Development of Bioactive Soft Tissue Scaffold Systems

Elizabeth Anne Boughton

A thesis submitted in partial fulfilment

of the requirements for the degree of

Doctorate of Philosophy (Biomedical Engineering)



THE UNIVERSITY OF SYDNEY

The School of Aerospace, Mechanical & Mechatronic Engineering,
The Faculty of Engineering and Information Technology
The University of Sydney, Australia

March 2011

STATEMENT OF ORIGINAL WORK

I hereby declare that the following outlines my work contained in this thesis. All discussions and conclusions are my own, although influenced by my supervisor's opinions and by advice from experts in their respective fields.

- I carried out the literature review
- I synthesized and characterized the ceramic osteochondral scaffolds, with some assistance from Chengtie Wu.
- I performed the chondrocyte extraction, isolation, culture, drug treatment and RT-PCR analysis, with initial supervision by Margaret Smith.
- I synthesized and characterized the variotis™ scaffolds.
- I synthesized the bioactive glasses, with assistance from Philip Boughton and Andrew Ruys for the melting process.
- I designed and carried out all in vitro experiments for the variotis scaffold and bioactive glasses, with some assistance with experimental design from Susan McLennan.
- I performed all the histology and data analysis for the in vivo study. Surgical procedures were performed by Susan McLennan and Jim.

ABSTRACT

There is a need for development of versatile soft tissue scaffolds which can interface with tissue junctions and a range of tissue architectures. Two approaches were developed. A bone capable ceramic scaffold was infused with gel and polymer components to suit cartilage resurfacing. Several biphasic prototypes were successfully developed and evaluated mechanically and biologically. Whilst they supported chondrocyte culture within the infused gel layer they lacked sufficient mechanical stability. Two therapeutic agents were investigated for potential roles in modulating cartilage degradation. Gene expression (RT-PCR) measurements demonstrated that whilst zoledronic acid reduced cartilage degradation, S100A9 increased ECM breakdown.

In a subsequent more substantive approach, a versatile polymer composite scaffold (variotis™) was designed and synthesised using a novel, high-throughput batch coagulation method. Methods were developed for formation of scaffolds with a range of shapes and properties. This novel scaffold could be readily post formed to impart graded interconnected porosity and mechanical response. Characterisation was undertaken for physical structure and mechanical behavior. The soft, elastic scaffolds were highly porous with excellent void interconnectivity and tensile properties within the range of skin.

A range of novel bioactive glass compositions were developed for incorporation with the scaffolds. Glasses were analysed compositionally, mechanically, for bioactivity and radiopacity. During in vitro studies, composites with bioactive glass and bulk metallic glass constituents were shown to support fibroblast cell culture and exhibited less inflammation than stainless steel and cell controls. negligible inflammation. In vivo subcutaneous implantation of 124 polymer and polymer-composite variotis™ scaffolds into rats demonstrated complete tissue filling by 14 days. Histological staining confirmed high proportions of mature collagen content and vascularization within the polymer-Bioglass® composite scaffolds. Low inflammatory levels were confirmed by circulating and wound fluid cell counts.

ACKNOWLEDGEMENTS

I would like to acknowledge all those who have played a part in bringing this project together. A special thanks goes to my supervisors, Susan McLennan and Andrew Ruys, for their encouragement, advice and the opportunities they have provided me. I have learnt so much during the past 4 years and am sure that the skills I have acquired have taught me how to learn, to persevere, design and carry out experiments, and have improved my skills in writing and delivering presentations. I am also grateful for the opportunity to work with and share friendship with others in the various labs I have been involved with. In particular, Alex Baume, Peter Lok, Lily Wong and Melanie Lim have been core to the development Biometic; the company which has begun from this work. Thankyou Mel for your superb job of drafting the patents. Thanks Alex and Peter for your tireless effort towards the research and supporting the other students. And for always being able to make me laugh or to have an opportunity to brainstorm about the latest ideas and inventions.

Thankyou to those who have given generously of their time to provide opportunities of training- particularly Jane Radford from Histology and Ian Kaplin, Alan Jones and the other staff at the Australian Centre for Microscopy and Microanalysis. Also thanks to Jim Bonner who helped with the animal study.

Thankyou to my biggest supporter- my husband Phil. I am so grateful for your constant support and friendship. It hasn't been easy going through the past 11 years of our combined PhDs, but- we've done it now! I very much look forward to spending the rest of my life enjoying my life with you. I am very grateful for the love shown by my family, in-law family and other friends. They have provided a sense of normality when my entire existence has been caught up in this thesis. I hope I have been able to make you proud and can now spend more time with you. My gratitude goes to everyone who has helped with the proof reading, references, and making me cups of teas!

This list wouldn't be complete without acknowledging God- the great designer. I am grateful to have had the oppoprtunity to immerse myself in understanding more about how wonderfully he has made us. I look forward to following his leading for my future, wherever that might be.

TABLE OF CONTENTS

Title Page *i*

Statement of Contribution *ii*

Abstract *iii*

Acknowledgements *iv*

Table of Contents *v*

Index of Figures *xx*

Index of Tables *xxxvii*

CHAPTER 1. INTRODUCTION & DESIGN CONCEPTUALISATION *1*

1.0. Chapter Overview *1*

1.1. Tissue Engineering Scaffolds *2*

1.1.1. A Regenerative Approach to Tissue Healing 3

1.1.1.1. Key Functions of a Tissue Scaffold 3

1.1.1.2. Hierarchical Device Design 4

1.1.1.3. Components of a Tissue Engineered Device 6

1.2. Problems with Alternative Tissue Replacement Options *6*

1.2.1. Limitations of Natural Grafts 6

1.2.2. Limitations of Conventional Implants 7

1.2.2.1. Adverse Implant-Tissue Interfaces 8

1.2.2.2. Inflammation 8

1.2.2.3. Stress Shielding of Implants 9

1.2.2.4. Tissue Integration 11

1.2.3. Clinical Experiences of Meshs/Scaffolds 11

1.2.4. Limitations of Current Tissue Scaffolds 11

1.2.4.1. Fibrovascular Tissue Infiltration into Scaffolds 12

1.2.4.2. Inflammation and Fibrous Encapsulation of Scaffolds 13

1.3. Commercialisation of Scaffold-based Devices ***13***

1.3.1. Tissue Scaffold Design Inputs 14

1.3.2. Limitations of Naturally Derived Materials 15

1.3.3. Biodegradable Materials 16

1.3.3.1. Case study: Dura Mater Substitutes 17

1.4. Bioactive Scaffolds ***18***

1.4.1. Bioactive, Bioresorbable Bioceramics 18

1.4.1.1. Calcium Phosphates 19

1.4.1.2. Calcium Silicates 19

1.4.1.3. Bioactive Glasses 19

1.4.2. Bioactive Polymer-Composites 22

1.4.2.1 PLA & PGA Based Polyesters 26

1.4.2.2. Poly-e-caprolactone 28

1.5. Native Tissue Architecture and Function ***31***

1.5.1. Cartilage Anatomy, Pathology and Physiology 31

1.5.1.1. Anatomy and Physiology of Cartilage 31

1.5.1.2. Cartilage Pathology 33

1.5.2. Skin Anatomy, Physiology and Pathology 34

1.5.2.1. Anatomy and Physiology of Skin 34

1.5.2.2. Skin Pathology 35

1.5.2.3. Skin Ulceration 36

1.5.3. Mechanical Properties of Native Tissue 36

1.6. Scaffold Structure and Factor Delivery ***37***

1.6.1. Vascularisation of Scaffolds 37

1.6.2. Scaffold Form 38

1.6.3. Degradation Rate 41

1.6.4. Surface Energy (Hydrophilicity/hydrophobicity) 42

1.6.5. Pre-Seeding of Scaffolds with Cells 43

1.6.6. Delivery of Therapeutic Agents from Scaffolds 44

1.6.6.1. Antibiotic Delivery 46

1.6.6.2. Tissue-Inducing and Angiogenic Growth Factors 46

1.6.6.3. Anti-Inflammatory Drugs and Bisphosphonates 48

1.6.6.4. Delivery of Organic and Inorganic Ions 48

1.6.7. Bioactive Soft Tissue Scaffold System Design 49

CHAPTER 2. CALCIUM SILICATE-BASED OSTEOCHONDRAL BED SCAFFOLD ***52***

2.0. Chapter Overview ***52***

2.1. Introduction ***53***

2.1.1. Approaches to Cartilage Repair 53

2.1.2. Osteochondral Tissue Engineering Constructs 54

2.1.2.1. Design Considerations for Osteochondral Scaffolds 55

2.1.2.2. Review of Osteochondral Constructs 55

2.1.3. Calcium Silicate-based Scaffolds for Bone Engineering 59

2.1.4. Hydrogels for Cartilage Engineering 60

2.1.5. Incorporation of Therapeutic Agents into Scaffold 61

2.1.5.1. Bisphosphonates 62

2.1.5.2. S100 Proteins 64

2.1.6. Characterisation Techniques 65

2.1.6.1. Gene Expression of Cartilage Modelling Markers 65

2.1.6.2. Micro Computer Tomography (MicroCT) 67

2.2. Design & Synthesis of Biphasic Ceramic/Hydrogel Scaffolds ***68***

2.2.1. Osteochondral Bed Construct Concept 68

2.2.2. Synthesis of Scaffold Precursor Powders 69

2.2.2.1. Synthesis of Wollastonite ($CaSiO_3$, WT) Powders 69

2.2.2.2. Synthesis of Sphene ($CaTiSiO_5$) Powders 69

2.2.3. Formation of Microspheres and Porous scaffolds 70

2.2.3.1. Synthesis of Bioceramic/Alginate Composite Microspheres 70
2.2.3.2. Synthesis of Porous Ceramic Scaffolds 70
2.2.3.3. Synthesis of Biphasic Bioceramic/PDLLA Scaffolds 71
2.2.3.4. Synthesis of Biphasic Bioceramic/Alginate Scaffolds 71
2.3. Physical Characterisation of Scaffolds ***72***
2.3.1. Methods 72
2.3.1.1. Scaffold Morphology 72
2.3.1.2. Mechanical Testing 72
2.3.2. Results 73
2.3.2.1. Scaffold Morphology 73
2.3.2.2. Mechanical Characterisation 75
2.3.3. Discussion 76
2.3.3.1. Osteochondral Bed Model 76
2.3.3.2. Synthesis Process 76
2.3.3.3. Scaffold Morphology 77
2.3.3.4. Gel Infusion 77
2.3.3.5. Comparison of Scaffold Morphology with Other Scaffolds 77
2.3.3.6. Mechanical Properties 77
2.3.3.7. Comparison of Mechanical Properties with Literature 78
2.4. Ovine Chondrocyte Seeded Biphasic Scaffolds ***79***
2.4.1. Methods 79
2.4.1.1. Isolation of Chondrocytes from Ovine Joints 79
2.4.1.2. Seeding of Chondrocytes onto Biphasic Ceramic/Alginate Scaffolds 80
2.4.1.3. Seeding of Chondrocytes onto Biphasic Ceramic/Gelatin Scaffolds 81
2.4.1.4. Scanning Electron Microscopy 82
2.4.2. Results 83
2.4.2.1. Morphology of Chondrocytes on Biphasic Ceramic/Hydrogel Scaffolds 83
2.4.3. Discussion 85

2.5. Effect of Zoledronic Acid on Chondrocytes 86

2.5.1. Methods 86

2.5.1.1. Cell Culture and ZA Treatment 86

2.5.1.2. Gene Expression using Real Time Polymerase Chain Reaction 86

2.5.2. Results 88

2.5.3. Discussion 90

2.6. Effect of S100 Proteins on Chondrocytes 91

2.6.1. Methods 91

2.6.1.1. Cell Culture and S100 Protein Treatment 91

2.6.1.2. Gene Expression using Real Time Polymerase Chain Reaction 91

2.6.2. Results 92

2.6.3. Discussion 96

2.7. Conclusion 97

CHAPTER 3. VARIOTIS DESIGN, SYNTHESIS & CHARACTERISATION 98

3.0. Chapter Overview 98

3.1. Introduction 99

3.1.1. Development of a Versatile, Soft Tissue Scaffold 99

3.1.1.1. Scaffold-Based Skin Graft for Chronic Wounds 99

3.1.1.2. Tissue Mechanostimulation via Elastic Scaffolds 100

3.1.2. Cutaneous Wound Healing 101

3.1.2.1. Acute vs Chronic Wounds 101

3.1.2.2. Phases of Acute Wound Healing 102

3.1.3. Development of Chronic Wounds 105

3.1.3.1. Bacterial Colonisation 106

3.1.3.2. Microbial Biofilms 106

3.1.4. Management of Chronic Ulcers 107

3.1.4.1. Principles Promoting Wound Healing 107

3.1.4.2. Wound Dressings 111
3.1.5. Skin Grafts 114
3.1.5.1. Native Skin Grafts 114
3.1.5.2. Engineered Skin Grafts 115
3.1.5.3. Gene Therapy and Stem Cell Delivery for Cutaneous Wound Healing 118
3.1.6. Bioresorbable, Bioactive Scaffold Fabrication Methods 120
3.1.6.1. Review of Synthesis Processes for Polymer Scaffolds 120
3.1.6.2. Limitations of Processing Techniques 124
3.1.6.3. Approaches for Bioactive Glass Incorporation into Scaffolds 126
3.1.6.4. Effect of Bioactive Glass Incorporation on Physical Properties of Scaffolds 130
3.1.7. Modular and Functionally Graded Scaffolds 131
3.1.8. Scaffold Sterilisation and Commercial Considerations 133
3.1.8.1. Gamma Irradiation 135
3.1.8.2. Ethylene Oxide 135
3.1.8.3 Effect of Sterilisation on the Properties of Polymers 135
3.1.8.4. Effect of Sterilisation on Properties of Glass 138
3.1.8.5. Shelf Life and Packaging 138
3.1.9. Mechanical Verification 139
3.2. Variotis™ Design, Synthesis and Physical Characterisation ***142***
3.2.1. Design Considerations 142
3.2.1.1. Materials Selection 142
3.2.1.2. Novel Batch Coagulation Synthesis Process 143
3.2.2. Methods 144
3.2.2.1. PCL Scaffold Synthesis via Coagulation 144
3.2.2.2. Synthesis of Composite Scaffolds via Glass Filling 147
3.2.2.3. Synthesis of Composite Scaffolds via Glass Coating 147
3.2.2.4. Consistency of Scaffold Batches 148
3.2.2.5. Manual Calculation of Porosity 148

3.2.2.6. Scaffold Morphology and Pore size using Optical Microscopy and SEM 149
3.2.2.7. 3D Scaffold Reconstruction using MicroCT 149
3.2.2.8. Calculation of Pore Size, Porosity and Interconnectivity using MicroCT 150
3.2.3. Results 151
3.2.3.1. Analysis of Scaffold Batch Consistency 152
3.2.3.2. Scaffold Porosity (Manual Calculation) 154
3.2.3.3. Scaffold Morphology and Pore Size using Optical Microscopy and SEM 154
3.2.3.4. Examination of Scaffold Morphology using MicroCT 160
3.2.3.5. Porosity, Pore size and Interconnectivity Calculations using MicroCT 162
3.2.3.6. Interconnectivity Path Calculations 166
3.2.4. Discussion 168
3.2.4.1. Scaffold and Synthesis Process Design 168
3.2.4.2. Scaffold Synthesis 168
3.2.4.3. Macrostructural Characterisation 169
3.2.4.4. Comparison with Literature 171
3.3. Post-Synthesis Modulation of Scaffold Geometry ***173***
3.3.1. Methods 173
3.3.1.1. Scaffold Fusion 173
3.3.1.2. Scaffold Compression 173
3.2.1.3. Addition of a Thin Film 173
3.3.1.4. Formation of variotis™ Sheet 174
3.3.1.5. Synthesis of Tubular Scaffolds 174
3.3.1.6. Functionally Graded Scaffold 174
3.4.2. Results 176
3.3.3. Discussion 180
3.4. Synthesis of Porogen Network Templates ***181***
3.4.1. Methods 181
3.4.1.1. Formation of Cylindrical Templates (method A) 181
3.4.1.2. Formation of Sheet Templates (method B) 181

3.4.1.3. Effect of Pressure on Template Synthesis (method C) 181
3.4.1.4. Template Formation using Small Porogens (method D) 182
3.4.1.5. Formation of Precursors with a Bimodal Porogen Distribution (method E) 182
3.4.1.6. Effect of Water Content and Pressure on Template Formation with Bimodal Porogen Distribution (method F) 182
3.4.2. Results 183
3.4.3. Discussion 186
3.5. Methods for Scaffold Sterilisation ***187***
3.5.1. Ethylene Oxide 187
3.5.2. Gamma Irradiation 187
3.5.3. Ultra-Violet Radiation 187
3.6. Mechanical Verification ***189***
3.6.1. Methods 189
3.6.1.1. Tensile Testing 189
3.6.1.2. Compressive Testing 191
3.6.2. Results 191
3.6.2.1 Effect of Strain Rate and Test Conditions on Tensile Properties 191
3.6.2.2. Effect of Glass Filler on Mechanical Properties 193
3.6.2.3. Effect of Glass Coating on Mechanical Properties 194
3.6.2.4. Methods to Enhance Variotis' Stiffness 196
3.6.2.5. Effect of Sterilisation on Mechanical Properties 198
3.6.2.6. Extension Ratio Comparison 201
3.6.3. Discussion 201
3.6.3.1. Influence of Test Conditions during Tensile Tests 201
3.6.3.2 Variotis™ has a High Capacity for Tensile Strain 202
3.6.3.3. Variotis™ has a High Capacity to Return to its Original Shape and Resists Tearing 203
3.6.3.4. Comparison of Tensile Properties to Literature 203

3.6.3.5. Effect of Glass Filler or Coating on Tensile Properties 204
3.6.3.6. Effect of Sterilisation on Tensile Properties 204
3.6.3.7. Comparison of Compressive Properties to Literature 206
3.6.4. Skin Ulcer Clinical Concept 208
3.6.5. Osteochondral Treatment Clinical Concept 210
3.6.5.1. Surgical Procedure 210
3.6.5.2. Pin Description 211
3.6.5.3. Scaffold Description 211

CHAPTER 4. BIOACTIVE COMPONENTS 215

4.0. Chapter Overview 215

4.1. Introduction 216

4.1.1. Bioactive Scaffolds 216
4.1.2. Bioactive Glasses 217
4.1.2.1. Biological Activity of Bioactive Glasses 217
4.1.2.2. Bonding Mechanisms of Bioactive Glasses 218
4.1.2.3. Effect of Bioactive Glass on Cell Behaviour 220
4.1.2.4. Variation in Bioactive Glass Composition 222
4.1.3. Bulk Metallic Glasses 223
4.1.4. Carbohydrates 225

4.2. Synthesis of Bioactive Glass 231

4.2.1. Precursor Powder Preparation 232
4.2.2. Precursor Powder Mixing 233
4.2.3. Powder Compression 234
4.2.3.1. 15mm Die Compression Method 234
4.2.3.2. 75mm Die Compression Method 234
4.2.4. Glass Formation 235
4.2.5. Glass Processing 238

4.3. Characterisation of Glass Particle Size Distribution 241

4.3.1. Methods 241

4.3.1.1. Digital Particle Size Distribution 241

4.3.2. Results 242

4.3.2.1. Particle Distribution for 45S5 Powder 242

4.3.2.2. Particle Distribution for 1393 Short Fibers 243

4.3.3. Discussion 244

4.4. Characterisation of Glass Composition ***244***

4.4.1. Methods 244

4.4.1.1. Scanning Electron Microscopy (SEM) and Energy Dispersive X-Ray Spectroscopy (EDS) 244

4.4.1.2. X-Ray Fluoroscopy 245

4.4.2 Results 245

4.4.2.1. Efficacy of Precursor Mixing 245

4.4.3. Discussion 253

4.5. Nanoindentation ***255***

4.5.1. Methods 256

4.5.2. Results 258

4.5.3. Discussion 261

4.6. Bioactivity and Dissolution ***262***

4.6.1. Methods 262

4.6.2. Results 263

4.6.3. Discussion 270

4.7. Measurement of Glass Radiopacity ***272***

4.7.1. Methods 272

4.7.2. Results 273

4.7.2.1. Radiopacity of Ba-doped Glasses 273

4.7.3. Discussion 274

4.8. Methods for Mounting Glass Powders onto Scaffold Disks ***275***

4.8.1. Methods 275

4.8.1.1. Method A. Synthesis of Glass-Coated Compact Scaffold Disks via Direct Heating 275
4.8.1.2. Method B. Synthesis of Glass-Coated Scaffold Disks via Warm Water 276
4.8.1.3. Method C. Synthesis of Glass-Coated Bulk PCL Disks 277
4.8.2. Results 278
4.8.3. Discussion
4.9. Honey-Coated variotis™ Scaffolds ***280***
4.9.1. Methods 280
4.9.1.1. Scaffold Honey Infusion Method 280
4.9.1.2. Honey Infiltrated Scaffold Method 280
4.9.2. Results 281
4.9.3. Discussion 281
4.10. Conclusion ***282***
CHAPTER 5. IN VITRO TESTING *283*
5.0. Chapter Overview ***283***
5.1. Introduction ***284***
5.1.1. Device Biocompatibility and Efficacy 284
5.1.2. Techniques for In Vitro Culture in Scaffolds 285
5.1.2.1. Cell Seeding 286
5.1.2.2. Cell Culture 286
5.1.2.3. Characterisation Techniques 286
5.1.2.4. Non-Destructive Cell Characterisation Techniques 287
5.1.3. Challenges Posed by Scaffold Systems 288
5.1.4. Previous In Vitro Studies on PCL/BG Composites 289
5.1.4.1. Studies with Hard Tissue Cells 289
5.1.4.2. Studies with Soft Tissue Cells 290
5.1.5. Previous *in vitro* studies on Bioactive Glasses 291
5.1.6. Detection of Wound Modelling Biomarkers 294

5.2. In Vitro Testing of Fibroblasts on Composite Scaffolds ***296***

5.2.1. Methods 296

5.2.1.1. Specimen Preparation and Cell Seeding 296

5.2.1.2. Optical and Fluorescent Microscopy Examination 297

5.2.1.3. Scanning Electron Microscopy (SEM) Examination 297

5.2.1.4. Measurement of Cellular Metalloproteinase Activity 297

5.2.1.5. Examination of Cells on Scaffold using MicroCT 297

5.2.2. Results 298

5.2.2.1. Examination of Cell Attachment and Morphology on 3D Scaffolds 298

5.2.2.2. Examination of the Effect of the Scaffolds on In Vitro Inflammatory Response 314

5.2.2.3. Examination of Cells in Scaffold using MicroCT 315

5.2.3. Discussion 316

5.2.3.1. In vitro Cell Culture on variotis™ Scaffolds 316

5.2.3.2. Visualisation of Cells on Scaffolds 316

5.2.3.3. Cell Morphology via SEM 316

5.2.3.4. Precipitate Formation on Scaffolds 317

5.2.3.5. Scaffold Micropores 317

5.2.3.6. Comparison with Literature 317

5.2.3.7. Investigation of MMP Levels 318

5.3. Investigation of Cell Number Measurement Techniques ***319***

5.3.1. Methods 319

5.3.1.1. MTS Assay 319

5.3.1.2. Fluorescence Measurement 319

5.3.2. Results 320

5.3.2.1. MTS assay 320

5.3.2.2. Fluorescence Readings 322

5.3.3. Discussion 324

5.4. In Vitro Testing of Fibroblasts on Bioactive Glasses ***325***

5.4.1. Methods 325
5.4.1.1. Specimen Preparation and Cell Seeding 325
5.4.1.2. Fluorescent Microscopy Examination 325
5.4.1.3. Measurement of Cell Spreading 325
5.4.1.4. Measurement of Cellular Metalloproteinase Activity 326
5.4.1.5. Protein Measurement 326
5.4.2. Results 326
5.4.2.1. Cell Attachment, Morphology and Spreading on Bioactive Glass Powders 326
5.4.2.2. Measurement of Protein Concentration 334
5.4.2.3. Examination of the Effect of the Glasses on MMPs 336
5.4.3. Discussion 339
5.4.3.1. Cell Spreading and Morphology on Glass Powders 339
5.4.3.2. Methods for Quantitating Cell Number 339
5.4.3.3. MMP Levels 340
5.4.3.4. Comparison with Previous Studies 340
5.5. In Vitro Biocompatibility Testing of Mg-Based and Ca-Based Bulk Metallic Glasses 342
5.5.1. Methods 342
5.5.1.1. Specimen Preparation and Cell Seeding 342
5.5.1.2. Examination of Disks using Light Microscopy 343
5.5.1.3. Measurement of Weight Loss 343
5.5.1.4. Scanning Electron Microscopy and Energy Dispersive X-Ray Spectroscopy 343
5.5.1.5. Total Protein Quantification 344
5.5.1.6. Measurement of Cellular Metalloproteinase Activity 344
5.5.1.7. Fluorescent Microscopy 344
5.5.2. Results 345
5.5.2.1. Particle Size Distribution 345
5.5.2.2. Chemical and Physical Changes in the Materials 346
5.5.2.3. Cellular Activity 348

5.5.3. Discussion 353

5.5.3.1. Findings of this BMG study 353

5.5.3.2. MMP Levels 354

5.5.3.3. Comparison with previous studies 354

5.6. Conclusion ***355***

CHAPTER 6. IN VIVO BIOCOMPATIBILITY STUDY *356*

6.0. Chapter Overview ***356***

6.1. Introduction ***357***

6.1.1. Animal Models 357

6.1.2. Tissue Ingrowth and Vascularisation of Scaffolds 357

6.1.3. In Vivo Scaffold Review 358

6.1.3.1. Hydrogels 358

6.1.3.2. Woven Meshes 363

6.1.3.3. Sintered Scaffolds 365

6.1.3.4. Rapid Prototyped Scaffolds 366

6.1.3.5. Freeze Drying/Porogen Techniques 369

6.1.4. Review of In Vivo Bioactive Glass Studies 374

6.1.4.1. In vivo Effect of Bioactive Glass on Tissue Ingrowth and Vascularisation 374

6.1.4.2. Effect of Bioactive Glass on *In vivo* Inflammation 375

6.1.5. Blood Vessel Counts 376

6.1.6. Inflammatory Cell Analysis 377

6.2. Methods ***378***

6.2.1. Synthesis of Bioactive Glass Powders and Scaffolds 378

6.2.2. Animal Study 378

6.2.2.1. Examination of Tissue Ingrowth into the Scaffold 379

6.2.2.2. Histological Examination 379

6.2.2.3. Immunohistochemical Examination 379

6.2.2.4. Scanning Electron Microscopic (SEM) Examination 380

6.2.2.5. Stereoscopic Microscopy Examination 380
6.2.3. Examination of the Effect of the Scaffold on Inflammatory Response 381
6.2.3.1. Measurement of Circulating Inflammatory Cell Number 382
6.2.3.2. Measurement of Cell Types in Scaffolds 381
6.2.3.3. Measurement of Wound Fluid Matrix Metalloproteinase Activity 381
6.2.3.4. Statistical Analysis 381
6.3. Results ***382***
6.3.1. Examination of Tissue Ingrowth into the Excised Scaffolds 382
6.3.2. Blood Vessel Ingress into the Scaffolds 395
6.3.3. Examination of the Effect of the Scaffold on Inflammatory Response 401
6.4. Discussion ***405***
6.4.1. Rapid and Complete Fibrovascular Tissue Ingrowth Inside Scaffold 405
6.4.2. Vessel Formation Inside Scaffolds 406
6.4.3. Inflammatory Response and Scaffold Bioresorption 407
6.4.4. Possible Adipose Tissue within Scaffold 408
6.4.5. Comparison with Literature- Tissue Infiltration and Vascularisation 408
6.5. Conclusion ***411***
CHAPTER 7. CONCLUSION ***412***
REFERENCES ***413***
APPENDIX ***455***

INDEX OF FIGURES

Figure 1.1. Thesis structure schema. 2

Figure 1.2. (a) The key functions of a scaffold are analogous to those of a house, (b) Cell-based and acellular tissue engineered constructs [23]. 5

Figure 1.3. A fibrous capsule forms around many conventional implants [32]. 8

Figure 1.4. Stress shielding in the femoral component of a cemented hip implant. The arrow indicates the resultant bone loss. [38] 9

Figure 1.5. Variation of relative strengths of osteotomy and fracture union with time [44]. 10

Figure 1.6. Incomplete tissue infiltration into a PDLA scaffold after 6 weeks in vivo [85]. 12

Figure 1.7. The Valley of Death. For tissue engineering, the Valley of Death is the gap and associated funding difficulties of taking tissue engineering technologies to tissue-engineered products 13

Figure 1.8. Tissue scaffold design inputs. 14

Figure 1.9. (a) Synthetically formed tropoelastin (E) [94] (b, c) Porous elastin hydrogels fabricated using CO2 gas and cross-linked via gluteraldehyde [95]. 15

Figure 1.10. (a) PCL/TCP scaffold, (b) PCL/collagen nanofibers, (c) PCL foam (d) PLGA woven textile mesh. Arrows: scaffold material [100]. 16

Figure 1.11. Preoperative computerised tomography scan demonstrating a calcified mass surrounding propylene Marlex mesh (arrow) [85]. 17

Figure 1.12. SEMs showing: (a) a cross section of a graded glass coating after a 6 month in vivo test in the pig model [134] (b) Hydroxyapatite crystals precipitated on a 6P57 bioactive glass coating on titanium alloy, after 30 days soaking in SBF [137]. 20

Figure 1.13. Filling of a dental socket with bioactive glass [36] 21

Figure 1.14. Photographs of sectioned full thickness skin demonstrating (a) No adhesion to uncoated silicone tubing (arrows) and (b) good adhesion to bioactive glass-coated silicone. (c) Scanning electron micrograph of the bioactive glass (BG) coated silicone tubing (S) [53]. 21

Figure 1.15. (a) 13-93 bioactive glass adherent spheres on a 70:30 P(L/(D/L)LA plate [160]. (b) Formation of an apatite layer on the polymer plate surface adjacent the microspheres after 3 days in PBS. 22

Figure 1.16. PLA particles from a biodegradable bone screw found in an osteolytic lesion 52 months after implantation [27]. 26

Figure 1.17. Comparison of degradation of PLLA and Biocryl Rapide (PLGA/TCP) devices in bone [238]. 28

Figure 1.18. Osteopore PCL mesh products: (a,b) Skull burrplug (c) Osteomesh orbital implant [251], (d) PCL-coated braided PGA suture Surucryl [254]. 29

Figure 1.19. Representative stress-strain curves from PLGA and PGCL scaffolds. Inset: PGCL scaffold morphology [262]. 30

Figure 1.20. Schematic diagram of the different zones of hyaline articular cartilage [263]. 31

Figure 1.21. Characteristics of a normal knee joint compared to joint degeneration due to osteoarthritis [271]. 33

Figure 1.22. The complex structure of skin [278]. 34

Figure 1.23. Classification of burns according to depth of tissue necrosis [279]. 35

Figure 1.24. The appearance and structure of a chronic skin ulcer [285]. 36

Figure 1.25. Angiogenesis is a process of capillary sprouting [335]. 37

Figure 1.26. Modelling of fluid flow through a bioactive glass scaffold (ref Fig. 1.24a). The pore throats are visible in red [322]. 41

Figure 1.27. Schematic of the interaction between water molecules and surfaces showing (a) Hydrophilic surface and (b) Hydrophobic surface [20] . 42

Figure 1.28. Scaffold seeded with cells [379]. 43

Figure 1.29. (a) Drug release from a biodegradable particle [357]. (b) In vitro accumulative release of Dexamethazone from PLGA/mesoporous bioactive glass (MBG) films with different proportions of glass [116]. 45

Figure 1.30. bFGF delivery increased the number and extent of capillaries formed inside porous PVA implants, which were subcutaneously implanted in mice [84]. 47

Figure 1.31.Design inputs and corresponding chapters where design verification and validation work is covered. 50

Figure 2.1 Autologous chondrocyte implantation [384]. 53

Figure 2.2. (a) PCL osteochondral scaffold [385] (b) Triphasic scaffold for tendon-bone interface. Histological images show tissue growth into the three regions of the scaffold after 4 weeks of implantation [410]. 58

Figure 2.3. Bioactive glass scaffolds formed using (a) Gas foaming [5], (b) Polymer sponge template [411]. 59

Figure 2.4. The chemical structure of Zometa [432]. 62

Figure 2.5. (a) Pooled Severity Index showing ZA attenuates arthritis, and evidence suggesting ZA treatment time does not alter arthritic outcome (b) Paw volume, (c) Radiology and (d) Histology. *Denotes significant difference from controls (saline), *p< 0.05 [436] 63

Figure 2.6. S100A8 immunolocalisation in rat articular cartilage (arrows). Animals treated with: a) Saline, b) Zometa 3 mg/kg and c) Zometa 10 mg/kg [441]. 64

Figure 2.7. Stages of the PCR reaction. 65

Figure 2.8. An example melt curve indicating a single product. 66

Fig. 2.9. Schematic diagram of an osteochondral defect and the osteochondral bed construct. 68

Fig. 2.10. Schematic diagram of the microsphere synthesis procedure. 70

Figure 2.11. Porous sphene scaffolds. 70

Figure 2.12. Schematic of synthesis process for bioceramic/alginate scaffolds 71

Fig. 2.13. Compression testing of bioceramic scaffolds. 72

Figure 2.14. SEMs of (a) WT scaffold (b) WTPL scaffold. WTPL scaffold viewed using (c) MicroCT 3D reconstruction (d) a single MicroCT cross-sectional slice. 73

Figure 2.15. SEM micrographs of mesoporous surface of the WTPL scaffold. 74

Figure 2.16. Alginate-infused sphene scaffolds. 74

Figure 2.17. Photographs of (a) WT and (b) WTPL scaffolds after compression testing. 75

Figure 2.18. Compressive properties for the wollastonite (WT) and wollastonite/PDLLA (WTPL) porous scaffolds. * indicates <0.05 significance 75

Figure 2.19. Protocol for synthesis of chondrocyte-seeded biphasic ceramic/alginate scaffolds. 81

Figure 2.20. Protocol for gelatine-seeded biphasic ceramic/alginate scaffolds. 82

Figure 2.21. Biphasic scaffolds after 4 weeks OACs culture: (a) sphene/alginate, (b) sphene/gelatine. 83

Figure 2.22. OACs cultured for 4 weeks on the sphene/alginate scaffold. 84

Figure 2.23. OACs cultured for 4 weeks on the sphene/gelatine scaffold. Arrows: cells which appear chondrocyte-like. 85

Figure 2.24. OACs cultured for 4 weeks on the WT/alginate scaffold. Arrows: chondrocytes. 85

Figure 2.25. OAC gene expression for GAPDH and ECM components after ZA treatment. 88

Figure 2.26. OAC gene expression for degradative proteases after ZA treatment. 89

Figure 2.27. OAC gene expression after S100 protein treatment (expt 1). 92

Figure 2.28. Gene expression for S100 protein treated chondrocytes (expt 2) 93

Figure 2.29. OAC Gene expression for GAPDH and ECM components after S100 protein treatment. 94

Figure 2.30. OAC gene expression for degradative proteases after S100 protein treatment (expt 3). 95

Figure 3.1. Repair of an acute wound versus an unhealing chronic wound [23]. 101

Figure 3.2. Phases of repair during wound healing [456]. 102

Figure 3.3. (a) Stages of bacterial infection [468] and (b) Number and types of bacterial isolates from patients with diabetic foot ulcers [469]. 106

Figure 3.4. (a) A schematic diagram and (b) scanning electron micrograph of a bacterial biofilm [470] 107

Figure 3.5. Treatment priorities as the wound progresses through various stages of healing (left to right) [471]. 108

Figure 3.6. (a) VAC GranuFoam [478], (b) Schematic diagram of NPWT [479], (c) Abdominal wound before and (d) after application of NPWT [478]. 110

Figure 3.7. Common wound dressings. 111

Figure 3.8. Healing of a large (28cm^2) diabetic ulcer which did not decrease in size with standard treatment, including negative wound pressure therapy. Following treatment with cryopreserved allogenic skin (TheraSkins), the wound closed in 19 weeks [505]. 114

Figure 3.9. A range of skin grafts. 115

Figure 3.10. The structure of Apligraf compared with human skin [522]. 117

Figure 3.11. The potential advantages of MSC-aided therapy for chronic wounds. 118

Figure 3.12. Stem cells have the ability to differentiate into a wide variety of cell types which are critical for wound healing [538]. 119

Figure 3.13. Schematic of (a) Interpenetrating network porogen (red), (b) Porogen and polymer (yellow) (c) Interpenetrating network polymer scaffold [221]. 125

Figure 3.14. (a) PDLLA foam (b) 40 wt% Bioglass®-filled PDLLA foam [196]. 127

Figure 3.15. Bioactive glass coated PDLLA foams synthesised via slurry dipping in ethanol [189]. 128

Figure 3.16. (a) Bioglass®-PDLLA coated Vicryl suture (b) Knotted Bioglass®-PDLLA coated Vicryl suture showing peeling of the coating (c) Vicryl coated with Bioglass®-PDLLA followed by a second PDLLA coating showed high structural stability [562]. 129

Figure 3.17. Changes in average molecular weights of P(CL/DL-LA) polymer (+) and 60 wt% S53P4 bioactive glass/P(CL/DL-LA) composite as a function of hydrolysis time [193] 130

Figure 3.18. Multi-phase scaffolds (a) two distinct phases (b) two distinct phases joined by a graded region (c) Step-wise gradient, (d) Seamless gradient. 132

Figure 3.19. Two cross-linking polyethylene molecules before and after radiation sterilisation. 136

Figure 3.20. Comparison of mechanical properties of PCL and PEO-PCL (70-30) before and after sterilisation with 25 kGy gamma irradiation. 137

Figure 3.21. Appearance of the polymers via Scanning Electron Microscopy before and after sterilization with 25 kGy gamma irradiation [608]. 137

Figure 3.22. Compressive properties for porous and dense polymers and ceramics. 139

Figure 3.23. The novel batch coagulation process used to synthesise variotis™ scaffolds. 143

Figure 3.24. (a) PCL pellets (b) PCL/acetone solution (c) variotis™ scaffold. 144

Figure 3.25. Steps in the original batch coagulation process. 145

Figure 3.26. Steps in the upscaled batch coagulation process. 146

Figure 3.27. 13-93 bioactive glass fibers. 147

Figure 3.28. (a) Skyscan 1172 MicroCT, (b) Specimen holder, (c) Reconstructed region (white cube) 149

Figure 3.29. A cross-sectional image of the scaffold, using MicroCT. 150

Figure 3.30. Steroscopic micrographs of a PCL scaffold. 151

Figure 3.31. Bioglass coated scaffolds 152

Figure 3.32. Scaffold weights for scaffolds made using the original process (a) Three PCL batches (b) PCL and 13-93-fiber filled scaffolds. 153

Figure 3.33. SEMs of (a) Macropores, (b) micropores and (c) surface texture on the PCL scaffolds. 154

Figure 3.34. SEMs of (a) 45S5 glass particle-coated scaffold (arrows: glass coating) (b) Cross-section of a 45S5 coated scaffold, showing the interconnected micropores through the struts. 155

Figure 3.35. High magnification SEMs of (a) PCL scaffold (b) 45S5 glass particle-coated scaffolds. (arrows: glass coating). 156

Figure 3.36. PCL & Bioglass scaffolds shown using negative microscopy (a-b) and reflective microscopy (c-h). (a) PCL, (b-d) PCL+20% 13-93-incorporated scaffold, (e-h) Glass powder coated scaffolds. The arrows indicate glass particles on the scaffold surface. 157

Figure 3.37. PCL scaffolds coated using milled E-glass powder. 158

Figure 3.38. PCL scaffolds coated with hollow borosilicate glass microparticles. 159

Figure 3.39. 3D MicroCT reconstruction of the variotis™ scaffold. 160

Figure 3.40. MicroCT images of a PCL scaffold: (a) Frame captures from video (b) Front view 161

(c) Cross-sectional view (d, e) Scaffold reconstructed with different grey thresholds. 161

Figure 3.41. Histogram of pore spacings and strut diameters measured using MicroCT for a single 2D slice. Insets: The cross-sectional regions of the scaffolds which were examined. 164

Figure 3.42 Histograms of strut diameters as measured using MicroCT, for regions selected from two adjacent slices. Insets: The cross-sectional regions of the scaffolds which were examined are the red highlighted regions 165

Figure 3.43. MicroCT sections for a range of different scaffolds for which the detour index was calculated. Indicated in 2D are the direct pathway (blue line) and shortest distance from a point to outer surface through interconnections (blue dotted line). These images have been inverted so the scaffold is seen in black and the empty pore space in white. 166

Figure 3.44. Detour indices calculated for the variotis™ scaffold and scaffolds reported in the literature [322, 323]. 167

Figure 3.45. Hierarchical structure of the scaffold and the corresponding biological features which could be accommodated: (a) Scaffolds used for the animal model (scale bar:5 mm), (b) MicroCT of a portion of the scaffold (scale bar:1 mm), (c) Optical microscopy of scaffold (Scale bar:500μM), SEM of the scaffold, showing: (d) Cross-sectioned scaffold showing pores and struts (e,f) Mesopores in the scaffold struts (Scale bar:100 μm) (g) Surface texture of the PCL scaffold (Scale bar: 10 μm) (h) Surface of the BG scaffold (Scale bar:10 μm) (i) Granules of BG (j) Powdered BG as used for the current study. 170

Figure 3.46. Longitudinal cross-sectional view of the apparatus used to form tubular scaffolds. 174

Figure 3.47. The method for the synthesis of FGM scaffolds. 174

Figure 3.48. (a) Shore Hardness Tester (b) Indentation Tip. 175

Figure 3.49. Hardness measurements of the scaffold were taken using an indentation methods 175

Figure 3.50. (a) Original scaffolds (b) Fusion of variotis™ scaffolds to form sheets (c) Teflon-coated steel plates for scaffold compression (c) Scaffolds before and after hot compression. 176

Figure 3.51. (a) Figure Fusion of a semi-permeable PCL membrane to the scaffold, (b) Precursor and scaffold formed using multiple sugar cubes. 177

Figure 3.52. Tubular scaffolds which were formed from variotis™ (scale bar: 1 cm). 178

Figure 3.53 (a) FGM scaffold viewed with optical microscopy. Hardness profiles of FGMs with (b) Shore Hardness Tester (c) ELF3400 Indentation technique. 179

Figure 3.54. Cylindrical sucrose templates with (a) d=11 and (b) d=16 mm. (c) Sheet template synthesised from sucrose granules. 183

Figure 3.55. Sucrose precursors synthesised using granulated sucrose and compressed with (a) zero, (b) low, (c) moderate and (d) high levels of compression. The delaminated scaffold shown in (d) as synthesised using 1.01% water (0.2mL water:19.58 g castor sugar) 184

Figure 3.56. A good quality cylindrical precursor formed using small porogens. 184

Figure 3.57. (a) Cylindrical precursors and (b) scaffold formed using 2 ranges of granule sizes (method E). (c,) Cylindrical templates formed using method F. 185

Figure 3.58. Sterilised scaffold samples. 187

Figure 3.59. Sterilised cylindrical scaffolds for cell culture plates. 188

Figure 3.60. Glasses sterilized using gamma irradiation. 188

Figure 3.61. (a) Specimen set-up for tensile tests (b) A stress-strain curve from a tensile test depicting regions from which mechanical properties were obtained. 190

Figure 3.62. A typical stress strain curve obtained from a compression test. 191

Figure 3.63. (a) A stress-strain curve of a typical PCL scaffold tested at a strain rate of 0.5 mm/s (b) A scaffold after tensile testing. 192

Figure 3.64. Effect of strain rate on tensile properties of the PCL variotis™ scaffold. 192

Figure 3.65. Comparison of the modulus and strength of variotis™ scaffolds under different environmental conditions. 193

Figure 3.66. Effect of 13-93 glass incorporation (5, 10, 15%) in the PCL matrix on the scaffold mechanical properties. 193

Figure 3.67. Tensile properties of PCL scaffolds after coating with 10% 45S5 powder. 194

Figure 3.68. The compressive stress-strain compression curve and associated moduli for the PCL and the BG powder-coated scaffolds. 195

Figure 3.69. Compression set values for the PCL and 10% BG powder coated scaffolds over 6 cycles. 196

Figure 3.70. Addition of a thin PCL film or coating with 20% bioactive glass fibers demonstrated the wide range of mechanical properties which the Variotis™ scaffold may demonstrate. 197

Figure 3.71. UTS and Linear Elastic Moduli calculated for Variotis™ scaffolds which had experienced sterilisation treatments. 198

Figure 3.72. Stress- Strain curve for sterilised scaffolds during compression tests. 199

Figure 3.73. Compression Moduli and densification points for sterilised PCL scaffolds. 200

Figure 3.74. Extension ratio for various scaffold conformations and sterilisation treatment. 201

Figure 3.75. Extension ratio of scaffolds (ref's provided in Table 3.8). RP: Rapid Prot., ES: Electrospun 202

Figure 3.76. Ultimate Tensile Strength vs modulus for a range of variotis™ scaffolds and other scaffolds from the literature (references listed in Table 3.8). 205

Figure 3.77. Comparison of compressive moduli with variotis™ and other scaffolds from the literature (references included in Table 3.9) 207

Figure 3.78. Procedure for delivery of the variotis™ scaffold to a skin wound. 209

Figure 3.79. A prototype scaffold mounted on a threaded bioresorbable pin, for osteochondral repair. 210

Figure 3.80. Schematic of the surgical delivery of an osteochondral repair pin. 212

Figure 4.1. Methods to impart bioactivity to a scaffold. 216

Figure 4.2. (a) Bioactive glass nanofibers made using laser spinning [634], (b) Bioactive glass scaffold [30], (c) Computer tompography image of blood vessel ingress into a bioactive glass scaffold [635], (d) Naturally-derived 'unbreakable' glass scaffold [636]. 217

Figure 4.3. SEM image of collagen fibres growing into cracks on the glass surface (G) at the tissue-implant interface at magnification ×100 [644]. 218

Figure 4.4. (a, b) Theraglass [647] (c, d) Immunostained transverse sections of tissue extracted from the lumen of a BG nerve conduit after 4wks implantation in rats. BG= previously occupied by a BG fiber, v=blood vessel, mf=minifascicle. Magnification: (c) x255, (d) x450 [643]. 219

Figure 4.5. (a) BMGs [679], (b) BMG foam [680]. Hydrogen bubbles evolving from (c) BMG and (d) Mg Metal [672]. (e) Crystalline vs Amorphous structure [681]. 224

Figure 4.6. (a) Sugar [690], (b) WoundCare™ Healing Powder [691] (c) Protein/sugar nanoparticles for drug delivery [692]. 225

Figure 4.7. Medical grade honeys. 227

Figure 4.8. (a) Propolis powder (b) Propolis is extracted from honeycomb (c) Propolis incorporation in toothpaste. 230

Figure 4.9. Flow diagram for glass synthesis. 231

Figure 4.10. Weighing of precursor powders. 232

Figure 4.11. (a) SPEX mill + its figure-of-eight motion, (b) Industrial scale mixer, (c) Comparison between the two batch sizes. 233

Figure 4.12. (a,b) The apparatus used for pressing the pellets, including the die and the press, (c) the completed pellets. 234

Figure 4.13. The various crucibles which were used. 235

Figure 4.14. Schematic showing the crucible synthesis procedure. 236

Figure 4.15. (a) Vertical tube furnace, (b) Molybdenum furnace, (c) Glass quenching, (d) The synthesised bioactive glass granules. 237

Figure 4.16 l to r: 13-93 bioactive glass fibers, crushing of the 13-93 fibers and 45S5 granules, sieving of the glass. 238

Figure 4.17. (a) The ball mill crushing process, (b) The ball mill which was designed & manufactured by our group. 238

Figure 4.18. Detection of 45S5 glass particles & 13-93 short fibers. 241

Figure 4.19. 45S5 powder (Ax1) crushed using the manual method. 242

Figure 4.20. Particle size distribution for length and area of 45S5 powder (Ax1). 242

Figure 4.21. 13-93 short fibers (Sx3) crushed using the manual method. 243

Figure 4.22. Particle size distribution for length and area of 13-93 particles (Sx3). 243

Figure 4.23. (a) Glass samples on conductive tape, (b) Carbon sputter coater, (c) Phillips XL30 SEM. 244

Figure 4.24. SEMs of the precursor powder after (a) 2min (PAx1) and (b) 8min mixing (PAx3). (c) EDAX spectrums after various periods of mixing (PAx1, PAx2, PAx3). 246

Figure 4.25. SEM and EDAX spectrums for 45S5 synthesised using a (a) small (Ax1) or (b) upscaled (Ax2) batch process. EDAX was performed on samples which had been crushed using the manual process. 248

Figure 4.26. (a) Manually milled 45S5 (Ax1), (b) 45S5 crushed using ball mill (Ax3). 250

Figure 4.27. EDAX analysis of the ball milled 45S5 glass (Ax3). 250

Figure 4.28. SEM image and EDAX spectrum of the 5%Fe45S5 (Fx1). 251

Figure 4.29. SEM image and EDAX spectrum of the 5%Zn45S5 (Nx3). 252

Figure 4.30. Hysitron triboindenter. 255

Figure 4.31. Appearance of some of the samples mounted for nanoindentation. Left to right: samples D, S, H, G. 256

Figure 4.32. Selection of the sample region and indentation points. 257

Figure 4.33. Force-displacement curve obtained using the Hysitron TI 900 Triboindenter. 258

Figure 4.34. Hardness results for experiment 1. 259

Figure 4.35. Dissolution curve of glasses after immersion in SBF. 263

Figure 4.36. SEM micrographs of the surface of a 45S5 particle (a) prior to immersion, and (b) 1 day (c,d) 7 days after immersion in in SBF at 37°C. (e) The corresponding EDAX spectrums. 264

Figure 4.37. (a,b) Spherical precipitates on 52S4.6 glass (Sx2) after 7 days SBF soaking, Arrow: rounded precipitates. (c) Corresponding EDAX spectrums. 266

Figure 4.38. 0.5mol%Ba4SS5 (a) prior to immersion and after (b-d) 7 days immersion in SBF at 37°, (e) EDAX analyses of the 0.5Ba45S5 glass sample after soaking in SBF. Arrows: precipitate formation. 267

Figure 4.39. 0.2%Zn45S5 glass after (a) 0 days (b, c) 1 day (d) 7 days.). 2%Zn45S5 glass after (a) 0 days (b) 1 day (c,d) 7 days soaking in SBF at 37 ° C. 5%Zn45S5 after (e) 1 day (f) 7 days sbf soaking. Arrows: Spherical precipitates. 269

Figure 4.40. Silicone/bioactive glass samples. 272

Figure 4.41. Calculation of pixel intensity using Phoretix 1D. 273

Figure 4.42. Measurements of radiopacity using fluoroscopy. 273

Figure 4.43. Synthesis of cylindrical shaped, glass coated scaffolds for cell culture wells (method A). 275

Figure 4.44. Synthesis of cylindrical shaped, glass coated scaffolds for cell culture wells (method B). 276

Figure 4.45. Synthesis of glass coated PCL cylinders for cell culture (Method C). 277

Figure 4.46. Fabrication of cylindrical shaped scaffolds using (a-c) method A, (d-f) method B and (g-i) dense PCL cylinders using method C. These images demonstrate coating with (c) Magnesium-rich BMG and (f, i) 45S5 bioactive glass. 278

Figure 4.47. Histogram of weights for the PCL disks and mounted glasses (average for each glass composition). 279

Figure 3.48. Manuka Honey UMF25+. 280

Figure. 3.49. The variotis™ scaffold with infiltrated and infused Manuka honey. Microscopy images are 200x magnification. 281

Figure 5.1. Osteoblastic cell proliferation after 4 days on (a) PCL, (b) Nanofibrous bioactive glass/PCL composite (c) Comparison of cell growth, as measured by MTS assay [147] 292

Figure 5.2. Scanning Electron Micrographs of MSCs proliferating on gelatin sponges incorporated with (a) 0, (b) 25%, (c) 75% TCP. Time course of MSC proliferation of gelatin sponges incorporating various levels of TCP by the (d) static or (e) stirring culture method. The TCP particles used in this study had an average diameter of 2.9μm [108]. 293

Figure 5.3. Cell proliferation assays on PDLLA scaffolds (a) Human osteosarcoma cell line (MG63) or (b) Human lung carcinoma cells (A549) cultured on PDLLA foams containing 0, 5 or 40wt% of 45S5 Bioglass® and compared with a plastic control surface [212]. 294

Figure 5.4. Scanning Electron Microscopy images of (a, c) Substrate surfaces (b, d) Osteoblasts on the surface after 7 days of culture. (a, b) PDLLA films (c, d) PDLLA/40% BG [208] 295

Figure 5.5. Nucleus pulposis cells on 45S5 bioactive glass. Some cells exhibited a rounded shape (R) and others had cytoplasmic processes (P) [202]. 295

Figure 5.6. The protocol for fibroblast seeding on variotis™ scaffolds. 298

Figure 5.7. Cellular growth on 3D 13-93 fibre coated BG/PCL scaffolds assessed using (a-c) optical and (d) fluorescent microscopy (DAPI). Images (c) and (d) show the same region. S: scaffold, G: glass, C: cells 300

Figure 5.8. Fibroblast proliferation on scaffold fragments using DAPI and Calcein fluorescent staining. 301

Figure 5.9. Histological sections of DAPI-stained fibroblasts cultured on PCL variotis™ scaffolds for 48hrs. C: cell, S: scaffold. 302

Figure 5.10. Scanning Electron Microscopy images of mouse fibroblasts on variotis™ scaffolds after culture for 14, 21 and 28 days. 303

Figure 5.11. SEMs of PCL scaffold after culture with fibroblasts for (a) 21 and (b) 28 days. 305

Figure 5.12. Images taken at the base of the PCL scaffold after 28 days of cell culture. 306

Figure 5.13. SEMs of PCL scaffold after culture with fibroblasts for 28 days. Arrow: cell reaching into a micropore. 307

Figure 5.14. SEMs showing spreading of fibroblasts over the 45S5/PCL scaffolds after 14 days. 307

Figure 5.15. SEMs showing spreading of fibroblasts over the 45S5/PCL scaffolds after 21 days. 308

Figure 5.16. Rounded precipitates were observed on the surface of the 45S5 glass and the polymer after in vitro culture for 28 days (red and white arrows, respectively). 309

Figure 5.17. Star-like morphology of cells on 45S5 BG/PCL scaffolds. S: Scaffold cross-section, showing microporosity. 310

Figure 5.18. A dehydrated cell observed stretching to a length of 200μm (45S5/PCL scaffold, 28days). Inset: cell philopodia attachment to glass particles. 311

Figure 5.19. SEM of fibroblast proliferation on the 1393/PCL scaffold (21 days). 312

Figure 5.20. Regions of (a) high and (b) low cell density on the 1393 Bioactive Glass coated PCL scaffold (21 days). 313

Figure 5.21. Highly magnified scanning electron micrographs of cells on 1393 BG/PCL scaffold (21 days). 314

Figure 5.22. Highly magnified scanning electron micrographs of cells on 1393 BG/PCL scaffold (21 days). Arrow: cell protrusions attaching to scaffold. 315

Figure 5.23. Gelatinase activity of mouse fibroblasts on composite variotis™ scaffolds, after 4, 7 and 14 days of culture. 316

Figure 5.24. (a) Fibroblasts stained with 1.25%phosphomolybdic acid, (b, c) MicroCT of media-filled scaffold with stained cells. 317

Figure 5.25. MTS readings for (a) Cells only (b) Cells remaining after scaffolds were moved (c) Scaffolds and attached cells. 323

Figure 5.26. Comparison of fluorescence measured for 1000 cells in ethanol, PBS and stained with DAPI. 324

Figure 5.27. Fluorescence for acellular and 5000 cell seeded PCL and BG/PCL scaffolds (in PBS). 324

Figure 5.28. Measurement of fluorescence after DAPI staining for a range of cell densities (in PBS). 325

Figure 5.29. Morphology of fibroblasts cultured on bioactive glasses for 24hrs for (a) 0.5%Ba45S5 and (b) 49S4.9 Bioactive Glass (Calcein, 40x). Arrows: cells tracking along glass edges or ridges. 329

Figure 5.30. Morphology of fibroblasts cultured on 52S4.6 bioactive glasses for 24hrs (Calcein, 40x). Arrow: Cells bridging between glass granules. 330

Figure 5.31. Morphology of fibroblasts cultured on 49S4.9 bioactive glasses for 24hrs (Calcein). Arrows: Cell accumulation in regions with collections of small glass particles 331

Figure 5.32. Morphology of fibroblasts cultured on 0.5%Ba45S5 bioactive glasses for 24hrs (Calcein). Arrows: Cells showing flat spreading on glass granules. 332

Figure 5.33. Morphology of fibroblasts cultured on tissue culture plastic for 24hrs (Calcein). 333

Figure 5.34. Cell fluorescence after 48hr culture on bioactive glass powders (a) DAPI, (b) Calcein. 334

Figure 5.35. (a) Original image (b) Selection of the cell area (c) Selection of the outer perimeter of glass particles (d) Selection of the area occupied by glass. (red: digital selections, green: calcein staining) 335

Figure 5.36. Digital cell coverage calculation for calcein-stained cells after 48hrs culture on glass powders. 336

Figure 5.37. Standard curve for protein measurement showing the BSA control and the samples (day 4, fibroblast proliferation on bioactive glass) 336

Figure 5.38. Protein measurement from supernatant taken from fibroblasts grown on glass after 4, 8 and 11 days. (a) All glass concentrations were 1% (b) Glass concentrations are included after the composition. 337

Figure 5.39. Gelatin zymography gels for fibroblast cultures on various bioactive glass compositions. 338

Figure 5.40. proMMP-9 and proMMP-2 expression for fibroblasts cultured on glasses (1% concentration in wells) for 4, 8 and 11 days. 339

Figure 5.41. proMMP-9 and proMMP-2 expression for fibroblasts cultured on glasses (1% concentration in wells) for 4, 8 and 11 days. 340

Figure 5.42. (a) BMG powder, (b) BMG mounted on PCL variotis disk, (c,d) Ultrasound treatment of the disks. 344

Figure 5.43. Particle distribution histograms for (a) Ca BMG and (b) Mg BMG. 347

Figure 5.44. (a) The appearance of the bulk samples after 1 day of soaking in media (b) Bubbles on the Ca BMG disk (c) Degradation products from the Mg-based BMG (d) Ca BMG (e) PCL/Mg BMG (f) PCL/Ca BMG (g) PCL/45S5 disk. 348

Figure 5.45. Light microscopy of the surface of the bulk disks after the culture period (a) S. Steel, (b) Mg, (c) Mg BMG, (d-f) Ca BMG. 349

Figure 5.46. Weight loss for the BMG, metallic and bioactive glass disks and scaffold samples. 350

Figure 5.47. Measurement of protein levels in the supernatant. 350

Figure 5.48. Gelatin zymography gel for matrix metalloproteinase expression. 351

Figure 5.49. Matrix metalloproteinase expression for proMMP-2 and proMMP-9 of fibroblasts cultured on bulk BMGs and variotis™ scaffold-mounted powders. 352

Figure 5.50. Representative images showing viable cells in the wells containing the PCL Variotis ™ disks. The three sets of images indicate plain PCL, PCL/Mg BMG and PCL/45S5. (DAPI, calcein). 353

Figure 5.51. (a) Cells on the edge of the Ca-BMG (b,c) Autoflouorescing cell material and BMG fragments from the Mg-based BMG well. (left) DAPI (right) Calcein 354

Figure 6.1. Elastin tubes before and after subcutaneous implantation for 28 days (H&E staining). S: scaffold, CP: capsule. The red line indicates the boundary between the scaffold and capsule [627]. 360

Figure 6.2. Two weeks after implantation in mice a marked inflammatory response was evoked. The implant (*) was surrounded by Polymorphonuclear Neutrophils and macrophages, which were also degrading the implant (arrows) [628]. 363

Figure 6.3. Histological images (H&E staining) of collagen scaffolds excised 4 weeks after subcutaneous implantation. (a) Collagen scaffold which degraded in 2 weeks, (b) Collagen which degraded in 4+ weeks. F: mature adipose, P: preadipocyces, S: scaffold [16]. 364

Figure 6.4. (a) Acellular porous hyaluronan-based scaffold and (b) Acellular, hyaluronan-based viscous gel scaffold, after 12 weeks subcutaneous implantation in rats. S: scaffold, F: mature adipose, T: tissue (collagen, fibroblasts etc) [57]. 364

Figure 6.5. (a) SEM of PGA/45S5 Bioglass® composite mesh. Subcutaneously implanted meshes with surrounding tissue at (b) 14 days and (c) 42 days (H&E and van Gieson staining, arrows show blood vessels, arrow heads show woven mesh fibers and * indicates Bioglass®) [86]. 365

Figure 6.5. (a, b) GORE PGA-TMC Hernia plug (c) Insertion of the plug into a gastrointestinal wound (d) Collagen ingrowth around the plug remnants at 8 weeks (10x, trichrome stain) during a gastrointestinal perforation study [775, 776]. 366

Figure 6.6. (a,b) Polyethylene Medpor implants for craniofacial reconstruction (c) Fibrovascular ingrowth into the scaffold after 4 weeks orbital implantation (white=scaffold) [7] 367

Figure 6.7. (a) Osteoplug implant, designed for a 14 mm burr hole, (b) Implantation into the burr hole. Axial CT image of a burr hole in the skull, taken at (c) 1 month post operation and (d) 1 year post operation. (e) A good cosmetic result [18]. 368

Figure 6.8. Fused deposition modeling PCL scaffold at (a) 0 months (b) and after 6 months in vitro degradation. (c) MicroCT of bone growth after 2 years of the scaffold in a rabbit calvarial defect

model. Soft tissue growth in the PCL scaffold at (d) 3 months and (e) 6 months. Soft tissue ingrowth into a PCL/TCP scaffold at (f) 3 months and (g) 6 months (Giemsa stain, scale bar 400 μm). The arrows indicate blood vessels, black dots are TCP particles, erythrocytes are grey/yellow, collagen is pink, mast cells are purple, leukocytes are red/orange and most cells are pale blue [83]. 369

Figure 6.9. A PGT/TBT scaffold after 21 days of (a,b) In vitro dynamic chondrocyte culture (c,d) In vitro dynamic culture followed by 21 days subcutaneous implantation (a,c) SEM (b,d) Stained with H&E. * denotes a thick fibrous capsule and arrows refer to the lacunae (spaces) left from polymer struts [59]. 370

Figure 6.10. SEMs of (a,c) Compression Molded and (b,d) Freeze Dried PLGA scaffolds. (a,b) Prior to implantation and (c,d) Incomplete tissue filling by 6 weeks. (e) Tissue infiltration was greater along the direction of the pores of the freeze dried foam. (f) The arrows indicate the granulation tissue layer surrounding the foam (F), in which blood vessels were counted [85]. 371

Figure 6.11. (a) Scaffold-filled polycarbonate chamber, indicating tissue level at 8 weeks- longitudinal view, (b) AV loop- horizontal view (c) PLGA scaffold after 2 weeks, demonstrating tissue growth into some pores. (*) an unfilled pore. CT: Connective tissue, F: Fibrin clot on scaffold edge, L: AV vessel loop. Scale: 100 μm [14]. 372

Figure 6.12. PVA sponges (pore size 250 μm) incorporating bFGF 3 weeks after subcutaneous implantation. Arrows indicate capillaries [84]. 373

Figure 6.13. (a) SEM of PGCL scaffold morphology, (b) H&E staining (c) α-smooth muscle actin staining after 3 weeks implantation [262]. 373

Figure 6.14. PLAC scaffold, and scaffold after 1 and 3 months of implantation. Red arrows: fibrous layers surrounding the scaffold [61]. 374

Figure 6.15. Polyurethane scaffold before implantation and after 28 days subctuaneously. V: Histological staining shows α-smooth muscle surrounding the vessels. S: Cross-sections of scaffold struts displaying microporosity [62]. 375

Figure 6.16. In vivo response to (a) Silicone implant (b) Bioactive glass-coated silicone implant. Note the increased presence of inflammatory cells associated with the bioactive glass. (c, d) Arrows: Multinucleated giant cells surrounding bioactive glass particles (100x mag) [53, 785]. 377

Figure 6.17. The number of blood vessels counted at 40x magnification within a PGA/45S5 mesh [86]. 378

Figure 6.18. Vessel counts surrounding PLGA scaffolds, with or without bioactive glass coating [85]. 378

Figure 6.20. Figure 6.19. (a) A subcutaneous pocket in rat skin showing the implantation site of the scaffolds (Day 4, BG), (b) Measurements of the volume of the excised scaffolds, (c) Photographs of the excised scaffolds (d) H&E stained cryosections from the centre of the scaffolds (PCL day 14), (e) Cross-section of the Bioglass® composite scaffold at day 28. 385

Figure 6.21. H&E- stained sections showing tissue ingrowth into the scaffolds (a) edge profiles and (b) scaffold centres. 386

Figure 6.22. PCL scaffold after 14 days tissue infiltration, taken using stereoscopic microscopy after preparation for SEM. 386

Figure 6.23. (a) PCL and (b) BG scaffold, after 21 days tissue infiltration, taken using stereoscopic microscopy after preparation for SEM. 387

Figure 6.24. Scanning Electron Micrographs of central cross-sections of the a) the PCL scaffold before implantation and (b) the tissue-infiltrated scaffold after 42 days in vivo. S: scaffold, T: tissue and arrow: blood vessel. (Scale: 500 μm) 387

Figure 6.25. Scanning Electron Micrographs of central cross-sections of the scaffolds showing the phases of wound healing 2, 7, 28 and 42 days. b) (top) Blood and inflammatory cells visible on the surface of the scaffold (Scale: 10 μm) (middle) A thromboplastin clot lining the surface of the scaffold struts (Scale: 100 μm) (bottom) The Bioglass® scaffold at 42 days, showing the presence of collagen bundles (Scale: 200 μm). 388

Figure 6.26. Fibrin provisional matrix between the pores (2 days, PCL scaffold). 389

Figure 6.27. High magnification images of the blood clot within the scaffold (2 days, PCL scaffold). 390

Figure 6.30. Quantification of collagen from PSR sections showing (a) % Collagen (b) Collagen intensity, which are both increasing over time and similar across the two scaffolds. 392

Figure 6.31. Images of a PSR section taken using (a) Optical and (b) polarised light, showing molecularly aligned collagen bundles in yellow (Scale bar: 200 μm). 393

Figure 6.32. PSR stained sections imaged using polarised light, showing mature collagen bundles in the centre of the scaffolds, (a) Day 14, PCL (b) Day 42, BG (Scale bars: 500 μm), (c-f) Day 14 and 42 images show increasing collagen maturity over time. At day 42, the Bioglass® shows less mature collagen formation in regions where the scaffold is partially degraded (Scale bar: 2 mm) 394

Figure 6.33. Collagen 1 staining of the BG scaffold after 21 days in vivo. 395

Figure 6.34. Micropores within the struts after 42 days subcutaneous implantation show the presence of collagen and cells. (a) H&E (b) PSR (c) Collagen 4/Eosin (Scale: 100μm). Nuclei (blue)

indicate cells within the pores in a & c, which are likely to include fibroblasts and macrophages. (d) DAPI (Scale: 500 μm). 395

Figure 6.35. Possible adipose tissue within a Bioglass® composite scaffolds excised at day 14. 396

Figure 6.36. Possible adipose tissue was observed in BG scaffolds excised at day 14. (a) SEM (b) H&E (c, d) Collagen IV. 396

Figure 6.37. (top) Blood vessels 500 μM into the BG scaffold at 7 days, (bottom) Blood vessel in the centre of the PCL scaffold at day 14 (CD31 immunofluorescence- green, DAPI-blue, scale bars: 200 μm). 397

Figure 6.38. Blood vessels in the centre of the scaffolds using CD31 & DAPI fluorescent stains. For the BG scaffold, the day 7 images are taken close to the edge, in order to capture the fibrovascular ingress. (scale:500 μm) 398

Figure 6.39. Blood vessels after 14 days in the centre of PCL and BG scaffolds (CD31, DAPI) 399

Figure 6.40. Blood vessels in the centre of the scaffolds (Collagen 4 immunohistochemistry, dark brown) (Scale: 500 μm) 400

Figure 6.41. Blood vessel counts inside the scaffolds. 401

Figure 6.42. The tissue surrounding the scaffolds was highly vascularised. (a) Large vessel lining the scaffold (day 21, PCL, collagen 4 immunostaining scale bar 500 μm) (b) Vascularisation surrounding the scaffold (day 42, BG, collagen 4 immunostaining, scale bar 200 μm) (c) cross-section of a vessel on the outer edge of the scaffold (day 7, PCL, PSR, polarised filter, scale bar 1 mm), (d & inset) 1 mm+ vessel inside the degrading scaffold (D42, BG, PSR, polarised filter, scale bars 1mm). (e,f) SEMs of tissue surrounding a PCL scaffold which was excised after 14 days in vivo. The round cells in these images could be endothelial cells. (scale bar: 10 μm) 402

Figure 6.43. Scaffold sections stained for macrophages, which particularly accumulate near the scaffold (CD68 immunostaining, dark brown, Scale bar: 200 μm, arrow indicates macrophages near disintegrating scaffold) 403

Figure 6.44. Circulating blood counts for various cell types. 404

Figure 6.45. Volume of wound fluid collected from scaffolds. 405

Figure 6.46. (a) Counts of neutrophils, eosinophils and macrophages from the wound fluid (MPO negative). 405

Figure 6.47 (a) Gelatin zymography results obtained from the wound fluid showing the concentration of MMP-2, MMP-9 (and their active forms), indicating increasing growth and decreasing inflammation over the first 7 days 406

Figure 6.48. Comparison of cellular polymer scaffold thickness with complete tissue infiltration (references included in Table 6.1). 412

INDEX OF TABLES

Table 1.1. Features and Applications of Bioceramics. 19

Table 1.2. Features and clinical applications of polymers [165]. 23

Table 1.3. Review of relevant polyester/bioactive glass composites and related studies. 24

Table 1.4. Properties of popular bioabsorbable polyesters [233]. 26

Table 1.5. Tensile properties of native tissues. 36

Table 1.6. Tissue scaffold prototypes and products 39

Table 2.1. Review of osteochondral scaffolds. 56

Table 2.2. Compressive properties of bioceramic scaffolds. 60

Table 2.3. Zoledronic Acid Action. 62

Table 2.3. Compressive properties for the wollastonite-based scaffolds (average±stdev of 4 samples). 76

Table 2.4. The process of Real-Time Polymerase Chain Reaction, as completed by the RotoGene 6000. 87

Table 3.1. Features of PCL, bioactive glass and composites that address key requirements 99

Table 3.2. Types of Wound Debridement [477]. 109

Table 3.3. Examples of materials used for wound dressings [481]. 111

Table 3.4. Examples of moist wound healing dressings. 112

Table 3.5. Commercially available engineered skin grafts [78, 515]. 116

Table 3.6. Features of polymer scaffold synthesis processes. 120

Table 3.7. Review of scaffolds formed using particulate leaching. 123

Table 3.8. Techniques for glass incorporation into scaffolds. 127

Table 3.9. Review of scaffold tensile properties. 140

Table 3.10. Review of scaffold compressive properties. 141

Table 3.11. Weights of scaffolds before and after coating with glass powder. 153

Table 3.12. Manual porosity calculations for the variotis™ scaffolds. 154

Table 3.13. Parameters for the 3D models. 162

Table 3.14. Morphological parameters for the PCL scaffold, calculated from MicroCT data. The 2D data is presented as the average±stdev and range. 163

Table 3.15. Conditions used for compression of scaffolds. The heating method and material used for the plate apparatus are specified in the second column. 176

Table 3.16. Specimen descriptions for mechanical tests. 189

Table 3.17. Tensile properties for various strain rates. 192

Table 3.18. Effect of glass incorporation on the tensile properties. 194

Table 3.19. Tensile properties for the BG powder coated scaffolds. 195

Table 3.20. Compressive properties for the PCL and glass-coated scaffolds. 195

Table3.21. Tensile properties of scaffolds which had been coated with BG or attached to a thin PCL film. 197

Table 3.22. Tensile properties for the sterilised scaffolds. 199

Table 3.23. Compressive properties for sterilised scaffolds. 200

Table 4.1. Formulation of the oxides used for bioactive glass synthesis. Measurements are in mol%(wt%). 232

Table 4.2. Glass batches and analysis techniques undertaken. 239

Table 4.3. Comparison of the composition of 45S5 precursor powder after 2, 4 and 8mins mixing (average of 3 regions). 247

Table 4.4. Composition of 45S5 precursor powder using x-ray fluoroscopy after 2, 4 and 8mins of mixing. 247

Table 4.5. EDAX results for 45S5 milled glasses. 250

Table 4.6. Composition for 5%Fe45S5 (Fx1) glass. 251

Table 4.7. EDAX results for 5%Zn45S5 (Nx3) glass. 252

Table 4.8. Parameters for the nanoindentation experiments. 258

Table 4.9. Nanoindentation results for experiment 1. 259

Table 4.10. Nanoindentation results for experiment 2. 260

Table 4.11. Nanoindentation results for experiment 3 260

CHAPTER 1

INTRODUCTION & DESIGN CONCEPTUALISATION



"Human subtlety will never devise an invention more beautiful, more simple or more direct than does nature because in her inventions nothing is lacking, and nothing is superfluous"

Leonardo da Vinci

1.0. CHAPTER OVERVIEW

Tissue scaffolds are currently needed to replace compromised soft tissues where native grafts are unavailable or inappropriate. Tissue engineering scaffolds designs aim to regenerate rather than simply substitute native soft tissue. Soft tissue engineering scaffolds and respective cross-disciplinary design considerations are critically reviewed. While biologically-derived scaffolds and biostable scaffolds have been under development and in use, they continue to be limited in terms of capability and long-term clinical results. Synthetic resorbable solutions provide an ideal match of device safety, therapeutic efficacy, regulatory compliance, and commercial viability. Challenges to current scaffolds include: lack of pathway for *de novo* tissue and blood vessels, poorly matched load transfer to developing tissue, aggravated inflammatory response, chronic infection, delayed healing and chronic pain. Methods for mitigating against these risks are discussed, including the use of bioactive surfaces to engage with tissues. Scaffold form should allow for high interconnected porosity, large mean pore size for tissue infiltration without compromising structural support requirements. Biomaterials should be selected with controlled degradation rate to avoid eliciting an aggravated inflammatory response or mechanical instability. Scaffolds designed with these aspects in mind have the potential to encourage tissue regeneration by recruiting cells and factors from the surrounding tissue to safely and efficaciously mediate soft tissue repair.

1.1. TISSUE ENGINEERING SCAFFOLDS

The following thesis outlines the design and development of novel soft tissue engineering scaffolds and methods. A broad literature review and scaffold design sections are provided in chapter 1. The methods for forming and characterizing a novel biphasic osteochondral scaffold and the evaluation of therapeutic additives are provided in chapter 2. Chapter 3 & 4 document the development of Variotis™; a novel and versatile soft tissue scaffold. Chapter 4

The thesis structure is summarized below in Fig. 1

Figure 1.1. Thesis structure schema.

1.1.1. A REGENERATIVE APPROACH TO TISSUE HEALING

Tissue engineering scaffolds play a vital role in providing ancillary support for tissue repair at sites of injury or disease [1]. Tissue scaffolds or matrices are used for regenerative treatment where both the form and function of the native tissue are restored to healthy conditions [2]. This approach marks a shift from replacement of tissues as provisioned in prosthetic devices [2, 3]. Increasing the life-span of medical implants is a critical area of development, particularly as society seeks strategies to cope with an aging population [4, 5].

Chief aims of tissue engineering approaches are therefore to improve the integration of implants within the body, to improve the health of damaged tissue by addressing underlying pathological issues and to be completely replaced and eliminated from the body in the long term [6]. Approaches to improve the attachment of tissue to medical devices have included the incorporation of bioactive materials and modulation of the implant shape/surface [7, 8]. Bioactive scaffolds which promote tissue regeneration have great potential for improving healing outcomes for a wide range of tissue types and conditions [5].

1.1.1.1. Key Functions of a Tissue Scaffold

Fully functional tissue is less likely to become a locus for infection and should be the ultimate goal of any tissue engineering approach [9]. A scaffold should perform several important roles to facilitate vascularised tissue repair [10]. These include:

- Provide a 3D framework in which cells can migrate, attach and proliferate;
- Provide space for hierarchical tissue formation and remodelling;
- Protect developing tissue from stresses such as high compressive forces and infection;
- Address underlying tissue pathologies through delivery of therapeutic factors;
- Promote good integration with the surrounding tissue;
- Facilitate the transport of wound fluid and blood through scaffold; and
- Facilitate the transfer of force to the developing tissue.

As shown schematically in Fig. 2.1a, these key functions of a scaffold are like those of a house. Similar to the role of a house, scaffold designs should provide a protective function, whilst also facilitating connection to the surrounding environment. Scaffolds should provide protection from deleterious forces and yet still allow physiologic stress to be transferred to the tissue within the scaffold [11, 12, 13]. If these concepts are not incorporated into the scaffold design, excessive displacement or forces can lead to tissue necrosis and hinder vessel development

[14]. Instead, controlled levels and directions of force transfer are important to enable mature, vascularised tissue to develop [11, 15].

Scaffolds should also ideally be designed to induce stasis or inhibition of bacterial colonisation and biofilm formation. This can be achieved through materials selection, removal of vacant space and localised, long-term therapeutic delivery from the scaffold. Nutrient delivery to the cells and extraction of waste products should be facilitated via good mass transfer and competent vascularisation throughout the scaffold. The scaffold must also provide a good connection with the surrounding tissue, so that the cells within the scaffold are not isolated via the formation of scar tissue.

Scaffolds play an important role in providing space for tissue regeneration [16]. This concept has been clinically confirmed through the use of guided tissue regeneration membranes for dental surgery. These non-biodegradable membranes were effective for space making and in the prevention of scar tissue ingrowth [17]. In many clinical examples, scaffolds increase the speed and quality of tissue compared to the absence of a scaffold [18].

1.1.1.2. Hierarchical Device Design

Long-term medical device acceptance is dependent on the macro-, micro- and nano-scale properties. Conventional prosthetics have focused on macroscale performance properties such as emulating the shape of the tissue, restoring the range of motion to the joint, and ensuring sufficient strength and toughness in load-bearing situations. Bulk implant designs have in most instances neglected the microscale needs of the cells and tissues, including chemical, biological and micromechanical considerations [19, 20]. This can lead to localised tissue erosion, regression, subsidence, adverse fibrous capsule formation, release of wear debris/ions and local aggravated inflammatory reactions around prosthetics.

Important microscale needs of the tissues include: cellular attachment, blood transport (nutrient delivery/waste removal), chemical environment (including release of ions from biomaterial and pH), protein absorption and the inflammatory response [21]. Regenerative tissue engineering approaches aim to consider the microscale needs of the biological environment, but can focus on biomaterial-cell interactions whilst neglecting broader performance requirements. The challenge is therefore to create scaffold-based devices with suitable multiscale properties, to restore the tissue form and function for the long-term.

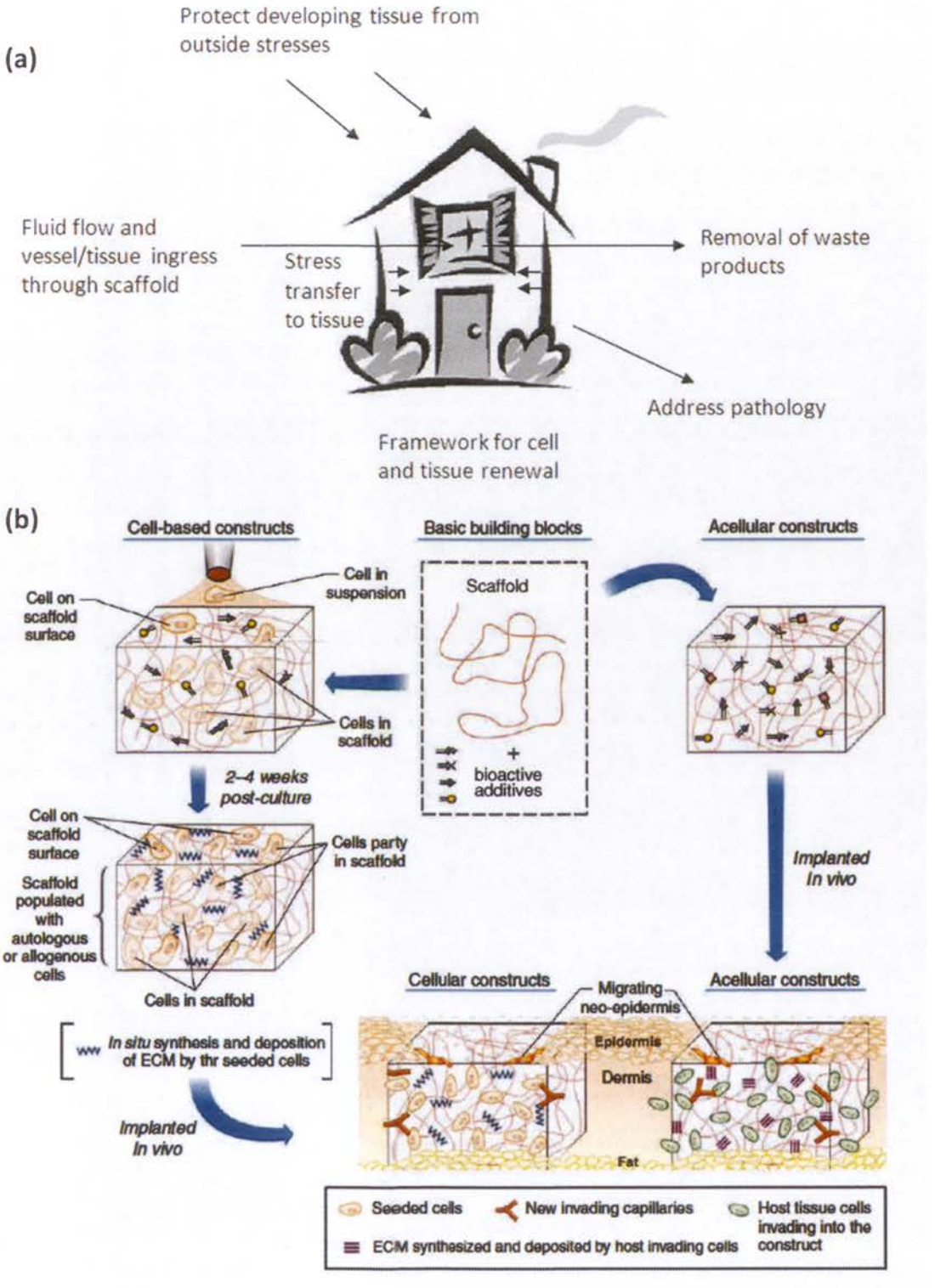


Figure 1.2. (a) The key functions of a scaffold are analogous to those of a house, (b) Cell-based and acellular tissue engineered constructs [23].

1.1.1.3. Components of a Tissue Engineered Device

Tissue engineered solutions can consist of the following:

(1) Scaffold/substrate;

(2) Bioactive molecules; and

(3) Cells.

Fig. 1.2b. demonstrates two different philosophical approaches to tissue engineering: cell-based constructs and acellular constructs. Cell-based constructs can be cultured *in vitro* (using a bioreactor) to achieve cell expansion and matrix deposition and implanted in the patient [22]. Alternately, acellular constructs harvest cells *in vivo*, from the surrounding tissue and fluids [16]. Acellular approaches can result in superior invasion by the surrounding tissue and capillaries due to the provision of vacant space and the influx of a diverse range of native cells.

1.2. PROBLEMS WITH ALTERNATIVE TISSUE REPLACEMENT OPTIONS

1.2.1. LIMITATIONS OF NATURAL GRAFTS

Tissue loss or damage can occur due to mechanical, chemical or metabolic causes. When significant loss of tissue occurs, healing can require medical intervention. Tissue loss can be treated using natural grafts, stem cells, metabolic drugs or engineered grafts. Graft material can be retrieved from an alternative site in the patient (autograft), from another human donor (allograft/homograft) or from other living or nonliving species (heterografts, xenografts). These options are, however, restricted by limited material availability, immunogenic rejection, lower engraftment rates, mechanical fragility, high costs, risk of disease transmission/microbial contamination and complicated multistage surgery [24, 25, 13].

Localised delivery of stem cells to the wound site is a recent approach which can assist regeneration. However, it is difficult to ensure stem cells are effectively delivered to the wound site and remain there for a sufficient period [19, 20]. In addition, this technique often does not provide mechanical stability for large defects, and generation of the relevant cell populations is a time-consuming process. Metabolic drugs are also useful for aiding the wound healing process; however, can be inadequate when substantial tissue loss has occurred. In addition, gradual, localised administration is preferred to injection in many cases.

A scaffold-based synthetic engineered graft has the capacity to overcome these limitations, whilst reducing the risk of harm to the patient. Scaffolds are particularly important for tissue which will not readily regenerate (e.g. cartilage), or where an injury effects a large area or volume and filling and augmentation are required.

1.2.2. LIMITATIONS OF CONVENTIONAL IMPLANTS

There has been a trend to import prosthetic design philosophy into the field of tissue engineering at the macro, micro, molecular and interfacial levels. The emphasis of this approach is to substitute rather than compliment or conduct native tissues. Key aspects of this design emphasis are:

1. The scaffold acts to substitute extracellular matrix (ECM) into which cells are seeded,
2. The modulus of native tissues is matched without accounting for tissue modelling.
3. Tissue-scaffold integration is assumed for materials deemed "biocompatible".

These assumptions can be overly simplistic. To gain further basis for scaffold design, relevant insight for the field of regenerative medicine can be gained by reviewing tissue integration of implants and biomaterials in the clinical context.

Conventional prosthetics are made from permanent materials (ceramics, metals, polymers, composites) in bulk form. Typical examples include intramedullary fixation, hip arthroplasty and breast implants [27]. Many medical devices which are currently used clinically show sub-optimal responses *in vivo*. Even though an implant is made from a 'biocompatible' material, its long-term acceptance can be poor [28, 29].

Conventional implants have a limited lifespan as they lack three of the most critical characteristics of living tissues: (i) the ability to self-repair; (ii) the ability to maintain a blood supply; and (iii) the ability to modify in response to stimuli such as mechanical load [30]. Implants often cause problems including excess pain, inflammation and fibrous encapsulation, stress shielding and lack of tissue integration [31, 29, 32]. Prosthetics can serve as a locus for infection and also suffer implant migration. This has resulted in premature implant failure, and subsequent removal for many patients. These difficulties will be now discussed in more detail, along with methods to address them.

1.2.2.1. Adverse Implant-Tissue Interfaces

Implants can develop capsules on their surface which consist of aligned, collagen rich fibrous tissue. These capsules can be fluid filled and isolate the implant from the adjacent tissue. This reaction can be due to both biological signalling but also movement at the tissue-implant surface and the mechanics of the implant as a whole. Implant encapsulation often causes pain to the patient. Fibrous capsules often develop surrounding silicone breast implants [26, 31, 32]. These isolating capsules are distinct from highly vascular tissue which can form adjacent to an implant or tissue engineered construct. Such tissue does not isolate the implant and provides vascular networks through to the surrounding tissue.

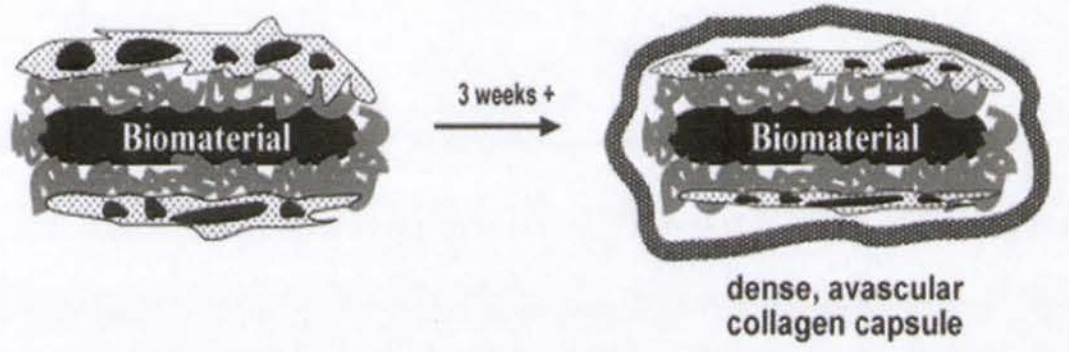


Figure 1.3. A fibrous capsule forms around many conventional implants [32].

1.2.2.2. Inflammation

When biomaterials are implanted, a series of events occurs, including protein absorption onto the surface and attraction of inflammatory cells, including neutrophils and macrophages to the area [33]. Inflammation is the first event which occurs in normal wound healing (ref 3.1.2) and if controlled, could be a useful tool in tissue engineering. Factors released due to inflammation can stimulate normal healing and vascularisation [34].

However, aggravated inflammatory responses can delay tissue regeneration and contribute to fibrous capsule formation [26, 33]. Adverse responses can be due to the nature of the proteins adsorbed onto the implant surface, or biological signalling due to the nature of the material. Wear debris or ions which are released from metal or polymeric implants can lead to an undesirable inflammatory response and fibrotic encapsulation of the particles. These particles can persist in the body for the long-term and experience migration and cause tissue necrosis and resorption [35].

Implants can modulate the pH of the local region, which also causes a high level of inflammation. In addition, corrosion of metals, chemical degeneration of ceramics or release of polymer constituents or crosslinking agents can also result in inflammation [36, 37]. For example, silicone breast implants demonstrate an aggravated immune response characterised by localised T-cell activation and high levels of macrophages and dendritic cells in the fibrous capsule surrounding the implant [26].

1.2.2.3. Stress Shielding of Implants

Stress shielding (Fig. 1.4.) is defined as the reduction in tissue density as a result of removal of normal stress from the tissue by an implant [39]. It is a common problem in bone due to the use of metallic hip prosthesis which have a high density and much greater stiffness (or modulus) than the natural materials they replace, and can lead to implant loosening and failure. A lack of mechanical stimulation in the adjacent tissue can induce resorption which will lead to the eventual failure and loosening of the implant [40]. The opposite effect is also true- if loading on the adjacent tissue decreases, the tissue will increase in strength to resist the loading.



Figure 1.4. Stress shielding in the femoral component of a cemented hip implant. The arrow indicates the resultant bone loss. [38]

The moduli of metallic implants are >5-10x higher than the native bone. For example, while the modulus of cortical bone is 7-25 GPa, the moduli of chromium based alloys/stainless steels and titanium are 200-300 GPa and 110 GPa, respectively [8]. Implant movement associated with stress shielding can also contribute to fibrous layers adjacent to the biomaterial.

Implantation of a medical device can cause changes in the loading patterns experienced by tissues, on both the macro- and micro-scales. Like hard tissue, soft tissue requires an optimal level and direction of force for healthy remodelling and vascularisation to occur. This includes development and maintenance of the correct cell type and tissue structure. Stress shielding in soft tissues as a result of device implantation can lead to implant calcification, implant encapsulation and a lack of strength.

Stress shielding can be reduced by designing an implant with a modulus which is similar to, or below that of the tissue it is replacing. Composite materials can deform to higher strains than metals and fibrous composite plates and rods have shown improved healing in bone [41, 42]. For example, intramedullary nails made from self-reinforced polylactic acid have shown similar levels of fixation to stainless steel nails in a porcine femur model [43, 44].

An alternate method to reduce long-term stress shielding using a biodegradable material which degrades at a similar rate as being replaced by the new tissue. This can lead to a gradual transfer of the load from the biomaterial to the native tissue, without losing mechanical stabilisation of the tissue [44]. This concept is shown in Fig. 1.5. Almost all bioabsorbable polymers exhibit a dramatic loss in mechanical properties during the first month of implantation. For example, a biomechanical study (rabbit model) conducted with PGA and PLLA rods demonstrated a drop in flexural strength by up to 90% within 3 weeks of implantation in bone [45]. Implants should be designed so that a sudden loss of support does not occur, and instead a stable transition is achieved. In this way, an implant can play a complimentary, rather than just substitutionary role.

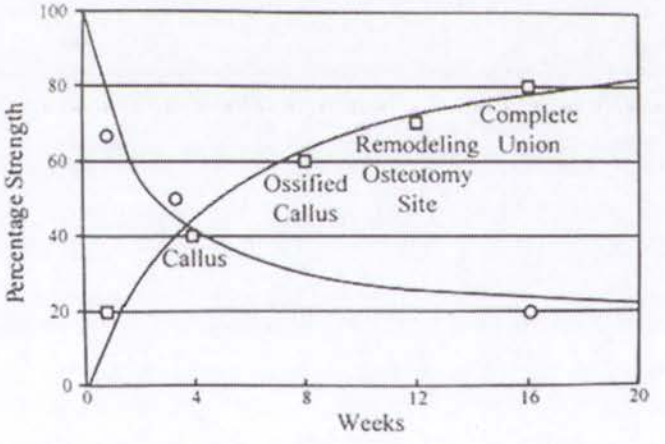


Figure 1.5. Variation of relative strengths of osteotomy and fracture union with time [44].

Modulus-matching of implants can be achieved not only through material selection but also via reduction of stress concentrations which occur due to implant shape [46]. Both macro- and micro-scale features of the implant can change the stress experienced by adjacent tissues. The stiffness of an implant can be reduced by decreasing the thickness of the implant or addition of porosity. For example, Ward and coworkers reported a reduction in the thickness of the fibrous capsule around polyurethane (PU) implants, when either a thinner or less stiff implant (PU/silicone/polyethylene oxide) was used [29]. Studies have also shown minimal stress concentrations within porous scaffolds, which should reduce stress shielding effects [46].

1.2.2.4. Tissue Integration

Immobilisation of an implant, especially during the initial months, is important for tissue healing. Lack of implant stability leads to increased healing rates and reduced integration with the surrounding tissue [44] which can exacerbate problems due to stress shielding and fibrosis. Implant-tissue fixation can be improved by composition and form improvements. Bioactive ceramic implant coatings have been used clinically to improve implant stability [47-53]. Soballe and coworkers [47] found the shear strength and stiffness of the bone adjacent to a ceramic-coated prosthesis and the canine femur increased 2-5 times. Good implant attachment helps avoid stress shielding and adverse loading conditions.

Tissue attachment is also achieved by using textured surfaces, meshes or porous scaffolds, compared to bulk materials [29, 54-63]. Textured surfaces reduce fibrous capsule thickness and increase the level of angiogenesis surrounding an implant [29]. Porous surfaces have been created on implants using titanium or ceramic particle coatings [56]. Superior soft tissue attachment has been achieved for nylon meshes which had large mesh spacings (200-500 μm), as compared to small mesh spacings (30 μm), when implanted subcutaneously into rats [64].

1.2.3. CLINICAL EXPERIENCES OF MESHS/SCAFFOLDS

Porous meshes and scaffolds have been used in many clinical settings [65]. These include both synthetic and natural polymers (permanent or bioabsorbable), decellularised biological matrices and other materials. Applications have included abdominal hernias [66-69], skull bone defects [58, 70, 71], eye prosthesis [7], dura mater repair [25, 73-76], bone [70, 77], engineered skin grafts [78, 79, 80], aortic stents [81] and spinal cages [82]. The most successful of these exhibit high levels of porosity and interconnectivity, good biocompatibility with low levels of inflammation and good tissue attachment. Most scaffolds employed clinically are for bone. There remains a need for development of versatile and optimised soft tissue scaffolds.

1.2.4. LIMITATIONS OF CURRENT TISSUE SCAFFOLDS

Key limitations of existing scaffold systems:

- Stress shielding of tissue within or surrounding construct [83];
- Lack of attachment and integration to surrounding host tissue [61];
- Rapid degradation [73, 14];
- Aggravated foreign body response [14, 57, 74-76];
- Fibrous encapsulation/isolation [62, 61]; and
- Poor levels of new tissue and vessels within porous scaffolds [83, 14, 86].

Like conventional prosthesis, many scaffolds still function to replace rather than complement and regenerate the host tissue. Case studies demonstrating these aspects are examined in detail in chapter 6 but some of these concepts will now be briefly introduced.

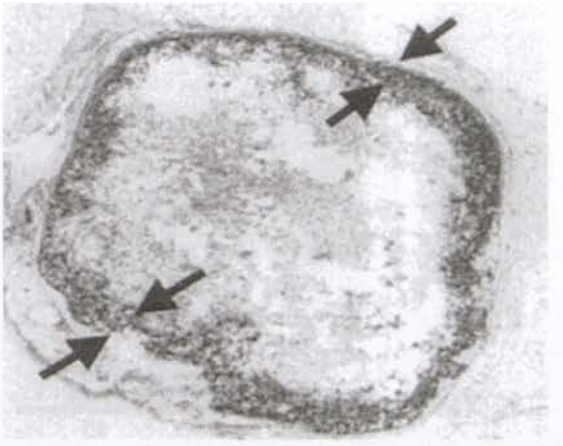


Figure 1.6. Incomplete tissue infiltration into a PDLA scaffold after 6 weeks in vivo [85].

1.2.4.1. Fibrovascular Tissue Infiltration into Scaffolds

Fibrovascular tissue is vascularised, high collagen content ECM which infiltrates a scaffold. New fibrovascular ingrowth is referred to as granulation tissue. Many scaffolds reported in the literature experience incomplete tissue ingrowth into the centre of the scaffold [14, 61, 83, 84, 86, 87]. These include scaffolds in clinical use, such as bone burr plugs [58]. Few soft tissue scaffolds achieve rapid vascularisation within the pore spaces throughout the scaffold, and this can lead to tissue necrosis [14, 84, 87].

In one example of a soft tissue scaffold, Day and coworkers designed a woven polyglycolic acid (PGA)/bioactive glass mesh [85]. They noted good cellular infiltration, but little collagen deposition after 42 days of subcutaneous implantation in rats. In another study by the same group, little granulation tissue and no vascularisation were observed within a PDLA scaffold, after 6 weeks subcutaneous implantation in rats.

In some cases, incomplete tissue ingrowth is due to rapid polymer degradation. Entenmann and coworkers [73] noted that a polydioxanone (PDS) mesh dissolved too rapidly for sufficient consolidation of ingrowing connective tissue to resist tensile forces present in the abdominal muscle. Optimally designed scaffolds would enable a wide variety of cell types to enter and migrate throughout a scaffold, in order to efficiently build ECM, rapidly develop a vascular network and effectively remove degradation products. Various biomaterials which are possible candidates for tissue scaffolds will now be discussed, along with their strengths and limitations.

1.2.4.2. Inflammation and Fibrous Encapsulation of Scaffolds

Scaffolds/meshes have also experienced high levels of inflammation and fibrous encapsulation, which can cause bleeding, pain and persistent fibrous growths whist inhibiting tissue infiltration within a scaffold [14, 61, 62, 74-76].

1.3. COMMERCIALISATION OF SCAFFOLD-BASED DEVICES

Along with considerations of biological efficacy, the ease with which a scaffold might be commercialised must be a key input into the design process [88]. Shown in Fig. 1.7, there is a chasm, or 'Valley of Death', between tissue engineering research and commercial products. This is a complex long-term process which requires a high level of funding and extensive testing to demonstrate the safety of the device, both in vitro and in vivo. Currently, there are high risks and poor clinical outcomes associated with many cultured tissue engineered systems which seek to replace the host tissue. While biologic tissue scaffolds are possible to develop they warrant more exhaustive developmental controls and regulatory constraints [88]. For these reasons, a synthetic *in* vivo approach is considered more commercially viable for regenerative scaffold design. There are numerous examples of clinical success utilizing this tissue engineering approach [7,71,83]. The limitations with using naturally derived materials will be discussed in the following section, followed by an analysis of synthetic candidates.

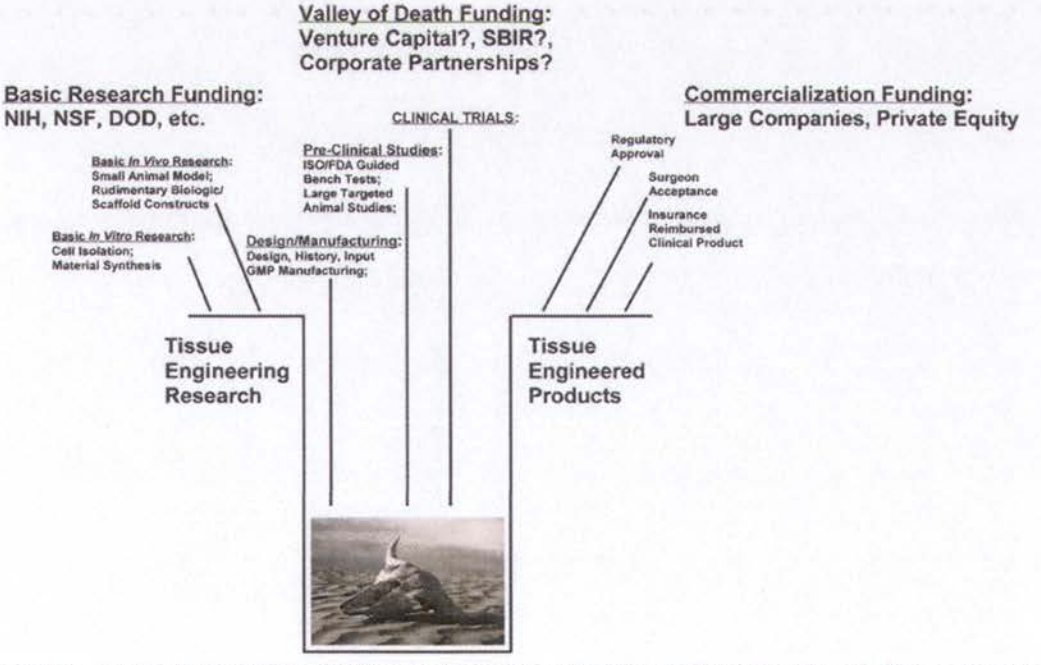


Figure 1.7. The Valley of Death. For tissue engineering, the Valley of Death is the gap and associated funding difficulties of taking tissue engineering technologies to tissue-engineered products. The Valley exists due to the need of obtaining funding to develop scalable/Good Manufacturing Practice design and manufacturing processes, the need for pre-clinical studies proving therapies in large animal models, and finally, the need to progress to clinical trials [88].

1.3.1. TISSUE SCAFFOLD DESIGN INPUTS

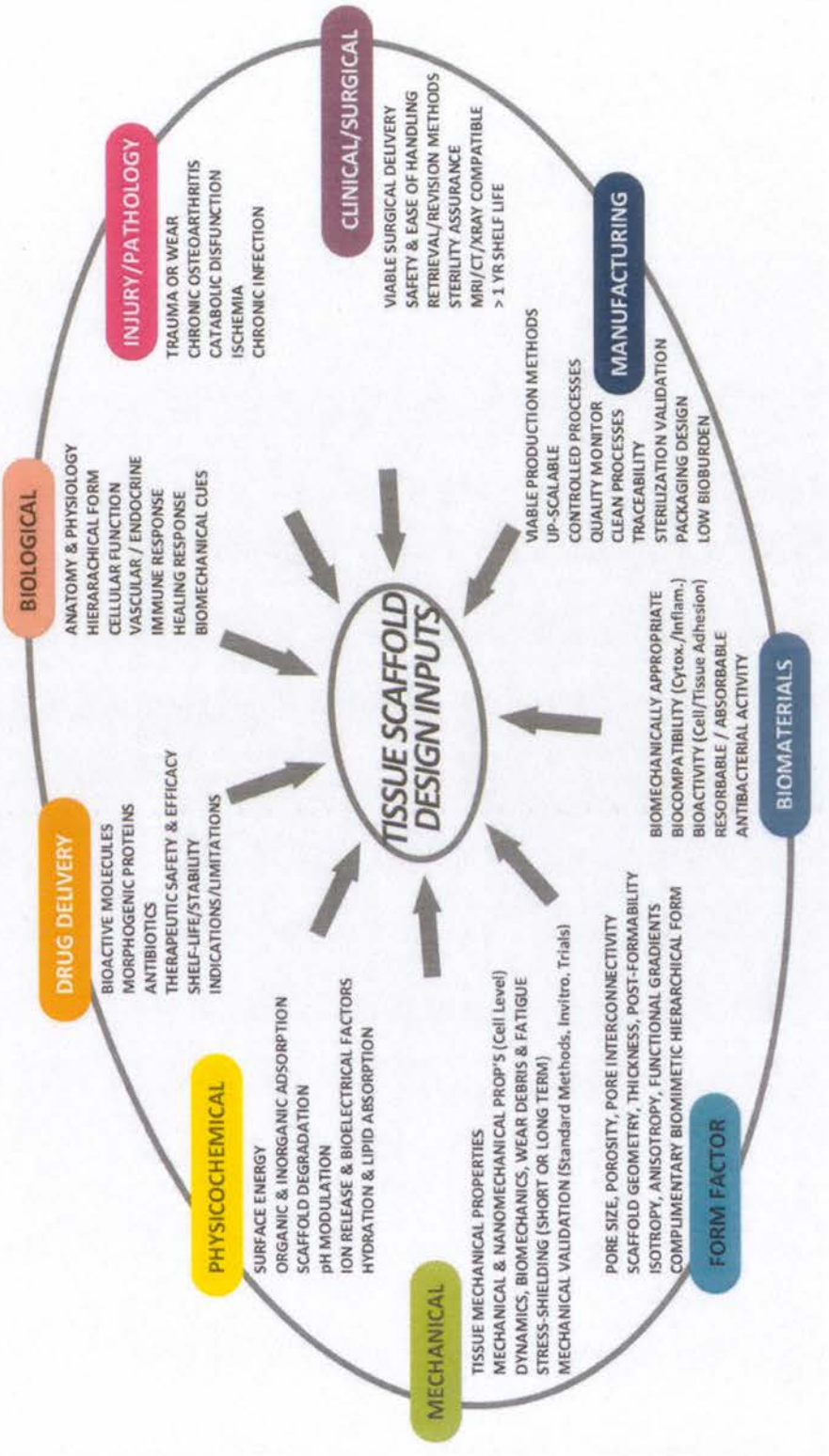


Figure 1.8. Tissue scaffold design inputs.

A schematic diagram listing key tissue scaffold design inputs is show above in Fig. 1.8. Most of the main areas pertinent to designing a soft tissue scaffold for clinical relevance are covered in this cross-disciplinary project.

1.3.2. LIMITATIONS OF NATURALLY DERIVED MATERIALS

Naturally derived hydrogels (Fig. 1.9) are polymer networks that are insoluble but swellable in aqueous medium. They offer an environment that resembles the highly hydrated state of natural tissues. Popular hydrogels include decellularised ECMs, collagen, alginate, agarose, hyaluronic acid, gelatine, chitosan and fibrin [10, 16, 89-92], as reviewed in detail previously [6, 57, 93-96]. Their key limitations are listed below.

- Poor shelf life;
- Expensive sourcing/processing, low availability;
- Risk of prionic disease transmission;
- Cross-linked samples were incompletely degraded, remodelling and elimination from body;
- Limited strength, often in both compression and tension. Limited elongation;
- Unwanted biological signalling;
- Unpredictable swelling behaviour in vivo (affected by infection, temperature, pH, lipid ingress etc); and
- Cytotoxic crosslinking agents.



Figure 1.9. (a) Synthetically formed tropoelastin (E) [94] (b, c) Porous elastin hydrogels fabricated using CO_2 gas and cross-linked via gluteraldehyde [95].

While many of these materials are partially or wholly naturally derived, they still substantially differ from native ECM, in terms of both structure and composition [10]. For this reason, these materials are remodelled by the body over a period of weeks-months. Some hydrogels are designed to be biostable materials [94]. *In situ* polymerizing tropoelastin developed by Weiss, Mithieux and coworkers, is described as "undergoing rapid localised gelation to form a persistent mass", following injection in the body [94] (Fig 1.9c). Although tropoelastin is elastic like native tissue, and contains synthetic human elastin, it actually performs an augmentative filling role rather than encouraging regeneration and eventual replacement. Other hydrogels are completely biodegradable and eliminated from the body. In order to attain sufficient structural integrity, however they are usually crosslinked, rendering them only partially degradable. This can lead to segments of the hydrogel persisting in the body for prolonged

periods. Hazardous and cytotoxic cross-linking agents are commonly used. These include gluteraldehyde, hexamethylene diisocyanate (HMDA) and dimethyl sulfoxide (DMSO) [95]. Naturally derived materials can lack the versatility to be cultured for both *in vitro* and *in vivo* applications. For example, Matrigel, is "unusable in clinical situations" [57, 96, 97], as it is derived from tumour ECM. Many clinically suited matrices are too costly for *in vitro* studies.

1.3.3. BIODEGRADABLE MATERIALS

Biodegradable materials (e.g. polymers, ceramics, glasses) are broken down in the body through the action of enzymes, cells (esp. macrophages), swelling due to moisture/lipid absorption and cross-linking. Polymers are susceptible to in vivo cross-linking which can eventually embrittle the polymer. Polymer degradation may occur via surface erosion resulting in mass loss. Alternately, a gradual loss of molecular weight can lead to softening of the polymer prior to bulk mass loss [88, 98].

Materials which are biodegradable are not necessarily bioresorbable. As they degrade, bioresorbable materials move away from the implant site and are completely eliminated from the body with no residual side effects [99].

Biodegradable materials are routinely used clinically for sutures, haemostatics, wound covers, drug delivery systems, artificial skins, bone fixation devices and dental membranes for guided tissue regeneration. A range of biodegradable scaffolds are shown in Fig. 1.9.

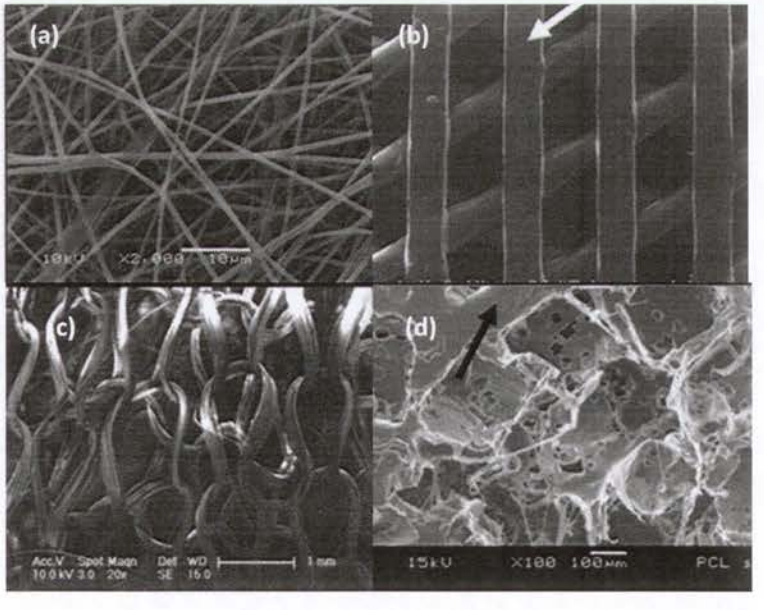


Figure 1.9. (a) PCL/TCP scaffold, (b) PCL/collagen nanofibers, (c) PCL foam (d) PLGA woven textile mesh. Arrows: scaffold material [100].

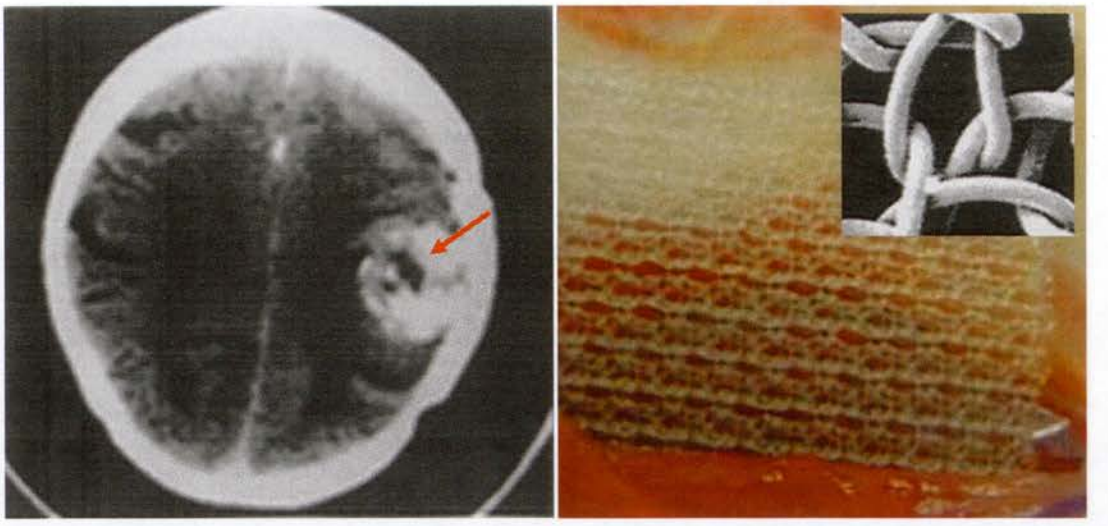


Figure 1.10. Preoperative computerised tomography scan demonstrating a calcified mass surrounding propylene Marlex mesh (arrow) [85].

1.3.3.1. Case study: Dura Mater Substitutes

The shift occurring in the industry from the use of native tissue grafts, to permanent biomaterials then to bioabsorbable materials can be illustrated through a case study of dura mater substitutes. The dura mater is one of the layers of the meninges which surrounds the brain and spinal cord. Replacement is required when it is lost in craniotomy.

Originally, a lack of donor sites for autografts led to the clinical use of allogenic and zenogenic materials, such as collagen, gelatin, human or bovine derived duras and pericardia. However, when some reports were published suggesting that freeze-dried duras induced the deadly Creutzfeldt-Jakob disease, synthetic options were urgently sought [25, 73].

Initially, non-degradable silicone membranes (Silastic) and silicone-coated Dacron were used. However, there were reports of bleeding, thought to be due to chronic foreign body inflammation [74]. Similarly, propylene meshes (Marlex) [75] and silicon-coated Dacron (Dura Film) [76] were reported to occasionally cause exuberant fibrous reactions, simulating a slowly growing tumour (Fig. 1.10).

During the 1980's, meshes based on Vicryl® sutures, were explored as bioabsorbable synthetic substitutes [101]. Initially the designs focused on a Vicryl®-based mesh in a hybrid with collagen. However, these meshes degraded rapidly and were excessively rigid. More recent meshes consisting of Vicryl® mesh/PDS (Dura Patch®, ETHISORB, Codman) [102], and also PLCL [103] have evolved. This Vicryl® mesh allows tissue ingrowth on one side, while the PDS film prevents leakage of the cerebrospinal fluid.

1.4. BIOACTIVE SCAFFOLDS

Bioactivity refers to the capacity of a material to be "tissue inductive". Bioactive materials materials can facilitate cellular attachment and even gene modulation. A stable interfacial bond can form between the material and the surrounding tissue. Both bioceramic coatings and porous surfaces contribute to the level of bioactivity of an implant [8]. Coatings are considered bioactive when they facilitate the formation of a bone-like hydroxyapatite (calcium phosphate) crystallite layer on their surface, after submersion in simulated body fluids.

Hench and Polak identified three classes of materials, depending upon the response they illicit from the biological environment [3, 104]. First generation materials are permanent and bioinert (e.g. alumina, stainless steel). Second generation materials are bioactive or biodegradable (e.g. poly-ε-caprolactone, tri-calcium phosphate). Third generation materials are those which are both bioactive and biodegradable (e.g. hydroxyapatite, bioactive glass).

1.4.1. BIOACTIVE, BIORESORBABLE BIOCERAMICS

Bioactive bioceramics have been used clinically since the 1970's [105]. Traditionally, they have been used as bone fillers, but more recently they have been common as implant coatings for their capacity to bond with bone [106, 107]. They can be produced almost completely inert or with varying degrees of interaction with the physiological environment. Bioceramics with a high level of bioactivity are completely bioresorbed by the body, forming products such as silica, calcium and phosphorous. Metallic or polymer surfaces can be rendered bioactive through the incorporation of ceramics or glass-ceramics. Applications of bioceramics are described in Table 1.1.

Bioceramics include calcium phosphates (e.g. hydroxyapatite, tricalcium phosphate), calcium silicates (e.g. wollastonite, hardystonite, sphene) and silica-based bioactive glasses (e.g. Bioglass®). Compared to the more stable hydroxyapatite, calcium phosphates exhibit a greater degree of bioactivity and are completely absorbed into the body [108]. The incorporation of silicon results in a further increase in bioactivity by leading to the formation of Si-OH groups on the surface, thus improves bone bonding by triggering the nucleation and formation of apatite layers on the surface. Silicon can be incorporated into calcium phosphate, and SiO_2 is the network former of silica-based bioactive glasses.

Table 1.1. Features and Applications of Bioceramics.

Ceramic	Features	Applications	Ref
Calcium Phosphates	Low strength, difficult to shape, HA: poor degradation, TCP: degrades in 8-24wks	Implant coatings, bone fillers, experimental wound dressing	49, 106, 109-111
Calcium Silicates	Extremely high bioactivity, poor strength	Experimental implant coatings/bone fillers	111, 112, 114-121
Silica-based Bioactive Glass	Good bond with soft/hard tissues, mechanically weak, low fracture resistance	Root canal therapy, bone fillers, cosmetics, implant coatings (Perioglas®)	107, 113, 122- 127

1.4.1.1. Calcium Phosphates

One of the most popular bioceramics is hydroxyapatite ($Ca_{10}(PO_4)_6(OH)_2$), HA), due to its biocompatibility and having a similar chemical composition as bone mineral. Hydroxyapatite coatings have been used since the late 1980's, and excellent clinical results on total hip replacements 15years+ after implantation have been attained [128]. These coatings remove the need for bone cement, while providing a seal against wear debris. Hydroxyapatite and TiCaP coatings have also been used clinically for coatings for spine implants (e.g. NuVasive®) [129-131]. Fibrous encapsulation was avoided by a particulate hydroxyapatite coating on a nucleus replacement implant (ultra-high-molecular weight polyethylene woven mesh) [130, 131]. This coating encouraged good tissue integration and physiological motion during the first 6 months. However, progressive stiffening occurred as scar tissue calcified to form bone.

1.4.1.2. Calcium Silicates

Calcium silicates ($CaO\text{-}SiO_2$) were developed in the 1990s for biomedical applications, particularly by De Aza and coworkers [112]. They are highly bioactive, with a faster rate of hydroxyapatite formation then glass ceramics. Their bending strength is close to human cortical bone (50-150 MPa). Calcium silicates as yet are not widely used clinically, but due to their high degree of osteoinductivity they have been investigated for their potential as bone fillers, implant coatings and incorporation into tissue scaffolds [112, 132].

1.4.1.3. Bioactive Glasses

Many silica-based bioactive glasses are highly biocompatible, bioactive and biodegradable. The original formulation, 45S5, was based on the SiO_2-CaO-Na_2O-P_2O_5 system. It was developed by Larry Hench in the 1970s and commercialised under the name 'Bioglass®' [3,8].

Bioactive glasses have been used for many years as implant coatings (e.g. for titanium alloys), and shown excellent bonding to both hard and soft tissue without any intervening fibrous layers [107, 112, 127]. In a study by Tomsia [134], a bioactive glass-coated titanium alloy was implanted in a pig bone model for 6 months, and showed the formation of a thin Ti_5Si_3 layer (Fig. 1.11). The bone matrix in the vicinity of the bone-implant interface of the coated implants had changed to mature lamellar-type bone, while the uncoated implants remained with woven-type bone. In addition to improving osseointegration, bioactive glass coatings also improve the corrosion resistance of implants. The role of the coating is twofold: (1) Protect the metal against corrosion from the body fluids, and (2) Protect the tissue from the corrosion products of the alloys [127].

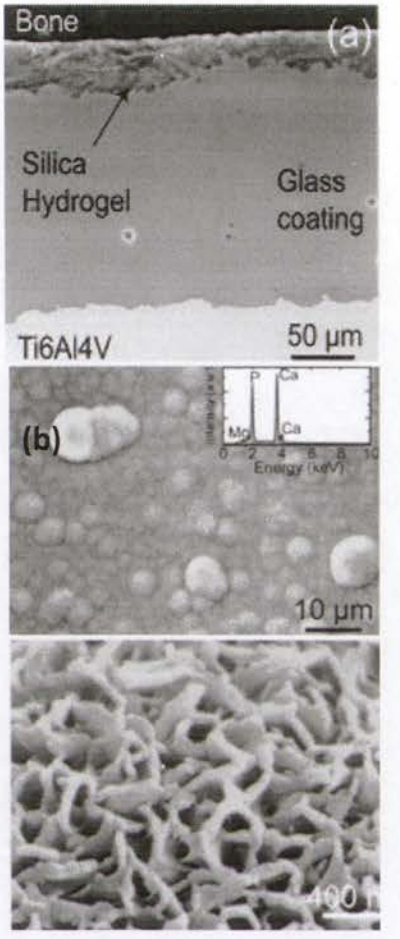


Figure 1.11. SEMs showing: (a) a cross section of a graded glass coating after a 6 month *in vivo* test in the pig model [134] (b) Hydroxyapatite crystals precipitated on a 6P57 bioactive glass coating on titanium alloy, after 30 days soaking in SBF [137].

Bioactive glasses are also widely used for root canal therapy [122, 123] and bone filler [135, 136] (Fig. 1.12).

Bioactive glass granules are available commercially as a synthetic bone graft (Perioglas®, Novabone, US Biomaterials), and can be made into composites using the patient's own bone. The bending strength of bioactive glass is 2-3x less than calcium silicates. The brittleness of bioactive glass has limited its clinical use as a bulk material for bone tissue engineering, although some researchers have developed porous glass scaffolds [138].



Figure 1.12. Filling of a dental socket with bioactive glass [36]

Bioactive glasses also display many properties beneficial for soft tissue regeneration, although little work has been done in this area. The excellent bond which can occur between Bioglass and tissue within a few hours can minimise infection (biofilm) and fibrous capsule formation [53, 127, 139]. Bioglass® increases the bioactivity of surfaces by facilitating deposition of biological molecules and the formation of a silica gel on its surface [3, 8]. The silica gel layer is thought to provide nano-mechanical cues to the approaching cells. This can be used for coating of silicone catheters. For example, Ross and coworkers demonstrated excellent soft tissue adhesion of a Bioglass®-coated silicone tube used for dialysis [53] (Fig. 1.13). Other possible roles for bioactive glasses are in wound repair. In this function, it has been shown to increase wound strength in a canine wound model [140].

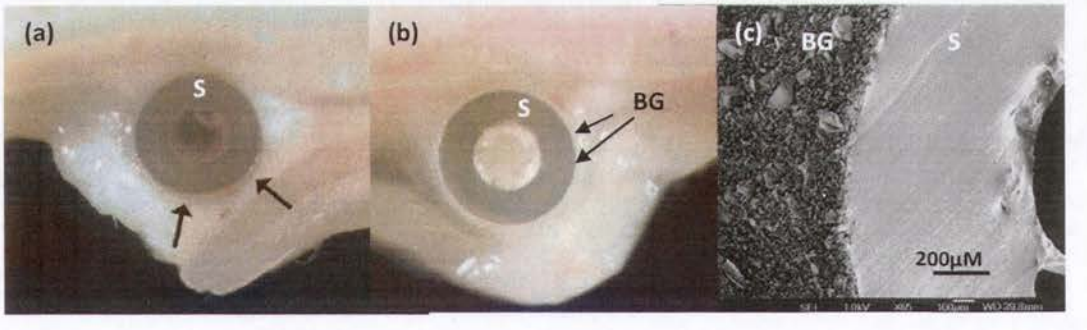


Figure 1.13. Photographs of sectioned full thickness skin demonstrating (a) No adhesion to uncoated silicone tubing (arrows) and (b) good adhesion to bioactive glass-coated silicone. (c) Scanning electron micrograph of the bioactive glass (BG) coated silicone tubing (S) [53].

Bioactive glasses have recently been included in topical cosmetics [141], due to evidence suggesting many benefits to skin. Research has suggested they can encourage vascularisation [84, 86, 142-146], encourage the attachment and proliferation of cells [84, 143, 147-152], increase collagen deposition [147, 153, 154], and also demonstrate antibacterial properties [139, 155-159]. The properties of bioactive glass are further discussed in 4.1.2.

1.4.2. BIOACTIVE POLYMER-COMPOSITES

Polymer-ceramic composites have been used for tissue engineering approaches such as bone fillers, coatings and scaffolds (Fig. 1.14). They are an attractive class of materials due to their biocompatibility, good handling properties, their capacity for long-term drug delivery and their capacity to reproducibly control their physical properties such as stiffness, strength and degradation rate [88]. Properties of biomedical composites are strongly affected by a number of factors [161], some of which are listed:

1. Reinforcement shape, size, and size distribution;
2. Reinforcement properties and volume percentage;
3. Bioactivity of the reinforcement (or the matrix);
4. Matrix properties (molecular weight, grain size, etc.);
5. Distribution of the reinforcement in the matrix; and
6. Reinforcement-matrix interfacial state.

A large number of polymers have been used clinically, which are candidates for inclusion with bioactive ceramics [22, 24, 162, 164]. These are summarised in Table 1.2. Table. 1.3. contains a review of studies which have investigated bioactive glass/polymer composites for tissue engineering.

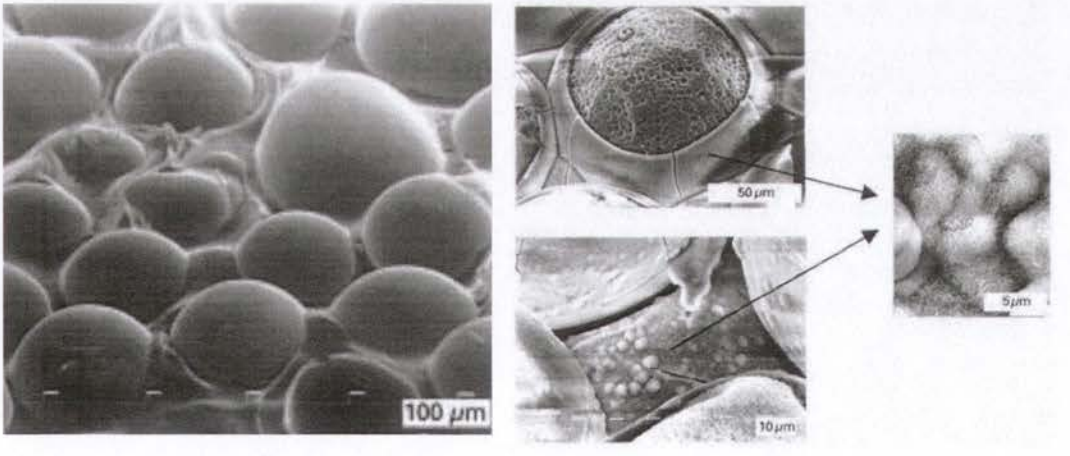


Figure 1.14. (a) 13-93 bioactive glass adherent spheres on a 70:30 P(L/(D/L)LA plate [160]. (b) Formation of an apatite layer on the polymer plate surface adjacent the microspheres after 3 days in PBS.

Table 1.2. Features and clinical applications of polymers [165].

	Polymer	Features	Applications	Ref
Permanent	Silicone		Breast implants, Subdermal contraceptive devices (Norplant®, Jadelle®)	26, 166
	Silk	Bacterial adherence, chronic inflammation/fibrosis	Sutures	118, 167
	Polyethylene	Permanent	Eye implant	7, 169
	PVA	Permanent, fibrous encapsulation	Negative pressure wound therapy foam, subcutaneous research models	170-172
Bioabsorbable	PLA	Slow degradation, can persist in body	Screws, nails, pins, prostatic stent, bone cement plug (Fixsorb®, Neofix®, Bio-Tenodesis®, Bio-Corkscrew®, SmartNail®, BioScrew®, SmartTak®, Bio-statak®)	27
	PGA	Fast degradation, rapid loss of strength, aggravated inflammatory response	Sutures, hernia mesh, prostatic stent (Biofix®, Dexon™, Bondek®, Valtrac™)	68
	PCL	High extensibility, low melting temperature, long degradation rate	Sutures, orthopaedic fixation, bony defects, craniofacial, drug delivery, staple	58, 71, 162, 173-180
	PDS		Sutures	102
	PDLGA		Suture, drug delivery, maxillofacial- screws, pins, meshes, periodontal, orthopaedic (Polysorb™, Lactosorb®, Vicryl- suture, mesh, Phusisline®, ResorPin®, Polypin®)	102, 101
	PDLCL	Good extensibility	Nerve regeneration, non-adhesive foil (Neurolac®, Polyganics, mesofol)	103
	PGCL		Sutures (Monacryl®)	165
	PCL-based composites		Tissue reinforcement, torn tendon replacement patch, interpositional spacer in osteoarthritis, root canal filling (Artelon® Sportsmesh™, Artelon® CMC spacer Arthro, Resilon™)	165

Table 1.3. Review of relevant polyester/bioactive glass composites and related studies.

Study	Composition	Form	Test	Ref
Vitale-Brovarone 2008	Novel glass composition	Sintered powder scaffold	Synthesis	181
Chouzouri 2007	PCL/45S5	Extruded nonporous composite	SBF soaking	182
Fu 2007	13-93	Scaffold (sintered particles)	SBF soaking	183
Jones 2006	70%SiO2, 30mol%CaO glass	Scaffold (sintered particles)	SBF soaking	138
Boccaccini, 2007	45S5	Scaffold (sintered powder)	SBF soaking	184
Brovarone 2006	PE/BG	Scaffolds	SBF soaking	185
Rainer 2008	PU/BG	Foam (polymer template)	SBF soaking	186
Boccaccini 2003	PLGA/45S5	Foam (TIPs)	PBS soaking	187
Bil 2007	PU/PDLLA/BG	Foam	SBF soaking	188
Boccaccini 2003	PDLLA/45S5	Foam (TIPs)	PBS soaking	189
Roether 2002	PDLLA/45S5	Foam (TIPs)	SBF soaking	190
Marquet 2003	PDLLA/45S5	Foam (TIPs)	PBS soaking	191
Niemela 2005	PDLA/1393	Composite rods	PBS soaking	192
Couto 2009	Chitosan/BG	Injectable hydrogel	SBF soaking	193
Rich 2002	PCL/DLLA/S53P4	Composites	SBF soaking	194
Li 2008	PCL/BG	Foam (particulate leaching)	SBF soaking	195
Jaakkola 2004	PCL/PDLA/S53P4	Composite disks	SBF soaking	196
Maquet 2004	Poly(alpha-hydroxyacid)/45S5	Foam (TIPs)	PBS soaking	197
Zhang 2002	Cellulose acetate/BG	Foam (phase separation)	SBF soaking	198
Haimi 2009	Zn-containing glass	Fibers (sintered)	Human Adipose Stem Cells	199
Brown 2008	13-93	Fibers (sintered)	Osteoblasts	200
Levy 2007	45S5	Powder	Mouse calvarian cells	201
Day 2004	45S5	Powder	Mouse Fibroblasts	86
Gan 2000	45S5	Powder	Nucleus Fibrosis Cells	202
Gao 2001	53S or 58S	Plates	Osteoblasts	203
Alcaide 2010	85S	Powder, or conditioned media	Osteoblast, fibroblast, lymphocyte	204
Bitar, 2008	Iron-phosphate glass	Fibers	Osteoblasts, fibroblasts	205
Wu 2010	Silk/BG	Foam (polymer template)	Human osteoblasts	118
Yeh 2009	PCL	Foam (precipitate casting)	Human foreskin fibroblasts	206
Leu, 2008	Collagen/45S5	Hydrogel sponge	Endothelial cells	143
Vance 2004	PLGA, PU, PCL	Vacuum dried textured films	Fibroblasts	207
Tsigjou 2007	PDLLA/45S5	Composite films	Human fetal osteoblasts	208
Day 2005	PDLLA/45S5	Compression Molding or TIPS foams	Mouse Fibroblasts	84
Blaker 2003	PDLLA/45S5	TIPS foams	Human Osteosarcoma	209
Helen 2007, 2008	PDLLA/45S5	TIPS foams	Human Annulus Fibrosis Cells	154, 210
Gough 2003	PDLLA/45S5	TIPS foams	Osteoblasts	211

Table 1.3 (Cont...).

Study	Composition	Form	Test	Ref
Verrier 2004	PDLLA/45S5	TIPS foams	Human Lung Carcinoma/ Osteosarcoma	212
Boccaccini 2005	PLGA/45S5	Freeze Dried Foam	Mouse Fibroblast	153
Keshaw 2009	PLGA/45S5	TIPS Microspheres	Myofibroblasts	213
Yao 2005	PLGA/45S5	Scaffold (sintered microspheres)	Marrow stromal cells	214
Lu 2003	PLGA/45S5		Human Osteosarcoma	215
Day 2005	PLGA/45S5	Disks	Mouse Fibroblasts	84
Day 2005	PLGA/45S5	Microspheres	Myofibroblasts	84
Haimi 2009	PLA/BG or PLA/TCP	Scaffold	Human Adipose Stem Cells	198
Kim 2008	PLA/BG	Dense composites (electrospun nanofibers)	Osteoblasts	216
Mo 2006	PCL-PGLA	Braided scaffold	Fibroblasts	217
Lee 2008	PCL/BG	Thin membrane	Murine Osteoblasts	147
Jo 2009	PCL/BG	Electrospun nanofibers	Osteoblasts	150
Yun 2010	PCL/BG	Foam (porogen leaching/rapid prototyping)	Human Bone Marrow Stromal Cells	218
Yun 2007	PCL/BG	Foam (porogen leaching/rapid prototyping)	Osteoblast	148
Cannillo 2010	PCL/45S5	Foam (porogen leaching)	Bone Cells (unspecified)	219
Whitehead 2008	PCL/silicon	Foam (porogen leaching)	Human Kidney Fibroblasts, Bone Marrow-derived MSCs	149
Wei 2009	PCL/wollastonite	Foam (porogen leaching)	Osteoblast	220
Lu 2009	PCL	Rapid Prototyping (sucrose porogen)	Endothelial hybridoma & osteoblasts	221
Lowery 2010	PCL	Fibers (electrospun)	Human Dermal Fibroblasts	222
Chen 2004	PCL/silk	Scaffold (porogen leaching)	Fibroblasts	223
Bretcanu 2009	P3H8/45S5	Bioglass scaffolds (polymer template)	Human Osteosarcoma	224
Bretcanu 2009	P3HB+PEO/45S5	Nanofibrous polymer (electrospun) coating on Bioglass®based pellets	Osteoblast	225
Miao 2008	HA/TCP/PLGA	PLGA-coated ceramic scaffolds (polymer template)	Bone Marrow Stem Cells	226
Wheeler 2000	58S, 77S, 45S5	Granules	Rabbits- bone	227
Pohunkova 1995	45S5, HA or shredded bone, with collagen	Hydrogel	Rats, guinea pigs- bone	228
Ross, 2003	45S5 coated silicone	Tube	Rats- subcutis	53
Ekholm 2005, Tommila 2008	HA* coated cellulose	Foam (hydrogel porogen)	Rats- bone	229, 230
Day 2005	PDLG/45S5	Foam (TIPs/compression molding)	Rats- subcutis	84
Day 2004	PGA/45S5	Knitted fibrous mesh	Rats- subcutis	86
Keshaw 2009	PLGA/45S5	Microspheres	Rats- subcutis	213
Shin'oka 2005	PLCL	Porous tube	Canine, human- artery	231
Lam 2009	PCL or PCL/TCP (Osteopore)	Scaffolds (rapid prototyping)	Rabbit- bone	83
Jo 2009	PCL/BG	Nanofibers (electrospinning)	Rats- bone	150
Acharya 2008	HA/BG	Bulk Composite	Human Clinical Trial	232

Table 1.4 lists some of the common polymers and their physical properties. These polymers will now be discussed, with the focus on PLA and PGA, and then PCL.

Table 1.4. Properties of popular bioabsorbable polyesters [233].

Polymer type	*Melting point (°C)*	*Glass trans. temp. (°C)*	*Degration time (months)*[a]	*Density (g/cm^3)*	*Tensile strength (MPa)*	*Elongation, %*	*Modulus (GPa)*
PLGA	Amorphous	45–55	Adjustable	1.27–1.34	41.4–55.2	3–10	1.4–2.8
DL-PLA	Amorphous	55–60	12–16	1.25	27.6–41.4	3–10	1.4–2.8
L-PLA	173–178	60–65	>24	1.24	55.2–82.7	5–10	2.8–4.2
PGA	225–230	35–40	6–12	1.53	>68.9	15–20	>6.9
PCL	58–63	−65	>24	1.11	20.7–34.5	300–500	0.21–0.34

[a]Time to complete mass loss. Time also depends on part geometry.

1.4.2.1 PLA & PGA Based Polyesters

Among the most popular bioabsorbable polymers for tissue engineered scaffolds are poly(lactic acid) (PLA), poly(glycolic acid) (PGA) and their poly(lactideco-glycolide) copolymers (PLGA) [6]. In the 1970's, the first FDA approved biodegradable suture (PGA) was placed on the market, by the name of DEXON® [24].



Figure 1.15. PLA particles from a biodegradable bone screw found in an osteolytic lesion 52 months after implantation [27].

Despite their utility, degradation results in the generation of acidic species, which potentially create local inflammation in tissues and initiate enzyme hydrolysis [14, 27, 28, 183, 234-236], which interferes with healthy wound healing. In addition, these polymers can initially be extremely rigid, and so do not often match the modulus of soft tissues. Despite these drawbacks these synthetic polymers remain a recurring feature in tissue engineering strategies.

Polymers based on PLA and PGA release glycolic and/or lactic acid as they degrade. Lactic acid particulates have been found in the body several years after implantation, particularly when used in bulk form [27, 28, 237, 238]. Fig. 1.15 shows PLA particles which were found in an osteolytic lesion 52 months after the implantation of a PLA bone screw [27]. Bergsma and coworkers [28] found swelling due to PLLA remnants which were surrounded by a dense fibrous capsule 3yrs post-implantation. Crystal-like PLLA was observed within the cytoplasm of

various cells. This engulfment or foreign-body reaction can be a result of overload of polymeric debris rather than an immunological response to the polymer chemistry.

PGA is amongst the least stable of the bioabsorbable polymers, taking as little as 1 week to degrade. Although this property has been utilised to increase the degradation rate of lactic acid-based materials [238], PGA often causes an aggravated inflammatory response. For example, PGA has been reported to contribute to synovitis developing in nearby joints [239, 240]. This fast degradation rate also makes PGA an unsuitable candidate for drug delivery [24].

Poor long-term tissue responses to rapidly degrading or persistent biodegradable polymers such as these have led to their slow acceptance. Complication rates of 7–48% for biodegradable plates and screws have been reported [241]. Frequently, these cases have necessitated incision and drainage and/or surgical debridement with ultimate removal of the material [237]. The precise nature of these soft tissue reactions has not been formally determined. Although poly(a-hydroxy) esters were assumed to completely degrade via nonspecific hydrolytic scission of their ester bonds to carbon dioxide and water [242], recent findings have shown the contribution of other factors, including pH, heat and free radical attack [243]. Further, the assumption that all poly(a-hydroxy) esters will completely degrade does not appear to be true in all cases.

To address the complications caused by acidic byproducts, Wang and coworkers [44, p525] suggest the inclusion of biocompatible buffers with low aqueous solubility to react with any evolving polymer acids thus preventing adverse decreases in pH [104]. Their studies showed that PLGA 50:50 polymer was found to drop pH sharply in an *in vitro* experiment to pH=2.6. Addition of 50% calcium carbonate filler provided a polymer of reasonable strength whilst ensuring the *in vitro* pH did not fall below 5.7 over the period studied (2250 hrs). In another *in vitro* experiment, Li and coworkers [133] found the pH of PLGA scaffolds to fall to 4.3 in 8 weeks. After the addition of hydroxyapatite, the pH exhibited a linear decrease from 7.4 to 5.6. However, with the addition of wollastonite or 45S5 Bioglass®, the pH was maintained between 7.7-7.3 and 8.15-7.1 respectively. This corresponded to acceleration in scaffold weight loss and initial water absorption. This effect was due to the increased alkalinity of wollastonite/Bioglass® compared to hydroxyapatite. Fig. 1.16. demonstrates the increase in degradation which was observed for the Johnson and Johnson Biocryl Rapide bone fixation material (PLGA/TCP) as compared to pure PLLA [238].

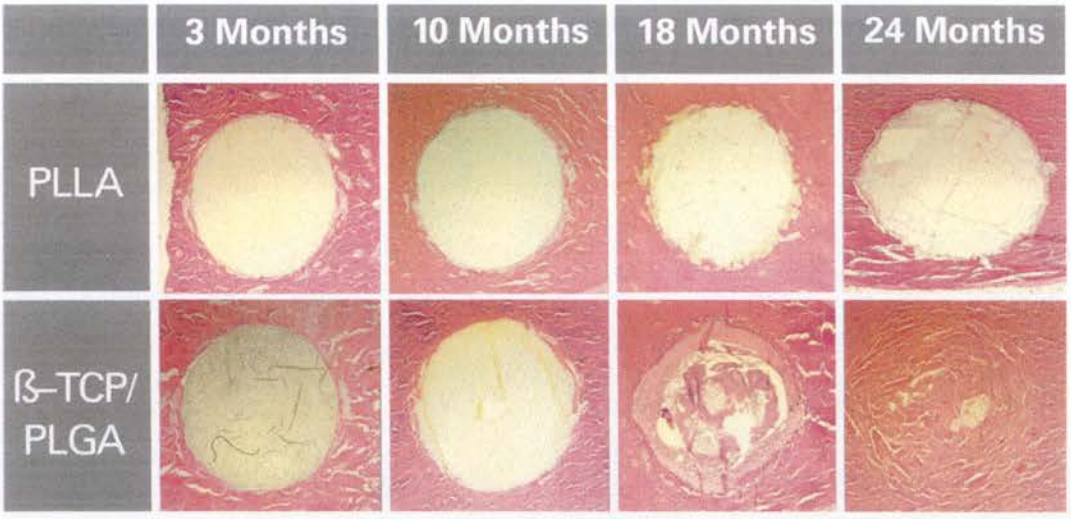


Figure 1.16. Comparison of degradation of PLLA and Biocryl Rapide (PLGA/TCP) devices in bone [238].

1.4.2.2. Poly-e-caprolactone

PCL is a well-established polyester with slow degradation rate and excellent elongation (300-500%) [175, 245]. Being thermoplastic in nature, PCL may be hot-formed with great ease into desired shapes by moulding, extrusion, solvent processing, or 3D porous matrices. PCL is an ideal polymer for a variety of processing techniques, due to its low melting point (59-64°C), ease of dissolution in a variety of solvents and excellent blend compatibility [165]. It is a semi-crystalline polymer having a glass transition temperature of -60°C. PCL displays a higher level of hydrophobicity than PGA and PLA, which contributes to its reduced degradation rate. Degradation of PCL is via the ingress of water and lipids which leads to swelling and hydrolysis, and subsequent surface erosion. Metabolism is via the action of biological enzymes and cells such as macrophages [246]. The sole metabolite of PCL is hexanoic (caproic) acid, which is an essential fatty acid found in fats and oils which is eliminated by the body [247].

PCL gained popularity in the 1970's and 1980's as a drug delivery device. For example, delivery of the hormone levonorgestrel from Capronor subdermal capsules [248]. Recently Sun and coworkers have developed a 2-year contraceptive device comprising PCL-based compounds filled with levonorgestrel powder which was approved for phase II clinical trials in China [249]. Preclinical studies using rats and dogs demonstrated good release kinetics of levonorgestrel from this device, with no adverse effects. After implant retrieval at 2 years the implant was physically stable with an associated drop in the molecular weight of the polymer from 66,000 to 15,000 Da [250].

PCL has been widely used for tissue regeneration, and recently in maxillofacial applications [58]. Burrplug™ (Osteopore International Pty, Ltd, Singapore), shown in Fig. 1.18a,b, is a rigid, isotropic mesh which, over 5 years of clinical use, has shown excellent bone ingrowth for repair of skull defects after brain surgery [58, 70, 71]. This technology was developed by the National University of Singapore, as a "platform" from which various implants can be developed. More recently, the company commercialised Osteomesh™ (Fig. 1.18c), a similar matrix for repair of soft tissue in the orbital floor of the eye [251].

PCL has also been incorporated into sutures. Examples include Monosyn® (Braun) [252], a - glycolide-trimethylene carbonate-caprolactone tri-composite P(GA/TMC/CL) [253], and Surucryl® (SURU International) [254] (Fig 1.18d), PCL Calcium Stearate-coated PGA. In Europe, PCL is in clinical use as a degradable staple for wound closure [255]. Monosyn® retains 50% of knot tensile strength after 14 days, and experiences complete mass absorption in 60-90 days [252]. Surucryl retains 81% of its strength at 14 days. Recently, PCL/TCP matrices [110] and nanofibrous PCL [256, 257] have been investigated for wound dressings, and for release of antibacterial agents [80, 258, 259].

Polyesters can be readily polymerized with PCL to improve biocompatibility, stability, extensibility, lubricity and handling [209, 231, 234, 260-262]. Barralet *et al.* demonstrated that PGA scaffolds degraded within 28 days *in vitro*, while PCL coated scaffolds remained *intact* beyond 3 months [260].

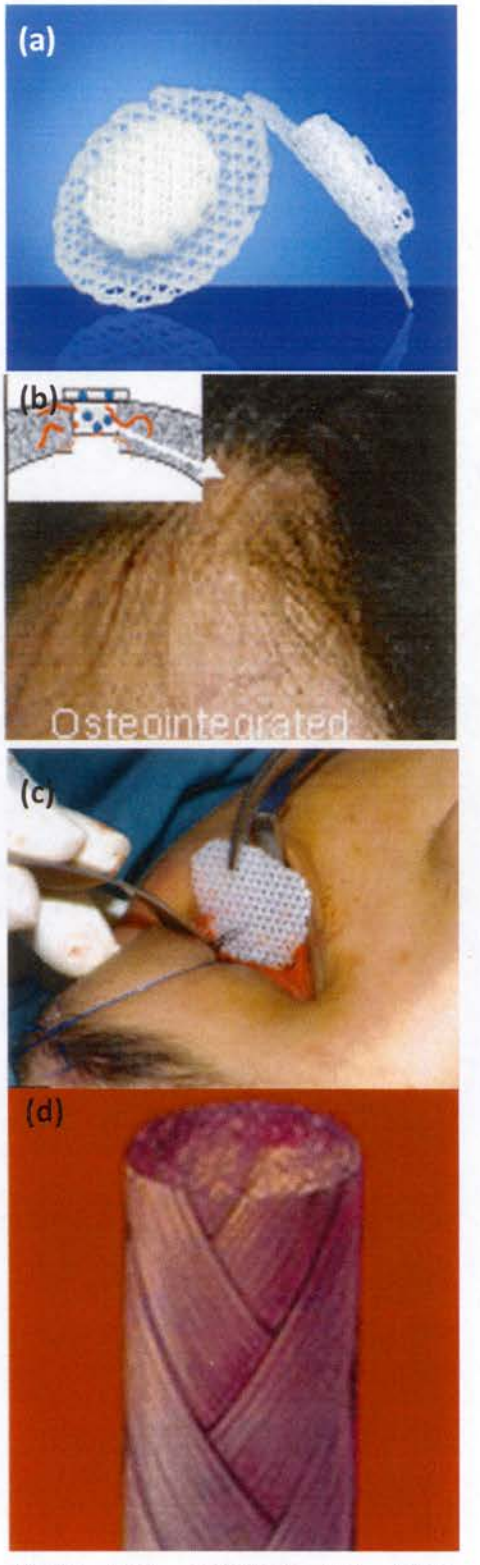


Figure 1.18. Osteopore PCL mesh products: (a,b) Skull burrplug (c) Osteomesh orbital implant [251], (d) PCL-coated braided PGA suture Surucryl [254].

Another study by Sung and coworkers [234] has demonstrated an increase in cell viability, cell mobilisation and angiogenesis for microporous PCL scaffolds as compared to PLGA scaffolds, both *in vitro* and *in vivo*. This was attributed to both the rate and the nature of the degradation products. The authors of this study concluded that *in vitro* cell viability and *in vivo* angiogenesis are inversely proportional to degradation rate. Addition of 5 wt% PCL to a PLA scaffold increased the strain to failure from <25% to more than 200% [261]. Shown in Fig. 1.19, a PGCL copolymer designed for blood vessel engineering showed a similar improvement in extensibility [262].

The scaffold also displayed excellent cyclic properties [262]. Poly(lactide-co-ε-caprolactone) co-polymer (PLCL) has shown an excellent response in clinical studies for tubular pulmonary artery scaffolds- an application where elasticity is particularly important [209]. An excellent recovery was observed for 22 patients implanted with scaffolds which had been pre-seeded with bone marrow stem cells. In a further study, urinary tract stromal cell attachment and proliferation were significantly enhanced on PCL scaffolds compared to PLGA [209]. This was attributed to the decreased modulus of the PCL scaffolds (2 MPa vs 4 MPa) being closer to the modulus of native bladder tissue [209].

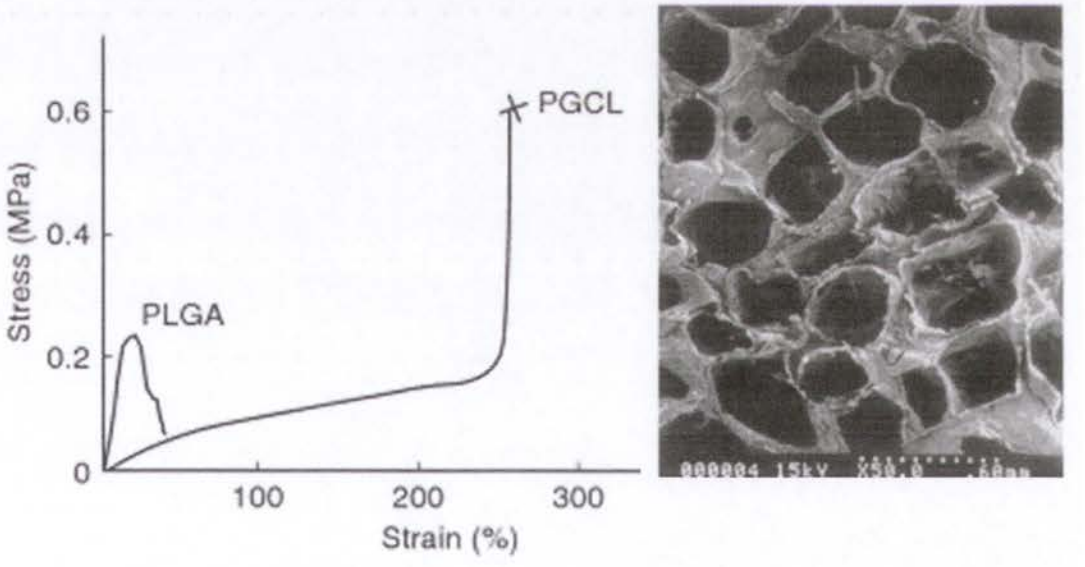


Figure 1.19. Representative stress-strain curves from PLGA and PGCL scaffolds. Inset: PGCL scaffold morphology [262].

1.5. NATIVE TISSUE ARCHITECTURE AND FUNCTION

Understanding the biology and architecture of soft tissues is important for scaffold development. In the following sections the anatomy and physiology of cartilage and skin tissues studied for repair in this thesis will be described in detail.

1.5.1. CARTILAGE ANATOMY, PATHOLOGY AND PHYSIOLOGY

1.5.1.1. Anatomy and Physiology of Cartilage

Cartilage (Fig. 1.20) is a flexible connective or articular tissue found in many areas of the human body, including joints between bones, the rib cage, the nose, the bronchial tubes and the intervertebral disks. Cartilage consists of cells (chondrocytes) suspended in a collagen matrix. Chondrocytes are small cells which produce the components of cartilage: the matrix material and the fibres. They are derived from mesenchymal stem cells, as are fibroblasts.

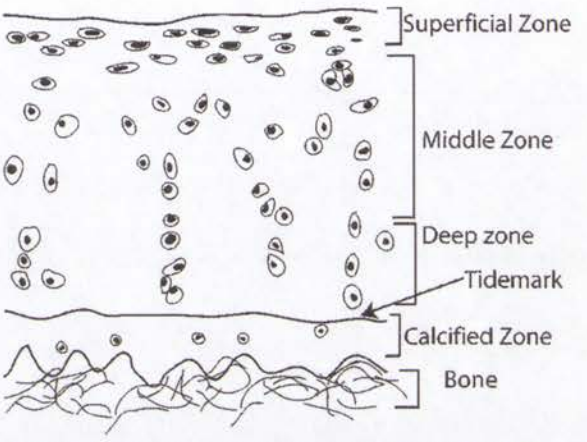


Figure 1.20. Schematic diagram of the different zones of hyaline articular cartilage [263].

In some cases, chondrocytes are thought to have the potential to change phenotype between the two. As the chondrocytes secrete matrix material, they become walled off into small chambers (lacunae). The cells are grouped into small clusters, consisting of several generations of daughter cells which arose from the same chondroblast progenitor cell [263, 264].

Cartilage ECM is a homogenous material principally composed of proteoglycans, most notably aggrecan containing several glycosaminogycans (GAGs; hyaluronic acid, chondroitin sulfate and keratin sulfate) and chondronectin [263]. This viscous, hydrated matrix provides osmotic resistance so cartilage is able to absorb compressive forces [265]. The fibrillar component of cartilage is largely a meshwork of collagen II, which provides the cartilage with shape retention and tensile strength. Dynamic compression of cartilage actually encourages ECM production [266]. Cartilage has a limited ability to regenerate due to its avascularity, low mitotic activity, and the inability of chondrocytes to migrate to the site of injury due to suspension in the matrix [267]. Nutrient diffusion in articular cartilage occurs through the matrix- from synovial fluid and the subchondral bone. This diffusion is facilitated via a pumping action generated by compression of articular cartilage or the flexion of the elastic cartilage.

The osteochondral junction (cartilage-bone interface) has a structure which varies in chondrocyte organization and phenotype [264, 266] (Fig. 1.17). Near the surface, in the superficial zone, chondrocytes are densely populated and have relatively low metabolic rates, but uniquely secrete molecules that may aid in boundary lubrication, including proteoglycan 4. Deeper into the tissue, in the middle and deep zones, chondrocyte density decreased, while biosynthesis rates of matrix molecules, including collagen II and aggrecan increase.

with the zonal cellular variations are changes in the content, organization and mechanical properties of the ECM [268]. Proteoglycan content increases with depth and is primarily responsible for the depth-increasing compressive modulus. Collagen content remains fairly constant with depth, but fibre orientation varies from parallel to the surface in the superficial zone, to perpendicular in the deep zone. Similar structural and compositional gradients are also present within the intervertebral disks, knee meniscus and ligament/tendon to bone interfaces [269].

There are three main types of cartilage as described below.

Hyaline, also known as articular cartilage, accounts for the majority of the cartilage present in the joints. Cartilage is responsible for providing lubrication, and reducing friction at joint surfaces.

Elastic cartilage contains a higher proportion of elastin fibres, and is therefore more flexible than other types of cartilage. This type of cartilage provides a balance between structure and flexibility, and is found in the outer ear, larynx and Eustachian tubes.

Fibrocartilage is the strongest and most rigid type of cartilage. It contains more collagen than hyaline cartilage, particularly type I collagen, which is tougher than type II. Fibrocartilage appears in high stress areas such as the intervertebral disks, temporomandibular joint, knee meniscus and connecting tendons and ligaments to bones. Damaged hyaline cartilage is often replaced with fibrocartilage, which unfortunately does not bear weight as well due to its rigidity. When compared to hyaline cartilage, fibrocartilage has low glycosaminoglycan content, a low compressive modulus, and a high tensile modulus. Fibrocartilage consists of a mixed cell population of fibroblasts and cells similar to chondrocytes, which predominantly secrete type 1 collagen [263].

1.5.1.2. Cartilage Pathology

Articular cartilage can be damaged due to trauma or disease. Initial defects can lead to further degeneration of the joint. The fibrocartilage-like scar tissue which forms is mechanically inferior to the native articular cartilage [270]. Two common conditions affecting the cartilage are: (1) rheumatoid arthritis- an autoimmune, inflammatory disease and (2) osteoarthritis- a degenerative joint disease, which results in the destruction of the ECM (Fig 1.21). During osteoarthritis, chondrocytes lose their differentiated phenotype, change their gene expression pattern and undergo localised cell death and degeneration. Surrounding tissues, such as the synovial capsule and membrane and the subchondral bone are involved in the progression of the disease. Joint destruction is accelerated through inflammation and stiffening within the joint capsule [272]. Osteoarthritic joints are characterised by fibrillation, fissuring and loss of proteoglycan 4 from the surface of the cartilage. The chondrocytes increase synthesis of collagen I and III, forming fibrocartilage [273]. Some researchers postulate that a deficiency in the subchondral circulation can be responsible for the development of osteoarthritis [274]. This is difficult to study due to the slow progression of degenerative changes during osteoarthritis.

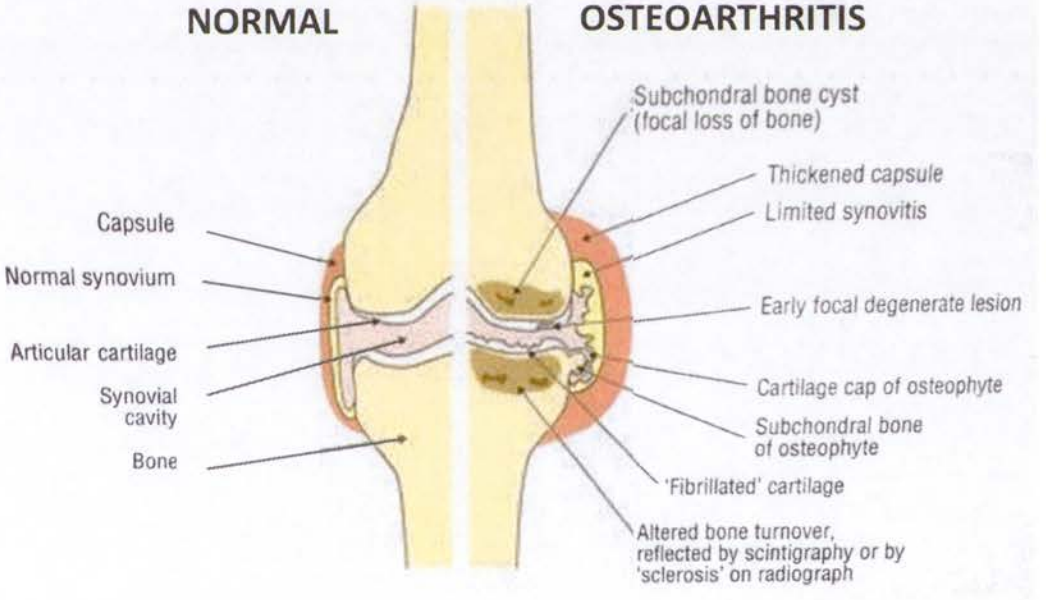


Figure 1.21. Characteristics of a normal knee joint compared to joint degeneration due to osteoarthritis [271].

Osteoarthritis affects as many as 3 million people in Australia (representing about 15% of the population) and 21 million people in the USA, resulting in over 50% of the total joint replacements, with societal costs of greater than US $15 billion per annum [275]. The most prominent risk factor for osteoarthritis is simply age, and so any treatment solution must

consider the aged cells which do not respond to the mechanical, inflammatory and traumatic assaults as well as their juvenile counterparts [276]. The composition of the ECM is known to change with age and with diseases such as arthritis. This affects the rate and characteristics of bone turnover.

1.5.2. SKIN ANATOMY, PHYSIOLOGY AND PATHOLOGY

1.5.2.1. Anatomy and Physiology of Skin

The skin, depicted schematically in Fig. 1.22), is the largest organ in the body, with a surface area of 1.5-2m^2 [277]. Skin plays a critical role in the sustenance of life through regulation of water and electrolyte balance, thermoregulation, and by acting as the body's first barrier to external impurities including micro-organisms.

The skin consists of three layers, the epidermis, dermis and hypodermis. The epidermis is primarily composed of keratinocytes which form a stratified squamous epithelium. Beneath the epidermis lies the basement membrane and the dermis, which consists of the papillary dermis and the deeper reticular dermis. The reticular dermis provides the skin with strength, elasticity and flexibility, due to a dense meshwork of thick collagen and elastic fibres. The hypodermis (or subcutis) layer, beneath the dermis, consists primarily of adipose, or fat tissue.

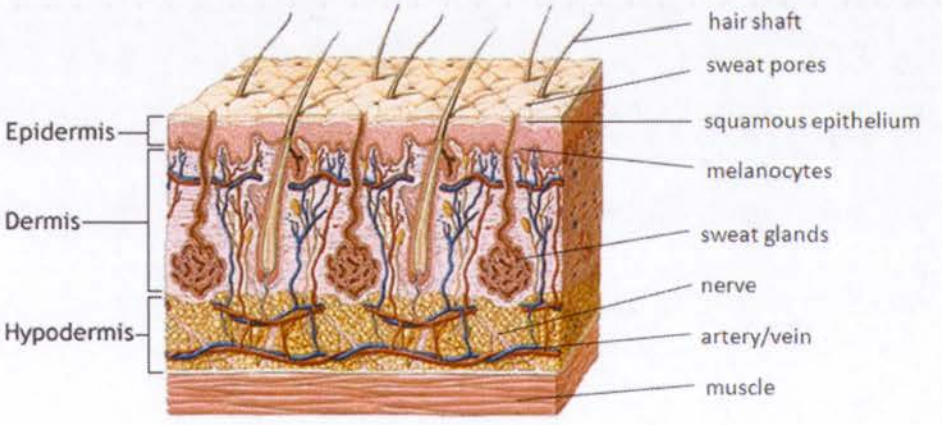


Figure 1.22. The complex structure of skin [278].

The skin is a complicated organ containing many specialised cells and structures. Immune cells (such as Langerhan cells) in the epidermis alert the adjacent keratinocytes and nerves to perturbations in the cutaneous environment, such as trauma, ultraviolet radiation, toxic chemicals and pathogenic organisms. Hair follicles are an important source of keratinocytes during reepithelialisation of severe wounds. The dermis provides connective tissue which supports an extensive vasculature, lymphatic system and nerve bundles [277].

1.5.2.2. Skin Pathology

When the skin barrier is disrupted its {1.8} necessary functions are no longer adequately performed. It is therefore vital to restore its integrity as soon as possible. A wound is defined as a break in the epithelial integrity of the skin. However, the disruption could be deeper, extending to the dermis, subcutaneous fat, fascia, muscle or even bone. Skin can be lost due to burns, ulceration, postsurgical and posttraumatic wounding. A lack of sufficient donor tissue and the high cost of bioengineered skin mean there is a need for readily available and cost-effective synthetic skin grafts.

Burns

Burns can occur due to contact with flame, liquid, hot surfaces, chemicals, electricity or harmful sun rays. They are classified according to the depth of tissue necrosis experienced (Fig. 1.23). First degree burns cause damage to the epidermis, and usually heal naturally. Second degree burns are more severe, causing damage to both the epidermis and the dermis. Treatment is usually by an occlusive dressing or a skin substitute, in order to maintain a moist surface layer. Third degree burns are very serious, resulting in damage to the deep dermal layer, blood vessels and nerve endings. Skin grafts are required for these injuries. In the meantime, a topical antibacterial cream and/or a temporary skin (natural or artificial) covering is vital to reduce the risk of infection and prevent moisture loss [279].

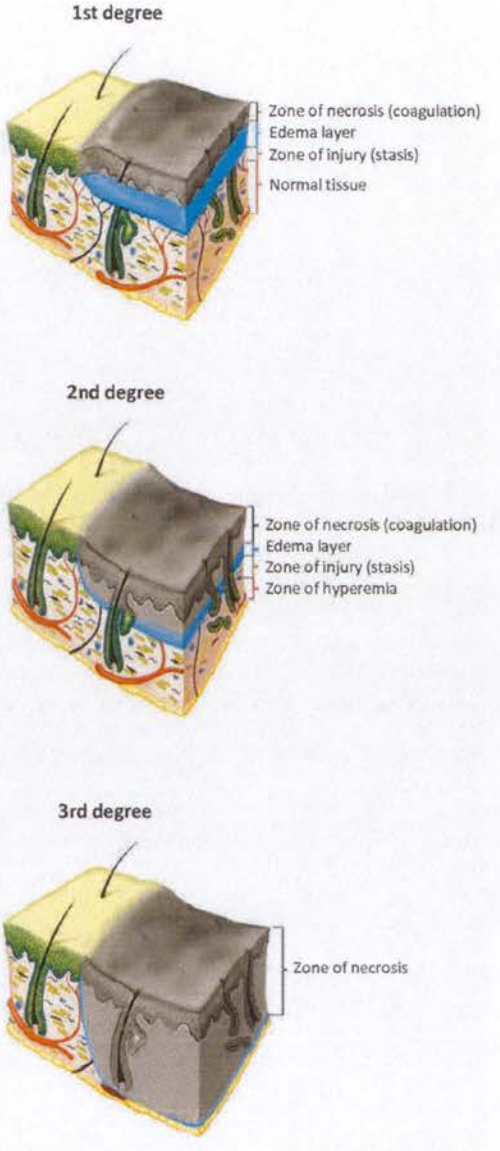


Figure 1.23. Classification of burns according to depth of tissue necrosis [279].

1.5.2.3. Skin Ulceration

Skin ulcers (refer Fig. 1.24) are persisting wounds commonly found on the foot or lower extremities of elderly persons or patients with diabetes. Other underlying conditions which can predispose a patient to ulceration include infection, deep venous thrombosis, osteoarthritis, rheumatoid arthritis, progressive arterial disease or tumours. Skin ulcers can be shallow and broad, or deep with a convoluted structure. Ulcers can easily become infected and an antibiotic-resistant biofilm can develop. If not treated promptly, gangrene can spread and limb amputation can be the only suitable treatment option [280, 281].

Diabetic patients are at high risk of ulcer development due to a combination of several risk factors, including abnormal cellular/inflammatory pathways, peripheral neuropathy and vascular disease/tissue hypoxia [282]. Chronic ulcers can also be induced by concentrated pressure on the body when a patient is stationary for prolonged periods. An aging population where the incidence of diabetes is increasing creates an environment where effective solutions for treating chronic ulcers are needed [283, 284].



Figure 1.24. The appearance and structure of a chronic skin ulcer [285].

1.5.3. MECHANICAL PROPERTIES OF NATIVE TISSUE

Tissues display a variety of tensile and compressive properties (Table 1.5). While bone is extremely stiff (Modulus:20-500 MPa), connective tissue found beneath the skin are far softer (Modulus: 2.75 kPa). ECM of skin also shows high ultimate strain. A single collagen fibre has the capacity to strain 50%, while fibrous ECM will strain to an even higher degree [286].

Table 1.5. Tensile properties of native tissues.

Tissue Description	Elastic Modulus	Tensile Strength	Ref
Skin (rat) (low/high strains)	4.8/240kPa	-	[287]
Subcutaneous connective tissue (rat)	2.75kPa	-	[288]
Knee Articular Cartilage (human)	2.1-11.8MPa	-	[289]
Bladder (human)	0.25MPa	-	[290]
Cartilage (human)	0.7-15.3MPa	3.7-10.5MPa	[291]
Ligament	65-54.1MPa	13-46	[292]
Cortical bone	20-500MPa	60-160	[293]

1.6. SCAFFOLD STRUCTURE AND FACTOR DELIVERY

1.6.1. VASCULARISATION OF SCAFFOLDS

Vascularisation of tissue is important to facilitate the delivery of nutrients, oxygen and minerals, and the removal of waste products, cell debris and biomaterial degradation products. Vascularisation improves tissue strength [294] and is important in reducing fibrous tissue formation which can lead to scarring [295]. Vascularisation of thick tissue engineered constructs remains a major challenge in the tissue engineering field [296]. Due to difficulties overcoming this obstacle, most soft tissue engineered constructs which are used clinically are either thin (heart valves, blood vessels), or avascular (cartilage, spinal disk) [297]. Nutrient transfer through such constructs must be facilitated by diffusion and mechanical actuation of the construct.

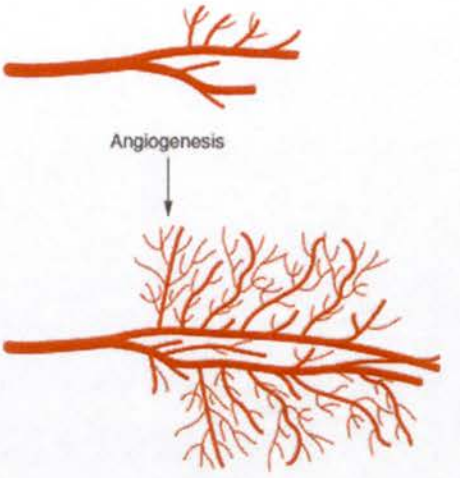


Figure 1.25. Angiogenesis is a process of capillary sprouting [335].

There are two mechanisms of vessel development; (1) angiogenesis- the formation of new blood vessels from existing ones, driven by endothelial cell proliferation and migration and (2) vasculogenesis- the formation of blood vessels de novo. Commonly both these processes are incorporated in the term 'angiogenesis'. Rapid angiogenesis is important for early stages of healing and long-term tissue survival for all tissue types, including bone, skin, muscle, ligaments and particularly adipose tissue [14].

Strategies to improve *in vivo* vascularisation and tissue integration have generally included incorporation of growth factors and/or supplementing with pre cultured cells into tissue engineering models, which have shown some success and will be discussed in detail later in this section [152, 298]. However, the importance of the physical structure, chemical composition and degradation rate of the scaffold itself are often underestimated. Ideally, vascularisation could be achieved without the need for additional growth factor delivery. The use of the angiogenic growth factor FGF has a risk of encouraging the progression of lung cancer [299].

Several studies have reported vessel formation inside porous, polymer scaffolds [7, 14, 58, 62, 68, 83, 84, 86], as further reviewed in section 6.1.3. Often the vascularisation which is reported

in studies is actually in the tissue surrounding the scaffold, rather than throughout the pore network [84]. Generally, vascularisation is more likely to occur in scaffolds with large pores (>350 μm), good pore interconnectivity and slow degradation rates. Most of the synthetic scaffolds which have reported good vascularisation have been rigid anisotropic scaffolds synthesised using rapid prototyping techniques [18, 58, 71]. Occasionally, vascularisation has been reported in softer, more elastic scaffolds using the Thermally Induced Phase Separation process or porogen leaching [14]. However, these vessels were limited in size and did not form rapidly.

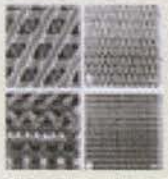
1.6.2. SCAFFOLD FORM

Healthy tissues are composed of viable cells held within a supportive matrix of proteins and circulating fluids. The ECM is an important component that acts to space and suspend, connect and transfer mechanical forces, conduct signals and cells, allow perfusion, facilitate growth and repair.

Table 1.6 summarises a range of products and prototypes that are gauged at physically supporting cells in a similar manner to natural matrix and tissues. Microspheres or beads have been excluded as a class as they generally do not act as connective matrix. Beads or spheres can be fused together (eg. orthopaedic implant coatings) or constrained in a net, but this is less common. A number of ceramic, glass and metallic candidates have been included for completeness, however, the majority are unhelpful as they shield the developing cell cultures from important strain and stress conditioning.

There are three main classes included in the table: hydrogel, foam, 3D Mesh/Fabric [24]. Some of the candidates are combinations of classes. Combinations can better approximate the complex hierarchical structure found in natural tissues (at nano, micro, macro connectivity). Hydrogels can be described as nanoscopic sponges filled with water. These can support cell seeding and growth, however, they can prevent cells from migrating, proliferating and connecting due to their fine nanoscopic structure. These gels are commonly synthesised from human, animal or plant proteins that can contain contaminating species such as viruses, prions, and toxins. There also remains a risk of rejection with animal and human derived proteins.

Table 1.7. Tissue scaffold prototypes and products

Class		Name	Material	Comment	Available Forms	Company	Ref.
	Hydrogel	Fibrogen	Recombinant proteins	Expensive and poor mechanical/perfusion prop's	Gel, Beads	BD Biosciences	1-5
		Collagen I,II etc	Recombinant collagens	Expensive and poor mechanical/perfusion prop's	Gel, Beads	BD Biosciences	
		Omniflow II	Collagen-polyester composite	Expensive and only partially resorbable	Gel, Foam, Sheet, Tubing	Bio Nova	6-36
		Tropoelastin	Recombinant Human Tropo-Elastin	Expensive and poor mechanical/perfusion prop's	Gel, fibre, Closed foam	Elastagen	37-41
		Keratin	Recombinant ovine keratin	Expensive and poor mechanical/perfusion prop's	Gel, Foam	Keratec/Keraplast	42-74
		TR Matrix	Collagen composite	Expensive and only partially resorbable	Gel, Beads	TR Biosurgical	75-110
		PuraMatrix	Polypeptide	Synthetic, safer, but lacking bioactivity/signalling	Gel, injectable fragments	3DM/BD Biosciences	111-136
		3D Collagen	Type I & III Collagens	Expensive and poor mechanical/perfusion prop's	Gel, Beads	Chemicon (Millipore)	
	Foam	BD CaP Foam	Calcium phosphate	Brittle and stress shielding	Foam	BD Biosciences	137-147
		Sphene	Calcium silicate / PLA coated	Brittle and stress shielding	Foam, Coating		148-150
		Bioglass Foam	Bioactive glass	Brittle and stress shielding	Foam		151-153
		Polymer Bioglass	Bioabsorb. polymer / bioactive glass	Poor interconnectivity and stiff	Foam		154-156
		Variotis	PCL / bioactive glass-gel	Variable modulus & porosity, interconnectivity	Foam, FGM, sheet	Biometic	
		BD 3D Comp/OPLA	PDLA & Collagen filled variant	lactic acid release and animal derived collagen	Foam	BD Biosciences	157-180
		Pelnac	3mm Collagen & 150micron Silicone	Expensive and animal or human derived	Bilayer foam	Gunze	
		Actipore	Porous TiNi	Non resorbable and stress shielding	Porous foam	Biothex	
		UHMWPE Scaffold	UHMWPE & NaCMC/PVA/HA	Poor interconnectivity / non resorbable	70% Porous Scaffold	S Pal	181
	3D Mesh/Fabric	UHMWPE 3DF	UHMWPE Plasma-treated 3D Fabric	Non resorbable, slow and expensive processing	3D Woven Fabric		182
		Osteomesh	PCL polymer / Calcium phosphate	Slow and expensive processing	3D FDM Printed PCL Mesh	Osteopore	183-186
		Cartilage Scaffold	PEGT/PBT	Not bioactive - slow and expensive prototyping	3D Fabric		187
		SLS PCL Scaffold	PCL polymer	Slow and expensive processing, coarse structure	3D SLS PCL Mesh		188-191
		MEMS Scaffold	Bioabsorbable polymer	Slow and expensive processing	0.5mm unit assemblies		192-198
		Novosorb	Bioabsorbable Polyurethanes	Alcohol degradation product, not bioactive	Woven/Knitted/FDM/E.spun	CSIRO, Polynovo	199-201
		3D Insert	PCL, PLGA, or PS	Not bioactive - relatively stiff scaffolds	Mesh >0.25mm spacing	3D Biotek / Rutgers Uni	
		Electrospun Fibre	PCL composites	Difficult to replicate for 3D cell culture use	Sheets, wool/felt	UQ	202-204

Foam, or 'cellular solids' are common structural forms for supporting tissue ingrowth. Only interconnective open-celled foams allow cells to readily infiltrate, proliferate and migrate, induce connective tissue formation, and permit vascularisation to develop unhindered. Foams allow the greatest range of strain in compression, tension, torsion and shear. Porous foams also enable the volume of biomaterial being implanted to be minimised, in contrast to hydrogels or bulk materials. Foams are generally classed as random (stochastic), in contrast to periodic structures based on repeating units. Repeating structures include 3D mesh and fabrics, as well as 3D prototyped meshes. These structures are relatively coarse in structure compared to random foams. They tend to be less suited to large strains when compared to foams and can result in creasing and buckling instability. Wool or felts consist of randomly arrayed long fibres. They can be readily manufactured but can vary in consistency from batch to batch. Felts and wool are poor in resisting compression, tensile and torsional loads and can tangle and agglomerate when wet, thus lending to poor handling.

In summary, polymer composite foams provide an ideal blend of manufacturing versatility, mechanical properties, porosity, interconnectivity, and compositional variation to suite the dynamic culture of cells *in vitro* and *in vivo*. Automated manufacture of 3D mesh/Fabric scaffolds is still in infancy, although commercially available competitive products have recently been released ($AUD 36 each) on the market for 3D cell culture [317]. The 3D inserts are designed to fit into standard culture plates. They are not readily suited to dynamic cell culture due to their rigidity and are not bioactive. An ideal scaffold should allow dynamic mechanical loading of the cell culture and encourage cell attachment, proliferation, migration, while ensuring adequate perfusion can take place as toxins are removed and nutrients are replenished.

Permeability is defined as the rate of flow of a fluid or gas through a porous material (Fig 1.26) [331]. Scaffold permeability has been shown to be the result of:

1. Porosity
2. Pore size and distribution
3. Interconnectivity
4. Fenestration size and distribution and
5. Orientation of pores with respect to flow direction

Permeability is also a function of compressive strain. A positive correlation exists between porosity and permeability, provided that most pores are well connected [331]. Further work needs to be done to determine the threshold permeability a scaffold must possess for tissue conductance [331]. Hui and coworkers [332] reported a threshold fluid conductance to achieve union for freeze–dried cancellous bone allografts implanted into rabbit tibial defects. Below this threshold, sufficient revascularisation could not be attained. Permeability is a more suitable parameter to use for scaffolds, as it is a specific property of macroporous materials, independent of the sample size and the fluid used in the tests.

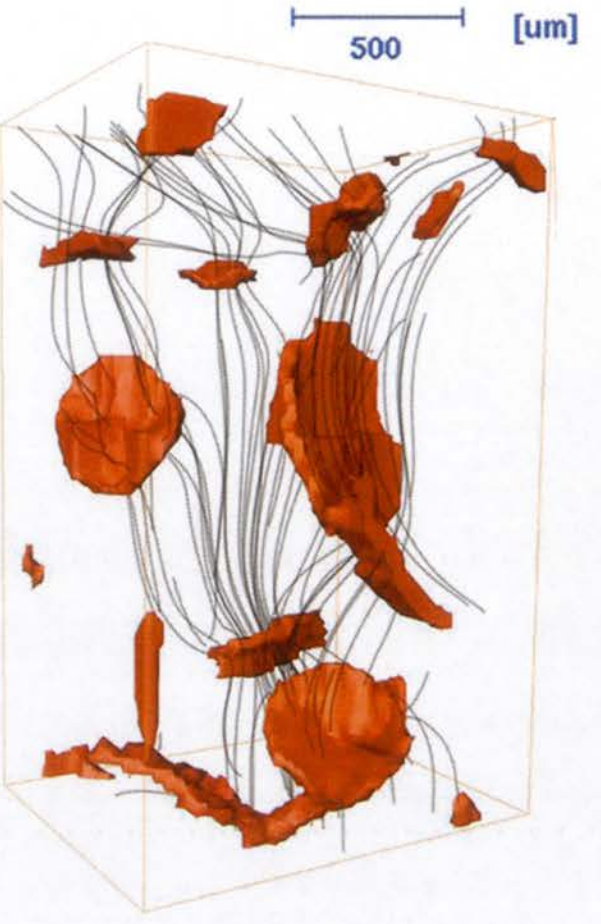


Figure 1.26. Modelling of fluid flow through a bioactive glass scaffold. The pore throats are visible in red [322]. (Refer to Fig 4.2b for an image of the scaffold structure.)

1.6.3. DEGRADATION RATE

The rate of degradation of a biomaterial can have a major effect on the level of tissue ingrowth. Many factors can affect the rate of degradation of a biomaterial, in order to achieve complete degradation over a period of weeks or years. Factors include the chemical composition of the polymer, its molecular weight distribution, copolymer ratios and the crystalline/amorphous ratio [365, 334]. Amorphous regions of allow easier access for water and therefore the polymer degrades faster [334]. Additional factors are the size, shape and pore structure of the implant, polymer processing methods, implantation site and the age/metabolic condition of the patient [336]. High porosity and surface area increases the degradation rate.

Some polymers, including PLA and PGA lose most or all of their strength before their mass is significantly altered. There have also been cases of polymers dissolve faster than expected. An example is the use of PGA sutures in the infected urogenital tract. It is considered that the bacterial urease digests urea in the tract and decrease the environmental pH, which accelerates the degradation of the PGA suture [337]. Thus, the degradation of PGA is suppressed in the acidic environment and accelerated in the alkaline environment. Other polyanhydrydes are also affected [338].

A study by Kimura and coworkers demonstrated less adipose tissue formation in rapidly degrading collagen sponges, when compared to slower ones [10]. This was likely to be due to their inability for space making. An optimal balance of scaffold degradation is a key factor in order to induce cell-based tissue regeneration.

1.6.4. SURFACE ENERGY (HYDROPHILICITY/HYDROPHOBICITY)

Hydrophilic surfaces are polar surfaces onto which water molecules tightly bind, disrupting water self-association (Fig. 1.27a). The proteins in proximity of these surfaces are trapped within bound water layers. On the other hand, water layers tend to reduce their contact with hydrophobic (non-polar) interfaces, compelling proteins to associate with non-polar surfaces via hydrophobic interactions (Fig. 1.27b).

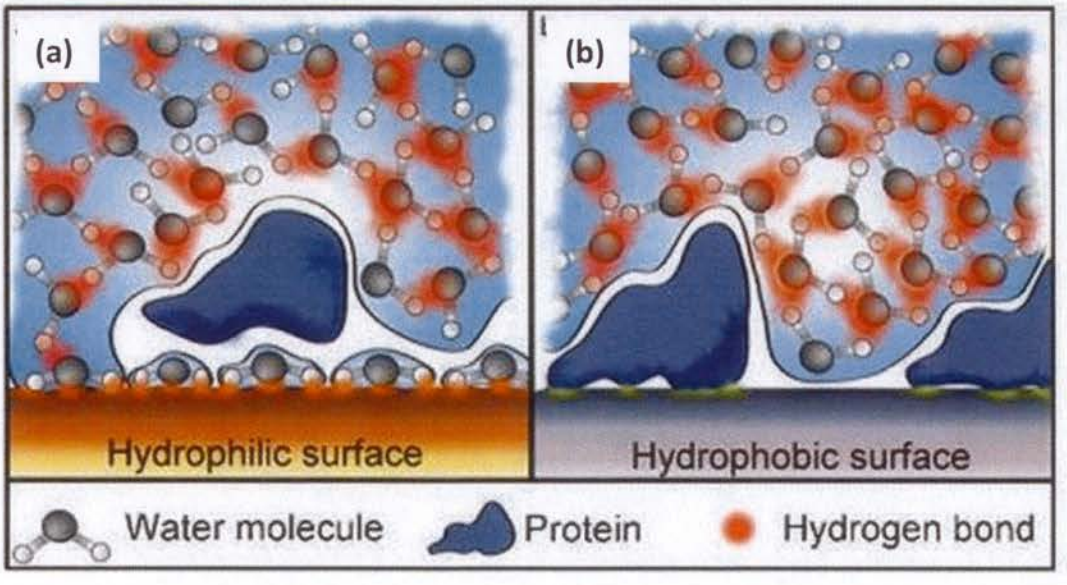


Figure 1.27. Schematic of the interaction between water molecules and surfaces showing (a) Hydrophilic surface and (b) Hydrophobic surface [20] .

1.6.5. PRE-SEEDING OF SCAFFOLDS WITH CELLS

Tissue engineering and synthetic skin grafts have incorporated cells with the aim of providing deficient cells and cell-produced factors (shown in Fig. 1.28). Healing rates may be increased and result in widespread tissue repair. Cells are most commonly suspended in beads or hydrogels and injected into the wound site. Cells can either be mature, for example chondrocytes, myoblasts, osteoblasts, or immature stem cells [299, 340].



Figure 1.28. Scaffold seeded with cells [379].

Scaffolds are increasingly important as a delivery vehicle for exogenous cells, as they allow large numbers of cells to be delivered and retained at the implant site. Collagen II/GAG scaffolds induced more reparative tissue formation when precultured with chondrocytes for 24 hrs [262]. However, this was predominantly hyaline cartilage, not articular cartilage. There have been reports of a lack of healing and degenerative changes occurring in cartilage, after the injection of expanded autologous chondrocytes [341]. Although an improvement was seen in the amount of cartilage developed at 3 and 6 months, with chondrocyte injection, by 1 year there were no differences between the two groups [341]. By 18 months, the defects were not completely filled and the surrounding cartilage showed degenerative changes [341]. This highlights the importance of the role of a scaffold in protecting the cells and providing mechanical cues to aid tissue development.

However, there are potential problems and significant expenses associated with cell-based approaches. Surgery must be performed for the isolation of autologous cells, followed by expansion of the cells on the scaffold for several weeks before implantation. This process is both time and resource consuming [342]. In addition, cultured scaffolds can be difficult to keep free of contamination, and must be implanted without ensuring terminal sterilisation. Many scaffolds, such as collagen, also significantly degrade within a few weeks, limiting the time possible for pre-culturing. It is important to either use autologous cells or immunosuppressants, to ensure host acceptance of the expanded cells. Whether delivery of cells on a scaffold is optimal is uncertain. A study by Luong-Van found that when human mesenchymal stem cells (MSC) were loaded onto electrospun PCL/heparin sulfate scaffolds and implanted subcutaneously in rats, the human cells did not show optimal survival. This was thought to be due to the reaction of the biomaterial-induced inflammatory cells to the MSCs.

In other studies, protection of the MSCs from the inflammatory cells has been achieved using more rigid or dense scaffolds, such as hydroxyapatite or a collagen sponge [343]. However, these scaffolds are not ideal for long-term soft tissue use.

1.6.6. DELIVERY OF THERAPEUTIC AGENTS FROM SCAFFOLDS

Conventional delivery routes for therapeutic agents include orally, intravenously or via injection. Although injection of therapeutic agents provides a bolus dose which can aide tissue repair, these factors are unable to maintain their effectiveness throughout the remodelling phase of wound healing. This occurs weeks/months after the injury.

Three-dimensional scaffolds have the ability for short, medium or long-term localised delivery of factors beneficial for tissue regeneration. Scaffolds have the potential to deliver a higher concentration to a local area, compared with systemic delivery. In addition, lower costs can be incurred as less therapeutic is used when it is delivered locally, and in a controlled way. Scaffolds have the potential to release drugs, natural factors (e.g. cytokines, hormones, proteins), plasmid DNA [344] or antibiotic agents. These agents are used to stimulate cellular adhesion, proliferation and differentiation, and/or to address infection and other tissue conditions. The challenge for engineers is to direct the release of multiple growth factors at various time intervals from a scaffold as to stimulate and enhance the natural healing process [345].

Several points need to be considered when incorporating therapeutic agents for release from scaffolds [346]:

- loading capacity - defined as the amount of therapeutic that can be mixed into the scaffold;
- load distribution - the therapeutic needs to be dispersed evenly throughout the scaffold;
- binding affinity - defined as how tightly the therapeutic binds the scaffold; this binding affinity must be sufficiently low to allow release;
- release kinetics - need to be controlled to allow the appropriate dose of growth factor to reach the cells over a given period of time; and
- long-term stability - the stability of the therapeutic when incorporated within the scaffold at physiological temperature; therapeutics need to maintain their structure and activity over a prolonged period of time.

Therapeutic agents can be directly coated, infused or embedded into a scaffold, or combined with a bioabsorbable material. Coating of a drug onto a polymer scaffold is often via solubilisation followed by diffusion through a network of fluid-filled pores and channels. Therapeutics which are incorporated in a biodegradable material, and either formed into microparticles, scaffolds or coatings, are released as the material degrades (Fig. 1.31).

Bioabsorbable polymers are the most widely used class of biomaterials for achieving controlled factor release. Examples of drug delivery candidates include PCL [347, 256, 15], gelatin [348], chitosan [349], PLA [350], PLGA [116] and thermoresponsive hydrogels [327].

Therapeutic release has also been achieved from systems incorporating ceramics [321], including calcium phosphates [352, 353, 354] and silicate-based bioactive glasses [116, 146, 355]. Rai and coworkers [356] combined PCL/TCP/fibrin and 20 µg/mL BMP-2 to form scaffolds. The *in vitro* release kinetics of these scaffolds consisted of burst releases at 2h, and days 10 and 21, with release being complete at day 21. The addition of TCP appeared to cause a delay in BMP-2 release and also improved the loading efficiency, possibly due to the increase in hydrophilicity which it provided to the PCL. In another study, Wu [116] observed a huge increase in the initial *in vitro* release (0-200 hr) of dexamethazone (anti-inflammatory agent) from PLGA films when mesoporous bioactive glass was incorporated, due to the increased degradation rate of the PLGA (Fig. 1.31b).

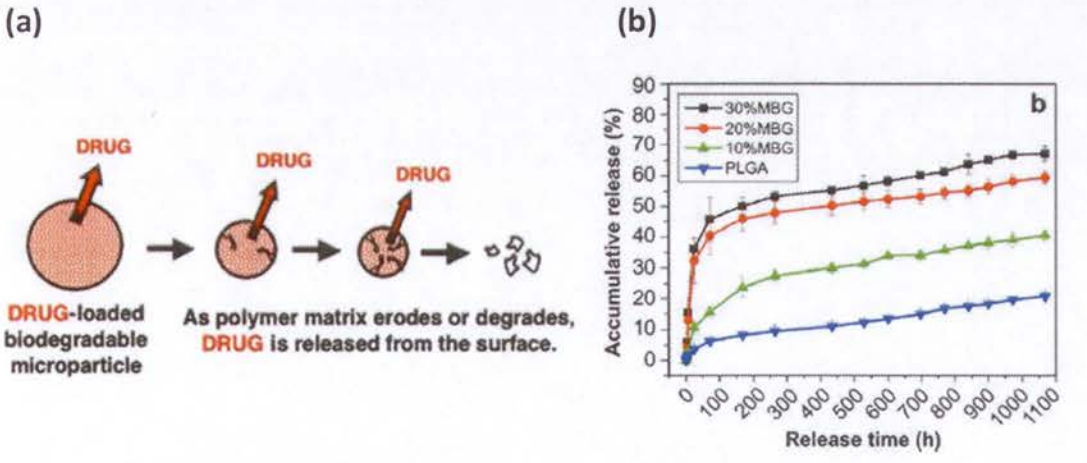


Figure 1.29. (a) Drug release from a biodegradable particle [357]. (b) *In vitro* accumulative release of Dexamethazone from PLGA/mesoporous bioactive glass (MBG) films with different proportions of glass [116].

1.6.6.1. Antibiotic delivery

Antibiotics are chemicals which inhibit the growth of microorganisms such as bacteria which can cause infection. Scaffold composition and form have been shown to alter the rate of the release of antibiotics. Nandi and coworkers [146] observed delivery of the antibiotic cefuroxime axetil over a period of 6 days, when incorporated into a porous bioactive glass block. Zhang and coworkers [358] created composite pellets from chitosan, bioactive glass particles and teicoplanin (antibiotic) powder, and found it provided an effective treatment for osteomyelitis induced by Staphylococcus aureus. Implantation of the pellets into a rabbit tibia osteomyelitis model resulted in the detection of teicoplanin in the blood for about 9 days. Another group, Zhang and coworkers [359] loaded gentamicin sulphate onto chitosan/calcium phosphate scaffolds via dipping in an antibiotic/PBS solution. *In vivo*, these scaffolds showed a sustained release for more than 3 weeks, as compared with the burst-release exhibited by the pure chitosan scaffolds. Chang and coworkers [360] loaded gentamicin sulphate onto PCL matrices via suspension of the antibiotic particles in the PCL solution, prior to forming scaffolds using precipitate casting. They demonstrated the *in vitro* release of 80% of the gentamicin sulphate over 11 weeks, with low levels of antibiotic being measured up to 20 weeks. Further it was possible to increase the amount of drug loaded onto the PCL by cooling the PCL solution to 4°C prior to casting.

1.6.6.2. Tissue-Inducing and Angiogenic Growth Factors

Growth factors which play important roles in wound healing and tissue building have demonstrated increased tissue ingrowth and neo-vascularisation in 3D scaffolds, and can also act to modulate inflammatory pathways. Factors which promote cell proliferation and wound healing include BMPs (part of the TGF-β super family), insulin-like growth factors (IGF), fibroblast growth factor (FGF) and platelet-derived growth factor (PDGF) [320]. Park and coworkers demonstrated that injection of bFGF significantly increased fibrovascular ingrowth into a porous polyethylene orbital implant (Medpore®) [7]. Fujita [361] demonstrated increased angiogenesis and fibrous tissue formation in animals when FGF-2 was released via heparin, when used in combination with a modified injectable chitosan hydrogel. Bone growth has been stimulated via delivery of BMP-2 from carboxymethyl-cellulose hydrogel/PLGA microspheres [350], and CaP/PLGA microspheres [362].

The two main growth factor families shown to directly stimulate angiogenesis are vascular endothelial growth factor (VEGF) and fibroblast growth factor (FGF). VEGF plays an important role in endothelial cell proliferation, which leads to capillary formation. In addition, TGF-β and

the PDGF family have an indirect effect on angiogenesis *in vivo*. Angiogenic growth factors have been used to induce capillary formation in porous scaffolds [363, 364]. Inclusion of VEGF increased vascular perfusion in at polyurethane scaffold by 20% [365]. Shown in Fig. 1.30, bFGF (delivered from gelatin microspheres) increased the number of capillaries inside 2 mm porous PVA sponges [84] and also in Matrigel matrices [10] in subcutaneous rat models. However, FGF is known to have a high risk of encouraging the progression of cancer [299] and so elimination of the need for its use would be ideal.

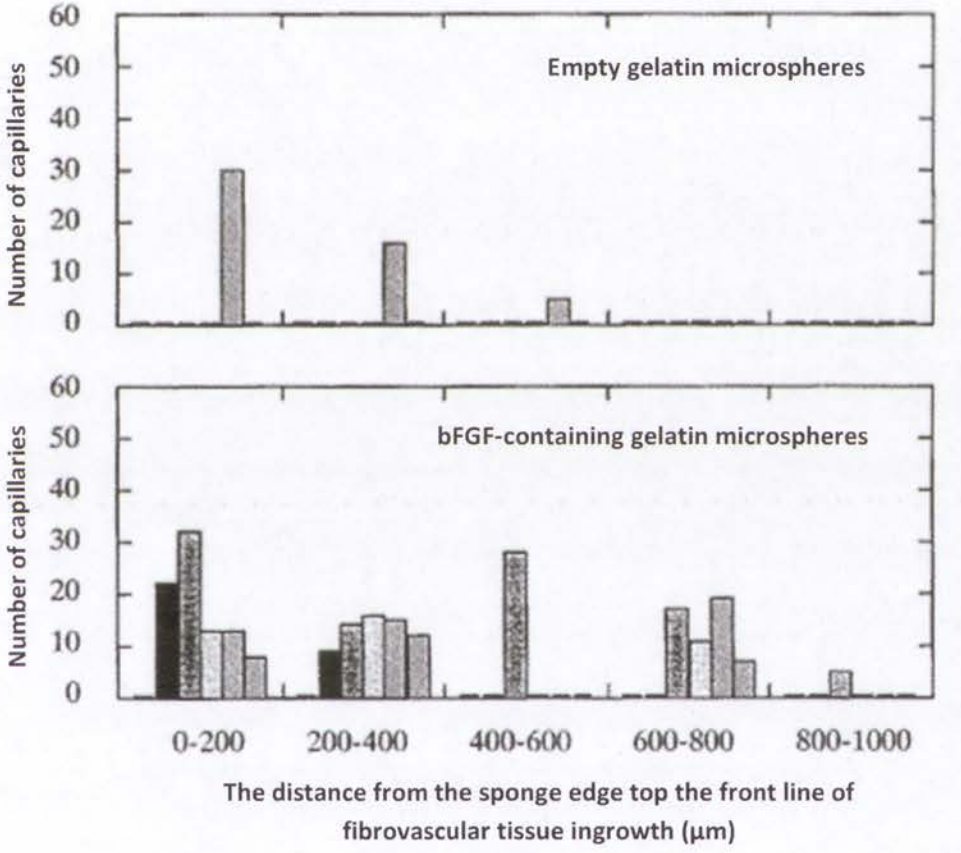


Figure 1.30. bFGF delivery increased the number and extent of capillaries formed inside porous PVA implants, which were subcutaneously implanted in mice [84].

Nillesen and coworkers [371] included 2 growth factors; FGF2 and VEGF, into acellular collagen-heparin scaffolds. Staining of collagen IV and smooth muscle actin demonstrated a higher density and more mature blood vessel formation compared to collagen alone or delivery of a single factor. Less hypoxic cells were detected in the scaffold which delivered the 2 factors (2.2%, 0.2%) as compared to the collagen sponge (36%, 21%), at 7 and 21 days respectively.

1.6.6.3. Anti-Inflammatory Drugs and Bisphosphonates

Anti-inflammatory drugs can be classified as steroids (glucocorticoids) or non-steroids. Glucocorticoids are commonly used to treat rheumatoid arthritis and have shown to have strong inhibitory effects on cytokine-related inflammation by downregulating transcription of interleukin (IL)-1, -3, -4, -5, -6, -8 and tumour necrosis factor (TNF-α) [367]. As previously mentioned, dexamethasone (a common glucocorticoid) has been released from starch/PLLA scaffolds over a period of 21 days [368] and also from PLGA-coated Bioglass® scaffolds [116].

Other anti-inflammatory agents include the non-steroidal ibuprofen, which has been adsorbed onto the surface of bioactive glass-ceramic scaffolds by immersing the scaffolds into a solution of ibuprofen for 3 days [355]. The *in vitro* drug release study showed a fast release of ibuprofen over the first 8 hours followed by a slower release between 8 and 120 hrs. Ibuprofen has also been delivered from a polyurethane dressing for diabetic ulcer treatment [369]. Bisphosphonates have been widely used since the 1970's for bone diseases characterised by bone resorption [370]. Examples of materials which have been used to deliver bisphosphonates include a silica based scaffold [371] and calcium-deficient apatite [372].

1.6.7.4. Delivery of Organic and Inorganic Ions

Various metallic or non-metallic ions or salts can be delivered to the healing tissue via incorporation in the biomaterial. These can have tissue-stimulating, anti-inflammatory or antibiotic properties. Organic ions such as calcium and silicon have been widely used for their ability to stimulate gene expression in osteoblasts due to their ability to increase proliferation and bone ECM production [373].

Numerous essential elements have also been demonstrated to possess antibacterial activity, including zinc [374-377], copper [378] and iron [205]. Other elements which are vital for body function include manganese, aluminium and magnesium. Metallic ions have been incorporated into bioactive glasses for delivery to tissues [145, 198]. This approach will be explored in chapter 4.

1.6.7. BIOACTIVE SOFT TISSUE SCAFFOLD SYSTEM DESIGN

In this thesis, two distinct scaffold system concepts were conceptualized for soft tissue clinical applications. Both systems are bioactive composite systems with potential to facilitate tissue attachment. In these composite scaffolds, two or more phases are combined to provide advantageous bulk material properties. The first calcium silicate (CaSi) ceramic-based scaffold concept addresses osteochondral defects. This ceramic based scaffold is reinforced with a polymer coating and also incorporates a gel phase. The second scaffold concept is designed to primarily address chronic dermal wounds as well as other soft tissue needs, including osteochondral defects. This mechanically versatile scaffold consists of a polymer matrix combined with bioactive glass.

While the specific needs for each application will vary significantly, it was deemed helpful to identify general requirements that would provide a means to assess the clinical and commercial viability of these soft tissue scaffold platforms. The tissue scaffold design inputs or requirements shown in figure 1.31 correspond to majors sections of this developmental thesis. A variety of specific scaffold design requirements are listed in Table 1.7. These were determined from the preceding literature review in this chapter, reviews included in subsequent chapters, and personal communication with clinicians and medical device industry-experts. The proceeding chapters summarize design development and verification and validation work carried out for soft tissue engineering systems. While two distinct scaffold platforms are investigated in this project, there is good commonality and overlap between the two approaches. Findings from both developmental facets provide a broad insight into the development and validation of clinically and commercially relevant soft tissue scaffold systems.

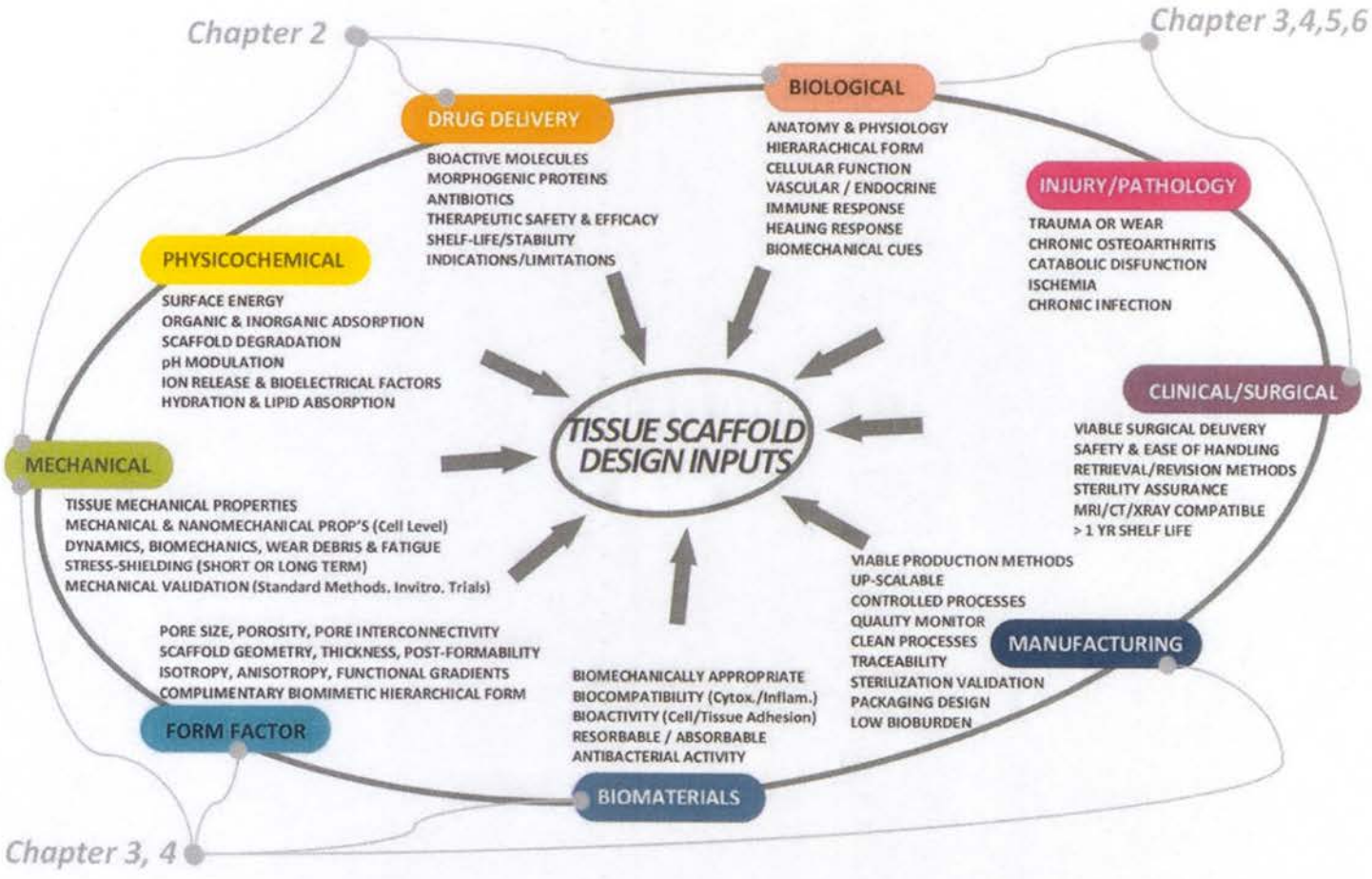


Figure 1.31.Design inputs and corresponding chapters where design verification and validation work is covered.

Table 1.7. A summary of key tissue engineering scaffold design requirements

Tissue Engineering User Requirements		Category	Chapter
1	Non or low-cytotoxicity	Materials	1,2,5,6
2	Non or low-inflammatory	Materials	2,5,6
3	Pure and controlled composition	Materials	2,5,6
4	Controlled resorbability	Materials	2,4,5
5	High porosity	Physical	1,2,3
6	Bulk volume and thickness	Physical/Clinical	2,3
7	Hierarchical porosity	Physical	2,3
8	High void interconnectivity	Physical	2,3
9	Adjustable porosity	Physical/Biologic	3
10	Functional gradient capable	Physical/Biologic	3
11	*In vivo* & *in vitro* adaptable	Biological/Clinical	2,3,4,5
12	Soft & hard tissue attachment	Biological/Mechanical	2,3,4,5
13	Cyclic strain capable-bioreactor use	Biological/Mechanical	3
14	Adjustable modulus	Biological/Mechanical	3
15	Low trauma to adjacent tissues	Mechanical	3,5
16	Physiological-range support	Mechanical	3
17	Compressible/Extensible (>50%)	Mechanical	3
18	Avoid stress shielding	Mechanical	3
19	Resist failure by impact-loading	Materials/Mechanical	3
20	Terminal Sterilization	Clinical	3
21	Researcher & Surgeon handling	Biologic/Clinical	3
22	Packaging & Shelf Life Req's	Clinical	3
23	Regulatory recognized biomaterial	Clinical	1,3
24	Partially radiolucent	Clinical	3,4
25	Vehicle for therapeutics	Clinical	2,3
26	Modular / Shapable	Clinical/Manufacture	3
27	Suturable / Joinable	Clinical	3
28	Cuttable	Manufacture	3
29	Consistent quality	Manufacture	2,3
30	Up-scalable	Manufacture	3
31	High through-put	Manufacture	3
32	Low cost production	Economical	3
33	Low cost constituents	Economical	3
34	Low energy processes	Economical	3

CHAPTER 2-

CALCIUM SILICATE-BASED OSTEOCHONDRAL BED SCAFFOLD

2.0. CHAPTER OVERVIEW

Novel osteochondral bed scaffolds were developed with a bioactive ceramic scaffold as the bone integrating component and gel phase for the cartilage component. Calcium silicate-based scaffolds were synthesised from wollastonite ($CaSiO_3$, WT) and sphene (Ti-$CaSiO_3$) using a polymer foam replication technique. SEM and MicroCT indicated the scaffolds were highly porous (~82%) and interconnected (~99.5%) with large pore voids (300-700 μm). Compression tests revealed the WT scaffolds were extremely brittle with a compressive strength of 262 kPa, however PDLLA coating improved the scaffold strength to 1048 kPa. The Young's modulus was also increased from 13 to 47 MPa- which is within the range of cancellous bone. The scaffolds afforded low strains till unrecoverable deformation was observed (<5%). SEM of chondrocyte culture on gelatin or alginate-filled scaffolds showed cell attachment and spreading. Therapeutic agents, including zoledronic acid (ZA) and S100 proteins (A8, A9, A8/9) were used to treat chondrocytes before gene expression was measured using RT-PCR. Genes included markers active in cartilage remodelling from the MMP, TIMP and ADAMTS families. Zoledronic acid reduced degradation of cartilage by lowering ADAMTS-1 and -5 expression. S100A9 increased breakdown of the ECM, as shown by an increase in ADAMTS-5 and decreased TIMP-1 and TIMP-2 expression. These results indicate that it could be beneficial for ZA and S100A9 to be locally released from a scaffold for addressing catabolic-related osteochondral tissue erosion.

2.1. INTRODUCTION

2.1.1. APPROACHES TO CARTILAGE REPAIR

Human articular cartilage lesion repair is a challenging clinical problem. This is because the ability of cartilage to respond to injury is poor [267]. Once cartilage damage has occurred, an irreversible degenerative process can occur. The resulting defects may lead to osteoarthritis. Current attempts to treat articular cartilage lesions include chondral shaving, spongialisation, and microfracturing of the subchondral plate, mosaicplasty, implantation of artificial matrices and/or growth factors, and drilling through the subchondral bone to allow pluripotent cells from the marrow space to invade and repair the lesion [380, 381]. To date, no reliable reproducible approach has been identified [382]. Even fewer options are available for the repair of osteochondral (bone-cartilage defects). Many techniques lead to the formation of fibrocartilage, which is higher in collagen I than the original hyaline cartilage. Fibrocartilage does not have the necessary load-bearing capability and undergoes degeneration over time.

Although treatment of cartilage defects with autologous or allogenic cells or osteochondral grafting (Fig. 2.1) has shown some success, these approaches still have still significant limitations. These include inadequate donor tissue availability, donor site morbidity, risk of infection and poor integration with the native cartilage [383]. These approaches also require healthy cartilage surrounding the defect [381]. Cartilage does not integrate well with transplanted tissue of any kind- including grafts and engineered constructs. This phenomenon is due to, in part, the

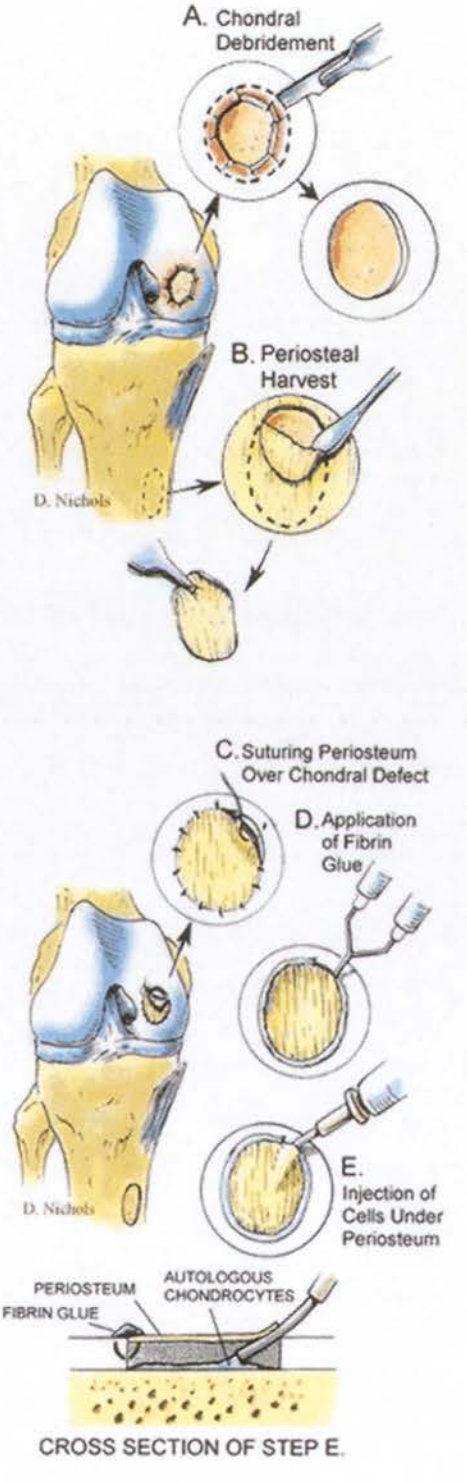


Figure 2.1 Autologous chondrocyte implantation [384].

thick ECM and avascular nature of cartilage [267, 382]. Arthroscopic techniques often provide temporary repair, although efficacy fades with time. This is especially the case for large injuries (>1cm^2).

In addition to these approaches, autologous cells are cultured *in vitro* in a biomaterial prior to implantation. The goal of this process can be either to expand the cell population or to create more mature cartilage which can be replaced like a natural prosthetic. Growth factors can also be delivered to the wound site via the biomaterial. Both synthetic and natural materials are commonly used as a matrix. Matrices can be formed into gel, bead, fibrous, woven fabric or porous structures. Mature cartilage formation can be encouraged through mechanical actuation using an *in vitro* bioreactor prior to implantation into the joint defect. The challenge for cartilage integration in tissue engineering is twofold: the initial biomaterial scaffold must be stabilised in the joint and the subsequent developing tissue must integrate with the surrounding native tissue [15]. These are extremely important in the mechanically harsh environment of the joint [15].

2.1.2. OSTEOCHONDRAL TISSUE ENGINEERING CONSTRUCTS

Synthetic scaffolds have the potential to reduce complications associated with grafts and other biologically-derived solutions. These approaches allow donor site morbidity associated with autografts to be minimised [385].

Device designs which replace osteochondral tissue, in contrast to just the cartilage, have many advantages. A bone anchorage scaffold section is an important component because a bone-to-bone interface integrates better and faster than a cartilage-to-cartilage interface [386, 387]. In addition, the health of the cartilage is dependent on the health of the subchondral bone. Thus, an approach which addresses the pathology of the bone could aid cartilage regeneration. 3D biphasic scaffolds include a bone interfacing component, and a cartilage component. Each component is suited for the particular needs of the two tissue types, in terms of chemistry, structure and biological factors. This was the approach followed in the current study.

A wide variety of conformation has been investigated for filling of osteochondral defects, as reviewed previously [381, 388]. These include synthetic constructs which use:

- A scaffold for the bone component, but scaffold-free approach for the cartilage
- Different scaffolds for the bone and cartilage sections, which are combined at implantation
- A single, but heterogeneous composite scaffold

- A single homogenous scaffold for the entire osteochondral defect

These scaffolds can be loaded with cells, which include:

- A single cell source, with a chondrogenic capacity
- Two cell sources having either chondrogenic or osteogenic capacities
- A single cell source having both chondrogenic and osteogenic differentiation capacity, OR
- A cell-free approach

2.1.2.1. Design Considerations for Osteochondral Scaffolds

Optimal osteochondral scaffold designs will possess the following characteristics [385]. The device will facilitate good mechanical anchorage to the bone, which may be achieved through the use of pins or other anchorage devices [381]. The scaffold should be made from materials which are biocompatible, as well as osteoinductive/osteoconductive and chondroinductive/chondroconductive. The scaffold structure should provide a framework to guide the new osteochondral tissue development, whilst being capable of facilitating revascularisation. Even though cartilage is avascular, a scaffold is required to support diffusion of blood and nutrients in the cartilage section. The chosen material should also be affordable, storable and sterile. The device should have a high initial stiffness which is similar to bone to allow primary union, followed by gradual resorption and reduction in stiffness corresponding to the ability of the healing tissue to serve in a load-bearing capacity [389].

2.1.2.2. Review of Osteochondral Constructs

Table 2.1 contains a review of some examples of osteochondral scaffolds reported in the literature, some of which will now be highlighted. Further examples of osteochondral scaffolds are reviewed by Martin and coworkers [388]. Bone components are often synthesised from PCL, PLA/PCL, PLA/PGA or bioceramics, usually in porous form. Cartilage components utilise a mesh (woven or unwoven), gel or porous polymer component.

Table 2.1. Review of osteochondral scaffolds.

	Scaffold Description	Study	Ref.
Hydrogel	Cellmatrix® collagen gel (concentration gradient)	MSCs, rabbit articular cartilage defect	390
	Microchanneled agarose hydrogels	Chondrocytes- rotating cultures for 28days	381
	PVA/BG composite hydrogel	Mechanical properties	381
	Photopolymerising hydrogel with TGF-β1	MSCs	393
	Agarose reinforced with 3D woven mesh	Mechanical properties, porcine articular chondrocytes	394
	Collagen sponge/calcium phosphate crystals	Chondrocytes	395
	Injectable hyaluronan/calcium phosphate	Autologous bone marrow-derived progenitor cells	327
Woven/Fibrous Mesh	Electrospun PCL	hMSCs	396
	PLLA fibers, bioreactor 42 days	Bioreactor culture 42 days with bovine chondrocytes	395
	PCL/PLLA fibrous scaffolds		398
	PGA meshes (cartilage), PLGA/PEG (bone)	Chondrocytes, peristoneal cells	399
	Graded electrospun PCL/TCP	Mouse preosteoblast cells	400
BP	PCL/fibrin (cartilage), Bone: PCL/HA scaffold (bone)	Bone marrow derived stem cells	70
	PCL scaffold	Chondrocytes, osteoblasts	385
	PLGA/PLLA (cartilage), PLGA/TCP (bone)	Chondrocytes- rotational culture for 4 weeks	401
Porous Foam	Tutobone® devitalised spongiosa (bone) Chondro-Gide® collagen-based matrices (cartilage)- joined with fibrin glue (Tisseel®)	Chondrocytes	90
	Calcined bovine bone/gelatin	Porcine chondrocytes- bioreactor 2 or 4 weeks	402
	PLA or PCL elastic PCL scaffolds	Chondrocytes, Rabbit defect model	403, 404
	PLCL foam	Mice- subutaneous	405
	PLGA or PLA porous scaffolds	Chondrocytes	406
	Biocoral® (calcium carbonate-based) (bone), Ethisorb® 3D PGA/PLLA/PDS mesh (cartilage)- joined with fibrin glue	Bovine chondrocytes	407
	PCL scaffold	ESCs- 3-4week culture, mice- subutaneous	408
	Multilayered: PDLGA with PGA fibers, 45S5 bioglass or calcium sulphate. Dense film on articulating surface.	Goat chondrocytes, goat osteochondral defect	409

As illustrated in Fig. 2.2a, Cao and coworkers [385] synthesised a high strength PCL scaffold and precultured chondrocytes and osteoblasts in opposite sides of the scaffolds. During *in vitro* culture, the cells each produced different ECMs in each scaffold compartment, with mineralised nodules being deposited in the osteogenic seeded compartment. Similarly, Hutmacher and coworkers [70] synthesised a scaffold using the same technique, consisting of PCL/fibrin (cartilaginous) and PCL/10%HA (bone) components. In theory, each component would be cultured separately with the appropriate cell type, then joined together for a further culture period. Osteogenic stem cells spread between the pores and formed mineralised nodules. Chondrocytes showed good proliferation within the fibrin/PCL section. Splazzi and coworkers [410] created a tri-phasic scaffold to mimic the tendon-bone interface, for repair of the anterior cruciate ligament. Although this is not an osteochondral implant, there are similarities with this tissue interface. Shown in Fig 2.2b, the three layers of the scaffold were: (A) PLGA knitted mesh sheets- Vicryl (ligament) (B) PLGA microspheres in water/oil/water emulsion (interface) (C) Sintered composite microspheres- PLGA/45S5 bioactive glass (bone). Interface-relevant cells (fibroblasts, chondrocytes and osteoblasts) were cultured on the construct and matrix formation was analysed over 8 weeks in a subcutaneous rat model. Distinct mineral and fibrocartilage-like tissue regions were formed in this scaffold. Cell seeding had a positive effect on both host infiltration and matrix elaboration compared to the acellular control. This translated into increased mechanical properties in the seeded groups. These studies demonstrate biomimetic and multiphasic design coupled with spatial control of cell distribution enables the potential for regenerating the interface between soft tissue grafts and bone. Development of porous constructs with increased pore size and porosity could have the potential for increasing the speed and quality of bone ingrowth. In the current study, a porous scaffold was developed consisting of a porous calcium silicate bone component and hydrogel cartilage section.

Scotti and coworkers [90] formed bilayered scaffolds from devitalised spongiosa (bone component) and collagen-based matrix (cartilage component). Preculture of the chondral layer allowed for (i) more efficient cartilaginous matrix accumulation than no pre-culture, and (ii) superior biological bonding to the bony scaffold than 14 days of preculture. The integration of the bilayered materials was assessed using a peel-off mechanical test. An acellular bone component was conceptualised since osteoprogenitor cells are abundantly present in the bleeding subchondral bone during implantation and are expected to colonise the scaffold and efficiently promote new bone formation. Schaefer and coworkers [399] also found the tissue integration was better when chondrocytes were cultured for a short period (1 week) as

compared to long-term (4 weeks) in PGA mesh (cartilage component)/PLGA/PEG (bone component) bilayered scaffolds.

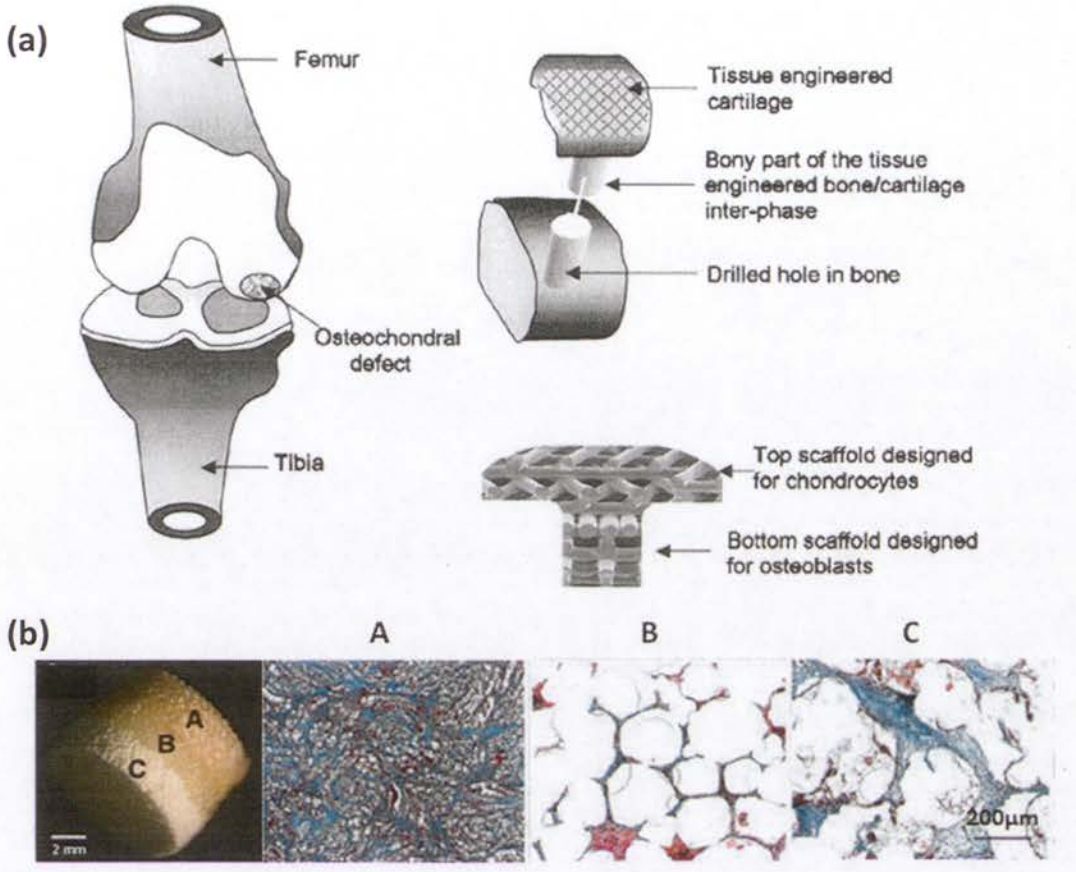


Figure 2.2. (a) PCL osteochondral scaffold [385] (b) Triphasic scaffold for tendon-bone interface. Histological images show tissue growth into the three regions of the scaffold after 4 weeks of implantation [410].

An alternate approach is formation of a seamless gradient in the composition and properties of the scaffold. Erisken and coworkers [400] created non-woven PCL meshes incorporated with varying concentrations of tricalcium phosphate nanoparticles using a new hybrid twin-screw/electrospinning process. This technique can enable the creation of scaffold with varying degrees of porosity, mechanical properties, wettability, biodegradation rate distribution and concentrations of drugs/growth factors, aiming to mimic the complex distributions found in native tissue. When mouse preosteoblast cells (MC3T3-E1) were cultured on the scaffolds for 4 weeks, the tissue constructs revealed the formation of continuous gradations in extracellular matrix with various markers including collagen synthesis and mineralization. These were akin to the type of variations observed in the typical bone-cartilage interface in terms of the distributions of the concentration of Ca particles and of mechanical properties associated with this.

Bioactive bioceramics (ref section 1.4.1), particularly calcium phosphates, are clinically popular as bone fillers and implant coatings and can be formed into scaffolds for tissue engineered bone. Calcium silicates are less widely utilised but are potential candidates for bone scaffolds as they are biocompatible, biodegradable and display osteoinductive and osteoconductive properties [8]. However, they exhibit insufficient strength, high brittleness and high ionic dissolution, which limit their biological applications [224]. Others have tried to address these drawbacks by developing composite $CaSiO_3$/polymer scaffolds using traditional methods [224]. Solvent casting/particulate leaching and freeze-drying methods have been used to produce porous $CaSiO_3$/PDLLA, $CaSiO_3$/polyhydroxybutyrate-polydroxyvalerate and $CaSiO_3$/collagen scaffolds [114, 244]. However, the composite scaffolds thus produced are not mechanically strong due to the use of unsintered $CaSiO_3$ powder. The challenge remains to produce scaffolds that combine high porosity with increased mechanical strength.

Alternate synthesis techniques which can be used to create highly porous ceramic scaffolds include gas foaming and the replication technique [4, 186, 224, 411] (Fig. 2.3). The latter uses porous polymer foams as a sacrificial template. Following infusion of the ceramic into the polymer matrix, the particles are sintered at a high temperature, leaving an interconnected network of pores [411]. Highly porous calcium phosphate scaffolds (80%+) with macropores (>200 μm) have been reported. These scaffolds have been filled with PLGA or 58S bioactive glass (33 wt%)-PLGA composite coating [413].

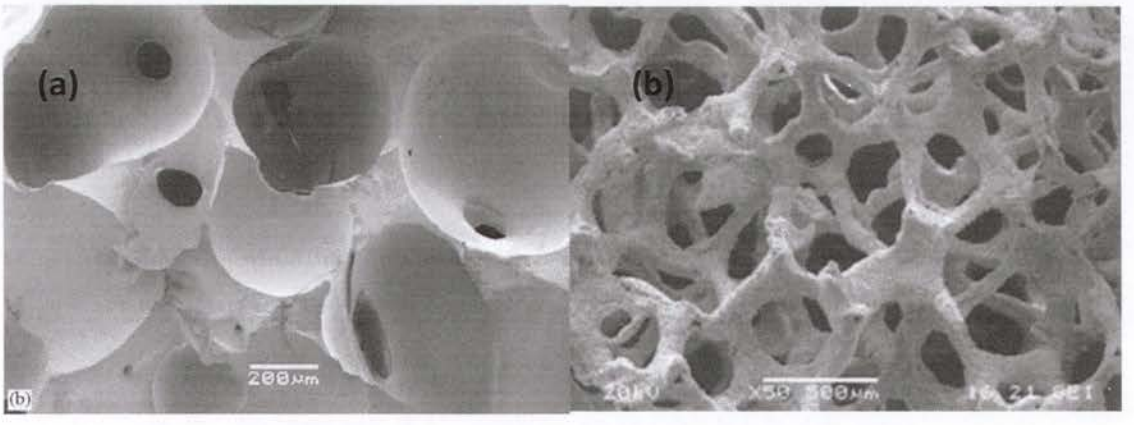


Figure 2.3. Bioactive glass scaffolds formed using (a) Gas foaming [5], (b) Polymer sponge template [411].

Shown in Table 2.2 are the porosity and compressive strength of some scaffolds reported in the literature. These scaffold designs attempt to match the strength of the native cancellous bone.

Table 2.2. Compressive properties of bioceramic scaffolds.

Author	Scaffold	Porosity (%)	Compressive Strength (kPa)	Ref
Kim 2005	HA	69-86	30-290	414
Chen 2006	45S5 Bioglass	82-89	600-420	411
Miao 2007	Calcium phosphate (bioactive glass-PLGA coating)	-	7.7MPa	413
Wu 2010	Cancellous bone	70-90	200-4000	117

A variety of calcium silicate-based 3D porous scaffolds have been previously synthesised by our group using the replication technique [119]. These scaffolds have been shown to be effective for bone cell attachment, proliferation and stimulation of bone ECM components. Recent work has demonstrated the improvement of the mechanical and biological stability of these scaffolds via doping with titanium (Ti-$CaSiO_3$, Sphene, zinc ($Ca_2ZnSi_2O_7$, Hardystonite, HT), strontium ($Ca_2ZnSi_2O_7$, Sr–HT), magnesium ($CaMgSi_2O_6$, diopside) and zirconia [117, 119, 415-417].

The approach in the current study is to prepare porous $CaSiO_3$ scaffolds at high temperature using a polymer sponge method and then to modify these scaffolds using biodegradable and biocompatible PDLLA in an attempt to improve the mechanical strength and biological properties of the scaffold. The scaffolds will also be filled with hydrogels to facilitate chondrogenesis.

2.1.4. HYDROGELS FOR CARTILAGE ENGINEERING

Hydrogels (e.g. alginate, gelatin) are good candidates for cartilage scaffold components. Cell proliferation and maintenance of a chondrogenic phenotype is heavily reliant on the cells being suspended in a supportive 3D environment and the overall compressive forces experienced by the tissue engineered structure [418, 402, 394, 381, 390]. A chondrogenic phenotype displays a rounded morphology and is characterised by gene expression of markers such as collagen 2, aggrecan and Sox-9 [381]. 3D hydrogels (Fig. 2.6.) with high water content can be used to support rounded cell morphologies and rapid diffusion of soluble nutrients [419-421]. Liu and coworkers [421] have demonstrated that although chondrocytes become dedifferentiated when subcultured in monolayer (and exhibited a fibroblastic morphology), when transferred to 3D beads of alginate, the cells quickly regained their spherical shape. Kolambkar and coworkers [423] encouraged a chondrogenic lineage by expanding human annulus fibrosis cells and MSCs in alginate gel. In fact, chondrocytes have been shown to retain their chondrogenic phenotype for 8 months of culture in alginate beads [424]. Oxygen

consumption of chondrocytes was 2-fold higher in agarose than in collagen, indicating that the nature of the material, including its stiffness, strongly influences metabolic behavior [425].

Hydrogels can differ in properties including degradation, drug delivery, surface interaction and cell recognition characteristics. Examples of therapeutic delivery from gelatin have included protein [426] and bFGF release [61]. Some hydrogels undergo an *in situ* curing experience in a phase transition triggered by stimuli such as pH, temperature, ionic strength and redox state.

Bulk hydrogels are unable to support the significant loads experienced by cartilaginous tissues *in vivo*. For these reasons, hydrogels are often reinforced by a matrix phase [394] or bioactive fillers [381]. Moutos and coworkers [394] demonstrated that composite constructs composed of agarose reinforced with a woven fibre mesh showed mechanical properties of the same order of magnitude as native articular cartilage, as measured by compressive, tensile and shear testing. In addition, these scaffolds reproduced the anisotropy, viscoelasticity and tension-compression nonlinearity of native cartilage.

2.1.5. INCORPORATION OF THERAPEUTIC AGENTS INTO SCAFFOLD

Therapeutic agents can be incorporated into the scaffold through the hydrogel phase, and/or biodegradable polymers; as coatings, micro/nanospheres or fillers. The factors can also be functionalised directly to the sphene scaffolds. Therapeutic products could include anti-inflammatory agents such as bisphosphonates or S100A8 proteins. S100A8 can be functionalised to the scaffold via heparin: with negatively charged heparin binding to Ca^{2+} in the scaffold and via both N-and O-linked sulfates [427]. Numerous proteins contain heparin-binding domains that specifically interact with heparin and heparin sulfate glycosaminoglycans (GAGs). GAGs enhance the biological activities of growth factors involved in chondrogenesis and act as a reservoir to concentrate growth factors close to cells and inhibit proteolytic digestion by trypsin, plasmin and other proteases [428]. Heparin can be readily incorporated into scaffolds and retains its biological activity despite being subjected to harsh fabrication methods that would normally destroy protein [429]. This property makes heparin suitable for attachment to scaffolds and for the delivery of proteins such as S100A8.

Conventional therapeutic treatments used for osteoarthritis/rheumatoid arthritis are successful in suppressing the pain and inflammation associated with the disease, however they do not always inhibit the underlying tissue catabolism, allowing the disease to progress into irreversible ECM loss and chronic disability [430]. Common treatments aim to minimise pain and inflammation, including analgesics, corticosteroids (e.g. prednisone), bisphosphonates, immune suppressors and other anti-inflammatory agents (e.g. methotrexate, cyclosporin,

Arava). Dietary supplements such as glucosamine sulfate and chondroitin are also taken. COX-2 inhibitors are popular with osteoarthritis patients, however although they alleviate the pain they do not favorably affect the outcome of the disease. Therapeutic targets often target cytokines which mediate early inflammation, including tumour necrosis factor alpha (TNF-α), interleukins IL-1, IL-6, IL-8, transforming growth factor beta, fibroblast growth factor and platelet-derived growth factor.

2.1.5.1. Bisphosphonates

As introduced earlier (Chapter 1), bisphosphonates (BP) are widely used in the treatment of osteoporosis, osteoarthritis and rheumatoid arthritis and are effective as anti-inflammatory agents. Therefore, they were chosen as potential candidates for incorporation in an osteochondral scaffold. Zoledronic Acid (ZA) (Fig. 2.10) is one such BP. It is available through Novartis Oncology under the trade name Zometa and has been shown effective for not just arthritis treatment, but also multiple tumour types which have secondary metastases in bone (eg. breast, prostate, lung cancer) as well as prevention of skeletal events such as pathological fractures [431].



Figure 2.4. The chemical structure of Zometa [432].

ZA (Fig 2.4) is a nitrogen-containing bisphosphonate, and as such has a unique mechanism of action related to its ability to inhibit the mevalonate biosynthetic pathway. This effects cell proliferation, regulation of cytoskeletal architecture and cell survival [431-435]. The mechanisms for ZA action is summarised in Table 2.3 below.

Table 2.3. Zoledronic Acid Action.

Action	Ref
Inhibition of osteoclast maturation	[430-432]
Inhibition of osteoclast recruitment to the site of bone resorption	[430-432]
Suppression of mature osteoclast function	[429-432]
Reduced production of cytokines (eg, interleukin-1)	[431-432]
Direct antitumour activity (cytostatic and cytolytic) and Inhibition of tumour-cell dissemination, invasion, and adhesion to bone matrix.	[431-433]

ZA has superior potency and pharmacologic properties compared with other bisphosphonates. ZA has also demonstrated chondroprotective actions; it inhibits cartilage matrix breakdown. Previous work by Zreiqat [436] demonstrated that ZA was found to dose-dependently reduce arthritic severity by as much as 75.6 ± 5.7% (Pooled Severity Index) when administered subcutaneously to rats. This was the case when ZA was administed at day 0 (disease onset), 12 (disease established) or every 3 days throughout the timecourse (days 0-19). Shown in Fig 2.5, the Pooled Severity Index was drawn from indexes calculated from the paw volume, radiology and histology. Treatment with ZA was equally effective in attenuating adjuvant arthritis when administered during disease onset (day 0) or established disease (day 12) and a single injection was as effective as multiple injections.

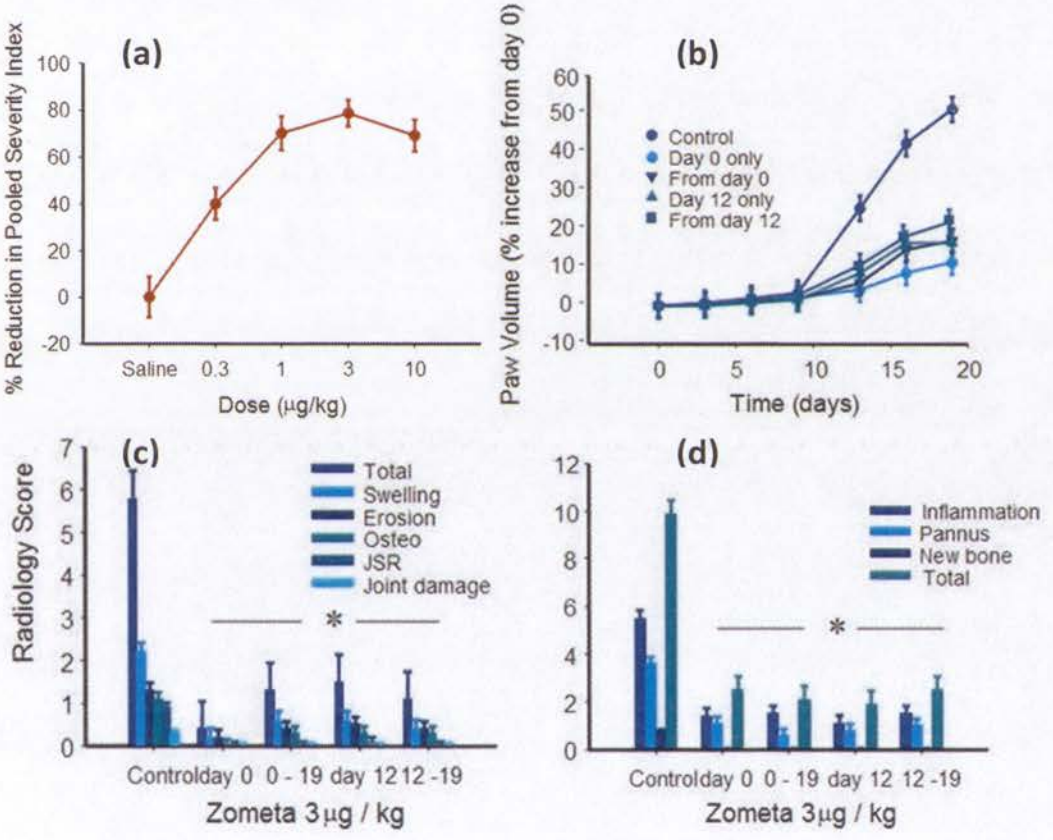


Figure 2.5. (a) Pooled Severity Index showing ZA attenuates arthritis, and evidence suggesting ZA treatment time does not alter arthritic outcome (b) Paw volume, (c) Radiology and (d) Histology. *Denotes significant difference from controls (saline), *p< 0.05 [436]

This study demonstrates ZA can slow the progression of arthritis. Although the effects of ZA on bone are extensively reported in the literature, the mechanisms by which ZA can act directly on cartilage are not well understood. Therefore in this thesis *in vitro* studies were undertaken investigating the mechanisms by which ZA can affect the gene expression of chondrocytes. Low concentrations were chosen as *in vivo* rates of 3 µm are effective. Studies investigating *in vitro* effects of ZA have usually been performed at high concentrations (100 or 150 µm) to anti-

tumour activity and inhibition of cancer cell proliferation [428]. Table 2.3 contains a summary of the dosage applied, cell type and conclusions from the literature.

2.1.5.2. S100 Proteins

S100 proteins are present naturally in the body, and are found in high concentrations in synovial fluid and blood plasma/serum during inflammation. They were also considered as candidates to enhance chondrogenesis in the scaffold. S100 proteins are expressed by keratinocytes and inflammatory cells in human/murine wounds and by appropriately activated macrophages, endothelial cells, epithelial cells and keratinocytes *in vitro*. They regulate intracellular processes including cell cycle regulation, transcription and differentiation. S100A8, S100A9, and S100A12 are calcium-binding proteins expressed in the cytoplasm of phagocytes. They are rapidly secreted by activated monocytes or neutrophils, which are abundant in inflamed synovial tissue [437]. Elevated levels of S100A8, S100A9 and S100A12 proteins have been found in the serum of patients with erosive disease compared with patients with nonerosive rheumatoid arthritis (RA) or healthy individuals [438]. Both the S100A8/S100A9 complex and S100A12 have been proven to be useful as diagnostic markers of inflammation especially in non-infectious inflammatory diseases such as arthritis, chronic inflammatory lung and bowel disease. [437] S100A8 is expressed constitutively with S100A9 in neutrophils and is regulated by inflammatory stimulants [439].

Although S100 proteins are present during inflammation, they may also show anti-inflammatory actions in some situations and cell types [440]. In an OA model in rats, Zreiqat and coworkers [441] demonstrated through immunolocalisation staining that S100A8 increased in articular chondrocytes in animals treated with ZA (Fig 2.6). This corresponded to a significant reduction in joint damage, indicating that S100A8 could have a protective role against OA. In addition, meniscal fibrochondrocytes, osteocytes and occasional osteoblasts in the subchondral bone also showed positive immunostaining for S100A8. There was loss of S100A8 early in OA and progressively as cartilage degeneration ensued. Interestingly, S100A8 staining was not altered in subchondral bone or meniscus. Together, these findings suggested that loss of S100A8 could be associated with cartilage pathology.

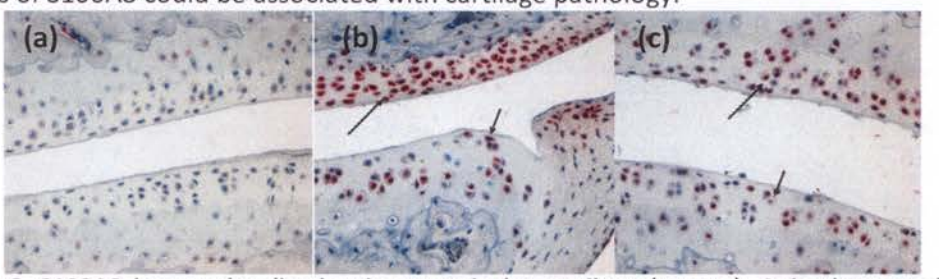


Figure 2.6. S100A8 immunolocalisation in rat articular cartilage (arrows). Animals treated with: a) Saline, b) Zometa 3 mg/kg and c) Zometa 10 mg/kg [441].

Further studies indicated that S100A8 significantly downregulated *in vitro* MMP13 expression in normal chondrocytes, after 24 hrs. This finding indicates that S100A8 acts to accumulate the cartilaginous matrix and augment new tissue in-growth by way of controlled proteolytic degradation. No effect was found on other genes such as ADAMTS-4 and-5, also important in degradative pathways. These previous studies indicate a potential therapeutic role for S100A8. Studies in this thesis were undertaken to determine the gene expression of chondrocytes in response to various S100 proteins, particularly to confirm whether MMP13 downregulation in chondrocytes is a repeatable result.

2.1.6. CHARACTERISATION TECHNIQUES

Techniques used to characterise the efficacy of the therapeutic agents, and the structure of the scaffold are described with detail in the following section of this thesis.

2.1.6.1. Gene Expression of Cartilage Modelling Markers

To determine the effect of ZA and S100 proteins on cartilage cells, gene expression was measured using Real Time Polymerised Chain Reaction (RT-PCR). This was done by extracting RNA from cells and conversion to cDNA. Primers specific for the gene of interest were used to amplify the cDNA in a Realtime PCR machine, as shown in Fig. 2.7. The amplification products were then measured and compared.

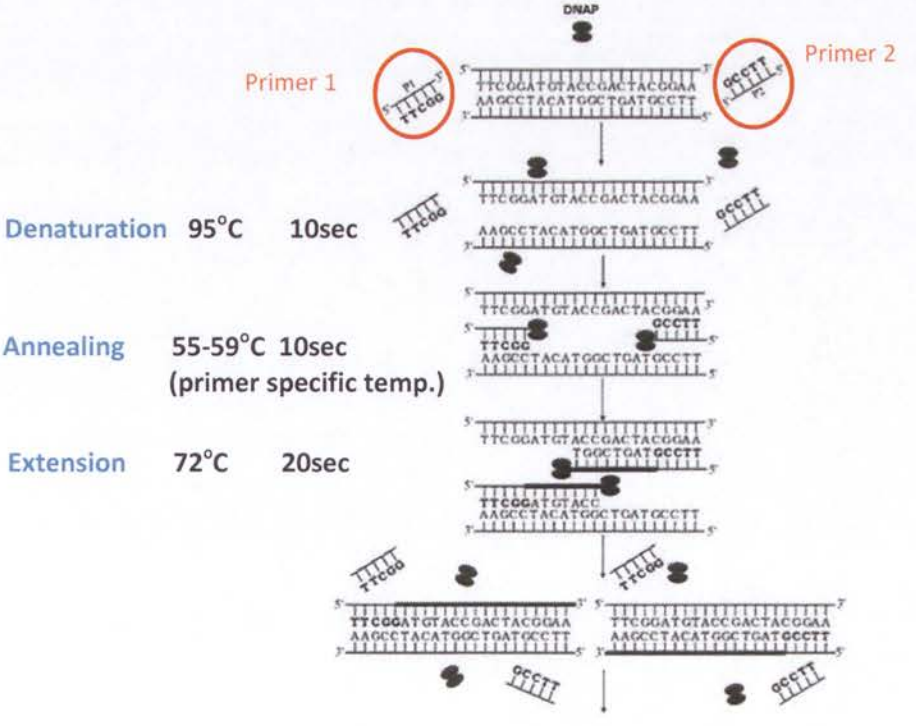


Figure 2.7. Stages of the PCR reaction.

Genes examined are listed below and included markers of matrix accumulation (Aggrecan, collagen 1, collagen 2) and matrix turnover such as members of the ADAMTS and the MMP families. GAPDH was used as a control for loading. Metalloproteinases (MMPs) are a large family of proteolytic enzymes which target ECM components within articular cartilage. Important stage-dependent metalloproteinases involved in the mediation of ECM degradation during OA include MMPs-1, -2, -3, -9 and -13 [431]. The Adamylasin family (ADAMTS; A Disintegrin and Metalloproteinase Protein) are responsible for the activation of inflammatory mediators such as TNF-α, and shed extracellular portions of transmembrane proteins. Important ADAMTS proteins include ADAMTS -1, -4 and -5. Tissue Inhibitors of Metalloproteinases (TIMPs) are major *in vivo* mediators of ECM degradation in osteoarthritis. They control activity of the MMPs and could be possible therapeutic targets. Four TIMPs are known but only TIMPs -1, -2 and -3 are found in cartilage [431].

In preparation for the PCR reaction, the quality of the DNA is measured using a UV spectrophotometer. The absorption maximum of DNA or RNA is ~260 nm. The degree of purity of the nucleic acids can be assessed by examining other wavelengths in which protein and polysaccharides have known absorption maxima (280 or 230 nm). A sample containing RNA is judged as being uncontaminated if the 230:260:280 ratio is 1:2:1. If there is significant deviation from the ratio, then it is evident that contaminants are present and that further purification of the sample is necessary. For the current experiments, a range of 1.7-2.2 for the 260:230 ratio was considered acceptable.

After the DNA is amplified using PCR, the temperature is raised for a melting sequence. SYBR green enables the detection of the melting point of distinct products to be detected. Peaks occurring at a single melting temperature indicate a pure product, as shown in the melt curve in Fig. 2.8. Multiple peaks indicate the presence of any double stranded DNA, including primer dimmers, contaminating DNA and PCR product from misannealed primer and these results are rejected.

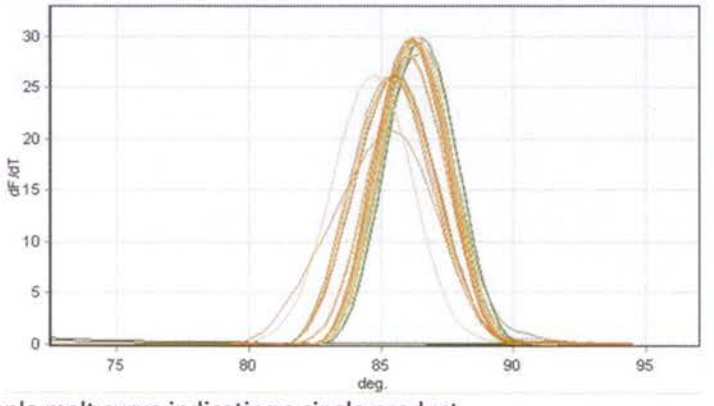


Figure 2.8. An example melt curve indicating a single product.

2.1.6.2. Micro Computer Tomography (MicroCT)

MicroCT is one of the few methods which enables characterisation of the 3D microstructure of a scaffold [2, 100, 442- 445]. This method was utilised in both chapters 2 and 3. With recent advances it also has the potential for the imaging of cells, tissue and vasculature within the 3D space of the matrix [2, 442, 446]. MicroCT involves acquisition of X-ray images at multiple angles around the object, through a rapid and nondestructive process. This is followed by reconstruction of the acquired images into a 3D computer model of the object's microstructure. MicroCT is capable of achieving a spatial resolution up to at least 0.3 μM; about three orders of magnitude higher than conventional CT systems, which can resolve 0.5 mm [442].

With MicroCT it is possible to:

1. Obtain transmission shadow images of tissue or biomaterials;
2. Reconstruct any cross-section of the complete 3D object microstructure;
3. Calculate distance, surface area and volume;
4. Analyse density and porosity of an object; and
5. Achieve 3D rendering and realistic visualisation through animation of the reconstructed images.

MicroCT has been widely used to quantify the 3D microstructure of calcified tissue such as bone, and to provide quantitative information about its functionality, porosity and mineral density. Soft tissue has also been studied, including both vascular and renal structures [447, 448]. MicroCT has more recently been used to characterise the physical properties of scaffolds [117, 322, 442-446, 449].

It has also been used to visualise cells on scaffolds, including chondrocytes embedded in porous gelatin scaffolds [446]. Zehbe and coworkers [446] were able to visualise 7 μm chondrocytes as 2-3 voxels on the MicroCT reconstruction, when they were stained with combined gold and silver. While cell clusters were easily detected, some individual cells exhibited a low level of contrast, and non-specific staining was also present. Doping soft tissue with phosphomolybdic acid is an approach which has been used by Golding and Jones at the University of Sydney to enhance the contrast of molluscan anatomy. This method was trialled in chapter 3.

In this chapter, wollastonite (calcium silicate) and sphene (ti-doped calcium silicate) scaffolds were formed using a polymer template technique. The scaffolds were characterized for pore morphology and compressive properties. Methods were developed for infusion of the scaffolds with alginate and gelatin. Chondrocytes were cultured on the biphasic scaffolds. The effect of Zoledronic acid and S100 proteins on chondrocytes were then examined using RT-PCR, as potential therapeutic candidates for scaffold inclusion.

2.2. DESIGN & SYNTHESIS OF BIPHASIC CERAMIC/HYDROGEL SCAFFOLDS

2.2.1. OSTEOCHONDRAL BED CONSTRUCT CONCEPT

Fig.. 2.9 shows the concept for a biphasic scaffold, with a hydrogel cartilage component embedded in a porous, sintered calcium silicate-based scaffold. Chondrocytes could be seeded in the gel section and the ceramic scaffold could be acellular, being infiltrated by osteoprogenitor cells from the surrounding blood [90].

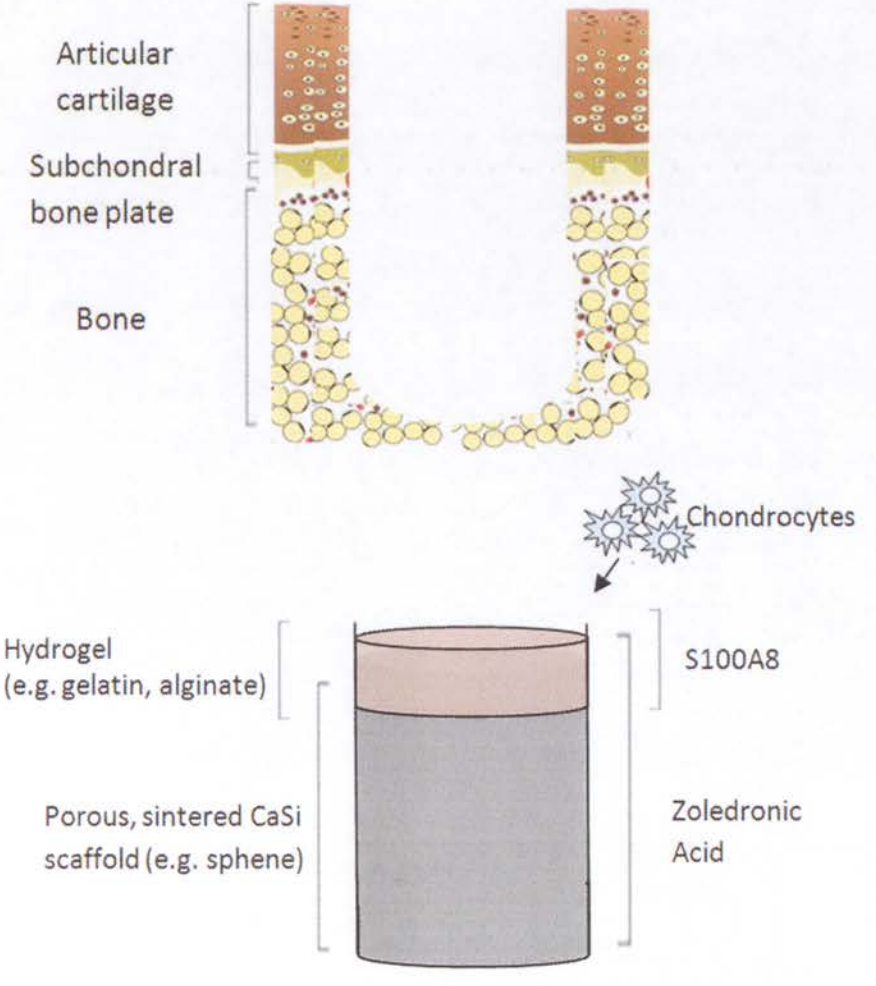


Fig. 2.9. Schematic diagram of an osteochondral defect and the osteochondral bed construct.

2.2.2. SYNTHESIS OF SCAFFOLD PRECURSOR POWDERS

The following sections of this chapter will describe the formation of bioceramic powders, which were used to synthesise biphasic microspheres and scaffolds. Physical characterisation was performed to investigate the macrostructure, porosity and mechanical properties of the scaffolds. *In vitro* testing of chondrocytes was performed on scaffolds.

2.2.2.1. Synthesis of Wollastonite ($CaSiO_3$, WT) Powders

$CaSiO_3$ powders were synthesised by the reaction of sodium meta-silicate nonahydrate (Na_2SiO_3-$9H_3O$, Thermo Fisher Scientific) with calcium nitrate tetrahydrate ($Ca(NO_3)_2$-$4H_2O$), Sigma Aldrich). 1000 ml of 0.4 M calcium nitrate tetrahydrate solution with a pH 11.4 was vigorously stirred at room temperature, and 1000 ml of 0.4 M silicate was added drop wise over 40–60 min to produce a white precipitate. The white precipitate was then stirred for 12 hrs followed by washing four times with distilled water to remove the Na^+ and NO_3^- ions, and then washed two times with 100% ethanol to improve the dispersion characteristics. After washing, the remaining liquid was removed by vacuum filtration, and the precipitate was dried at 80°C for 24 h, and then calcined at 800°C for 2 h. The obtained $CaSiO_3$ powders were sieved to obtain 38–45 mm particulates, and mixed with 6 wt% polyvinyl alcohol binder. The obtained dry gel was ground using a mortar and pestle and transferred into a corundum crucible and calcined at 1100°C. The calcined powders were sieved through a 230 mesh sieve to obtain a particle size <66 μm.

2.2.2.2. Synthesis of Sphene ($CaTiSiO_5$) Powders

$CaTiSiO_5$ powders were synthesised by sol–gel process using tetraethyl orthosilicate ($(C_2H_5O)_4Si$, TEOS, Sigma Aldrich), titanium (IV) butoxide ($Ti(O(CH_2)_3CH_3)_4$, $Ti(Bu)_4$, Sigma Aldrich) and calcium nitrate tetrahydrate ($Ca(NO_3)_2$-$4H_2O$, Sigma Aldrich). TEOS and $Ti(Bu)_4$ were mixed with ethanol and 2 M HNO_3 (mol ratio: TEOS/$Ti(Bu)_4$/ethanol/HNO_3 5 1:1:10:0.08) and hydrolyzed for 30 min while stirring. The $Ca(NO_3)_2$-$4H_2O$ were added into the mixture (mol ratio: TEOS/$Ti(Bu)_4$/$Ca(NO_3)_2$-$4H_2O_5$ 1:1:1), and reactants were stirred for 5 hr at room temperature followed by incubation at 60°C for 1 day before drying at 100°C for 2 days. The obtained dry gel was ground using a mortar and pestle and transferred into a corundum crucible and calcined at 1100°C. The calcined powders were sieved through a 230 mesh to obtain a particle size <66um.

2.2.3.1. Synthesis of Bioceramic/Alginate Composite Microspheres

Bioactive sphene/alginate composite microspheres (diameter: ~2 mm) were formed using a similar protocol previously described by our group [117] (Fig 2.10).

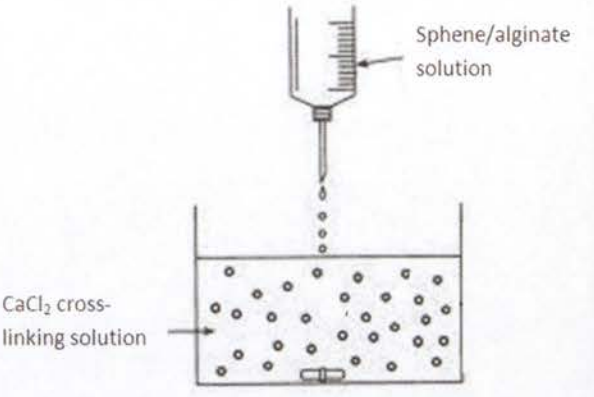


Fig. 2.10. Schematic diagram of the microsphere synthesis procedure.

Alginate powder (viscosity 20–40Cp, Sigma), was dissolved in water at a 3% (w/v) concentration, and the alginate solution was then added to $CaTiSiO_5$ powders. The mixture was stirred for 1 hr and ultrasonicated for 5mins to form homogenous mixtures. The mass ratio of inorganic powders/alginate was 1.67. The mixtures were extruded drop-wise with a 0.65 mm diameter needle into a 0.1 M $CaCl_2$ crosslinking solution to form spherical particles. The microspheres were hardened by 30 min immersion in the crosslinking solution, then filtered and dried at 50°C overnight to obtain composite microspheres. The microspheres were not characterised or used further, as porous scaffold were deemed more suitable for load bearing applications.

2.2.3.2. Synthesis of Porous Ceramic Scaffolds

Porous wollastonite or sphene scaffolds (Fig. 2.11) (dimensions: 10 x 10 x 10 mm^3) were prepared using a polymer sponge template method as previously described [119]. The porosity and interconnectivity could be controlled via adjusting the thickness of the slurry coating on the foams. To prepare ceramic scaffolds, $CaSiO_5$ or $CaTiSiO_5$ powders were suspended in a 10 wt% polyvinyl alcohol aqueous solution (PVA, Sigma Aldrich, USA) water solution binders (weight ratio:PVA solution/powders=1:9). A polyurethane foam template (density 25 parts per inch, porosity> 97 vol% was cut to the desired shape (5 x 7 x 7 mm^3) to replicate a porous scaffold. The prepared sponge was immersed in a glass beaker containing the target material slurry and the mixture was compressed with a glass stick to force the slurry to migrate into the pores of the foams. The struts of the foams were uniformly coated, with the ceramic slurry whilst maintaining open pores. The impregnated sponge was



Figure 2.11. Porous sphene scaffolds.

sintered (at 1100 and 1250°C for 3 hrs with a heating rate of 2°C/min to remove the polymer to form porous sphene scaffolds. Sphene scaffolds were sterilised via heat treatment in an autoclave.

2.2.3.3. Synthesis of Biphasic Bioceramic/PDLLA Scaffolds

The wollastonite/PDLLA scaffolds (known as 'WTPL') were prepared by surface modification of WT scaffolds with PDLLA. Briefly, PDLLA powders (molecular weight: 75,000–120,000; Sigma Aldrich, USA) were dissolved in chloroform (Sigma Aldrich, USA) at a concentration of 10% (w/v) under stirring. The sintered WT scaffolds were immersed in PDLLA solution for 3 min and centrifuged to remove any excess PDLLA solution with a centrifugal speed of 1000 rpm. The modified scaffolds were air-dried under a fume hood for 1 day followed by heating at 60°C for 1 day to remove chloroform solvent.

2.2.3.4. Synthesis of Biphasic Bioceramic/Alginate Scaffolds

The process for synthesis of the biphasic scaffolds is shown schematically in Fig 2.12. Alginate powder (viscosity 20–40Cp, Sigma), was sterilised in a small glass jar via heat autoclaving. Alginate was dissolved in serum-free culture media (DMEM; GIBCO°, Invitrogen) at a 2% (w/v) concentration. The mixture was stirred for 1 hr to form a homogenous solution. The solution was extruded into the scaffold using a 20 µL pipette. The gel was dropped in at least 3 positions on the top surface of the scaffold, to evenly distribute the gel. Scaffolds were carefully transferred into a small (diameter: 10 cm) glass tube, using tweezers. Some scaffolds were kept upright at room temperature for 3 hrs. Other scaffolds were mixed for 3 hrs using an electric rotary mixer. This was to ascertain the best method for gel distribution when the scaffolds were seeded with cells. The scaffolds were immersed into a 0.1 M $CaCl_2$ crosslinking solution for 10 min. Specimens were kept in clean, sealed glass tubes, at 37°C, 5% CO_2 for 2 hrs for either 3 or 20 days.

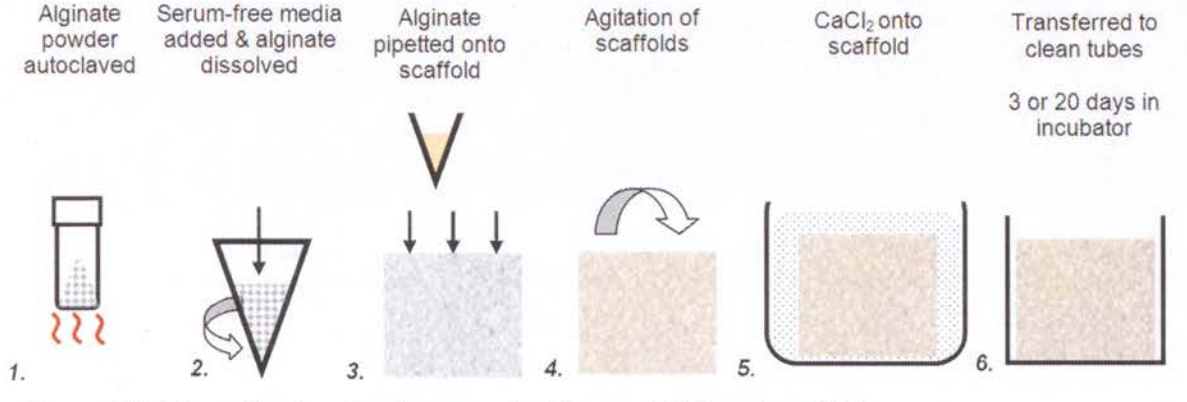


Figure 2.12. Schematic of synthesis process for bioceramic/alginate scaffolds.

2.3. PHYSICAL CHARACTERISATION OF SCAFFOLDS

2.3.1. METHODS

Microspheres and scaffolds were successfully formed using the above methods. The morphology and mechanical properties of representative scaffolds were investigated using the following methods.

2.3.1.1. Scaffold Morphology

Scanning Electron Microscopy (SEM, Philips XL 30 CP, The Netherlands) and Micro-computerised tomography (MicroCT, Skyscan 1072, The Netherlands) and were performed with Chengtie Wu to investigate the morphology of representative scaffolds. The full protocol is included in section 3.2.2.7. WT and WTPL scaffolds were visualised. The porosity (P) of these scaffolds was calculated according to the equation:

$$P = [(V_{total\ pore})/(V_{scaffold})] \cdot 100\%,$$

where $V_{total\ pore}$ is the total pore volume and $V_{scaffold}$ is the scaffold volume.

The interconnectivity (I) was calculated according to the equation:

$$I = [(V_{total\ pore} - V_{disconnected\ pore})/V_{total\ pore}] \cdot 100\%,$$

where $V_{disconnected\ pore}$ stands for the disconnected pore volume.

Biphasic ceramic/alginate scaffolds were investigated using SEM to determine the effect of rotary mixing, or of periods of incubation, on the appearance of the scaffold and gel. Specimens were fixed using 2% gluteraldehyde and dehydrated by serial ethanol dilutions. Scaffolds were coated with 15 nm gold and imaged using the Philips SEM505 Electron Microscope.

2.3.1.2. Mechanical Testing

Mechanical testing (Fig 2.13) was performed with the assistance of Chengtie Wu and Philip Boughton. Mechanical testing was performed in phosphate buffered saline using an ELF 3400 Uniaxial Tensile Tester with a load cell of 50N. For compressive tests, scaffolds (dimensions: 10 x 10 x 10mm^3) were compressed at a speed of 0.5mm/s. The compression strength was defined as the peak stress which was experienced by the scaffold. The effect of PDLLA coating on the WT scaffold



Fig. 2.13. Compression testing of bioceramic scaffolds.

was ascertained for compressive strength, modulus and strain. Four scaffolds were used for each test and the results are expressed as mean ± standard deviation.

2.3.2. RESULTS

2.3.2.1. Scaffold Morphology

SEM micrographs and MicroCT analysis of the WT and WTPL scaffolds (Fig. 2.14) demonstrated the formation of porous structures with an interconnected porous network and open macropores ranging from 300-500 μm in diameter. The porosity of the WT scaffolds was calculated as 81.5 vol%. The scaffolds had an interconnectivity of ~99.5%, meaning that 99.5% of the pores had some form of interconnectivity to the other pores. The strut thickness was 175 ± 82.9 μm. PDLLA modification of the WT scaffolds led to the formation of a PDLLA layer (3-5 μm) on the surface of the pore wall. PDLLA modification did not decrease the pore size, porosity or interconnectivity on the surface of the pore wall. The coated scaffolds were calculated to also have a high porosity (82.2%) and interconnectivity (99.9%).

Micropores were visible within the WT scaffold; however, these pores were filled when the scaffolds were coated with a PDLLA film (Fig 2.15). Micropores were typically ~2x10 μm in diameter, and their degree of interconnection was unclear.

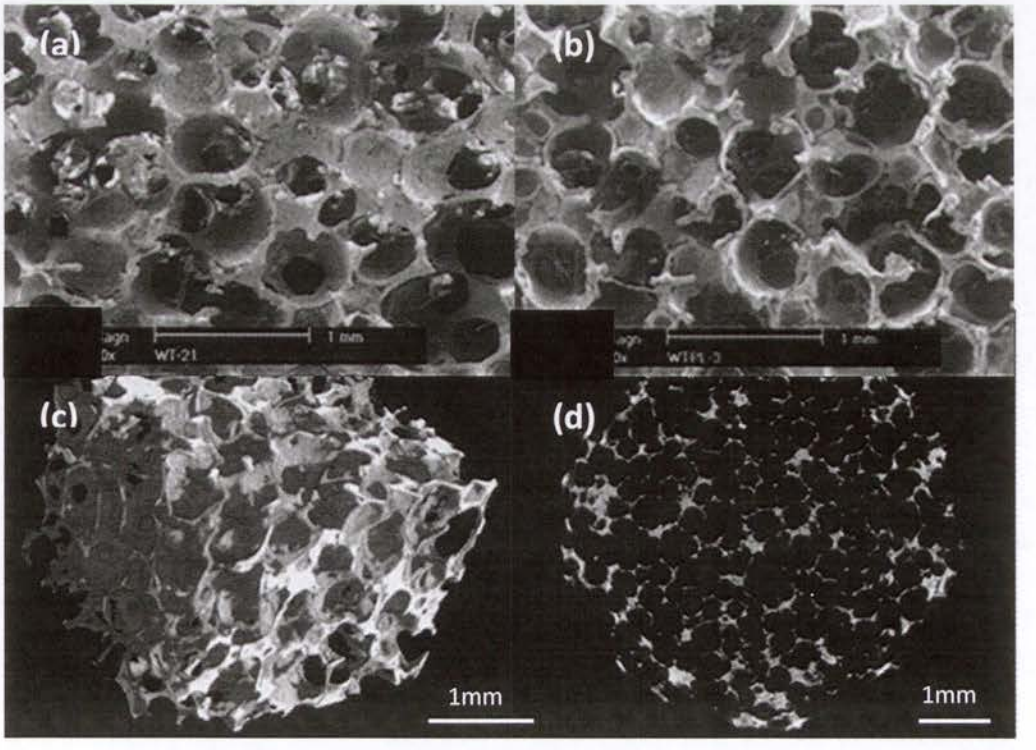


Figure 2.14. SEMs of (a) WT scaffold (b) WTPL scaffold. WTPL scaffold viewed using (c) MicroCT 3D reconstruction (d) a single MicroCT cross-sectional slice.

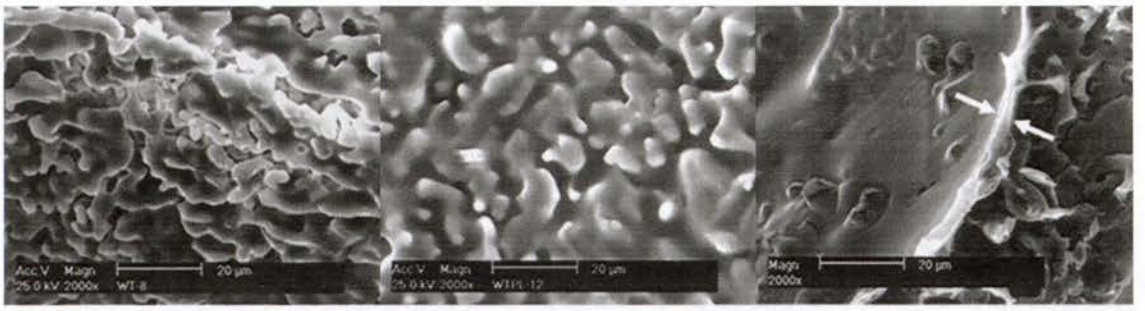


Figure 2.15. SEM micrographs of mesoporous surface of the WTPL scaffold.

SEM micrographs suggested that the sphene scaffolds had a pore size ranging from 300-700 μm. Their porosity and interconnectivity could not be confirmed, as MicroCT was not done on these specimens. The levels of interconnectivity appeared lower than the WT scaffolds, when examined visually using SEM.

SEM investigations demonstrated that when alginate was infused into the ceramic scaffold, the alginate fully filled many of the pore spaces (Fig 1.16). A slight improvement in gel distribution was observed when the scaffolds were subjected to 3 hrs rotary mixing. The scaffolds which had been incubated for 20 days exhibited a higher degree of cracking in the alginate.

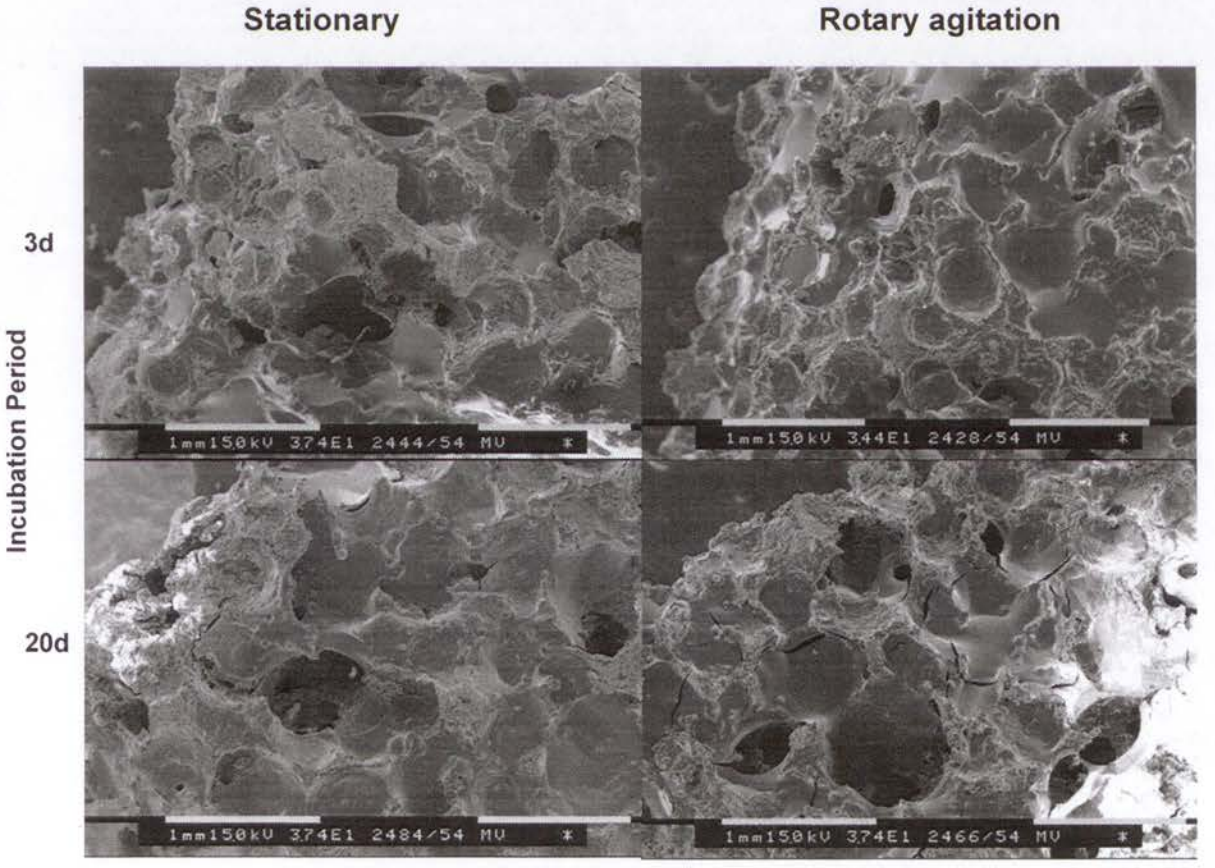


Figure 2.16. Alginate-infused sphene scaffolds.

2.3.2.2. Mechanical Characterisation

The ceramic scaffolds were observed to be extremely brittle and experience cracking of the ceramic struts at extremely low loads. Fig. 2.17a depicts the crumbled appearance of the WT scaffold after the compression test. This was in contrast to the coated scaffold (Fig. 2.17b), which showed increased shape retention, but still experienced internal cracking early in the compression test.

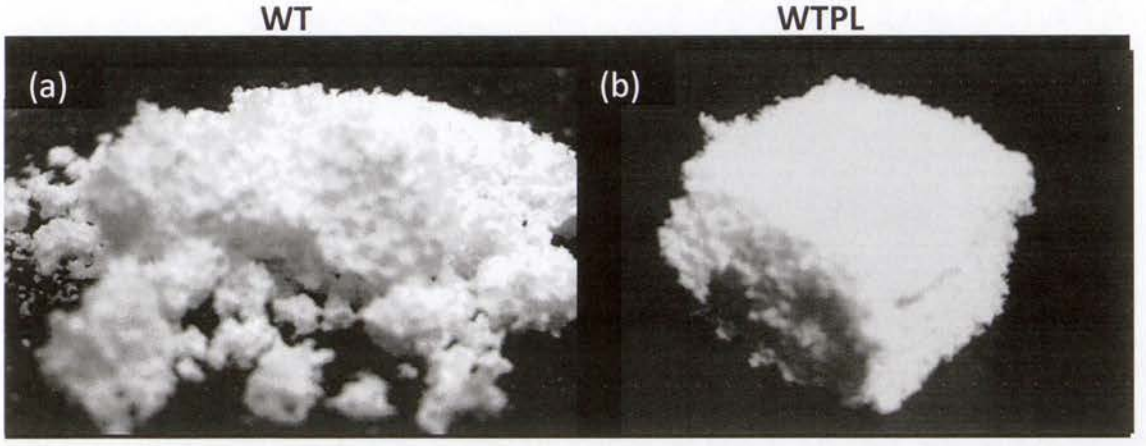


Figure 2.17. Photographs of (a) WT and (b) WTPL scaffolds after compression testing.

Compression testing demonstrated an increase in compressive strength and modulus (>3x) for the PDLLA coated WT scaffolds, compared to the pure WT scaffolds (Fig. 2.18, Table 2.3). The compressive strength results reported here are indicative of the maximum load which was held by the crumbled scaffold. The strain was also recorded at this point. Levels of strain were extremely low for both scaffolds (average: <5%) though were increased for the WTPL scaffold.

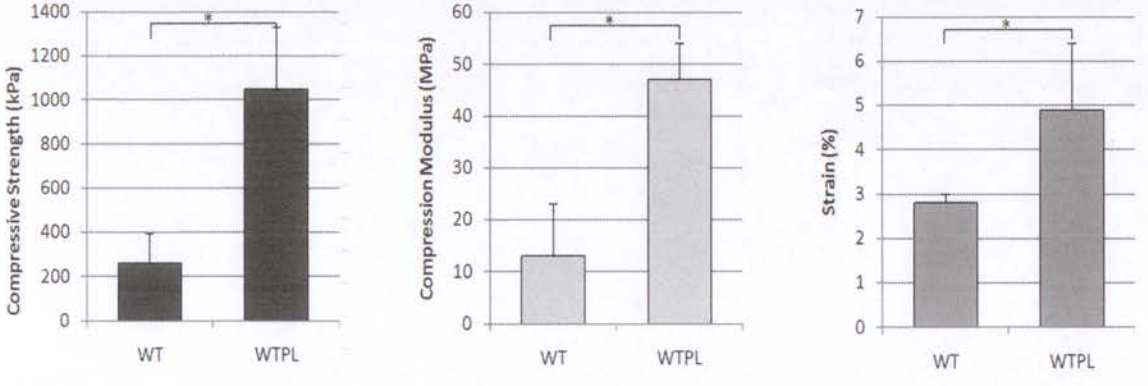


Figure 2.18. Compressive properties for the wollastonite (WT) and wollastonite/PDLLA (WTPL) porous scaffolds. * indicates <0.05 significance

Table 2.3. Compressive properties for the wollastonite-based scaffolds (average±stdev of 4 samples).

	Comp strength (kPa)	Comp Modulus (MPa)	Strain (%)
WT	262±133	13±10	2.8±3
WTPL	1048±282	47±7	4.9±1.5

2.3.3. DISCUSSION

In this study, novel calcium silicate-based scaffolds were successfully synthesised using a polymer foam replication technique. The biocompatibility of hydrogel-filled scaffolds were examined to help determine whether such constructs may have potential for osteochondral bed engineering. The composition of these scaffolds (pure calcium silicate- WT) or sphene (titanium-doped) were chosen for proof of concept, but other compositions have been made by our group which may provide further benefits for stimulation of bone gene expression (discussed earlier). In order to address cartilage pathology such as arthritis, therapeutic actions of ZA or S100 proteins were investigated as potential candidates for release from the cartilage layer of the scaffold. To the author's knowledge, this is the first study to synthesise biphasic calcium silicate-based scaffolds and to test the mechanism of action of ZA directly on chondrocytes.

2.3.3.1. Osteochondral bed model

An osteochondral bed model was designed to test a bioceramic-based scaffold construct. It is well established that the health of the cartilage is highly dependent on the health of the underlying bone. Inclusion of a bioactive bone scaffold may help to provide initial and long-term anchorage to and attachment within the bone. This should improve the long-term response to the implant and address some of the difficulties with current solutions. The scaffold could be used to address the pathology of both the cartilage and bone, through the localised delivery of therapeutics to the specific tissue type.

2.3.3.2. Synthesis process

The scaffold synthesis process could be readily performed with minimal specialised equipment. However, it was a time consuming process, with a small number (~8 scaffolds) requiring several days to form. Milling of the ceramic powders was a labor intensive process. Scaffolds were difficult to handle, due to the tendency of cracking within the porous structure and breaking off of scaffold portions.

2.3.3.3. Scaffold Morphology

When visualised using SEM and MicroCT, the WT scaffolds were confirmed to have a highly porous structure (81.5%) with large pore size (300-500 μm), micropores (~2x10 μm) and high interconnectivity. After surface modification by the addition of a thin PDLLA layer (3-5 μm), the porosity (82.2%), pore size (300-500 μm) and interconnectivity (99.9%) were maintained. The struts had an inherent thickness of ~175 μm which was anticipated to provide rigidity and strength for load-bearing bone applications. The pore sizes of the sphene scaffolds were measured to be 300-700 μm. Differences in pore size (and probably interconnectivity and porosity) between the WT and sphene scaffolds were attributed to differences in strut thickness formed during the slurry dipping process, rather than the ceramic powder composition. In addition, a variation in scaffold morphology was evident due to minor scaffold breakage during handling.

2.3.3.4. Gel infusion

After gel infusion, the porosity and interconnectivity of the scaffolds reduced to almost zero as the gels filled the pore spaces. Infusion of gel for the chondrocyte layer of the scaffold was anticipated to be necessary for maintenance of the chondrogenic phenotype [418]. Even though an increase in the uniformity of the gel distribution in the scaffold was observed after rotary agitation, it was decided that during cell seeding the scaffolds would not be agitated. This was to minimise the possible risk of cell damage and death due to compression during the agitation process, in addition to a prolonged period removed from the incubator. The distribution of gel at different positions within the scaffold could not be observed using SEM, due to the inability to readily cross-section the ceramic scaffolds because of their fragility.

2.3.3.5. Comparison of scaffold morphology with other scaffolds

Other researchers have explored the potential for a porous ceramic scaffold or decellularised biological matrix (sourced from bone or coral) to serve as a bone component [4, 5, 90, 402, 407, 411]. Generally, these scaffolds have a mean pore diameter between 300-600 μm and porosity of 50-70%. These parameters are often chosen to mimic the structure and composition of native bone [4]. The scaffolds synthesised in the following chapters of this thesis have a similar pore size but a higher porosity, in order to facilitate filling of the scaffold with host tissue.

2.3.3.6. Mechanical Properties

When subjected to the compressive test, the WT scaffolds were brittle and crushed to powder. However, the WTPL scaffolds maintained their composite configuration. The compression strength of the WTPL scaffold increased almost 4 fold when compared to the WT scaffold (262 kPa and 1048 kPa, respectively). The compressive modulus increased from 13 MPa to 48 MPa with the scaffold coating. The scaffolds both showed a low capacity to strain, however this was increased slightly for the WTPL scaffold (WT: 2.8%, WTPL: 4.9%). This improvement in mechanical properties can be attributed to two possible reasons. (1) The WT scaffold possesses some micropores on the pore wall and some collapsed networks inside the scaffold, which results in decreased mechanical strength. PDLLA coating fills the micropores and induces a more uniform and continuous network in the scaffolds which prevents it from collapsing (2) PDLLA has a high mechanical strength and provides reinforcement to the inorganic phase.

2.3.3.7. Comparison of mechanical properties with literature

The compressive strengths reached in this study are significantly higher (>6x) than $CaSiO_3$/PDLLA and $CaSiO_3$/collagen scaffolds (<160 kPa) prepared using solvent casting/particulate leaching and freeze drying methods which are reported in the literature [113, 114, 397]. Previous studies have shown that the compressive strength of porous hydroxyapatite scaffolds (porosity 69–86%) and 45S5 Bioglass scaffolds (porosity 84–89%) prepared via a polymer sponge template method were about 30–290 and 420–600 kPa, respectively [414, 411]. The strength of the WTPL scaffolds prepared in this study was higher than that for hydroxyapatite and Bioglass scaffolds. The compressive strength of the WTPL scaffold falls within the range of the strength of cancellous bone, which is 0.2-4 MPa [117].

In summary, although the calcium silicate-based scaffolds which were produced in this study are likely to be bioactive and biocompatible, they lack sufficient compressive strength and modulus for load bearing applications. In addition, in order for optimal chondrogenesis to occur, a scaffold would ideally possess a higher capacity to strain, in order to ensure sufficient mechanical cues are passed to the developing tissue and ensure chondrogenesis occurs.

2.4. OVINE CHONDROCYTE SEEDED BIPHASIC SCAFFOLDS

2.4.1. METHODS

2.4.1.1. Isolation of Chondrocytes from Ovine Joints

Articular cartilage was dissected from the trochlear groove of 6 month old sheep. Ovine Articular Chondrocytes (OACs) were isolated from the cartilage extracellular matrix via a sequential enzymatic digestion performed with Pronase then Collagenase/Dnase. Cells were expanded in cell culture flasks prior to seeding onto biphasic scaffolds.

A few days prior to the dissection, 6-8 ovine knee joints were ordered by calling Steve at Pear Meats (Ph: 9631 9866). Ovine joints were collected from local butchers as convenient for the abattoir (e.g. Leichardt Marketplace). Extraction was done within 24 hrs of joint pick up, preferably on the same day. Joints were stored in the fridge until usage. 2 sterile bottles were prepared for cleaning the scalpels, the first containing sterile phosphate buffered saline (PBS, GIBCO°, Invitrogen), and the second containing 70% Ethanol. PBS was placed into the petri dishes for collection of the cartilage. Ovine joints were sprayed (over the sink) with 70% ethanol. Joints were dissected on bench paper in the laminar flow cabinet. Using a sterile scalpel (#22, BD Bard-Parker™) attached to an autoclaved surgical blade handle, excess meat was removed from around the knee. Deliberate cuts were made along the side of the knee to remove the joint capsule. Care was taken not to damage the articular cartilage. The articular cruciate ligament was carefully cut. The capsule was gently opened to expose the trochlear groove (a smooth, curved, cream coloured region). Scalpels were regularly rinsed in the ethanol then PBS bottles, when necessary. A sterile stainless steel scalpel (#11 or #15) was used to score square regions of approx. 5mm^2. The cartilage was removed from the bone by gently sliding the scalpel under the cartilage. Care was taken to avoid collecting the blood. Cartilage explants were placed into the petri dishes. The cartilage was finely diced using 2x scalpel blades (#11) as scissors. Some PBS was removed from the petri dish so the cartilage was not floating. The end was cut off a plastic transfer pipette, using a sterile scalpel (#22). This was used to transfer the cartilage and PBS to a 50mL centrifuge tube (Corning®). The volume was adjusted to 40mL using PBS. The volume of PBS was adjusted to 20 mL. Tubes were capped and mixed gently by inversion. Centrifuge tubes were spun at 20°C, 1500-2000 rpm for 10 mins (Beckman Bench Centrifuge). In the laminar flow hood, excess PBS was slowly removed using a sterile transfer pipette, until 10 mL remained.

The first step of enzymatic digestion to isolate the chondrocytes was performed by addition of 1 mg/mL pronase and incubation at 37°C for 2 hrs. Meanwhile, the second digestion solution

was prepared as follows. Dulbecco's Modified Eagle Medium: Nutrient Mixture F-12 (DMEM/F12, GIBCO®, Invitrogen) was combined with 10% heat-inactivated Foetal Calf Serum (FCS, Invitrogen), 0.05% collagenase 1 (0.5 mg/mL, type 1A; Sigma-Aldrich) and 0.01% DNase 1 (10 mL per sheep joint, Sigma-Aldrich). For example, for 6 joints, 30 mg/60mL collagenase and 6 mg/60 mL DNase were used. This solution was sterilised by passing through a 0.22 micron filter (Millipore) into a sterile 50 mL centrifuge tube. The cell/pronase-containing centrifuge tubes were spun at 1500-2000 rpm for 10 min at 20°C. The pronase solution was removed to waste until 15mL was remaining in the tube. The prepared collagenases digestion solution was added to each tube. The tubes were capped and mixed gently by inversion. The cartilage was digested at 37°C, 5% CO_2 overnight, until the extracellular matrix had been completely removed. The centrifuge tubes were spun at 1500-2000 rpm for 10 min at 20°C. The digestion solution was removed to waste and fresh DMEM/F12/10%FCS was added to each tube. The cell pellet was gently resuspended using a transfer pipette. The centrifuge tubes were spun at 1500-2000 rpm for 10 min at 20°C. The media solution was removed to waste and fresh DMEM/F12/10% FCS was added to each tube. Pellet was again gently resuspended using a transfer pipette. The centrifuge tubes were spun at 1500-2000 rpm for 10 min at 20°C. The media solution (including fat) was removed to waste. 15 mL DMEM/F12/10%FCS was added to each tube. The pellet was again gently resuspended using a transfer pipette. Undigested cartilage was removed by passing through three layers of nylon mesh (cell sieve- size 70 μm, Falcon™ BD). Cells were counted with a hemocytometer chamber in the presence of trypan blue (Invitrogen, 1:4 dilution in PBS) (ref Appendix A1). The viability was between 93-97%. The inclusion of serum in the digestion medium was found to be essential for the retention of good viability. The cells were either expanded or cryopreserved. Cells were pipetted into 150 mm^2 tissue culture flasks at a cell density of 3-6 million cells per flask.

2.4.1.2. Seeding of Chondrocytes onto Biphasic Ceramic/Alginate Scaffolds

OACs were seeded onto biphasic alginate scaffolds as shown schematically in Fig. 2.19. below. Alginate powder (viscosity 20–40Cp, Sigma), was sterilised in a small glass jar via heat autoclaving. The jar was carefully sealed prior to autoclaving using tape, and foil (to avoid water penetration). Serum-free culture medium was prepared consisting of DMEM (GIBCO®, Invitrogen) and antibiotics- 1% penicillin/streptomycin (Invitrogen). The culture medium was added to the alginate powder at a 2% (w/v) concentration. For example, 100 mg alginate to 5 mL medium. A magnet, which had been rinsed with 100% ethanol, was added to the solution. The solution was stirred overnight to form a homogenous solution. The solution was stored in the fridge. Confluent cells (6mth, P1 Ovine Articular Chondrocytes) were removed from flasks

and counted. The cells were seeded at a density of 1 million cells/scaffold in 320µL (i.e. 3.125 million cells/mL). 1 million cells were placed into each of 3 tubes and centrifuged at 20°C at 2000 rpm for 10min to form a single cell pellet for each scaffold. 320µL of alginate gel was added to each of the cell pellets. Cells were resuspended using a transfer pipette. Ceramic scaffolds (sphene, wollastonite; 10 x 10 x 10 mm^3) were gently placed into a sterile petri dish using sterilised curved tweezers. 320 µL of alginate gel/cell solution was deposited onto each scaffold. The scaffolds were immersed into a 0.1 M $CaCl_2$ crosslinking solution for 5 mins. The scaffolds were placed into a 24 well tissue culture plate and incubated at 37°C, 5% CO_2 for 2 hrs to allow cells to attach. 0.5 mL culture medium consisting of DMEM, antibiotics and 10% FCS was added to each well. Media was changed every 2-4 days and cells were allowed to proliferate for 4 weeks.

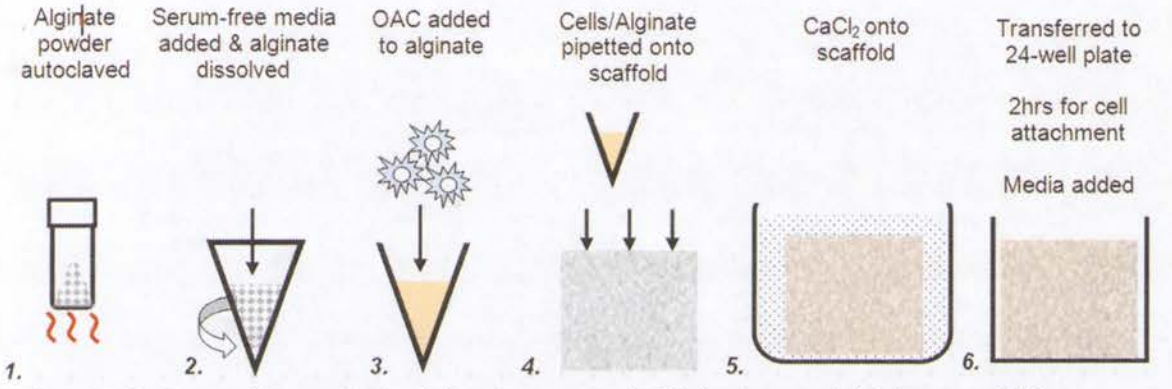


Figure 2.19. Protocol for synthesis of chondrocyte-seeded biphasic ceramic/alginate scaffolds.

2.4.1.3. Seeding of Chondrocytes onto Biphasic Ceramic/Gelatin Scaffolds

Gelatin and cells were infused into the scaffolds using the following method, as shown in the schematic diagram in Fig. 2.20. A 10% (w/v) solution was made from bovine-derived gelatin powder (Sigma-Aldrich) and DMEM (GIBCO®, Invitrogen). The powder was dissolved by carefully heating (in microwave) for short time intervals. The gelatin solution was sterilised by passing through a 0.2 µm filter (Millipore) with a syringe (BD). The gelatine was used immediately after reconstitution, as gel setting would occur rapidly. Confluent cells (6mth, P1 Ovine Articular Chondrocytes) were removed from flasks and counted. The planned cell density was 1 million cells/scaffold in 320 µL (i.e. 3.125 million cells/mL). 1 million cells were placed into each of 3 tubes and centrifuged at 20°C at 2000 rpm for 10min to form a single cell pellet for each scaffold. 320µL of gelatin solution was added to each of the cell pellets. Cells were resuspended using a transfer pipette. Ceramic scaffolds (sphene, 10 x 10 x 10mm^3, ref 2.2.2) were gently placed into a sterile petri dish using sterilised curved tweezers. 320µL of gelatin gel/cell solution was deposited onto each scaffold. The scaffolds were immersed into a 0.1 M $CaCl_2$ crosslinking solution for 5 min. The scaffolds were placed into a 24 well tissue

culture plate and incubated at 37°C, 5% CO_2 for 2 hrs to allow cells to attach. 0.5 mL culture medium consisting of DMEM, antibiotics and 10% FCS was added to each well. Media was changed every 2-4 days and cells were allowed to proliferate for 4 weeks.

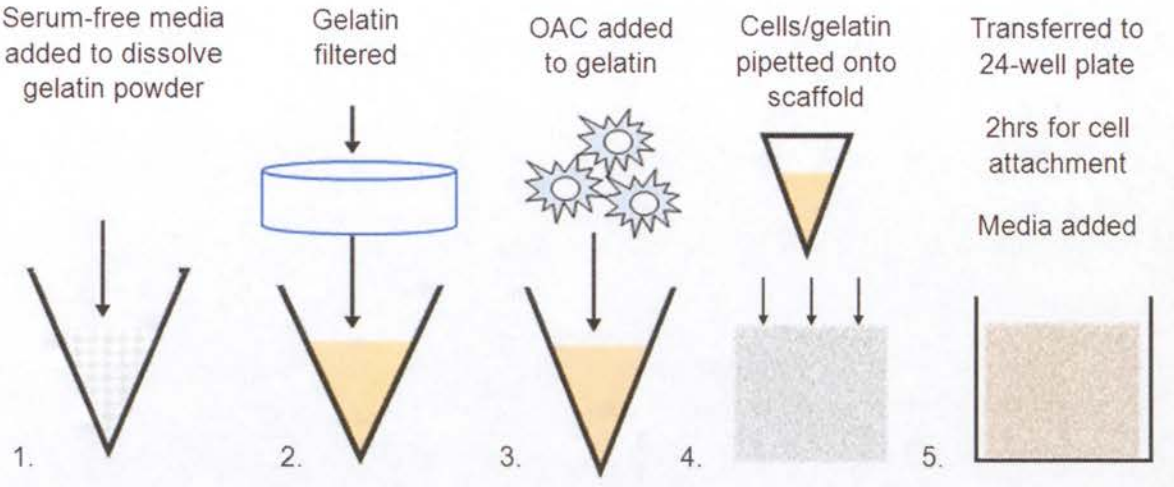


Figure 2.20. Protocol for gelatine-seeded biphasic ceramic/alginate scaffolds.

2.4.1.4. Scanning Electron Microscopy

Specimens were prepared for SEM after 4 weeks of culture (ref Appendix A2). Primary fixation was achieved by immersion in 2% gluteraldehyde (in 0.1 M Na-cacodylate buffer) for 1 hr at 37°C and post-fixation with 1% osmium in 0.1 M Na-cacodylate buffer for 1hr. Samples were dehydrated in ethanol solutions at 70%, 80%, 90% and 3 x 100% for 10min each, before being immersed for 3 min in 100% hexamethyldilazane (HMDS) for dehydration. Whole scaffolds were mounted on alumina stubs, sputter-coated with coated with 15 nm gold and imaged with a Philips Electron Microscope (SEM505).

2.4.2.1. Morphology of Chondrocytes on Biphasic Ceramic/Hydrogel Scaffolds

Biphasic scaffolds were observed using scanning electron microscopy after 4 weeks culture with primary OACs. Additional scaffolds were also cultured in order to visualise using optical microscopy, however due to infection some samples were discarded. The macro-scale appearance of the sphene/alginate and sphene/gelatin scaffolds is shown in Fig. 2.21. After 4 weeks of culture, the gels no longer completely filled the pores but did form a coating on the ceramic scaffold. Degradation of both the hydrogels and ceramic were presumed to have occurred during the 4 week culture. Indications of this included: the reduced volume of hydrogel, increased cracking, absence of pore struts and evidence of precipitates on the scaffold.

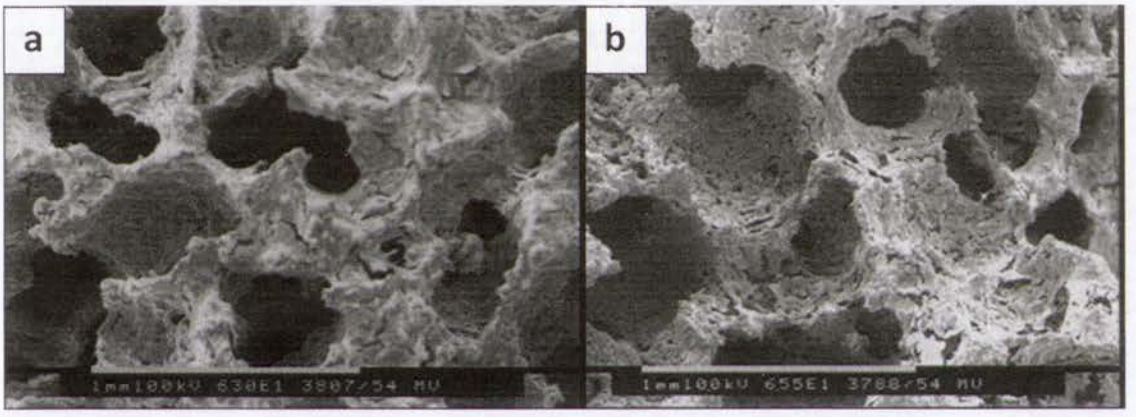


Figure 2.21. Biphasic scaffolds after 4 weeks OACs culture: (a) sphene/alginate, (b) sphene/gelatine.

At increased magnifications (Fig 2.22-2.23), the gel coatings were clearly evident but were not uniform throughout the scaffolds. Chondrocytes were observed attached to the scaffolds of all three compositions, when the top surface was examined. Fig. 2.22 depicts cells spreading on the sphene/alginate scaffold. These cells attached to precipitates on the scaffold. Cells exhibited 3D stretching behaviour with multiple, short protrusions (Fig 2.22b). Chondrocytes which were more fully embedded in the alginate demonstrated a rounded morphology, with long, filopodia-like processes (Fig. 2.22d). This is likely to correlate with retention of the chondrogenic phenotype within these regions.

The sphene/gelatine scaffold (Fig. 2.23) had a highly irregular surface texture with many features <1 μm. It was more difficult to distinguish the cells from the hydrogel for this scaffold. This could have indicated a good level of integration of the cells with the hydrogel which may have been due to a slower degradation rate for the gelatine. Most of these cells showed a star-like morphology.

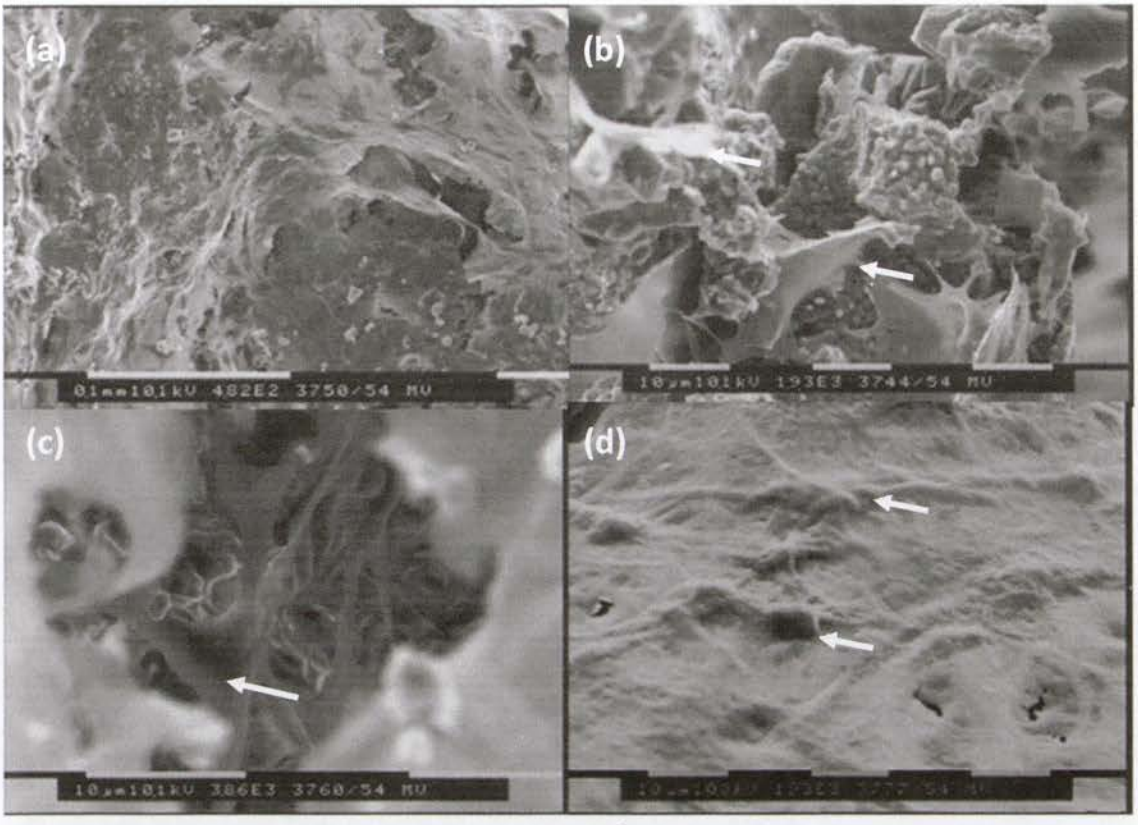


Figure 2.22. OACs cultured for 4 weeks on the sphene/alginate scaffold.

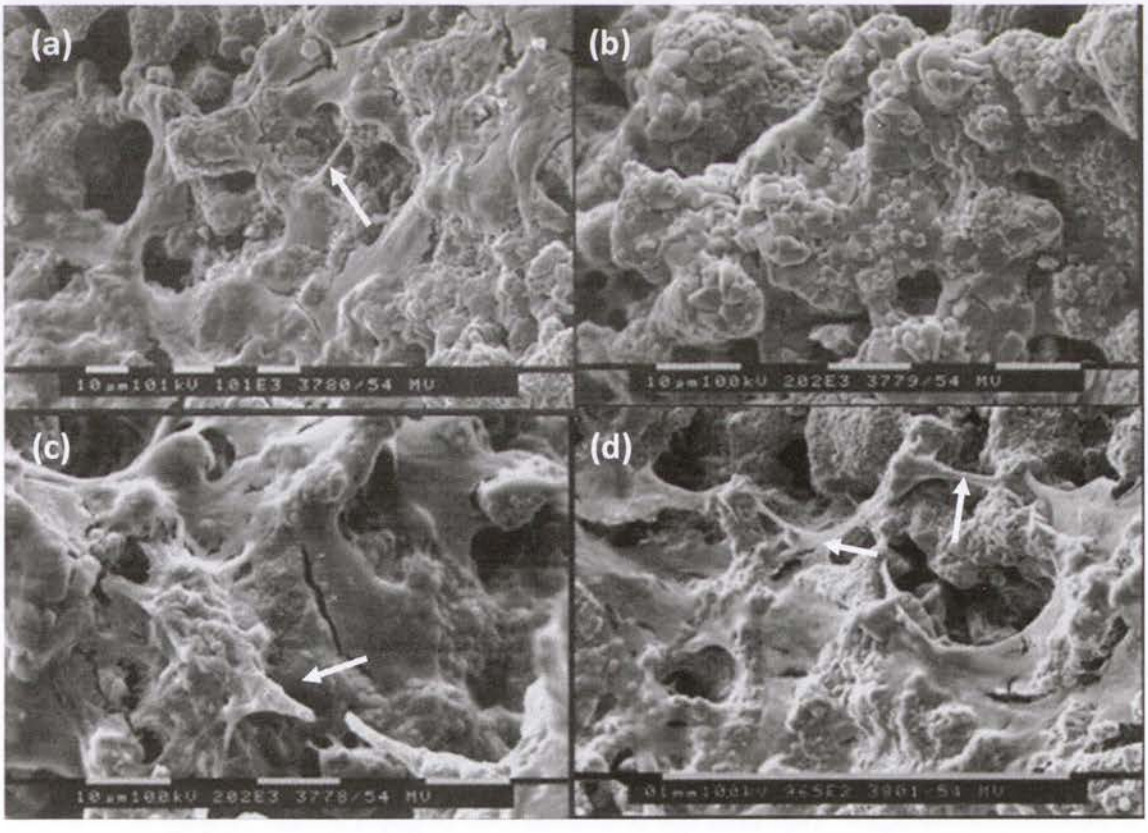


Figure 2.23. OACs cultured for 4 weeks on the sphene/gelatine scaffold. Arrows: cells which appear chondrocyte-like.

Micrographs of the WT/alginate scaffold are shown in Fig. 2.24. Cells were observed with a flat, sheet-like appearance, stretching between parts of the scaffold.

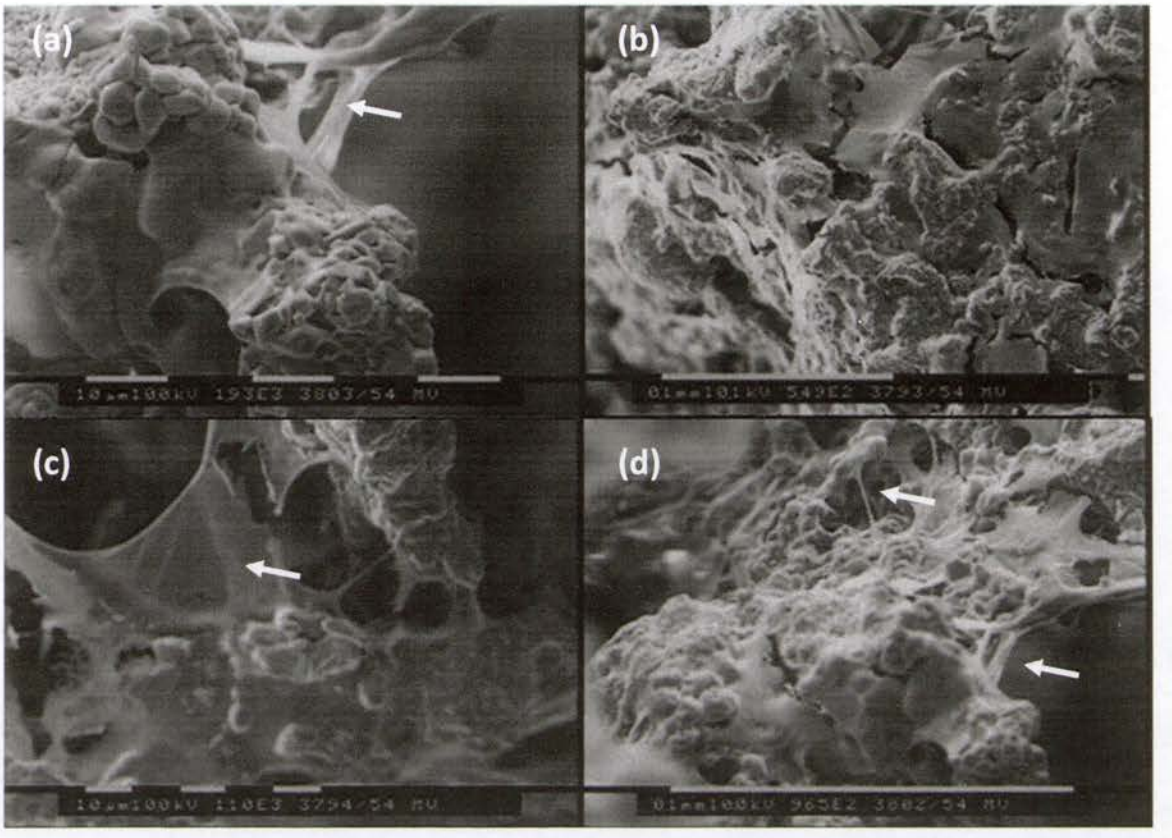


Figure 2.24. OACs cultured for 4 weeks on the WT/alginate scaffold. Arrows: chondrocytes.

2.4.3. DISCUSSION

Preliminary biocompatibility of the novel osteochondral bed scaffold was demonstrated by *in vitro* culture of ovine articular chondrocytes on biphasic scaffolds. Protocols were developed for the sterile infusion of sphene and calcium silicate scaffolds with cells and hydrogels (alginate or gelatin). These protocols could be applied for a range of scaffold types, including the soft tissue scaffold developed in chapter 3. While gel coatings initially filled the pore voids (Fig 2.16) after 4 weeks of culture with chondrocytes the gels only coated the strut surfaces (Fig. 2.21). This indicated some degradation of the gels had occurred. Articular chondrocytes were able to attach, spread and proliferate on all the biphasic scaffolds for a period of 4 weeks (Fig 2.22-2.24). Cells were observed stretching in 3D and attaching to precipitates on the scaffolds (Fig 2.22b, c, Fig 2.24a, c). In other areas, they were also embedded in the gel and took a rounded shape, suggesting a chondrogenic phenotype (Fig 2.22bd). Higher volumes of hydrogel were observed on the sphene scaffolds compared to the WT scaffold. This can be attributed to the increased stability imparted by the addition of titanium [416]. On the WT

scaffold, cells were not rounded and were likely to have lost their phenotype already (Fig 2.24). Some cracking was observed of the scaffolds (Fig 2.21), which probably occurred during handling due to the fragility of the scaffolds. Cracking of the gels were visible in the SEM images (Fig 2.24b), probably due to the dehydration and fixation process during specimen preparation.

2.5. EFFECT OF ZOLEDRONIC ACID ON CHONDROCYTES

OACs were treated with a range of ZA concentrations and the gene expression was measured. This was to determine whether ZA showed a direct effect on cartilage.

2.5.1. METHODS

2.5.1.1. Cell Culture and ZA Treatment

OACs were isolated from 6 month old ovine joints and expanded in tissue culture flasks. Complete media was made consisting of: DMEM/F12 (GIBCO®, Invitrogen), 10% heat inactivated Fetal Calf Serum (FCS) and antibiotics- 200 g/mL gentamicin, 2 mM glutamine (Invitrogen). Primary chondrocytes were removed from 70% confluent culture flasks using 1-2 mL of 0.2% (w/v) Trypsin/0.1% (w/v) EDTA (Invitrogen). Cells were subcultured in 6 well tissue culture plates at a density of 200,000 cells/mL in 2mL pre-warmed complete media (ref Appendix A1, A3). This yielded a concentration of 400,000 cells/well. Cells were cultured at 37°C, 5% CO_2 for 2 hrs. Cells were rinsed with serum-free DMEM/F12, which was removed. ZA (Zometa®; Novartis Oncology) was diluted to the following concentrations, in DMEM: 0, 10, 20 μM. ZA was added to the OAC cultures, at a volume of 2 mL per well. Control wells were used consisting of media alone (i.e. 0 μm ZA). 6 replicates were used for each treatment.

2.5.1.2. Gene Expression using Real Time Polymerase Chain Reaction

RT-PCR was performed to determine the effect of ZA on the gene expression of OACs. Total RNA was isolated from the cells using an RNeasy Mini Kit (Qiagen; Valencia, Ca, USA), according to the manufacturer's protocol (ref Appendix A5). Briefly, 300 μL Chloroform (ACS reagent, Sigma-Aldrich) was added to the samples and the tubes vortexed vigorously before centrifugation to pellet the tissue residue. The clear supernatant solution (aqueous phase) was recovered and mixed by inversion with an equal volume of 70% ethanol, and then loaded onto spin columns. Following several washing steps and an on-column DNase digestion (Qiagen, Hilden, Germany), RNA was eluted from the column with 32 μL of RNAse free distilled H_2O.

Total RNA was quantified using a Nanodrop ND-1000 Spectrophotometer and each sample was assessed for purity to confirm the absence of detectable DNA.

Reverse Transcription reactions were undertaken in order to convert the RNA to cDNA. 1ug total RNA was transcribed using the Omniscript RT kit (Qiagen; Valencia, Ca, USA), according to the manufacturer's protocol (ref Appendix A6).

Aliquots of cDNA were amplified by Polymerase Chain Reaction (PCR) using a RotoGene 6000 RT-PCR Machine (Corbett Research). Samples were prepared as described in Appendix A7. Primers used for this experiment were for anabolic genes (build ECM); aggrecan, collagen I, collagen 2 and catabolic genes (break down ECM); ADAMTS 1, ADAMTS 5, MMP 13 and the housekeeping gene; GAPDH. Specific primer sets (Sigma Genosys, Castle Hill, New South Wales) were used (ref Appendix A8). The RotoGene cycling parameters were set as described in Table 2.4.

Table 2.4. The process of Real-Time Polymerase Chain Reaction, as completed by the RotoGene 6000.

Step	Procedure	Temperature/Time
1	Initial Denaturation	Hold @ 95°c, 10 min
2	Cycling (40 repeats): Denaturation Annealling Extension	 Step 1 @ 95°c, hold 10 secs, Step 2 @ 58°c, hold 15 secs, Step 3 @ 72°c, hold 20 secs
3	Melt	Melt (72-95°c), hold secs on the 1st step, hold 5 secs on next steps.

Reactions generated single PCR products that were identified by sequencing (SUPAMAC, Sydney, Australia) and specificity confirmed by BLAST searches. Each primer set had previously undergone a process of cycle optimisation, performed by Chris Little and coworkers from the Raymond Purves Laboratory, Royal North Shore Hospital. For all reported experiments amplification levels were compared in the linear range of the PCR reaction. All samples underwent RT and cDNA amplification at the same time to avoid potential variations in experimental conditions. All RT-PCR data was normalised to the quantity of total RNA.

Levels of gene expression obtained via RT- PCR for ZA-treated OACs are shown in Fig. 2.25 and 2.26. As expected, the level of the housekeeper GAPDH was unchanged with treatments. Aggrecan and collagen 1 were slightly altered with ZA. ADAMTS-1 and -5 were significantly decreased for 10 µM and 20 µM. MMP13 was unchanged with treatments.

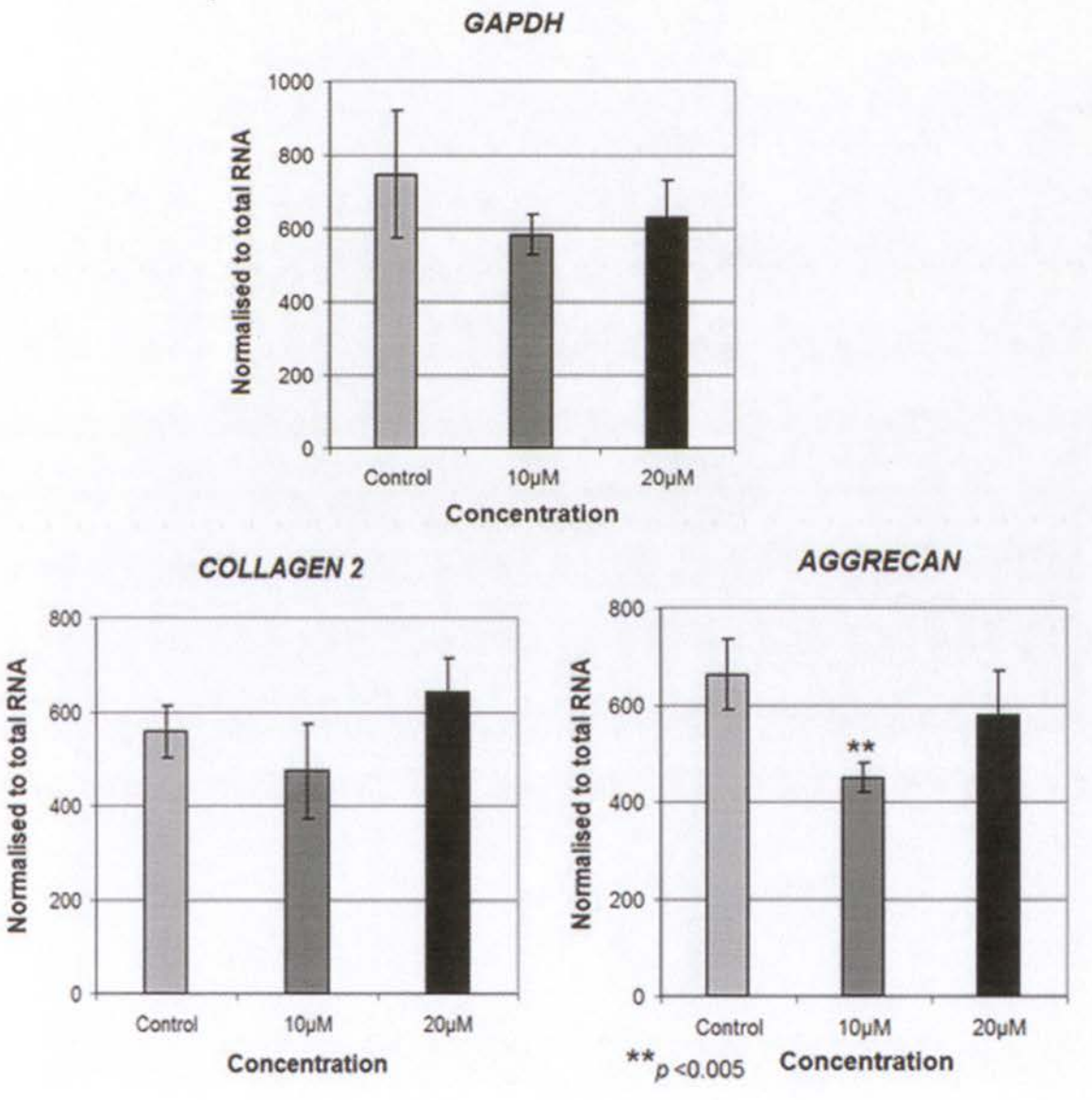


Figure 2.25. OAC gene expression for GAPDH and ECM components after ZA treatment.

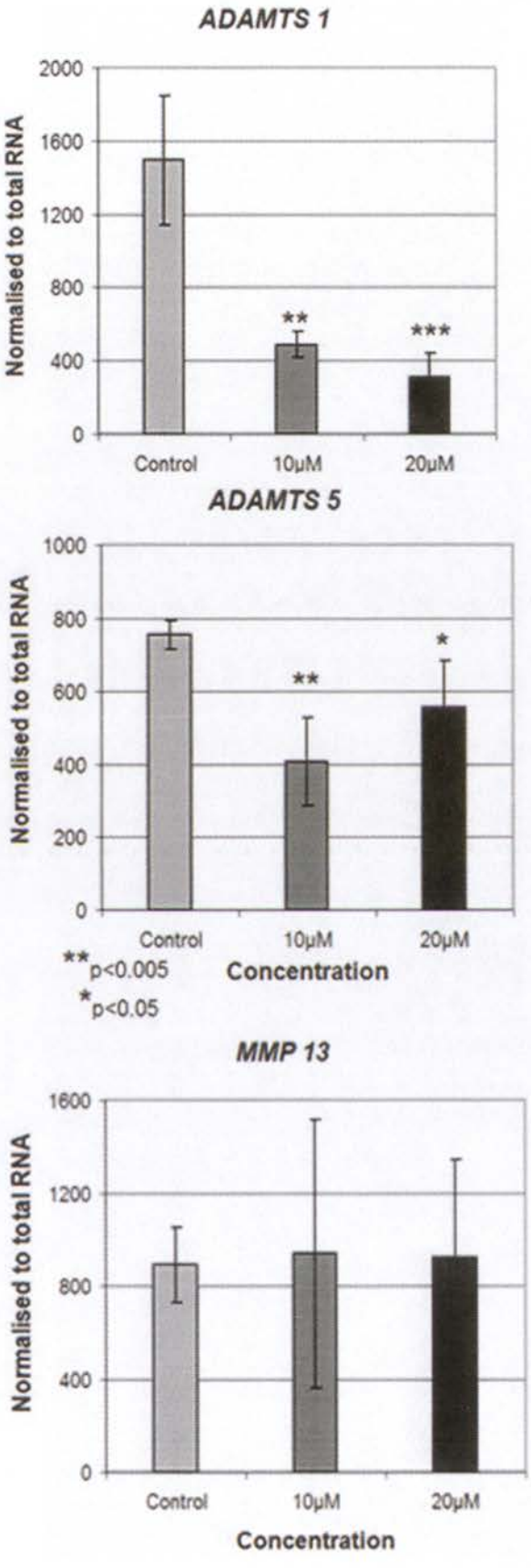


Figure 2.26. OAC gene expression for degradative proteases after ZA treatment.

2.5.3. DISCUSSION

Delivery of therapeutics from osteochondral scaffolds has the potential to help address tissue pathologies including osteoarthritis and rheumatoid arthritis. Previous *in vivo* studies have shown that ZA attenuated arthritis and reduced inflammation *in vivo*, regardless of treatment time. Although the mechanisms by which ZA affect the bone are well established, whether ZA has a direct effect on cartilage are not well understood. This is the first study to examine the *in vitro* effect of ZA on articular chondrocytes.

Characterisation of gene expression of chondrocytes using RT-PCR suggested that ZA significantly decreases ADAMTS-1 and -5 over a 24 hour period (for 10 μM, 20 μM ZA) (Fig.2.26). This indicates that ZA has a potential role in reducing *in vitro* cartilage degradation by direct action on the chondrocytes. Further replicates of this experiment will confirm whether ZA shows any direct effect on chondrocyte gene expression. It is possible that ZA shows a time effect and loses potency *in vitro* over 24 hrs. For this reason further studies should also include shorter timepoints. Zoledronic acid is a good candidate for delivery from this osteochondral scaffold due to its proven effectiveness, widespread clinical acceptance and potency. Its modulation of arthritis by changing the gene expression of bone would improve the health of both the bone and the cartilage, therefore aiding restoration of joint health.

2.6. EFFECT OF S100 PROTEINS ON CHONDROCYTES

2.6.1. METHODS

2.6.1.1. Cell Culture and S100 Protein Treatment

OACs were isolated from 6 month old ovine joints and expanded in tissue culture flasks. Complete media was made consisting of: DMEM/F12 (GIBCO®, Invitrogen), 10% heat inactivated Fetal Calf Serum (FCS) and antibiotics- 200g/mL gentamicin, 2mM glutamine (Invitrogen). Primary chondrocytes were removed from 70% confluent culture flasks using 1-2mL of 0.2% (w/v) Trypsin/0.1% (w/v) EDTA (Invitrogen). Cells were subcultured in 6 well tissue culture plates at a density of 250,000 cells/mL in 2mL pre-warmed complete media. This yielded a concentration of 500,000 cells/well. Cells were cultured at 37°C, 5% CO_2 for 24 hrs. The media was replaced with serum-free DMEM for 3-4 hrs. S100 proteins (A100A8, S100A9, S100A8/9) were applied to the cells at a concentration of 0.1 μM (in complete media). This resulted in a final concentration of 1 μM in the cell wells. Cells were incubated at 37°C, 5% CO_2 for 24 hrs. Three experiments were undertaken, consisting of 3-4 repetitions of each treatment.

2.6.1.2. Gene Expression using Real Time Polymerase Chain Reaction

Gene expression was determined by following the procedures of RNA Isolation, Reverse Transcription and RT-PCR (ref Appendix 85-A9). Primers used for this experiment include anabolic genes (build ECM); aggrecan, collagen I, collagen 2, TIMP 1, TIMP 2 and catabolic genes (break down ECM); ADAMTS 1, ADAMTS 5, MMP 1, MMP 2, MMP 3, MMP 13 and the housekeeping gene; GAPDH. All RT-PCR data was normalised to the quantity of total RNA.

Fig. 2.27 and 2.28 show the results for experiment 1. Levels of collagen 1 and 2 remained steady for all treatments groups. TIMP-2 showed a downward trend for S100A9, however this was not significant.

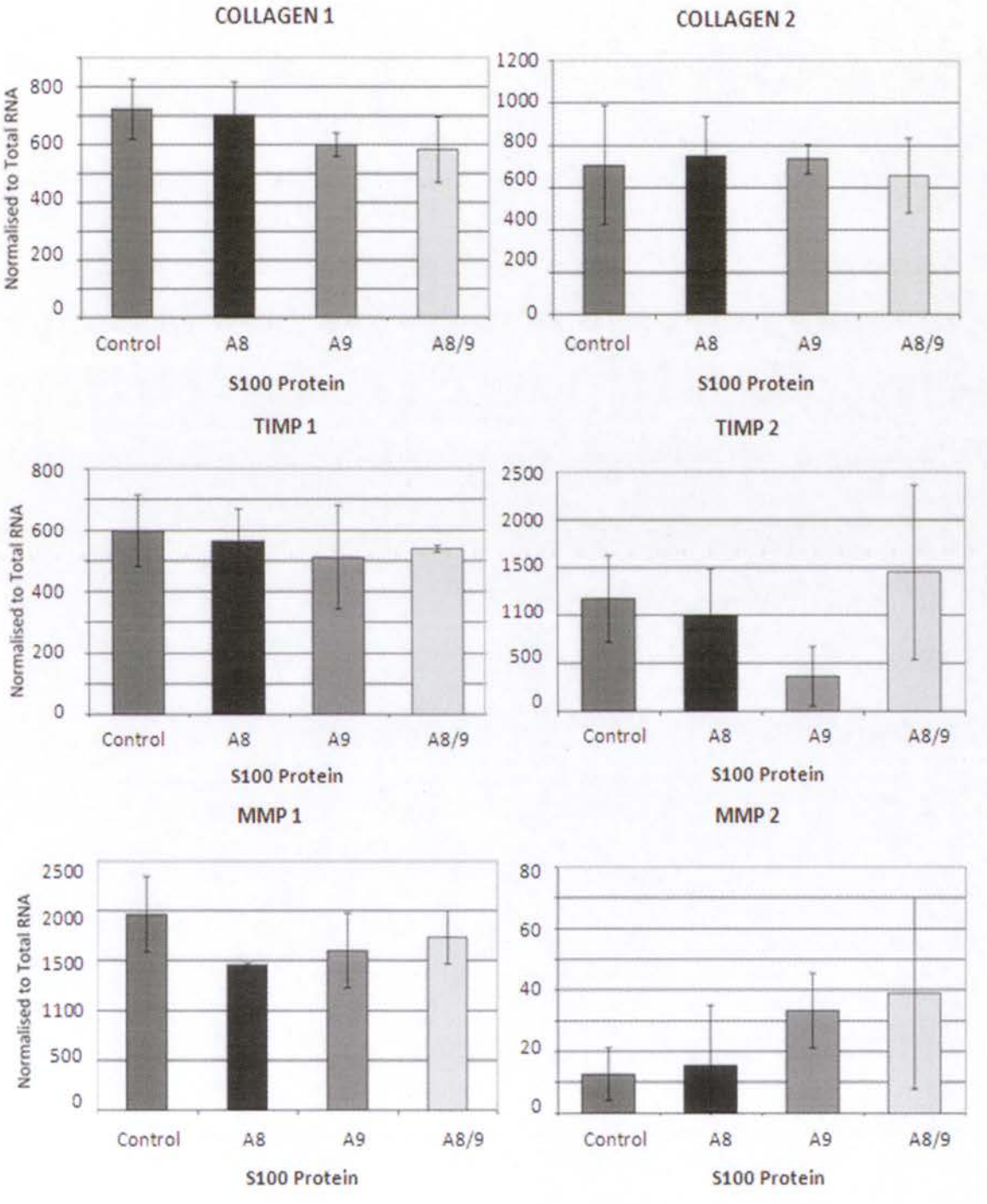


Figure 2.27. OAC gene expression after S100 protein treatment (expt 1).

The results for experiment 2 are shown in Fig. 2.28. An increase in ADAMTS4 was measured for S100A8. ADAMTS5 and TIMP1 increased significantly for the S100A9. S100A8 increased ADAMTS 4, and S100A9 significantly increased ADAMTS 5 and TIMP 1.

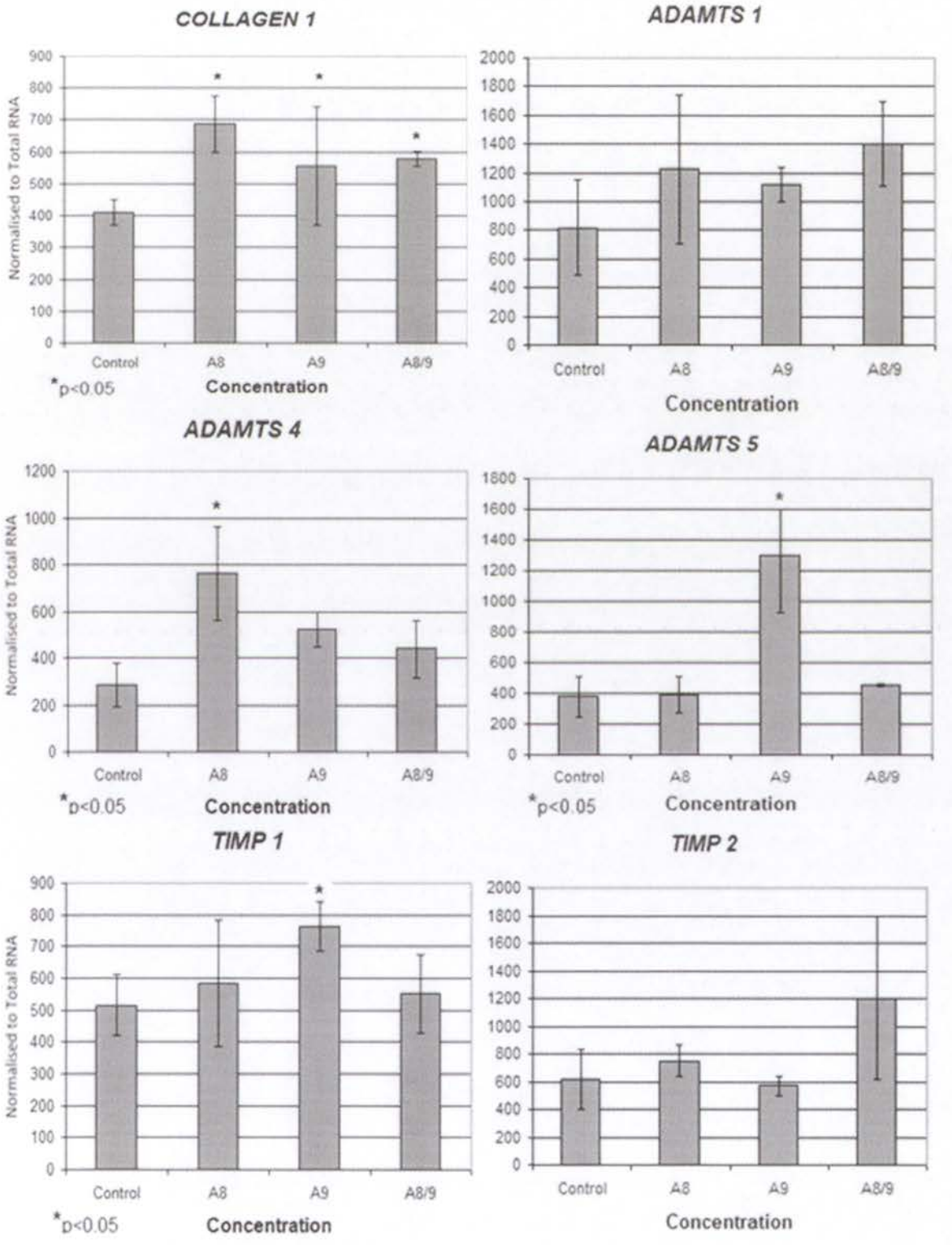


Figure 2.28. Gene expression for S100 protein treated chondrocytes (expt 2)

The results for experiment 3 are shown in Fig. 2.29 and Fig. 2.30. Levels of ADAMTS-5 decreased for S100A8/9. Both MMP-3 and MMP-13 increased for S100A9 (7x and 3x) respectively. S100A9 and S100A8/9 decreased TIMP-3 expression.

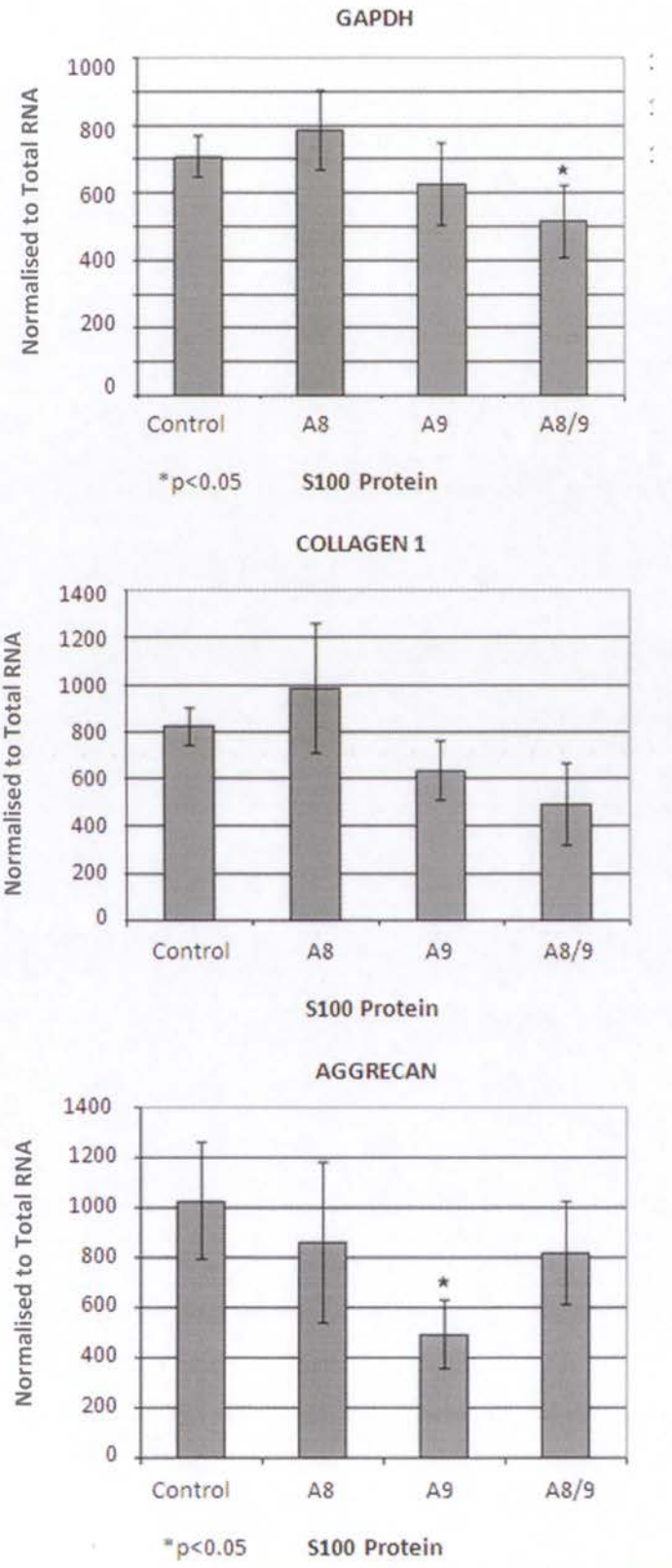


Figure 2.29. OAC Gene expression for GAPDH and ECM components after S100 protein treatment.

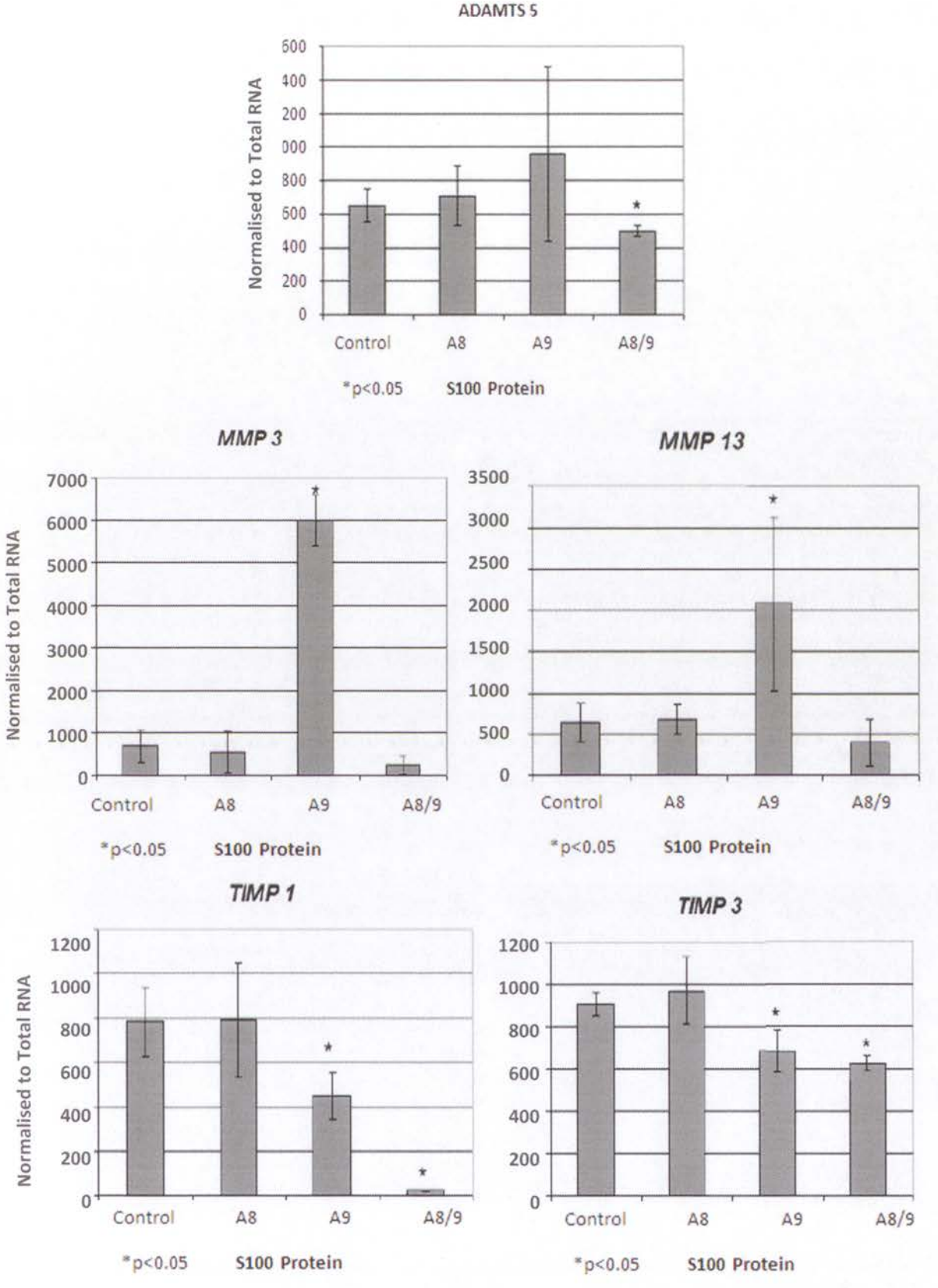


Figure 2.30. OAC gene expression for degradative proteases after S100 protein treatment (expt 3).

2.6.3. DISCUSSION

In this study, the gene expression of S100 protein-treated chondrocyte culture was measured using RT-PCR. To the author's knowledge, this is the first study to examine the effects of S100 proteins on cartilage culture.

Results showed substantial difference over the three experiments undertaken. The most comprehensive experiment (expt 3) showed several significant trends. An increase in the catabolic ADAMTS-5 (non-significant) was evident for S100A9 (Fig. 2.30); a trend which was also noted with significance in experiment 2 (Fig. 2.28). In addition, an increase in MMP-3 and MMP-13 were measured for S100A9 (7x and 3x). This indicates that S100A9 could play a role in progression of ECM degradation in cartilage. ADAMTS proteins, particularly -4 and -5, degrade aggrecan during diseases, leading to a loss of compressive resilience. Mice deficient in ADAMTS-5 have been shown to be protected against early cartilage degeneration in inflammatory arthritis [451].

Decreases were observed in TIMP-1 and -3 for S100A/9 and S100A9, respectively (expt. 3) (Fig. 2.30). This is evidence that these proteins are showing a protective action against degradation. A decrease in TIMP-2 was also observed in experiment 1 for S100A9. However, a different trend was present in experiment 2, where S100A9 showed an increase in TIMP-1 expression.

Conclusive results cannot be drawn from these experiments. These results did not replicate the trend which was observed in a previous rat model [441] and *in vitro* experiment (unpublished) by our group. These studies suggested a protective role for S100A8, modulated by a downregulation of MMP-13. ADAMTS proteins did not show any changes. In the current study, no change was noted in MMP-13. Generally, S100A8 did not show any significant trends. However an increase in MMP-13 and other degradative proteases were observed for S100A9, indicating the opposite trend for this protein.

Sample variation in this study was attributed to the following possible reasons: animal age, state of animal prior to slaughter (e.g. exercise, food), health of animal joint and. Pooling the cells taken from several animals (6-8 knee joints) does reduce this variation and this was a measure taken in the current study. Experimental differences may also play a role such as cell confluency and saturation and stagnation within the *in vitro* environment.

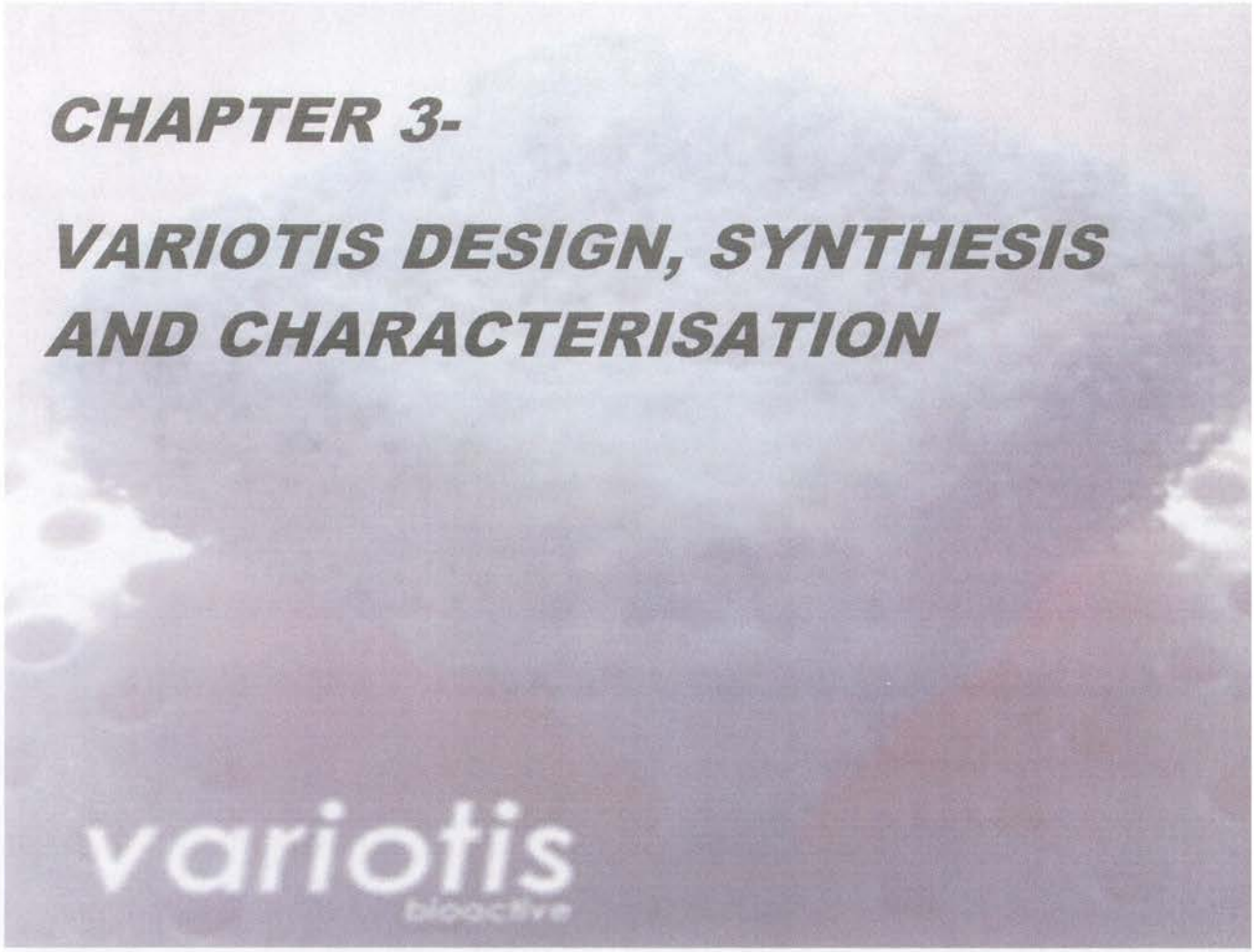
Further replicate experiments are required to confirm the actions of S100 proteins on regulation of ECM degradation.

2.7. CONCLUSION

- Biphasic calcium silicate-modified scaffolds and microspheres were formed, incorporating gelatin, alginate or PDLLA.
- Scaffolds had rounded macropores (d<500 μm), micropores (2x10 μm) and high levels of porosity (~82%) and interconnectivity (~99.5%).
- Fabricated PDLLA coated calcium silicate scaffolds showed increased mechanical strength and modulus compared to the neat scaffolds (3x increase). The strength was within the range for bone.
- Chondrocyte culture was demonstrated on the alginate and gelatin infused scaffolds.
- Zoledronic Acid was confirmed to have a protective effect on chondrocytes, as demonstrated by a decrease in ADAMTS-1 and ADAMTS-5 expression *in vitro*. This is the first study to investigate a direct action of ZA on chondrocytes. This finding is consistent with previous animal studies which found ZA reduced the severity of arthritis [346].
- *In vitro* chondrocyte studies suggest that S100A9 increases the breakdown of ECM. This is by increasing ADAMTS-5 levels while decreasing the protective actions of TIMP 1 and TIMP 2. No change was noted in MMP-13 expression.
- These calcium-silicate based scaffolds not only demonstrate a low stability, but also poor handling characteristics (low toughness) and so are difficult to use clinically. Although these ceramics show potential for implant coatings, in bulk form they lack strength, extensibility and could lack the ability to transfer stresses to developing soft tissue such as cartilage. These scaffolds cannot be easily tailored by a surgeon to fit a defect site.

CHAPTER 3-

VARIOTIS DESIGN, SYNTHESIS AND CHARACTERISATION



3.0. CHAPTER OVERVIEW

The development of a novel scaffold, variotis™, is documented in this chapter. The physical form and cell-attachment requirements raised in Chapter 2 are addressed by variotis™, while also being adjustable in elastic modulus and readily transferable to clinical use. Though relevant for cartilage engineering, there is also immediate clinical opportunity in developing a treatment for chronic dermal wounds. 10 mm-thick PCL scaffold units were fabricated using a novel high-throughput batch coagulation process. Bioactive glass composite scaffolds were formed by incorporating glass into the matrix and as adherent coatings. SEM and microCT confirmed high levels of interconnective porosity (>94.3%), large pore size (300-500 μm), micropores (2-40 μm) and rippled surface texture. These thermoplastic scaffolds were hot-pressed into a variety of shapes, sheets. By this method pore sizes were readily set. Novel functionally graded scaffolds were formed and characterized using indentation hardness techniques. Mechanical testing of the variotis™ scaffolds using an ELF3400 confirmed the high extensibility of the elastomeric scaffolds (up to 2.5x original length). Mechanical variations caused by glass additions, sterilization techniques and membrane additions were found. A range of moduli were demonstrated to be within the physiologic range for skin. A variety of scaffolds were developed for *in vitro* culture and *in vivo* applications.

3.1. INTRODUCTION

3.1.1. DEVELOPMENT OF A VERSATILE, SOFT TISSUE SCAFFOLD

3.1.1.1. Scaffold-Based Skin Graft for Chronic Wounds

Amongst increasingly aging populations, there is a clinical and commercial need for cost-effective and convenient treatments for chronic wounds such as persistent diabetic skin ulcers. There is a particular urgent need for effective treatments for diabetic wounds among rural indigenous populations that have the highest rates of loss of limb and morbidity in Australia [452]. There is also general need among people in remote communities or developing nations who cannot regularly access a hospital for chronic wound care and treatments utilising costly skin graft systems. Chronic wounds experience poor wound strength and could benefit from a reinforcing and adherent resorbable scaffold. Owing to the versatility of the variotis™ scaffold and immediate clinical research opportunity from a collaboration with The Royal Prince Alfred Hospital (Sydney, Australia) the focus for scaffold design in this chapter relates to specifically dermal chronic wounds. The ability of the scaffold to be further manipulated to be used for cartilage engineering and other applications is also outlined later in this chapter.

Established biomaterials used for both soft and hard tissue applications were selected to ensure patient safety, simplify development objectives necessary for attaining clinical outcomes, and minimize time for commercialization [165]. The benefits of PCL and Bioactive Glass, and the thesis sections in which they are discussed further, are listed in the following table.

Table 3.1. Features of PCL, bioactive glass and composites that address key requirements

Biomaterial	Features	Thesis section ref.
PCL	Slow degradation rate (>2yrs bulk form). Naturally occurring degradation products. High extensibility. Ability to utilise with a range of synthesis techniques. Thermoplastic. Clinically utilised for a range of implants. Degradation via surface erosion-> no loss in molecular weight so maintains mech. stability, predictable degradation for drug delivery, does not induce chronic inflammation at early timepoints.	1.4.2.2., 1.3.3., 3.1.6.1., 3.1.8.3.
Bioactive Glass	Potential stimulation of angiogenesis, antibacterial, High bioactivity- soft/hard tissue attachment. Clinically utilised for soft and hard tissue applications, including skin.	1.4.1.3., 1.6.6.4., 3.1.8.4.
PCL + Bioactive Glass	Modulate mechanical properties, e.g. increased stiffness. Increase PCL degradation rate. Increase hydrophilicity of the matrix. Increased surface area and bioactivity. Encourage protein absorption. Increases bonding strength to tissue-> reduces fibrous capsule.	1.4.2., 1.6.7., 3.1.6.3., 3.1.6.4., 3.2.1.

Additional design considerations for this novel skin graft will now be discussed. Areas which are considered include:

- Tissue mechanostimulation via elastic scaffolds
- Healing process for normal and chronic wounds;
- Current methods to treat chronic wounds (including dressings, native grafts and engineered grafts) and their limitations;
- Potential synthesis methods for the novel composite skin graft; and
- Commercial considerations (e.g. post-form., sterilisation, mechanical verification);

Following these discussions, the requirements for the skin graft are summarised and a conceptual design is proposed. In section 3.1.4, potential models are described for using the scaffold for chronic skin wounds and also in osteochondral defects.

3.1.1.2. Tissue Mechanostimulation via Elastic Scaffolds

For many tissue types, generating functional tissue requires using a mechano-active scaffold which can transmit mechanical signals to its adherent cells in both bioreactor systems and dynamic bodily environments [11, 223, 453, 454]. The mechanical signals received by cells affects their phenotype (i.e. fibroblasts, osteoblasts, chondrocytes) and the type of extracellular matrix they produce (i.e. fibrous tissue, cartilage, bone) [11]. The mechanical properties of the scaffold or engineered tissue before implantation are therefore key determinants of its success [11].

Jung and coworkers [403, 404] reported a study examining the quality of cartilage formed within rigid PLA or elastic PLCL scaffolds. While the PLA scaffolds showed little recovery to applied strain, the PLCL scaffolds could return to 97% of its original length after being strained up to 500%. *In vitro* (chondrocytes) and *in vivo* (rabbit osteochondral defect) studies demonstrated the PLCL scaffolds could significantly enhance chondrogenic differentiation. Mechanical stimulation of the dynamic *in vivo* environment promoted deposition of chondral extracellular matrix onto the PLCL, compared to an empty control or PLGA scaffolds. Mechanotransduction is particularly important for osteochondral tissue due to the high loads it experiences, but the same concept could be applied to a range of other soft and hard tissues, on various scales [455].

3.1.2.1. Acute vs Chronic Wounds

Acute (normal) wound healing is a dynamic process involving the coordinated actions of both resident and migratory cell populations within the extracellular environments, leading to the repair of injured tissues. In contrast to this, some wounds fail to heal in a timely and orderly manner, resulting in chronic non-healing wounds which can require skin grafting. A discussed previously, chronic wounds can encounter impairment of one or more of the phases of normal wound healing, particularly the inflammatory phase. As shown in Fig. 3.1, compared with acute healing wounds, chronic wounds have high levels of protease activity, bacterial pathogens, neutrophils, free radicals and continual bacterial infection can form a biofilm [23].

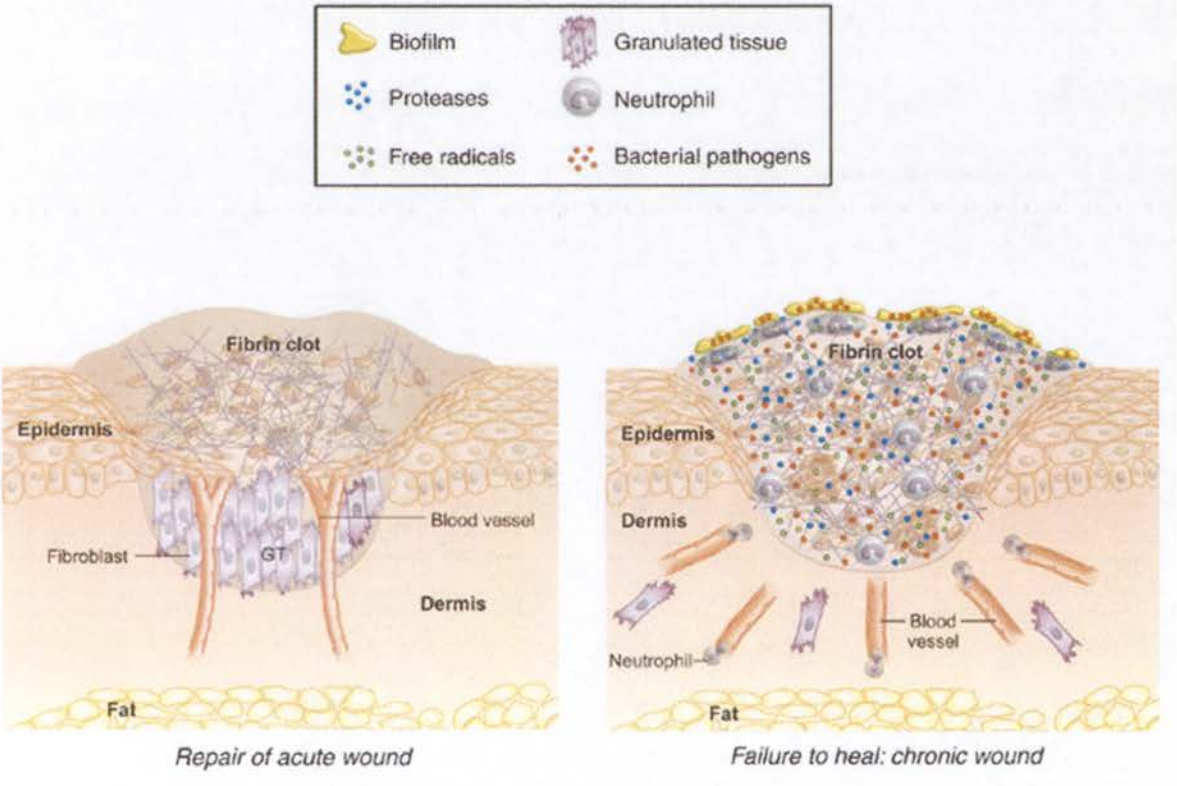


Figure 3.1. Repair of an acute wound versus an unhealing chronic wound [23].

3.1.2.2. Phases of Acute Wound Healing

Depicted in Figure 3.2, acute wound healing occurs as a sequential cascade of overlapping processes that requires the coordinated completion of a variety of cellular activities. Healing occurs through four overlapping but well defined phases.

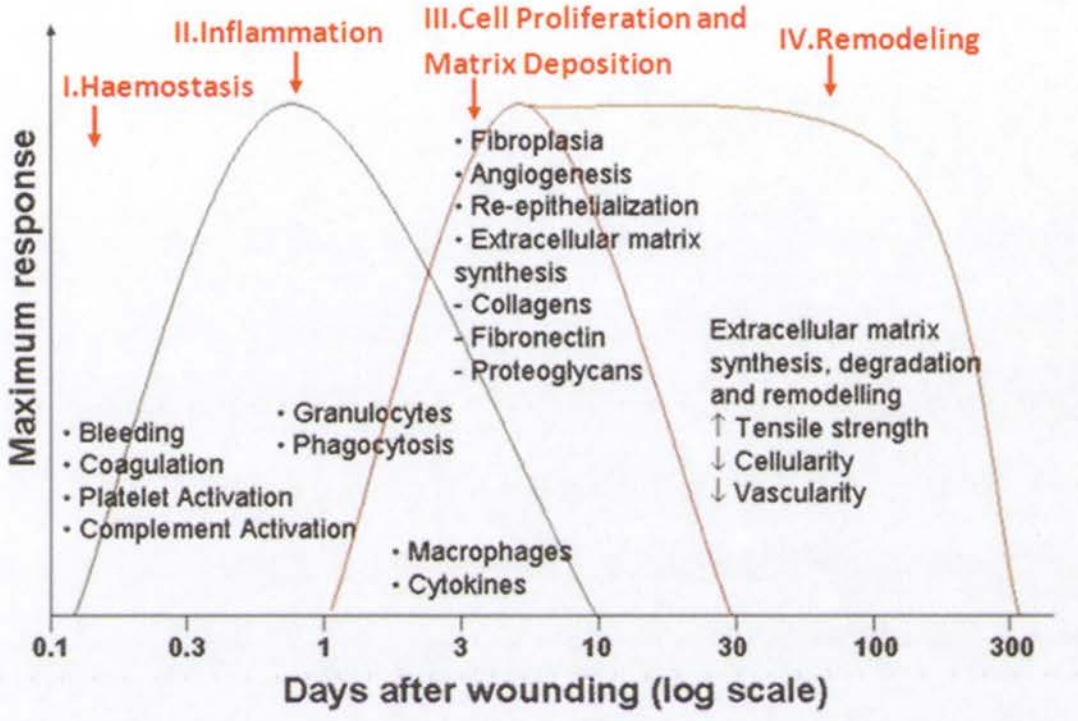


Figure 3.2. Phases of repair during wound healing [456].

3.1.2.2.1. Haemostasis

Tissue injury is characterised by microvascular injury and therefore extravasation of blood into the wound. Injured vessels constrict rapidly and the coagulation cascade is activated to limit blood loss. A blood clot forms within the wound consisting of fibrin, fibronectin and other components provides the provisional matrix for cellular migration [457]. Platelet aggregation within the clot is essential for haemostasis as well as a normal inflammatory response. The platelets contain growth factors, including platelet-derived growth factor (PDGF), insulin-like growth factor-1 (IGF-1), epidermal growth factor (EGF) and transforming growth factor-beta (TGF-β). These proteins initiate the wound healing cascade by attracting and activating fibroblasts, endothelial cells and macrophages. Exudation of fluid into the extracellular space is triggered by an increase in microvascular permeability.

3.1.2.2.2. Inflammation

Within 24-48 hrs of injury, granulocytes or polymorphonuclear leucocytes (PMNs) are attracted to the wound site. The PMNs move through the vessel walls and into the wound environment, where they phagocytose bacteria and other foreign particles, killing them by releasing degrading enzymes and oxygen-derived free radical species. PMNLs usually cease activity once invading bacteria has been cleared. Redundant cells are cleared away from the wound by extrusion to the wound surface as slough or phagocytosis by macrophages.

Blood monocytes undergo a phenotypic change on arrival at the wound site to become tissue macrophages. Macrophages appear to act as the key regulator for tissue repair, and are very important 48-72 hours after wounding. They release further cytokines and growth factors into the wound, recruiting fibroblasts, keratinocytes and endothelial cells to repair the damaged blood vessels [8]. Macrophages are capable of releasing proteolytic enzymes such as collagenases that can debride tissue. The PMNLs release further growth factors to stimulate the inflammatory response, such as basic fibroblast growth factor (bFGF) and transforming growth factor-aloha (TGF-α). Lymphocytes enter the wound environment at least 72 hrs after injury. The role of lymphocytes has not been clearly defined; however they can be attracted by interleukin-1, which is believed to play a key role in the regulation of collagenases. This suggests that lymphocytes can be involved in collagen and extracellular matrix (ECM) remodelling.

3.1.2.2.3. Cell Proliferation and Matrix Deposition

The proliferative phase starts at about day three and lasts for two weeks after wounding. It is characterised by the replacement of the provisional fibrin/fibronectin matrix with newly formed granulation ("fibrovascular") tissue.

- **Fibroblast migration:** Fibroblasts and myoblasts are attracted to the wound 2-4 days after injury, by a number of factors, including PDGF and TGF-B [9]. Fibroblasts proliferate and start to build the ECM, by producing matrix proteins -firstly fibronectin and hyaluronic, and during later stages collagen and proteoglycans. Interactions between the fibroblasts and the ECM help to determine the synthesis and remodelling of the matrix [458].
- **Collagen synthesis:** Collagens, particularly I and III are produced by fibroblasts. Collagens are a key component of all phases of wound healing and provide strength and integrity for the tissue.
- **Angiogenesis:** The process of forming new blood vessels occurs concurrently during all stages of the healing process. The macrophages in particular, play a key

role in angiogenesis by releasing a number of angiogenic substances such as tumor necrosis factor-α and bFGF. Angiogenic capillary sprouts invade the blood clot and organise into a microvascular network within a few days [459]. As collagen accumulates in the granulation tissue, the density of blood vessels diminishes.

- **Granulation tissue formation:** Granulation tissue is the pink, capillary-rich tissue which invades the wound. It consists mainly of proliferating fibroblasts, capillaries and tissue macrophages in a matrix of collagen, glycosaminoglycans (GAGs) including HA, and the glycoproteins fibronectin and tenasin [460].
- **Epithelialisation:** A single layer of epidermal cells start to migrate from the wound edges within a few hours of wounding to form a delicate covering over the raw area exposed by the loss of epidermis. The basal cells on the wound edges loosen their normally firm attachments to the underlying dermis, allowing them to migrate in a leap-frog fashion across the provisional matrix [461]. The rate of epithelial coverage is increased if the wound is kept moist; a dry eschar (scab) slows the rate of epithelialisation.

3.1.2.2.4. Matrix Remodelling

Matrix synthesis and the remodelling phase are initiated concurrently with the development of granulation tissue and continue over prolonged periods of time. As the matrix matures, fibronectin and HA are broken down. Collagen bundles increase in diameter, due to cross-linking of collagen fibrils. This corresponds with increasing wound tensile strength [Clark 1995]. However, these collagen bundles never regain the original strength of normal unwounded skin and only a maximum of 80% unwounded skin strength can be achieved [463].

There is ongoing collagen synthesis and breakdown as the ECM is continually remodelled, equilibrating to a steady state about 21 days after wounding. Collagen degradation is achieved by specific matrix metalloproteinases (MMPs) that are produced by many cells at the wound site, including fibroblasts, granulocytes and macrophages. As remodelling of the wound continues, MMP activity decreases and tissue inhibitors of metalloproteinases (TIMPs) activity increases. TGF-β plays an important role in promoting matrix accumulation through the mediation of these activities [464].

Early collagen deposition is highly disorganised but its subsequent organisation is primarily achieved by wound contraction. Wound remodelling occurs when the underlying contractile connective tissue shrinks in size to bring the wound margins closer together. Contraction occurs through the interactions between fibroblasts and the surrounding ECM [458, 465]. These interactions can be influenced by a number of extracellular factors including TGF-β,

PDGF and FGF [458]. Over time, the density of macrophages, fibroblasts and capillaries is reduced, and the wound has been healed by a scar.

3.1.3. DEVELOPMENT OF CHRONIC WOUNDS

Chronic wounds are disrupted at one or more of the phases described above. In most wounds, the process is thought to be 'stuck' in the inflammatory or proliferative phases. This can lead to hypertrophic scarring, microbial contamination and inability for the wound to close. As growth factors, cytokines, proteases, and cellular and extracellular elements all play important roles in different stages of the healing process, alterations in one or more of these components could account for the impaired healing observed in chronic wounds. In addition, oxidative damage by free radicals or condition-specific factors such as neuropathy in diabetes or ischaemia in peripheral vascular disease can lead to the non-healing nature of chronic wounds. Healing can also be impeded by the accumulation of necrotic tissue or slough, a feature of chronic wounds [464].

The wound fluid from a chronic wound is characterised by a significant increase in proteolytic activity, elevated pro-inflammatory cytokines (e.g. tumour necrosis factor-α (TNF- α) and interleukin-1β (IL-1 β), proteases (e.g. matrix metalloproteinases). TNF- α has a demonstrated ability to increase production of MMPs, which in turn inhibits production of TIMPs. This then causes an extension in pro-inflammatory cytokine expression, which can change a normal healing wound into an environment rich in proteases and extremely toxic for connective tissue proteins and growth factors [466]. Not surprisingly, chronic wounds have reduced levels of growth factors, such as PDGF, basic fibroblast growth factor (bFGF), EGF and TGF- β [283, 467].

Ulcers are breaks in the skin which fail to heal, which often develop on the leg or foot. Patients in nursing homes or hospitals can develop pressure ulcers if they remain lying in the same position for prolonged periods. People at risk of developing skin ulcers include those with diabetes, circulatory problems, tumors, traumatic injury or paralysis [284]. Diabetic patients with uncontrolled hypoglycemia have the highest risk of skin ulcer development. Ulcers are difficult to heal as poor circulation leads to decreased removal of waste, and an increased risk of infection. This is the case for both diabetic and chronic venous ulcers.

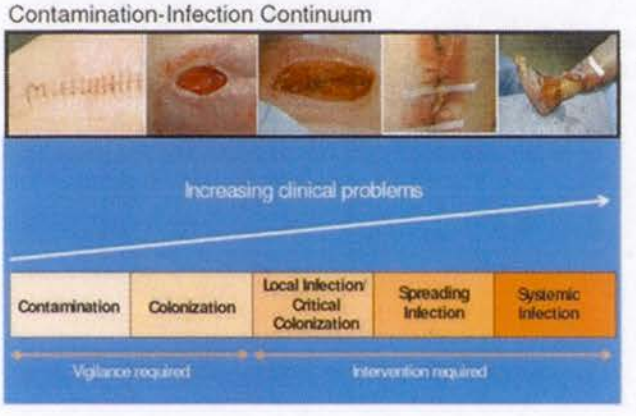
In chronic wounds, poor wound closure leads to increased risk of infection. This section will focus on types of bacteria commonly infecting wounds and the function of biofilm which together can decrease wound healing.

3.1.3.1. Bacterial Colonisation

Bacteria in ulcers usually act along a continuum from contamination through colonisation to critical colonisation and finally to infection [468]. In wounds less than one month old, cutaneous and Gram-positive organisms tend to predominate. As ulcer healing becomes prolonged, a broader spectrum of organisms can colonise the wound, including Gram-negative organisms such as coliforms, anaerobes and Pseudomonas species [469]. This increasing complexity of bacterial colonisation of the wound is represented in Fig. 3.3 below.

If the wound becomes infected bacterial activities overcome the host's immune response and injury occurs. Many factors affect the risk of infection, such as nutrition, tissue perfusion and medical conditions (e.g. diabetes). Infection in a wound results in devitalised tissue and can ultimately lead to systemic infection which can be life threatening.

(a)



(b)

Bacteria	*n (%)*
Staphylococcus aureus	11 (26.19)
Escherichia coli	10 (23.8)
Staphylococcus epidermidis	6 (14.3)
Proteus mirabilis	4 (9.5)
Pseudomonas aeruginosa	2 (4.76)
Enterobacter spp.	2 (4.76)
Morganella spp.	2 (4.76)
Proteus vulgaris	1 (2.4)
Klebsiella spp.	1 (2.4)
Citrobacter spp.	1 (2.4)
Diphtheroid	1 (2.4)
Yeast	1 (2.4)

Figure 3.3. (a) Stages of bacterial infection [468] and (b) Number and types of bacterial isolates from patients with diabetic foot ulcers [469].

3.1.3.2. Microbial Biofilms

When critical levels of infection are reached, bacteria can make a biofilm, as shown in Fig. 3.4. These are broadly defined as adherent microorganisms within a polymer matrix (polysaccharides), typically containing water channels between the stacks of microorganisms [281]. Biofilms usually consist of a range of species bacterial species [470] and these have higher level of resistance to standard antibacterial agents, than cultures grown in suspension [280]. Whilst the mechanism for the resistance of biofilm bacteria is not generally agreed on, it is thought to be due to a combination of innate and induced factors [280].

Biofilms are a common cause of failure for artificial joints, prosthetic heart valves and catheters. Studies have shown that regular debridement and flushing of ulcers removes biofilm and contributes to increased wound healing rates, as discussed later.



Figure 3.4. (a) A schematic diagram and (b) scanning electron micrograph of a bacterial biofilm [470]

3.1.4. MANAGEMENT OF CHRONIC ULCERS

3.1.4.1. Principles Promoting Wound Healing

Approaches to promote wound healing focus on these main principles [481]:

- Overall healthcare e.g. control of diseases such as diabetes, weight control, nutritional balance;
- Wound debridement and treatment of infection;
- Maintenance of a moist wound environment and stable temperature;
- Restoring arterial flow to the foot and allow the wound exudates to drain freely;
- Minimisation of pressure over the wound and the surrounding area;
- Minimisation of dead space but not packing the wound too tightly; and
- Minimisation of scarring and restoration of function.

As depicted in Fig. 3.5, depending on the wound characteristics, particularly the level of exudates, the wound should be managed via debridement of necrotic tissue, absorb wound fluid (exudates) or provide hydration to the wound. If healing does not occur within 4 weeks, reconstructive surgery such as angioplasty or bypass surgery can be needed to improve blood flow in the extremities, or skin grafting can be performed.

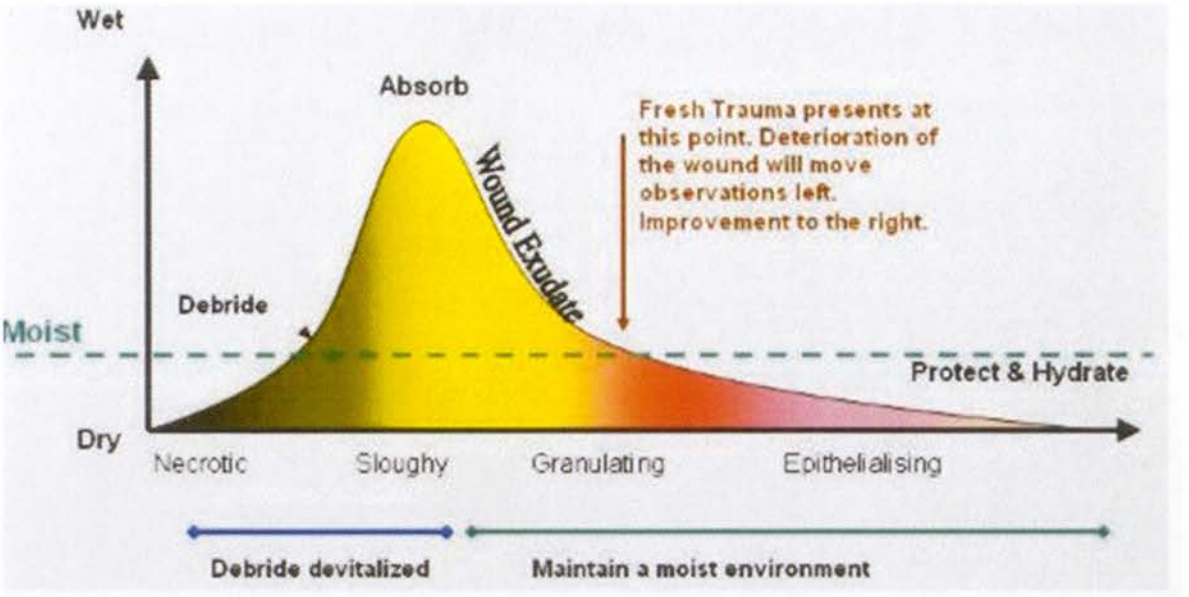


Figure 3.5. Treatment priorities as the wound progresses through various stages of healing (left to right) [471].

3.1.4.1.1. Wound Debridement

Debridement (Fig. 3.6) is the process of removing necrotic tissue (yellow slough or black eschar) from a wound bed [472]. Clinical evidence suggests that debridement aids healing via: (1) reduction of inflammatory cytokines, fibronectin, and metalloproteinases (2) promotion of DNA synthesis and growth of keratinocytes; and (3) reduction of bacterial bioburden in the wound bed [473-475].

The most common debridement techniques are described in Table3.2. The method chosen depends on the amount of necrotic tissue within the wound, the extent of the wound, the patient's medical history and overall condition. Clinicians sometimes use debridement methods in conjunction with each other. Debridement methods are classified as either selective or non-selective, depending on whether they discriminate between viable and nonviable tissues. Surgical debridement remains the standard of care for the removal of necrotic tissue, although enzymatic debridement is often recommended for chronic wounds.

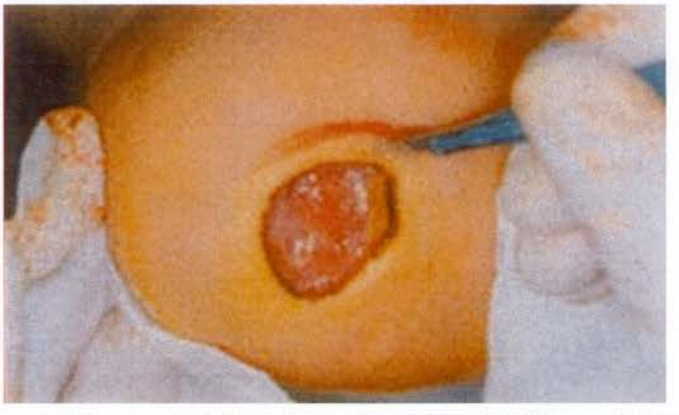


Figure 3.6. Removal of dead tissue via surgical debridement [476].

Table 3.2. Types of Wound Debridement [477].

	Technique	Indications	Examples	Advantages	Disadvantages
Selective	Surgical	*Wounds with large amount of necrotic and infected tissue*		Fast & selective Can be extremely effective	Painful Costly, esp. if operating room required May require transport of patient
	Autolytic	*Non-infected wounds*	Hydrogels Hydrocolloids Honey Semiperm. films	Little damage to surrounding skin Safe, easy, versatile Little pain	More time consuming than surgical
	Chemical (some not selective)	*Wounds with a large amount of necrotic debris, eschar formation*	Enzymatic agents (e.g. Collagenase)	Fast acting With proper application, minimal damage to healthy tissue	Expensive, requires a prescription Must carefully be applied to only necrotic tissue Inflammation or discomfort may
	Biosurgical	*Non-healing, necrotic wounds*	Larval therapy	Low cost Safe and effective	Requires further clinical studies to further popular acceptance
Non-selective	Mechanical	*Wounds with moderate amounts of necrotic debris*	Wet-to-dry Saline Irrigation Hydrotherapy Ultrasonic	Costs of actual material (gauze) is low	Time consuming May traumatize healthy tissue, pain Gauze fibers may become embedded in tissue Fluid evaporation from dressing may result in local tissue cooling of wound bed Hydrotherapy contains many risks. It can can cause tissue masceration. Waterborne pathogens can cause infection. Disinfecting additives may be cytotoxic.

3.1.4.1.2. Management of Wound Exudate

Management of wound exudate is important if the optimal moist environment necessary for wound healing is to be created. They are produced as a result of vasodilation of vessels during the early inflammatory stage of normal healing. When the wound becomes chronic with persistent inflammation or infection, exudates contain proteolytic enzymes and other components not seen in acute wounds. This type of exudates has the capacity to degrade growth factors and predispose skin to inflammation. The appearance of exudate can range from thin, pale yellow to thick and red. The volume of exudate increases following infection. The volume and viscosity of exudates are good indicators of whether healing is progressing normally. In the case of a leg ulcer, pressure ulcer or diabetic foot ulcer, exudates levels in the non-infected wound are generally higher in the early stages of healing and reduce as healing progresses. Exudate can be removed using Negative Pressure Wound Therapy (NWPT) or controlled using wound dressings [34].

3.1.4.1.3. Negative Pressure Wound Therapy

NWPT has been used successfully for many years to remove exudate, under brand names including V.A.C® Therapy™ (Vacuum Assisted Closure™). As shown in Fig. 3.6 below, sterile foam dressings are placed within or on a wound. A suction tube is placed within the foam and

covered with an occlusive dressing. NPWT introduces both macrostrain and microstrain into the wound. Macrostrain, the visible deformation of the foam which occurs under negative pressure, draws the wound edges together and evenly distributes the negative pressure. This facilitates the removal of exudate, bacteria, protease enzymes and free radicals- all barriers to healing. Microstrain is microdeformation at the cellular level, which leads to cell stretch. This reduces oedema, promotes blood flow and promotes granulation tissue formation by facilitating cell migration and proliferation [478, 479].

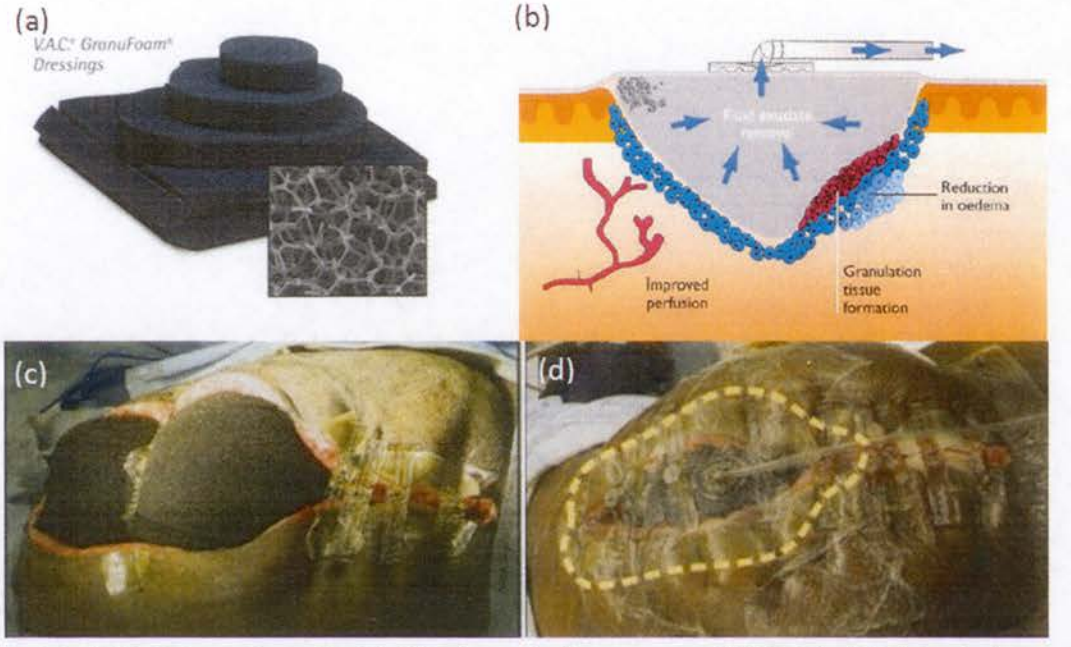


Figure 3.6. (a) VAC GranuFoam [478], (b) Schematic diagram of NPWT [479], (c) Abdominal wound before and (d) after application of NPWT [478].

Commonly used foams for NPWT are V.A.C GranuFoam and V.A.C WhiteFoam (KCl). V.A.C. GranuFoam dressing is a black, polyurethane foam dressing with a reticulated, open cell design that provides uniform distribution of pressure at the wound site. The 400-600μm pore size induces the promotion of granulation tissue formation and new cell growth. The foam is hydrophobic, facilitating effective removal of fluid and infectious materials, allowing wound healing progression. GranuFoam Dressing is also available with a metallic silver coating, which provides the sustained release of silver ions for antimicrobial activity to the wound. V.A.C. WhiteFoam dressing is a polyvinyl alcohol foam with a dense, open pore design and high tensile strength. WhiteFoam is hydrophilic and comes premoistened with water.

NPWT involves the removal of many beneficial components of wound fluid and for this reason is contraindicated in wounds containing eschar or necrotic tissue. Recently the US Food and Drug Administration (FDA) have reported safety risks associated with NPWT. These include bleeding, worsening infection, retention of foam dressing pieces within the wound and foam adhering to tissues or becoming embedded in the wound [480]. Moreover NPWT has been reported to be the cause of 6 deaths and 77 injuries in the two years preceding November

2009. Reduction of the risks associated with NPWT can lead to increased use of this type of therapy. Whether a bioabsorbable foam, such as variotis™, which shares many physical similarities with the VAC foams, could be used is not known and remains a possibility.

3.1.4.2. Wound Dressings

Ideally, a wound dressing (Fig. 3.7) will keep the wound moist, prevent maceration, protect from contamination, contain the wound fluid and protect the granulation tissue. A wide variety of dressing materials have been developed [481]. The materials currently in use are summarised in Table 3.4.

Table 3.3. Examples of materials used for wound dressings [481].

Origin	Source	Examples of fibres and polymers
Natural	Animal	Silk (spider, silkworm)
	Vegetable	From seed (cotton) Bast (linen, hemp)
Man-made	Synthetic polymers	Polyester Polyamide Polypropylene Polyurethane Polytetrafluoroethylene
	Natural polymers	Regenerated cellulose Proteins (collagen, catgut, branan ferulate) Alginates Polyglycolic acids Polylactic acids Chitin Chitosan Hyaluronan
	Other (non-fibrous material)	Carbon Metals (silver, etc.)



Figure 3.7. Common wound dressings.

Traditionally, dry dressings have been used and these are made from cotton or other gauzes. However, their use has decreased as they are associated with increased pain/itching, decreased collagen production and increased levels of scarring and contamination. More recently, it has been recognised that dressings which contain an optimal level of moisture within the wound bed will lead to increased healing rates, increased cosmetic outcomes, decreased pain, decreased infection rates and reduced overall healthcare rates [482].

For heavily exudating wounds, moisture-absorbing dressings can be used such as alginates or foams. Absorbent dressings require fewer dressing changes and therefore cause less wound disturbance and consume less labor time by the caregiver. As the wound progresses and

begins to granulate, exudate levels decrease and the natural level of moisture can be maintained within a wound using a hydrocolloid or transparent film dressing. Wounds which require moisture maintenance can be covered with hydrocolloids or transparent films. Tegaderm and Transeal are semi-permeable polyurethane films. Both have shown to be not only effective for moisture maintenance but also for killing bacteria in wounds [483].

Other types of dressings include moisture-donating dressings (hydrogels). These can be required when wounds are already dehydrated. They are occlusive dressings which act as a bacterial barrier, prevent the formation of an eschar (scab), enhance the role of macrophage/lymphocytes and retain fluid which encourages autolytic debridement and healing [484]. Polyurethane foams are another example of a dressing. These not only absorb exudates but also release therapeutic substances. For example, Biatain® Ibu foam releases pain-relieving ibuprofen to the wound site over a period of 2-3 days [485].

Table 3.4. Examples of moist wound healing dressings.

Dressing function	Dressing type	Dressing name	Manufacturer
Absorb exudate	Alginate	Sorbsan	Bertek Pharmaceuticals, Research Triangle Park, NC
	Alginate	Curasorb Calcium Alginate Dressing	Tyco Healthcare/Kendall, Mansfield, MA, USA
	Hydrofiber	Aquacel Hydrofiber Wound Dressing	ConvaTec, Skillman, NJ, USA
	Foam	Optifoam Nonadhesive Dressing	Medline Industries, Inc, Mundelein, IL, USA
	Foam	Tielle Hydropolymer Adhesive Dressing	Johnson & Johnson Wound Management, Somerville, NJ, USA
Maintains Moisture	Hydrocolloid	Duoderm CGF Sterile Dressing	Convatec, Skillman, NJ, USA
	Hydrocolloid	Replicare Thin Hydrocolloid Dressing	Smith & Nephew, Inc, Largo, FL, USA
	Transparent film	Tegaderm Transparent Dressing	3M Health Care, St. Paul, MN, USA
	Transparent film	Transeal	DeRoyal, Powell, TN, USA
Donate Moisture	Hydrogel—amorphous	Purilon Gel	Coloplast Corp, Marietta, GA, USA
	Hydrogel—amorphous	Skintegrity Hydrogel	Medline Industries, Inc, Mundelein, IL, USA
	Hydrogel—wafer	Nu Gel Wound Dressing	Johnson & Johnson Wound Management, Somerville, NJ, USA
	Hydrogel—wafer	FlexiGel Hydrogel Sheet Dressing	Smith & Nephew, Inc, Largo, FL, USA

Whilst these types of dressings form part of the standard care to improve wound healing, there are some disadvantages with this approach. These include the following aspects.

- Incorporation into the wound, causing tearing of fragile tissues and discomfort upon removal
- Ineffective barrier to bacterial contamination
- Frequent dressing changes (e.g. every 24-48 hrs)
- Introduction to contamination during dressing changes
- Often contra-indicated for infected wounds

These negative features may be improved upon in the future by the use of scaffolds such as variotis™ which can deliver antibiotics, growth factors and/or provide structural support.

3.1.4.2.1. Addressing the Local Biochemical Environment

Advanced wound dressings that account for biochemical aspects of the wound aim to speed wound healing. Key biochemical parameters include the local levels of tissue proteases, the levels of cytokines and growth factors, the presence and duration of tissue hypoxia and reactive oxygen species, and the level of bacteria and other bioburden in the wound. Chronic wounds have been characterised by local populations of senescent cells which can benefit from correction of biochemical imbalances [483, 487].

Frequently, broad-spectrum antibiotics are used for treatment of chronic skin wounds [488-490]. Antibiotic delivery to the skin from biomaterials have included tobramycin delivery from calcium sulfate (Osteoset-T™, Wright Medical Tech, Memphis TN) gentamicin sulphate from chitosan/calcium phosphate [197], PCL/hydroxyapatite [414] or teicoplanin from chitosan/borate glass [490]. Chang and coworkers demonstrated that gentamicin sulphate demonstrated a gradual release from PCL fibers, and recommended PCL for further investigation for treatment of infection associated with periodontal disease, musculoskeletal injuries, vascular prosthesis and other tissue substitute applications [360]. Merrell and coworkers [256] investigated the feasibility of curcumin-loaded PCL nanofibers as a diabetic wound dressing with both anti-oxidant and anti-inflammatory properties. Protein release has also been investigated for its antibacterial action. Kim and coworkers [491] demonstrated controlled release of lysozyme over an extended period from PCL/PEO electrospun fibrous meshes. Antibiotic delivery could be facilitated from Variotis™ via either PCL [L347, 256, 15] or bioactive glass [116, 146, 355]- this could be the subject of a future study.

Silver has been incorporated into wound dressings as either silver nitrate, silver ions or silver sulphadiazine [60]. Examples of silver-incorporating dressings include Aquacel® Ag (ConvaTec, Ickenham), Contreet® Foam (Coloplast, Peterborough) or POMOGRAN PRISMA® (Systagenix). Silver has proven efficacy against a wide spectrum of bacteria, fungi and yeasts and has proven advantageous in the management of ulcers [492]. However, silver is nonessential to the host and can be toxic and lead to tissue death [493, 494].

3.1.4.2.2. Addressing Elevated Protease Levels in the Local Wound Environment

An active dressing (POMOGRAN®, Systagenix 2011) specifically targeted toward reducing local levels of MMPs in non-healing wounds is composed of a freeze –dried mixture of 55% bovine collagen and 45% oxidised regenerated cellulose. When placed in the wound bed, this dressing appears to facilitate wound healing progress in complimentary ways—both by reducing elevated levels of destructive proteases and by protecting local growth factor viability [495, 496]. Other dressings have also modulated protease expression [464, 497-499].

3.1.5. SKIN GRAFTS

While wound dressings are generally temporary covers on the wound, skin grafts (which can be naturally or synthetically derived constructs) are generally placed within the wound for long periods or permanently. While skin grafts are used most extensively for the treatment of burns, they are also used for non-healing wounds such as diabetic ulcers, venous ulcers or pressure sores [23, 79, 500, 501]. Skin grafts aim to prevent infection, obtain wound coverage and minimise protein and fluid loss [501]. Appropriate wound debridement should still be undertaken before graft application, as this is a crucial factor contributing to healing rates [502].

3.1.5.1. Native Skin Grafts

Native skin grafts, such as allografts, xenografts or autografts, are used as either temporary or permanent coverings to prevent fluid loss and aid healing (Fig. 3.8). Epithelial autografts or dermal allografts are often expanded in area using splits. However, lack of sufficient donor tissue and high rates of donor site morbidity mean this is not always a good option. Native grafts can experience failure due to inadequate preparation of the wound, poor blood flow to the injured area, infection, contraction or haematoma [465]. Donor sites can be extremely painful and vulnerable to infection [503]. Native grafts also often experience failure due to inadequate integration with the host tissues. Allograft transplants are particularly in limited supply, are very expensive (>$10,000 /$m^2$) and can transmit viruses such as HIV if screening guidelines are not followed correctly [504]. The use of immunosuppressive agents increases the risk of infection [504]. Allografts are only a temporary covering, and graft replacement causes pain to the patient [23].



Figure 3.8. Healing of a large (28cm^2) diabetic ulcer which did not decrease in size with standard treatment, including negative wound pressure therapy. Following treatment with cryopreserved allogenic skin (TheraSkins), the wound closed in 19 weeks [505].

3.1.5.2. Engineered Skin Grafts

A variety of engineered skin grafts ("bioengineered skin substitutes") have therefore been made consisting of natural and synthetic components, with varying degrees of success [296, 505-511]. These products, depicted in Fig. 3.9, fall into three categories, depending on the presence and source of seeded cells; A. Cellular, allogenic, B. Cellular, autogenic, C. Acellular. Shown in Table 3.5. is a summary of these grafts, and are described according to their dermal and epidermal substitute components.

Some engineered skin grafts, including Dermagraft, Apligraft and Orcel, have been used to treat persistent venous leg ulcers, diabetic ulcers or chronic wounds with good healing rates and reduction of scarring in many patients [76, 78, 507, 509, 510, 512]. Dermagraft was the first engineered substitute available on the market and is approved by the Food and Drugs Administration (FDA) (in the US) and the Therapeutic Goods Administration (in Australia) for the treatment of diabetic foot ulcers. It is a cryopreserved dermal substitute consisting of neonatal foreskin fibroblasts on a biodegradable PLA/PGA matrix, which secrete collagen, growth factors and structural proteins. Dermagraft can be kept on a wound for 3 months without changing [514].

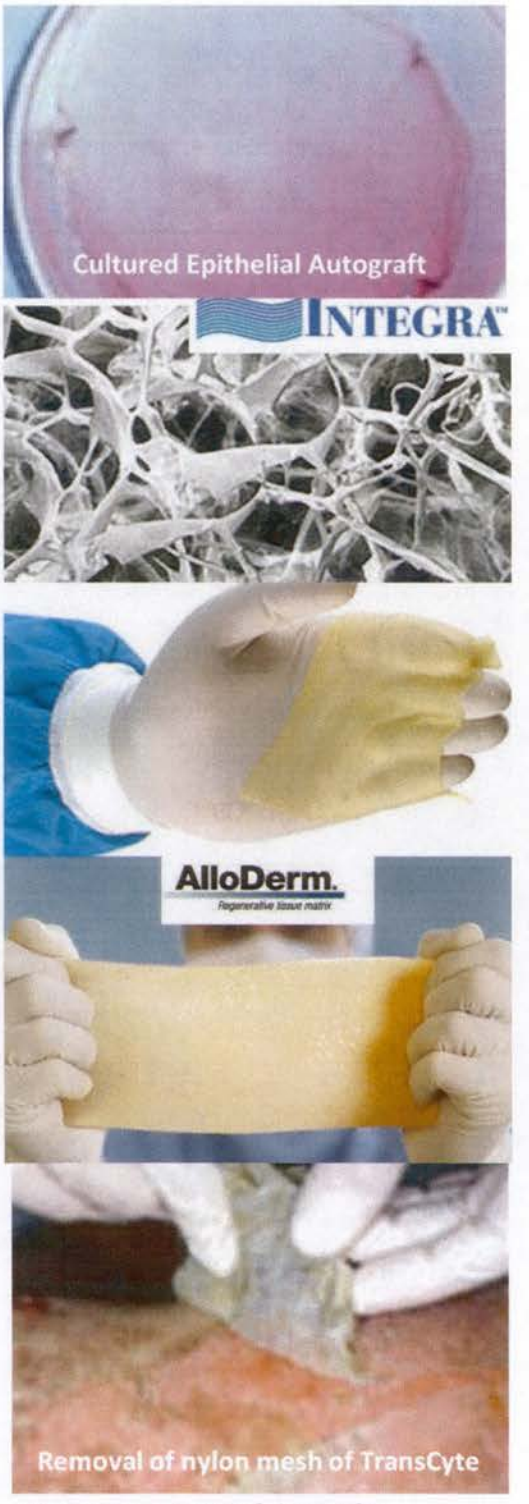


Figure 3.9. A range of skin grafts.

Apligraf (Fig. 3.10) consists of neonatal foreskin-derived fibroblasts suspended in a lattice of bovine collagen 1, with a layer of neonatal keratinocytes to represent the epidermal layer. Apligraf has been approved for treating venous leg ulcers since 1998 and diabetic foot ulcers since 2000 [516]. Vascularisation of the collagen lattice begins 5 days after grafting . Apligraf has been shown to heal >6mth old leg ulcers quicker than a compression therapy alone group (92 days vs 190 days) [509]. Researchers found that the

Table 3.5. Commercially available engineered skin grafts [78, 515].

		Product	Company	Dermal Component	Epidermal Component
A. Cellular, allogenic		Apligraf	Novartis, Organogenesis	Collagen gel with allogenic fibroblasts	Allogenic keratinocytes
		Dermagraft	Advanced BioHealing	PLA/PGA mesh scaffold with allogenic fibroblasts	-
		Melanoderm	MatTek Corporation	Collagen coated cell culture insert	Allogenic keratinocytes and melanocytes
		OrCel	Forticell	Collagen sponge with allogenic fibroblasts	Allogenic keratinocytes
		SkinEthic	SkinEthic Laboratories	Cell culture insert	Allogenic keratinocytes (with or without melanocytes)
		SureDerm	Hans Biomed	Allogenic acellular human dermis	-
		TransCyte	Smith & Nephew	Dermal matrix secreted by allogenic fibroblasts	Nylon mesh
B. Cellular, autologous		CEA*	Uni. of Cincinatti	Collagen-based polymer with autologous fibroblasts	Autologous keratinocytes
		Epicel	Genzyme Biosurgery	-	Autologous keratinocytes sheet
		Epiderm	MatTek Corporation	Collagen coated cell culture insert	Autologous keratinocytes
		EpidermFT	MatTek Corporation	Allogenic fibroblasts on cell culture insert	Autologous keratinocytes
		Epidex	Modex Therapies	-	Autologous keratinocytes with silicone membrane support
		Myskin/Transcell	CellTran Limited	-	Autologous keratinocytes on acrylic acid polymer
C. Acellular		Alloderm	LifeCell Corp.	Allogenic acellular human dermis	-
		Biobrane	Smith & Nephew	Nylon mesh coated with collagen	Semipermeable silicone membrane
		Integra	Integra Life Sciences	Collagen-chondroitin-6-sulfate matrix	Silicone polymer coating

CEA: Cultured Epithelial Autograft

presence of hyaluronan in Apligraf was the essential component responsible for repair in the diabetic model. Apligraf restores hyaluronan levels in the wound, leading to an increased ability of monocytes to differentiate into repair macrophages [517]. Orcel is fairly similar to Apligraf and has also shown good healing of ulcers in research trials.

In addition to providing a structural scaffold for wound healing, fibroblast-containing grafts provide growth factors, cytokines and regulatory factors that stimulate wound healing [518]. However, these skin substitutes cannot be used in wounds which are infected or in patients who are allergic to animal products, as both products contain bovine-derived materials [519]. As these products use allogenic products, these components are remodelled and removed from the body within the first few weeks- in a phenomenon known as silent rejection [23, 520, 521]. The presence of Apligraf DNA can only be detected in healing wounds up to 4-6 weeks

[521]. Apligraf is also a difficult product to use as its shelf life is only 10 days and it is extremely expensive [512].

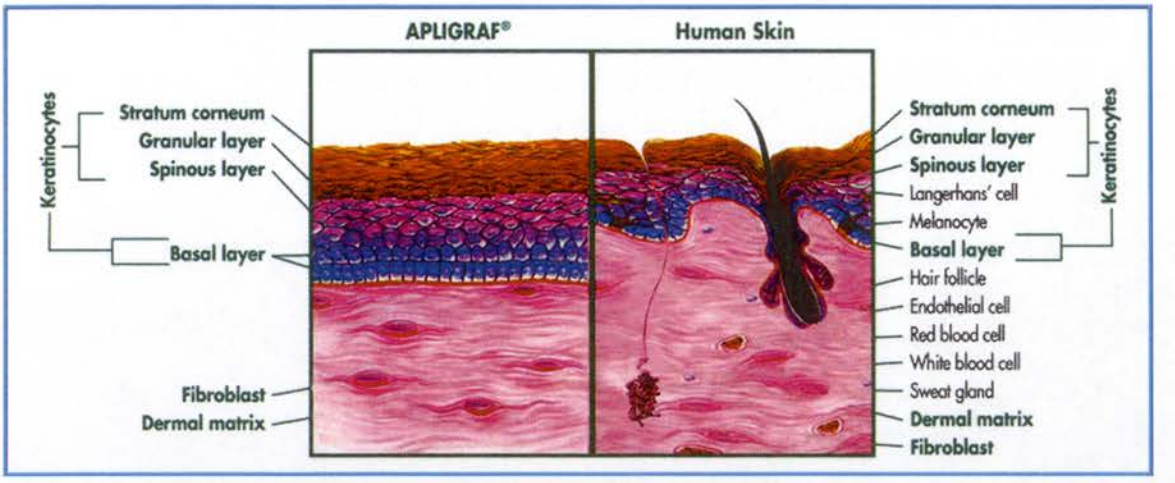


Figure 3.10. The structure of Apligraf compared with human skin [522].

Non-living matrices have also been used for deep wounds. Integra®, a matrix composed of bovine type 1 tendon collagen and chondroitin-sulfate, has displayed potential for use in the healing of deep postsurgical wounds and deep chronic diabetic ulcers [523, 524]. The epidermal silastic cover is removed 2-3 weeks after application. Integra provides good wound coverage and a long shelf life, with low risk of disease transmission. Alloderm® is composed of a freeze dried dermal component of human cadaveric skin and has shown reduction in wound contracture and scar formation in deep wounds [525]. Alloderm® is usually used in conjunction with a split-thickness skin graft and carries a risk of disease transmission.

Common problems associated with engineered grafts include [23, 3]:

- Limited availability, low shelf life
- Production intensive
- Extremely high costs (e.g Integra: ~AUD$1,200 per A4 sheet) [527]
- Often provide only partial skin replacement
- Poor handling properties
- Use of animal derived products
- Risk of immune rejection
- Long, costly hospital stays
- Scarring and wound contraction
- Multiple surgical procedures
- High risk of infection

- Risk of transmission of infection agents incl. prions
- Some are temporary grafts
- Grafts degrade during cryopreservation (e.g. Apligraf, Dermagraft→ cell viability and protein synthesis reduced by >50%)

A synthetic, bioabsorbable scaffold-based skin graft has the potential to address these limitations and could deliver stem cells to the wound site.

3.1.5.3. Gene Therapy and Stem Cell Delivery for Cutaneous Wound Healing

Chronic wounds can suffer from a myriad of defects, including fewer endothelial progenitor cells, diminished macrophage function, lower levels of chemokine stromal-derived factor 1 alpha and growth factors, fibroblast growth factor, especially epithelial growth factor and platelet-derived growth factor, decreased levels of endothelial nitric oxide synthase synthesis, reduced collagen deposition, greater proteolysis in the extracellular matrix, less angiogenesis and diminished keratinocyte and fibroblast migration and proliferation [283]. Therefore, any treatment strategy must address multiple aspects of this wound-healing impairment simultaneously.

New therapies have attempted to improve one or more of these wound aspects, through approaches such as gene therapy and stem cell delivery [481, 528-530] (Fig. 3.11). Enhanced wound closure and angiogenesis have been reported when gene therapy has been used to insert DNA encoding the angiogenic factors VEGF and PDGF into host cells [528-530]. REGRANEX® Gel, (Systagenix Wound Management, US) is the only FDA approved prescription medicine which contains human platelet-derived growth factor for the treatment of deep neuropathic diabetic foot ulcers [531]. The non-sterile gel consists of the active ingredient becaplermin, in a gel which largely consists of sodium carboxymethyl-cellulose which has been

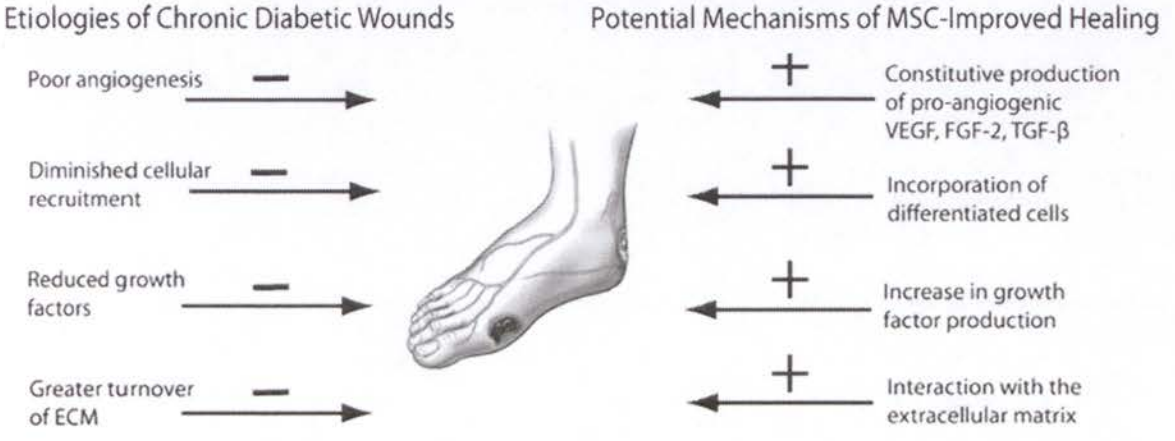


Figure 3.11. The potential advantages of MSC-aided therapy for chronic wounds.

modified to contain sodium chloride and pH levels which resemble physiological salt concentrations and to optimise the stability of the protein. The PDGF-B is thought to be efficacious in the treatment of ulcers as it enhances the granulation tissue thickness [532].

Stem cell therapy can offer even greater advantages to gene therapy. Pluripotential (haemopoietic or mesenchymal) stem cells, the precursors to more specialised stem cells, are capable of differentiating into a variety of cell types, including fibroblasts, endothelial cells and keratinocytes, all of which are critical cellular components for healing (Fig. 3.12). Mesenchymal stem cells (MSCs) are an ideal candidate for treatment of diabetic ulcers, due to their capacity to affect the wound in multiple ways and their ability to self-renew. MSCs do not require immunosuppression, as they possess immunosuppressive properties that likely occur through T-cell suppression [533]. Their immune characteristics mean they can be extracted and expanded from an unrelated donor.

Bone marrow contains both pluripotential and haemopoietic stem cells [534] and has been shown to accelerate healing of chronic wounds [535]. Yoshikawa and coworkers [536] demonstrated that use of a collagen sponge impregnated with autologous bone marrow-derived MSCs promoted closure in chronic wounds of multiple etiologies.

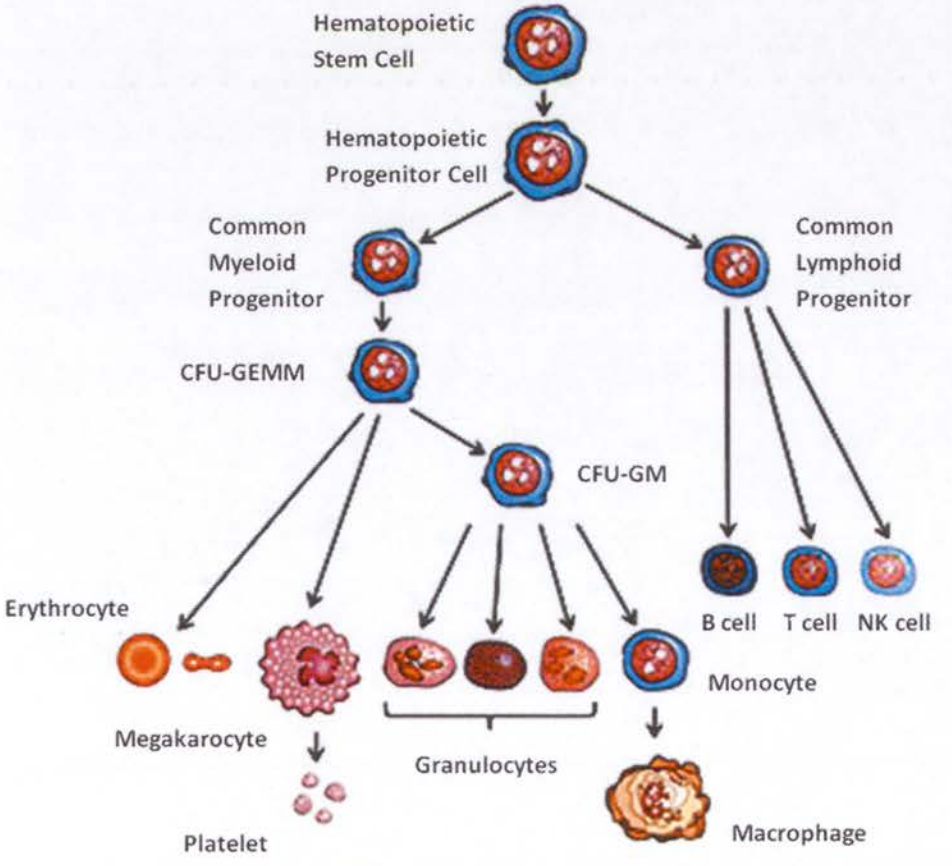


Figure 3.12. Stem cells have the ability to differentiate into a wide variety of cell types which are critical for wound healing [538].

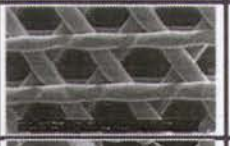
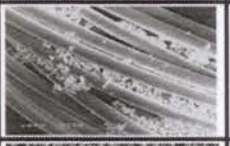
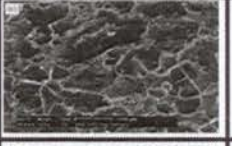
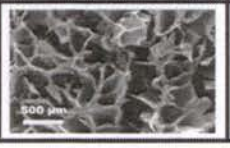
3.1.6. BIORESORBABLE, BIOACTIVE SCAFFOLD FABRICATION METHODS

For the development of a scaffold suitable for soft tissue repair, a fabrication method was sought to produce an elastic PCL/Bioactive composite with an interconnective, open celled structure. This form of scaffold could readily provide opportunity for tissue and cells to rapidly integrate and repair. A key aspect of this is to mediate infiltration of blood and vascular tissue. The scaffold was also required to have a good capacity for strain and adequate stability in all directions.

3.1.6.1. Review of Synthesis Processes for Polymer Scaffolds

Many techniques have been used to manufacture porous polymer scaffolds, resulting in a wide variety of architectures and corresponding physical properties, as reviewed in detail elsewhere [328, 538, 539]. Whilst the scaffold structure is important, critical consideration must be given to the viability of the manufacturing method, including its consistency, affordability and convenience. Table 3.6 contains a review of the features of key processes used for polymer scaffold formation. A selection of these methods is discussed in detail below.

Table 3.6. Features of polymer scaffold synthesis processes.

Process	Image	Process Features	Refs
Rapid Prototyping		Expensive, time consuming Pores (300-600um), porosity (60-80%) High compressive strength, low strain Isotropic structure, lacks heirachical pore structure	83, 59, 58
Sintered Particles		Very low porosity High rigidity Cost effective, simple process- no organic solvents Uses established ceramic/metal techniques	7
Fibrous Mesh		Cost effective, convenient Lack long-range interconnectivity May delaminate when layered Mechanically unstable	86 68
Thermally Induced Phase Separation		Directional, inhomogenous pore shape/dimension Difficult to control scaffold structure precisely Porosity (90%), Pore size (few microns to 250um) Can exhibit high strains	85
Solvent Casting/ Porogen Leaching		High porosity (<90%), Pores (75-500um) Cost effective, Crystallinity can be tailored Multi-directional high strains & good tensile properties Limited thickness (3mm)	85
Batch Coagulation		High porosity (64-90%) Heirachical porosity Rapid batch process Multi-directional high strains & good tensile properties	540

3.1.6.1.1. Fibrous Meshes

Fibrous meshes are popular for soft tissue grafts such as skin and cartilage [68, 73, 86, 244, 261, 394, 396, 398-400]. They consist of individual fibres which are either woven, non-woven or knitted into three-dimensional patterns of variable pore size. Fibrous meshes provide a large surface area for cell attachment and allow a rapid diffusion of nutrients.

A popular technique to create non-woven, continuous fibre scaffolds is electrospinning. These fibres, with a diameter 1-10 μM, may be made from natural, synthetic or blended polymers and are designed to mimic the structure of the native ECM. Electrospinning provides control of fibre diameter, orientation, composition and packing density, which can be advantageous for aligned tissues such as tendons. Although cost-effective and versatile, electrospinning techniques have a lack of control over the 3D pore structure. Pores are often very small (<5 μm) and lack long range interconnectivity, so cell migration and tissue ingrowth are often poor [245]. As such, these scaffolds act more as a filler than a porous matrix which facilitates native tissue ingrowth. Attempts to form meshes with good pore interconnectivity have included forming scaffolds via bonding PGA fibres using heat [541] or by spraying with an atomised PLLA or PLGA solution [541].

Although fibrous meshes show reasonable levels of strain (~60-150% for a PGA mesh) [261] and can exhibit some tensile strength, they often lack compressive stability. Biaxial instability (shrinkage) of the electrospun collagen scaffolds has also been reported to contribute to wound contraction and dermal scarring [544]. This effect was reported to be reduced by utilising a freeze drying process.

3.1.6.1.2. Thermally Induced Phase Separation (TIPs)

Thermally Induced Phase Separation [14, 61, 62, 85] involves solid-liquid phase separation during freeze drying. Highly porous scaffolds can be created with macropores up to 400 μm [61]. However, many pores are often smaller than this diameter (e.g. 10 μm), particularly on the surface [14]. Several authors have reported hierarchical porosity with this method. In addition to the macropores, micropores were observed with dimensions of 20-50 μm [1, 187].

Using this process, pore sizes can be adjusted depending on processing parameters (cooling rate) and formulation conditions (nature of the solvent, polymer concentration). As the freezing temperature is increased, the average pore size increases due to a low crystal nucleation and growth rate of the solvent. Pores formed via this technique are often interconnected, tubular, highly oriented and parallel to each other as a result of the unidirectional cooling process [187]. Pores of this shape were observed in PLGA/Bioactive glass foams in a study by Boccaccini and coworkers [187]. This was a major contributor to

suboptimal tissue ingrowth into these scaffolds (ref 6.1.3) [85]. The oriented pores lead to tissue ingress which is more pronounced in one direction but limited in plane which is perpendicular to this.

TIPs scaffolds often display reasonable tensile strength, good flexibility and a high capacity for strain (>200%) [1]. However, one of their main limitations are the narrow pore interconnects which are approximately the diameter of a single cell. As a result, these scaffolds have difficulty producing rapid tissue ingrowth to a significant depth within the scaffold. As mentioned above, they also display poor homogeneity of the poor structure; with regions of small pores. Additional limitations of the TIPS method are the requirements for well controlled processing parameters, and that it is user and technique sensitive.

3.1.6.1.3. Solvent Casting/Porogen Leaching

Porogen leaching techniques can enable the synthesis of highly porous scaffolds with large, interconnected pores. Scaffolds with porosities of 45-90% and pore sizes <100 μm-710 μm have been reported [221, 540, 545, 546]. This technique also allows scaffolds to be formed in a range of shapes and sizes. Table 3.7. reviews scaffolds formed using particulate-leaching based techniques.

This process involves several steps:

(1) Dispersion of particulate porogens into a polymer solution;

(2) Casting of the solution in a mold;

(3) Removal of the solvent via evaporation/ precipitation; and

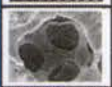
(4) Leaching out the porogen.

The most common porogens are NaCl salt crystals [85, 87, 219, 223, 540, 548, 549] however recently sucrose crystals and fibers have been investigated [221, 326, 550-552]. Solvent removal can be facilitated via water or evaporation in air, nitrogen, or other gases via a freeze drying process [540, 545, 553, 554]. Porogen leaching is usually achieved using water. The porosity (or void volume fraction) corresponds to the amount of leachable particles [540]. The pore size and pore shape of the porous structure can be modified independently of the porosity, by varying the leachable particles characteristics [84, 540].

Porogen leaching has been used to form scaffolds with hierarchical porosity. In one case, Gao and coworkers [548] used NaCl porogens to synthesise PGS scaffolds. The scaffolds contained both macropores (15-150 μm) and micropores (5-20 μm). The micropores were generated by glycerol vapor formed during the polymer curing.

Porogen leached scaffolds show a high capacity for strain and good multi-directional stability. However, major challenges remain with this process, as discussed in the following sections. A method was sought which could overcome these limitations.

Table 3.7. Review of scaffolds formed using particulate leaching.

	Image	Study	Material	Porogen; Additional Process	Pore Size	Porosity	Ref.
Porous Foams		Gao 2006	PGS	NaCl crystals; TIPS	bimodal: 65-150um, 5-20um	90%	548
		Chen 2004	PCL	NaCl crystals; scaffolds coated with silk	<100um	-	223
		Nam 2000	PLLA	NH_4HCO_3 particles; coagulation	300-400um	-	545
		Reignier 2006	PCL/PEO	NaCl crystals; extrustion	bimodal: unspecified	75-88%	549
		Lu 2009	PCL	3D printed solid free form sucrose mixture	<500um	-	221
		Lu 2009	PLLA	3D printed sucrose mixture	250-500um	-	221
		Bezuidenhout 2008	PU	Gelatin spheres	147um	-	62
		Hofer 2003	PLGA	NaCl crystals; extrusion	95um	81%	87
		Day 2005	PLGA	NaCl crystals; extrusion	<100um	-	85
		Hou 2003	PCL	NaCl crystals; compression, coagulation	250-425um, 500-710um	64-90%	540
		Yamamoto 2000	PVA	Starch particles	30, 60, 110, 250, 350, 700um	88-91%	84
		Misaki 2007	PLAC	NaCl crystals; TIPS	200-400um	-	61
		Lee 2003	PLGA or PGCL	NaCl crystals; TIPS	200-300um	93%	60
		Cannillo 2010	PCL/BG	NaCl crystals	<150um	-	219
		Rhodes 2007	Hyaluronan	NaCl crystals	400um	-	57
		Olah 2006	PCL, PCL/$CaCO_3$	NaCl crystals	250-500um	50-88%	546
		Meretoja 2006	P(CL-PLLA), PCL/BG	NaCl crystals	<250um	45-85%	555
		Nazarov 2004	Silk fibroin	NaCl crystals; TIPS	>100um	84-98%	556
		Oates 2007	PLLA	NaCl crystals	<250um	70, 80, 90%	557
		Wang 2007	PCL	Gelatin or lactose	bimodal: 500um, 25-33um	10%	15
		Yun 2011	PCL	NaCl; RP	bimodal: 190um, 5um	84%	218
		Perera 1997	Iron	Sucrose; Hot pressing	<150um	<45%	546

3.1.6.2. Limitations of Processing Techniques

Several challenges remain for particulate leaching techniques [70], including:

- Poor pore interconnectivity
- Limited to thin scaffolds (<3 mm)
- Residual particles in the polymer matrix
- Porogen agglomeration leading to non-uniform porosity and pore size
- Long processing times
- Labor intensive fabrication process
- Use of toxic solvents
- Low batch yield

These will be discussed in detail in the following sections.

3.1.6.2.1. Poor Pore Interconnectivity

Scaffolds made using solvent casting/particulate leaching processes often exhibit poor pore interconnectivity which limits tissue infiltration [14] (ref section 6.1.3.5). This attributed to inadequate porogen connectivity. In addition, a dense skin layer forms on the porogens and surrounding the entire scaffold during solvent evaporation.

There have been several attempts to improve pore interconnectivity and homogeneity. For example, particulate leaching has been combined with thermal processing techniques such as compression and extrusion. However, these techniques can result in fragile structures and can preclude the incorporation of growth factors/drugs due to the use of high heat and pressure. Thermal degradation of the polymer during processing could also be a concern. For example, PCL/PEO scaffolds were created by the combination of salt leaching with twin extrusion method [549]. The salt particles experienced damage during the extrusion process, resulting in a reduction in pore size and narrow interconnectivity channels.

A superior technique is utilisation of an interpenetrating network porogen [221]. For example, Lu and coworkers used rapid prototyping to print a porogen network in anatomical shapes, from a mixture of sucrose, water, alum, honey and butter (Fig 3.13). Molten PCL was injected into the porogen network, cooled to room temperature and placed in water to separate the sucrose porogen material from the PCL. The resulting PCL scaffolds were allowed to air-dry at room temperature, and sintered to improve mechanical integrity for bone applications. This rigid scaffold displayed a fully interconnected porous structure.

Another instance of these porogens is interconnected salt porogens [548]. Salt particles were fused in a humid environment for 4-8 hrs. PGS scaffolds formed with these porogens demonstrated high levels of pore interconnectivity and mass transfer, as shown by the ability of fibroblasts to penetrate and deposit collagen in the scaffold interior.

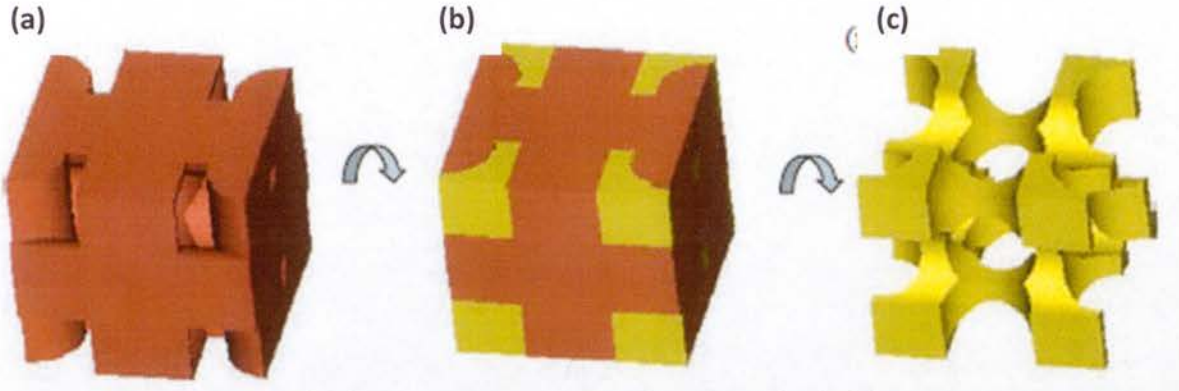


Figure 3.13. Schematic of (a) Interpenetrating network porogen (red), (b) Porogen and polymer (yellow) (c) Interpenetrating network polymer scaffold [221].

3.1.6.2.2. Inadequate Scaffold Thickness

Researchers have difficulty creating thick scaffolds using porogen leaching [60, 62, 84, 85]. Deeply embedded porogens become too distant from the surface, so they are difficult to remove via aqueous immersion. Residual porogens left in the final structure can have a cytotoxic effect on the contacting cells. Some groups have investigated layering thin scaffolds to provide depth, however this only allows for a limited number of interconnected pore networks [558]. Such structures also lack mechanical stability and can delaminate easily.

Interpenetrating networks can be used to reduce residual porogens [221]. Residual porogens occur due to insufficient interconnectivity caused by narrow pore channels (fenestrations) which become easily blocked. Wider pore throats facilitate water flow throughout the scaffold as the porogens are removed.

3.1.6.2.3. Time and Labor-Intensive Processes

Many scaffold synthesis processes have processing limitations which prohibit easy translation from the lab to a commercial setting. Many processes require a high degree of manual intervention, making it practically impossible to transform to industrial scaled-up methods. Often a technique is dependent on the user's skills and reproducibility is very difficult to achieve. The majority of common processes produce a low scaffold yield- perhaps one or just a few scaffolds. This can be limited by molds or other equipment, and it is often difficult to increase the batch yield.

Most processes are also time intensive [206, 219]. Solvent evaporation requires days-weeks to create one batch. When solvent evaporation is achieved using freeze drying, the process is particularly time consuming. The porogen leaching step is also time-consuming. For example, Cannillo and coworkers [219] created PCL/bioactive glass scaffolds involving 1 day of solvent evaporation (dichloromethane) and 5 days of rinsing NaCl crystals out using water. These scaffolds would therefore take >6 days to make a single batch. PCL scaffolds made by Yeh and coworkers required 24 hrs for a precipitate casting step, followed by 3 days rinsing in water [206].

3.1.6.2.4. Organic Vehicles for Polymer Scaffolds

Solvents used in polymer scaffold processing are often cytotoxic and/or carcinogenic. Common solvents include naphthalene, chloroform, methylene chloride, acetic acid, Dimethyl sulfoxide (DMSO), benzene, xylene and ethanol [14, 558]. DMSO is a common solvent, being used for both solvent dissolution and polymer cross-linking; however it is a tumorigen, mutagen, reproductive effector and irritant [14]. Some techniques must be performed with a limited solvent selection (e.g. Freeze drying) [14]. Jo and coworkers [150] created thin film scaffolds by dissolving PCL and nanofibrous bioactive glass in tetrahydrofluran. Yun and coworkers [148] dissolved PCL into chloroform.

Acetone is a ketone organic compound that plays an important role in the body's metabolism and has also been widely used by researchers for tissue engineering scaffolds [206, 326]. Yeh and coworkers [206] used acetone to make PCL scaffolds using precipitate casting. The resulting scaffolds with 62-72.5% were not found to be cytotoxic. The choice of molecular weight of the PCL can vastly alter the scaffold mechanical properties along with the concentration of the polymer solution. Yeh and coworkers [206] reported that the tensile strength of scaffolds (pore size 10-20 μm) prepared using 12.5% w/v polymer solution tended to increase from 0.83 MPa to 1.42 MPa and the elongation rate was improved from 35.2% to 117.8% when increasing PCL molecular weight. The porosity of this scaffold was found to decrease with increasing PCL solution concentration and molecular weight. Changes in molecular weight resulted in little change in the crystallinity. Crystallinity was measured to be approximately 67%.

3.1.6.3. Approaches for Bioactive Glass Incorporation into Scaffolds

Bioactive fillers can be added to the scaffold as fibers or powders with range of methods. These have been reviewed in detail previously [153, 187, 538]. Table 3.8 describes the types of techniques which could be used, and their effect on the scaffold properties.

Table 3.8. Techniques for glass incorporation into scaffolds.

Image	Method	Features	Refs
	**Bioactive Filler**	May show a pronounced effect on PCL degradation rate Large particles may cause physical damage to the matrix	209, 559, 150, 193, 198
	**Bioactive Glass Coating**	Increases surface texture/ wettability/bioactivity Encourages protein adsorption & tissue attachment May increase scaffold stiffness & decrease strain	189, 560, 561, 567
	**Composite Glass/Polymer Coating**	Drug delivery can be achieved according to the dissolution profile of the second polymer Increases scaffold toughness May decrease elasticity/strain	562

3.1.6.3.1. Bioactive Glass Filler

Bioactive glass can be integrated into the polymer melt or solvent solution prior to scaffold formation. This is the most common method for the incorporation of a bioactive phase. However, prolonged contact of the glass with water during a porogen leaching step can promote the development of calcite and alter the glass composition, which can suppress the development of hydroxyapatite *in vitro* [219]. This was found to be the case when Cannillo and coworkers removed NaCl porogens during a 5 day rinse step [219].

Rich and coworkers [193] synthesised composites consisting of 40, 60 and 70% bioactive glass by incorporating glasses of 2 granule sizes (<45 μm and 90-315 μm) into a batch mixer with a P(CL/DL-LA) copolymer. Haimi [198] incorporated 10 or 20% S53P4 BG into a polymer melt (PLA), followed by freeze drying to form porous scaffolds. Figure 3.14 depicts scaffolds formed via incorporation of 45S5 into a PDLLA/dimethylcarbonate solution, and formed using the TIPs process [209, 196]. BG concentrations up to 40 wt% were achieved, with the porosity decreasing with increasing glass content above 10 wt%. Jo and coworkers mixed Bioglass® powders or nanofibers with a PCL/tetrahyrofuran solution for 24 hrs before formation of 0.2 mm thick thin films [150].

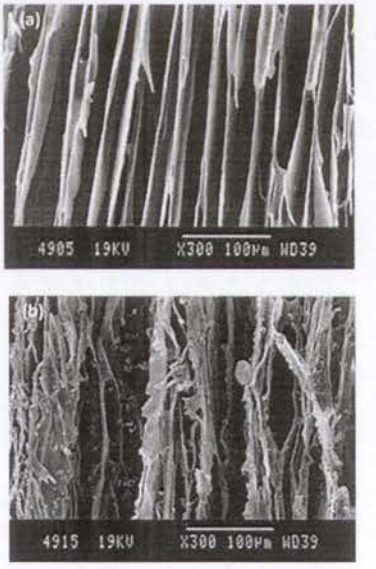


Figure 3.14. (a) PDLLA foam (b) 40 wt% Bioglass®-filled PDLLA foam [196].

Niemela and coworkers [191] added spherical 13-93 bioactive glass particles to a PLA solution and formed composites using an extrusion method. The incorporation of the glass was shown to reduce bending strength, but increase bending modulus, shear/compressive strength and increase torsional strain at maximum bending load.

3.1.6.3.2. Bioactive Glass Coating

Glass can be coated onto scaffolds using either dry [564] or slurry-dipping [187-189, 565, 566] techniques. Tussa and coworkers [564] pressed dry bioactive glass granules (diameter=315-500 μm) onto the surface of a bioactive glass fibre/polymer composite. Samboulis [560] coated bioactive glass powders (d<5 μm) onto the surface of sutures, by coating in a bed of dry powder, followed by pressing between two plates. Although the bioactivity of the surface is vastly improved, dry coating techniques have been shown to occasionally cause mechanical damage to suture surfaces [561]. In some cases, it has been difficult to adhere the particles to the polymer.

Slurry dipping involves the suspension of bioactive glass particles in an aqueous phase, followed by dipping of the scaffold into the solution, and then allowing it to dry at room temperature. Often, the solution is mixed using sonication or magnetic stirring, to avoid sedimentation [187, 188, 565, 566]. A typical process involves a 30 min period of stirring followed by an immersion time of 5 mins [189]. Roether, Boccaccini and coworkers [189] used the slurry-dipping technique to deposit Bioglass® onto PDLLA foams (Fig. 3.13). This was achieved with slurries of ethanol and 45S5 bioactive glass powder (0.01-10% wt/vol). The ethanol used in Roether's study resulted in a greater degree of Bioglass® infiltration and improved coating homogeneity. This was due to an increase in hydrophilicity, and hence water adsorption by the PDLLA [189]. However, the slurry-dipping technique results in closure of the interconnected pores due to an accumulation of Bioglass® particles [189].

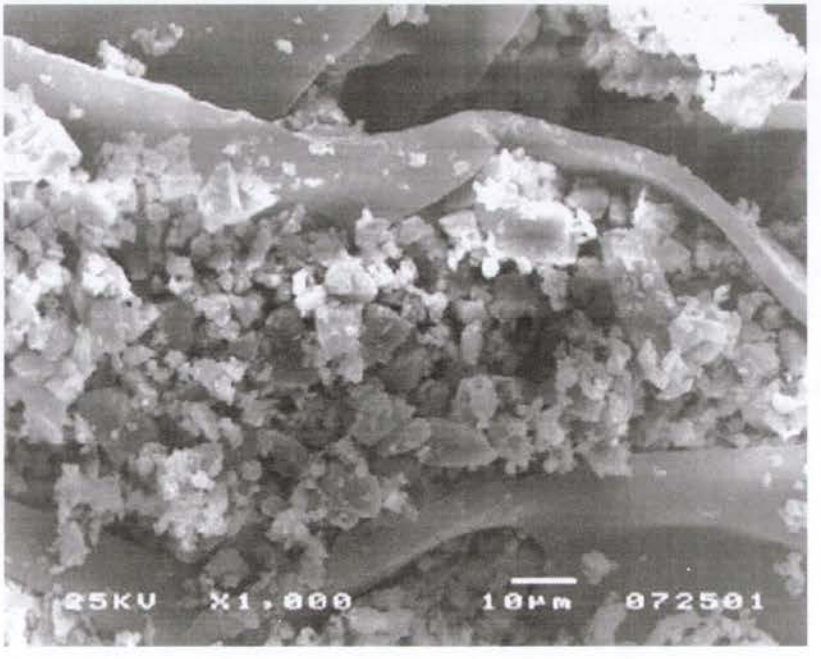


Figure 3.15. Bioactive glass coated PDLLA foams synthesised via slurry dipping in ethanol [189].

Other less common coating techniques include electrophoretic deposition [189] and electrospinning [567]. Electrophoretic deposition was also used by Roether [189] to coat PDLLA foams; however the coating thickness throughout the foam was less uniform and more difficult to control than the slurry dipped coatings. Shin and coworkers [567] created PCL nanofibrous scaffolds coated with a film of silica sol-gel using co-electrospinning.

3.1.6.3.3. Composite Glass/Polymer Coating

Scaffolds can be coated with a composite coating, where the polymer is used as a binding agent so the glass particles adhere to the surfaces of the polymer. Chen [562] coated Vicryl (polyglactin 910, Ethicon Inc) and Mersilk (silk, Ethicon Inc) sutures with a film of 45S5 Bioglass®-containing PDLLA (in a dimethyl carbonate solvent) (Fig. 3.16a). The composite coating became detached from the suture when the suture was knotted and the coating experienced deformation and friction (Fig. 3.16b). A second PDLLA coating was then applied to improve adherence of the glass to the sutures (Fig. 3.16c) [562]. These coated sutures are not ideal for *in vivo* use, as excessive friction when the suture penetrates the tissue would abrade the tissue.

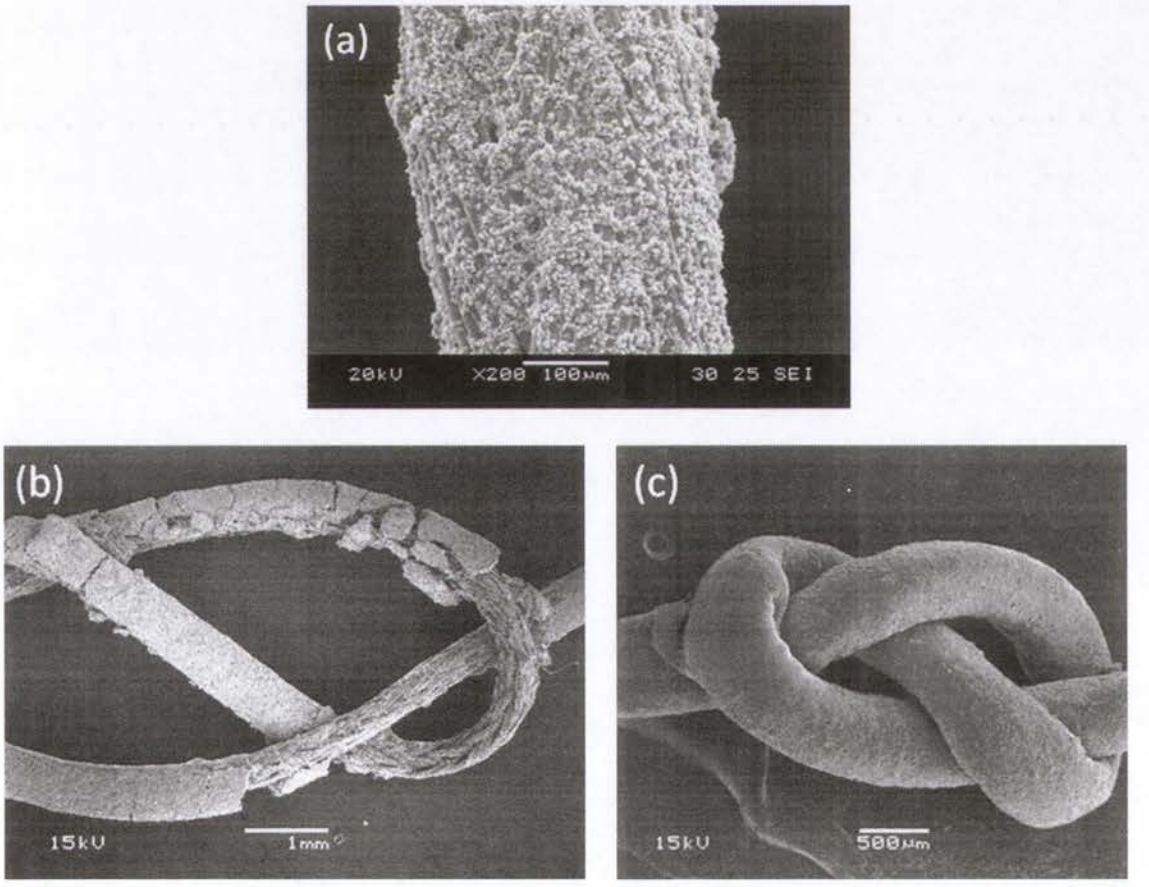


Figure 3.16. (a) Bioglass®-PDLLA coated Vicryl suture (b) Knotted Bioglass®-PDLLA coated Vicryl suture showing peeling of the coating (c) Vicryl coated with Bioglass®-PDLLA followed by a second PDLLA coating showed high structural stability [562].

3.1.6.4. Effect of Bioactive Glass Incorporation on Physical Properties of Scaffolds

Bioactive glass incorporation can change the physical properties of the scaffold, such as the water adsorption, degradation rate and mechanical properties [187, 190, 193]. The effect is highly dependent on the incorporation method, particle size and the composition and structure of both the glass and polymer.

3.1.6.4.1. Water Adsorption and Degradation

Bioactive glass is known to improve the water adsorption (hydrophilicity) and increase the degradation rate of polymers. This occurs via acceleration of the ester hydrolysis of the polymer matrix. This effect was observed by Maquet [190] who showed an increase in water adsorption in 45S5-filled PDLA scaffolds compared to PDLA scaffolds, for the first 10 weeks of soaking in PBS at 37°C. Rich [193] demonstrated an increased degradation rate when S53P4 bioactive glass filler was added to a P(CL/DL-LA) matrix (Fig. 3.17). This effect was especially pronounced for small particle sizes (<45 μm) with high surface areas.

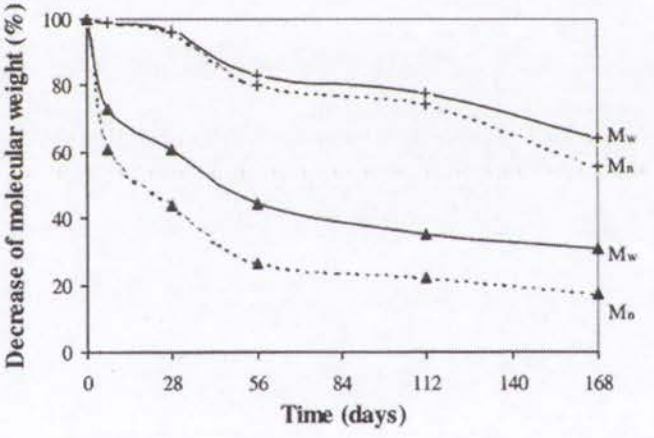


Figure 3.17. Changes in average molecular weights of P(CL/DL-LA) polymer (+) and 60 wt% S53P4 bioactive glass/P(CL/DL-LA) composite (▲) as a function of hydrolysis time [193]

3.1.6.4.2. Mechanical Properties

The addition of rigid fillers to polymer matrices is common in composite technology to improve the stiffness, mechanical strength and structural integrity of components. In the case of porous scaffold materials, however, the interrelationship between filler concentration and pore structure and their combined effect on mechanical properties is multi-factorial. This is discussed by Zhang and coworkers [197].

In compression, bioactive fillers usually have the effect of increasing the modulus and compression strength [187]. Boccaccini, Day and coworkers demonstrated that the addition of 50 wt% 45S5 bioactive glass to a PLGA foam increased the modulus by more than 200% and

the compression strength by 10% [187]. In tension, nanosized particles display a stiffening effect, whereas microsized Bioglass® usually do not [568]. This was observed by Misra and coworkers when films of solvent casted, Bioglass®-filled poly(3hydroxybuterate) were tested [568]. Boccaccini's study found the tensile strength of Vicryl sutures actually reduced when coated with bioactive glass/polymer composite films (88 and 83 MPa respectively) [187].

3.1.7. MODULAR AND FUNCTIONALLY GRADED SCAFFOLDS

Several researchers have reported the ability to cut, form and join scaffolds together in a modular fashion to fill anatomical defects [314, 315, 327, 789]. Often, thick, broad, contoured or tubular scaffolds are required to suit particular tissues. For example, Tran [789] reported a technique of bonding together layers of 200 μm - thick polyurethane-doped polyester scaffold sheets either chemically or through cell culture. This group also reported the fabrication of tubular scaffolds by molding around a Teflon rod. In an alternate approach, Gao and coworkers [327] fabricated flat and tubular poly(glycerol sebacate) (PGS) scaffolds using fused NaCl templates. Fused templates were made by packing NaCl crystals into a tubular mold consisting of an outer Teflon mold and an inner sacrificial mandrel composed of paraffin wax, and placing in a humid environment. The porogen was infused with a PGS/tetrahydrofuran mixture and the solvent and paraffin were removed during several subsequent steps before the scaffold was lyophilized. The resultant scaffolds had an inner diameter of 5mm, a wall thickness of 1 mm, and a length of 60 mm. This process was not ideal due the use of toxic solvents and the chance of residual paraffin. Fusion of PCL rapid prototyped scaffolds have also been reported to form anatomically shaped bone scaffolds upon immersion in warm saline [314, 315].

As introduced in section 1.5.1, many native tissues including skin and osteochondral junctions contain a variety of tissues which differ in histological characteristics and mechanical function. This is a common feature of materials in nature, also being found in bamboo and tree trunks. A seamless, graded transitional region often joins regions of soft and hard tissue together. Some examples include; the osteochondral junction, spinal disk and ligament-bone interface [569, 570]. In recent years, interest has been shown in developing scaffolds which meet the needs of the different tissue types. The scaffolds should match mechanical properties with native tissue to prevent stress shielding [571] and give the cells mechanical cues which they would receive in their native environment [572]. Scaffolds can be formed with a transition in either structure, composition and/or delivery of therapeutic factors/cells [569]. Mechanically, a seamless gradient is superior to a 2-part scaffold. This can prevent delamination, stress shielding and improve implant lifespan [569]. Biologically, a gradient is desirable and more closely mimics the composition and function of tissues [569]. Ideally, the mechanical stimuli experienced by

the cells/tissue within the scaffold must be appropriate to guide the new tissue to behave like the original tissue and ensure optimal ECM remodelling.

Multi-phasic scaffolds can be synthesised in 4 forms, as depicted in Fig. 3.18. Although seamless gradients are mechanically superior to the other options, they can be challenging to synthesise, and the alternate options are often pursued.

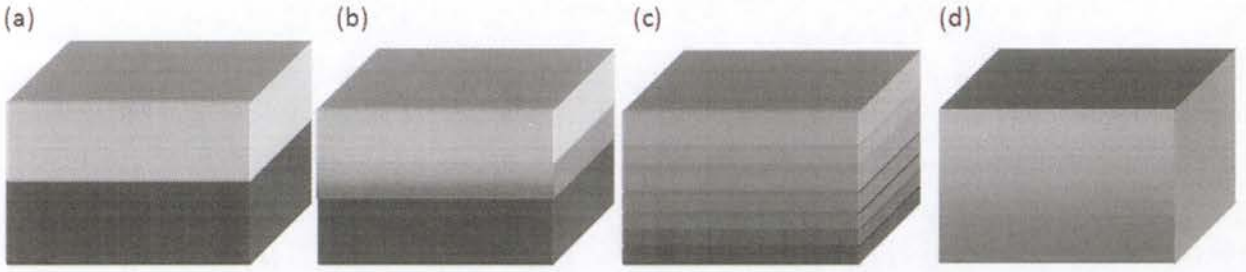


Figure 3.18. Multi-phase scaffolds (a) two distinct phases (b) two distinct phases joined by a graded region (c) Step-wise gradient, (d) Seamless gradient.

Biphasic, layered scaffold designs (Fig. 3.18a) are relatively common in the literature (ref section 2.12). This was the approach used in the scaffold in Chapter 2. Biphasic scaffolds with a central graded region (Fig. 3.18b) were synthesised by Sherwood and coworkers using 3D rapid prototyping methods [401]. The scaffold consisted of: 1) an upper, cartilage region which was 90% porous, composed of PLGA with macroscopic staggered channels, (2) a lower, bone portion which was 55% porous consisting of a PLGA/TCP composite, (3) a transition region which was graded in both composition and porosity [401].

Graded scaffolds (Fig. 3.18c, d) have been created by varying pore size/porosity, pore architecture, filler proportion and growth factors [59, 330, 569, 573-576]. A smooth modulus gradient (Fig. 3.18d) has been shown to increase the overall performance of the composite by avoiding internal stress peaks [577]. Oh and coworkers created PCL scaffolds using a centrifugation method, to achieve a gradual increase in pore size (from 88 to 405 mm) and porosity (from 80% to 94%) [574]. Woodfield and coworkers illustrated that scaffold design with anisotropic pore architecture could be used to instruct zonal cells and ECM distribution to a certain extent in constructing tissue engineered cartilage [59]. Scaffolds have also been synthesised with a graded composition consisting of PLA/glass fibers, collagen/nanohydroxyapatite or collagen/TCP [576, 578]. Buhler and coworkers [575] attempted to create PLA foams containing graded regions of glass fibers. By this method, a true gradient was not achieved, due to fiber agglomeration. Other scaffolds synthesised by Liu of collagen/nanohydroxyapatite displayed a gradient of Ca to P ratio across the scaffold [576]. When implanted into articular cartilage defects in rabbits, scaffolds encouraged complete healing at 12 weeks [578]. In addition to gradients in scaffold pore size, porosity and

composition, growth factor gradients have been investigated. For example, Wang and coworkers [573] delivered bone morphogenic protein 2 (rhBMP-2) in a concentration gradient fashion from silk fibroin microspheres in a hMSC-seeded, PLGA scaffold and found a corresponding gradient in bone cell differentiation [573].

Therefore, one of the design requirements for the scaffold in the current study was to ensure a functional gradient could be synthesised. The development of a graded scaffold with changing the porosity was thought to be a promising option. Porosity is thought to be more a more dominant factor in determining scaffold mechanical properties than pore size [579].

Practical considerations for development of a commercially relevant scaffold included considering sterilisation technique, shelf life and packaging, which will now be discussed.

3.1.8. SCAFFOLD STERILISATION AND COMMERCIAL CONSIDERATIONS

Appropriate sterilisation is a critical factor in ensuring long-term implant efficacy. Inadequate sterilisation can lead to infections which can cause product recalls and patient rehospitalisation and even death [580]. Implants bring a higher degree of risk of infection because: (1) Microorganisms left on the implant can cause infection- which is sometimes not be evident until a year after surgery (2) Implantation of biomaterials often involves the removal of tissue with the interruption of the blood supply- creating a vulnerable area in which microorganisms can multiply and which is difficult to reach using antibiotics (3) Implant removal is not always an option as it can kill or cripple the patient e.g. vascular graft, total joint replacement [580]. In 2004 it was reported that the mortality rate associated with infected total hip replacements approaches 50%- both from the infection itself and from complications associated with the resulting impaired mobility- such as blood clots and pneumonia [581].

Extensive sterilisation validation was therefore also a vital consideration for development of the soft tissue scaffold. For *in vivo* use, gamma radiation [583, 584] and ethylene oxide gas (EtO) were investigated as candidates, while for *in vitro* tests, UV radiation combined with ethanol rinses were deemed sufficient. Polymeric materials are susceptible to property changes during some sterilisation treatments, which can include mechanical properties, porosity, degradation rates and other scaffold characteristics [12, 70, 585-589]. It has only been recently that these property changes have been utilised in a controlled manner, to introduce positive changes in the material and thus achieve a property enhancement rather than a loss of properties [588]. In this way, sterilisation can become a part of the manufacturing process as it can alter the final properties and therefore the application of the device [588]. Due to their unique architecture, tissue engineering scaffolds require special consideration of the sterilisation process on the microbiological and physical characteristics.

Levels of bioburden (microorganisms) and the spores they produce must be minimized within an implant. Regulatory verification requires demonstration of terminal levels of contaminants. Microorganisms can release pyrogens, which cause fever *in vivo*, and can lead to septic shock and multiple organ failure resulting in death [590, 582]. A common pyrogen is endotoxin, found in the membrane of gram-negative bacteria (including Escherichia coli and Pseudomonas) [591]. Endotoxins are released from bacteria after death and lysis of the cell, which can occur during sterilisation procedures. Sources of pyrogens in medical devices are attributed to: the water used for the solvent or in the processing; packaging components; the chemicals, raw materials or equipment used in the product preparation. Endotoxins can be found in high levels in naturally-derived materials such as collagen, gelatin, chitosan, alginate and rubber.

Pyrogens are not commonly tested for during tissue scaffold development. This can compromise biocompatibility studies [593]. The presence of endotoxins can induce significant production of cytokines [582, 592] or cell maturation [594]. High levels of endotoxins have been detected in commercially available wound dressings (particularly calcium alginate) [582], collagen solutions [594], recombinant protein [592] and metallic microparticles [592]. Significant levels of adherent endotoxins have been detected on titanium disks which were prepared in a similar fashion to authentic implants [592]. There is some speculation that endotoxin can play a significant role in aseptic loosening [596]. Endotoxins are difficult to remove from products- the only way to effectively inactivate endotoxins is via dry-heat sterilisation at 250°C. Good manufacturing procedures can minimise the presence of microorganisms in some materials- particularly washing in pyrogen-free water [591].

Some bacteria produce dormant endospores which help them survive harsh environmental stresses, such as high heat, UV radiation, gamma radiation, chemical disinfectants and desiccation. Therefore it is not only the microorganisms, but also their spores which need to be carefully monitored to minimise the risk of contamination adversely affecting cell cultures, animals or humans.

Other commonly used techniques include UV light which is used in research laboratories, due to its low cost and efficiency [86, 587, 597-600]. However, although it can reduce bacterial count [591], it is not a FDA approved sterilisation technique for medical devices. Ethanol solution (70%) is often used to help clean a biomaterial [385]. However, ethanol has little effect on most bacterial spores and therefore does not always ensure sufficient elimination of microorganisms.

3.1.8.1. Gamma Irradiation

Gamma irradiation is powerful means of sterilisation which is widely used in industry. Gamma irradiation is a high energy form of electromagnetic radiation released from the radioactive isotope Cobalt 60. Bacteria are killed by the breakdown of bacterial DNA and inhibition of bacterial division. This is a popular process for polymers as it does not significantly increase the temperature of the product. Gamma rays have the capacity to totally penetrate the product (including through multiple layers of packaging) and will not cause packaging seals to come apart due to heat [601]. However, some materials undergo degradative changes making radiation unsuitable for some medical devices. Often, 25 kGy of gamma is sufficient for adequate sterilisation, however the level of microorganisms should be measured to ascertain the correct dose. Gamma irradiation results in dramatic changes in scaffold properties [583]. However, by testing these changes, this sterilisation technique can result in improvements in physical properties.

3.1.8.2. Ethylene Oxide

Ethylene Oxide gas is commonly used to sterilise temperature-sensitive objects such as plastics, optics and electrics. Ethylene Oxide is a small molecule which provides good penetrating power and alkylation activity, which prevents cell preproduction and thus leads to cell death. The ethylene oxide process involves raising the temperature to a maximum of 22°C with relative humidity levels of 40% [601]. However, ethylene oxide is highly toxic to humans, and therefore the products require a long period of aeration to ensure secondary residues are removed and the product is non-toxic. The scaffold geometry can also trap residues in its porous matrix [586, 588, 602]. For this reason, it is recommended that the specimen be placed in vacuum for at least 48 hrs at 50°C to degas the implant [588]. However, this often causes plastic deformation of the polymer, especially ones with low melting points such as PCL. Therefore, although ethylene oxide causes no polymer chain degradation, it can result in scaffold shrinkage and surface changes. This can reduce the porosity of the scaffold, which is an important design element for encouraging cell and tissue attachment [603].

3.1.8.3 Effect of Sterilisation on the Properties of Polymers

Irradiation is known to cause both immediate and time dependent changes in the mechanical properties of polymers [604]. This is influenced by the dose, material chemical structure and the atmosphere surrounding the polymer [604]. There is considerable experimental evidence that free radicals are formed during the adsorption of high energy radiation, and thus are responsible for changes in the material properties [604].

Some scaffolds are more susceptible to these changes than others. Aliphatic polymers (PGA, PLA, PCL) exhibit a high sensitivity towards radiation. At low doses, free radicals act to cause oxidative degradation (chain scission) in the polymer, resulting in a decrease in molecular weight. At high doses the general trend is for cross-linking to occur [588] (Fig. 3.19). Cottam and coworkers detected an increase in yield stress and degradation rate due to cross-linking induced in 25 kGy gamma-irradiated PCL thin films [585], however failure stress did not show a significant change. Scission and cross-linking were detected in this study by the decrease of molecular weight, but also an increase in the weight average molecular weight [585]. Plikk et al investigated the effect of radiation on a number of different copolymers, and it was demonstrated that, in general, scission and cross-linking increased with increasing doses of radiation [588]. Olah and coworkers demonstrated an increase in modulus and strength of porous PCL scaffolds with as the radiation dose increased from 25 to 150 kGy [586]. This has been one of the few studies investigating porous PCL scaffolds. As each scaffold varies in structure, it is important to test scaffolds for the impact of radiation, if irradiation processes are used for sterilisation.

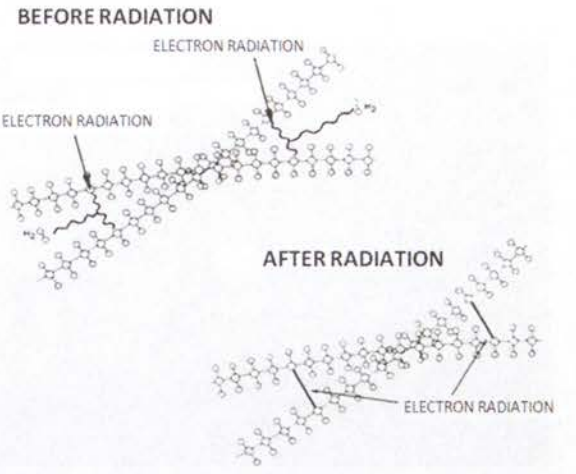


Figure 3.19. Two cross-linking polyethylene molecules before and after radiation sterilisation.

Chain scission processes are known to occur both during and after irradiation. Continual chain scission leads to release of inter-lamella tie chain material which then causes an increase in crystallinity [604]. Degradation due to gamma irradiation of articulating UHMWPE surfaces in total joint implants has posed a huge problem for their shelf life and implantation life [605]. Gamma-irradiated UHMWPE, when stored for 2 yrs at 23°C, has been shown to experience decay as well as changes from alkyl to peroxyl and polyenyl radicals [605]. This effect is due to continual reaction with oxygen, and was not observed when the polyethylene was stored in a vacuum [605]. The fatigue strength of UHMWPE (at 10 million cycles) has been shown to be lowered by gamma radiation, but not by ethylene oxide treatment [606]. Cross linking of UHMWPE due to gamma irradiation has been used to improve its capacity as a shearing and load bearing component on an articular surface [607]. For example, gamma radiation has been shown to be at least 50% more affective at increasing the stiffness than other cross-linking methods such as electron beam radiation and peroxide treatment [607]. However, it has been found that pieces taken from the fracture surfaces of the tensile specimens display a

significant decrease in stiffness, compared to the pieces prior to the test [607]. Gamma-irradiated specimens have also shown a decrease in storage modulus of about 95% [607].

The effect of radiation on the polymer is dependent on the hydrophilicity of the polymer. Goma and coworkers demonstrated that hydrophobic PCL suffered a decrease in molecular weight (12-30%) and tensile strength (12%) after 25 kGy gamma irradiation [608] (Fig. 3.20). Scaffolds which included hydrophilic polymers such as poly(ethylene oxide) (PEO) (mw=600) (70:30 with PCL), demonstrated an even greater decrease in both molecular weight (30-50%) and tensile strength (50%) [608]. The surface roughness was found to be unchanged for the PCL but to increase for the PCL/PEO [608] (Fig. 3.21). This study demonstrates PCL's increased resistance to damage which causes loss of tensile strength, when compared with more hydrophilic polymers. Gamma radiation has also been shown to increase the contact angle of PCL [608]. This increases the wettability of the polymer, and can increase the degradation rate and alter protein adsorption.

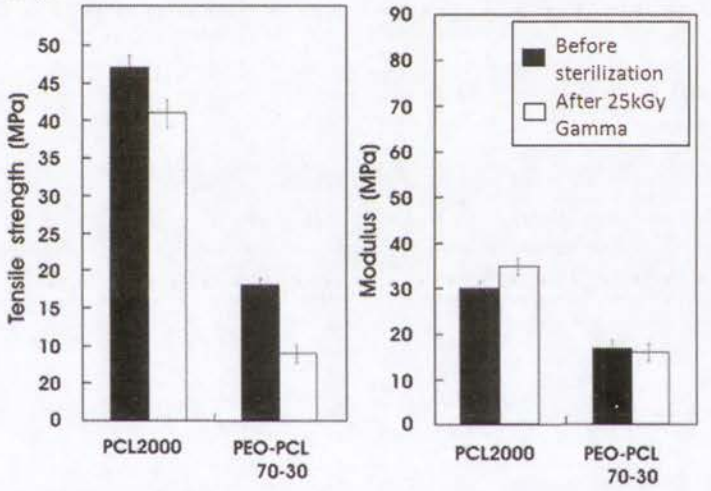


Figure 3.20. Comparison of mechanical properties of PCL and PEO-PCL (70-30) before and after sterilisation with 25 kGy gamma irradiation.

Sterilisation with UV light leads to less changes in the polymers. This is due to the use of lower energy radiation. However, degradative changes and cross-linking have also been demonstrated due to UV radiation [589]. A study by Yixiang and coworkers demonstrated a reduction in the average molecular weight of PLGA and P(LA-CL) nanofibre scaffolds (46% and 35% respectively) [598]. A corresponding reduction in the tensile strength was detected (26% and 28% respectively). This study again indicates the changes induced are dependent on the polymer

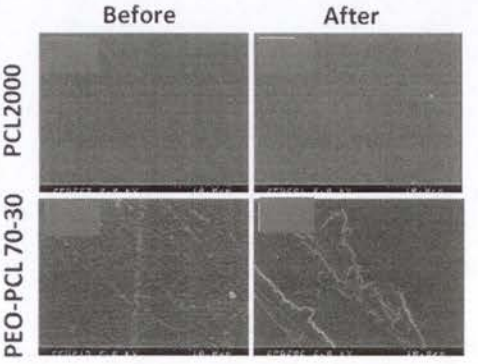


Figure 3.21. Appearance of the polymers via Scanning Electron Microscopy before and after sterilization with 25 kGy gamma irradiation [608].

structure. Burks and coworkers [620] found the following changes in a PCL film during tensile testing, before and after ethylene oxide treatment: Elastic modulus (18.62 kPa vs 68.57 kPa), elongation (854.38% vs 703%), UTS (8.55 MPa vs 6.09 MPa). Fischbach and coworkers determined that there was little effect of 2 hrs of UV radiation on the surface properties of biopolymer films [587]. It is important to ensure that sterilisation procedures don't change the cell adhesion to a surface, due to increasing the amount of unspecific protein adsorption.

3.1.8.4. Effect of Sterilisation on Properties of Glass

Glasses are much more resistant to physical changes than polymers. Zdaniewski and coworkers reported that gamma radiation (under 1 MGy) did not cause a change in the strength of borosilicate glass [609]. Sakurai [610] made the point that defects induced by gamma radiation, up to 1 MGy, have been reported to be generated through the bond breaking of manufacturing dependent point defect sites (precursors). This precursor dependency disappears or weakens in the defects induced by 10 MGy gamma irradiation. Crystalline glass shows much higher radiation resistivity than amorphous silica glasses, perhaps suggesting that strained silicon-oxygen bonds are the breaking sites at high dosages. Bharati and coworkers used the scratch test to demonstrate that gamma sterilisation improves the adhesion of 150 μm-thick silicate based bioactive glass coating onto Ti_6Al_4 V implants [611]. An increase in adhesion strength (critical load) was noted from 21 to 28 N. With increasing load, the glass coating then failed by chipping off the implant surface. Gamma radiation improved the crystallinity of the bioactive glass, resulting in better mechanical properties. It was thought to have penetrated the glass, creating defects, likely to affect the glass-metal interface and increase the adhesion. The authors also mentioned that the addition of nano-sized particles reduces the possibility of through thickness crack propagation, and this is a concept we could utilise in the design of our scaffold coating.

3.1.8.5. Shelf Life and Packaging

Another important requirement of the current design was that the scaffold would have a shelf life of at least two years. Ease and affordability of packaging and transportation were also important considerations. If a scaffold requires hydration before delivery to the surgeon, the design and manufacture of a suitable packaging system involves a much higher cost. A packaging system including a foil lining with an appropriate seal to contain a moist dressing/graft costs up to 10x the amount it costs to develop packaging for a dry medical device [612]. Hydrated systems are often metastable and have a high risk of reacting to air or other contaminants. For these reasons, a dry synthetic scaffold is preferred.

3.1.9. MECHANICAL VERIFICATION

Mechanical testing is routinely performed as an important design verification step for tissue engineering scaffolds [394,615, 616, 621]. Testing is required to ensure the scaffold does not cause stress shielding of the surrounding tissue, and yet provides appropriate support to the developing tissue structures. Tissue ingrowth throughout a porous scaffold will form an interpenetrating network composite, which displays different mechanical behavior from the scaffold or the tissue in isolation.

Tissue attachment to the scaffold will cause the scaffold to act synergistically with the tissue, increasing the stiffness and strength of the structure. Fig. 3.22 shows that the compressive strength and modulus of porous structures (ceramic or polymer) are markedly reduced by several orders of magnitude when compared to their dense counterparts. Porous biodegradable composites have the ability to display a range of properties, generally with a strength <1 MPa and elastic modulus <1 GPa, making them ideal for soft tissues such as skin. The tensile and compressive properties for a range of scaffolds are listed in Tables 3.9 and 3.10. These values are included in Figs. 3.81-3.83 in section 3.83 and compared to the properties of the novel scaffold which is developed in this chapter.

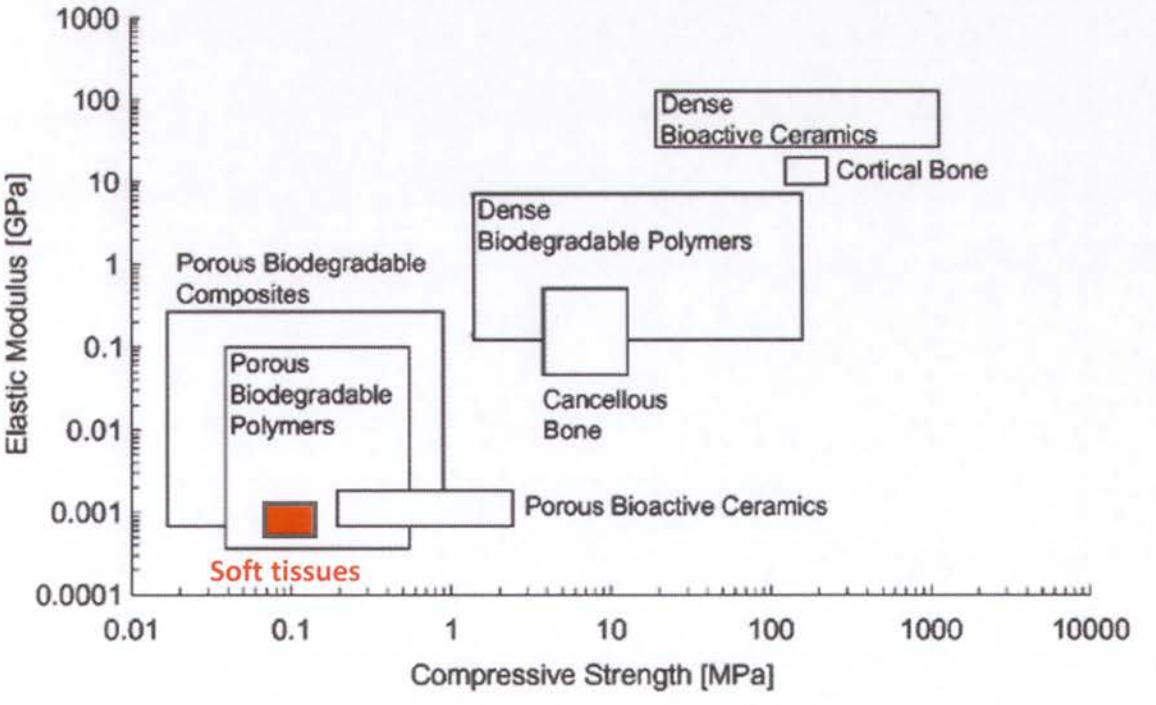


Figure 3.22. Compressive properties for porous and dense polymers and ceramics.

Table 3.9. Review of scaffold tensile properties.

Scaffold Description	Study	Elastic Modulus	Extension Ratio*	Ultimate Tensile Strength	Ref
Elastin blend hydrogel scaffolds	Annabi 2010	8.2-32.7 kPa	141-192%	3-38 kPa	[614]
PLGA (ES)	Li 2002	323.15 MPa	195.8%	22.67 MPa	[615]
P(LLA-CL) (ES)	Xu 2004	156 MPa	127%	5 MPa	[616]
PLCL	Kim 2006	1.22 MPa	500-600%	3.39 MPa	[617]
PCL (RP)	Eshraghi 2010	35.5 MPa	100.1%	1.1 MPa	[618]
PGA fibre/agarose	Moutos 2007	325-400 MPa	122-127%	75-85 MPa	[394]
Collagen-blend (CL)	Powell 2006	15.6-47.5 mN/mm	22.9-61.9%	33.6-74.8 kPa	[619]
PLCL film	Burks 2006	18.62 kPa	854.38%	8.55 MPa	[620]
PLCL film (EtO)	Burks 2006	68.57 kPa	703%	6.09 MPa	[620]
PCL (RP)	Corden 2000	470 MPa	-	-	[583]
PCL (RP, gamma)	Corden 2000	420 MPa	-	-	[583]
PCL (gamma, 90% porosity)	Olah 2007	0.99 kPa	-	-	[586]
PCL (gamma, 70% porosity)	Olah 2007	11.73 MPa	-	-	[586]

***The extension ratio is defined in section 3.8.1.**

Table 3.10. Review of scaffold compressive properties.

Scaffold Description	Study	Compressive Modulus	Ref
Bulk Bioglass®	Wang 2003	30-35 GPa	[161]
PVA hydrogel	Stammen 2001	1-18 MPa	[621]
Elastin hydrogel scaffolds	Annabi 2009	2-18 kPa	[622, 614]
Vicryl sutures (PLGA)	Boccaccini 2003	88 MPa	[187]
Vicryl suture (PLGA) coated with Bioglass®-PDLLA	Boccaccini 2003	83 MPa	[187]
PLLA scaffold	Nam 2000	66-240 kPa	[545]
PLGA foam	Boccaccini 2003	7 MPa	[187]
PLGA foam + 50% Bioglass®	Boccaccini 2003	22 MPa	[187]
PCL/PEO scaffold (NaCl porogens, extrustion)	Reignier 2006	1-5.2 MPa	[549]
PGS scaffolds (porogen leaching, freeze drying)	Gao 2002	5-7 MPa	[327]
PCL scaffold (NaCl porogens, coagulation)	Hou 2003	<2-25 MPa	[540]
PGA woven fibre-reinforced agarose	Moutos 2007	5-100 kPa	[394]
PCL scaffold (MW:80000) (rapid prototyped)	Eshraghi 2010	14.9 MPa	[618]
PLGA freeze-dried foam	Baker 2009	4.6 MPa	[623]
PCL freeze-dried foam	Baker 2009	1.9 MPa	[623]
PLLA nanofibrous/paraffin sphere porogens	Chen 2004	170 MPa	[223]
PCL/BG (NaCl porogens)	Yun 2010	500 kPa	[218]

In this current study, novel bioactive soft tissue scaffolds were designed, synthesized and characterized. Methods for manufacture and post-forming these scaffolds were developed.

3.2. VARIOTIS™ DESIGN, SYNTHESIS AND PHYSICAL CHARACTERISATION

3.2.1. DESIGN CONSIDERATIONS

The variotis™ scaffold was conceptualized to address key user requirements as listed in Table 1.7. These are broadly applicable for any tissue scaffold application. Envisioned improvements beyond a porous bioactive scaffold included controllable interconnective porosity and mechanical modulus, to the extent of replicating or complimenting tissue functional gradients. This embodiment and others were protected in the following patents:

1. E Boughton, A biocompatible pin, a method of treating joint articular cartilage defects in a bone and a method of accessing a joint surface..., Australian Provisional Patent 2009905343, 2009

2. E Boughton, Porous bioabsorbable composite scaffold, bioabsorbable pump, tissue repair system, method of manufacture a porous bioabsorbable composite scaffold..., Australian Provisional Patent, AU/2009/903433, 2009

While the original impetus for the design and development of the variotis™ scaffold was initially for cartilage engineering, the challenge was also to develop a truly versatile scaffold for broad use with soft tissues. An important opportunity for immediate clinical research towards developing a scaffold for chronic wound healing was offered in collaboration with Royal Prince Alfred Hospital, Sydney, Australia. The name "variotis™" stands for 'variable tissue', referring to the versatility of the scaffold to be adapted for a range of tissue architectures and functions.

3.2.1.1. Materials Selection

PCL and bioactive glass were chosen as key scaffold constituents, due to their proven safety, efficacy and widespread regulatory and clinical acceptance. There have been a number of studies focusing on the composites created by combining biodegradable polymers and bioactive glass [133, 214, 150, 194, 414]. Li and coworkers demonstrated that the addition of bioactive glass increased the bioactivity and hydrophilicity of a PCL matrix [194]. Pure bioactive glass scaffolds have been widely explored for bone engineering, however little development has been pursued for their incorporation in elastic matrices to facilitate skin attachment. Variotis™ scaffolds were filled and coated with bioactive glasses in order to tailor the bioactivity, degradation rate and mechanical properties of the scaffolds. Bioactive glass was chosen as the bioactive filler due to its increased bioactivity compared to ceramics such as TCP, and the extensive benefits it provides to the wound environment. For example, Bioactive glass has been shown to increase proliferation of cells and collagen deposition, enhance neovascularisation and demonstrate antibacterial and anti-inflammatory properties. Tissue attachment to both hard and soft tissue has been demonstrated.

3.2.1.2. Novel Batch Coagulation Synthesis Process

The current study overcomes the processing limitations discussed in section 3.1.6.2 through the development of a novel, batch coagulation method. This method was somewhat similar to the precipitation/porogen leaching process, but has distinct differences. These differences include an interpenetrating network sucrose porogen to create a fully interconnected, interpenetrating network scaffold. A PCL/acetone solution was then cast onto the sucrose network porogen. The scaffold was formed in a single batch coagulation step, removing the need for separate precipitation and porogen leaching processes [219].

During the batch coagulation step, as depicted in Fig. 3.23, the dissolution of the porogen in the water and the precipitation (coagulation) of the polymer struts occur concurrently. As the sucrose porogen dissolves, greater vacancies are formed. The scaffold strut precipitates on itself, forming non-solid, low density struts (containing interconnected microporosity). At this stage, the polymer solution is soft due to infiltration of water, enabling gradual formation of thin struts.

The struts which are formed are rod-shaped, rather than blades or plates, which usually form during the precipitation process [148]. In the current study, the concurrent dissolution of the porogen results in porogen aggregates with a lower surface area to volume ratio. This results in better pore interconnectivity of the resulting scaffold. The coagulation method is a low energy diffusion approach, which minimizes the specialised equipment needed. The coagulation step can be undertaken for large batches (>30 units), in less than ½ hr. A further rinsing step was added to ensure complete removal of the sucrose.

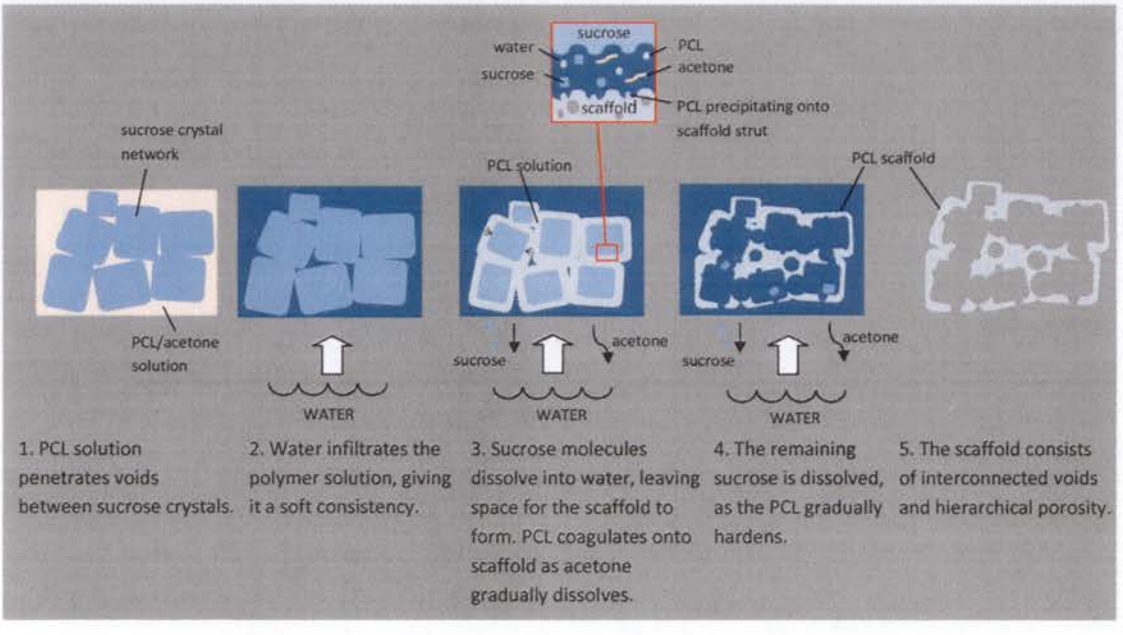


Figure 3.23. The novel batch coagulation process used to synthesise variotis™ scaffolds.

Although this is a novel process, coagulation methods have been used by a few researchers. Nam [545] dispersed ammonium bicarbonate salt particles in a PLLA-solvent gel (methylene chloride) and cast the scaffolds into a mold. When placed in boiling water, a coagulation process took place as ammonia and carbon dioxide gases evolved within the solidifying polymer matrix. This resulted in the expansion of pores within the polymer matrix, leading to well interconnected macroporous scaffolds having mean pore diameters around 300-400μM.

3.2.2. METHODS

The following section gives a detailed description of the PCL scaffold synthesis. Following this are protocols for composite scaffold synthesis via bioactive glass filling and coating procedures. Methods for physical characterisation of the scaffolds are then described.

3.2.2.1. PCL Scaffold Synthesis via Coagulation

3.2.2.1.1. Original Batch Process

Rectangular PCL scaffolds (10.5x16.5x17.8 mm) were formed using a novel Batch Coagulation process, using a sucrose network porogen (Fig. 3.24, 3.25). 10.17 g Poly-e-caprolactone granules (–[(CH2)5COO]n–, molecular weight: 80,000, density=1.15, Sigma–Aldrich, Australia) were placed in a 500 mL borosilicate vessel and melted using a heat gun set at >65°C. In a fume cabinet, 50 g acetone (ACS reagent, Sigma-Aldrich) was added to the vessel. A magnetic stirrer was preheated by setting the dial to 5-6 for 2 mins, and then turned off for later use. The PCL solution was heated using a microwave for 20-30 seconds and then stirred with a metallic stirring implement. This step was repeated until the PCL began dissolving. Care was taken not to overheat the mixture as it would boil over. A magnetic rod was added to the solution and the vessel was covered with cling wrap. The PCL solution was placed on the preheated magnetic stirrer. Stirring was commenced at low speed then increased to high. The solution was stirred for 10 mins until the PCL was dissolved and appeared distributed evenly throughout the acetone. Often, the solution was stirred overnight to ensure even distribution of the polymer chains.



Figure 3.24. (a) PCL pellets (b) PCL/acetone solution (c) variotis™ scaffold.

The porogens- sucrose cubes (CSR, Australia, granule size <800 μm) -were submerged in the PCL mixture. Approximately 10-15 scaffolds could be synthesised in one batch. The sucrose cube mixture was heated using a microwave for 10 sec x 2. The vessel was covered with 2 layers of plastic cling wrap and placed in the fume cabinet for 15 mins for infusion to occur. The solution was gently swirled intermittently. The scaffolds were individually held under running water for 3 sec. The outer PCL membrane was gently removed by hand in a single piece, as the scaffold was rotated. The scaffolds were placed in a plastic sieve under cold, moving water for 5-10 mins. This was achieved via either running water or intermittently submerging the sieve in a large vessel of water. Care was taken not to allow scaffolds to contact each other.

The scaffolds were placed in a tray of cold water. The water was refreshed regularly to prevent acetone accumulation in the water. Scaffolds were air-dried on a paper towel overnight then stored in a plastic container or bag. The remaining mixture could be re-used for a subsequent batch of scaffolds, by readjusting the PCL/acetone ratio. Subsequent batches were begun after step 8 of the previous batch.

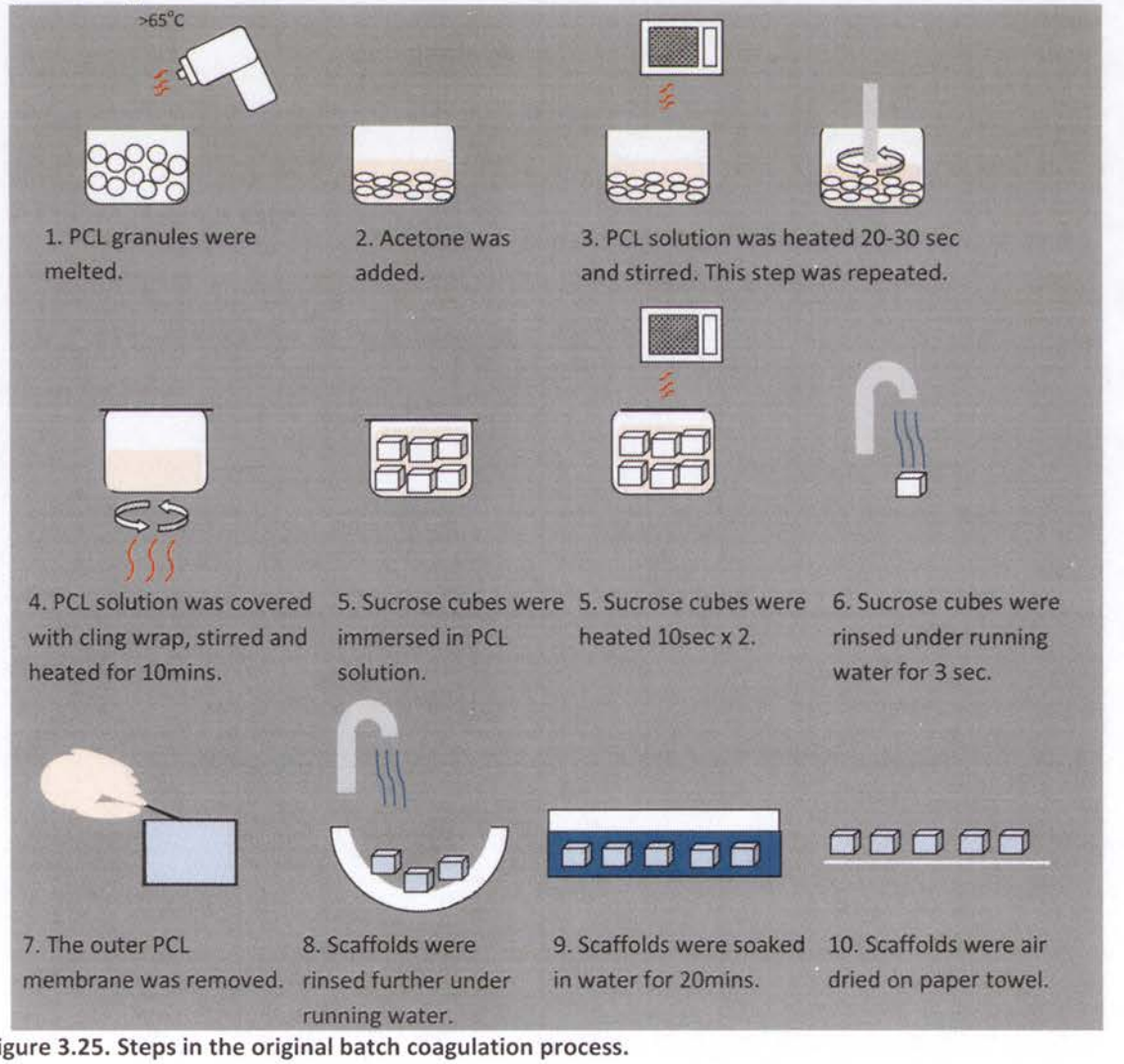


Figure 3.25. Steps in the original batch coagulation process.

3.2.2.1.2. Upscaled Batch Process

Once the small processing system was established we upscaled production. Details of the upscaled process are discussed below and shown schematically in Fig. 3.26.

In a fume cabinet, Poly-e-caprolactone granules (–[(CH2)5COO]n–, molecular weight: 80,000, density=1.15 g/cm^3, CAPA 6800, Solvay Capro-lactones, UK) were placed in an air-tight 1.5 L glass vessel with acetone (ACS reagent, Sigma-Aldrich) to a concentration of ~17% w/w. The glass vessel used had either a rubber or silicone seal around the class lid. A magnetic stirrer was added to the solution and the solution was stirred over low heat for at least 24 hrs, until the PCL was dissolved. Sucrose cubes (approx 30) (CSR, Australia) were immersed in the PCL solution for 24 hrs.

The cubes were placed on a custom-made aluminium alloy frame to enable stirring using a magnetic rod to continue under the sucrose cubes. The PCL-embedded sucrose cubes were immersed in a glass beaker with water for 5 sec. The outer PCL membrane was gently removed using a custom-designed roller. The scaffolds were placed in individual compartments in a polyethylene tray. The water was refreshed regularly to prevent acetone accumulation in the water. Scaffolds were air-dried in a custom-made box with circulating air.

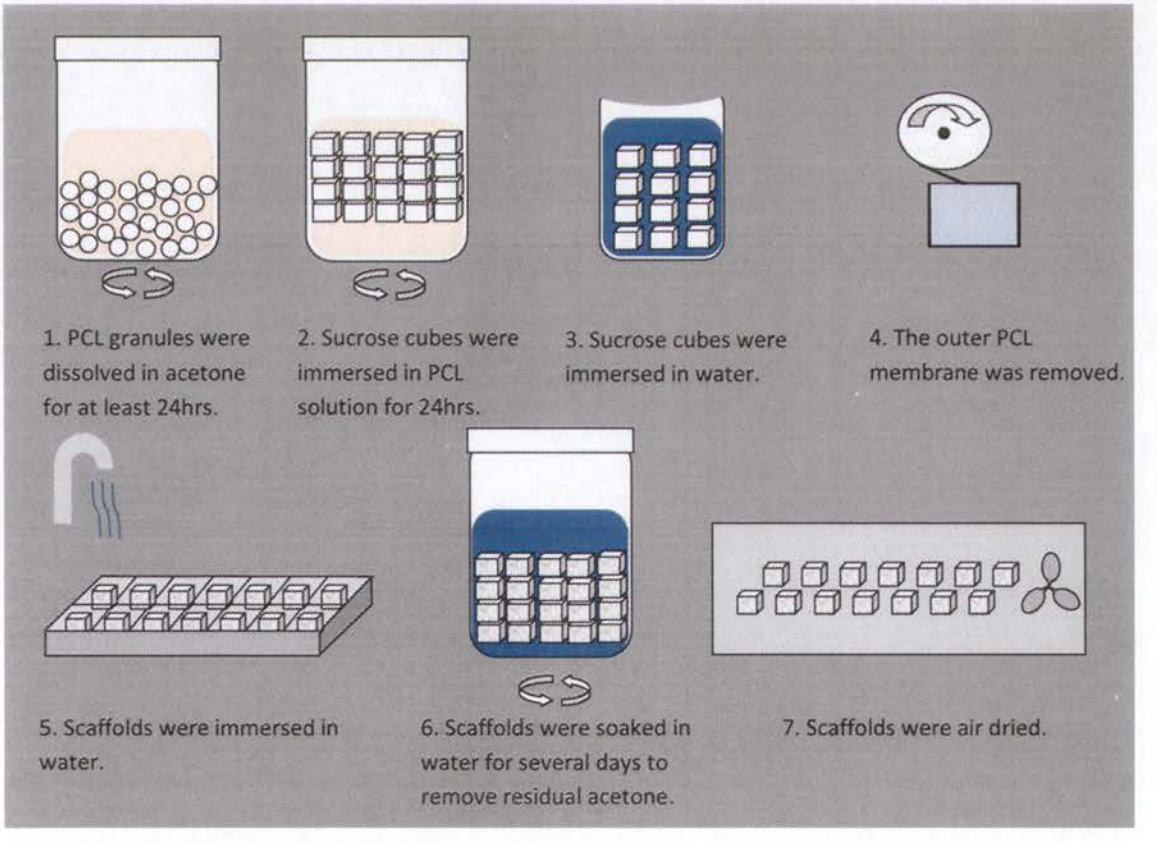


Figure 3.26. Steps in the upscaled batch coagulation process.

3.2.2.2. Synthesis of Composite Scaffolds via Glass Filling

For the composite scaffolds, 13-93 fibers (Mo-Sci Health Care, Rolla, MO) were ground into short fibers using a mortar and pestle. PCL scaffolds were synthesised using the protocol described previously. 13-93 fibers were added to the dissolved PCL/acetone solution. The solution was stirred for an additional 2 hours to ensure even distribution of the fibers. These scaffolds were tested mechanically in section 3.7.3.2.B.



Figure 3.27. 13-93 bioactive glass

3.2.2.3. Synthesis of Composite Scaffolds via Glass Coating

Several methods for glass coating were trialed. Method 3 was chosen for synthesis of the scaffolds which were used in the *in vitro* and *in vivo* studies, due to its ability to rapidly coat a large number of scaffolds, whilst contained in packaging pouches. Scaffolds which had been coated were weighed and contained ~20 wt% glass. These scaffolds were tested mechanically in section 3.7.3.2.B.

3.2.2.3.1. Manual Shaking

5 g 13-93 glass fibers (Fig 3.27) were ground into short fibers using a mortar and pestle and placed into a 100 mL plastic specimen jar with 3 scaffolds. The specimen jars were shaken by hand for 1 min. The scaffolds were heated in an oven at 55°C for 15 mins to gently melt the PCL and allow attachment of the glass to the scaffolds.

3.2.2.3.2. Rotisserie Oven- Jar

5 g glass was placed in a 100 mL plastic specimen jar with 8 scaffolds. The jars were agitated by hand for 1min to ensure even coating on all surfaces. The jars were placed in an oven for 10 mins at 48, 52 and 56°C. A method was trialed for rotating the scaffolds within the specimen jars, while heating was taking place. The jars were removed from the oven and the excess, unattached glass was removed by shaking the scaffolds. This technique was trialed with powdered 45S5, milled e-glass and borosilicate spheres.

3.2.2.3.3. Rotisserie Oven- Pouch

5 g glass was placed in a sterilisable paper pouch with 18 scaffolds. The pouches had excess length of 5 cm. Pouches were agitated by hand for 1 min to ensure even coating on all surfaces. Pouches were placed in an oven for 10 mins at 52°C. Pouches were removed from the oven and the excess glass was removed firstly by flicking the pouch by hand, and secondly by exposure to vibration of a range of frequencies for at least 10 mins. The excess glass was collected in one end of the pouch, which was removed via heat sealing and cutting. These scaffolds were tested mechanically in section 3.7.3.2.C.

3.2.2.4. Consistency of Scaffold Batches

The consistency in the polymer uptake between scaffolds and batches were ascertained by measuring scaffold weights. 6 PCL scaffolds from 3 different batches were compared. In addition, weights were recorded for scaffolds with 5, 10 and 15% w/w 13-93 glass fiber incorporated into the PCL/acetone mixture during scaffold synthesis (ref 3.2.2.2.). Results are expressed as mean±stdev.

Scaffolds were also weighed before and after coating with 45S5 glass powder, using method C. The % glass coating was determined. The volume occupied by the PCL and glass were calculated using the following equation.

$$\text{Polymer volume} = \frac{\text{Mass of polymer (g)}}{\text{Density of scaffold component/s } (\frac{\text{g}}{\text{cm3}})}$$

The density of scaffold component/s was taken as either ρ_{PCL} (PCL scaffolds) or ρ_{PCL}+ ρ_{glass} (glass coated PCL scaffolds).

Where ρ_{PCL}=1.15 g/cm^3, ρ_{glass}=2.7 g/cm^3.

3.2.2.5. Manual Calculation of Porosity

The porosity of the scaffolds was determined manually using the following equation [327]:

$$\text{Volume \% porosiy} = \frac{\text{Scaffold volume (mm3)} - \text{Polymer volume (mm3)}}{\text{Scaffold volume (mm3)}}$$

Where scaffold volume=10.5x16.5x17.8 mm.

Measurements were taken for PCL scaffolds (ref 3.2.2.1.A) as well as scaffolds with 5, 10 or 15 wt% bioactive glass fibers incorporated within the matrix (ref 3.2.2.2.A). Results were each expressed as average ± standard deviation (n=6 scaffolds).

3.2.2.6. Scaffold Morphology and Pore size using Optical Microscopy and SEM

Representative scaffolds were visualised using a stereoscopic optical microscope or a Leitz DMRXE optical microscope and images taken with a Leica DFC420 digital camera system. For SEM, cross-sectioned scaffolds were mounted on aluminium stubs using PVA/Superglue and conductive silver dag. The pore morphology, pore size and microstructure of the scaffolds were viewed using SEM (Philips XL30) with a current of 15mA.

3.2.2.7. 3D Scaffold Reconstruction using MicroCT

The inner structure and interconnectivity of the variotis™ scaffold were non-destructively visualised and characterized using micro-computerized tomography (microCT) (Skyscan 1072, SkyScan, The Netherlands) (Fig.3.28a). Operating instructions were obtained from the instruction manual [763]. Variotis™ scaffolds (10.5 x 8.5 x 17.8 mm) were prepared and mounted on a polymer stub (length: ~1 cm) using adhesive wax. A wide straw (length: ~1 cm, McDonald's) was placed over the scaffold, with an overlapping region around the polymer stub of ~3 mm (Fig. 3.28b). MicroCT projection images (16 bit TIFF) were collected as the specimen rotated over 360 °, with a rotation step of 0.23°. Data was collected for 3 pixel sizes: 2.0 µm, 3.4 µm and 6.8 µm. Images were reconstructed using NRecon2.0 to BMP slices of the 3D model.

3D volume rendering was accomplished using VGStudioMax1.2 (Volume Graphics), to produce RAW volume files. Parameters which could be varied include: region of interest, skip rate and grey scale. These parameters were varied to provide images which gave the most information about the actual structure of the scaffolds. The grey scale level was chosen that would best capture the fine scaffold fibers, whilst minimising noise.

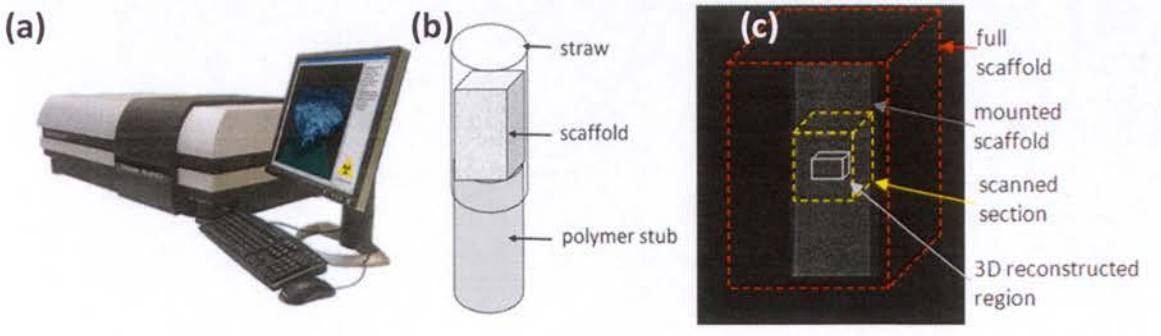


Figure 3.28. (a) Skyscan 1172 MicroCT, (b) Specimen holder, (c) Reconstructed region (white cube)

Videos were constructed using VGStudioMax1.2. Videos were taken by rotating the scaffold, and slicing through various planes. Fig. 3.28c indicates the regions of the original scaffold that were mounted, scanned and reconstructed.

3.2.2.8. Calculation of Pore Size, Porosity and Interconnectivity using MicroCT

MicroCT data was also used to quantify parameters associated with the macroporous scaffold structure (PCL variotis™ scaffold, batch 53r). Calculation methods were explored using Skyscan™ CT-analyzer and ImageJ. Detailed protocols can be obtained from the CTAn documentation [763]. CTAn was used to calculate porosity, using the algorithm "100-percent object volume". The porosity was measured using a range of settings, including scan resolution (2.0, 3.4, 6.8μM), voxel number (30-200^3), skip rate (0-15) and grey scale (10-31). These models consequently contained different numbers of elements when they were converted to an ABAQUAS Finite Analysis Model for analysis of tissue modelling and fluid flow (future study by Lucy Xiao).

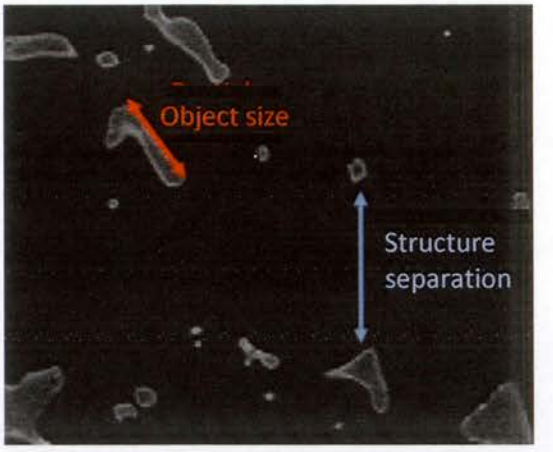


Figure 3.29. A cross-sectional image of the scaffold, using MicroCT.

Digital methods (CTAn) were also explored for their potential to calculate a range of morphological parameters, including surface area, porosity, pore size and strut thickness. These parameters were calculated in both 3D and 2D. 3D measurements were determined in a single calculation using CTAn. 2D measurements were calculated over 849 individual 2D cross-sectional slices and presented as average ± stdev and range. Shown in Fig. 3.29, an approximate indication of pore size was obtained by measurement of 'structure separation'. An idea of strut diameter was gathered by calculation of the 'object size'. A histogram was constructed which showed the distribution of these pore spacings over an entire 2D slice. In addition, a histogram was graphed showing the strut diameters, for a region selected from 2 adjacent 2D slices (slice numbers: 667, 668).

An indication of the nature of the scaffold interconnectivity was obtained by calculation of the detour index from MicroCT cross-sections. The method described by Otsuki was followed [322] (ref 1.6.3). The detour index was defined as the distance from a pore to the outer edge of the scaffold, divided by the shortest distance to the outside. This index was measured for 7 pores, chosen at random, and presented as the average±stdev. The detour index was measured for a range of scaffolds: (A) variotis™ scaffold; (B) Otsuki [322], a70% porous titanium scaffold made using polyhedral-shaped ammonium hydrogen carbonate porogens; (C) Moore [323], a 85% porous poly(propylene fumarate) scaffold made using a salt porogen; and (D) Wu [117], an 80% porous sintered diopside scaffold made using a polyurethane sponge template.

Large quantities of high quality scaffolds were synthesised using these methods. Using the original batch coagulation process, about 12 scaffolds were synthesised per batch. Using the upscaled process, at least 30 scaffolds could be synthesised in a single batch. Multiple batches could be run concurrently, dependent on the availability of several magnetic stirrers and glass vessels. Figure 3.30 shows the macroscopic appearance and dimensions of the PCL scaffolds.

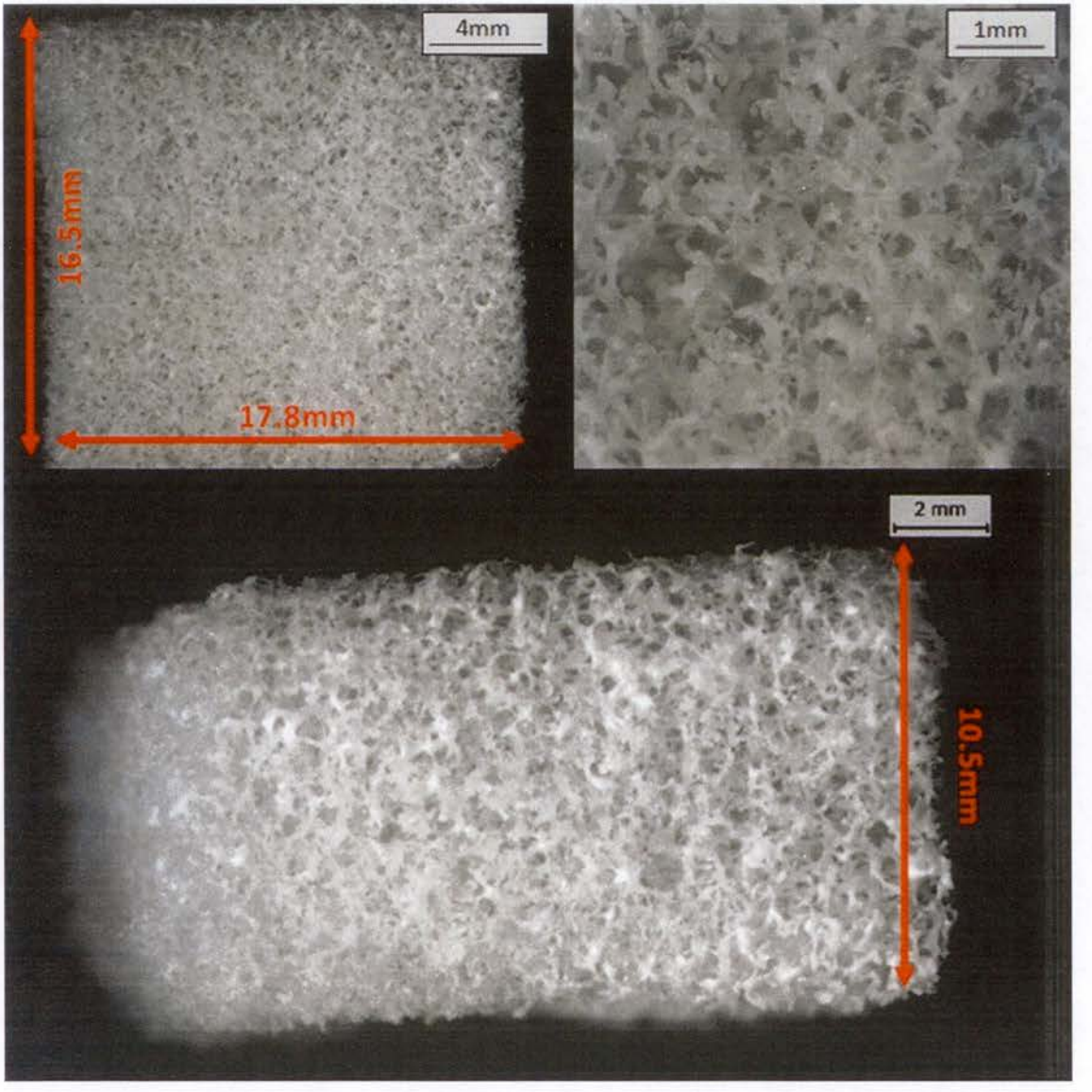


Figure 3.30. Steroscopic micrographs of a PCL scaffold.

Glass was successfully included into the scaffold by filling and coating approaches. Generally, glass inclusion did not change the macroscopic appearance of the scaffold. The scaffolds coated with 13-93 fibers often experienced more compression due to melting than did the other scaffolds (Fig. 3.31).



Figure 3.31. Bioglass coated scaffolds

3.2.3.1.Analysis of Scaffold Batch Consistency

Shown in Fig 3.32a are the weights of scaffolds synthesized using the original batch process. Each of these scaffolds was synthesized using sucrose templates which were the same dimensions. The trends across three consecutive batches are plotted. Within a single batch of PCL scaffolds, the standard deviation was <0.06 g, indicating 24% variation within a batch. Fig. 3.32b shows the measurements for the 13-93 bioactive glass fiber-filled scaffolds (ref 3.2.2.2A). The average weights were almost half that of the PCL scaffolds. There was a low standard deviation for the glass-filled scaffolds (0.2 g), indicating variation of 16% within one batch.

Table 3.12 lists the weights of PCL scaffolds using the upscaled process, before and after coating with 45S5 powder. The variation within one batch was only 4.17%. The glass coating was 9.92±2.06% w/w of the original scaffold, with 20.6% variation between scaffolds. The volume of the constituents was calculated to be 0.110 cm^3 for PCL and 0.005 cm^3. The proportion of glass was 4.36% v/v.

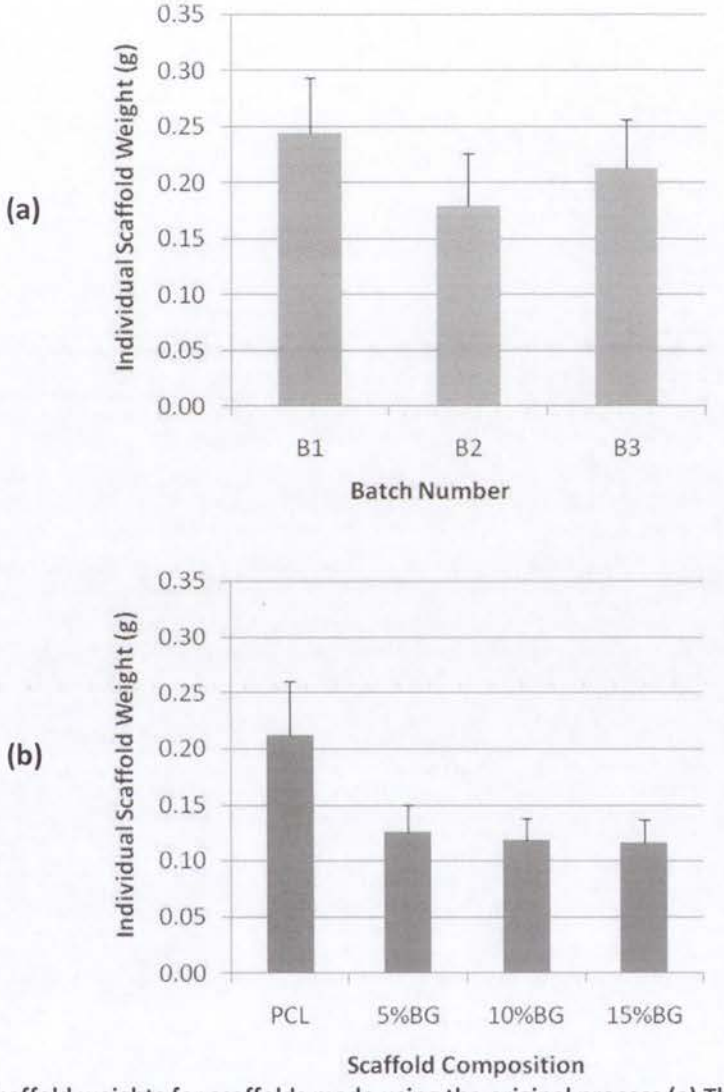


Figure 3.32. Scaffold weights for scaffolds made using the original process (a) Three PCL batches (b) PCL and 13-93-fiber filled scaffolds.

Table 3.11. Weight of scaffolds before and after coating with glass powder. Measurements in grams.

Scaffold	Scaffold Initial Weight	Scaffold Final Weight	Glass Weight	% Glass
1	0.135	0.145	0.009	6.950
2	0.133	0.149	0.017	12.594
3	0.123	0.134	0.011	8.943
4	0.121	0.135	0.014	11.663
5	0.125	0.138	0.013	10.400
6	0.128	0.140	0.012	8.984
AVERAGE	0.127	0.140	0.013	9.922
STDEV	0.006	0.006	0.003	2.053

3.2.3.2. Scaffold Porosity (Manual Calculation)

For the scaffold batch investigated in the previous section, the porosity of the PCL scaffold was 95.64%. For another batch, as shown in Table 3.12, the porosity of the PCL scaffolds was 94.5%, as compared to 97% for glass fiber-filled specimens.

Table 3.12. Manual porosity calculations for the variotis™ scaffolds.

	PCL	5%BG	10%BG	15%BG
Polymer volume (mm^3)	168.62±33.84	87.47±5.69	92.17±4.45	90.95±1.83
Porosity (%)	94.53±1.10	97.16±0.18	97.01±0.15	97.04±0.06

3.2.3.3. Scaffold Morphology and Pore Size using Optical Microscopy and SEM

A cross-sectional SEM of the variotis™ scaffold is seen in Fig. 3.33. The scaffolds were found to contain hierarchical, anisotropic porosity, consisting of large, interconnected macropores (300-500 μm) and micropores (2-40 μm). Surfaces were highly textured and contained micropores which appeared interconnected. Scaffold pores were of a similar size throughout the scaffold.

Figure 3.34a shows the surface of the 45S5 particle-coated scaffolds. About 70% of the surface area was estimated to be covered by the glass. The pore size and porosity were reduced about 8.7μm by the glass coating. So for example, a 300 μm pore could have been reduced to 291μm. The glass coated scaffolds still contained micropores (Fig. 3.34b). The surface texture on the PCL and glass coated scaffolds are shown in Fig. 3.35.

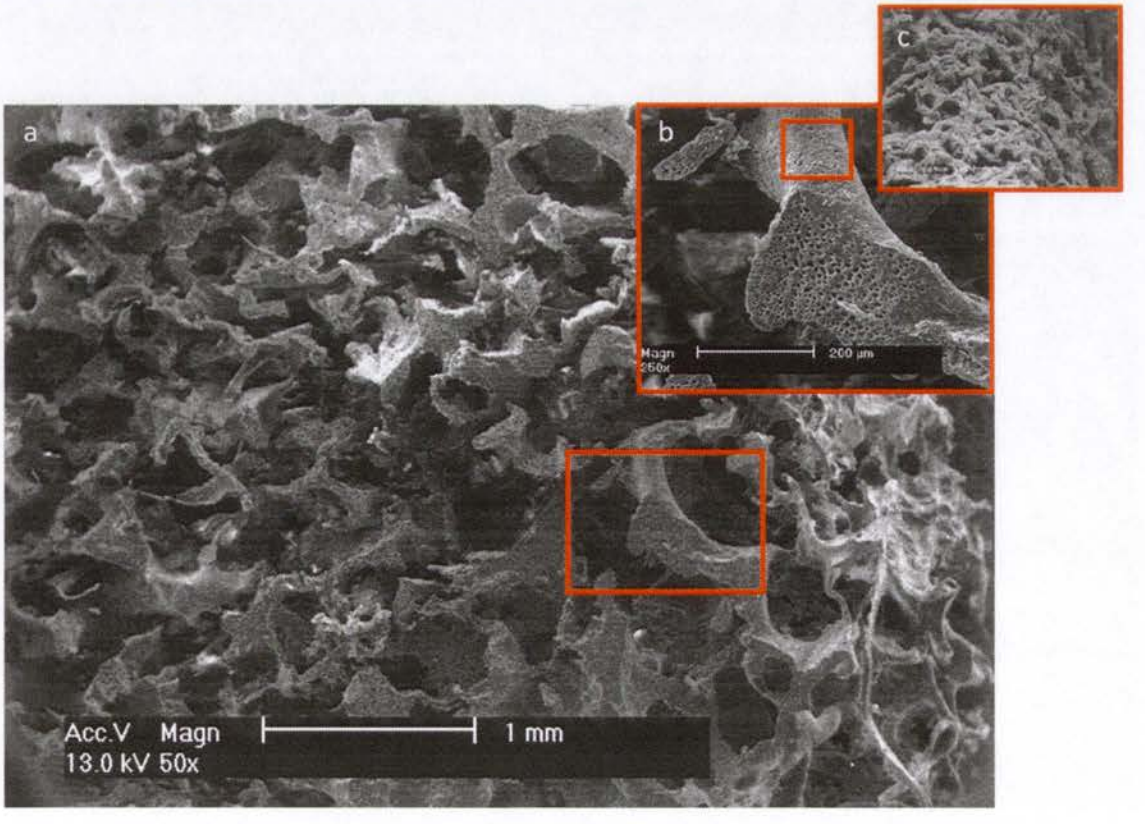


Figure 3.33. SEMs of (a) Macropores, (b) micropores and (c) surface texture on the PCL scaffolds.

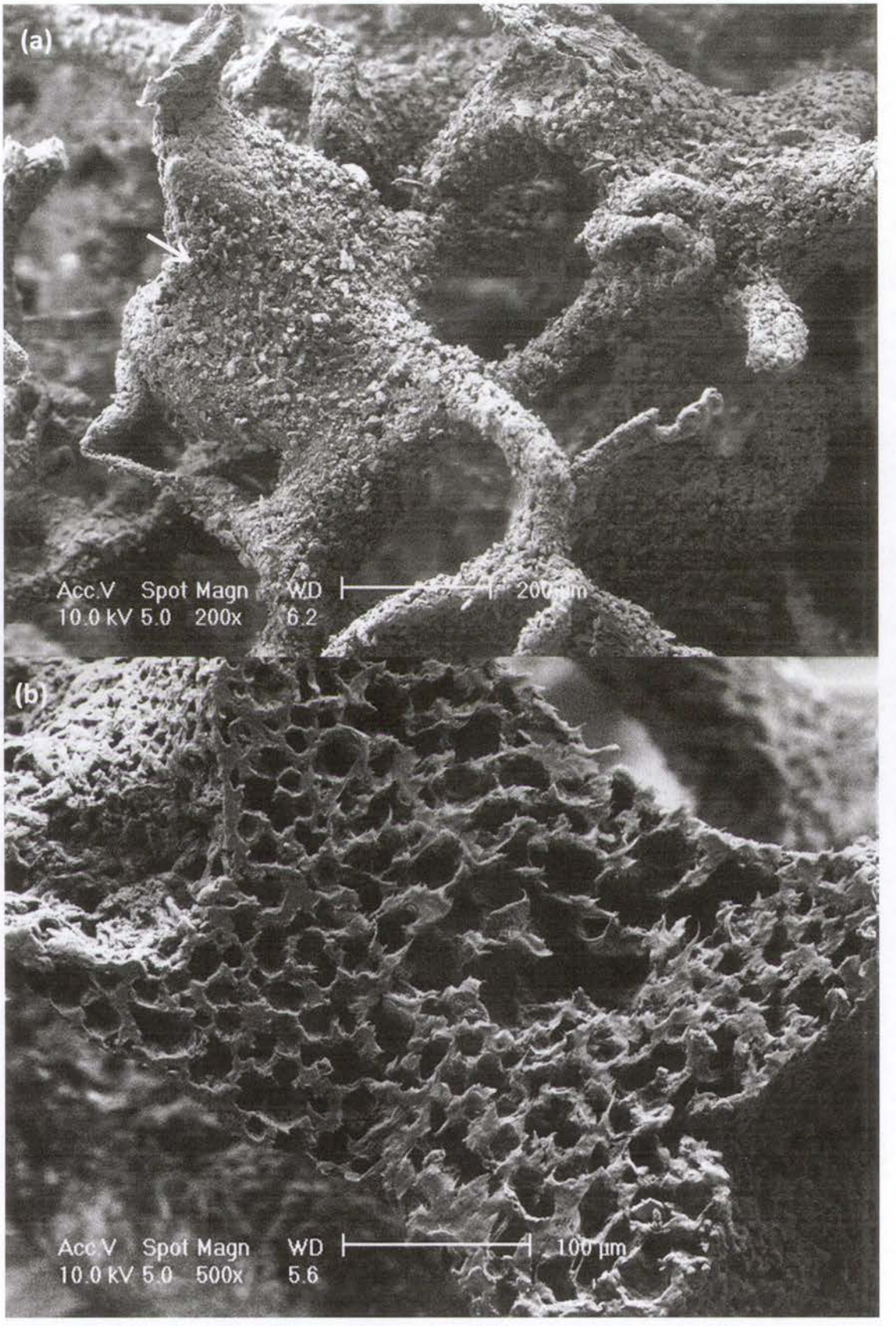


Figure 3.34. SEMs of (a) 45S5 glass particle-coated scaffold (arrows: glass coating) (b) Cross-section of a 45S5 coated scaffold, showing the interconnected micropores through the struts.

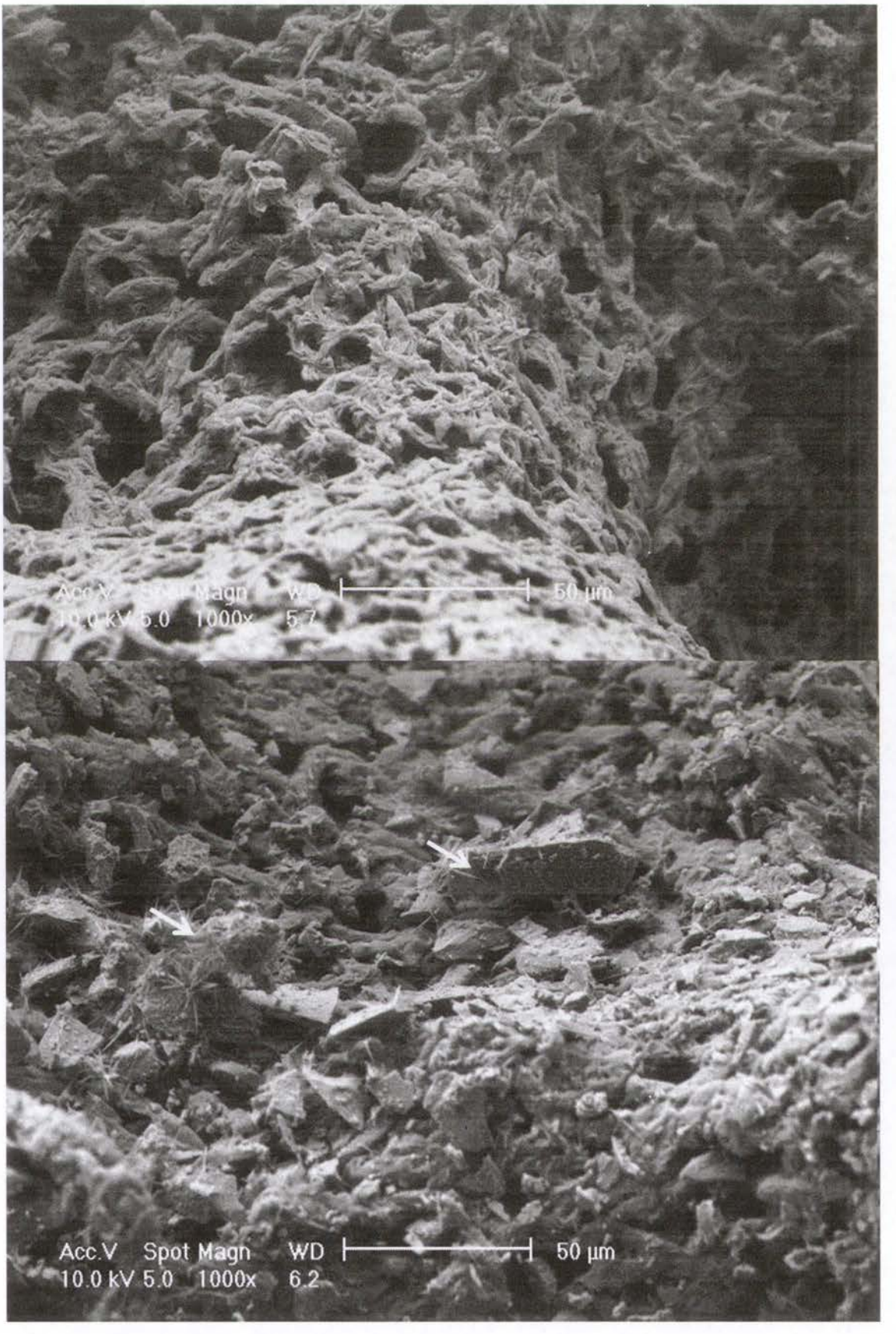


Figure 3.35. High magnification SEMs of (a) PCL scaffold (b) 45S5 glass particle-coated scaffolds. (arrows: glass coating).

Figure 3.36 shows the ~20 wt% 13-93 short fibre coating which was formed on the PCL variotis™ scaffolds. The fibers were firmly attached to the scaffold surface and occupied a high proportion of the surface area. Coating of the scaffolds with milled E-glass powder showed excellent coverage along the struts (Fig. 3.36, 3.37).

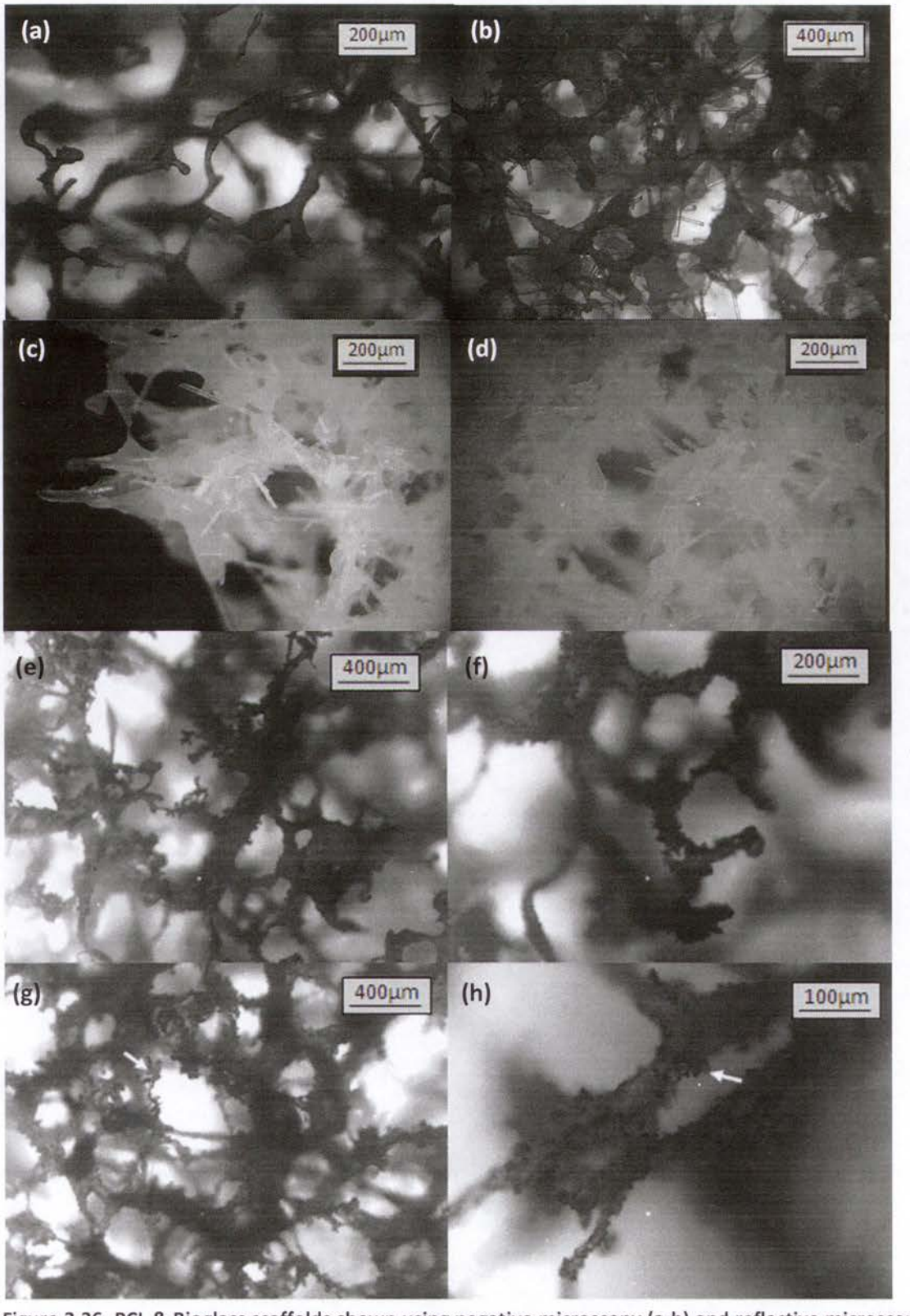


Figure 3.36. PCL & Bioglass scaffolds shown using negative microscopy (a-b) and reflective microscopy (c-h). (a) PCL, (b-d) PCL+20% 13-93-incorporated scaffold, (e-h) Glass powder coated scaffolds. The arrows indicate glass particles on the scaffold surface.

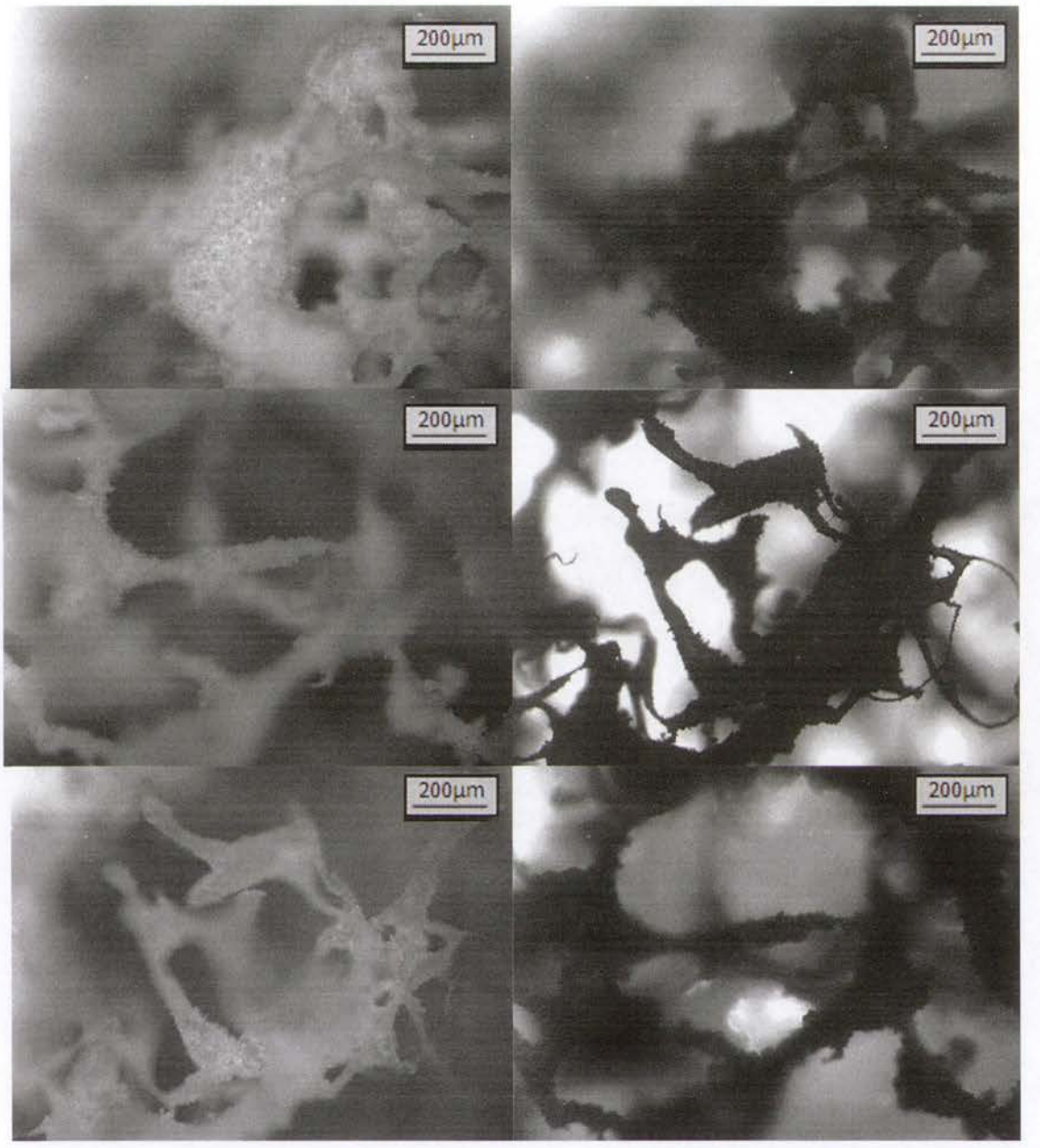


Figure 3.37. PCL scaffolds coated using milled E-glass powder.

Shown in Fig. 3.38, hollow borosilicate glass spheres also showed excellent distribution on, and bonding to, the scaffold. Approximately 85% coverage was obtained. The spheres vastly increased the surface area of the scaffold. Although not biodegradable, borosilicate is hydrophilic so may aid cell attachment, although this hypothesis was not tested. Hollow spheres could be useful in inducing buoyancy in culture systems, providing a passive actuation force to promote 3D culture, whether used alone or attached to a scaffold. Future work could include synthesis of hollow 45S5 spheres which could be useful for drug delivery.

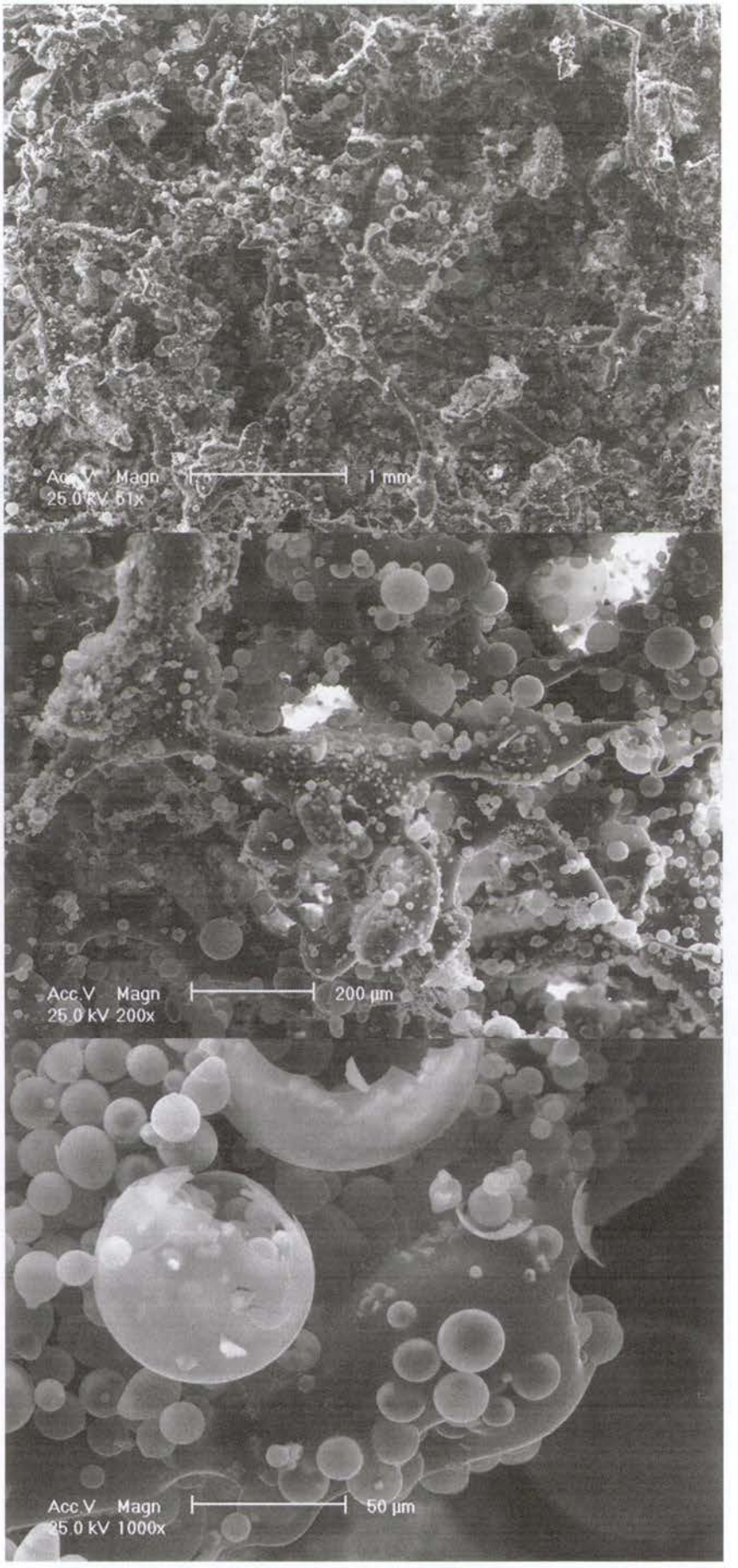


Figure 3.38. PCL scaffolds coated with hollow borosilicate glass microparticles.

3.2.3.4. Examination of Scaffold Morphology using MicroCT

Figures 3.39 and 3.40 show the 3D reconstruction of a PCL variotis™ scaffold using MicroCT. In these images, the scaffold is visible in white/grey, with black void pore space. Videos were created of the scaffold rotating and of the cross-sectional planes cutting away at various angles. Still frames from these videos are shown in Fig. 3.40a. The cross-section shown in Fig. 3.40c demonstrates the highly porous nature of the scaffold. An open an interconnected porosity was visible in all regions throughout the scaffold. Fig. 3.40 shows reconstructions of scaffold portions achieved using various grey scale levels. Optimal grey scale values were chosen to provide the maximum level of detail of the scaffold structure.

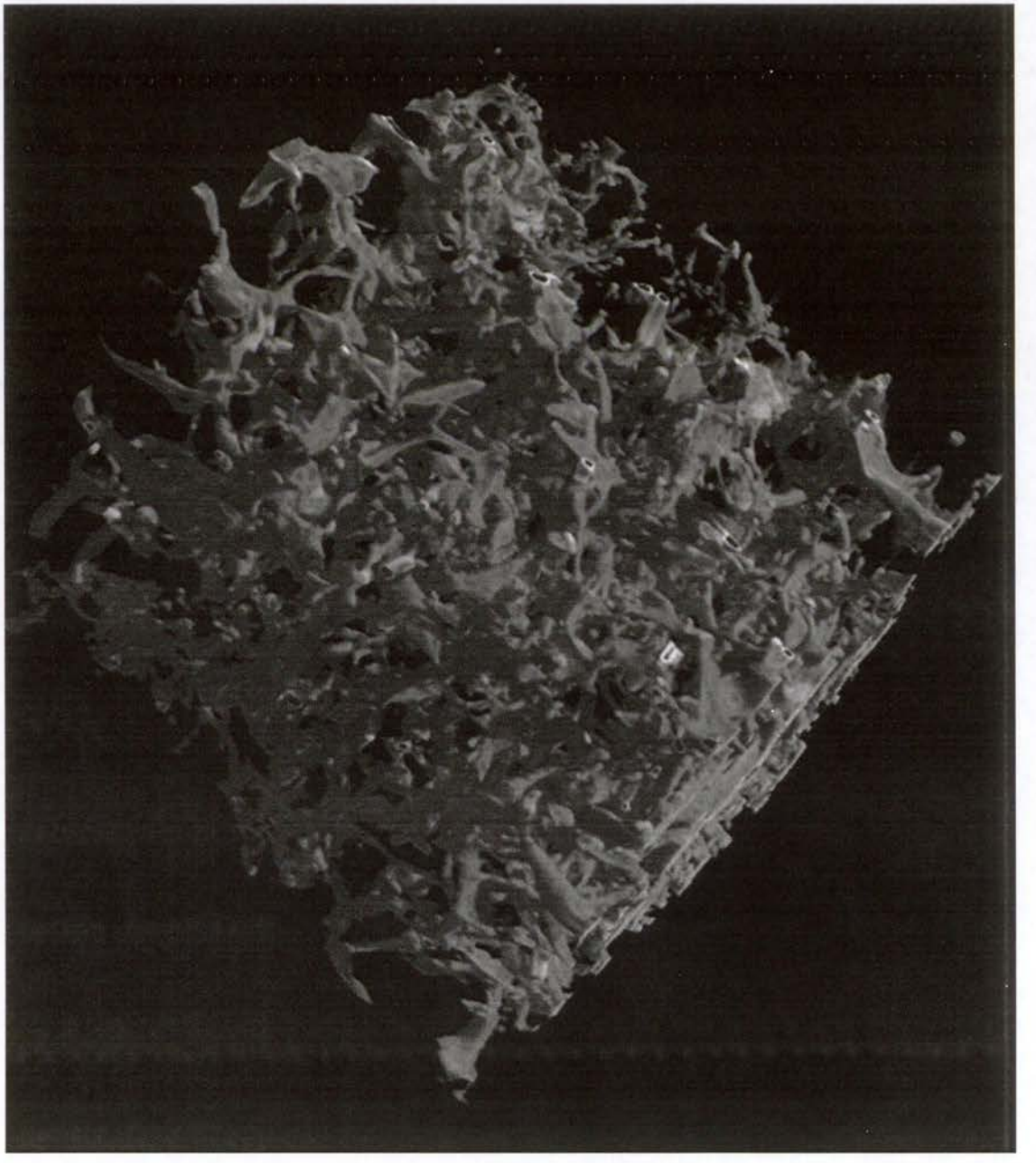


Figure 3.39. 3D MicroCT reconstruction of the variotis™ scaffold.

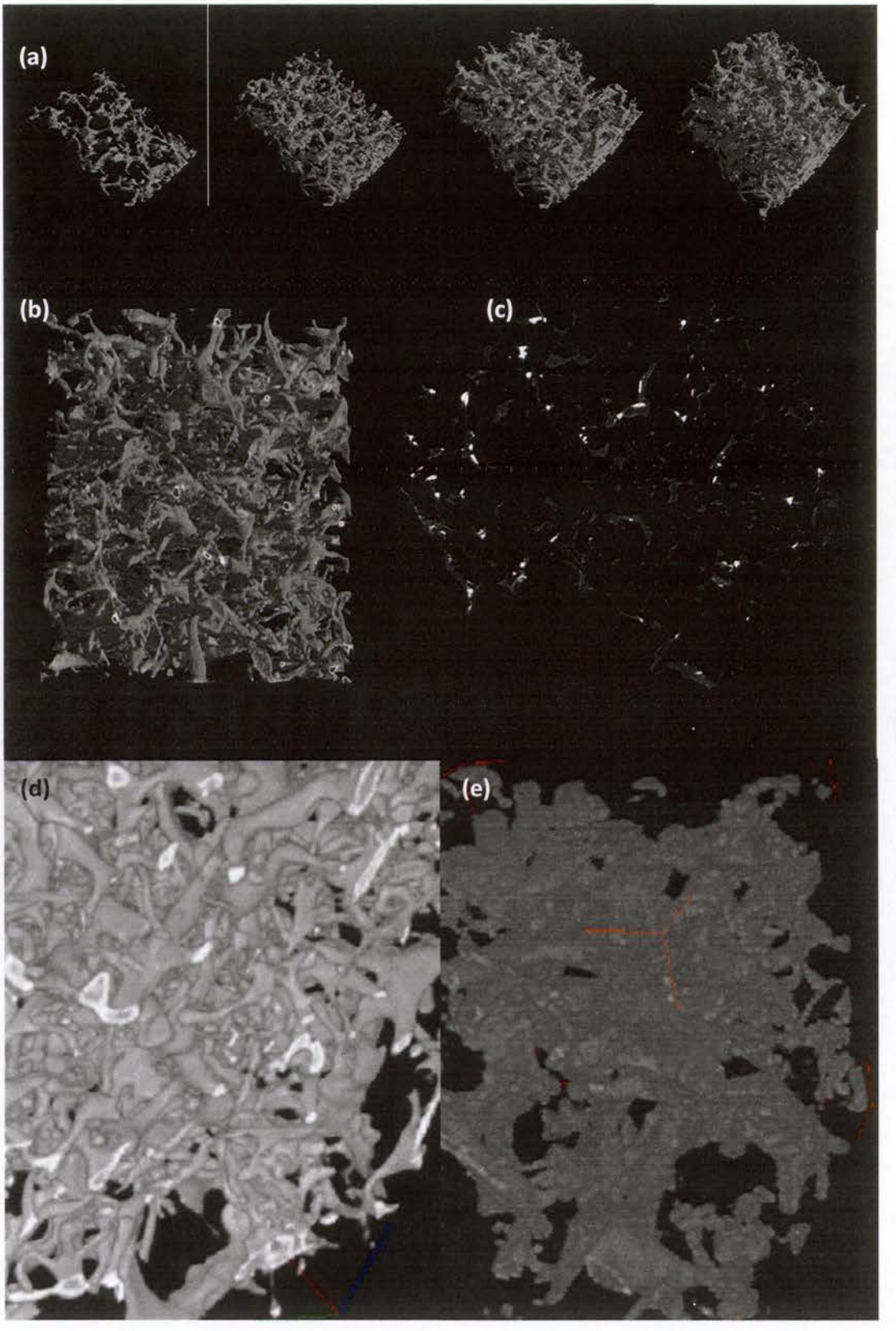


Figure 3.40. MicroCT images of a PCL scaffold: (a) Frame captures from video (b) Front view (c) Cross-sectional view (d, e) Scaffold reconstructed with different grey thresholds.

3.2.3.5. Porosity, Pore size and Interconnectivity Calculations using MicroCT

Shown in Table 3.12, porosity measurements varied slightly for scaffolds scanned using different resolutions and grey scale reconstruction thresholds. The porosity ranged from 81.01%-99.95% for these models. The average porosity was calculated to be 94.3±1.74%. Models were excluded which showed a porosity outside of 90-98%, as they were thought to not approximate the actual structure of the scaffold.

The porosity was highly dependent on the grey scale selected- the higher the grey scale, the more elements were rejected as background noise, resulting in a higher porosity value. The models with the most representative structure and porosity were chosen to be number 7, 8, 9, 13 and 14 from Table 3.13. These models had a resolution of 3.4 or 2.0 μm. The dimensions of model 7 were calculated. The side length was determined to be: 480 voxels (no. of voxels) x 3.4 μm (voxel size)=1.63 mm.

Table 3.13. Parameters for the 3D models.

Index	Resolution (pixel size)	Voxel Number	ROI (x=y=z)	Skip Rate	Grey Scale	Elements	Porosity
1	6.8um	30	240	7	22	345	98.72%
2	6.8um	50	400	7	22	700	99.44%
3	6.8um	50	500	9	22	310	99.75%
4	6.8um	100	400	3	22	83	99.99%
5	6.8um	100	500	4	22	77,711	92.23%
6	3.4um	30	480	15	16	5,128	81.01%
7	3.4um	60	480	7	16	14,959	93.07%
8	3.4um	100	900	8	28	43,030	95.03%
9	3.4um	201	201	0	34	566,380	93.03%
10	3.4um	100	900	8	10	1,527	99.85%
11	2.0um	50	800	15	21	4,450	96.44%
12	2.0um	50	800	15	28	3,500	97.20%
13	2.0um	100	800	7	31	62,761	93.72%
14	2.0um	100	900	8	31	68,840	93.12%
15	2.0um	100	900	8	10	129,928	87.01%

Table 3.14 shows calculation of morphological parameters for the scaffold. Calculations are presented in 3D, and in 2D (average of 849 slices). From this table, average porosities of 94.03 and 93.91% were calculated. Using the 2D slices, the average structure separation was measured to be 293±21.20 μm. This refers to the distance between 2D strut segments and can give some indication of pore size.

Figure 4.41 and 4.42 show histograms for the pore spacing and strut diameters of 2D cross-sectional slices. From these graphs it is clear that >30% of pore spacing measurements were between 280 and 300 μm. A large number of the strut segments were measured to have a diameter between 55.1 and 110.3 μm. More than 50% of the struts had a diameter <55.1 μm, and half of the struts were <6.9 μm. Measurements taken on adjacent slices were similar, although not identical.

Table 3.14. Morphological parameters for the PCL scaffold, calculated from MicroCT data. The 2D data is presented as the average±stdev and range.

Parameter	3D Data	2D Data
Pixel Size	3.4μm	3.4 μm
Total VOI Volume	9*10^10μm^3	9*10^10 μm ^3
Object Volume (Scaffold Volume)	5.4*10^9 μm ^3	5.4*10^9 μm ^3
Grey Thresholds	57-250	57-250
Porosity (100-%Object Volume)	94.03%	93.91%
Object Surface	7.4*10^8	9*10^8
Mean Eccentricity	-	0.38
Structure Separation (pore spacing)	-	293.88±21.20 μm (240.12-341.58)
Strut Porosity	-	7.8±1.07% (5.28-12.037)
Average Object Size per Slice (Strut Diameter)	-	46.11±1.55 (41.76-51.54)
Average Object (Strut) Area per Slice (Strut Area)	-	1671.56±112.88 μM ^2 (1369.64-2086.57)
Mean number of objects per slice	-	1124.95±191,49 (864-1386)

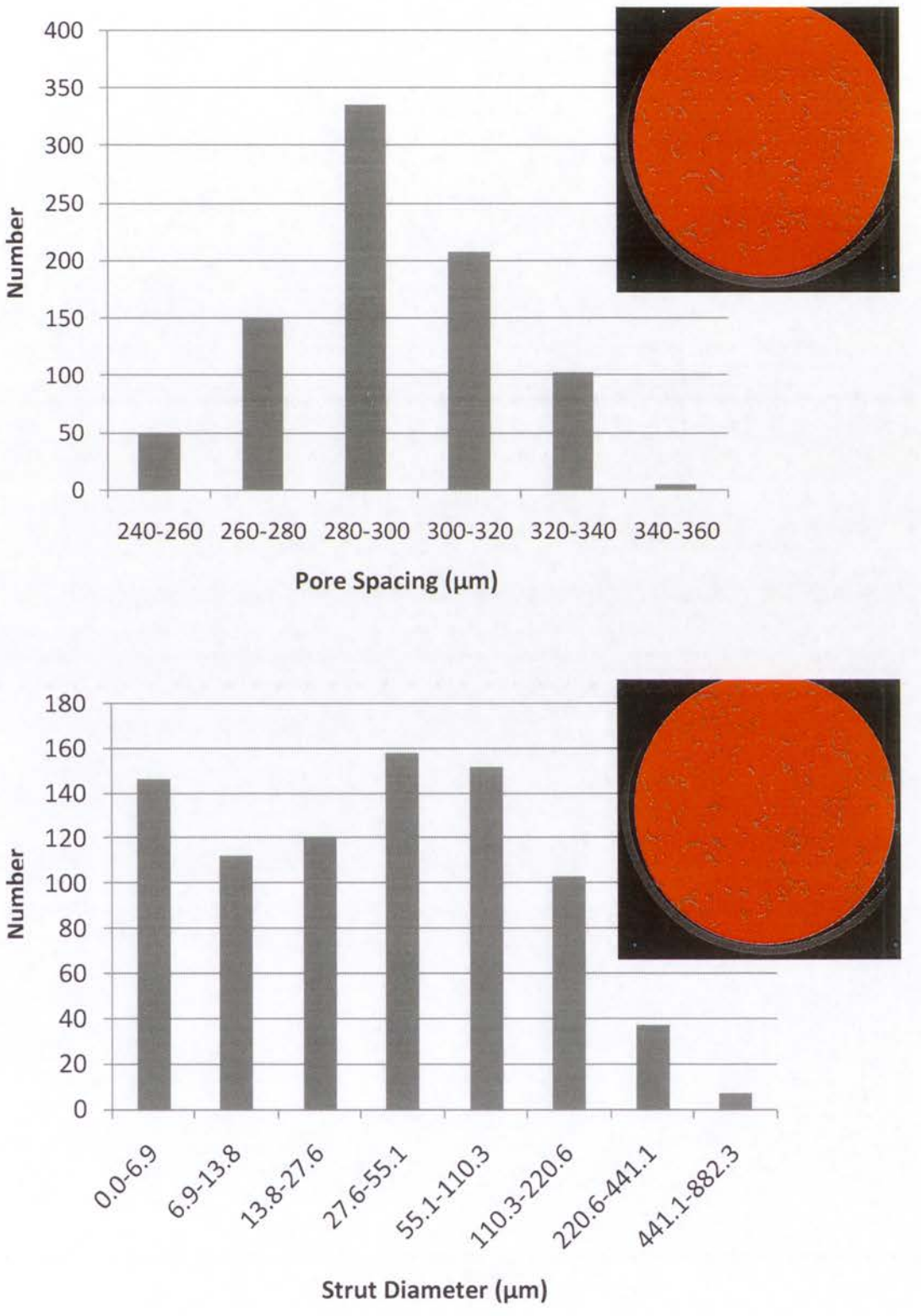


Figure 3.41. Histogram of pore spacings and strut diameters measured using MicroCT for a single 2D slice. Insets: The cross-sectional regions of the scaffolds which were examined

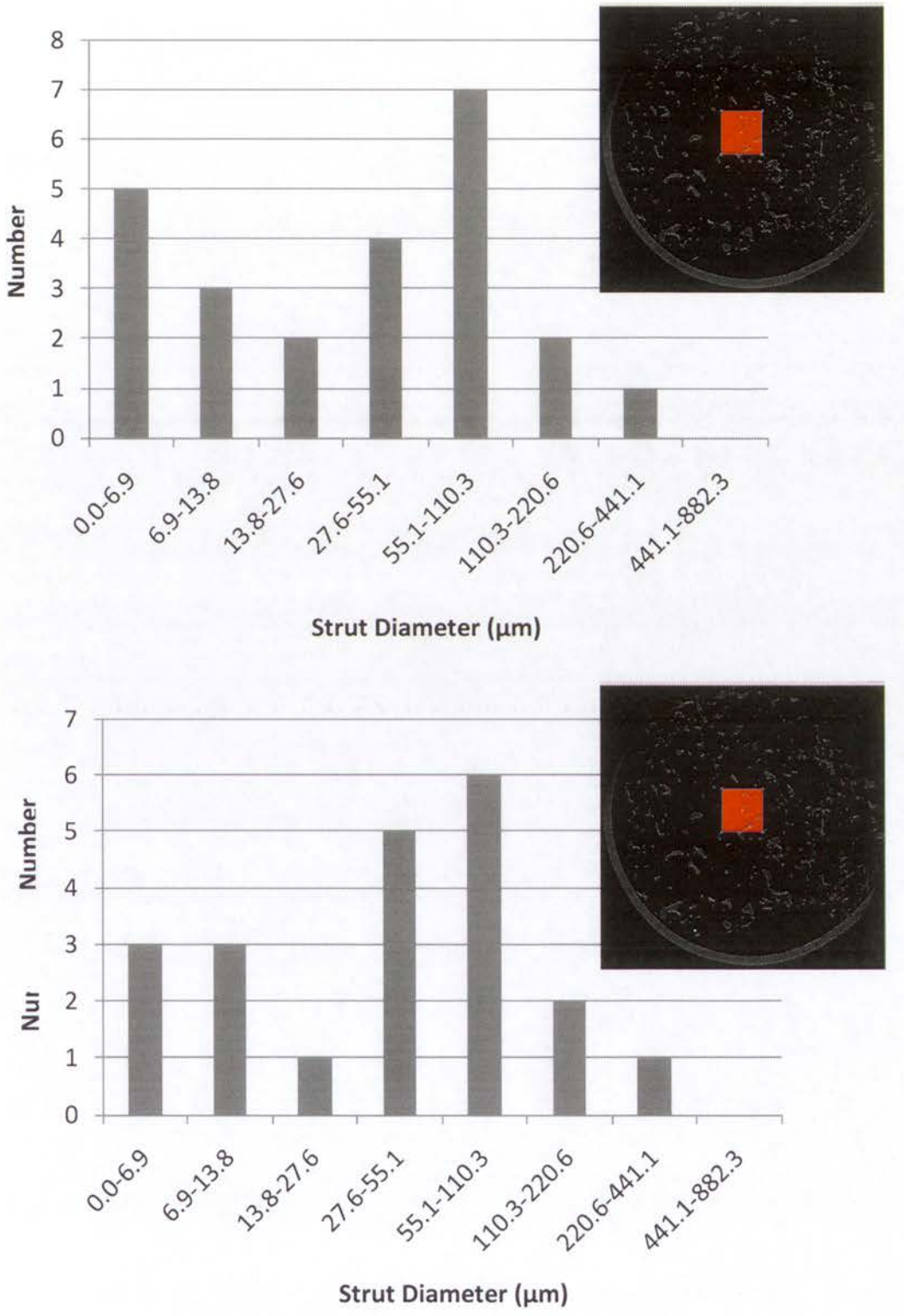


Figure 3.42 Histograms of strut diameters as measured using MicroCT, for regions selected from two adjacent slices. Insets: The cross-sectional regions of the scaffolds which were examined are the red highlighted regions.

3.2.3.6. Interconnectivity Path Calculations

Variotis™ contained 100% interconnected porosity, as there were no disconnected pores. Fig. 3.43 shows the range of scaffolds used for the calculation of the detour index. These results are summarised in Fig 3.44. The variotis™ scaffold had a detour index of 1.03, ~30% less than the other three scaffolds. This indicates that particles have the ability to travel from the inner pores of the scaffold, through to the outside edge, in a route which is almost a direct pathway. The inverse relationship is also true.

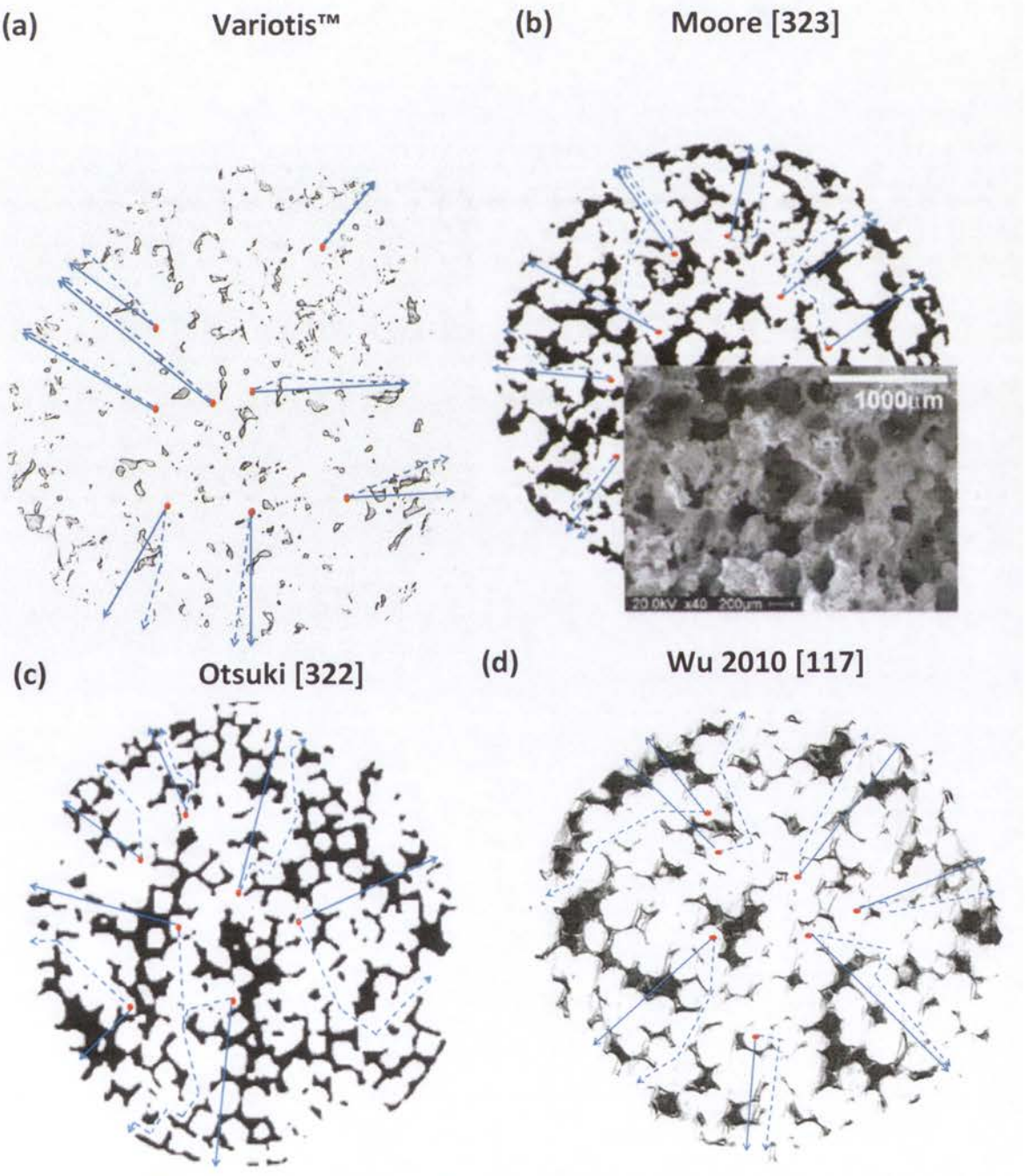


Figure 3.43. MicroCT sections for a range of different scaffolds for which the detour index was calculated. Indicated in 2D are the direct pathway (blue line) and shortest distance from a point to outer surface through interconnections (blue dotted line). These images have been inverted so the scaffold is seen in black and the empty pore space in white.

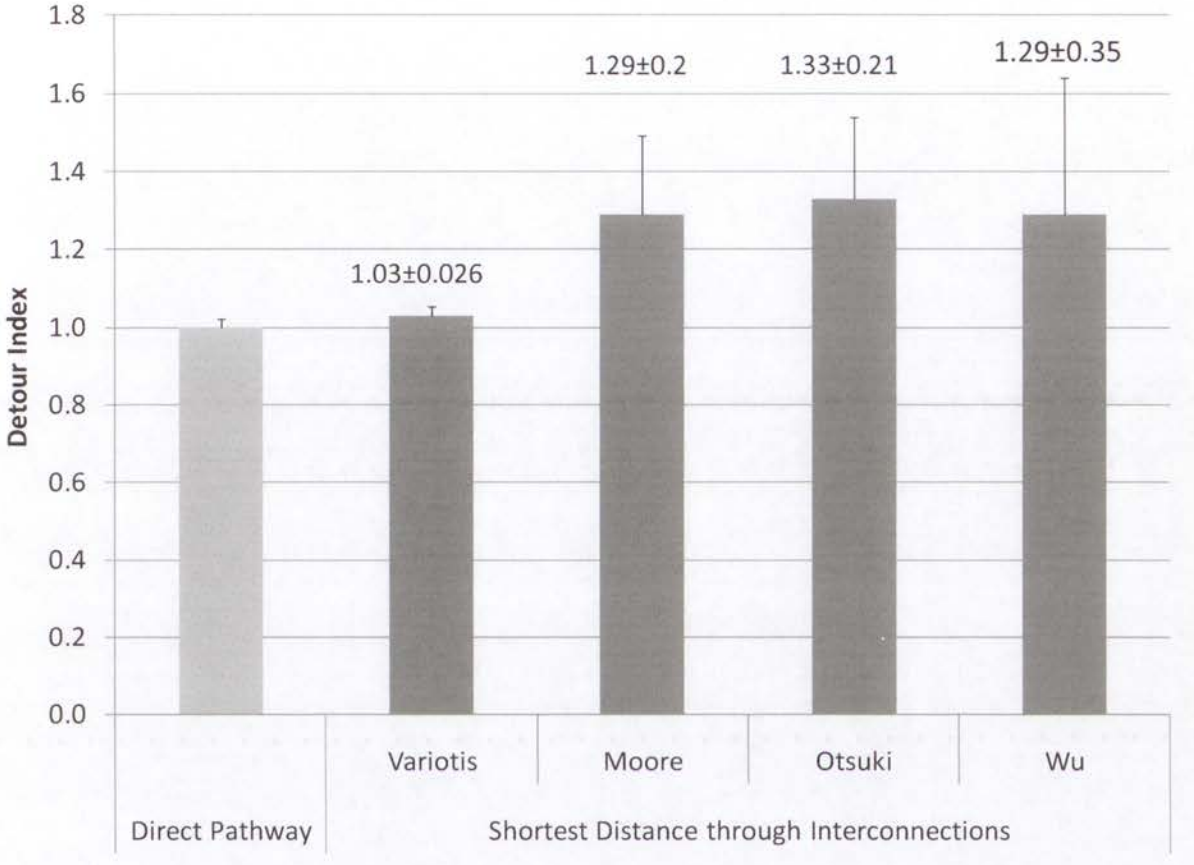


Figure 3.44. Detour indices calculated for the variotis™ scaffold and scaffolds reported in the literature [322, 323].

3.2.4. DISCUSSION

The synthesis of soft tissue scaffolds was demonstrated using a novel batch coagulation method. This high-throughput process enabled formation of highly porous 1cm-thick scaffolds which were of consistent quality and hierarchical porosity.

3.2.4.1. Scaffold and Synthesis Process Design

The key features which were sought in the design of a versatile, commercially viable soft tissue scaffold were: (1) a macrostructure with excellent pore interconnectivity, large pore size and high porosity (1.6.3), (2) soft and elastomeric structure (3.1.1) and (3) bioactive surface (1.4). These are important features for enabling tissue and vessels to form within the scaffold, for mechanostimulation of the developing tissue, facilitating attachment to the surrounding tissue and prevention of fibrous encapsulation. Current polymer processing techniques are limited in their ability to produce thick scaffolds with these features (3.1.6). This is due to difficulties including complete removal of the porogen, which limits the thickness and interconnectivity of the scaffolds that can be produced.

The synthesis process which was conceptualized and implemented overcame these limitations. This was by a unique process which involves simultaneous aqueous solvent and precursor removal, and polymer coagulation (Fig. 3.23). This process occurs at a rapid rate to allow sufficient solvent exchange, whilst the polymer solidifies. A highly densified and soluble commercial sucrose network porogen enabled fluid flow through the forming scaffold and promoted porogen removal.

The batch coagulation technique relies on a dual solvent system based on the exchange action of water and acetone. The following simultaneous sequence is proposed for this novel process, but has yet not been verified: (1) Acetone carries polymer in (2) Water gels the outer polymer which coagulates upon itself while the acetone leaves (3) Water removes porogen. This facilitates concurrent solvent exchange over an extremely high surface area; all surfaces within the scaffold.

3.2.4.2. Scaffold Synthesis

10 mm-thick scaffolds were formed using the batch coagulation technique, which was a rapid, convenient and reliable method. These are among the thickest scaffolds which have been reported in literature. The scaffolds showed an excellent ability to be handled. Large numbers of scaffolds could be synthesised with minimal labor times. Using this process, >500 scaffolds may be made per week with minimal apparatus, and requiring only 2-3 days of labor time. This is in contrast with many popular scaffold synthesis methods, such as rapid prototyping and

electrospinning which require several hours to create one 3D scaffold. Our process is therefore a great advantage for being able to provide a large number of scaffolds for various tests prior to commercialisation. In addition, our process has managed to eliminate the use of highly toxic solvents. The only substances the variotis™ scaffold contacts are sucrose, which can aid wound healing (ref section 4.1.4) and acetone (an *in vivo* metabolic by-product). The process is also extremely cost-effective, with the materials required to make a base scaffold costing <<50c.

Bioactive glass, both in particulate and fibrous form, was bonded to the scaffolds via gentle heating below PCL's melting temperature. The glass coatings formed a uniform coating on the scaffold surfaces which did not block the pores (Fig 3.38, 3.41, 3.42, 4.43). The scaffolds could likewise easily be coated with a range of polymer or ceramic particles if it were required e.g. for drug delivery.

Verification of the scaffold consistency showed 24% weight variation within a single batch, which was reduced to 4.17% when the process was upscaled (Fig 3.36, Table 3.11). Glass infiltration into the scaffolds reduced the weights by half, suggesting the glass fibers prevented infiltration of some molten PCL into the scaffold during the coagulation process. Glass coating of the scaffold achieved 10% w/w or 4.36% v/v of glass (Table 3.11).

3.2.4.3. Macrostructural Characterisation

Using SEM, the scaffolds demonstrated hierarchical porosities with interconnected macropores (300-500 μm), well distributed micropores (2-40 μm) within the pore struts, as well as surface texture (Fig. 3.45, 3.46). These large pores and microstructural features could provide sufficient space for tissue and vessel development, whilst providing microscale cues to the cells.

The interconnected micropores could improve mass transfer and cell communication; critical aspects for engineering 3D tissues. In addition, the micropores could increase surface sites for protein adsorption, cell attachment while increasing the hydrophilicity and degradation rate of the PCL. The micropores were likely to be formed during synthesis, due to the swelling of molten PCL and evolution of acetone gas which occurs upon the ingress of water. Fig. 3.45 demonstrates biological components which correspond with the multi-scale features of the scaffold which were examined in this chapter.

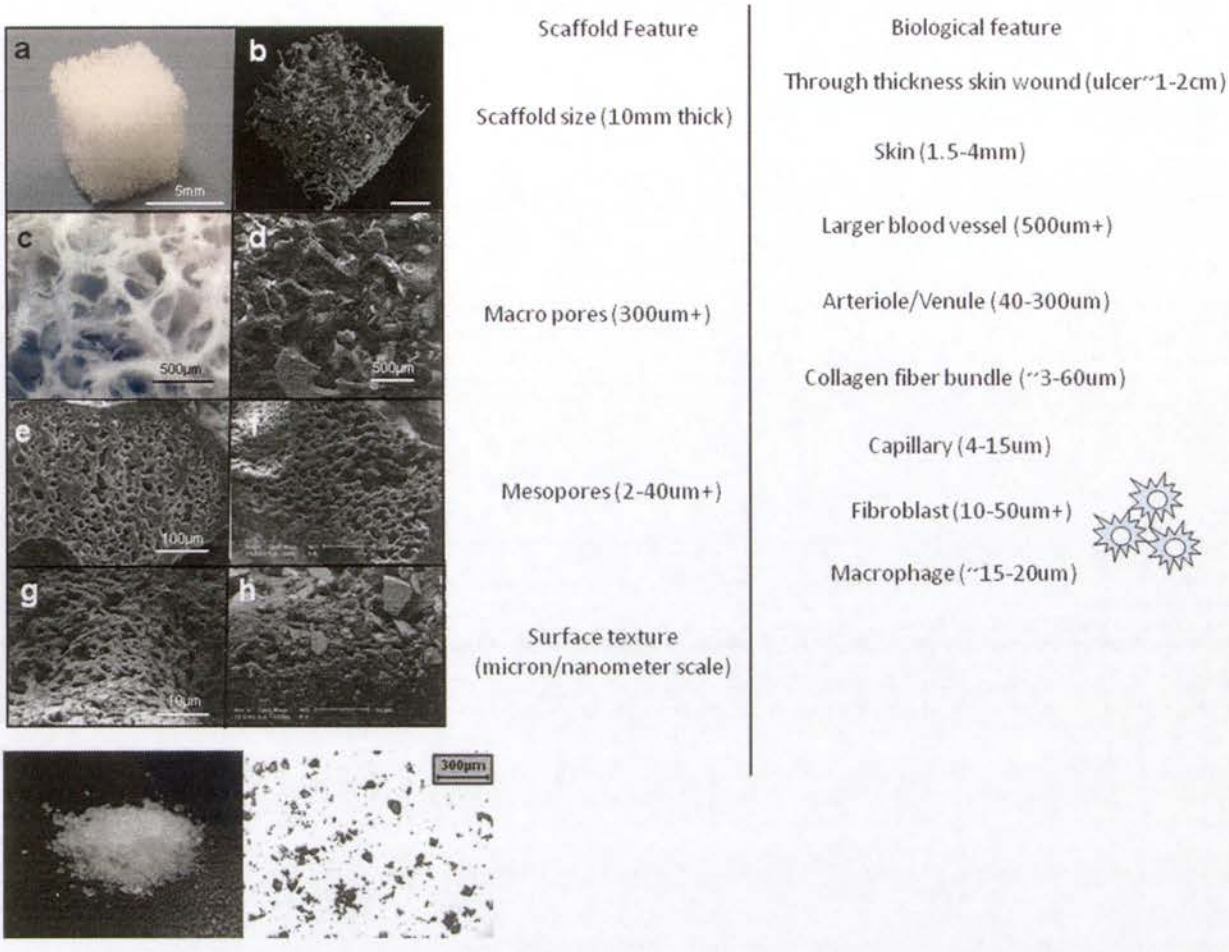


Figure 3.45. Hierarchical structure of the scaffold and the corresponding biological features which could be accommodated: (a) Scaffolds used for the animal model (scale bar:5 mm), (b) MicroCT of a portion of the scaffold (scale bar:1 mm), (c) Optical microscopy of scaffold (Scale bar:500µM), SEM of the scaffold, showing: (d) Cross-sectioned scaffold showing pores and struts (e,f) Mesopores in the scaffold struts (Scale bar:100 µm) (g) Surface texture of the PCL scaffold (Scale bar: 10 µm) (h) Surface of the BG scaffold (Scale bar:10 µm) (i) Granules of BG (j) Powdered BG as used for the current study.

High porosity measurements were achieved for the scaffolds using manual and MicroCT methods (PCL: >94%, 13-93 fiber filled PCL: 97%). These are thought to be underestimations ad the microporosity could not be considered. The porosity of the struts was calculated to be 7.8% (2D MicroCT measurement), however the actual value was thought to be much higher (>50%). The overall porosity of the variotis™ scaffold was therefore thought to be closer to 97%. The high porosity is attributed to the high density of the sucrose porogen and the low concentration of the PCL solution. This leads to the formation of low density scaffolds with thin scaffold struts which can ensure a minimal amount of foreign material is implanted in a clinical setting. This is expected to increase the degradation of the polymer (estimated:~6 months). Examination of the scaffold using MicroCT measured the pore size to be ~293 µm (Fig. 3.42). Most of the scaffold struts had diameters <55.1 µm (Fig. 3.43), which is <1/2 the thickness of many other scaffolds [445]. The scaffold was observed to be 100% interconnected with no disconnected pores.

An excellent level of interconnectivity was detected for the variotis™ scaffold, when compared to popular techniques such as salt porogen leaching. Dead pore space is a major inhibitor for tissue ingrowth, and has been a problem for many scaffolds [322]. Otsuki and coworkers [322] applied a custom-made algorithm to MicroCT models to demonstrate that the number of isolated pores within their scaffold could easily increase when narrow pore throats become blocked. This could occur when the scaffold thickens due to fibrin/collagen deposition or cell agglomeration/attachment. A detour index of 1.03±0.026 indicated only a 3-4% difference between the direct pathway and the shortest distance through the interconnections. This was in contrast to three other scaffolds [322, 323] which achieved detour indices between 1.29 and 1.33, indicating an increase of 30% in the tortuosity of the pathway. The lower detour indices are due to both the decreased porosity and the size and shape of the pores, partly due to inferior porogen density and interconnectivity.

Visually, the pore throats of the variotis™ scaffold are extremely wide and for this reason could have a low chance of experiencing blockages. In addition, the variotis™ scaffold exhibited multiple, efficient pathways to a single pore- a good indicator that the scaffold could show excellent fluid perfusion. The current calculations were performed examining the flow of fluid, or a small particle such as a cell. A more detailed examination would anticipate the flow of larger particles such as cell agglomerations, degraded scaffold segments and the accommodation of networks of biological structures such as vessels and collagen bundles. From the literature it would be anticipated that variotis™ would also easily outperform the other scaffolds in these respects. In the future, finite element analysis could be applied to the MicroCT models to help optimise the scaffold structure. Mechanical behaviour and modelling of the 3D flow of fluid/cells could be examined.

3.2.4.4. Comparison with Literature

In contrast with the variotis™ scaffold, the majority of scaffolds reported in the literature are extremely thin, <3 mm, and often have a high risk of delamination if layered [16, 60, 62, 83-85, 627, 628]. Some thick scaffolds have been reported from porogen-based techniques, including PLGA and PLAC scaffolds of 7-8 mm [61, 87]. Although both of these scaffolds reported *in vivo* vessel formation within the scaffold (ref ch 6), only one of these scaffolds (PLAC) achieved complete tissue ingrowth by 2 months during subcutaneous studies [61], highlighting the importance of optimising the scaffold structure and composition.

Previously reported scaffold synthesis methods including coagulation and TIPs processes all involve gas exchange, in contrast to the current aqueous approach [60, 61, 540, 585]. These multi-step techniques are more time consuming and lead to scaffolds which are not uniform. Gas exchange methods involve the action of a single solvent and diffusion effectively occurs only on the outer surfaces of the scaffold. For these processes, porogen removal is a secondary process to solvent extraction and takes several days. The porogen acts as a barrier around which the polymer forms in plate or blade shapes [148]. In contrast, our novel technique facilitates the formation of rod-shaped polymer struts which solidify as the porogen is already dissolving.

To the author's knowledge this is the first reported PCL scaffold with porosity in excess of 90% [540]. Langer and coworkers recommended a porosity of 90% for optimum diffusive transport within a cell–scaffold construct under *in vitro* conditions [309]. Most scaffolds in the literature range in porosity from 45-85% [546, 555, 624], although porosities as high as 93-98% have been reported for some scaffolds formed using porogen-based techniques [60, 556, 625] (ref Table 3.7), however, the pore size of these scaffolds were limited to <300 μm. Freeze-drying techniques are often used to achieve high void volumes, however the pore sizes and shapes vary considerably throughout the scaffold and large defects are often observed within the structure [540].

The variotis™ scaffold has a large pore size and excellent interconnectivity for a soft scaffold, which can be attributed to the network porogen and dual liquid solvent processes used. Pore sizes of soft tissue scaffolds are generally limited to 150μm [58, 85, 540, 548], although larger pores are often evident in rigid bone scaffolds [58]. Occasionally, scaffolds are reported in the literature with a bimodal pore distribution [15, 218, 327, 548, 549]. The network porogens in the current study consisted of tightly packed sucrose granules which were expected to consist of a wide range of particle sizes. This structure is ideal for formation of highly porous, interconnected scaffolds with thin pore walls. Gao [327] used an MTT assay to demonstrate superior levels of cell proliferation for scaffolds formed using salt fusion, as compared with the separated salt crystals, for up to 11 days after seeding. This is due to the superior level of fluid flow which can be achieved with a high degree of interconnection. Usually, discrete porogens are used for scaffold synthesis, leading to residual porogen within the scaffold. Interconnected porogens have been investigated previously by few researchers: fused salt crystals, [327], sintered paraffin spheres [625], 3D rapid prototyped sucrose template [221]. Such scaffolds display good interconnectivity and some have porosities up to 95% [625].

3.3. POST-SYNTHESIS MODULATION OF SCAFFOLD GEOMETRY

The PCL matrix of the scaffold is thermoplastic and therefore capable of being formed under thermal activation. Changes to the macroscopic and microscopic forms can be induced using heat and compression before setting at room temperature. The scaffold could be evenly heated using warm air, liquid or radiation. Osteochondral, intervertebral disk, tendon-bone and skin tissues exhibit unique form and properties. They also exhibit gradations in these properties (ref 3.1.7).

In this section, the versatility of the scaffold was verified by trialing post-forming methods. These methods could allow the scaffold to approximate and complement various forms and inhomogeneities of tissues. A thin film of PCL was added to the scaffold, in order to attempt to approximate the modulus of human dermis. A tubular scaffold was formed which could be used for blood vessel engineering or explant laboratory models (e.g. Cancer tumor models).

3.3.1. METHODS

3.3.1.1. Scaffold Fusion

Scaffolds were fused together by quickly dipping in water at 65°C to soften the polymer. Light pressure was applied, holding the components together, to complete the bond.

3.3.1.2. Scaffold Compression

Scaffolds (h=9.8 mm) were compressed between two custom-made plates; either Teflon-coated steel plates (Fig. 3.5.4c) or perspex plates. The plates were separated by a particular distance and pressure was applied using die components as weights. The polymer was heat-set to achieve permanent deformation using one of three heating approaches: i. Molybdenum element oven (Tetlow), ii. Heat gun or iii. Water bath. A range of conditions were trialed, ranging from 48-65°C for 30 sec - 18 min. The conditions were sought which would provide enough heat for the PCL to become heat set whilst retaining a distinct pore structure.

3.2.1.3. Addition of a Thin Film

A semi-permeable membrane of PCL (estimated thickness: 500-800 μm) was fabricated using a PCL/acetone solution (ref section 3.2.1.1.). The solution was poured onto a Teflon lined tray, forming a thin layer. The film was allowed to dry overnight at room temperature to ensure complete evaporation of the acetone. The membrane was cut to size using scissors. The membrane was fused to the scaffold by warming the bonding surface of the scaffold using 65°C water. Components were held together and light pressure applied to the bonding surface. These scaffolds were tested mechanically (ref section 3.8.2.4).

3.3.1.4. Formation of variotis™ Sheet

A large rectangular prism scaffold template (0.9x8.5x7.5 cm) was formed by joining 9 sugar cubes (CSR, Australia) using elastic bands as shown in Fig. 3.55. The porogen template was submerged in a PCL/acetone solution and scaffolds formed (ref section 3.2.1.1.). The elastic bands were kept in place whilst the sucrose granules were rinsed out, in order to provide compression and prevent displacement of cubes.

3.3.1.5. Synthesis of Tubular Scaffolds

Tubular scaffolds were formed with a stainless steel mandrill (0.6 cm) (Fig 3.46). Three variotis™ scaffolds (10.5x16.5x17.8 mm) were pierced with the mandrel, and held slightly in compression with a ring of Teflon tape on both the inner and outer edges of tube. The ends of the tubes were held in compression using silicone putty. Scaffolds were heated to 58°C for 10 or 15 mins.

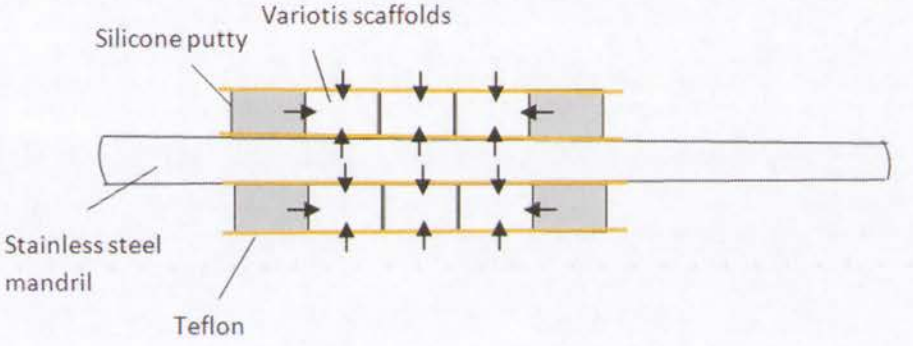


Figure 3.46. Longitudinal cross-sectional view of the apparatus used to form tubular scaffolds.

3.3.1.6. Functionally Graded Scaffold

Variotis™ scaffolds (10.5x16.5x17.8 mm) were cut diagonally in ½ using a sharp blade. Triangular prism shaped scaffolds were vertically compressed to a height of 2.5 mm (depth: 10.5 mm, breath: 16.5 mm) (Fig. 3.47). The functionally graded scaffolds were examined using a Leitz DMRXE optical microscope and Leica DFC420 digital camera system.

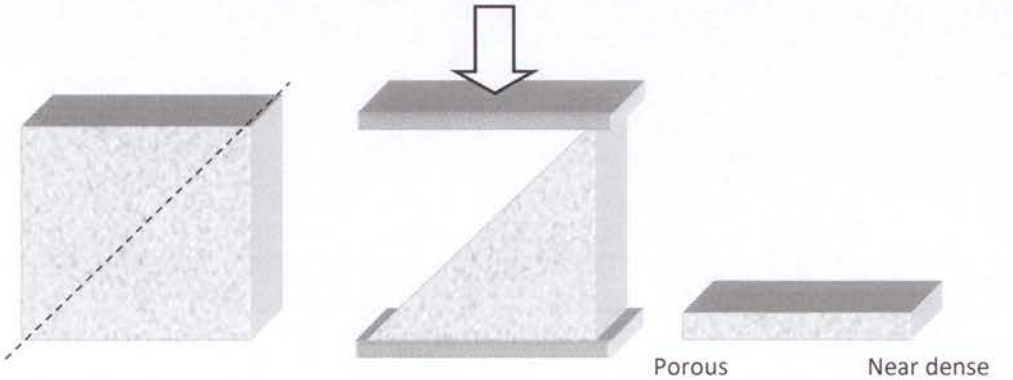


Figure 3.47. The method for the synthesis of FGM scaffolds.

Hardness indentation tests were performed to verify the method was successful for fabricating a functionally graded scaffold. Two techniques were used, as detailed below.

A. Shore Hardness Profile

Hardness was measured using a Shore S1 Durometer with a frustum cone indenter (max force 821 g) (Fig 3.48), which conforms to the ASTM D 2240 standard procedure. Hardness measurements were taken at various points along a functionally graded scaffold by firmly pressing the durometer against the sample, so it is perpendicular to the sample. The calibrated spring within the durometer induced a known load upon the indenter. The depth of penetration was recorded when the spring pushed the indenter into the sample. A deeper penetration indicated a softer material. A constant force and time was used for each indentation point. A hardness profile was graphed, showing the average/stdev of 3 points for each position.

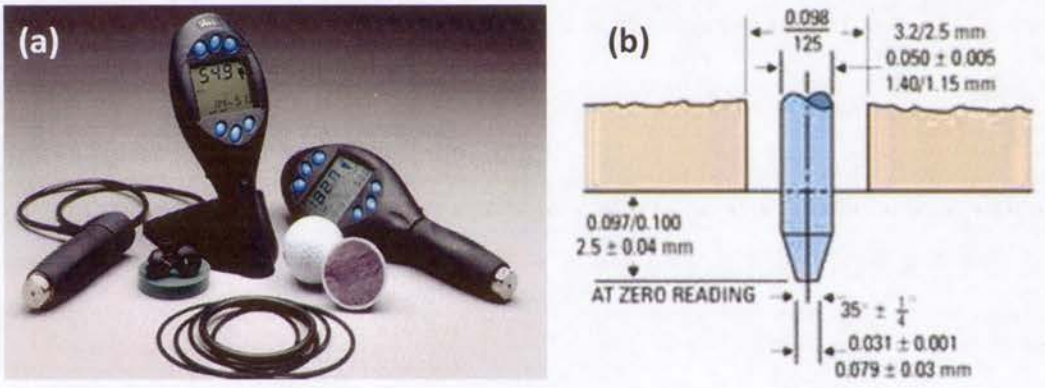


Figure 3.48. (a) Shore Hardness Tester (b) Indentation Tip.

B. ELF3400 Indentation Profile

A silicon nitride indenter (d=4.2 mm) (Fig 3.49) was attached to the compression plates of the ELF3400 and used to measure the hardness of the functionally graded scaffold at various positions located by the rotational actuator of the axial-torsion system. A speed of 1 mm/s was used and the peak indentation load was measured using a 50 N load cell.

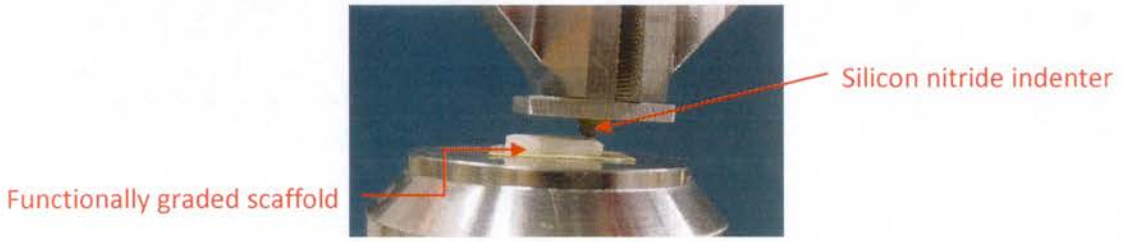


Figure 3.49. Hardness measurements of the scaffold were taken using an indentation methods

Scaffold tiles were successfully fused together as described in method A (Fig. 3.50a, b). Permanent deformation of the scaffolds during compression (Ref 3.3.1.2) was successfully achieved using all three heating approaches (Fig. 3.50c, d).

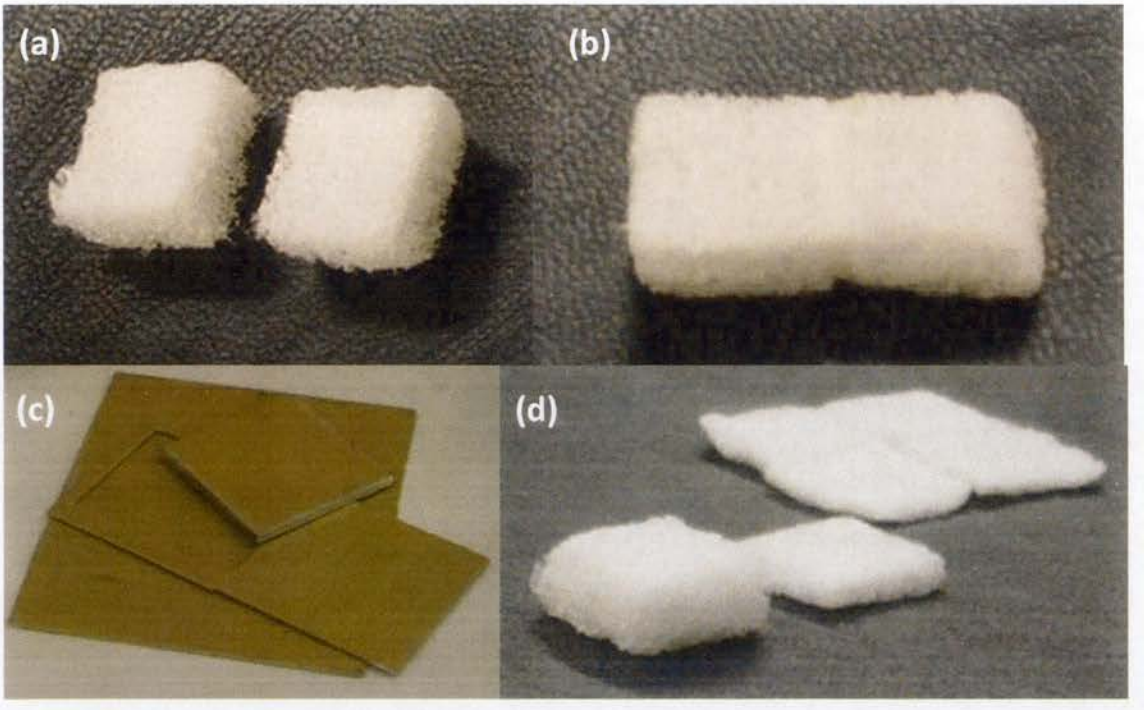


Figure 3.50. (a) Original scaffolds (b) Fusion of variotis™ scaffolds to form sheets (c) Teflon-coated steel plates for scaffold compression (c) Scaffolds before and after hot compression.

The scaffold heights achieved under various compression configurations are reported in Table 3.15. The change in height was assumed to correspond to a change in pore size- presumably a decrease in one direction and an increase in the other, in the x-y plane.

Table 3.15. Conditions used for compression of scaffolds. The heating method and material used for the plate apparatus are specified in the second column.

	Method and Apparatus	Plate Separation	Temp.	Heating Time	Final scaffold height (cm)	% of original height
A	1- perspex*	3.8mm	54°C	10min	3.8mm	39%
B	1- steel	2mm	54°C	10min	6.82mm	70%
C	1- steel	4.18mm	65°C	18min	6mm	61%
D	2- steel	2mm	-	20sec	5.48mm	56%
E	3-steel	2mm	48°C	30sec	4.93mm	50%
F	3-steel	2mm	51°C	30sec	4.3mm	44%
G	3-steel	2mm	55°C	30sec	3.7mm	37%
H	3-steel**	2mm	51°C	30sec	4.56mm	47%

* Metal sheets were surrounding this apparatus
** Scaffolds were in a plastic autoclave pouch

The thin PCL film formed using method C, contained mesopores which formed during evaporation of the acetone. The film formed a good bond with the scaffold, when fused using warm water (Fig. 3.51a). Heating of the membrane itself using saline or warm water was unnecessary as this would result in premature, self-adhesion. A large scaffold sheet was also synthesised (Ref 3.3.1.4) (Fig. 3.51b).

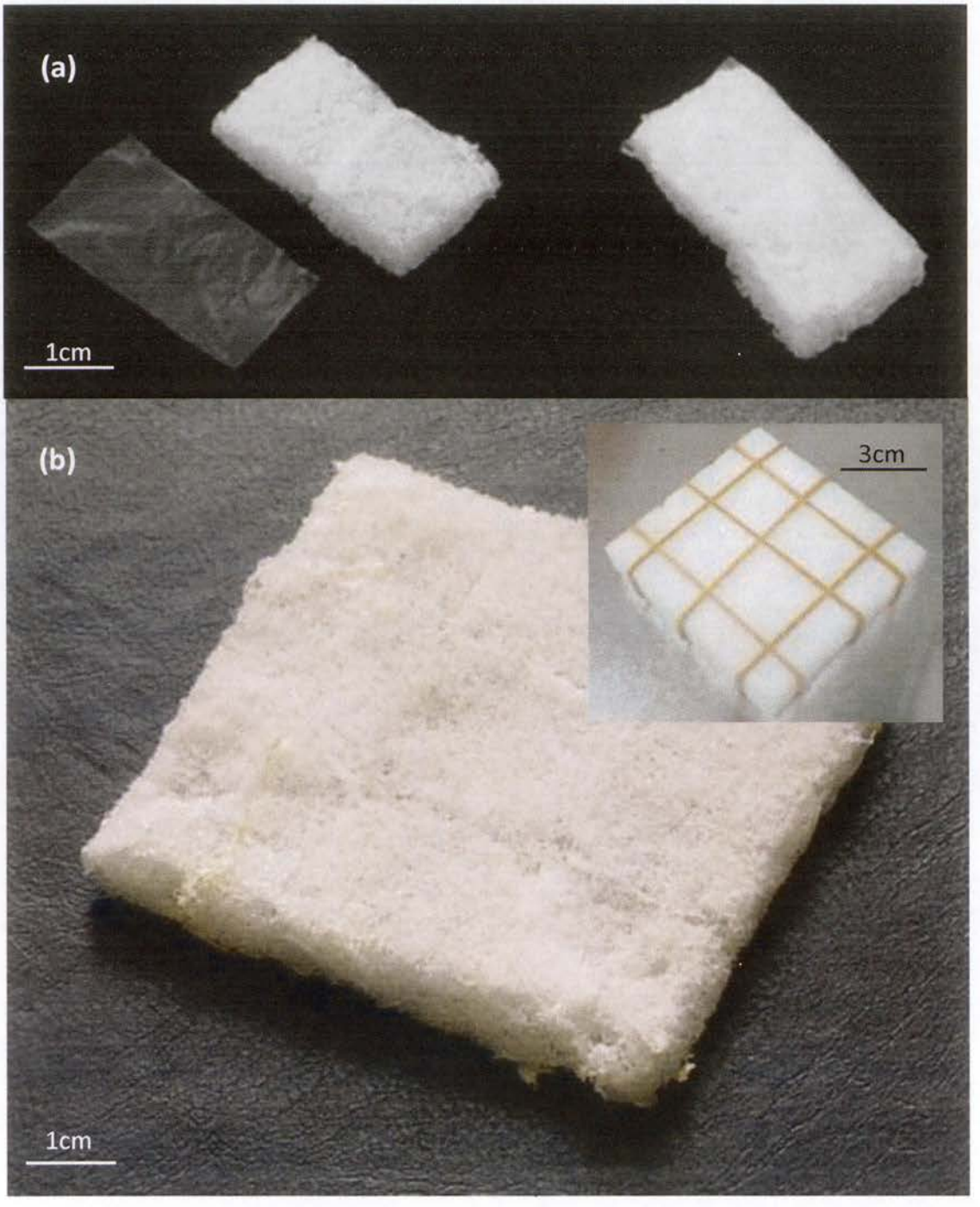


Figure 3.51. (a) Figure Fusion of a semi-permeable PCL membrane to the scaffold, (b) Precursor and scaffold formed using multiple sugar cubes.

Four tubular scaffolds were fabricated (Ref 3.3.1.5) (Fig. 3.56). The first two were heated for 15 mins, resulting in a high level of melting of the scaffold. The final two were well-formed tubular scaffolds with uniform thickness. These tubes measured 1.6cm in diameter and 2.6cm in length, with a 0.5 cm thick scaffold portion and a 0.6cm diameter lumen.

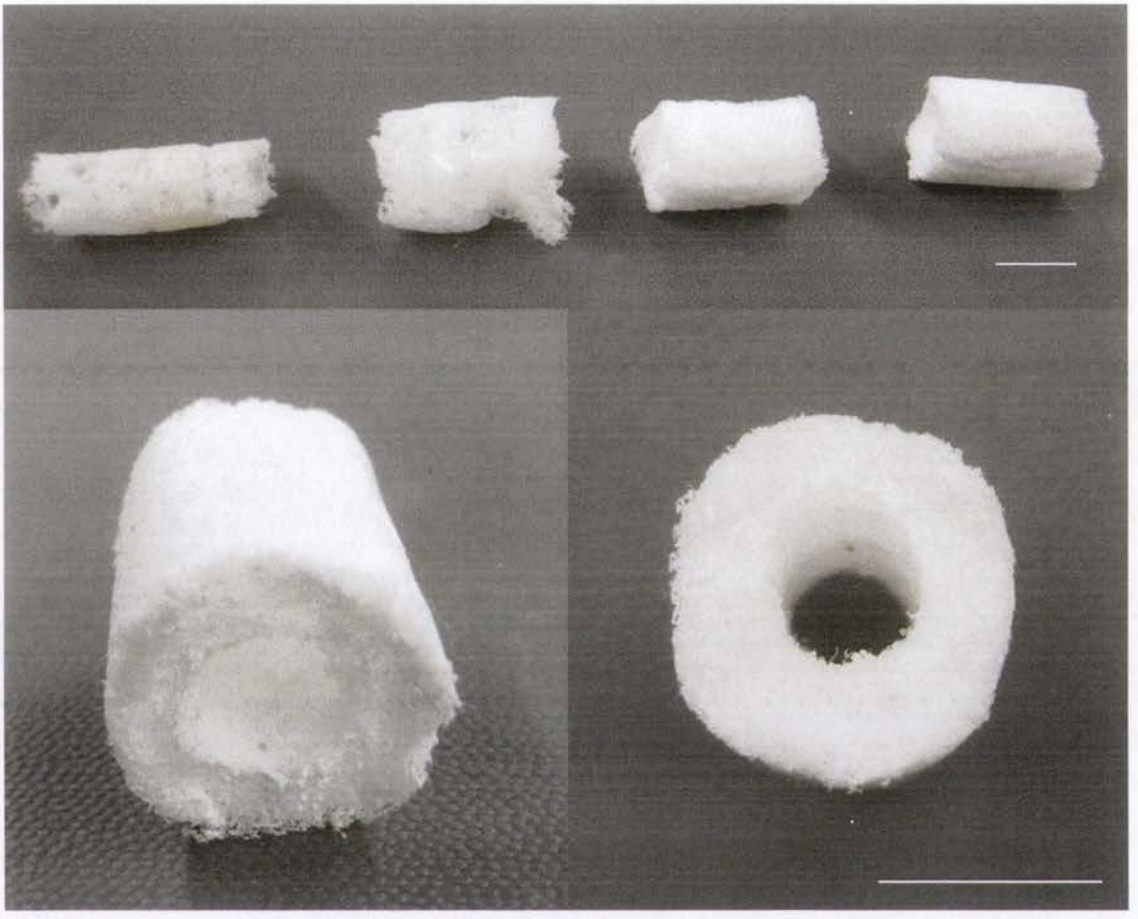


Figure 3.52. Tubular scaffolds which were formed from variotis™(scale bar: 1cm).

The functionally graded scaffold synthesised (Ref 3.3.1.6) displayed a gradient in porosity and pore size, from highly porous to a fully dense structure (Fig 3.57a). Shore A hardness measurements confirmed the scaffold displayed a gradually increasing hardness gradient (Fig. 3.57b). Measurements ranged from 30 units in the sparse region to 85 units in the dense region. Measurement of peak indentation load using the ELF3400 showed a similar trend, ranging from very low loads to a maximum of 12 N (Fig. 3.57c). The variation in hardness was due to changes in porosity and pore size. At the right hand edge the scaffold had a softer region, however this could easily be eliminated in future scaffolds. [178]

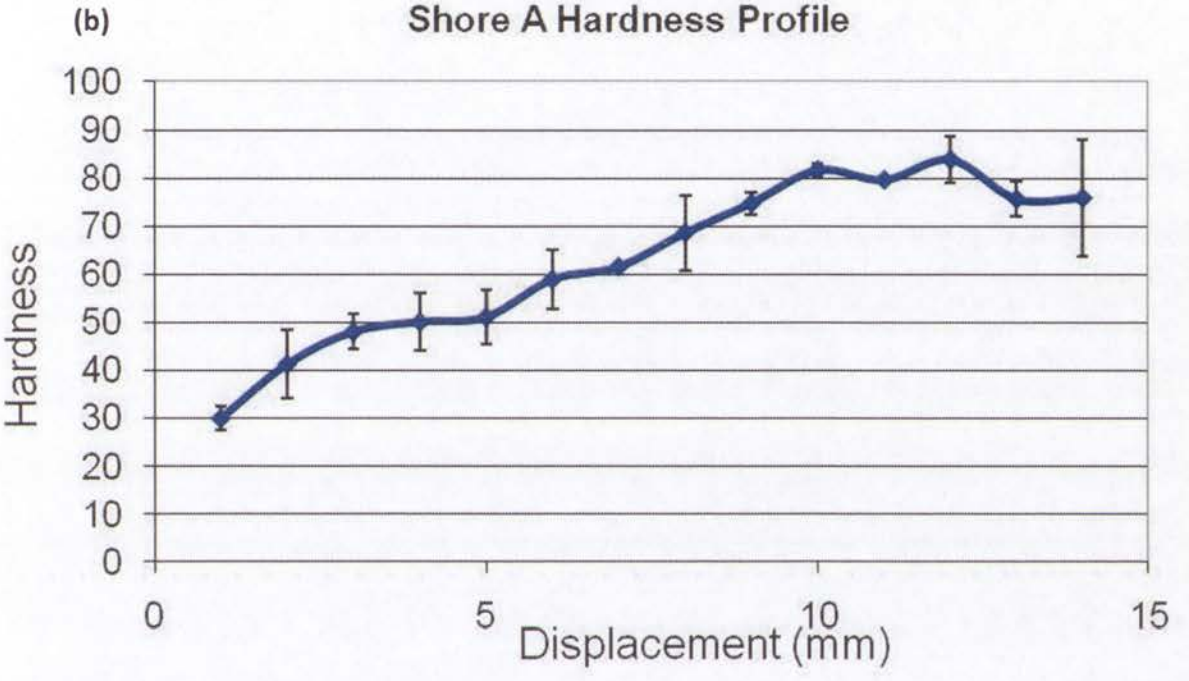
(a)



Porous: 100 µm pore diameter

Near dense

(b)



(c)

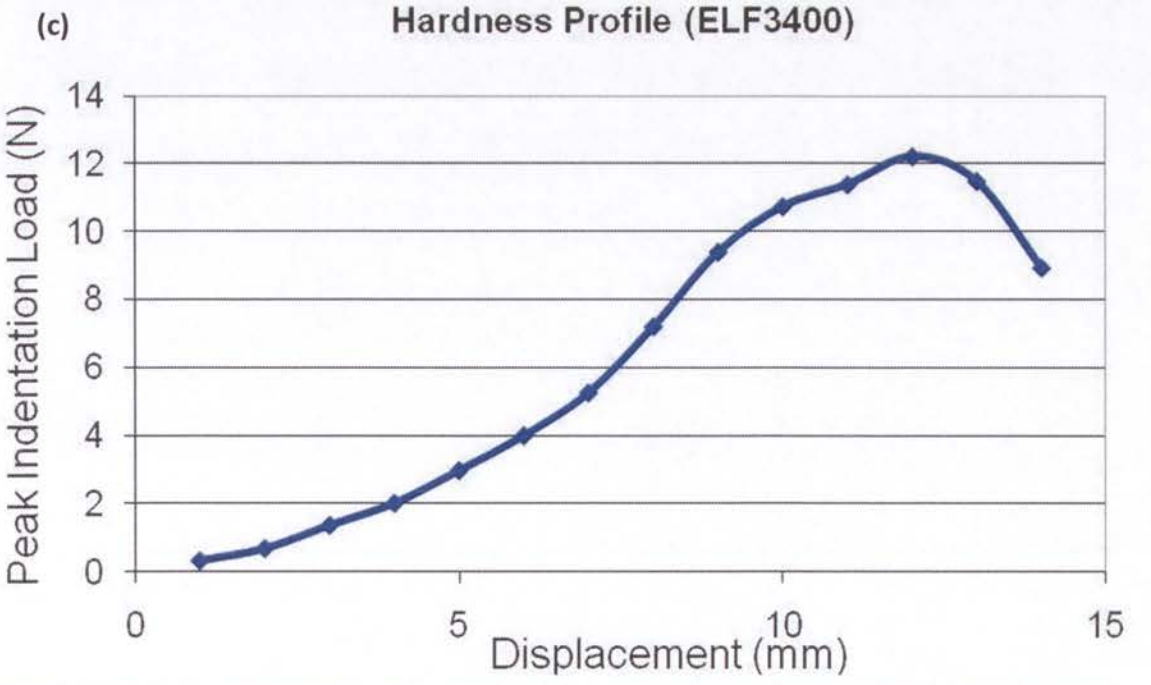


Figure 3.53 (a) FGM scaffold viewed with optical microscopy. Hardness profiles of FGMs with (b) Shore Hardness Tester (c) ELF3400 Indentation technique.

3.3.3. DISCUSSION

The versatility of the variotis™ scaffold was demonstrated through post-formation of scaffolds into a variety of shapes and sizes. Post-formation modulation was possible due to the low melting point and thermoplastic nature of PCL. Using these techniques, large, interconnected constructs may be formed in a modular fashion, such as organ precursors. Examples of applications for large scaffolds include chronic wounds, blood vessels and tendons.

Scaffolds could be easily cut and fused using gentle heating to <65°C, through either direct heat or warm saline whilst in slight compression (Fig 3.54b). Modulation of the porosity, pore size (and modulus were possible by compression setting the polymer. A range of scaffolds of varying heights were formed (Fig 3.54d, Table 3.15). Proof of concept studies showed the ability of a thin film to be attached to the scaffold using the same technique (Fig 3.55b). This could change the modulus of the scaffold to within the range of human dermis and could be suitable as a keratinocyte layer for a skin construct. This composite scaffold could therefore perform a similar function to intact skin, by presenting dehydration through excessive loss of electrolytes, and providing a protective barrier against bacterial invasion. The semi-permeable film could also be useful as a capsule, used for localised delivery of therapeutic agents or cell cultures to the wound site. It may also be used to slow the degradation of the scaffold, but is likely to hinder tissue formation.

A large sheet scaffold was formed using multiple network porogens (Fig. 3.55b). Stress concentrations at the intersections of the sucrose cubes are likely to lead to increased risk of failure in these zones. In addition, the interconnectivity at these joins could be compromised if contact between individual grains is not maintained during fabrication. PCL membranes could form between the cubes if a tight junction is not formed between them during the coagulation process. This could also slow tissue ingrowth into the scaffold. Tubular scaffolds were also formed, which could be used for laboratory explant models or blood vessel engineering (Fig 3.56). Dynamically stimulated vessel engineering could be facilitated using a bioreactor. Tubular scaffolds have been formed previously using mandrel [789] and tubular network porogen techniques [327].

Formation of a functionally graded scaffold was successfully achieved. A gradual gradient in modulus was demonstrated using two different hardness indentation techniques. To the author's knowledge, this is the first scaffold which has the ability to be thermoplastically post-formed into a functional gradient in pore size, porosity and modulus. Previous researchers have reported the ability for rapid prototyped PCL scaffolds to be joined using similar techniques for maxillofacial applications [314, 315].

The ability of the variotis™ scaffold to be formed into a variety of shapes and properties suggests a great versatility in modulation which could be achieved by researchers and surgeons alike. Scaffolds could be easily tailored to fit defect sites and experimental models.

3.4. SYNTHESIS OF POROGEN NETWORK TEMPLATES

A wide range of sucrose porogen templates were formed to enable the variotis™ scaffold to be formed in various sizes and shapes. Template shapes included cylindrical scaffolds which could fit in culture wells, and scaffold sheets for broad tissue defects.

3.4.1. METHODS

3.4.1.1. Formation of Cylindrical Templates (method A)

Cylindrical scaffold templates were formed by adding 0.5 mL water to 19.58 g sucrose (granulated sugar (particle size: ~500-800 μm, CSR, Australia) (2.49%). The porogen mixture was placed into cylindrical polystyrene molds with an inner diameter 11 or 16 mm and height 17 mm. The height of the cylindrical precursors was 5 mm or 15 mm. Porogens were manually compressed into the mold using a cylindrical, plastic rod. Precursors were allowed to dry at room temperature and removed from the mold.

3.4.1.2. Formation of Sheet Templates (method B)

Rectangular prism scaffold templates were formed by adding 0.5 mL water to 19.58 g sucrose 58 g sucrose (granulated sugar (particle size: ~500-800 μm, CSR, Australia) (2.49%). The porogen mixture was placed into a square, plastic mold (w=64 mm, d=64 mm, h=5 mm). Porogens were manually compressed using a cylindrical, plastic rod to a height of 4 mm. Precursors were allowed to dry at room temperature and removed from the mold.

3.4.1.3. Effect of Pressure on Template Synthesis (method C)

Cylindrical scaffold precursors were formed by adding 0.5 mL water to 19.58 g sucrose 58 g sucrose (granulated sugar (particle size: ~500-800 μm, CSR, Australia) (2.49%). The precursor mixture was placed into a custom-made, cylindrical, Teflon coated aluminium mold (d=50mm, h=7 mm). The height of the cylindrical precursor was 6 mm. Porogens were compressed using a vice, to various degrees: (a) uncompressed, (b), compressed lightly (1/2 turn of vice), (c) compressed moderately (1 turn of vice) or (d) high levels of compression (2 turns of vice). Precursors were allowed to dry at room temperature and removed from the mold.

3.4.1.4. Template Formation using Small Porogens (method D)

Cylindrical scaffold templates were formed by adding 0.4 mL water to 19.58 g sucrose (castor sugar (particle size: ~350 μm, CSR, Australia) (2.02%). The porogen mixture was placed into a cylindrical, Teflon coated aluminium mold (d=50 mm, h=7 mm). The height of the cylindrical template was 6 mm. The templates were then moderately compressed using a vice. The porogen templates were allowed to dry at room temperature and removed from the mold.

3.4.1.5. Formation of Precursors with a Bimodal Porogen Distribution (method E)

Cylindrical porogen templates were formed by adding 0.4 mL water to 19.79 g granulated and 19.79 g castor sugar (particle size: ~500-800 μm and ~350 μm respectively, CSR, Australia) (2.0%). The precursor mixture was placed into a cylindrical, Teflon coated aluminium mold (d=50 mm, h=7 mm). The height of the cylindrical precursor was 6 mm. The templates were manually compressed using a cylindrical, Teflon-coated rod. The templates were dried at 90°C for 45 min. PCL scaffolds were formed using these templates (ref section 3.2.1.1.)

3.4.1.6. Effect of Water Content and Pressure on Template Formation with Bimodal Porogen Distribution (method F)

Cylindrical scaffold templates were formed by adding 0.6 mL water to 19.79 g granulated and 19.79 g castor sugar (particle size: ~500-800 μm and ~350 μm respectively, CSR, Australia) (2.97%). The porogen mixture was placed into a cylindrical, Teflon coated aluminium mold (d=50 mm, h=7 mm). The height of the cylindrical precursor was 6 mm. The templates were compressed by application of a cylindrical, Teflon-coated rod and using moderate pressure in a vice. The templates were dried at 90°C for 45mins.

Cylindrical precursors were successfully made using method A to fit the dimensions of 24- and 96-well cell culture plates (Fig. 3.54). Some precursors fragmented during removal from the mold.

A sheet template (rectangular prism) was successfully synthesised using method B. The flexibility and rounded corners of the mold enabled easy removal without breakage. The compression method would need to be optimized to obtain a precursor with sufficient strength.

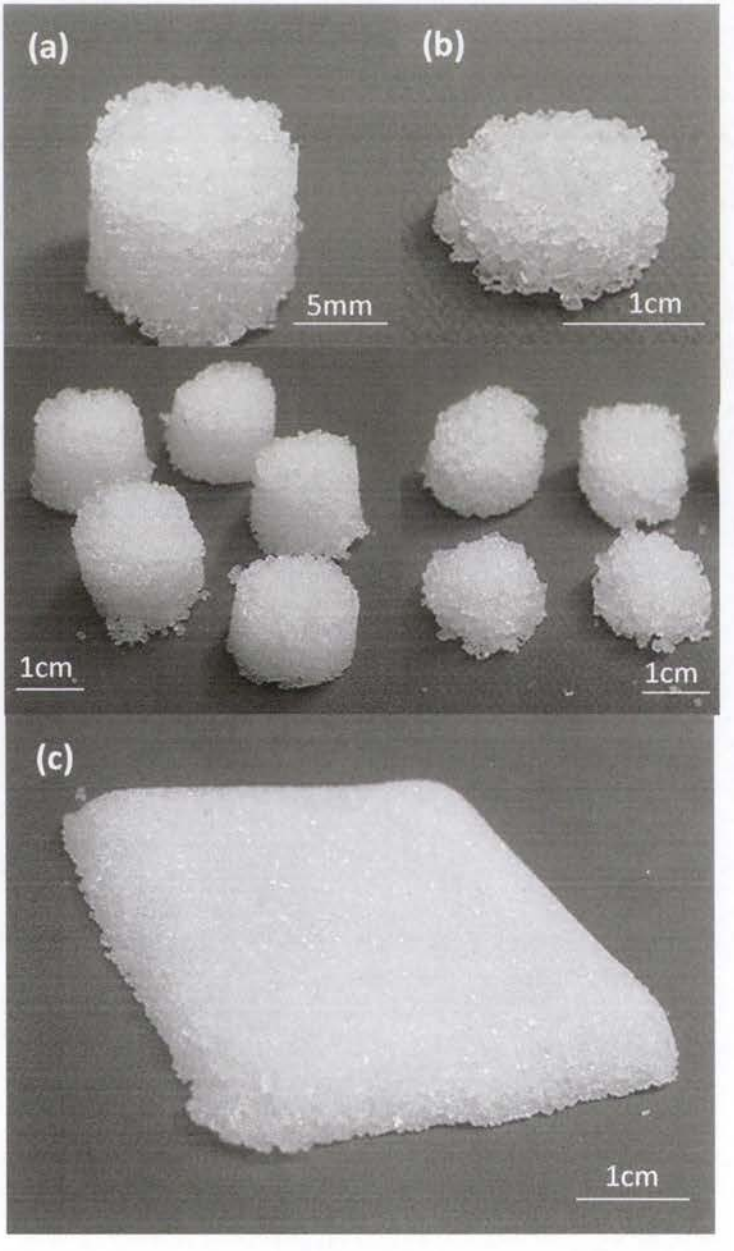


Figure 3.54. Cylindrical sucrose templates with (a) d=11 and (b) d=16 mm. (c) Sheet template synthesised from sucrose granules.

Method C enabled the synthesis of cylindrical precursors which could fit into 6-well culture plates (Fig 3.55). The sucrose templates displayed increasing levels of compaction according to the force used. The moderate/high levels of compression caused fracturing of the sucrose particles. High levels of compression caused delamination of the sucrose template, especially when <0.4mL water was used per 19.58 g sucrose (<2% water). This phenomenon occurred for both castor and granulated sucrose. It was concluded that >2% water was necessary for a stable precursor.

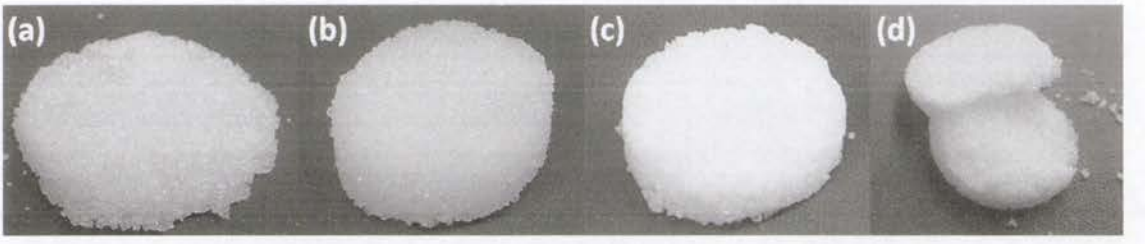


Figure 3.55. Sucrose precursors synthesised using granulated sucrose and compressed with (a) zero, (b) low, (c) moderate and (d) high levels of compression. The delaminated scaffold shown in (d) as synthesised using 1.01% water (0.2mL water:19.58 g castor sugar)

Using method D, a dense template was formed with good mechanical integrity (Fig. 3.56). However, synthesis of a scaffold using this template was not able to be achieved.



Figure 3.56. A good quality cylindrical precursor formed using small porogens.

Templates formed using method E exhibited excellent mechanical integrity (Fig 3.57a,b), indicating this is an ideal technique for precursor formation. The scaffolds formed appeared to be of good quality. The combination of castor and granulated sugar would give a wider range of granules to seamlessly fill the gaps between each other, leading to a higher level of interconnectivity and the possibility of scaffold formation. A variotis™ scaffold was successfully formed using these precursors, by following the original batch process. Precursors synthesised using method F were excellent and thought to be optimal (Fig. 3.57 c).

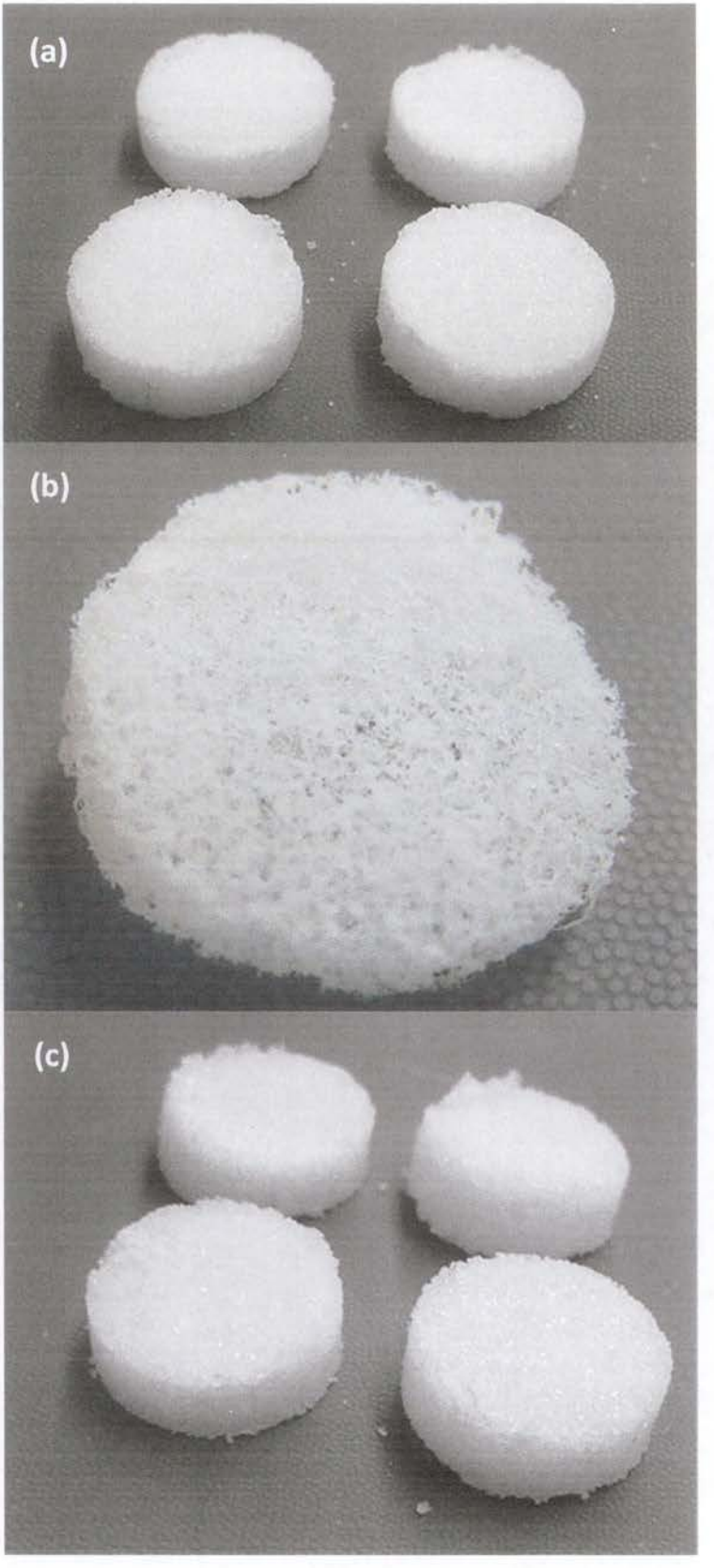


Figure 3.57. (a) Cylindrical precursors and (b) scaffold formed using 2 ranges of granule sizes (method E). (c,) Cylindrical templates formed using method F.

3.4.3. DISCUSSION

Customised precursor synthesis is an effective method which has the potential for the formation of scaffolds of virtually any shape, to suit anatomical or laboratory requirements.

Network sucrose precursors were formed using moisture, pressure, heat and a variety of grain sizes. A variety of shapes and sizes of precursors were successfully made. These included cylinders suited for 6, 24 or 96 well plates (Fig 3.54a, b, 3.55, 3.56, 3.57) and broad, rectangular prism shaped sheets. Scaffolds were successfully synthesised using a cylindrical disk precursors (Fig. 3.57b).

Cracking occurred for precursors which did not contain sufficient water or were subjected to high levels of compression (Fig 3.55d). For a stable precursor, it was deemed necessary to use >2% water and apply moderate pressure. An optimal protocol was thought to be 0.6mL water, 9.79 g granulated and 9.79 g castor sugar (2.97% water), with moderate pressure applied using a vice, followed by drying of the template at 90°C for 45mins. These parameters were chosen due to the good density achieved for the network porogens synthesised using method D.

Several previous studies have synthesised customized porogens [87, 221, 545]. Some examples include sucrose network porogens using rapid prototyping [221] and salt porogens by fusion [327]. However, the majority of these lack the compaction and interconnectivity achieved in the current study.

3.5. METHODS FOR SCAFFOLD STERILISATION

Scaffolds and bioactive glasses were packaged in paper/plastic pouches and the ends were heat sealed. Specimens were sterilized according to one of the following methods and scaffolds were tested mechanically (section 3.8.2.4) to determine whether any changes occurred to the polymer.

3.5.1. ETHYLENE OXIDE

A standard sterilisation cycle was undertaken by Steritech, consisting of an AQUIS cycle with a maximum temperature of 58°C.

3.5.2. GAMMA IRRADIATION

A standard dose of 25 kGy was used by Steritech to irradiate the specimens. The source of the Gamma rays was Cobalt-60.

3.5.3. ULTRA-VIOLET RADIATION

Scaffolds were exposed to ultra-violet radiation via a UV box (constructed by Michael West). The UV light box consisted of an array of four Philips TUV 8 watt low pressure mercury vapour discharge lamps that emitted shortwave UV radiation with a radiation peak at 253.7 nm. According to the manufacturer's specifications each lamp emits 2.1 watts in the UV range. The temperature within the UV box was found to be relatively stable at 27.5°C.

Scaffolds and glasses which had been sterilised using the various methods are shown in Fig. 3.58-3.60. Gamma sterilized samples displayed yellow discolouration. Ethylene oxide did not change in appearance.

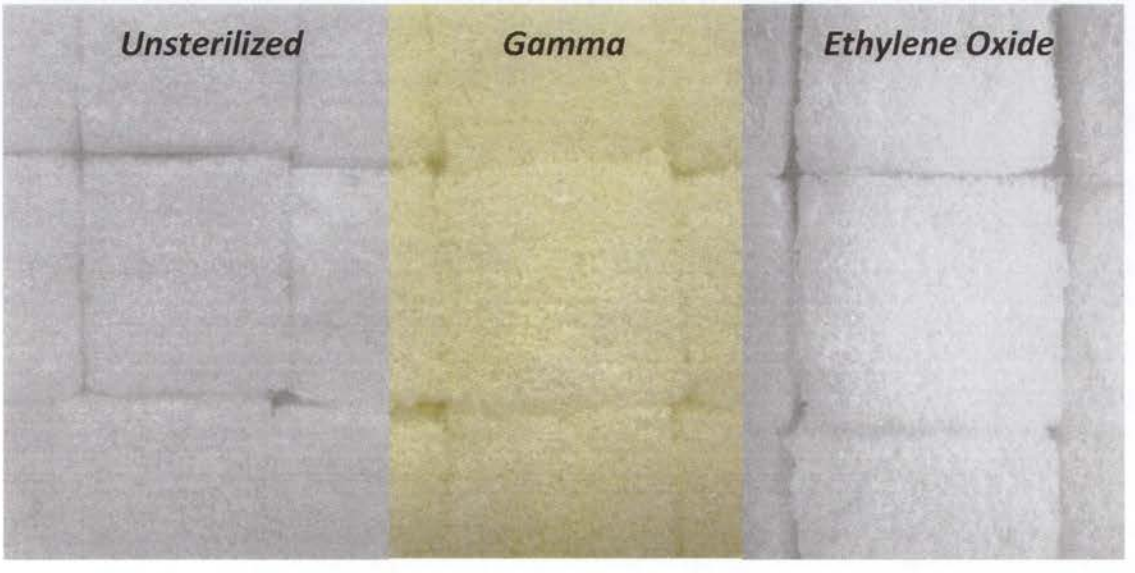


Figure 3.58. Sterilised scaffold samples.



Figure 3.59. Sterilised cylindrical scaffolds for cell culture plates.



Figure 3.60. Glasses sterilized using gamma irradiation.

3.6. MECHANICAL VERIFICATION

3.6.1. METHODS

3.6.1.1. Tensile Testing

Mechanical testing was performed using an electromagnetic multiaxial spine simulator (Bose, Minnesota, USA) or an ELF 3400 Uniaxial Tensile Tester with a load cell of 50 N. All tests were done using a strain rate of 0.5 mm/s, unless otherwise specified. This rate was chosen as it approaches physiological rates of strain for a viscoelastic material (skin) [562]. Uniaxial tensile tests were performed on various scaffolds with dimensions of ~6x10.5 (cross-section) x10 mm (test region length) (Fig 3.61a). Specimens were prepared using Teflon tape to help the grips to attach to the scaffold. Testing was generally performed under standard lab conditions (SLC), although some specimens were analysed under simulated body conditions (SBC). These specimens were immersed in a chamber containing simulated body fluid at 37°C throughout the test.

Data was converted using Excel and stress vs strain curves were obtained for all samples. Various information was obtained using these graphs, including the tensile modulus (linear elastic region, toe region), ultimate tensile strength and extension ratio at failure (Fig. 3.61b). The extension ratio was defined as the ratio between the final and initial length of the sample. This was provided as % (i.e. 100% refers to the original length). The effect of various scaffold forms and sterilisation treatments (as described in Table 3.16) on the tensile properties, were ascertained. At least four scaffolds were tested for each condition and the results were expressed as mean ± standard deviation. Specimens which encountered tearing near the grips were disregarded due to poor specimen mounting.

Table 3.16. Specimen descriptions for mechanical tests.

Scaffold Description	Protocol Ref.	Strain rate
PCL	3.2.2.1.	0.1667, 0.5, 3 mm/s
PCL + 5, 10, 15% 13-93 BG fiber incorporated	3.2.2.2.	0.5 mm/s
PCL + 45S5 powder coating	3.2.2.3C	0.5 mm/s
PCL + 20% 13-93 BG fiber coating	3.2.2.3A	0.5 mm/s
PCL + film	3.2.1.3.	0.5 mm/s
PCL (sterilized- gamma, ethylene oxide,	3.7	0.5 mm/s

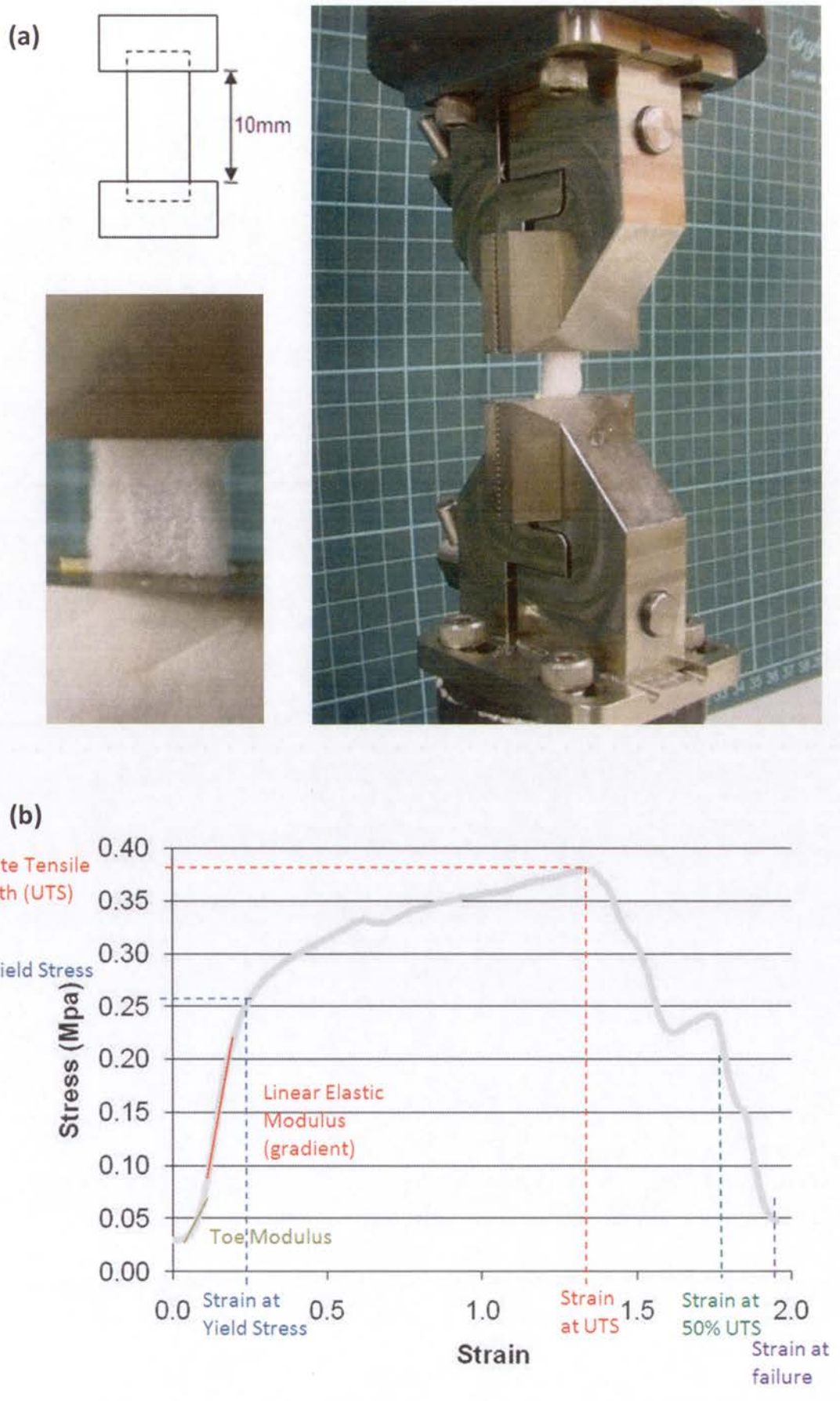


Figure 3.61. (a) Specimen set-up for tensile tests (b) A stress-strain curve from a tensile test depicting regions from which mechanical properties were obtained.

3.6.1.2. Compressive Testing

For compressive tests, scaffolds (dimensions: 10.5x16.5x17.8 mm) were compressed for 6 consecutive cycles at a speed of 0.5 mm/s, to 2 mm [223]. Young's modulus was determined at 20% and 40% strain for the 1st cycle. The dens strength corresponds to the point where the scaffold becomes dense due to compression of the empty pores. It was defined to be the strength which corresponds to the intersection of tangents along the plateau and the dens regions, as shown in Fig. 3.62.

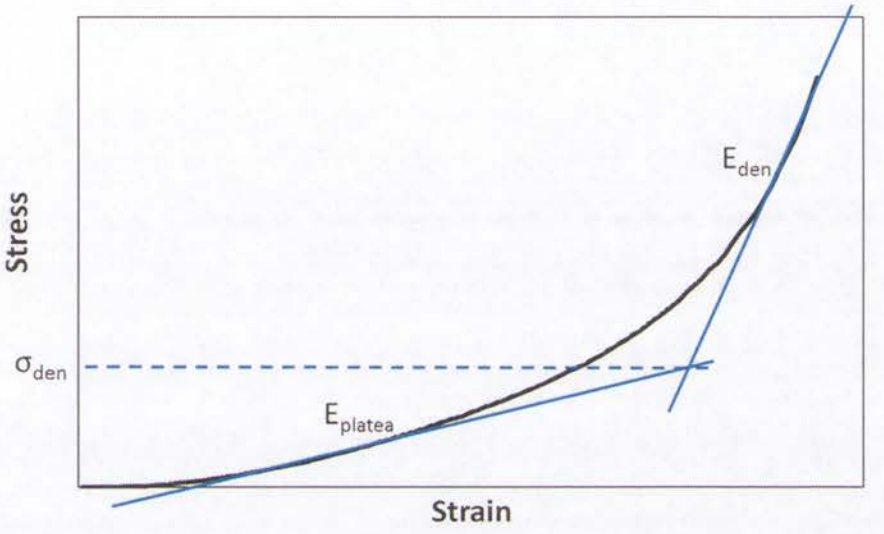


Figure 3.62. A typical stress strain curve obtained from a compression test.

The effect of the addition of bioactive glass to the scaffold and of various sterilisation techniques was determined for each of these values. For some specimens the maximum stress was also determined. Four scaffolds were used for each test and the results are expressed as mean ± standard deviation.

3.6.2. RESULTS

3.6.2.1 Effect of Strain Rate and Test Conditions on Tensile Properties

The stress-strain curve of the scaffolds during tensile testing (Fig 3.63) exhibited a long linear elastic region followed by a gradual decrease in stress, corresponding to gradual breaking of the struts. Extremely high strains were achieved before failure, with many scaffolds demonstrating an extension ratio of almost 400%. This did vary depending on the scaffold batch- with some of the more recently synthesised scaffolds demonstrating a decreased extension ratio (~250%). The scaffolds were highly pliable, being elastic up to 80% strain.

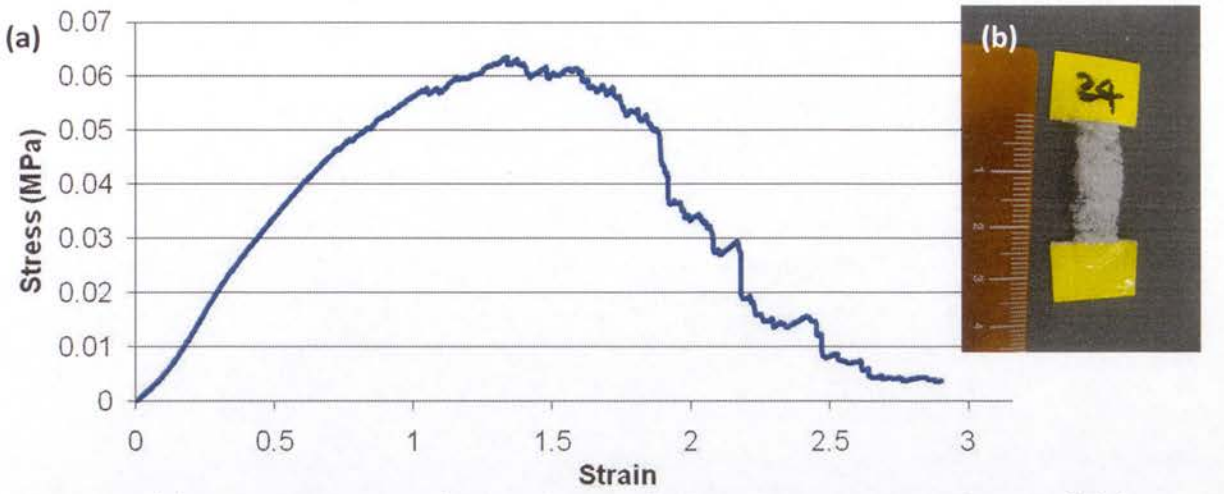


Figure 3.63. (a) A stress-strain curve of a typical PCL scaffold tested at a strain rate of 0.5 mm/s (b) A scaffold after tensile testing.

Fig. 3.64 shows bar graphs of the modulus and UTS obtained for strain rates of 0.1667 mm/s, 0.5 mm/s and 3 mm/s. These results are listed in Table 3.17. The scaffold was the stiffest at 0.5 mm/s; with a linear elastic modulus of ~0.09 MPa. This was almost double the modulus achieved at a strain rate of 0.1667 mm/s. The UTS was similar for all strain rates.

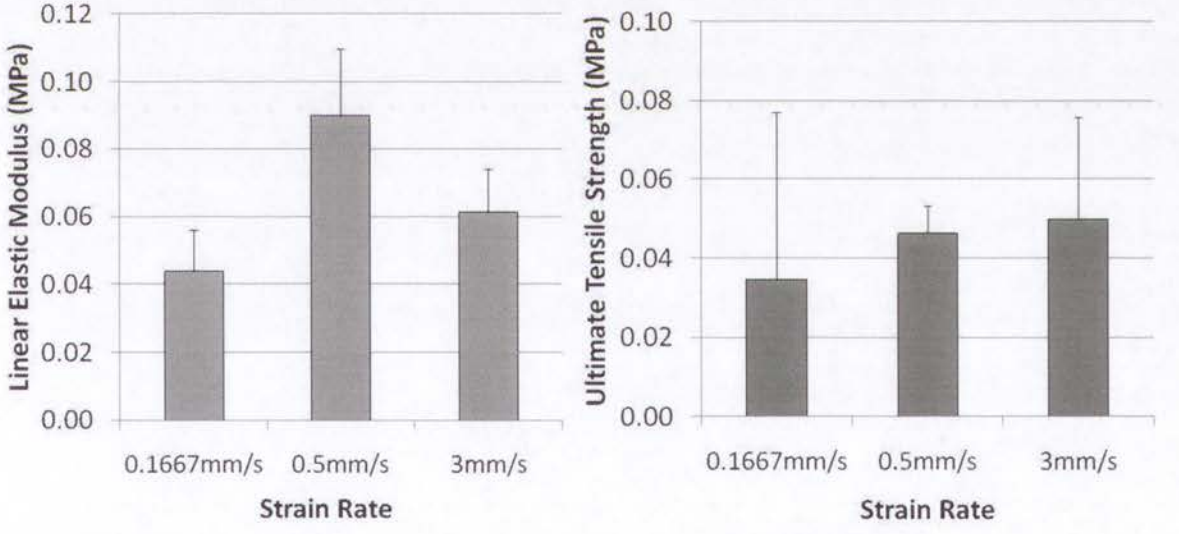


Figure 3.64. Effect of strain rate on tensile properties of the PCL variotis™ scaffold.

Table 3.17. Tensile properties for various strain rates.

Specimen (strain rate)	Ultimate Tensile Strength (MPa)	Linear Elastic Modulus (MPa)	Toe Modulus (MPa)	Extension Ratio (%)
PCL (0.1667 mm/s)	0.0344±0.0425	0.0437±0.0499	0.0251±0.01876	367.5±21
PCL (0.5 mm/s)	0.0464±0.0068	0.090±0.02256	0.0642±0.0188	400±66
PCL (3 mm/s)	0.049±0.026	0.0614±0.0067	0.0579±0.0410	386±38

Under simulated body conditions, the PCL scaffold decreased in stiffness by 1/3, and UTS also decreased (Fig. 3.65). Scaffold dimensions did not change.

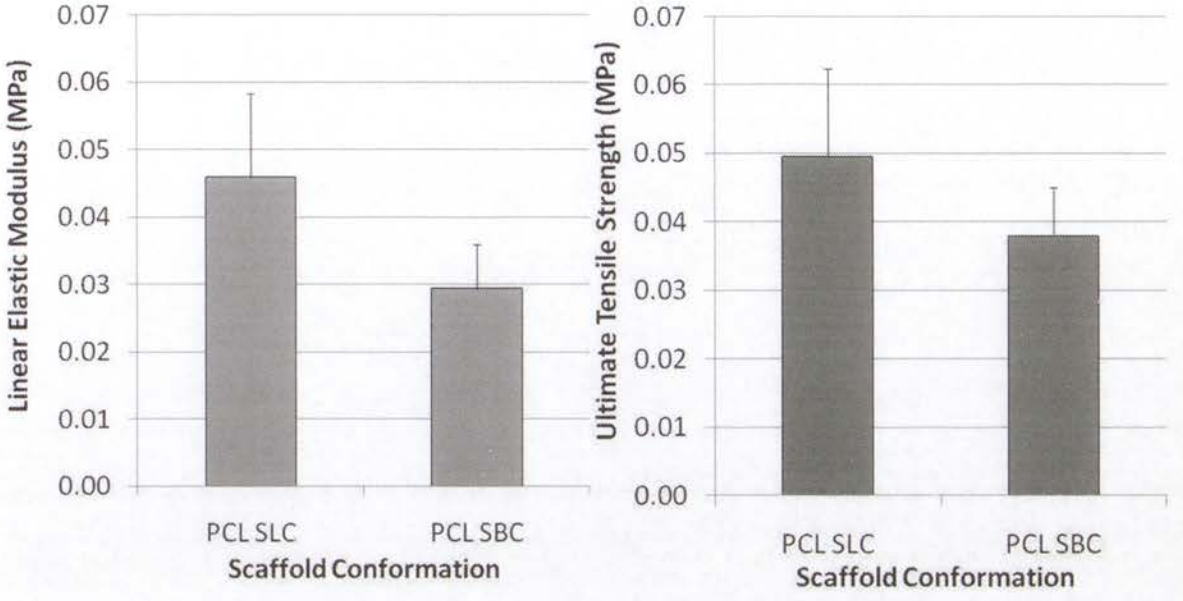


Figure 3.65. Comparison of the modulus and strength of variotis™ scaffolds under different environmental conditions.

3.6.2.2. Effect of Glass Filler on Mechanical Properties

Mechanical properties of the variotis™ scaffold were compared when bioactive glass was added to the matrix via inclusion during polymer processing or via coating. Incorporation of 5 or 10% 13-93 short fibers into the PCL matrix during solvent dissolution (ref 3.2.2.2) (Fig. 3.66, Table 3.18) resulted in little change to the elastic modulus or UTS. A marked decrease was noted for 15 wt% glass filler, with the modulus and UTS decreasing by approximately half.

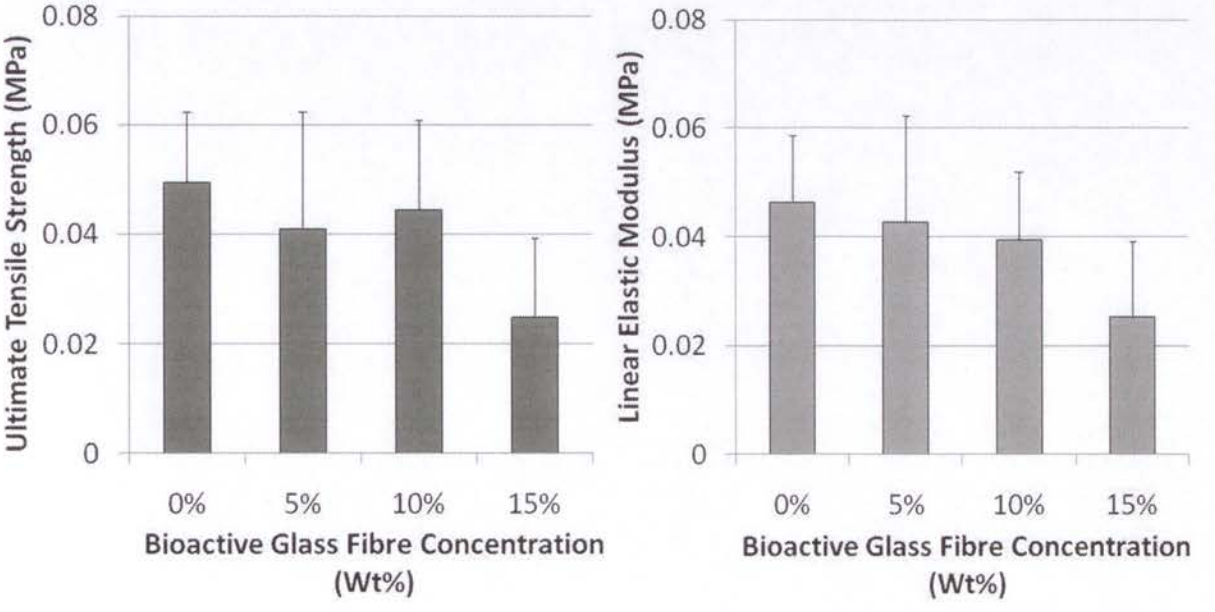


Figure 3.66. Effect of 13-93 glass incorporation (5, 10, 15%) in the PCL matrix on the scaffold mechanical properties.

Table 3.18. Effect of glass incorporation on the tensile properties.

Specimen	Ultimate Tensile Strength (MPa)	Linear Elastic Modulus (MPa)
PCL	0.049±0.013	0.046±0.012
PCL+ 5% BG fiber incorporation	0.041±0.021	0.043±0.020
PCL+ 10% BG fiber incorporation	0.0445±0.0163	0.039±0.013
PCL+ 15% BG fiber incorporation	0.025±0.0144	0.0253±0.014

3.6.2.3. Effect of Glass Coating on Mechanical Properties

Shown in Fig. 3.67 and Table 3.19, coating with 10 wt% Bioglass® particles (ref 3.2.2.3C) resulted in little change to the tensile properties of the scaffold. No change was observed in the extension ratio either.

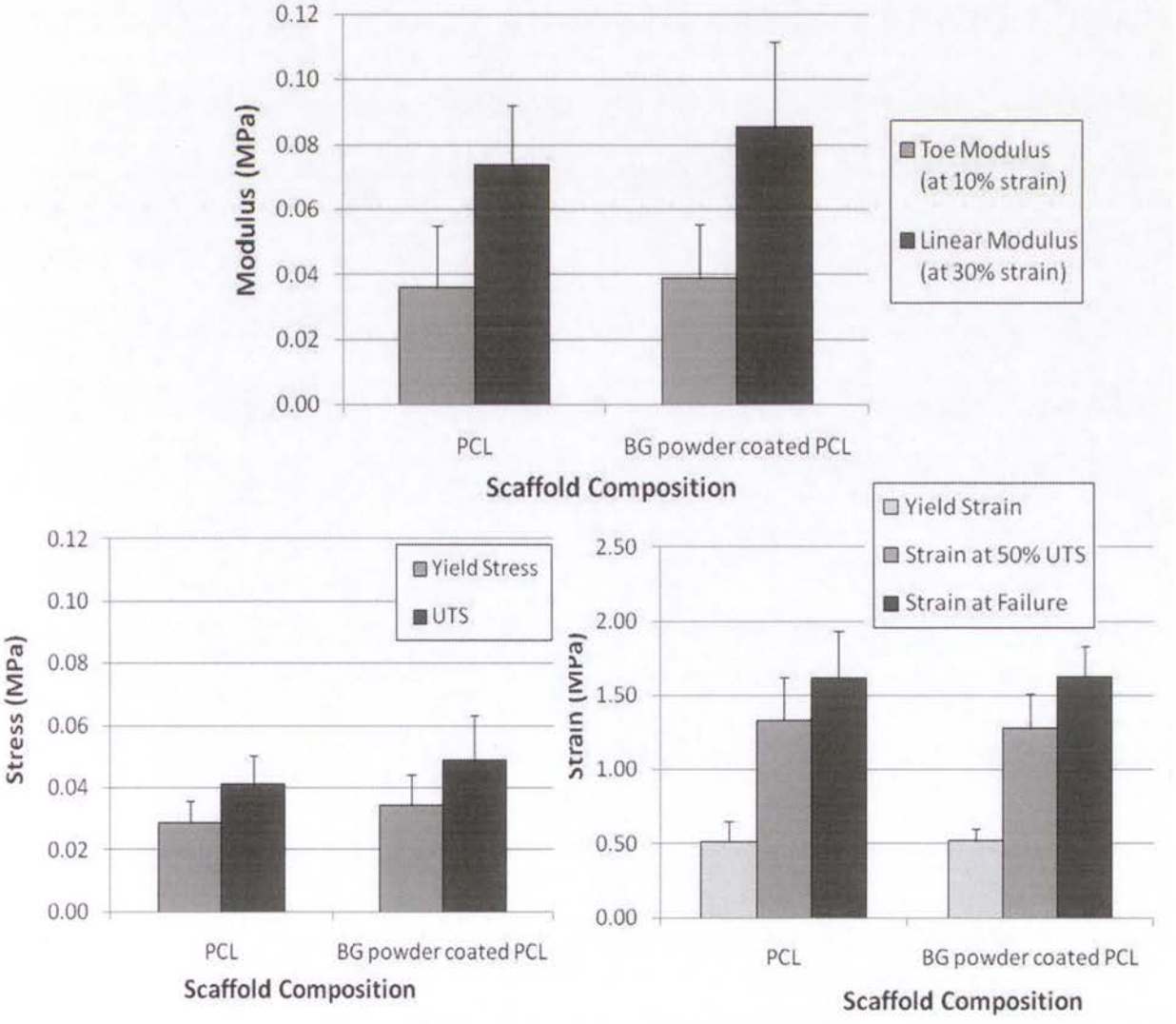


Figure 3.67. Tensile properties of PCL scaffolds after coating with 10% 45S5 powder.

Table 3.19. Tensile properties for the BG powder coated scaffolds.

Specimen	Ultimate Tensile Strength (MPa)	Linear Elastic Modulus (MPa)	Elongation Ratio
PCL	0.049±0.013	0.046±0.012	340±24.5
PCL + BG powder coating	0.049±0.014	0.039±0.017	263±20

The results for the compressive tests are shown in Fig. 3.68 and Table 3.20. For the bioactive glass powder coated scaffolds, no change was measured in compressive properties.

After cycling compression to 20% of the original height, a stabilisation in the permanent compression set was achieved within 3 cycles (Fig. 3.69). The compression set was 28% of the original height after 6 cycles.

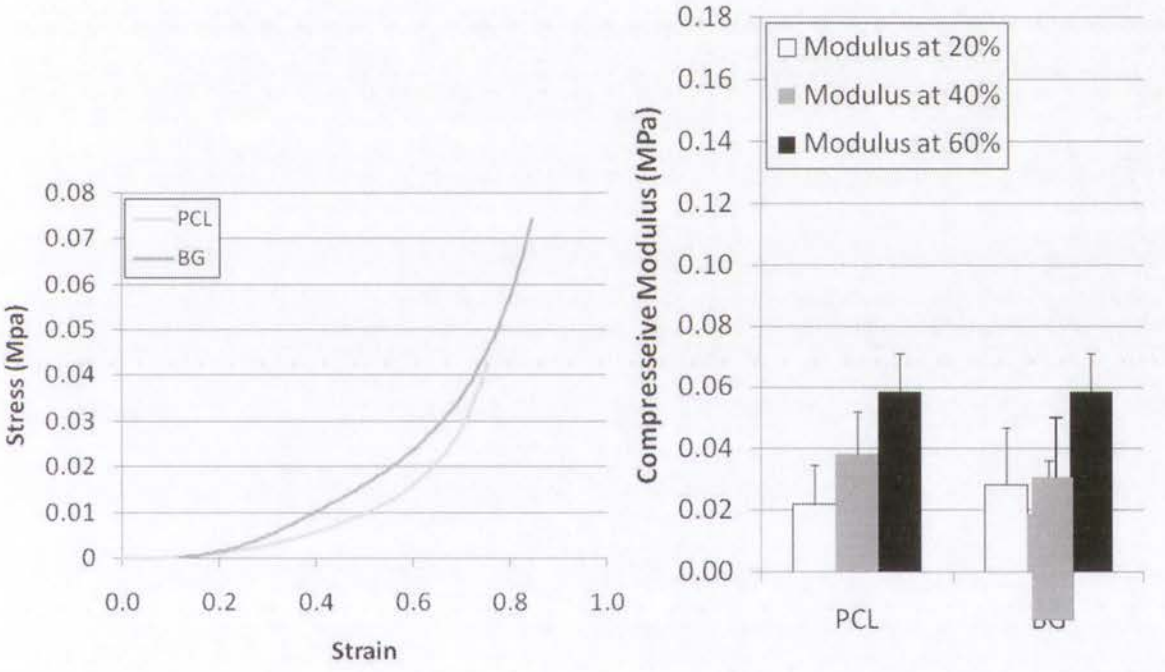


Figure 3.68. The compressive stress-strain compression curve and associated moduli for the PCL and the BG powder-coated scaffolds.

Table 3.20. Compressive properties for the PCL and glass-coated scaffolds.

Specimen	Compression Modulus @20% (MPa)	Compression Modulus @40% (MPa)	Compression Modulus @60% (MPa)	Densification Point- σ_{dens}
PCL	0.21±0.014	0.039±0.014	0.059±0.013	0.018±0.008
PCL + BG powder coating	0.027±0.020	0.047±0.029	0.059±0.013	0.0234±0.015

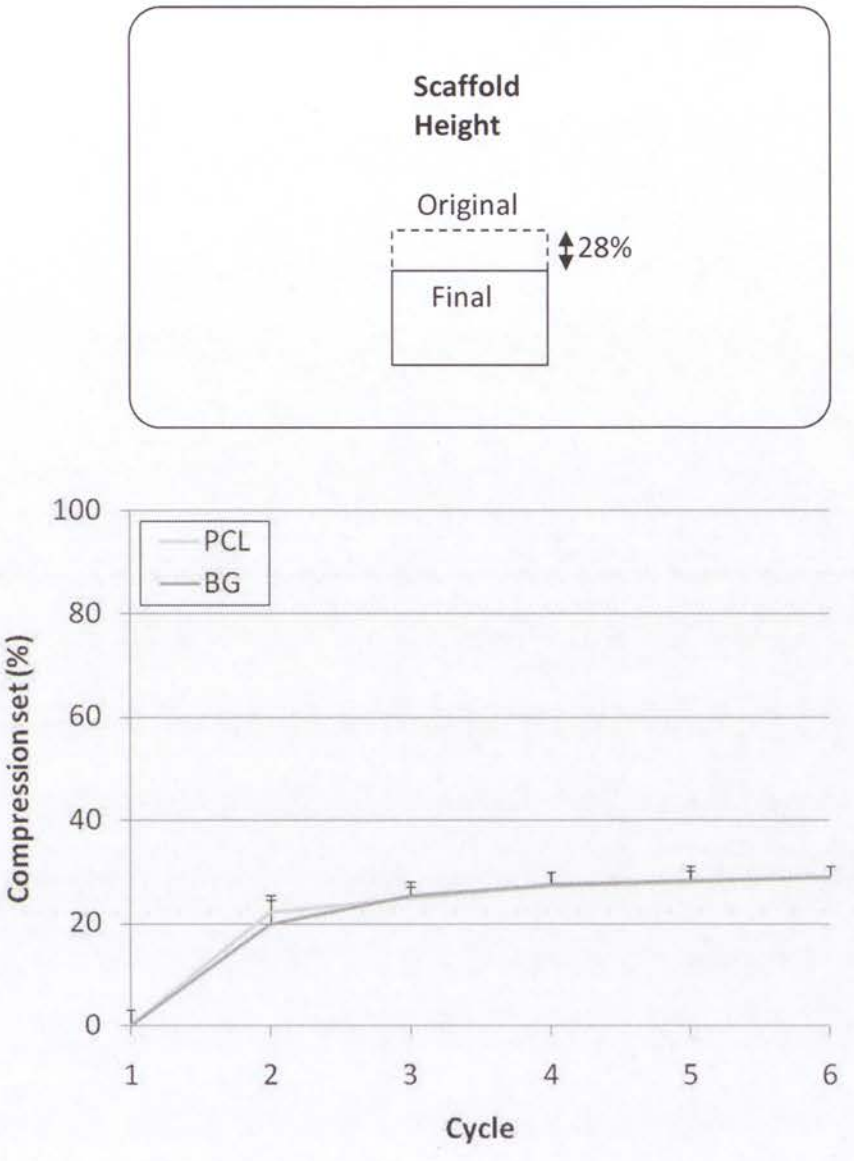


Figure 3.69. Compression set values for the PCL and 10% BG powder coated scaffolds over 6 cycles.

3.6.2.4. Methods to Enhance Variotis' Stiffness

Shown in Fig. 3.70 and Table 3.21, a marked increase in modulus and UTS was achieved when the scaffolds were coated with 20% glass fibre or attached to a thin PCL film. For the scaffolds with the thin films, the modulus increased ~3500%, while the UTS increased >1200%. For the fiber coated specimens, the modulus increased >18000x, while the UTS increased 230x. Addition of a thin PCL film to one edge of the scaffold (ref 3.2.1.3) also resulted in increases to the modulus and UTS (13 and 35% respectively). These changes both led to a decrease in the extension ratio.

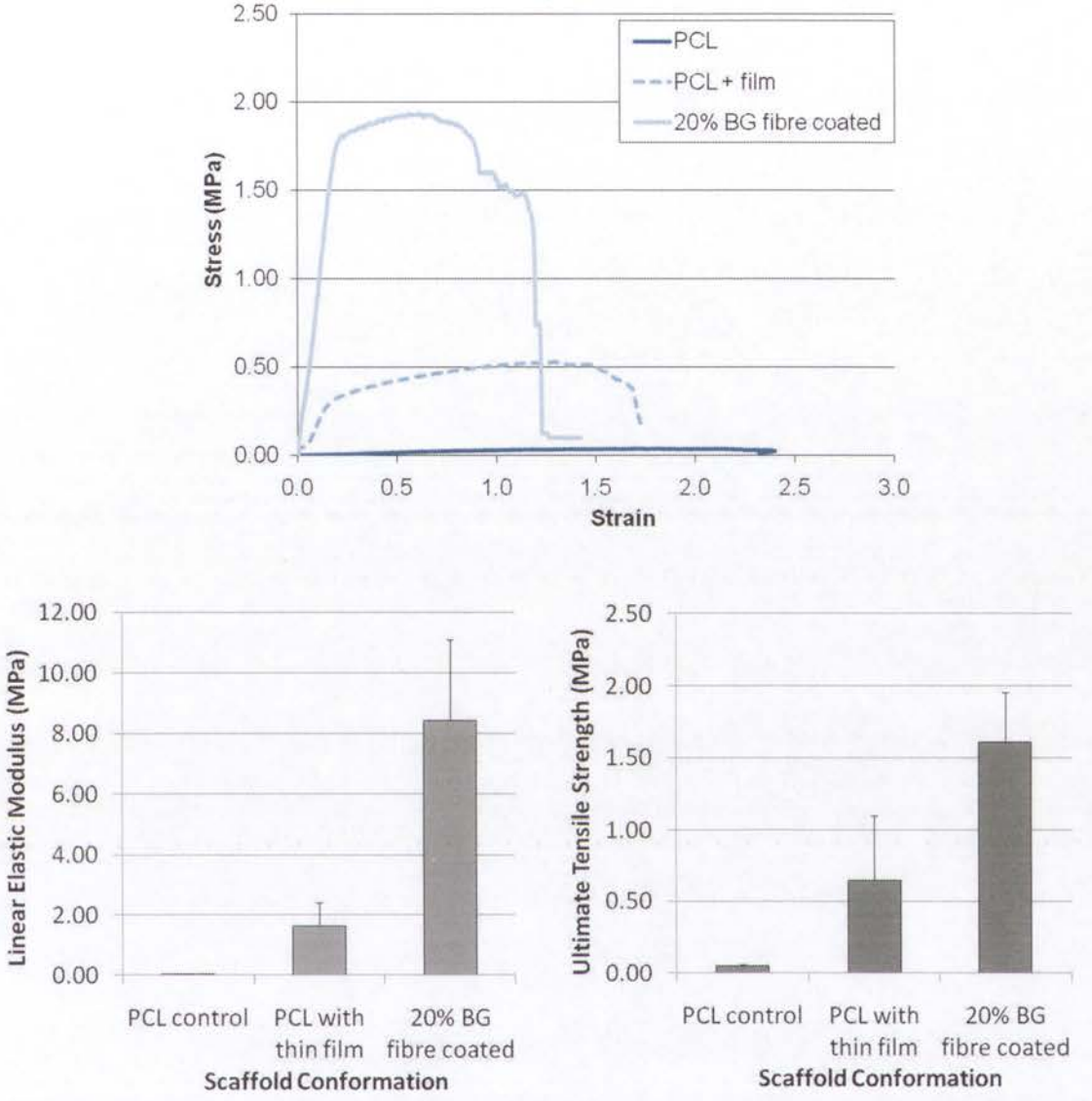


Figure 3.70. Addition of a thin PCL film or coating with 20% bioactive glass fibers demonstrated the wide range of mechanical properties which the Variotis™ scaffold may demonstrate.

Table3.21. Tensile properties of scaffolds which had been coated with BG or attached to a thin PCL film.

Specimen	Linear Elastic Modulus (MPa)	Ultimate Tensile Strength (MPa)	Elongation Ratio (%)
PCL	0.046±0.012	0.049±0.013	340±24.5
PCL + film	1.632±0.764	0.648±0.451	265±25.1
PCL + 20% BG fiber coated	8.431±2.685	1.610±0.035	229±18.6

3.6.2.5. Effect of Sterilisation on Mechanical Properties

The results for the tensile tests on sterilised scaffolds are shown in Fig. 3.71 and Table 3.22. Ethanol and UV radiation caused an increase in the linear elastic modulus. While UV showed little change to the UTS, ethanol treatment decreased the UTS by 30%. 25kGy Gamma increased the modulus by 10.4% but decreased the UTS by 30%. Ethylene Oxide exhibited the most change in modulus (131%), however showed only a 25% decrease in modulus. All treatments also reduced the elongation ratio. The most change was seen for the ethanol treated sample, and the least change was observed for the ethylene oxide sterilised scaffolds.

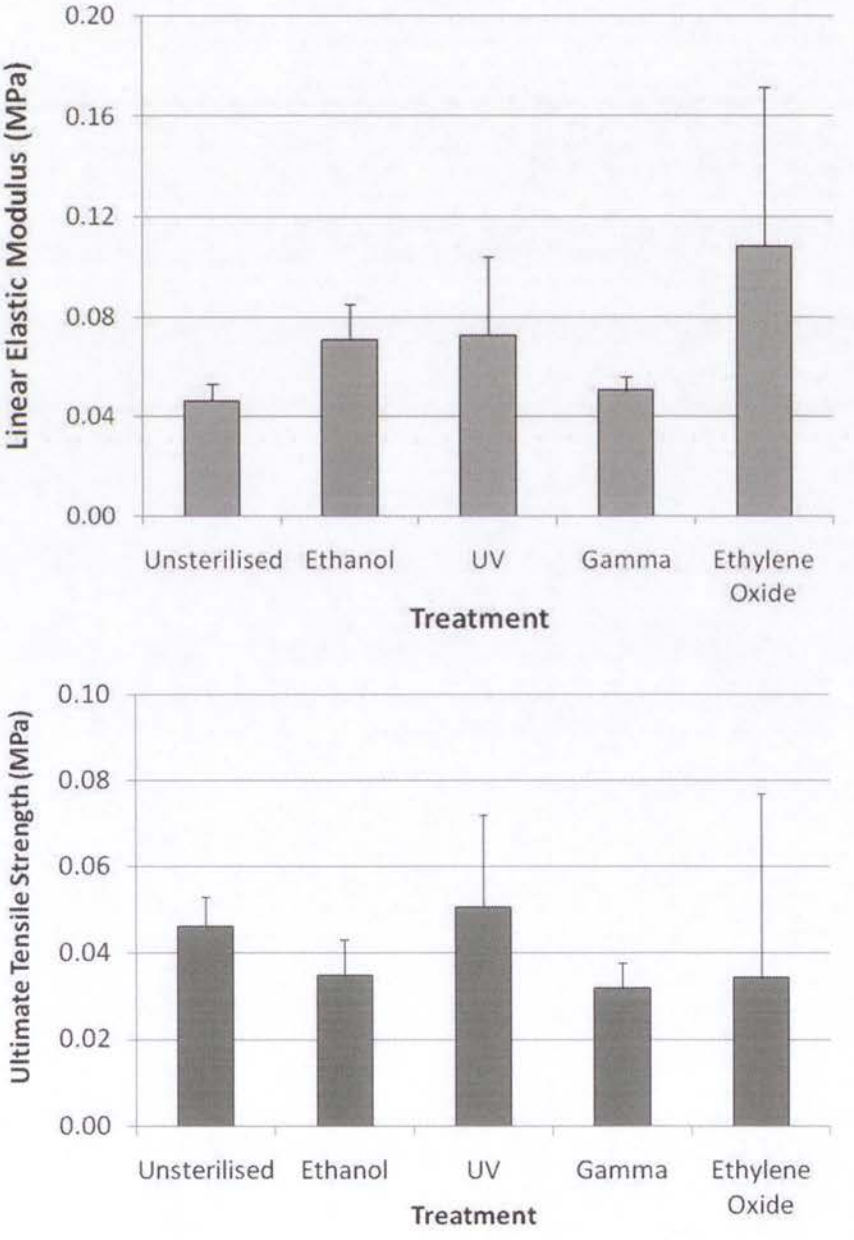


Figure 3.71. UTS and Linear Elastic Moduli calculated for Variotis™ scaffolds which had experienced sterilisation treatments.

Table 3.22. Tensile properties for the sterilised scaffolds.

Specimen	Linear Elastic Modulus (MPa)	Ultimate Tensile Strength	Extension Ratio (%)
PCL	0.048±0.072	0.047±0.096	340±24.5
PCL (Ethanol)	0.071±0.163	0.033±0.091	289±24.9
PCL (UV)	0.076±0.031	0.041±0.213	314±29.7
PCL (Gamma)	0.053±0.05	0.033±0.072	298±27.6
PCL (Ethylene Oxide)	0.111±0.058	0.035±0.425	320±22.6

Figure 3.72 shows a typical stress-strain curves for the sterilised scaffolds. The elastic modulus, as calculated at 20 and 40% strain, are included in Fig. 3.73. Table 3.23 shows the values for the compressive moduli as well as the densification point. Gamma sterilisation led to an increase in modulus (34% at 40% strain) and densification strength (22%). With ethylene oxide treatment, the compressive modulus increased by 21% (at 40% strain) and the densification strength decreased by 15%. UV radiation increased the modulus by 22% and the densification strength by 15%.

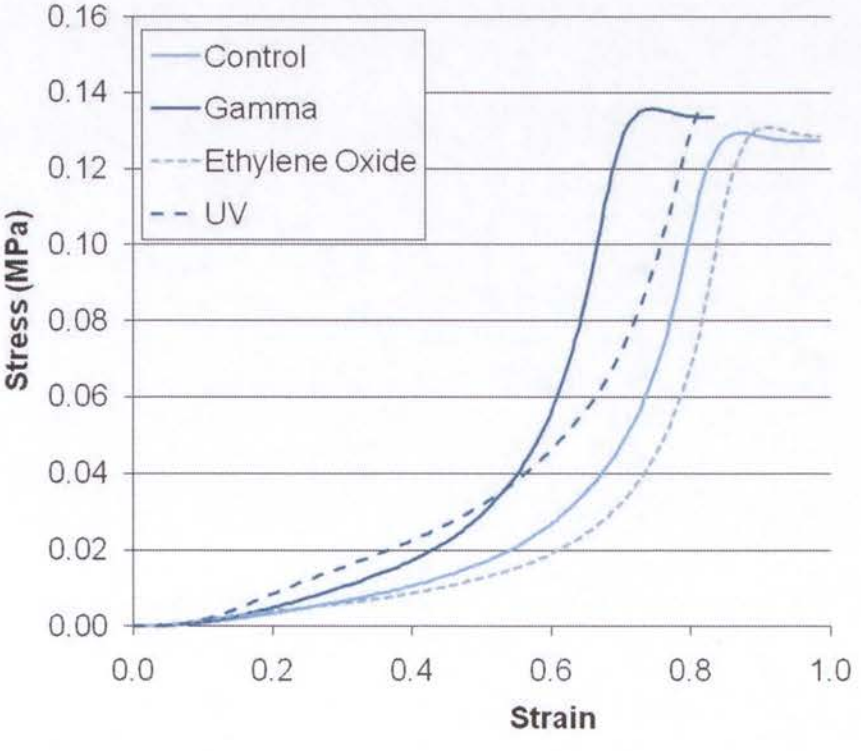
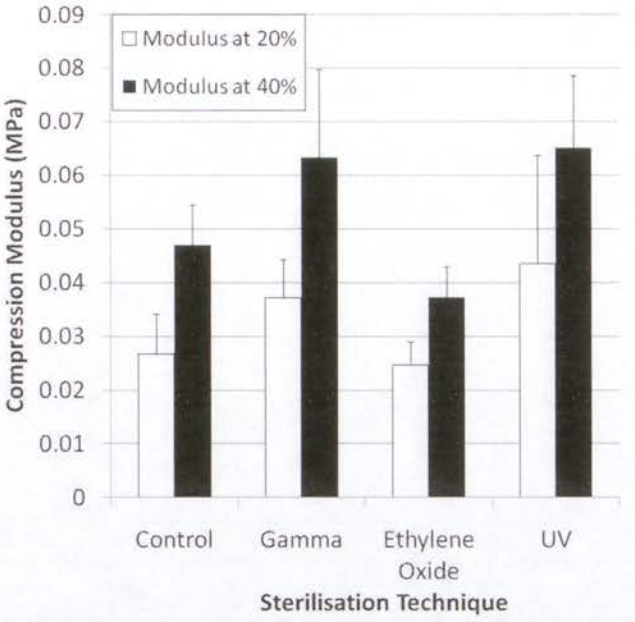


Figure 3.72. Stress- Strain curve for sterilised scaffolds during compression tests.



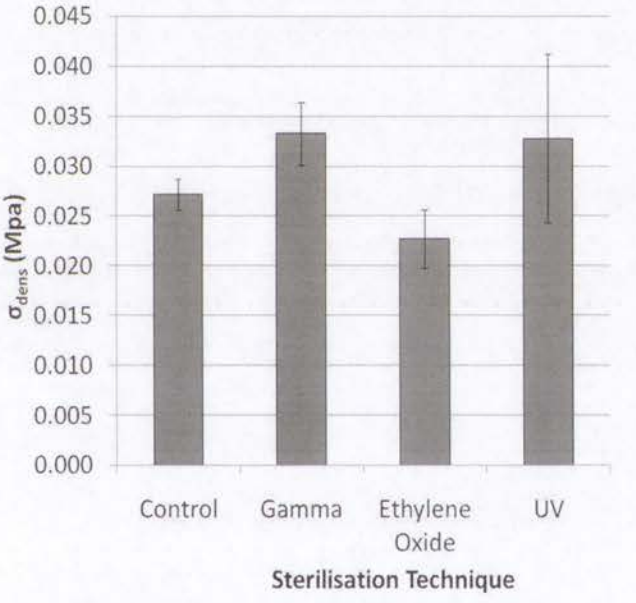


Figure 3.73. Compression Moduli and densification points for sterilised PCL scaffolds.

Table 3.23. Compressive properties for sterilised scaffolds.

Specimen	Compression Modulus (20%)	Compression Modulus (40%)	Densification Point- $\sigma_{dens)}$
PCL	0.027±0.0074	0.047±0.0075	0.027±0.0015
PCL (Gamma)	0.037±0.0722	0.063±0.0165	0.033±0.0032
PCL (Ethylene Oxide)	0.025±0.0433	0.037±0.0059	0.023±0.0029
PCL (UV)	0.044±0.020	0.065±0.013	0.033±0.0084

3.6.2.6. Extension Ratio Comparison

Fig. 3.74 shows a comparison of the extension ratios for the scaffolds from the previous sections. All of the scaffold treatments resulted in a decrease in extension before failure. In particular, coating the scaffolds with bioactive glass resulted in the highest restriction to the strain.

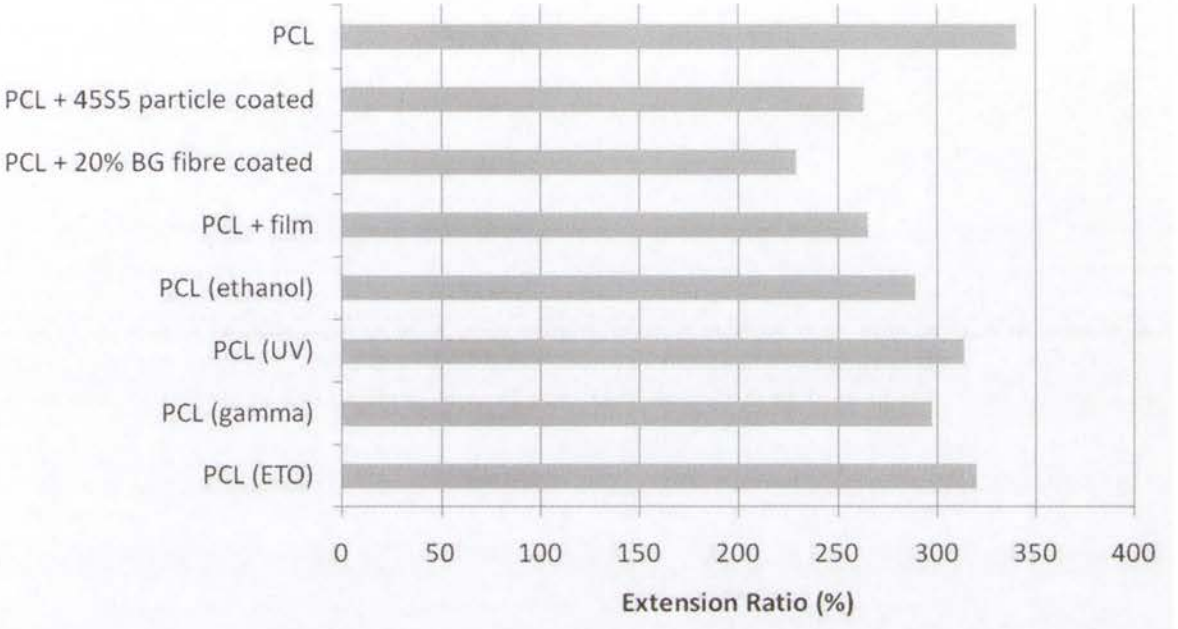


Figure 3.74. Extension ratio for various scaffold conformations and sterilisation treatment.

3.6.3. DISCUSSION

Mechanical testing of the variotis™ scaffold demonstrated an elastic nature with high capacity to strain before failure. This was whilst possessing the ability to absorb compressive stress and regain most of its original shape after being subjected to compressive or tensile strains.

3.6.3.1. Influence of Test Conditions during Tensile Tests

The variotis™ scaffold was easy to mount and test in both compression and tension. The rapid and convenient synthesis process ensured there were many samples available for a variety of tests. Other scaffolds, such as hydrogels, are difficult to mount in the test grips due to their fragility or high water content. Long processing times and expensive compositions often lead to limited sample numbers which can lead to inaccurate mechanical data.

Mechanical properties must be investigated over time and under different conditions (e.g. speed, temperature, moisture). In this study, variation of strain rate (0.167, 0.5, 3 mm/s) did not change the UTS, but altered the elastic modulus (Fig 3.64). The modulus at 0.5 mm/s was almost double for 0.167 and 3 mm/s. Many physiological motions occur at rates which

approach 1Hz (1 cycle/sec). For movement such as breathing or walking, this is at least 0.5 mm/sec (30 mm/min). This is much faster to 1 mm/min which is often specified for standard materials testing. Previous tissue and engineered grafts have also been tested using 30 mm/min [622]. Changing the strain rate gave the standard response for a viscoelastic polymer. A strain rate was chosen that would be comparable across various materials. The effect of temperature and liquid on the tensile properties of the variotis™ scaffold was also investigated (Fig 3.76). A <30% decrease in modulus and tensile strength was measured. Scaffold properties may change dramatically under physiological conditions. The presence of short-chain lipids and polymers in the body can alter the behavior of many polymers. Ingress of these substances can result in a softening of the polymer, and ultimately cause crosslinking- resulting in a hard and brittle material which may degrade sooner. The variotis™ scaffold is less susceptible to these changes than polymers based on lactic/glycolic acid or hydrogels.

3.6.3.2 Variotis™ has a High Capacity for Tensile Strain

The unique interpenetrating structure of the variotis™ scaffold provides it with a high capacity to strain before failure. Figure 3.81 demonstrates variotis™ high extension ratio (up to 400%) when compared to other scaffolds from the literature. The only scaffold in this figure which surpassed this strain was a PLCL fibrous mesh which achieved an extension ratio of 600%, however, this strain was only in one direction. Many electrospun and woven fiber scaffolds also experience most of their strain in one or two directions. Rapid prototyped PCL and PGA woven-fibre reinforced agarose demonstrate extremely low levels of extension (100.10 and 127% respectively). The variotis™ scaffold has the ability to strain equally in 3D, an important quality for many tissue engineering applications.

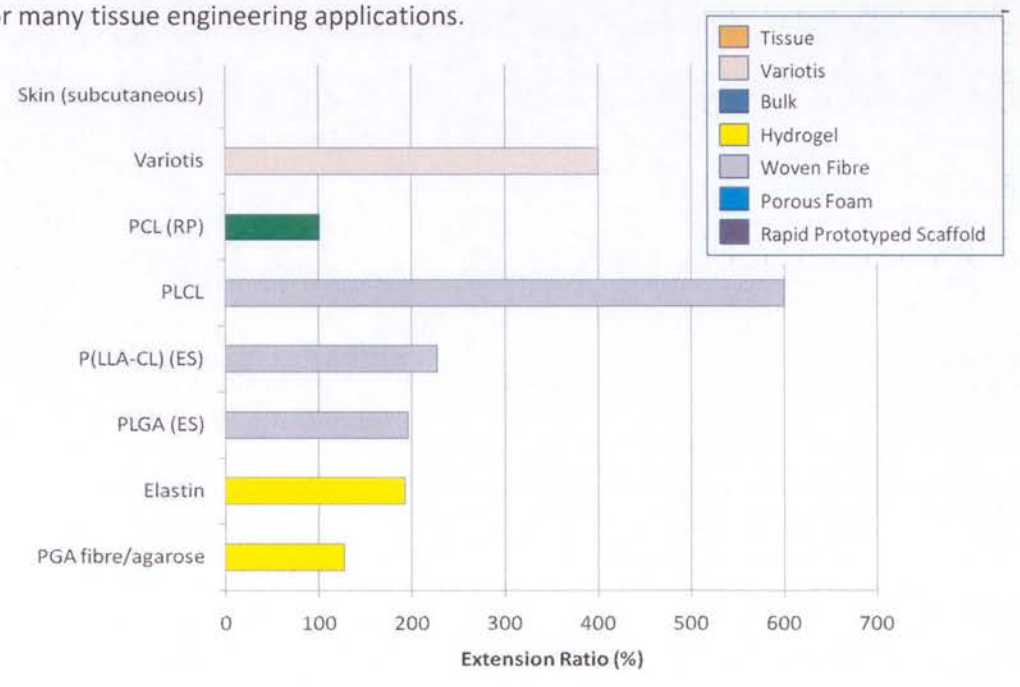


Figure 3.75. Extension ratio of scaffolds (ref's provided in Table 3.7). RP: Rapid Prot., ES: Electrospun

3.6.3.3. Variotis™ has a High Capacity to Return to its Original Shape and Resists Tearing

During tensile testing, variotis™ displays a long linear elastic zone during which it is able to return to its original shape upon removal of the tensile load (Fig 3.62). After this, it enters a shorter region of permanent (plastic) deformation from which it cannot recover. The high elastic region is due to properties of the PCL, as well as the high porosity and thin struts, which enable high strain of the scaffold as a whole. After the ultimate tensile strength is reached, the scaffold does not suffer catastrophic failure, but instead the individual struts stretch further and experience uncoiling, necking and strain hardening (increase in crystallinity) before gradually breaking. Furthermore, due to the microporosity, individual struts also act as an elastic, cellular solid and display a high level of elongation. Thus the structure of variotis™ can hold a higher level of stress over a longer elongation than many other structures. When filled with tissue, the scaffold would act as a reinforcing network which would prevent tearing of the tissue itself. Crack propagation through the scaffold would not be a problem, as it is with many hydrogels.

3.6.3.4. Comparison of Tensile Properties to Literature

The base variotis™ scaffold demonstrated a low elastic modulus and ultimate tensile strength. This was anticipated to be beneficial for facilitating stress transfer to the developing tissue (preventing stress shielding), whilst reducing the risk of fibrous encapsulation or ulceration. This would increase the lifespan of the scaffold and improve the strength and health of the wound. *In vivo* cyclic loading and hydrostatic pressure is likely to lead to an increase in crystallinity and thus increase the strength of the polymer further.

Fig. 3.76 contains a comparison of the elastic modulus and ultimate tensile strength of variotis™ compared to scaffolds from the literature, of various forms and compositions. On this graph, values were included for the mechanical properties of the 'bulk material' of the scaffold. This took into account the highly porous nature of the scaffold (~95%). Properties were multiplied by approximately 20 to find this value. Taken together, the forms of the variotis™ scaffold showed the ability to be tailored to possess a wide range of properties. The basic variotis™ scaffold displayed a low elastic modulus and ultimate tensile strength, which is of the same order of magnitude to soft collagen and elastin-based scaffolds [614, 619] (Fig. 3.72). When a thin PCL film was added to the scaffold or BG fiber coating was used, the properties approximated that of a PLCL fibrous mesh. This graph includes some stiff, strong scaffolds such as electrospun P(LLA-CL), rapid prototyped PCL and electrospun PLGA which may be mechanically more suited for bone, or perhaps ligaments/tendons, but unsuitable for subcutaneous connective tissue applications.

3.6.3.5. Effect of Glass Filler or Coating on Tensile Properties

For glass fiber filled scaffolds, the tensile strength and modulus showed little change for concentrations of 5 and 10 wt%. However for 15 wt% (as is expected for greater concentrations), a substantial decrease (50%) in strength was evident. It is likely that for concentrations approaching and exceeding 15% the fibers cause defects within the scaffold. This many not necessarily become a problem for the variotis™ scaffold if utilized within connective tissues that mechanically adhere to Bioglass and provide a complimentary mechanical couple. With glass powder coating, the tensile properties did not alter.

This constitutes a substantive finding: that the bioactivity of the scaffold can be adjusted without deleterious effects on the scaffold mechanical properties. Furthermore, the coating method ensures that most of the surface area interfacing with soft tissue is bioactive glass. These findings are typical of what would be expected for microsized particles [568]. Stiffening may result if nanosized particles of a higher proportion are used [568]. Some previous studies have a reported mechanical damage caused by dry glass coating techniques [561]. Boccaccini and coworkers found their bioactive glass coatings decreased the tensile strength of Vicryl sutures [153]. The risk of inducing mechanical damage on scaffolds is avoided with the coating methods outlined in this chapter.

3.6.3.6. Effect of Sterilisation on Tensile Properties

These results indicate the importance of testing scaffolds for changes to their physical behavior after sterilisation procedures. Whilst PCL shows higher levels of resistance to changes when compared to many other polymers [608], important polymer-dependent changes can still be induced which must be considered in the scaffold design. Whilst glassy natured polymers such as UHMWPE tend to exhibit an increase in strength, those which have a low glass transition temperature tend to show a decrease in strength and become embrittled [608]. Goma and coworkers [608] measured a decrease in tensile strength (12%) in PCL scaffolds after irradiation with 25 kGy Gamma, corresponding to a decrease in molecular weight (12-30%). The PCL scaffolds in our study experienced an even more pronounced decrease in tensile strength (30%). This indicates embrittlement due to microdefects which are exacerbated by the increase in rigidity due to crosslinking. Changes in the mechanical properties due to UV radiation have also been reported in the literature. A reduction of 28% in the UTS of P(LA-CL) nanofiber scaffolds was found by Yixiang and coworkers. This is very similar to our result (30% decrease).

Although some studies have reported no change in the tensile properties of PCL after ethylene oxide [629], others have reported significant changes. Burks and coworkers [620] reported a

268x increase in modulus and 28% decrease in UTS when thin PCL films (0.5-1.5 mm) were sterilised using ethylene oxide. Very similar trends were observed in the current study. These findings may be in part due to an increase in crystallinity, which has been reported for PCL [629]. In addition, heating of the specimen during the sterilisation process was likely to close of some of the micropores. This probably increased the modulus and led to a high standard deviation. Specimens may have been be subjected to temperatures of up to 50°C during the degassing process in order to remove residues of the highly toxic ethylene oxide [586, 588, 602].

In compression, the effects of embrittlement due to microdefects that are obvious in tensile or flexural modes of loading are not as obvious. Crosslinking induced by irradiation increases the stiffness of all materials. In compression we therefore saw an increase in modulus after gamma and UV radiation. The closure of some micropores due to heating during ethylene oxide processes also increased the compressive modulus.

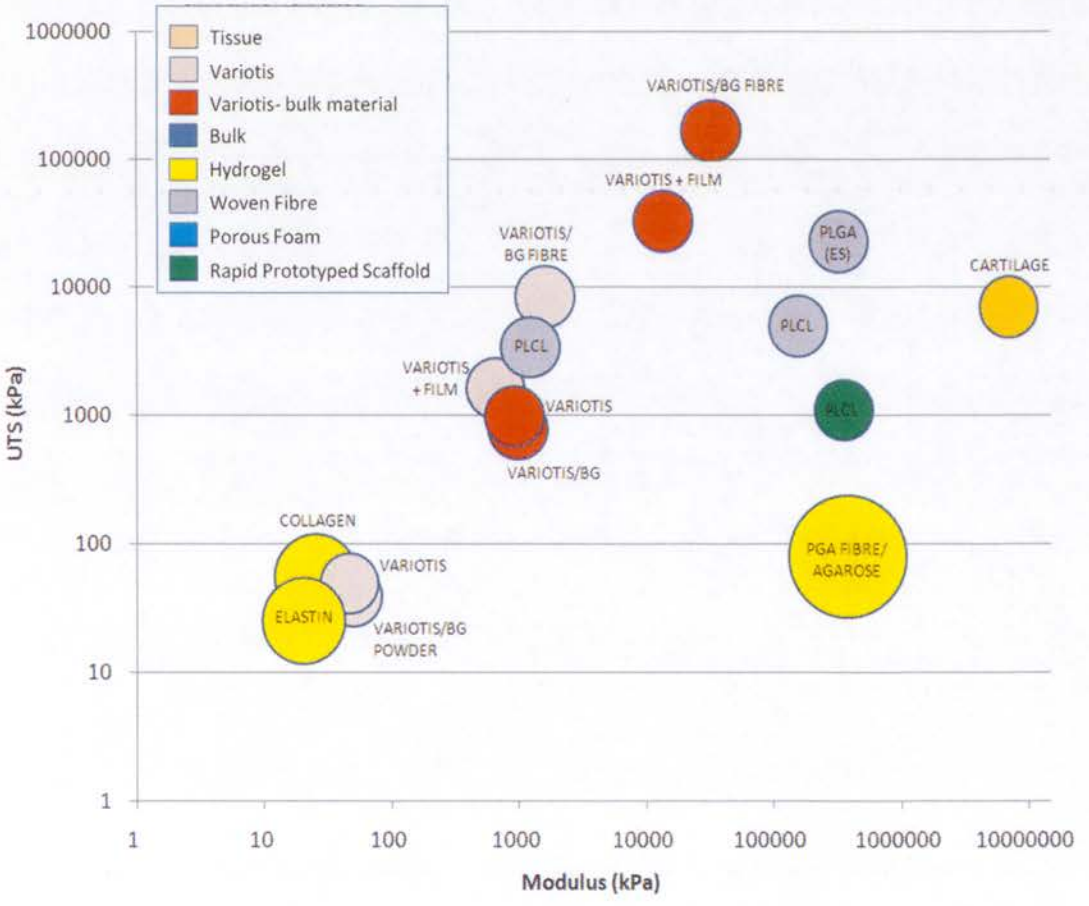


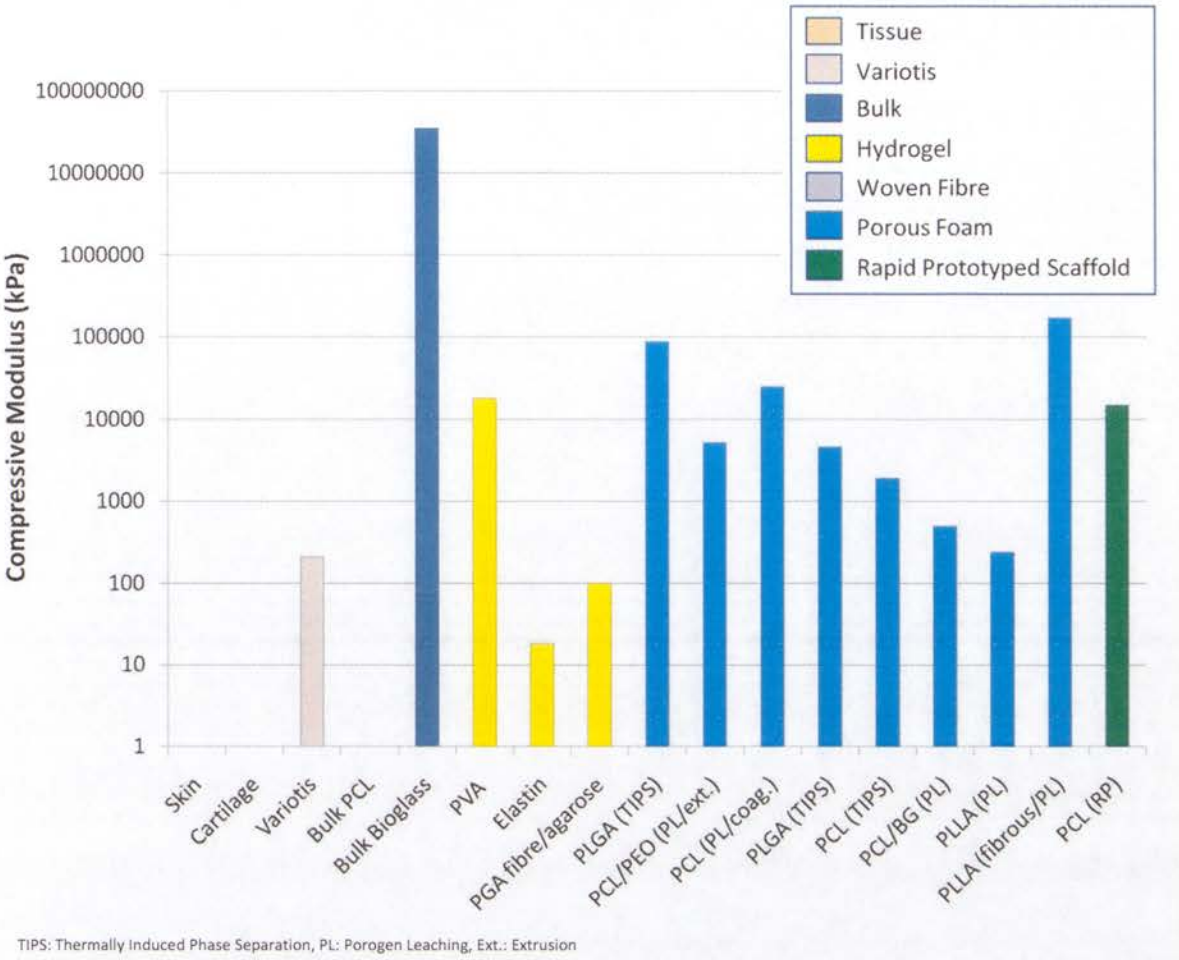
Fig. 3.76. Ultimate Tensile Strength vs modulus for a range of variotis™ scaffolds and other scaffolds from the literature (references listed in Table 3.8).

3.6.3.7. Comparison of Compressive Properties to Literature

The compressive modulus of variotis™ (0.29 MPa) was 2-3x lower than many of the scaffolds reported in the literature (e.g. PLGA) 394, 545, 614, 622] (Fig 3.77). In compression, variotis™ was 2x more supportive than elastin scaffolds. Although variotis™ has a compressive modulus the same order of magnitude as some PLLA scaffolds and PGA fibre-reinforced agarose, it much higher levels of extension, as mentioned earlier. With the addition of glass powder coating, no change was noted in compressive properties. This was different to previous results which have found a stiffening effect from the glass [153]. The high stiffness achieved by the glass fiber coating contrasts with the results from the glass powder coated/filled scaffolds and is in line with previous findings [153]. This highlights the vast effect that the shape and size of the glass particles, and the method of glass addition may have on the scaffold properties [547].

The shape of variotis' compression curve was different to many polymeric foams [613]. The scaffold in the current study showed gradual linear elasticity over the majority of the strain, with three regions identified (20, 40, 60% strain). Following this is a rapid increase in stress corresponding to the scaffold densification. The variotis™ scaffold is easily compressible- with densification occurring at a strength of ~180 kPa. This behaviour is different to closed-cell foams, which are filled with air which cannot escape. This leads to linear elasticity for low strains, followed by a long collapse plateau before the scaffold densification [549]. Such scaffolds are initially relatively rigid, and then during the collapse plateau do not have any resistance to further deformation and become unstable. Although initially pressure concentrates on the outer edges of the foam, allowing a higher load to be borne, ultimately such a structure collapses.

In contrast, variotis™ gradually increases in the resistance it offers the surrounding tissue. This mimics physiological behavior, where the structure allows for movement but also provides support. *In vivo*, variotis™ scaffold is likely to rapidly fill with liquid and thus be incompressible- increasing its stiffness and load-bearing capability. This property may be utilised in hydrated tissue such as the nucleus pulposus of the spinal disk. Similarly, when filled with blood vessels, collagen and wound fluid in the skin, the variotis™ scaffold has the capacity to provide superior compressive support. In this way the highly porous and interconnective nature of variotis™ actually provides more support to new tissue than water or air-filled closed-celled scaffolds, which reach a maximum compressibility and experience failure *in vivo*.



TIPS: Thermally Induced Phase Separation, PL: Porogen Leaching, Ext.: Extrusion

Figure 3.77. Comparison of compressive moduli with variotis™ and other scaffolds from the literature (references included in Table 3.9)

3.6.4. SKIN ULCER CLINICAL CONCEPT

The variotis™ scaffold platform has been proposed for clinical use in a graft for persisting skin wounds such as diabetic foot ulcers or pressure sores by use as a dermal graft. This graft could be acellular or precultured with stem cells. The scaffold could be infused a layer of antibiotics, a coherent nanofilm of either biostable or bioabsorbable metal (e.g. bulk metallic glass-ref section 4.1.3). The bioabsorbable metal (Mg based metallic glass) will also be antibacterial and disrupt biofilms (ref Fig. 3.78a). Bioactive silicate glass is incorporated into the polymer matrix to impart further antibacterial activity and soft tissue conduction (ref section 4.1.2). This concept is being further developed in collaboration with The Royal Prince Alfred Hospital, The School of Molecular & Microbiology, The University of Sydney, Biomedical Engineering, School of AMME, The University of Sydney and The School of Materials Science, University of New South Wales. Proposed procedures for delivery are described below and also in schematic form in Fig. 3.78b.

1. Tissue necrosis occurs in soft tissue near bony processes, due to mechanical trauma combined with other risk factors.
2. Ulceration occurs, forming an hourglass shaped wound. Alternate wound shapes may be broad and shallow, or narrow and deep with a tortuous pathway. Appropriate cleaning and debridement methods are followed. Attempts may be made to address systemic conditions such as diabetes as well as reduced blood flow.
3. The variotis™ scaffold is delivered via one of the following methods:

    a. Variotis™ scaffold is compressed into a syringe and delivered into the wound site. Once in place, the scaffold expands to fill the voids.

    b.Variotis™ scaffold fragments, suspended in a bioresorbable vehicle (such as Sodium Carboxymethyl-cellulose) are injected into the wound void. Similar bioresorbable vehicles have been used previously. Scaffold fragments form an interconnecting, assembled scaffold once within the body.
4. The wound may be covered with an epidermal split thickness skin graft and a gauze dressing. Appropriate measures are taken to protect the wound, such as off-loading and a total contact cast, if necessary.

Blood and wound fluids, cells and factors fill the scaffold within the first few minutes and hours. A provisional fibrin matrix is formed within the scaffold (blood clot). Therapeutic factors are released from the scaffold, such as antibiotics and beneficial antibiotic/nutrients from bioactive glass and biometallic glass coatings. New tissue (granulation tissue), including collagen, fibroblasts and adipose tissue fills the scaffold over a period of two weeks. The scaffold gradually resorbs. The skin is restored to health and the scaffold has completely degraded (estimated ~6 months). The degradation rate can be tailored by adjusting the type of bioactive fillers, coatings and polymer composition.

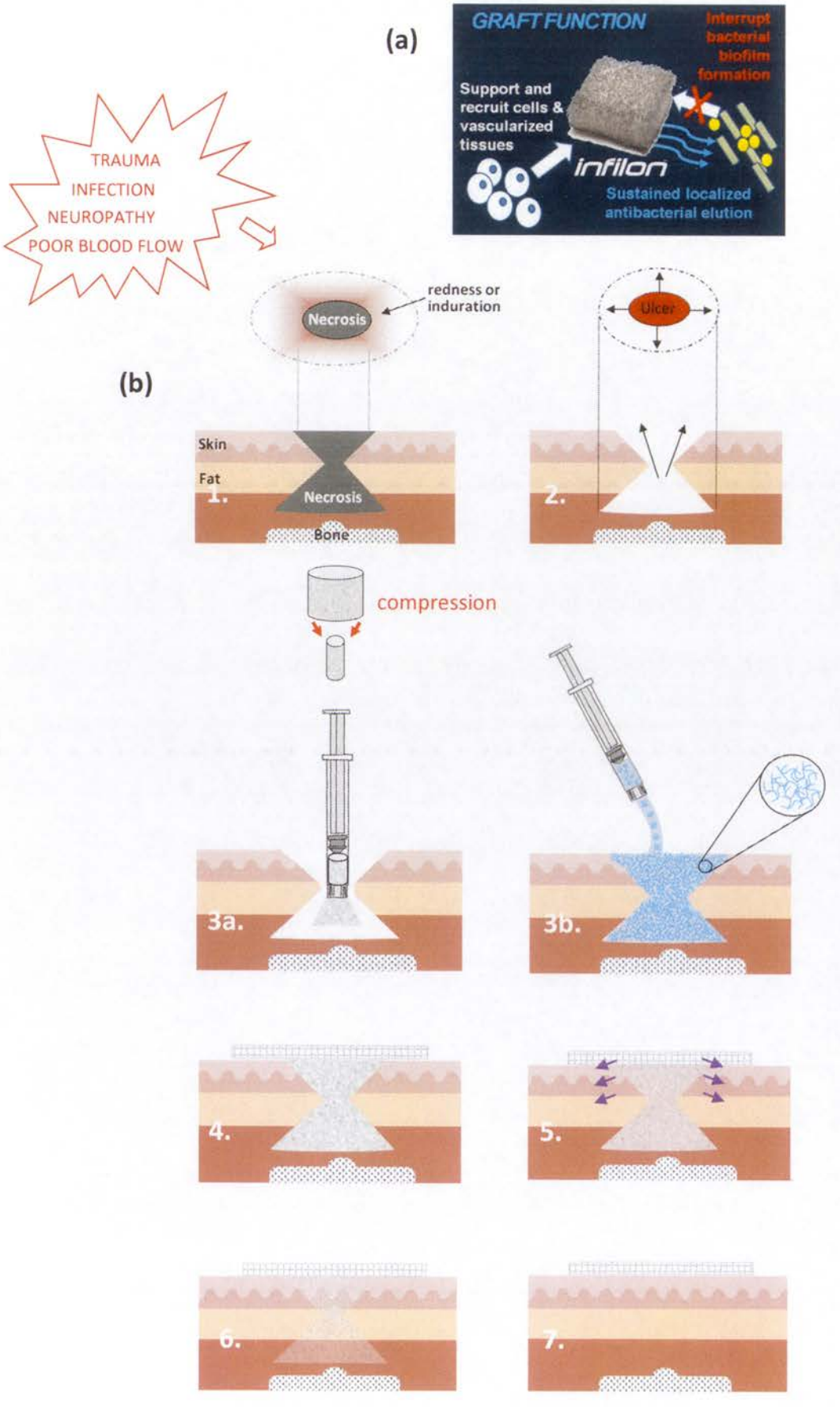


Figure 3.78. Procedure for delivery of the variotis™ scaffold to a skin wound.

3.6.5. OSTEOCHONDRAL TREATMENT CLINICAL CONCEPT

A functionally graded variotis™ scaffold, mounted on a bioabsorbable pin, was conceptualised as a device which could be used to repair osteochondral segments (Fig. 3.79). A minimally invasive surgical approach was conceptualised for access to articular cartilage surfaces, as described in a patent by the author [Refer to patent: A biocompatible pin, a method of treating joint articular cartilage defects in a bone and a method of accessing a joint surface] (Fig 3.80).

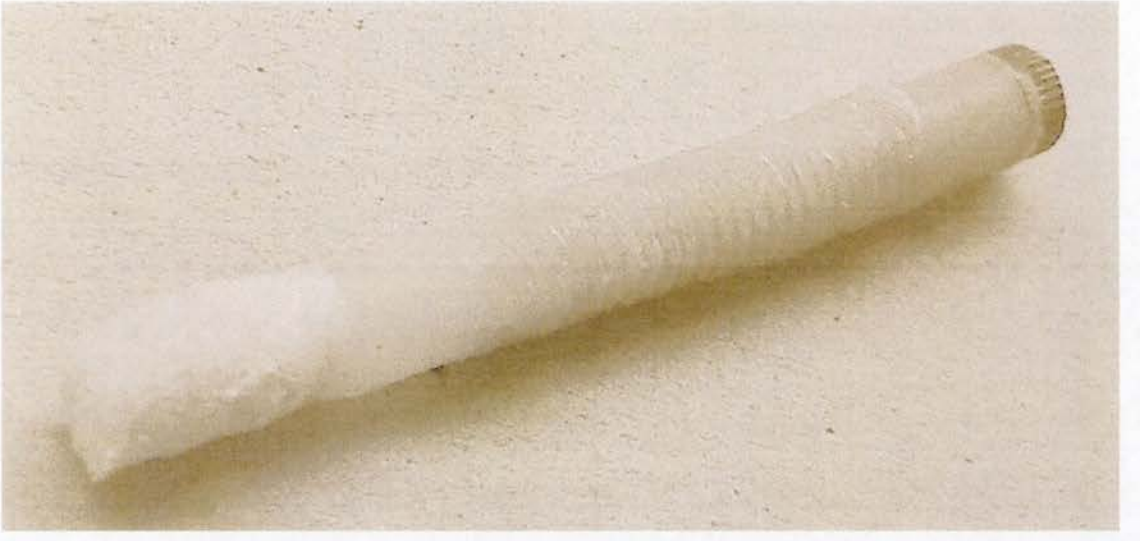


Figure 3.79. A prototype scaffold mounted on a threaded bioresorbable pin, for osteochondral repair.

3.6.5.1. Surgical Procedure

The next section describes the surgical delivery of this pin. The process is described for access to the femoral head, for treatment of the osteochondral surface of the knee (Fig 3.80). The device could be adapted to a range of alternate sites.

1. A defect is formed in the cartilage due to injury or a disease such as arthritis.
2. An osteomy is performed in the femur to form an oblique pilot hole with a proximal opening located at the surface of the bone and a distal opening at an articular cartilage surface.
3. The joint is pressed against the damaged cartilage surface. The outer pin is screwed through the pre-drilled shaft. Screwing is accomplished by a spanner twisting the internal metal pin, which in turn leads to the delivery of the outer pin. The pins are screwed in until the scaffold becomes pressed against the meniscal surface. The scaffold will be slightly protruding out of the cartilage. During load bearing, the scaffold becomes compression set within the cartilage. This provides a smoother articulating surface.
4. A central duct through the outer pin can receive a cannula to deliver additive agents such as stem cells, antibiotics or other therapeutic factors.

5. Fibre optics is used to deliver ultraviolet radiation to a localised region. This causes the hydrogel to set, fixing them in their conformed shapes.
6. A second inner pin would be screwed in through the inner shaft. This would form a plug to prevent the loss of synovial fluid, blood and stem cells.

The components of the device are now described.

3.6.5.2. Pin Description

The outer pin (e.g. 6 mm) consists of molded PCL and may include composite fillers such as bioactive glass or calcium phosphate in powder or fiber form. The PCL is relatively soft, and prevents stress shielding of the bone. Alternately, the pin may be made from glass-reinforced-glass, as described by a patent developed by Advanced Surgical Design and Manufacture (St Leonards, Australia). The pin is threaded on the outside to provide mechanical stability.

The pin contains a central shaft through which a metal shank is placed (e.g. 2 mm wide, titanium). This metal shaft contains a shape (e.g. hexagon) which mates with a spanner for screwing into the bone. A second inner pin consisting of PCL or PCL composite (similar to outer pin), of similar specifications to the metal pin, is used as a plug.

3.6.5.3. Scaffold Description

A functionally graded variotis™ scaffold is positioned on the end of the pin. The scaffold acts as a template for the formation of bone and cartilage, on the osteochondral interface. Blood and synovial fluid will fill the scaffold with blood, growth factors and other nutrients. This will be facilitated by the initial bone drilling process. The scaffold will act as a 'pump', and encourage the exchange of waste products from the scaffold, stimulated by forces on the joint when the patient moves. Bone integration into the porous subchondral bone scaffold will help healthy cartilage to develop. Development of the functional gradient present native cartilage will be encouraged in the pore spaces, including gradual changes in collagen fiber orientation, type and chondrocyte phenotype.

The scaffold is graded in porosity, and perhaps composition. The scaffold is made from PCL, reinforced with bioactive glass. The cartilage component of the PCL composite scaffold is up to 95% porous, changing to a dense bone region which seamlessly joins the outer pin. The bone phase may contain a higher composition of bioactive glass powder than the cartilage component. The bone component may also contain calcium phosphate powder. As the bioactive fillers dissolve (at different rates), the porosity of the PCL will increase, leading to stable bone integration. Fibrous encapsulation and stress shielding will be discouraged due to the porous nature of the scaffold and elastic modulus of the material.

The cartilage component of the PCL composite scaffold has a dehydrated hydrogel (or hydrocolloid) lining. This lining is preferably from a synthetic source, such as polyvinyl alcohol (PVA), carbomethyl-cellulose (CMC). The lining may alternately be from naturally derived materials such as chitosan, gelatin, collagen or alginate. Following implantation into the tissue, the hydrogel becomes hydrated, and increases in volume. This encourages the scaffold to expand to fill the voids in the implant site. The expanded hydrogel may still consist of an interconnected porous network, enabling cell migration to occur. The hydrogel will degrade relatively rapidly, enabling cartilage to develop. The hydrogel lining may be used to facilitate the delivery of therapeutic additives such as antibiotics, factors to slow cartilage erosion, factors to stimulate cartilage repair, proteins, cells or tissue components.

The surface of the scaffold near the articulating joint may be coated with a thin, bioabsorbable film (e.g. PCL) which is impermeable to the hydrogel. The function of the skin is to shield the scaffold from mechanical abrasion until the underlying osteochondral tissue is mechanically competent and the scaffold is compression set.

The pin and the scaffold will completely resorb over time, as new cartilage is formed, thus completely healing the joint defect and restoring the functionality of the joint. The period for resorption can be tailored according to the characteristics of the bioactive filler components.

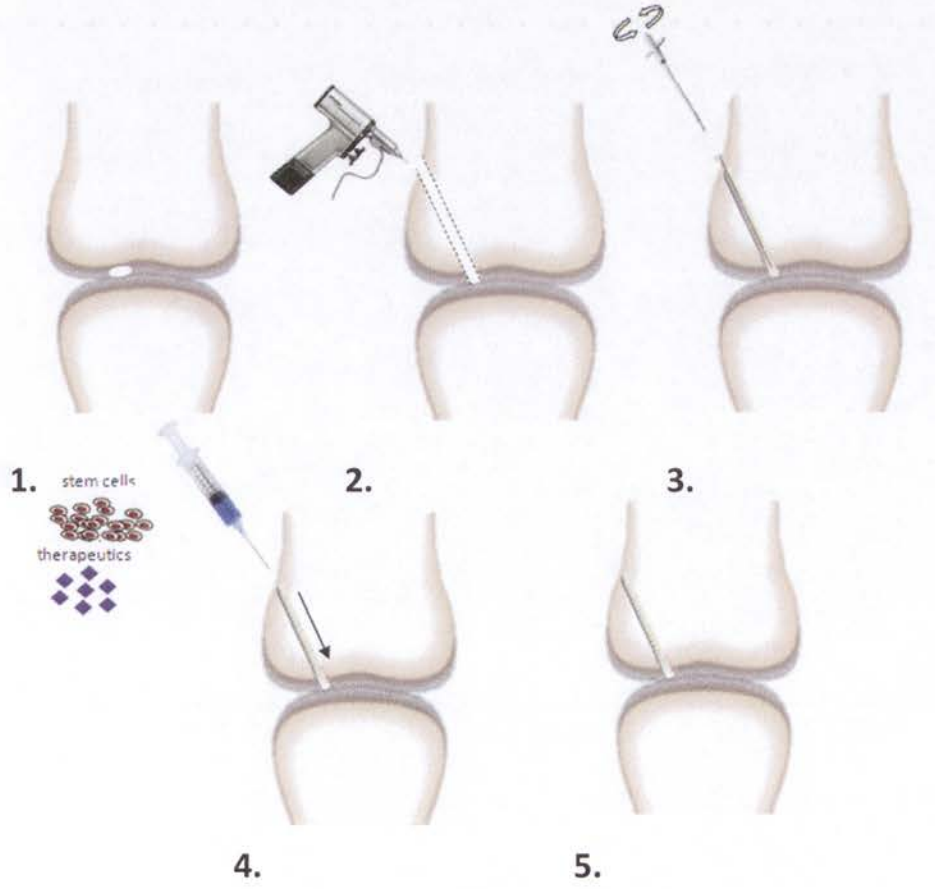


Figure 3.80. Schematic of the surgical delivery of an osteochondral repair pin.

CONCLUSIONS

- The variotis™ scaffold was designed and large quantities of PCL scaffolds were synthesised using a novel batch coagulation process. The process was rapid, repeatable and cost-effective. Variotis™ has been patented and commercialized by Biometic Pty Ltd.
- Bioactive glass (13-93, 45S5) was successfully added to the PCL matrix in the form of a filler and coating.
- The scaffolds were shown using SEM and MICROCT to have a high porosity (>95%) and large pore size (300-500 μM). MicroCT models and animations were constructed. The pores were highly interconnected with wide throats and short pathways to the outer edges of the scaffold, when compared with other scaffolds in the literature.
- The scaffold was easily post-formed into sheets, cylinders, tubes and functionally graded (porosity and pore size) geometries, via the application of heat and pressure. Glass powders were adhered to scaffold disks for biocompatibility tests. These procedures could easily be conducted by a surgeon or researcher.
- Custom-made sucrose network porogens and corresponding variotis™ scaffolds were synthesised.
- Scaffolds showed a high extensibility (300% increase in length) and an excellent ability to resist tearing and return to its original shape after stretching. The scaffolds showed a higher capacity to strain compared to other porous scaffolds examined from the literature.
- The mechanical properties which could be achieved with various conformations of the variotis™ scaffold were shown to fall within the range of the modulus and strength of human skin and subdermal tissue. The scaffold achieved superior strength and extensibility compared to other candidates for skin engineering, particularly naturally-derived gels (e.g. elastin, collagen). The scaffolds were shown to have lower moduli (more elastic) compared to other synthetic, bioabsorbable scaffolds (e.g. PLCL, PLGA, PCL commonly formed using TIPS or rapid prototyping processes).
- After sterilisation, tensile testing demonstrated that ethylene oxide gas-sterilised scaffolds more than doubled in linear elastic modulus (130%), whilst showing some

reduction in ultimate tensile strength (25%). Gamma sterilised scaffolds showed little change in modulus (10.4% increase) but had a reduction in strength (30%).

- Clinical models were conceptualised, for which the scaffold may be used for skin and osteochondral applications. Surgical delivery concepts were proposed. Scaffolds may be delivered to a skin wound in a compressed form, or as a fragmented scaffold (in gel phase). Functionally graded scaffolds, mounted on a bioabsorbable pin, were proposed as a model for osteochondral defect repair. Tissue pathology and metabolic problems could potentially be addressed through coating of the scaffold with biometallic glasses, bioabsorbable silica-based glasses and/or antibiotics.

CHAPTER 4-

BIOACTIVE COMPONENTS

4.0. CHAPTER OVERVIEW

The bioactivity of a scaffold can be enhanced by its physical structure, addition of therapeutics or through bioactive biomaterials. This chapter examines the synthesis and physical characterisation of a range of silicate-based bioactive glasses to promote tissue attachment to the scaffold, elicit desirable cell behavior, as well as modulate the physical and chemical characteristics of a scaffold. Bioactive glasses are known to increase the dissolution rate, surface area, wettability and bioactivity of polymer scaffolds, and may also stimulate angiogenesis and impart antibacterial/anti-inflammatory properties. Bioactive glasses were synthesised with varied compositions (Si, Ba, Zinc and Iron proportions). The physical properties of the glasses were examined to determine whether these changes would affect the mechanical properties, bioactivity and radiopacity of the glasses. Using Energy Dispersive Spectroscopy (EDS), the compositions of the 45S5 were verified as the expected formulations. Hardness measurements using nanoindentation techniques confirmed the modulus of 45S5 glass was similar to literature (31 GPa). Iron-doped glass showed a high modulus (135 GPa). Addition of Zn may have resulted in a less stiff glass (modulus:16 GPa). The bioactivity of the glasses was confirmed using a SBF dissolution study. The addition of zinc slowed calcium phosphate precipitation in the short term (1 day) but did not affect medium term apatite formation (7 days). Fluoroscopy analysis showed the radiopacity of Ba-doped glasses increased with the proportion of Ba dopant.

4.1. INTRODUCTION

4.1.1. BIOACTIVE SCAFFOLDS

Tissue conduction and wound healing could potentially be stimulated through a range of bioactive components in the variotis™ scaffold (Fig. 4.1). As previously discussed, the physical structure plays an important role in providing a framework for tissue to proliferate and mature. Tissue attachment could be stimulated through the porous structure and surface texture on the scaffold. Of particular interest in this chapter is the role that bioactive biomaterials can play in directing cell and tissue behavior. Two materials, silica-based bioactive glasses and bulk metallic glasses (BMGs) will be examined in further detail. These glasses have the ability to release elements into the body which are essential for wound healing and tissue growth, which can include zinc, calcium, silica, magnesium and iron. Incorporation of these agents into a soft tissue scaffold amounts to a substantial challenge. Following this, various carbohydrates, including sugar and honey will be investigated for the potential benefit they could provide the wound. These components have many potential benefits over standard antibiotics or other therapeutics, which can include: cost effectiveness, ease of synthesis, good shelf life, multiple biological actions, ability to treat antibiotic-resistant biofilms, long-term localised delivery and the ability to combine multiple modes of action together.

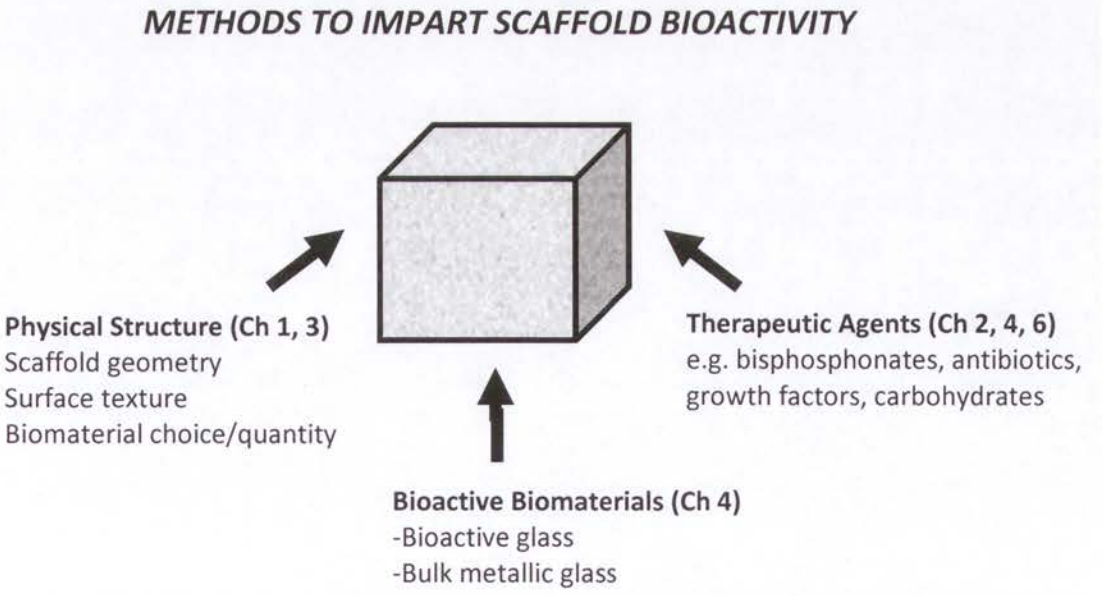


Figure 4.1. Methods to impart bioactivity to a scaffold.

4.1.2. BIOACTIVE GLASSES

Silica-based resorbable bioactive glasses can be incorporated into tissue engineering scaffolds in order to encourage bonding to both soft and hard tissue. Bioactive glasses are known to improve the bioactivity, surface area and hydrophilicity of the polymer, increase tissue attachment to the scaffold, alter the degradation rate of the scaffold and to buffer the pH of the surrounding fluid [153, 187].

The most common composition of bioactive glass is known as '45S5' or 'Bioglass®', and was developed by Larry Hench [3, 8, 74, 412, 570, 631, 632, 656, 661].

Bioglass® demonstrates tissue conductive behavior, including tissue conduction and production, and is thus classified as a class A bioactive material [632]. Bioglass® exhibits a higher level of bioactivity than hydroxyapatite, which is a class B material; exhibiting only tissue conductive behavior [188]. Bioactive glasses impart a high level of hydrophilicity to the implant surface, which is much more pronounced than with conventional bioceramics [633, 584]. When immersed in simulated body fluids, a rapid mineral precipitation is observed during the 1st week on bioactive glass, as compared to a more linear increase over a 1 month period on calcium phosphate [169].

4.1.2.1.Biological Activity of Bioactive Glasses

Certain bioactive glasses have demonstrated: [53, 147-150, 637, 638, 641-643, 648]

- Good biocompatibility;
- Good hard and soft tissue adhesion;
- Increased cell proliferation and attachment;
- Increased ECM production;

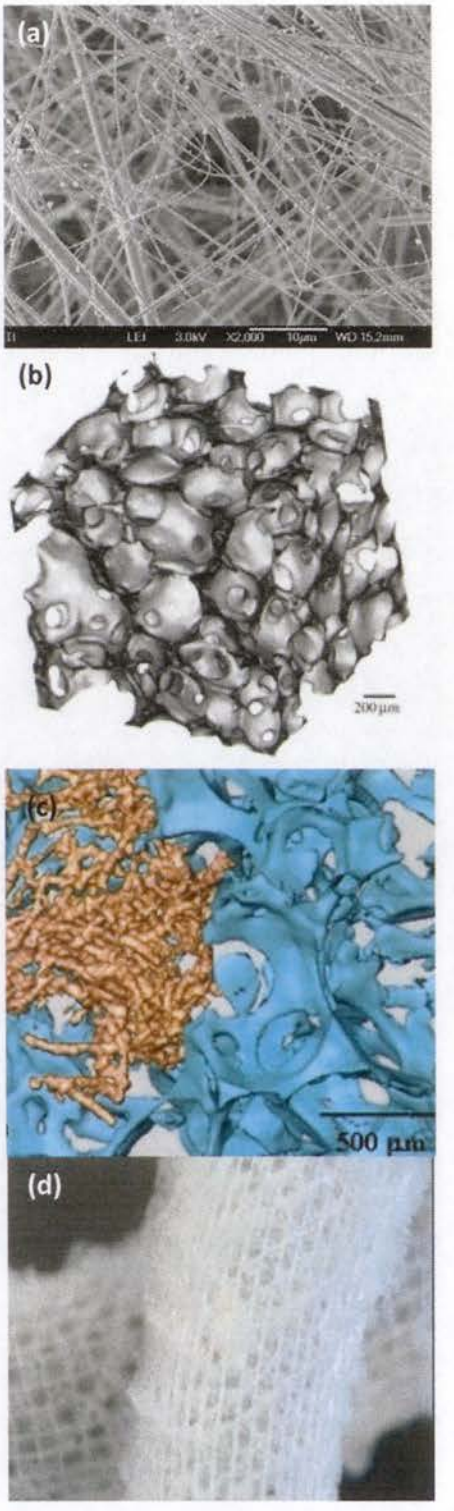


Figure 4.2. (a) Bioactive glass nanofibers made using laser spinning [634], (b) Bioactive glass scaffold [30], (c) Computer tompography image of blood vessel ingress into a bioactive glass scaffold [635], (d) Naturally-derived 'unbreakable' glass scaffold [636].

- Wide-spectrum antibacterial effects;
- Anti-inflammatory properties;
- Good bonding strength- elimination of fibrous encapsulation;
- Increased blood vessel formation;
- Differentiation of bone cells;
- Retention of chondrogenic phenotype; and
- Nerve regeneration.

The biological activity of the glass depends on the culture conditions or implantation site, glass composition, form and dimensions of glass particles and the concentration of the glass.

4.1.2.2. Bonding Mechanisms of Bioactive Glasses

Upon contact with body fluids, a silica gel layer and calcium phosphate precipitate forms on the surface of bioactive glass, according to the following steps [656].

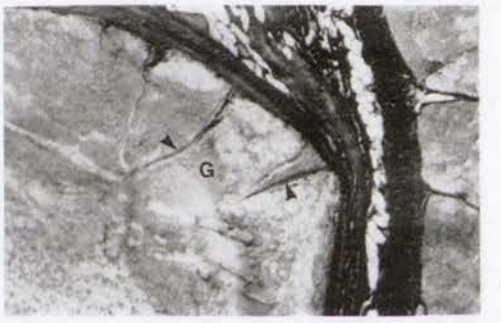


Figure 4.3. SEM image of collagen fibres growing into cracks on the glass surface (G) at the tissue-implant interface at magnification ×100 [644].

1. Rapid exchange of Na+ and Ca+ with H+ or H_3O^+ from solution. The pH of the solution increases as a result of H+ ions in the solution being replaced by cations.
2. The cation exchange increases the hydroxyl concentration of the solution, which leads to attack of the silica glass network. Soluble silica is lost in the form of $Si(OH)_4$ to the solution, resulting from the breaking of Si-O-Si bonds and the continued formation of Si-OH (silanols) at the glass solution interface.
3. Condensation and repolymerisation of a SiO_2-rich layer on the surface.
4. Migration of Ca^{2+} and PO_4^{3-} groups to the surface through the SiO_2-rich layer. A CaP_2O_5-rich film forms on top of the SiO_2-rich layer. As soluble calcium and phosphates from the solution are incorporated, an amorphous CaP_2O_5-rich film forms. This layer crystalises via incorporation of OH- and CO_3^{2-} anions from solution to form a mixed hydroxyl carbonate apatite (HCA) layer.

5. Adsorption and desorption of biological growth factors in the HCA layer activates the attachment & differentiation of stem cells. Macrophages are activated to remove debris from the site.

Bioactive glass bonds to tissue via chemical and biological routes. HCA crystallites have been found to nucleate and bond to osteoblast cell products, both collagens and noncollageneous proteins, thus forming a direct chemical bond between bioactive glass and bone structure [645]. Bioactive glasses have demonstrated increased protein adsorption on the surface of polymer composites [568]. Early protein adsorption, particularly of fibronectin, is a key process which leads to various cellular processes which dermine the fate of the biomaterial in the body [646]. This adsorption of a diverse range of proteins facilitates bonding via biological means. With this unique property, bioactive glasses and glass ceramics have been widely used clinically in orthopaedic, oral and maxillofacial surgery for bone and cartilage reconstruction but require further development for many skin applications.

45S5 Bioglass® (sol-gel derived) is commercially available as TheraGlass® (Imperial College London), for uses such as sustained release of anti-cancer therapies, drug eluting dressings, sprays and device coatings and repair of protein containing surfaces (e.g. teeth, bone, nails, hair eyelashes, skin) [647]. Bioactive glasses have also been used for some of the most challenging tissue engineering cases. For example, 45S5 bioactive glass fibers have been used for nerve regeneration, where there are extensive, long-term gaps to be bridged [643, 648]. Axonal regeneration on glass fibers has demonstrated to be indistinguishable after 4 weeks *in vivo*, to that which occurs across an autograft (Fig. 4.4c,d). Recently, silver-doped bioactive glasses have

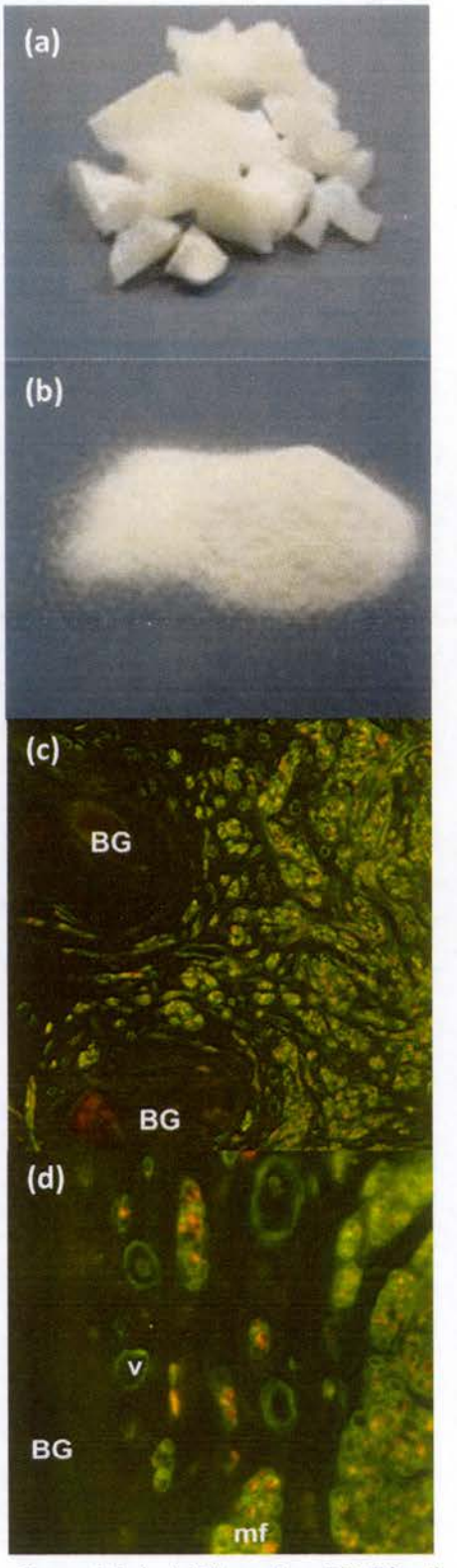


Figure 4.4. (a, b) Theraglass [647] (c, d) Immunostained transverse sections of tissue extracted from the lumen of a BG nerve conduit after 4wks implantation in rats. BG= previously occupied by a BG fiber, v=blood vessel, mf=minifascicle. Magnification: (c) x255, (d) x450 [643].

been coated on Vicryl and Mersilk sutures [566]. However, suture coatings are likely to cause tissue damage during the surgical procedure. The current study aims to capitalise on the advantageous bonding properties of bioactive glass, whilst minimizing damage to the surrounding tissue.

4.1.2.3.Effect of Bioactive Glass on Cell Behaviour

Attachment and proliferation of cells on bioactive glasses have been demonstrated for a variety of cell types including bone cells [214, 649, 650], spinal disk cells [154], fibroblasts [85, 653] and cancer cells [212]. Changes to cell behavior are largely attributed to the release of calcium and silica ions into the surrounding fluid [202, 552, 651]. Calcium is a modulator of intracellular events which can increase ECM production. Another element which promotes cell attachment is the surface roughness and increased surface area imparted to the scaffold surface [630, 653]. Helen & Gough demonstrated that coating of PDLLA foams with bioactive glass (5 or 30 wt%) resulted in more clusters of human annulus fibrosis cells than compared with the polymer foam alone [154]. An increase in collagen production was also observed for the composite foams, after 1 or 2 weeks in culture.

Some studies have indicated inhibition of cells for high concentrations of bioactive glass. In particular, Helen & Gough reported better proliferation for 5%BG/PDLLA than compared with 30%BG/PDLLA [154]. Cells grown on the 30%BG/PDLLA foams had lower cell counts between weeks 2 & 3, however by week 4 this had recovered and higher levels of collagen & proteoglycan were produced on this scaffold.

In vitro studies using bone cells have shown stimulation of osteogenic factors such as Akaline Phosphotase (ALP), Osteocalcin (OCN) [203, 654, 642]. When bioactive glass is used as an implant coating (e.g. alumina hip implants [655] and auditory implants [656]), good osseous tissue attachment has been observed and bone cement is not needed. Increased bone formation has been observed on porous implants with bioactive glass coatings [227].

Studies have also shown an upregulation in chondrogenic markers, for example collagen X, collagen II and aggrecan [642]. Intervertebral disk (annulus fibrosis and nucleus pulposis) cells, which are likely to consist of fibroblasts and chondrocytes, have been shown to keep their phenotype when cultured on bioactive glasses. This is partly due to micro-mechanical cues experienced by the cells when they come into contact with a highly textured, hydrated silica surface. This encourages the cells to keep their rounded shape and phenotype. Therefore, bioactive glasses have been explored for cartilage and osteochondral engineering. For example, Ylänen & coworkers used sintered bioactive glass microspheres to repair osteochondral defects in rabbit femurs [657].

4.1.2.3.1. Antibacterial Effect of Bioactive Glasses

Bioactive glasses have shown antibacterial properties against a wide range of species. A study by Munukka and coworkers [658] demonstrated an antibacterial effect on 29 clinically relevant bacterial species, including those present in infection of surfaces of prostheses after implantation. Waltimo and coworkers [659] showed antibacterial activity of bioactive glass nanopowders on oral microorganisms common in root canal defects. The antibacterial potency of Bioglass® is increased with the use of nanopowders, as compared to microsized particles. This is due to a 10x fold higher specific surface area, leading to an increase in alkaline species released [659]. Antibacterial activity is also increased as the glass becomes less stable. For this reason, glasses which include 45, 58 or 63% silica show the highest levels of antibacterial activity [158, 658]. Mortazavi and coworkers [158] demonstrated antibacterial potency of 58S and 63S toward E. coli and S. aureus for concentrations above 50 mg/mL. Silver-doped bioactive glasses have shown antibacterial activity which surpasses that of undoped bioactive glass [157].

4.1.2.3.2. Angiogenic Effect of Bioactive Glasses

Bioactive glasses have also been shown to upregulate VEGF and increase tubule formation [143]. This was demonstrated by Leu & coworkers [143] who cultured BG/collagen composite sponges with endothelial cells. The proangiogenic capcatity of bioactive glasses was related to their soluble dissolution products and the subsequent production of cell-secreted angiogenic factors by stimulated cells [143]. The effect of bioactive glass on angiogenesis has been reviewed by Gorustovich [144]. Increasing blood supply to a wound is very important for individuals suffering chronic wounds, who could be also experiencing poor vascularisation due to other health issues, due to age or diabetes.

4.1.2.3.3. Approaches for Synthesis and Characterisation of Bioactive Glass

The majority of previous studies using bioactive glasses involve commercially sourced glass [53, 77, 86, 132, 139, 143, 154, 189, 195, 202, 584, 639, 651], although this can be difficult and expensive to source. Some researchers synthesise their own glass, however this is usually mesoporous glass formed using a sol-gel technique [5, 117, 127, 132, 392]. The sol-gel method, however, is time-consuming (several days) and involves expensive precursor materials.

Synthesis by the melt-derived process first involves mixing of precursor powder, followed by melting and quenching the glass. Usually glass is formed in granules and crushed into powders. In one study, Aina and coworkers [145] produced 100 g batches of zinc-doped 45S5 via a precursor mixing step of 1 hr (in a polyethylene bottle), followed by melting at 1400-1550°C for 2 hrs in a 50mL platinum crucible [145]. Formation of glass fibers has also been reported by

several groups [205, 643]. Bunting and coworkers [643] formed continuous Bioglass® fibers by dipping a 10 mm diameter rod into moltern glass and removing it at a rate of 1 m/second. Fibers of 150-200 μm in diameter were used for cell tests. In an alternate method, reported by Bitar [205], iron phosphate glass fibers were formed by drawing fibers on a rotating drum. Fibers with diameters of 20-25, 15-20 and 10-15 μm were created with rotational speeds of 800, 1200 and 1600 rpm. A stepper motor shaft was added to the rig which resulted in parallel alignment of fibers at equal spatial intervals during the drawing process. The composition of glass can be analysed using Electron Density Scanning (EDS). In one study, Vargas and coworkers [774] used EDS to demonstrate the composition of 45S5 glass which was formed into sintered, porous scaffolds. Five days post implantation in a chick embryo angiogenesis model, the amount of silica on the glass had increased 5 fold while the calcium had dissolved into the surrounding fluid.

4.1.2.4. Variation in Bioactive Glass Composition

Groups which have synthesised glass using the melt-derived technique usually use the established 45S5 composition [643] or altered silica levels [203, 553]. Changes in the composition of the glass can affect properties such as stability (alter resorption rate), nutrient delivery, anti-inflammatory response, radiopacity and antimicrobial properties. This can be done via altering the proportions of the constituents of the glasses and/or addition of metallic or other ions. Small changes in composition can dramatically alter whether a glass is bioinert, resorbable or bioactive and the other effects they exhibit. The levels of SiO_2, CaO and Na_2O required for a glass to be bioresorbable are explored by Shackelford [660]. Bulk glasses which are bioinert cause a fibrous capsule adjacent to the surface, probably due to the high stiffness [644]. This was observed by Hench et al [661] when 45S5 bioactive glass rods were implanted into rat muscle. Soft tissue bonding has been demonstrated by Wilson et al [644] for specimens with compositions approximately 42 to 52% silica (SiO_2). Silica variation is often used to adjust the degradation rate of glasses [203]. This alteration also modulates the release of the other elements.

Some researchers have investigated doping glass with metals or other elements such as zinc, boron, silver, titanium, potassium, fluorine or magnesium, which provide nutrients to the tissue [145, 199, 553, 639, 669, 670]. Aside from its known role in aiding bone fracture healing [15, 662], zinc can also be useful for soft tissue repair [663]. Zinc plays a vital role in DNA synthesis and growth and development during pregnancy, childhood and adolescence [664]. The healing benefits of zinc have been observed through zinc supplementation [668]. Zinc is important for wound healing due to its necessity in synthesis, enzyme function, cell mitosis and fibroblast proliferation [663]. Zinc also plays a vital role in supporting the immune system,

and is thought to inhibit bacterial growth [377]. It also has a critical role in the development and activation of T-lymphocytes which help fight infection [664]. Aina and coworkers showed endothelial cell adhesion was enhanced by the presence of zinc in 45S5 glass [145].

Iron is a major trace element which is essential for hydroxylation of proline and lysine for collagen synthesis and haemoglobin and tissue oxygenation. It also boosts the bacteriocidal activity of leukocytes [665]. Iron-phosphate glass fibers have been tested with human osteoblasts & fibroblasts [205] for incorporation into bone scaffolds. Ferrimagnetic glass-ceramics have also been investigated as potential candidates for magnetic induction hypothermia [666]. Madanat and coworkers [795] explored the addition of 10% barium sulphate to bioactive glass, for its potential to replace permanent tantalum bead markers used in radiosterometric analysis. Radiosterimetric analysis involves the quantitative assessment of *in vivo* micromotion of joint replacements and fracture fixation devices, and is also used to measure polyethylene wear. Barium sulphate is frequently used as an opacifier in bone cements [790].

Other trace elements important in wound healing include magnesium, copper, selenium, manganese and folic acid [667, 668]. Magnesium is required for collagen synthesis and neuronal function. Copper is required for collagen cross-linking. Selenium is an antioxidant which impacts on macrophage and polymorphonuclear cell function. Manganese is thought to promote enzyme activity.

4.1.3. BULK METALLIC GLASSES

Bulk metallic glasses (BMGs) (Fig. 4.5) represent a new class of biodegradable materials which exhibit superior mechanical and chemical characteristics compared to their crystalline counterparts. Recently, glasses based on magnesium, calcium and zinc (MgZnCa) have been explored by two key groups; Löffler and coworkers (ETH Zürich, Switzerland) and our collaborators at University of NSW, Ferry and coworkers [671-677, 682]. Their light weight nature yet good elasticity (with minimal plastic deformation) have led to interest for bone fixation (e.g. pins, screws) [132, 678]. However, little research has been performed on other applications, including soft tissue.

BMGs could provide the following effects when coated as an impermeable barrier on a scaffold:

- Adjust scaffold degradation rate

- Impart antibacterial/antifungal activity
- Provide nutrients
- Modulate release of active agents (e.g. antibiotic coating under the metallic glass)
- Prevent UV degradation of the antibiotic
- Modulate mechanical properties of the scaffold- dependent on thickness/nature of the coating

The constituents of MgZnCa metallic glasses are naturally occurring in the body as salts or ions [676, 682]. Magnesium is an important regulator of cell proliferation, protein synthesis and other pathways. Calcium is abundant in the body, particularly in bone, and is vital for regulation of intracellular pathways. Zinc is essential for the immune system and is a co-factor for specific enzymes in bone and cartilage.

Magnesium alloys have been used as biomaterials from as early as 1907. However, their high corrosion rate (mainly by pitting corrosion) and associated rapid hydrogen gas evolution limited their success [683]. Hydrogen evolution leads to gas voids that cause adverse reactions and inhibit bone growth. These drawbacks can be altered by the amount of added elements (e.g. zinc) to the base Mg-based system [675]. Recent BMGs show high stability, good biocompatibility and osteoconductive properties [675, 676]. Unlike crystalline materials (e.g. conventional metallic alloys), metallic glasses lack long range order and feature high atomic packing efficiency of atomic clusters that result in high strength, chemical homogeneity and the lack of microstructural defects [132, 684-686]. Metallic glass has these desired properties by nature, it does not need alloy additions to achieve superior mechanical and corrosion

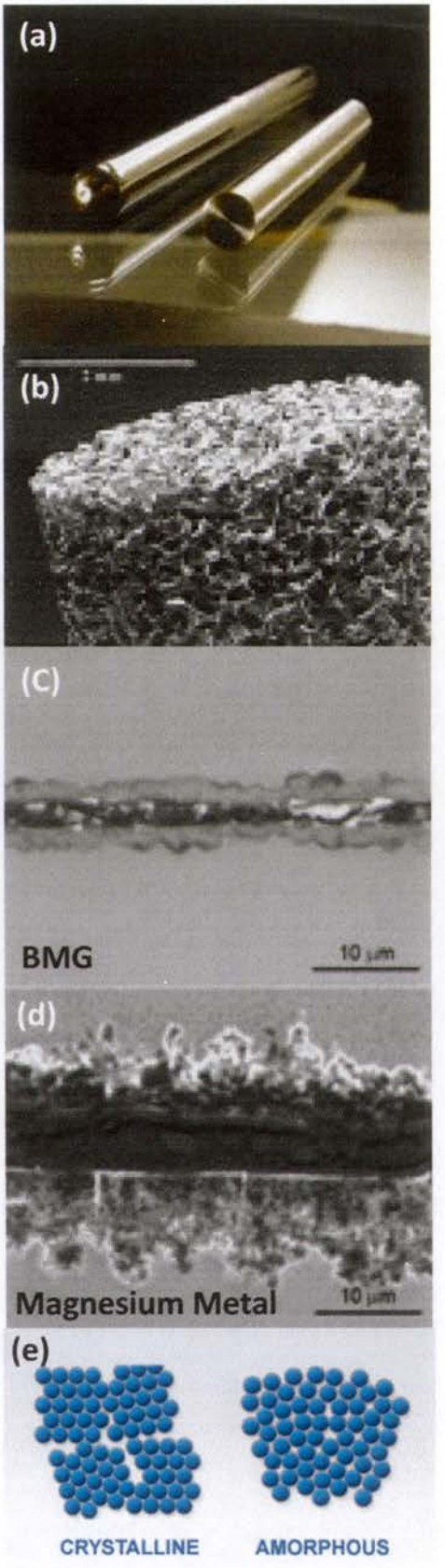


Figure 4.5. (a) BMGs [679], (b) BMG foam [680]. Hydrogen bubbles evolving from (c) BMG and (d) Mg Metal [672]. (e) Crystalline vs Amorphous structure [681].

properties. Commonly used alloying materials include rare earth elements, and aluminum which is a known neurotoxin [675]. A study by Loffler and coworkers [671] demonstrated a lack of significant hydrogen evolution from metallic glass discs ($Mg_{60}Zn_{35}Ca_5$) which were implanted into the abdominal tissues of domestic pigs. *In vitro* cytotoxicity studies by Gu and coworkers [677] demonstrated attachment of murine fibroblast (L929) and human osteosarcoma (MG63) on $Mg_{66}Zn_{30}Ca_4$ and $Mg_{70}Zn_{25}Ca_5$ metallic glasses using SEM.

4.1.4. CARBOHYDRATES

Various naturally occurring carbohydrates have been used in wound treatment throughout history. The most common are sugar (sucrose), honey (main constituents are glucose, fructose, and maltose) and molasses (main constituents are sucrose and glucose). These monosaccharaides are thought to demonstrate anti-inflammatory and anti-microbial activities, and encourage granulation tissue formation and re-epithelialisation of the wound [687]. In many cases, the wounds have healed without the need for debridement of necrotic tissues or any other surgical procedure [688, 689]. Healing is reported of many wounds which fail to respond to conventional therapies. The benefits of sucrose can be employed using the variotis™ scaffold, as it is used as the porogen and residual amounts could be present. It is also possible to incorporate other carbohydrates into our novel skin graft or other tissue engineered constructs.

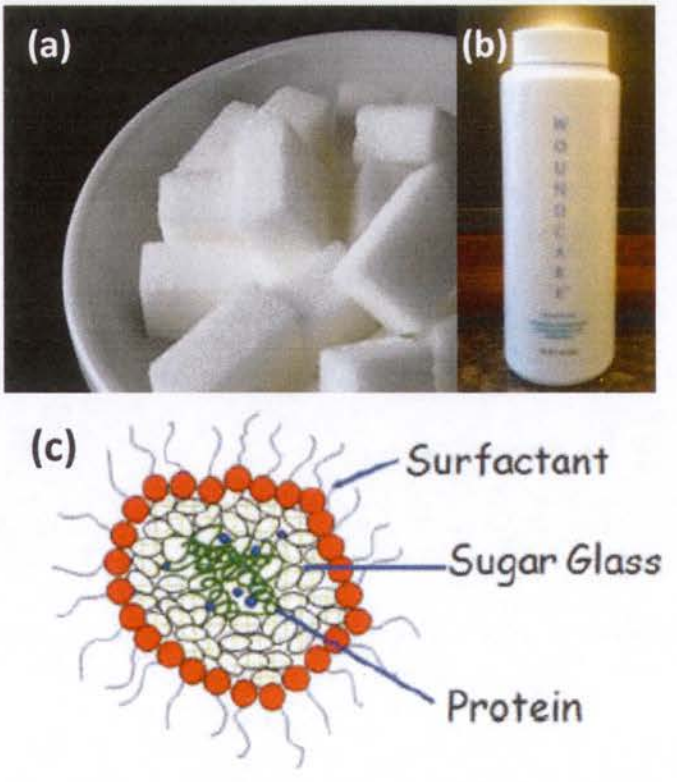


Figure 4.6. (a) Sugar [690], (b) WoundCare™ Healing Powder [691] (c) Protein/sugar nanoparticles for drug delivery [692].

4.1.4.1.Sugars

Sucrose has been shown to aid chronic wound healing when applied in granular or paste form [693]. In 1980, Herszage and Montenegro of Argentina reported on the use of granulated sugar in 120 infected wounds, and recorded a cure rate of 99.2% [688]. The odor and secretion from the infections began to subside within 24 hrs and disappeared totally after 72-96 hrs of treatment. Sugar pastes have since been developed, consisting of castor (fine granular sucrose) and icing sugar (powdered sucrose), polyethylene glycol and hydrogen peroxide, at proportions described in a patent held by Marraccini [694]. Marraccini's patent also covers application of free sugar (sold under the name WoundCare™, by Universal Healing Solutions) or sugar encased in a dissolvable capsule (e.g. gelatin) to a wound [691, 694]. The sugar paste can be made in a thick form, with a similar consistency to clay, for packing of deep wounds, or in a thin form, similar to the consistency of honey, for use in narrow cavities [694]. Sugar pastes are applied twice daily to infected and malodorous wounds [695]. Sugar pastes have been demonstrated to be rapidly bactericidal against a range of organisms including Staphylococcus aureus, Streptococcus faecalis, Escherichia coli, Candida albicans and Proteus mirabilis [696, 697].

Carbohydrate moieties have been used in the tissue engineering field to graft onto polymer surfaces to mediate cell attachment [698]. Recently, galactose-conjugated biodegradable polymeric scaffolds, such as alginate and/or chitosan [453l, 699] and PLGA [700] have been used for hepatocyte culture. Galactose targets asiaglycoprotein receptors on the hepatocyte membrane, causing spheroid formation and increased hepatocyte functions such as urea and albumin secretion. Modification of poly(2-hydroxyethyl methacrylate (pHEMA) with aminosugars to improve biocompatibility with neurons, for spinal cord tissue engineering [701]. Sugar particles containing proteins can be dispersed in solvents and incorporated into tissue engineering scaffolds, after coating with a surfactant [692].

4.1.4.2.Honey

Honey (Fig. 4.7) is the most ancient wound dressing material, being used by the ancient Greeks and Egyptians. There have been many reports of honey being effective as a topical antibacterial agent for the treatment of infected wounds, burns and skin ulcers [702-714]. These include cases which did not respond to standard antibiotic and antiseptic therapy [710] and diabetic patients [715].

Along with antibacterial, anti-inflammatory and angiogenic properties, honey is easy to apply, creates a moist healing environment improves blood and lymph flow in the wound [49] and provides nutrition [716]. Honey contains a wide range of nutrients including amino acids, vitamins and trace elements [717]. Honeys derived from particular floral sources, such as the Leptospermum species, including Manuka honey (Australia/New Zealand) (Fig. 4.7) have demonstrated particularly potent activity [708]. These honeys have been approved for therapeutic use, as Medihoney, Active Manuka Honey and WoundCare 18+ [708].

Honey has been demonstrated an effective debridement agent which can rapidly clear necrotic tissue and the infecting bacteria; important stages before tissue healing can occur [707, 712, 718]. In this respect, honey is superior to the expensive modern hydrocolloid wound dressings as a moist dressing. Usually, moist conditions favor the growth of infecting bacteria and antibiotics are ineffective in this situation (ref section 3.1.3, 3.1.4). Antibiotics cause tissue damage and slow the healing process [483, 719]. However, honey reduces tissue necrosis and does not cause damage upon dressing removal [720]. Honey is reported to have a powerful deodorizing action, probably due to the rich provision of glucose, which is used by bacteria in preference to amino acids, resulting in the formation of lactic acids and not malodourous compounds [709].

Honey also prevents scarring and deformity of the new skin. Scarring can occur when a dry scab forms on a wound and the skin cells can only grow across the wound deep down where it is moist. Honey causes the scab and dead cells to lift off the surface of the wound, leaving a clean and healthy wound bed in which regrowth of tissue can occur.



Figure 4.7. Medical grade honeys.

Honey must be incorporated into absorbent dressings, to ensure sufficient honey remains in contact with the wound bed [708]. Anti-microbial dressings with Manuka honey have been approved for sale in Europe, Canada, Australia, New Zealand and the US. One of the companies which sell such dressings is Derma Sciences, which is approved to sell Waikato-based Comvita LTD's dressing for wounds and burns in the US.

4.1.4.2.1. Osmotic Effect of Honey

The antibiotic effect of honey has been reviewed by Molan [708]. It has often been assumed that the antibacterial effect of honey is entirely due to the osmotic effect of its high sugar content [712, 721, 722], as is the case for other sugar syrups. The hygroscopic nature of honey means moisture is drawn out of the environment, and thus bacteria are dehydrated. A low pH (mean 4.4) also aids wound healing, causing more oxygen to be released from haemoglobin. However, usually upon contact with wound exudate, sugar syrups are diluted to levels which become ineffective against controlling infection [723]. However, honey has shown the ability to render sterile wounds which are infected with the common pathogen Staphylococcus aureus, which is known for its osmotolerance. Honey has the ability to prevent growth of Staphylococcus aureus even when diluted a further 7-14 fold beyond the point where osmolality ceases to be inhibitory [724]. The antibacterial potency of honey at low concentrations can be partially explained by the production of hydrogen peroxide which occurs upon dilution [725]. The importance of the additional antibacterial actions of honey is highlighted in comparisons between the therapeutic effects of honey and sugar [711, 726, 727]. An experimental study conducted on burns created on the skin of pigs [727], there were fewer bacterial colonies seen histologically in wounds treated with honey compared with those treated with sugar. Honey also possesses other advantages such as requiring fewer dressing changes than sugar dressings [712].

4.1.4.2.2. Hydrogen Peroxide Effect of Honey

Hydrogen peroxide is a well-known antimicrobial agent, which forms when honey is diluted, in the presence of oxygen. In recent times, it has lost favor because of cases of inflammation and tissue damage. However, the hydrogen peroxide levels in diluted honey are around 1 mol/L [703, 704] about 1000 times less than in the 3% solution commonly used as an antiseptic. Levels of 0.02-0.05 nmol/l hydrogen peroxide have shown to be effective at inhibiting Escherichia coli, whilst not damaging fibroblast cells from human skin [728].

4.1.4.2.3. Other Mechanisms of Honey

Additional non-peroxide wound healing effects have been identified, thought to be due to methylglyoxal (MG) and an unidentified synergistic component. MG is present in high levels in the Leptospermum-derived honeys [729]. However, MG plays a role in the pathogenesis of impaired diabetic wound healing, so further research is required in this area [730]. MGs are an important precursor for advanced glycation end products (AGEs) which accumulate in the ECM, resulting in decreased vessel elasticity and hindering keratinocyte migration, and which can enhance the activation of neutrophils in diabetics [730]. Recent research has indicated honey provides stimulation lymphocytes, and release of cytokines, TNF-a, IL-1 and IL-6 from monocytes, which activate the immune response to infection [731]. Honeys are also known to have antioxidant effects [732].

4.1.4.2.4. Animal Studies and Clinical Evidence for Healing Benefits of Honey

Reports of animal and clinical trials involving honey have been reviewed by Molan [689, 708, 710, 733]. Improved healing rates have been observed of burns created on the skin of rates, when treatment was of honey, as compared to a sugar solution similar to honey [734]. Epithelialisation was evident in 21 days for burns made on pigs which were treated with honey and sugar, as compared to silver sulfadiazine, which took 28-35 days to heal [724]. Full-thickness skin wounds on buffalo calves, injected with Staphylococcus aureus were treated with honey, saline or amphicillin ointment. The honey treated wounds exhibited a faster healing rate, lower inflammatory response and increased fibroblastic, angiogenic increased deposition of fibrous connective tissue and fastest re-epithelialisation. Clinical trials are difficult to perform due to the variations in age, multiple disease conditions and variations in wound site/characteristics/size. In a randomised, multicentre trial involving 156 patients, Manuka Honey (WoundCare 18+) increased the incidence of healing, desloughing & lowered the incidence of infection when compared to IntraSite Gel [735]. In a randomised control trial, 26 patients with postoperative wound infections had their wounds treated with honey and 24 had their wounds washed with 70% ethanol and povidone iodine applied [736]. The group treated with honey had infection eradicated and achieved complete healing in less than half the time compared with the antiseptic-treated group. Two randomised controlled clinical trials have compared honey with silver sulfadiazine ointment on partial-thickness burns [737, 738]. Both of these showed that honey gave better control of infection.

4.1.4.2.4. Propolis for Wound Healing

Propolis is a resinous substance present in honeycomb, which consists of at least 180 different compounds, including flavonoids, caffeic acid phenethyl ester, amino acids, and trace minerals such as iron and zinc. The main identified pharmacologically active components, flavonoids, phenolic acids, and their esters provide Propolis with the ability to act as a free radical scavenger and suggest potential anti-inflammatory and anti-microbial actions [739-741]. Antimicrobial activity has been observed against organisms including S. aureus, Streptococcus pyogenes, S. mutans, gram-positive and gram-negative bacteria species [742]. *In vitro* synergy between propolis and antimicrobial drugs has been investigated [709] and preparations combining propolis with antibiotic and antifungal agents are of potential medical interest [743]. In a rodent model, our coworkers, McLennan and group, demonstrated that the application of Propolis to diabetic wounds accelerated wound healing in diabetes, possibly through anti-inflammatory pathways [744]. Propolis prevented the persistent neutrophil infiltration and increased myeloperoxidase activity which is evident in diabetic wounds. Further work on the use of propolis in a clinical setting is required, although this preliminary evidence is promising.



Figure 4.8. (a) Propolis powder (b) Propolis is extracted from honeycomb (c) Propolis incorporation in toothpaste.

In the current study, a range of novel bioactive glasses were synthesised using a melt-derived process. These glasses were evaluated in terms of composition, bioactivity, mechanical hardness and radiopacity. In addition, methods were developed for mounting these glasses on variotis™ disks for cell testing. Manuka honey infused scaffold prototypes were also formed.

4.2. SYNTHESIS OF BIOACTIVE GLASS

Silica-based bioactive glass was synthesised with various levels of the following elements, with the corresponding proposed benefits. A corresponding code is assigned for easy reference to glass compositions used in this thesis.

ELEMENT	*BENEFIT*	*CODE*
Silica	Stability	S
Barium	Radiopacity	R
Zinc	Nutrient delivery	N
Iron	Antibacterial/magnetic	F

The flow diagram in Fig. 4.9 demonstrates the stages encompassed in the glass making process, which is described in this section. Various methods were trialed for each step, in order to determine a reliable way of upscaling the initial process. The synthesised glasses were subsequently characterised physically for their composition, bioactivity, nanoindentation and radiopacity (section 4.3-4.7). The glasses were also tested in an *in vitro* study in section 5.4.

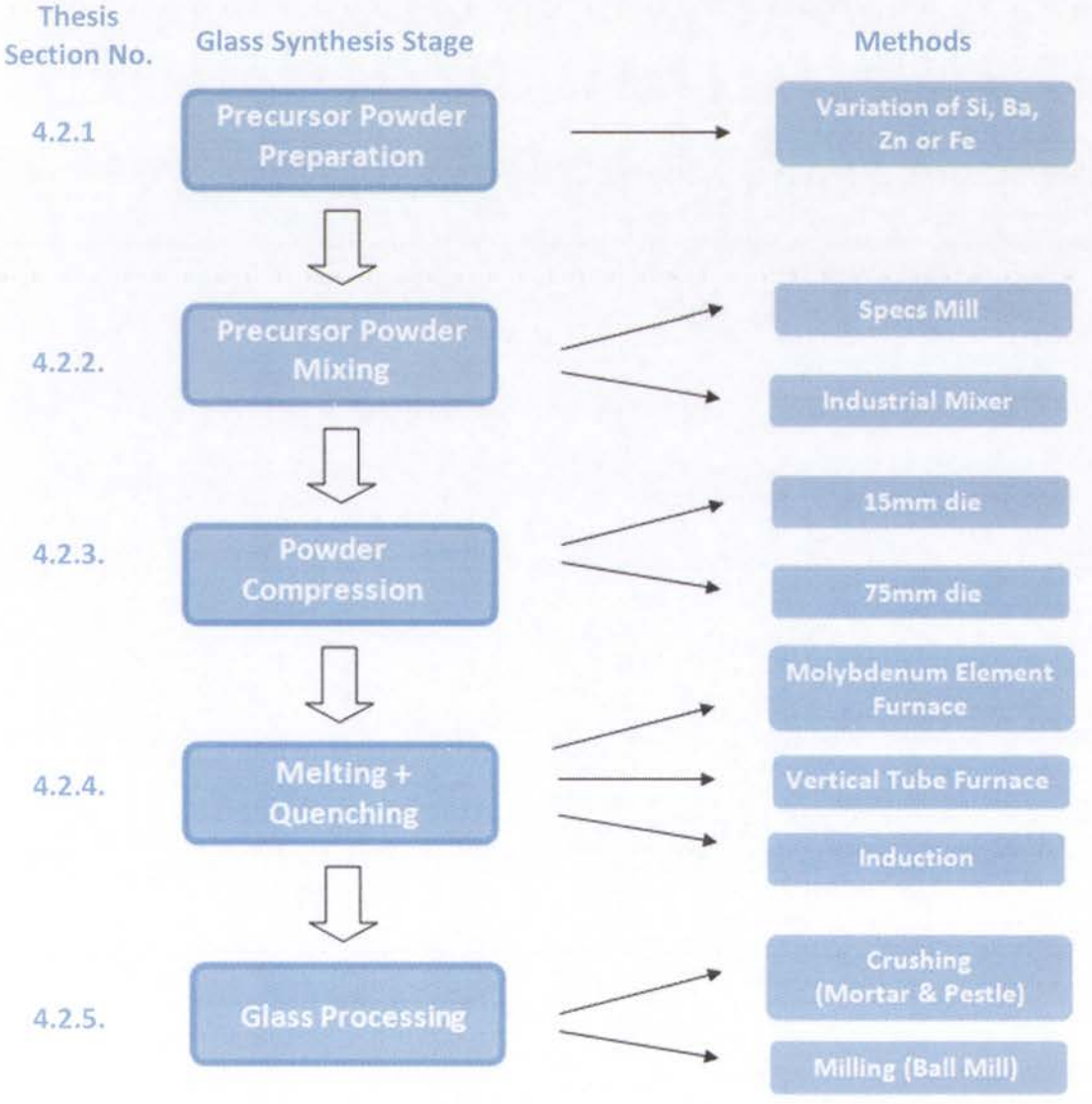


Figure 4.9. Flow diagram for glass synthesis.

4.2.1. PRECURSOR POWDER PREPARATION

Raw materials for the glasses were prepared according to following protocols. Raw materials were individually weighed according to the proportions described in Table 4.1. Two sizes of batches were prepared: 5.4 g in 100mL specimen jar ('original batch') & 300g in a 5L metal container ('upscaled batch'). Glasses with varying quantities of silica (45S5, 49S4.9 and 52S4.6) were synthesised. Glass was also formed using 0.5 mol% Ba and varying proportions of silica. In addition, glasses were formed by substituting the CaO component with 0.2, 2 and 5 wt% ZnO. The materials used were:

- Fumed silica, high purity (SiO_2, Sigma Aldrich, particle size 0.007 μm, surface area 390m^2/g)- MW: 60.1
- Calcium hydroxide (CaOH, Sigma Aldrich, 95+%, A.C.S. reagent grade)- MW:74.09
- Sodium carbonate (Na_2CO_3, Sigma Aldrich, granular, ≥99.5%, A.C.S. reagent grade)- MW:105.99
- Ammonium phosphate dibasic ($(NH_4)_3HPO_4$, Sigma Aldrich, reagent grade ≥98%): 132.06
- Barium carbonate ($BaCO_3$, Sigma Aldrich, 99.98%)- MW: 81.38
- Zinc Oxide (ZnO, Sigma Aldrich)- MW: 81.41
- Ferric Oxide (Fe_2O_3, Sigma Aldrich)- MW:159.69



Figure 4.10. Weighing of precursor powders.

Table 4.1. Formulation of the oxides used for bioactive glass synthesis. Measurements are in mol%(wt%).

Glass	SiO_2	P_2O_5	CaO	Na_2O_3	BaO	ZnO	Fe_2O_3
46S5.2 (45S5)	46.1 (45)	2.5 (6.0)	26.9 (24.5)	24.4 (24.5)	-	-	-
49S4.9	49.1 (47.9)	2.6 (6.0)	25.3 (23)	23.0 (23.1)	-	-	-
52S4.6	52.1 (50.8)	2.6 (6.0)	23.8 (21.6)	21.5 (21.6)	-	-	-
0.5Ba45S5	45.9 (44.8)	2.6 (6.0)	26.8 (24.4)	24.3 (24.5)	0.5 (1.2)	-	-
0.5Ba49S4.9	48.9 (47.7)	2.6 (6.0)	25.2 (22.9)	22.9 (23.1)	0.5 (1.2)	-	-
0.5Ba52S4.6	51.8 (50.6)	2.6 (6.0)	23.7 (21.6)	21.4 (21.5)	0.5 (1.2)	-	-
0.2%Zn45S5	46.2(45.0)	2.61 (6.0)	26.7 (24.3)	24.37 (24.5)	-	0.2 (0.2)	-
2%Zn45S5	46.5 (45.0)	2.6 (6.0)	24.9 (22.5)	24.5 (24.5)	-	1.5 (2.0)	-
5%Zn45S5	46.9 (45.0)	2.7 (6.0)	21.8 (19.5)	24.8 (24.5)	-	3.9 (5.0)	-
5%Fe45S5	56.74 (45.0)	3.44 (6.0)	19.94 (19.5)	17.51 (24.5)	-	-	2.37 (5.0)

The raw materials were mixed according to small and upscaled procedures, as described in this section.

4.2.1. Original Batch (SPEX Mill)

The 100mL specimen jar, containing 5.4g of precursor powder, was placed in a laboratory-scale, high-energy shaker mill (SPEX CertPrep Mixer/Mill 8000) and shaken for at least 5mins prior to pressing into pellets (Fig. 4.11a). This mixer shakes a single container backwards & forwards several times a minute, with the end of the container describing a figure of eight motion (Fig 4.11a). The length of the swing is approx. 2 inches, about the length of the vial itself. The SPEX mill can also be used as a ball mill with one or more balls, but is limited to samples around 10g or less. Overheating is a problem with this apparatus, so sessions are limited to 5-10mins.

4.2.2. Upscaled Batch (Industrial Mixer)

The 5L metal container, containing 300g precursor powder, was placed in a Blendor Mix M10 industrial scale mixer (Fig. 4.11b). A comparison between the size of this container and the smaller specimen jar are shown in Fig. 4.11c.

Mixing was performed for 2, 4 or 8mins, in an attempt to determine the minimum time required to yield the optimum ratio of raw materials for the melting process. This machine was originally designed for mixing fluids in 5L metal containers, therefore other containers could not be used.

5L paint tins were used for this process, and prepared by the following protocol. Residual paint was rinsed using cold water & tins were wiped using a clean cloth. The tins were filled with hot water for 30mins, then rinsed using cold water. They were dried by leaving in the sun for a day, followed by complete drying using a heat gun.

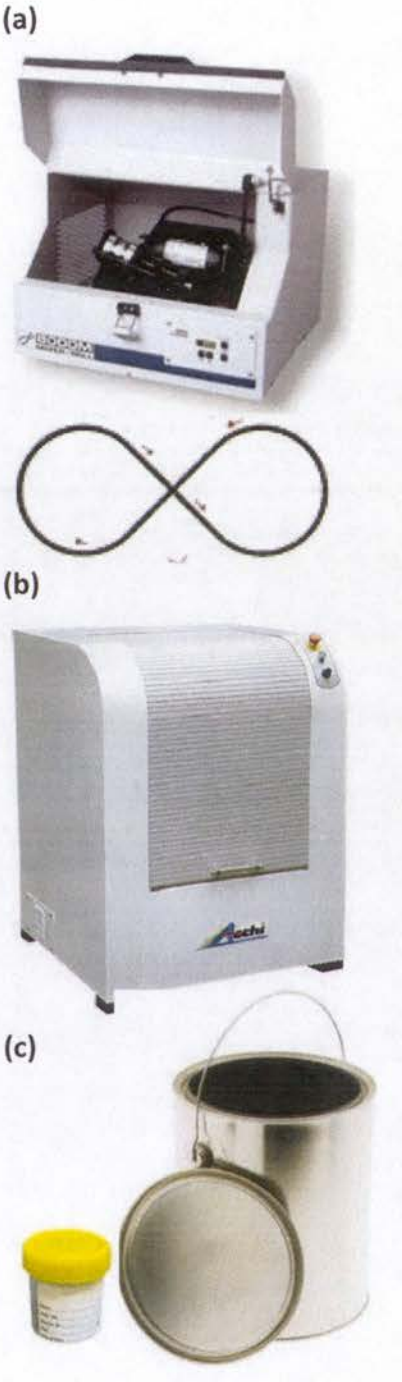


Figure 4.11. (a) SPEX mill + its figure-of-eight motion, (b) Industrial scale mixer, (c) Comparison between the two batch sizes.

The precursor powder was compressed into pellets in order to maximise the amount of bioactive glass powder which could be fit into one crucible during the melting process. This was particularly necessary due to the low density of the fumed silica, the major component in the mixture. Fig. 4.12 shows examples of the dies, the press and the powder disks which were made.



Figure 4.12. (a,b) The apparatus used for pressing the pellets, including the die and the press, (c) the completed pellets.

4.2.3.1. 15 mm Die Compression Method

The internal surfaces of a 15 mm diameter pellet die were wiped cleaned and lubricated with a stearic acid and acetone solution. A 1 g quantity of the raw material mix was weighed out on a clean sheet of paper and fed into the 15 mm diameter pellet die. Due to the low density of the raw material mix, small portions of each quantity were required to be fed into the die at a time and compressed by hand in order to fit the entire 1 g quantity within the pellet die. The filled die was compressed to a pellet pressure of 100 MPa (equivalent to 7.1 MPa or 1025.18 psi gauge pressure) using the 10 tonne load press. This pelletised the raw material mix into a 15 mm diameter pellet. The pressure was slowly released and the 15 mm diameter raw material pellet was removed and stored. This process was repeated for each composition of bioactive glass.

4.2.3.2. 75 mm Die Compression Method

The pellet compression process described above was upscaled using at 10 tonne load press and a 75 mm diameter pellet die. The compressive stress was kept at 100 MPa. The compression of the powders into pellets was not required, but was a means to a greater glass yield due to fitting more powder into the crucibles. The second method required the 75 mm pellets to be crushed into granules before melting. The second method resulted in a great increase in the time saved for compression. In

the time it took to compress 5.4 g using method 1, up to 40 g could be compressed in the same time.

The compression force required was calculated as:

For the 15 mm die:

Stress=Force/Area

*Force=Area*Stress*

*Force= (πx(0.015/2)^2 m^2 * 100x10^{6}Pa*

Force=17.670kN for the 15mm die

Stress=force/area =4MPa for the 75mm die

4.2.4. GLASS FORMATION

4.2.4.1. Crucible Preparation

Glass was melted by placing the precursor pellets or granules in crucibles. Glass formation was trialed using commercially sourced crucibles, made from platinum, porcelain or graphite (Fig. 4.13). For the majority of glasses, custom-made alumina crucibles were formed using the slip casting method, according to the following protocol (Shown schematically in Fig 4.14).



Figure 4.13. The various crucibles which were used.

To make the molds, pottery plaster was mixed with water according to the manufacturer's instructions. Crucible molds of two sizes were made: (1) d=5 cm, h-6 cm (2) d=10 cm, h=12 cm. The mixture was vibrated to remove any bubbles. A template lubricated with petroleum jelly was introduced (e.g. inner template: 1 L aluminium thermos, outer template: base of a disposable plastic drink bottle). Other molds were also synthesised, including a flat plate (10 x 15 mm). The mold was dessicated in an oven at 50°C for 48 hrs.

An alumina slurry was made according to the following. A 6 wt% Sodium Carboxylmethyl-cellulose (NaCMC) solution was made by weighing 1 L distilled water and 6 g NaCMC into a glass beaker, and stirred overnight using a magnetic stirrer. The solution was mixed with alumina powder and magnesia in the proportion 450 g NaCMC solution to 550 g alumina and

0.33 g magnesia in a pot mill with 2 kg of 1 cm alumina balls. The jar was tightly sealed and the alumina solution was placed on a rotating ball mill for 2 hrs. The solution was poured into a jug and used immediately. The alumina mixture was poured into molds using a glass funnel. Crucibles were dried at room temperature for 40 mins, until the required thickness had achieved. As the crucibles were drying, extra SiC solution was added to the mold to ensure an even wall thickness at the top of the crucible. This was added at the rate of approx. 3 mm per 5 mins for the first 15 mins. The remaining alumina slurry was poured out of the mold. This slurry could be reused immediately if convenient. The molds were turned upside-down for 1-2 mins to allow excess slurry to come to the top of the crucible. A paint brush was used to remove excess slurry from the top of the crucible. A sharp tool was used to cut away the top edge of the crucible, to ensure a smooth surface. Approx. 10 crucibles were synthesised in total using this method. Silica carbide crucibles were also synthesised using a similar process, however these were not needed for glass synthesis. For SiC crucibles, 425.52 g silica Carbide and 47.28 g clay were used. The crucibles took 45-60 mins to dry.

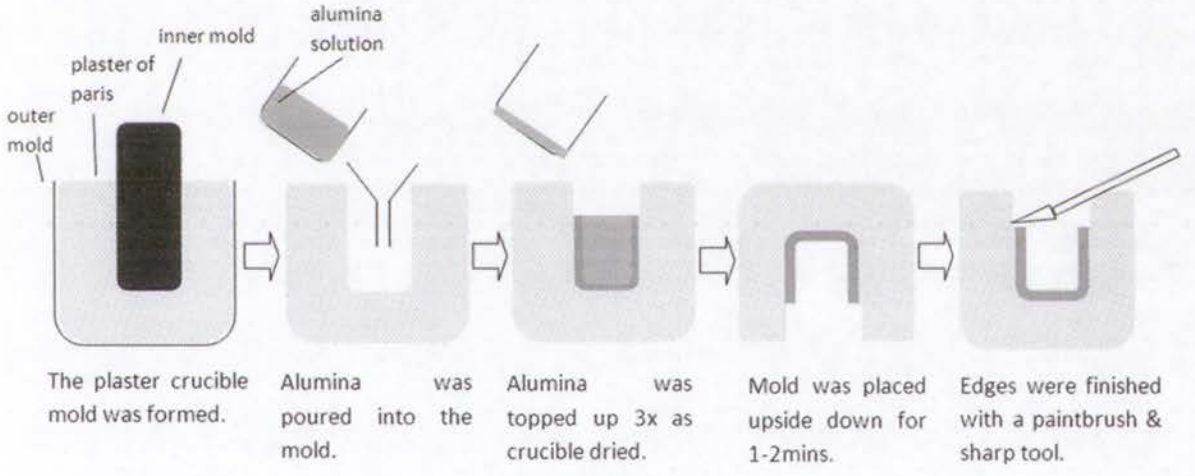


Figure 4.14. Schematic showing the crucible synthesis procedure.

4.2.4.2. Melting and Quenching of Glass

To form the glass, raw material pellets or granules were placed into crucibles, for example platinum (2-5 pellets) or large alumina (10 pellets). The crucible was slowly heated (to 1200-1350°C) in an oven. The melted glass was quenched using a bucket of iced water. The following section describes the various ovens which were trialed for the glass making process (Fig. 4.15).

4.2.4.2.1. Molybdenum Element Furnace

Glass melting using a molybdenum furnace (either Tetlow or MOS12) was the most widely used process. Initially, 10 g batches in a single, large alumina crucible were made using this method. This was termed the 'original' method.

The molybdenum furnace process was further optimised replacing the large crucible by 4 smaller alumina crucibles, and lightly packing precursor granules rather than pellets into the crucibles. The temperature of the oven was set to increase at 300°C/hr until 800°C and 100°C/hr until 1200°C. During this process, further precursor powder was added to the compacted mixtures, to maximise yield. The yield from these crucibles was 68.7-82.5 g each. This method was termed the 'revised' method.

4.2.4.2.1. Vertical Tube Furnace

The Tetlow vertical tube furnace allowed a continuous melting process to be undertaken, thus eliminating the steps involving repetitive preheating & loading of the crucibles. 20 g of glass was synthesised using this method.

4.2.4.2.1. Induction Furnace

An induction furnace operates by heating the glass via heating a coil of copper wire which surrounds the sample, using the principle of Lenz's Law. However, using this process the maximum temperature reached was 100°C. The advantage of induction heating is the total low energy consumption required compared to the molybdenum element furnace. The induction furnace reaches its peak temperature in a matter of minutes, eliminating the need for ~5 hrs of preheating. Induction heating was performed in porcelain or graphite crucibles.

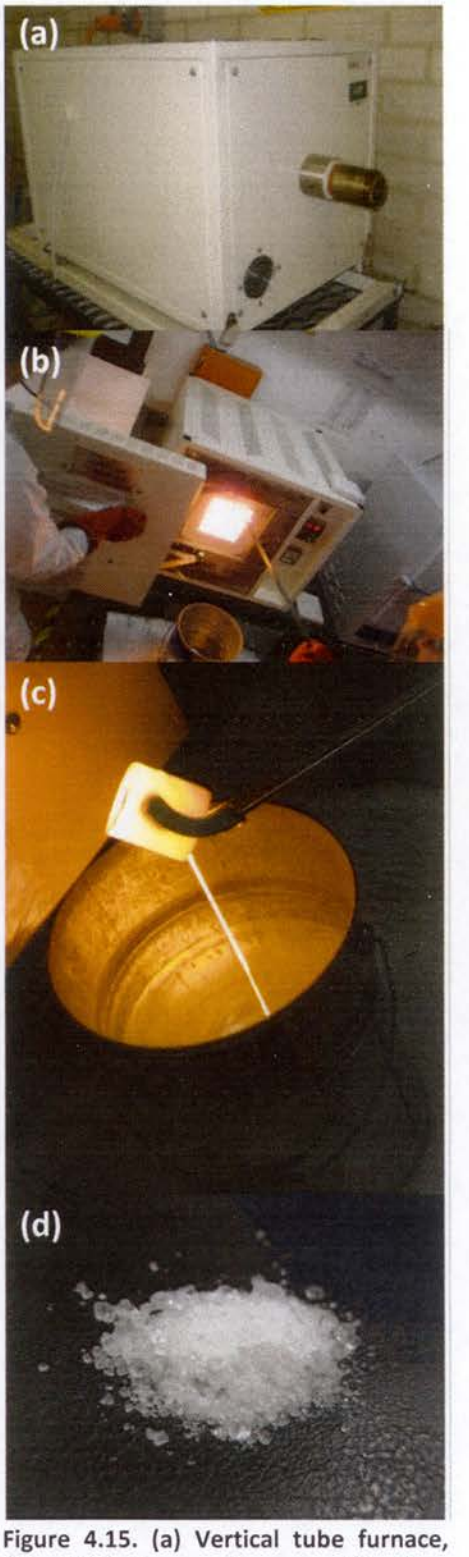


Figure 4.15. (a) Vertical tube furnace, (b) Molybdenum furnace, (c) Glass quenching, (d) The synthesised bioactive glass granules.

4.2.5.1. Manual Process for Glass Milling

Glass granules were crushed using a mortar & pestle made from either glass, plastic or granite (Fig. 4.16). Glass was passed through a sieve with 104-234 μm diameter apertures. This was a time & labour-intensive process, often requiring further crushing of the particles to obtain the desired particle size. Commonly a few grams of glass would take at least 15mins to crush to the appropriate size.

For the particle size characterisation, 45S5 granules were crushed using a plastic mortar & pestle. Commercially sourced 13-93 glass fibers (Mo Sci Health Care, Rolla, MO) were also crushed and sieved using this method, into short fibers.



Figure 4.16 l to r: 13-93 bioactive glass fibers, crushing of the 13-93 fibers and 45S5 granules, sieving of the glass.

4.2.5.2. Ball Milling of Glass

In order to automate the glass crushing process, a ball mill was utilised to mill the glass within an alumina-ball filled plastic or alumina jar (Fig 4.17). A ball mill was designed and manufactured by Jonathan Bruck. To demonstrate the feasibility of the milling process, commercially obtained E-glass was used as a model and coated on the scaffold (ref 3.2.2.3.A). In future studies, 45S5 could be milled in order to obtain micron-sized particles, if high dissolution rates and surface areas are required.

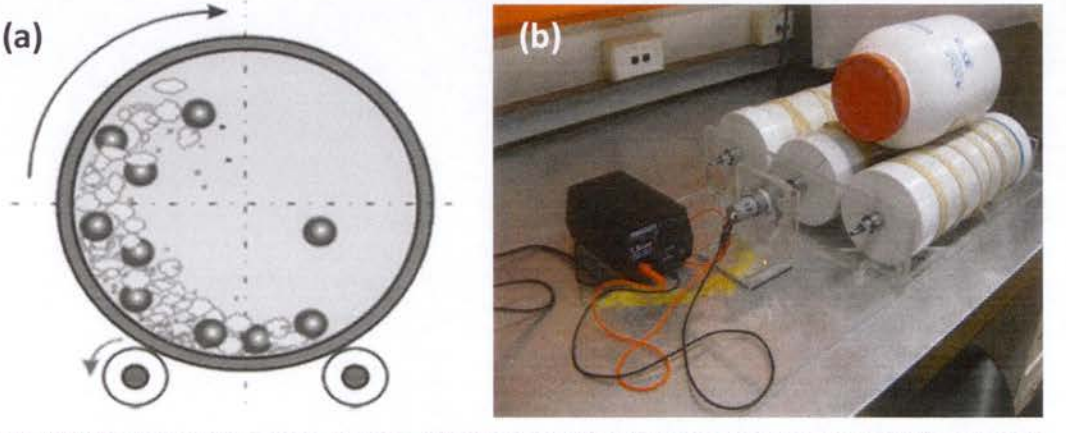


Figure 4.17. (a) The ball mill crushing process, (b) The ball mill which was designed & manufactured by our group.

Table 4.2. describes the glass batches which were synthesised. The analysis methods which were used for physical characterisation of the glass are listed, with the corresponding thesis sections indicated. Characterisation techniques included:

1. Particle size;
2. Composition (via SEM/EDAX/XRF);
3. Bioactivity/Dissolution (via SBF soaking);
4. Mechanical properties via nanoindentation (NI); and
5. Radiopacity measurements (via Fluoroscopy).

Table 4.2. Glass batches and analysis techniques undertaken.

Batch	Composition	Mixing Process	Melting Process	Processing	Analysis Techniques (thesis section)
PAx1	45S5	Industrial Mixer (2min)	-	Precursor Powder Pellets	SEM/EDAX, XRF (4.4)
PAx2	45S5	Industrial Mixer (4min)	-	Precursor Powder Pellets	SEM/EDAX, XRF (4.4)
PAx3	45S5	Industrial Mixer (8min)	-	Precursor Powder Pellets	SEM/EDAX, XRF (4.4)
Ax1	45S5	SPEX	Molybdenum Furnace (original)	Manual Process	Particle size (4.3), SEM/EDAX (4.4), Bioactivity (4.6), Radiopacity (4.7) NI (4.6)
Ax2	45S5	Industrial Mixer (8min)	Molybdenum Furnace (revised)	Manual Process	SEM/EDAX, XRF (4.4)
Ax3	45S5	Industrial Mixer (4min)	Molybdenum Furnace (revised)	Ball Mill (80min)	SEM/EDAX (4.4)
Fx1	5%Fe45S5	SPEX	Induction	-	SEM/EDAX (4.4), NI (4.5)
Nx3	5%Zn45S5	SPEX	Molybdenum Furnace (original)	Manual Process	SEM/EDAX (4.4), NI (4.5)

Sx3	13-93 fibers	Commercially Sourced	-	Manual Process	Particle size (4.3), NI (4.6)
Sx4	E-glass fibers (with sizing)	Commercially Sourced	-	Ball Mill (80min)	NI (4.5)
Sx1	49S4.9	SPEX	Molybdenum Furnace (original)	-	NI (4.5), Bioactivity (4.6), Radiopacity (4.7)
Sx2	52S4.6	SPEX	Vertical Tube Furnace	-	NI (4.5), Bioactivity (4.6), Radiopacity (4.7)
Rx1	0.5Ba45S5	SPEX	Vertical Tube Furnace	-	NI (4.5), Bioactivity (4.6), Radiopacity (4.7)
Rx2	0.5Ba49S4.9	SPEX	Vertical Tube Furnace	-	NI (4.6), Bioactivity (4.6), Radiopacity (4.7)
Rx3	0.5Ba52S4.6	SPEX	Vertical Tube Furnace	-	NI (4.6), Bioactivity (4.6), Radiopacity (4.7)
Nx1	0.2%Zn45S5	SPEX	Molybdenum Furnace (original)	-	NI (4.5), Bioactivity (4.6)
Nx2	2%Zn45S5	SPEX	Molybdenum Furnace (original)	-	NI (4.5), Bioactivity (4.6)
Ax4	45S5	SPEX	Vertical Tube Furnace		NI (4.6), Bioactivity (4.6)

4.3. CHARACTERISATION OF GLASS PARTICLE SIZE DISTRIBUTION

4.3.1. METHODS

4.3.1.1. Digital Particle Size Distribution

Bioactive glass powders (45S5: Ax1, 13-93: Sx3) were visualised using a Leitz DMRXE optical microscope and Leica DFC420 digital camera system. The particle dimensions were characterised using Leica QWin Plus (version 3.5.0) image analysis and processing software. Glass particles were placed onto a glass microscope slide. A drop of ethanol was placed onto the glass to enable dispersion of the particles into a single layer. The slide was placed onto the microscope & the focus and lighting was adjusted. The image was captured using Leica QWin Plus > Image>Image preview>acquire. Features were detected by selecting Image>Detect (Fig. 4.18). Features were measured by selecting measure>measure feature>measure. The minimum area for feature detection was set. A table was formed specifying the area, dimensions, roundness and aspect ratio of all the particles. A histogram of the particle features was created using Measure>feature histogram. Graphs were formed of the feature number vs area and feature number vs length.

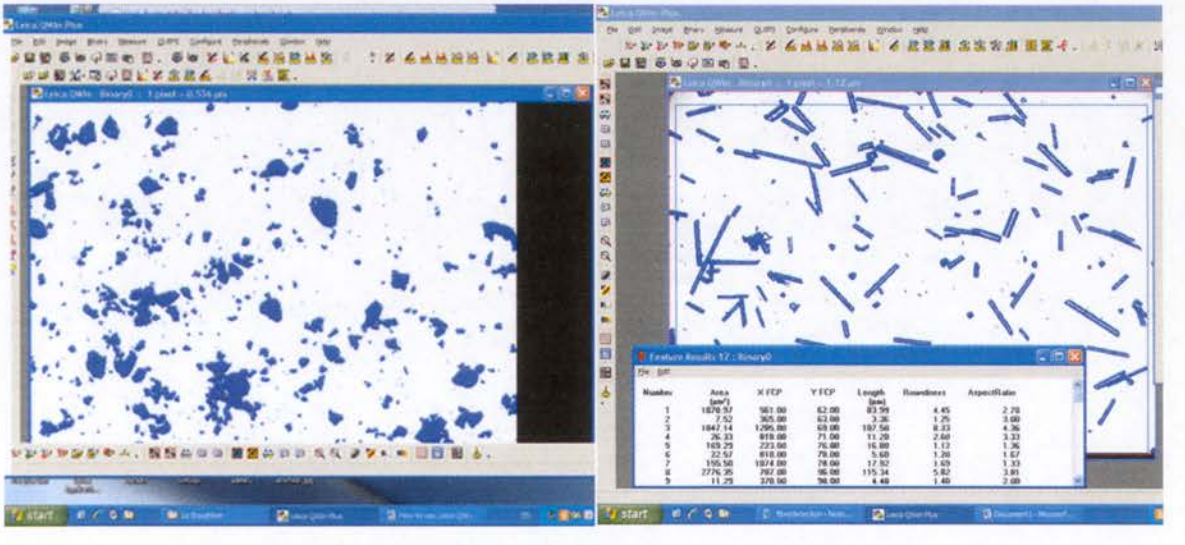


Figure 4.18. Detection of 45S5 glass particles & 13-93 short fibers.

Particle size distributions for 45S5 and 1393 powders are shown below. When crushed using a ball mill, E-glass powder was made with a consistent diameter <5um (not shown).

4.3.2.1. Particle Distribution for 45S5 Powder

Fig. 4.19 shows an image of the 45S5 glass powder (Ax1) taken using optical microscopy and particle size distribution for the 45S5 sample. The particle distribution histogram (Fig. 4.19) shows that 80% of the particles were <30μm in length. The remaining 20% were between 30 & 100μm. The mean length was 19.04±17.77μm. 88.83% particles were <200μm^2 in area, with 11.16% between 20 & 100μm^2. The mean area of the particles was 90.8±5.27μm^2.

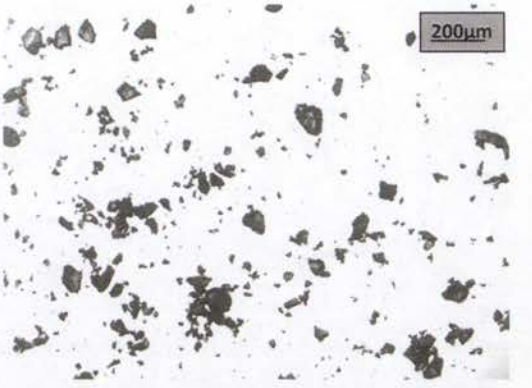


Figure 4.19. 45S5 powder (Ax1) crushed using the manual method.

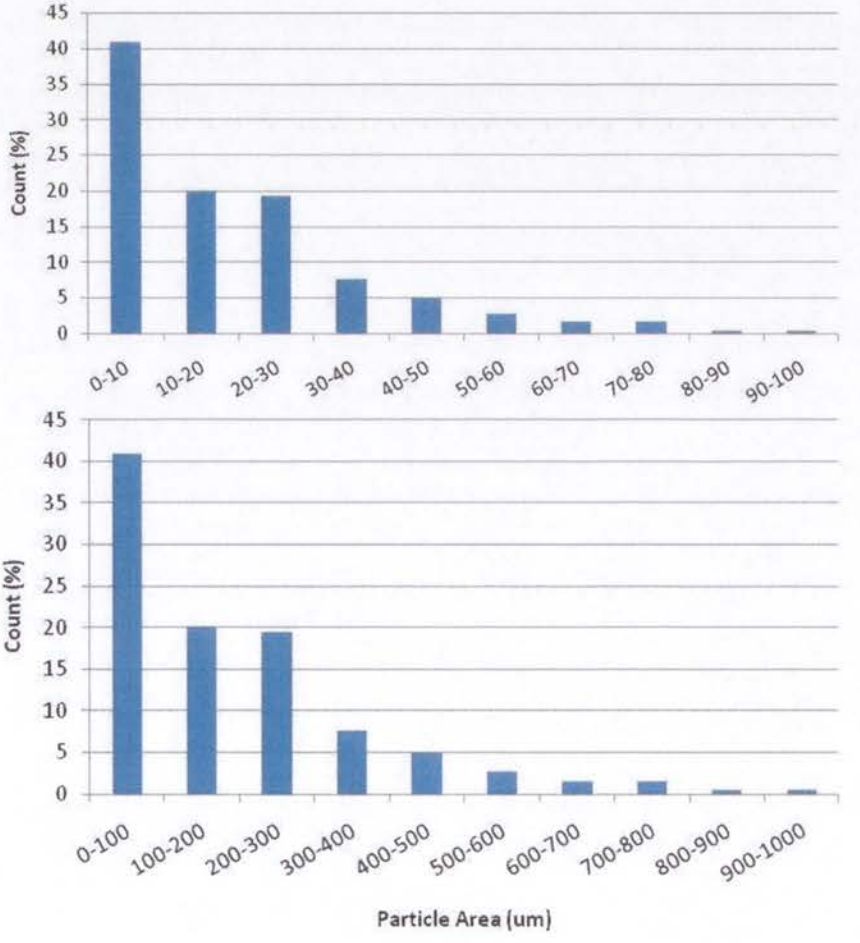


Figure 4.20. Particle size distribution for length and area of 45S5 powder (Ax1).

4.3.2.2. Particle Distribution for 1393 Short Fibers

The 1393 short fibers are shown visually in Fig. 4.21 and a histogram of their lengths is shown in Fig. 4.22. 5% of the particles were <10um in length, 31% were 10-50μm, and the remaining 4% were between 50-300μm. The mean length was 15.34±27.42μm. 82% particles were <100μm^2 in area, with 15% between 100 and 500μm^2. The mean areas of the particles were 95.51±230.16μm^2.

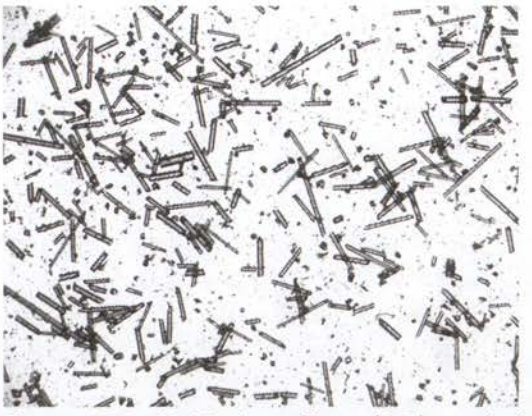


Figure 4.21. 13-93 short fibers (Sx3) crushed using the manual method.

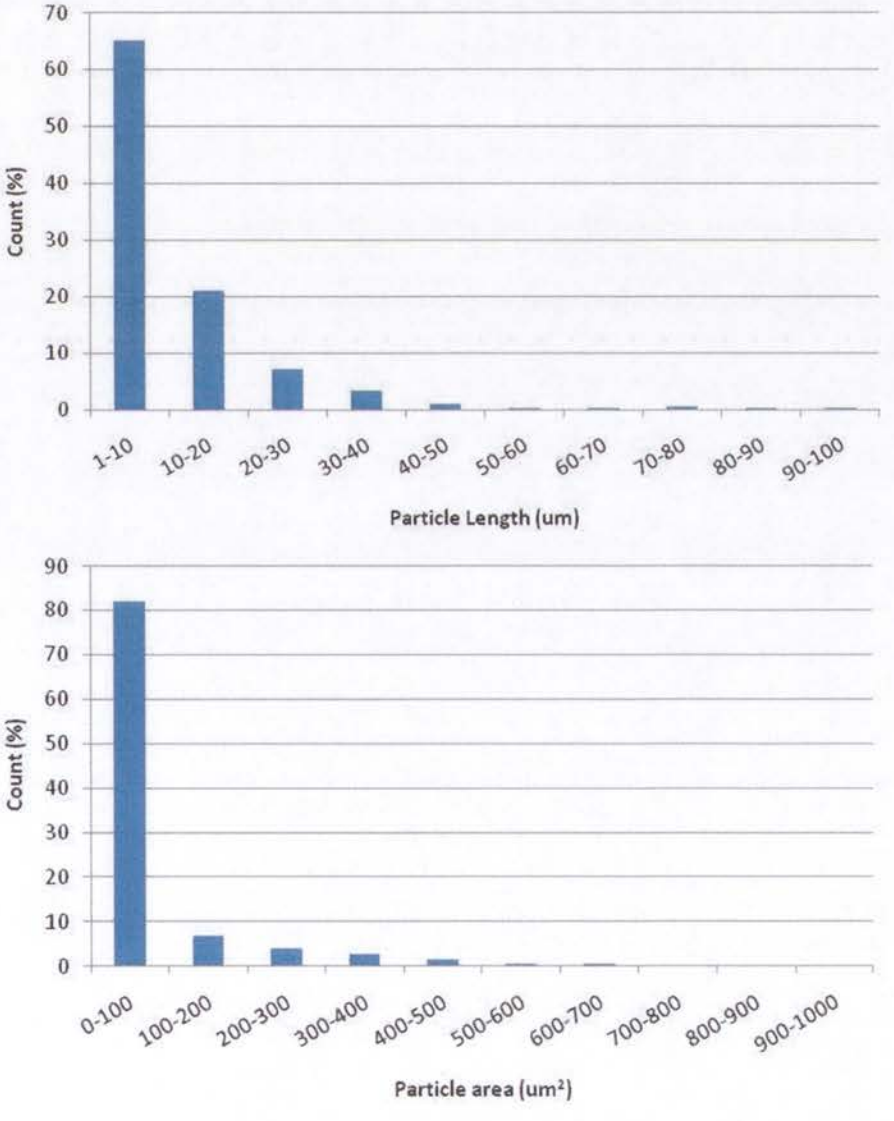


Figure 4.22. Particle size distribution for length and area of 13-93 particles (Sx3).

4.3.3. DISCUSSION

Fine glass particles were made using the manual crushing method. Observation of E-glass milled using the ball mill showed that all glass was <5μm in diameter. Digital quantitation of the particle sizes achieved showed that all 45S5 glass particles were reduced to <100μm (Fig. 4.20). The 1393 short fibers were reduced to <300μm (Fig. 4.22). A narrow particle size range was difficult to achieve for the 1393 fibers. This was due to the large difference between their length and diameter. This meant that long fibers were not always excluded using a sieve.

4.4. CHARACTERISATION OF GLASS COMPOSITION

4.4.1. METHODS

4.4.1.1. Scanning Electron Microscopy (SEM) and Energy Dispersive X-Ray Spectroscopy (EDS)

Samples were prepared for SEM by attaching to aluminium stubs using double-sided conductive carbon tape (Fig 4.23a). Circular tabs were not used as they exhibit microscopic texture on the surface which can interfere with imaging of the powders. Conduction to the alumina was further facilitated by the use of silver conductive dag on the edges of the specimens. Excess powders were removed using a hand-held air pump. Specimens were coated with 15μm of carbon using an automatic carbon sputter coater (EMITECG K550X) (Fig 4.23b). Specimens were imaged with a Philips XL30 SEM (Fig 4.23c), with a current of 25kV and spot size 50nm, and captured using Image slave software.

The elemental composition of the glasses was measured using an integrated EDS detector (EDAX) and EDX-ZAF software. The collection time was 100s and spot size 100 mm. The composition was measured over regions occupying an entire screen. The results are presented as the mean ± standard deviation of 3 regions. The mean Si:Ca ratio was also

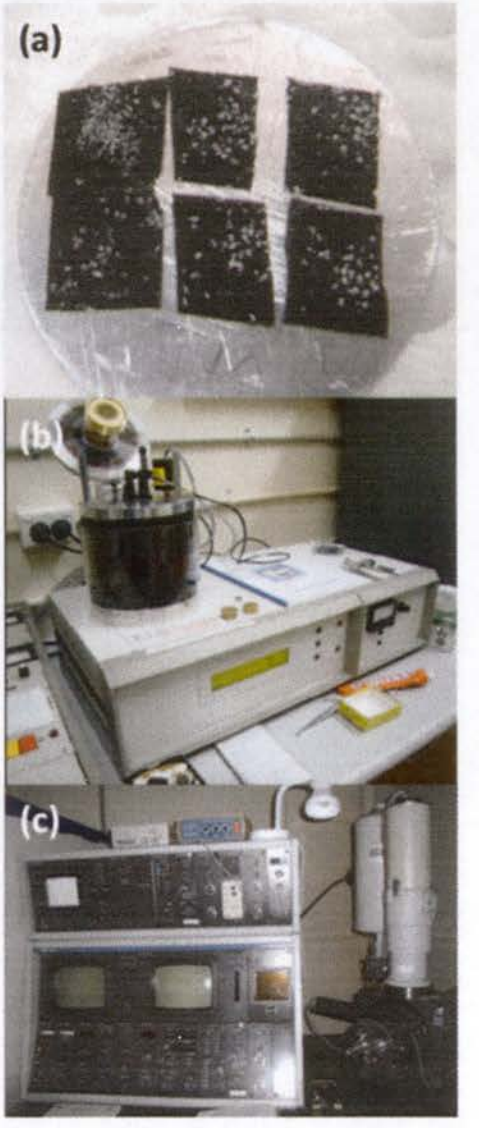


Figure 4.23. (a) Glass samples on conductive tape, (b) Carbon sputter coater, (c) Phillips XL30 SEM.

calculated. Glass compositions were verified by comparison with the correct glass formulations (ref Table 4.1). EDS was performed to examine the following:

- Efficacy of precursor mixing (PAx1, PAx2, PAx3)
- Glass melting (Ax1, Ax2)
- Glass processing (manual vs ball milling) (Ax1, Ax3)
- Glass doping (iron, zinc) (Fx1, Nx3)

4.4.1.2. X-Ray Fluoroscopy

X-ray fluoroscopy was performed by Irene Wainwright at University of New South Wales, using a Philips PW2400 XRF machine, with SUPERQ software. Samples tested included: 45S5 precursor powder (PAx1, PAx2, PAx3) and 45S5 glass (upscaled process) (Ax2).

The fluoroscopy procedure included the following steps.

1. Generation of channels for the desired elements;
2. Assembly of an analytical program with background channels;
3. Measurement of samples with different adsorption coefficients;
4. Calculation of background correlation factors;
5. Measurement of a set of standards with known composition;
6. Calculation of calibration factors; and
7. Measurement of unknown samples.

4.4.2 RESULTS

4.4.2.1. Efficacy of Precursor Mixing

The appearance of the 45S5 precursor powder after mixing for 2 or 8 mins using the industrial mixer is shown in Fig. 4.24a and Fig. 4.24b. After 8mins of mixing, the powder exhibited less clumping. The elemental spectrums obtained from EDAX analysis on the precursor powder are shown in Fig. 4.24c and summarised in Table 4.3. Peaks were evident for silica and calcium for all mixing times. There was an absence of phosphorous for all samples. The Si:Ca ratio was very low for 2 & 4mins (0.44±0.56 & 0.69±0.56 respectively) and high for 8mins (2.76±0.18). This indicates the optimal mixing time could lie between 4 & 8mins. However, high standard deviations and the absence of phosphorous and sodium could indicate incomplete mixing at all timepoints.

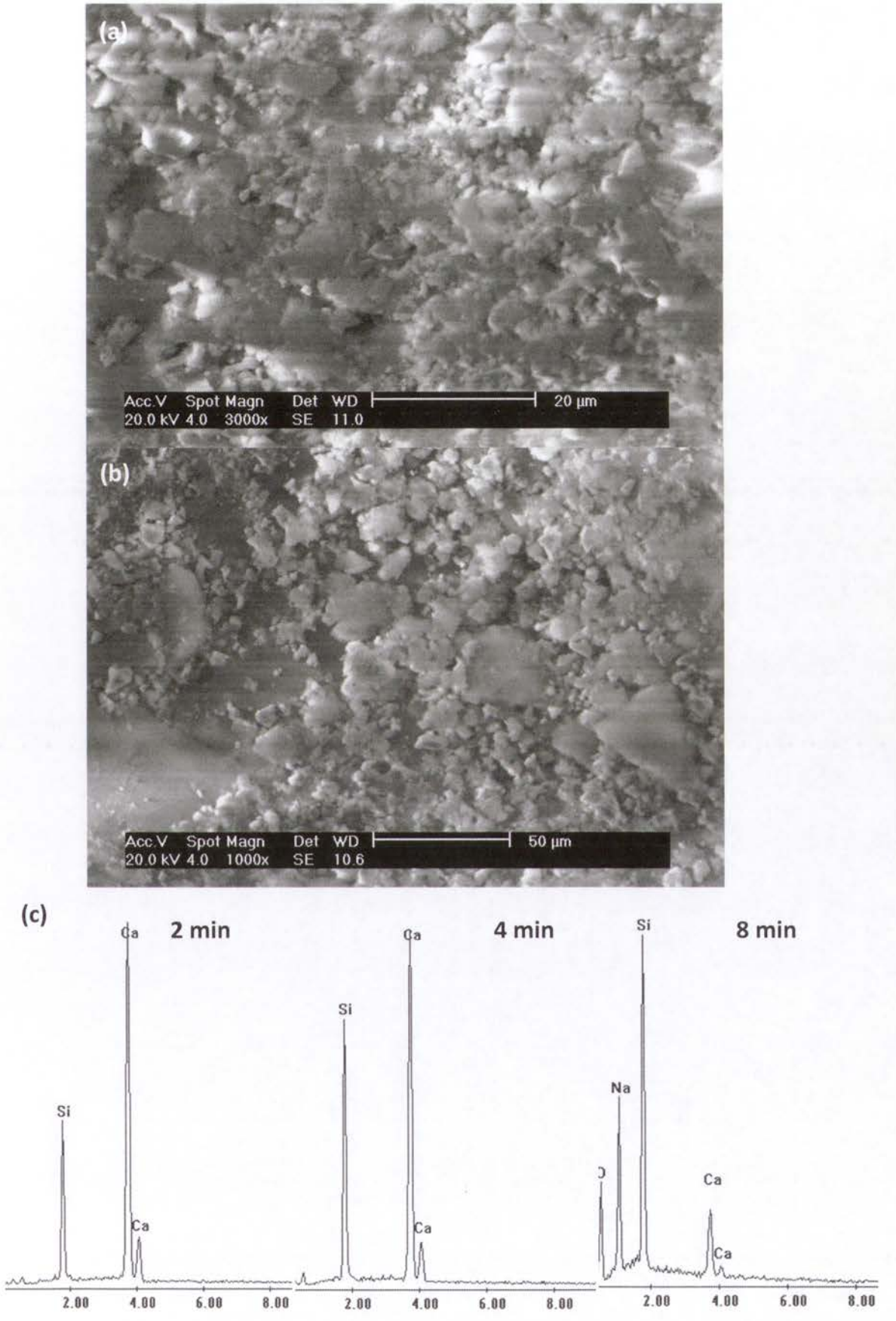


Figure 4.24. SEMs of the precursor powder after (a) 2min (PAx1) and (b) 8min mixing (PAx3). (c) EDAX spectrums after various periods of mixing (PAx1, PAx2, PAx3).

Table 4.3. Comparison of the composition of 45S5 precursor powder after 2, 4 and 8mins mixing (average of 3 regions).

Element	Time in industrial mixer			Correct Composition (mol%)
	2min (mol%) (PAx1)	4min (mol%) (PAx2)	8min (mol%) (PAx3)	
SiO_2	30.82±14.58	40.66±8.02	64.04±10.10	46.1
CaO	69.18±2.41	59.34±8.02	23.23±10.51	26.9
Na_2O	-	-	12.98±15.24	24.4
Si:Ca RATIO	0.44±0.56	0.69±0.56	2.76±0.18	1.71

However, the X-ray fluoroscopy results for these samples indicated very different compositions, as shown in Table 4.4. Using x-ray fluoroscopy, the levels of P_2O_5 and Na_2O for all samples were close to the expected levels. The ratio of Si to Ca was also very similar for all the samples, and somewhat close to the expected proportion, although actual Si and Ca levels differed from the actual formulation. The level of CaO decreased slightly with increasing periods of mixing. The amount of SiO_2 reduced for the sample which was mixed for 4min, but for the 8min mixed sample, returned to the same level as the sample which was mixed for 2min.

Table 4.4. Composition of 45S5 precursor powder using x-ray fluoroscopy after 2, 4 and 8mins of mixing.

Oxides	Time in industrial mixer			Correct Composition (mol%)
	2min (mol%) (PAx1)	4min (mol%) (PAx2)	8min (mol%) (PAx3)	
SiO_2	21.77	17.89	21.01	46.1
CaO	15.32	13.11	12.82	26.9
Na_2O	23.33	27.47	24.02	24.4
P_2O_5	6.59	6.90	6.99	2.5
Si:Ca RATIO	1.42	1.36	1.64	1.71

Trace Elements	Time in industrial mixer		
	2min (PPM) (PAx1)	4min (PPM) (PAx2)	8min (PPM) (PAx3)
Zn	15.8	8.3	42
Sr	45.2	40	43.1
Zr	11.2	11.1	16.1
V	10.1	11.3	8.9

Levels of Cu, Cr, Sr, Pb, Rb, Y, Ni, Ga, Ba, Nb were low (<10PPM) for all samples and are not shown.

4.4.2.2. Verification of Glass Composition

Figure 4.25 and Table 4.4 show the appearance and composition of 45S5 Bioglass® granules melted using the conventional furnace method using the original small or upscaled batch process. Si:Ca ratios measured with both EDAX and x-ray fluoroscopy were similar to the theoretical levels. Similar quantities of all components were also achieved. For most of the components, there was little difference between the small and upscaled batches. Surprisingly, the upscaled batch showed a higher level of phosphorous and alumina than the small batch.

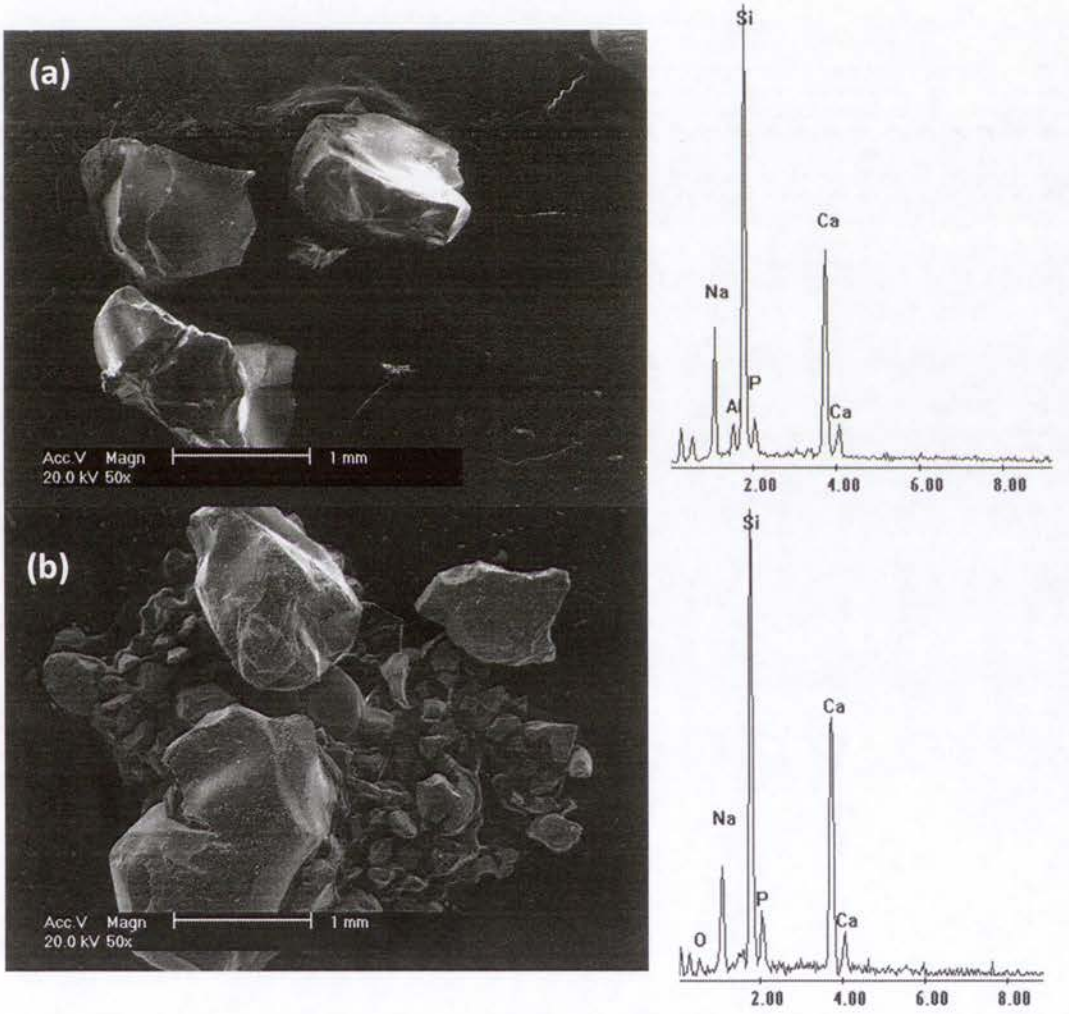


Figure 4.25. SEM and EDAX spectrums for 45S5 synthesised using a (a) small (Ax1) or (b) upscaled (Ax2) batch process. EDAX was performed on samples which had been crushed using the manual process.

Table 4.4. EDAX and XRF results for 45S5 glass.

Oxides	EDAX		XRF	Correct Composition (mol%)
	Small Batch (Ax1) (mol%)	Upscaled Batch (Ax2) (PPM)		
SiO_2	53.75±1.05	55.19±0.95	47	46.1
CaO	25.43±1.26	27.94±1.15	24.79	26.9
Na_2O	15.34±0.98	15.59±1.02	21.99	24.4
P_2O_5	3.48±0.08	8.53±0.12	4.97	2.5
Al_2O_3	3.16±0.20	1.27±0.18	1.14	0
Si:Ca RATIO	2.11±0.83	1.98±0.83	1.90	1.71

Trace Elements	XRF
	Upscaled Batch (Ax2) (PPM)
Pb	15.5
Sr	71.3
Y	10.1
Zr	20.5
Cu	19.5
Zn	29.2
Cr	14.8
V	11.3

Levels of Rb, Ni, Ga, Nb were low (<10) and are not shown.

4.4.2.3. Comparison of Glass Processing Technique

The appearance and composition of the 45S5 glass milled using either the manual process or the ball mill are shown in Figs. 4.26, 4.27 and Table 4.5. The Si:Ca ratio for the manually milled glass was close to the theoretical value. A high Si:Ca was measured for the ball milled glass. The ball milled glasses contained high levels of alumina compared to manually-milled glass (2.6x). For the other components, the level achieved using the manual milling process was close to the ideal value. An absence of phosphorous was observed for the ball milled sample.

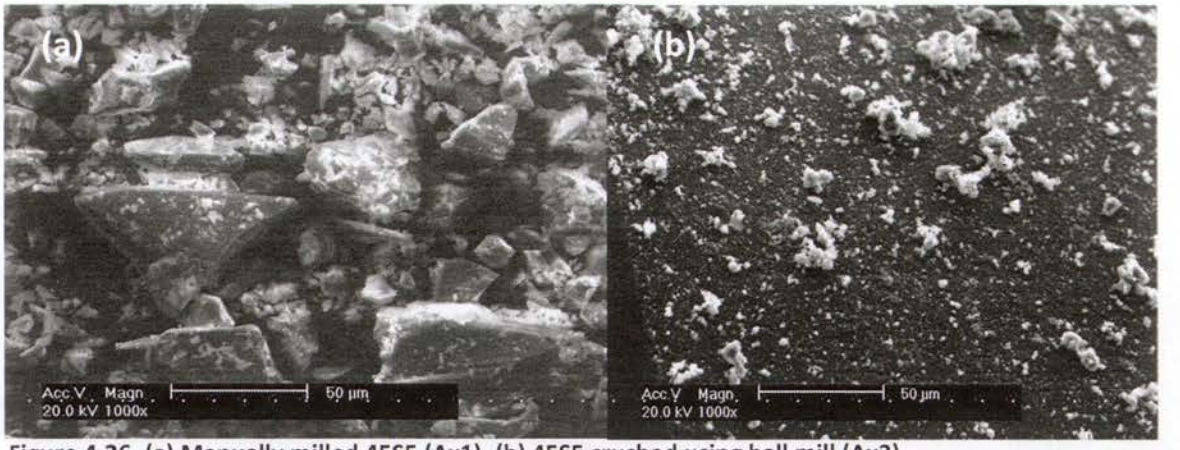


Figure 4.26. (a) Manually milled 45S5 (Ax1), (b) 45S5 crushed using ball mill (Ax3).

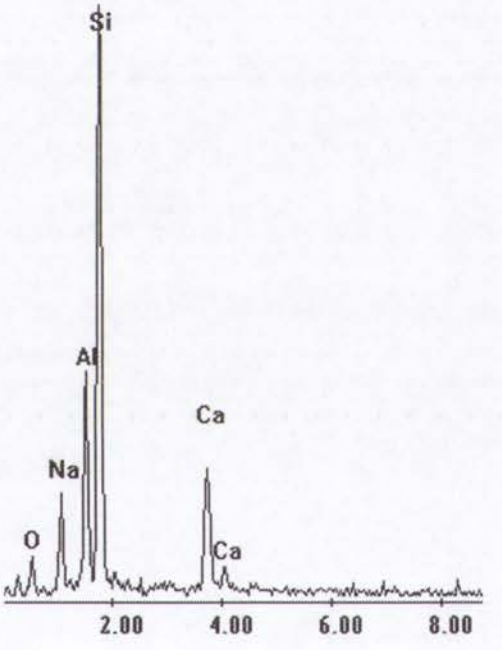


Figure 4.27. EDAX analysis of the ball milled 45S5 glass (Ax3).

Table 4.5. EDAX results for 45S5 milled glasses.

Oxides	Manual Process (Ax1) (mol%)	Ball Millled (Ax3) (mol%)	Correct Composition (mol%)
SiO_2	53.75±1.05	67.11±1.03	46.1
CaO	25.43±1.26	14.64±0.23	26.9
Na_2O	15.34±0.98	10.02±0.82	24.4
P_2O_5	3.48±0.08	-	2.5
Al_2O_3	3.16±0.20	8.22±0.40	0
Si:Ca RATIO	2.11	4.58	1.71

4.4.2.4. Glass Doping

4.4.2.4.1. Composition of Iron-Doped Glass

Iron-doped 45S5 glass (Fx1) was successfully made and displayed a clear, blueish appearance. An SEM image and EDAX measurements of the elements are shown in Fig. 4.28 and Table 4.6. Peaks were visible for all expected elements, including P_2O_5. The Si:Ca ratio was low compared to the correct composition. A low level of silica and high level of ferric oxide was detected compared. Again, alumina contamination was evident.

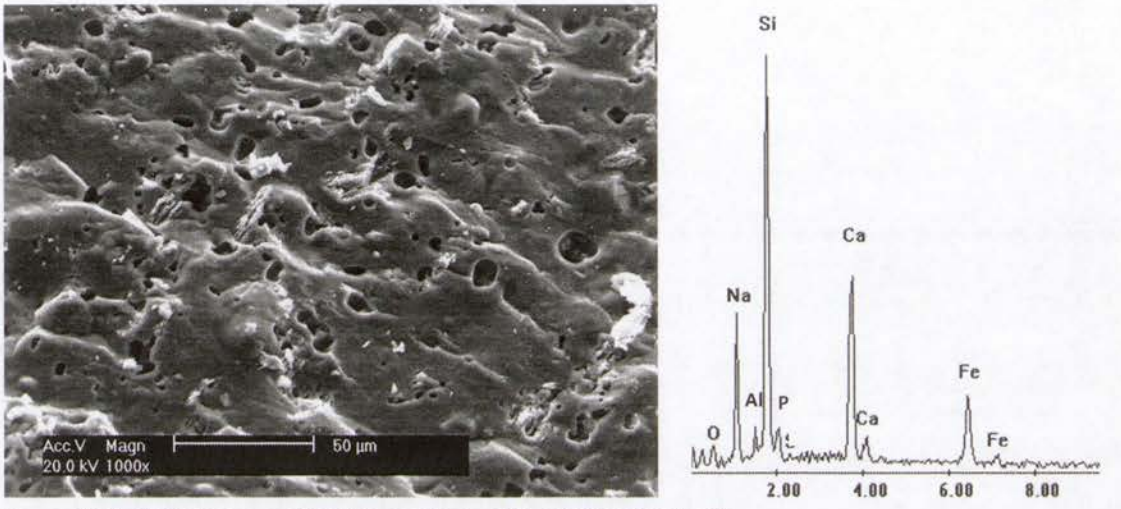


Figure 4.28. SEM image and EDAX spectrum of the 5%Fe45S5 (Fx1).

Table 4.6. Composition for 5%Fe45S5 (Fx1) glass.

Oxides	Iron-doped Glass (Fx1) (mol %)	Correct Composition (mol%)
SiO_2	38.40±8.57	56.74
CaO	23.90±3.71	19.94
Na_2O	27.36±7.69	17.51
P_2O_5	6.15±3.41	3.44
Al_2O_5	4.6±2.3	0
Fe_2O_5	4.19±2.1	2.37
Si:Ca RATIO	1.60±2.31	2.84

4.4.2.4.2. Composition of Zinc-Doped Glass

Zinc-doped 45S5 glass (5wt%Zn45S5) was also synthesised and compositionally characterised (Fig. 4.29, Table 4.7). The Si:Ca ratio was slightly higher than the theoretical composition. Levels of all oxides were similar to the correct amounts, except for low levels of calcium. High levels of alumina were noticed in some regions, but lower amounts were detected in other areas.

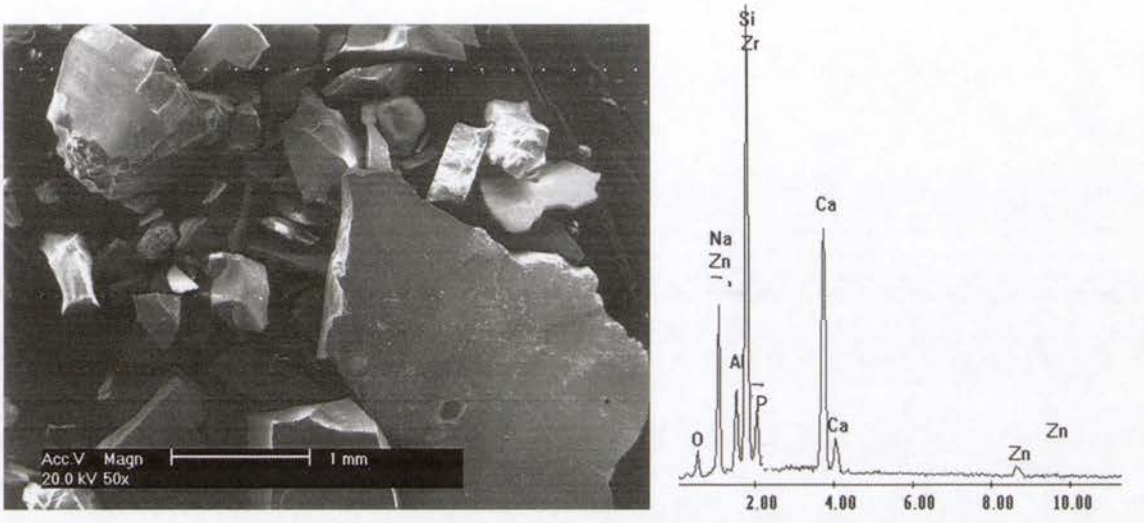


Figure 4.29. SEM image and EDAX spectrum of the 5%Zn45S5 (Nx3).

Table 4.7. EDAX results for 5%Zn45S5 (Nx3) glass.

Oxides	Zinc-doped Glass (Nx3) (mol%)	Correct Composition (mol%)
SiO_2	43.40±1.87	46.9
CaO	12.47±7.20	21.8
Na_2O	19.41±2.92	24.8
Al_2O_3	16.38±9.77	0
P_2O_5	3.40±1.38	2.5
ZnO	4.93±2.26	3.9
RATIO	3.48±0.26	2.15

The purposes of these experiments were to validate the mixing process, glass melting process, glass processing and doping methods by compositional analysis. These results would assist in refining upscaled protocols for the various steps of the glass making process.

4.4.3.1.Efficacy of precursor mixing

The composition of precursor powders with 2, 4 and 8mins of mixing were determined using EDAX and x-ray fluoroscopy (Fig. 4.24, Table 4.3). The results suggest measurements with x-ray fluoroscopy are more accurate than EDAX. The x-ray fluoroscopy data indicated that 8min of mixing could be most suitable for obtaining a Si:Ca ratio close to 1.8. The levels of calcium oxide decreased with increasing mixing time using both x-ray fluoroscopy and EDAX. This could be due to calcium hydroxide having the highest density of all the reagents (2.24g/mL). Fumed silica, in contrast, has an extremely low density of 0.04g/mL, giving a density difference of 2.20g/mL. As the precursor powders are mixed, the calcium hydroxide becomes more homogenous within the mixture. After a certain period of mixing, the calcium hydroxide would be expected to begin to settle out again, and form agglomerates. Due to its high density, calcium hydroxide is likely to concentrate on the base of the mixing container and also in the subsequently formed precursor pellets. Lightweight fumed silica will correspondingly be more prominent towards the top of the mixture. Fumed silica does not agglomerate in the same way as the other salts in the mixture. In addition, the CaO could also settle out during the stationary period between mixing and pellet formation, which was on the order of days or weeks. Settling could also occur when pouring the precursor mixture from the mixing vessel into the pellet molds. This would result in an excess level of silica entering the molds. As the measurements for this experiment were taken from regions on the top of the pellets, these factors are likely to have contributed to these spectral readings.

Several recommendations can be made for future studies with regards to precursor homogeneity. Careful attention should be paid to the positioning of the sample region. A number of measurements should be taken from regions at the top, base and centre of the pellets, to determine if there is a relationship between position and mixture homogeneity. Pellet formation should occur as soon as possible after the powder has been mixed, to reduce the occurrence of settling. This can be difficult to ensure in a timely fashion, as the industrial mixer is offsite. A secondary mixing step could instead be useful immediately prior to pellet synthesis- perhaps consisting of agitation, inversion or rotation procedures. Ideally, the entire batch of precursor (300g for the upscaled batch) would be melted into glass at the same time, which would increase the accuracy of the final formulation. However, current upscaled melting

processes can only account for a maximum of 80g of precursor- the limiting factor being the size of the crucible, which is partially dependent on the oven size. In contrast, using the small batch, melting can occur in a single batch in a crucible. In order to improve homogeneity of the glass, future synthesis procedures could follow the method documented by Gao [203]. This involved annealing the glass, crushing and then remelting.

4.4.3.2. Verification of Glass Composition

45S5 glasses synthesised using the melt-derived technique showed similar compositions to literature values (Fig. 4.25, Table 4.4) [202, 745]. This was the case for both the small and large batch processes. Both batches, however, contained alumina contaminant particles from the alumina crucible- 3.16 and 1.27% respectively. The contaminant level from the large alumina crucible was an acceptable level. The reason for the reduced amount of alumina was due to a higher proportion of precursor powder relative to the size of the crucible. This was evidence that not only had the process become commercially viable from the upscaling, but the produced glass was also of a higher quality.

4.4.3.3.Comparison of Glass Processing Technique

The composition of the 45S5 glass milled using the manual, mortar and pestle process, was close to the theoretical value (Fig. 4.27). However, the sample milled with the ball mill did show some differences. The most pronounced change was the presence of a high level of alumina. This could be due to the continual abrasion of alumina balls during the milling procedure. Friction existed between both the balls and the balls against the glass, which would have created a high level of wear debris. The absence of phosphorous also observed could be due to inadequate precursor mixing consistency and time, as discussed earlier.

4.4.3.4. Glass Doping

Glass made with iron and zinc doping were also compositionally characterized (Fig.4.28, Table 4.6, Fi. 4.29, Table 4.7). Ca:Si ratios did differ from the theoretical values, perhaps indicating insufficient mixing of the precursors. Alumina contamination was present in both samples from the alumina crucible. Most glass batches made after these samples were made using platinum crucibles with no risk of contamination. To improve the ball milling process, in the future 45S5 glass balls could be molded to replace the alumina balls. Although some researchers intentionally add alumina to bioactive glasses to control solubility [113], others have found it could inhibit bone bonding [174]. Banchet and coworkers found that glass containing up to 71% silica oxide, as well as network formers 3% magnesium oxide and 2% alumina prevented the dissolution of the glass so no surface layers formed within 24hrs of

exposure to biological solution (DMEM culture media). For another glass containing 50% silica, 1% magnesium oxide and 2% alumina, the solubility was reduced and the formation of an electron dense (Si, O) layer rich in $Si(OH)_4$ groups formed which permitted the formation of an amorphous apatite layer. This study highlights the high sensitivity of bioactivity to composition. These two glasses show small differences in composition which lead to important changes in surface reaction kinetics which must be considered when a material is chosen for a medical application.

4.5. NANOINDENTATION

Nanoindentation studies were performed at the School of Materials Science, University of New South Wales on a Hysitron TI 950 Triboindenter™ (Fig 4.30). A diamond Berkovich tip (triangular pyramid) and a 1DSN539432 transducer (10,000uN upper load limit) were used.

Nanoindentation is a technique used to measure the hardness of small volumes of material. An indenter made of a hard material is pressed onto the sample, with the load increasing as the tip penetrates further into the specimen. At this point it could be held constant for a period or removed. The area of the residual indentation in the sample is measured and the hardness, H, is defined as the maximum load, P_{max}, divided by the residual indentation area, A_r.

Nanoindentation techniques improve on macro and micro indentation tests by providing indentation on the nanoscale, high spatial resolutions to place the indents, and providing real-time load-displacement data while the indentation is in progress. Nanoindenation enables the characterisation of the surface the cells will experience. Characterisation of the young's modulus using this method was different to the young's modulus obtained from the universal tensile test.

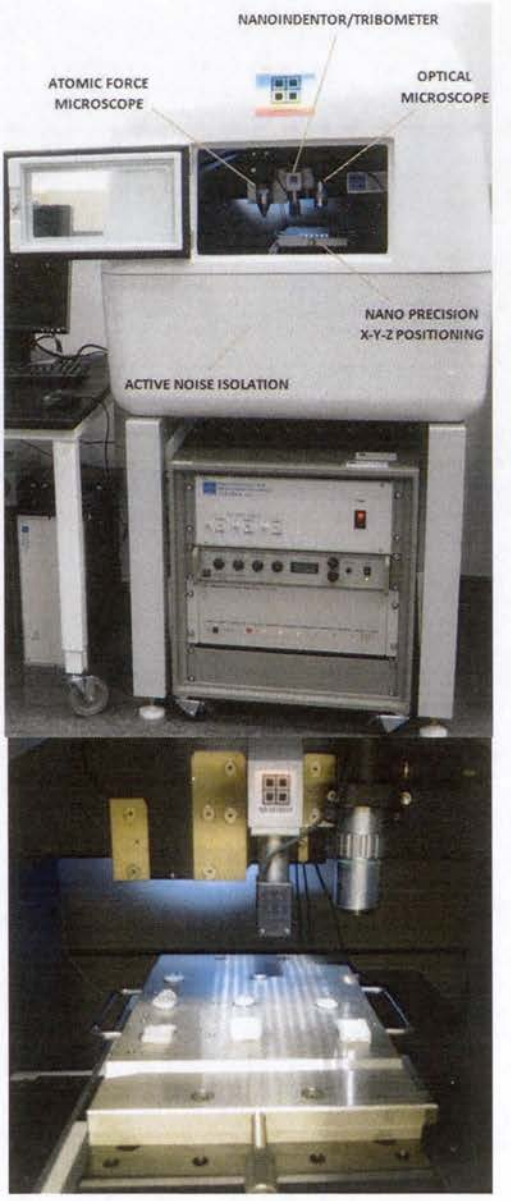


Figure 4.30. Hysitron triboindenter.

4.5.1.1. Calibration Procedure

During the calibration procedure, the load measured from the transducer was kept close to zero, by adjusting the black knobs to the right of the Triboscope controller. 'Indentation' mode was selected within the 'ranish' workspace. Calibration system settings were as follows:

i. Low pass filter: 300
ii. Displacement gain: 100
iii. Microscope feedback gain: 100
iv. NanoDMA: 100

The 'calibrate' function was selected on the transducer calibrations page within the indentation axis menu. A 20sec ramp graph was displayed (in the load function>Quasi tab). The peak force was changed to 1200uN. The "Cal Air Indent" function was selected and started. The load was adjusted to zero by turning the black dials to the upward position and selecting "rezero". The course and fine tuning were adjusted and OK was selected. The microscope feedback on the Triboscope Controller was adjusted to 100 and OK was selected. A plot appeared of the indenter pushing in air. The maximum value of this graph was confirmed to be 42000 with no hysteresis, and OK was selected. The load was adjusted to zero and the microscope feedback was returned to 1000. These windows were closed and the 'calibration' tab was selected.

4.5.1.2. Specimen Preparation

Pieces of unsterilised glass were chosen for nanoindentation. Ideally, samples consisted of large crystals with relatively flat top surfaces. Crystals were mounted on steel disks using polycaprolactone, which was softened at 65°C using a heat gun (Fig. 4.31).

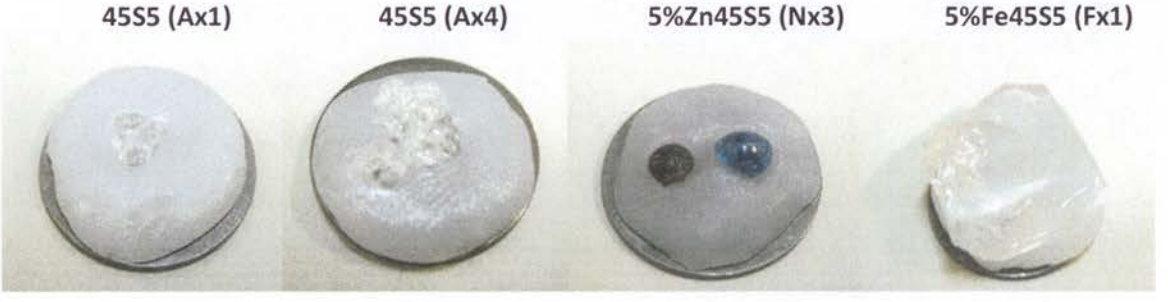


Figure 4.31. Appearance of some of the samples mounted for nanoindentation. Left to right: samples D, S, H, G.

A range of glass compositions were tested, including silicon, barium, zinc and iron modified glasses. Samples were all made via precursor mixing in a small batch in the SPEX mill, with some glasses melted in the molybdenum furnace and others in the vertical tube furnace or the induction furnace. The samples for experiment 1 were: Sx3, Sx4, Ax1, Sx1, Sx2, Rx1, Rx2, Rx3, Nx1, Nx2 and for experiment 2 & 3: Ax1, Ax4, Nx3, Fx1. Attempts were also made to mount PCL variotis™ scaffolds, however nanoindentation results could not be obtained, due to the softness of the scaffolds.

4.5.1.3. Indentation Procedure

The samples were placed onto the Hysitron stage and the Berkovich tip was inserted. The following test settings were used for these tests:

i. Low pass filter: 300
ii. Displacement gain: 100
iii. Microscope feedback gain: 1000
iv. NanoDMA: 100

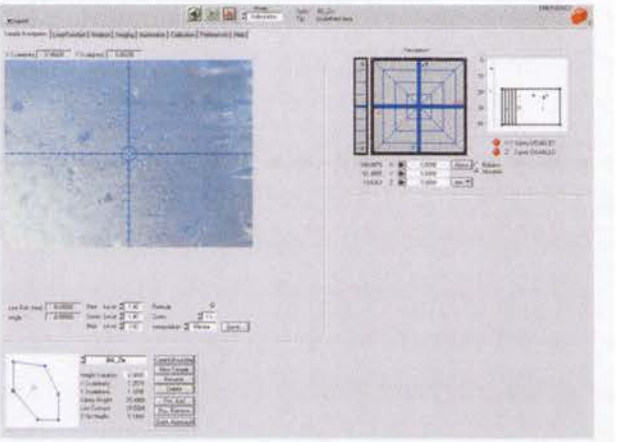


Figure 4.32. Selection of the sample region and indentation points.

The optical lens of the microscope was positioned above the first sample. The Berkovich tip was above the sample, slightly to the left. The microscope was carefully moved down the z-axis. The stage was moved in the x-y direction until the sample was visualised on the computer screen. The stage was adjusted so the probe tip was 8mm above the sample. A region was defined around this point, within which indentation tests would later be performed (shown in Fig 4.32). Neighbouring indents were not expected to affect each other as these were not metallic samples. The region was selected using 'position add', and moving the stage in the x-y plane. These steps were repeated until a complete 3D fence was formed. The specimen was confirmed to be in focus at all points. The region was defined by right clicking in the centre of the region and selection of 'quick approach'. A region was defined around all the other specimens using a similar procedure of selection of the specimen, focusing and adding new positions. The Berkovich tip moved in a 10-5-10 profile, consisting of the following steps:

1. 10 seconds ramping up
2. 5 seconds rest
3. 10 seconds ramping down

The settings for the indentation points are shown in Table 4.8.

Table 4.8. Parameters for the nanoindentation experiments.

	Indentation Load (μN)	Number of Points per sample	Distance between points (μm)
Experiment 1	50	6	7.5
Experiment 2	100	6	7.5
Experiment 3	100	20	7.5

4.5.2. RESULTS

An example force-displacement curve recorded for bioactive glass is shown in Fig 4.33.

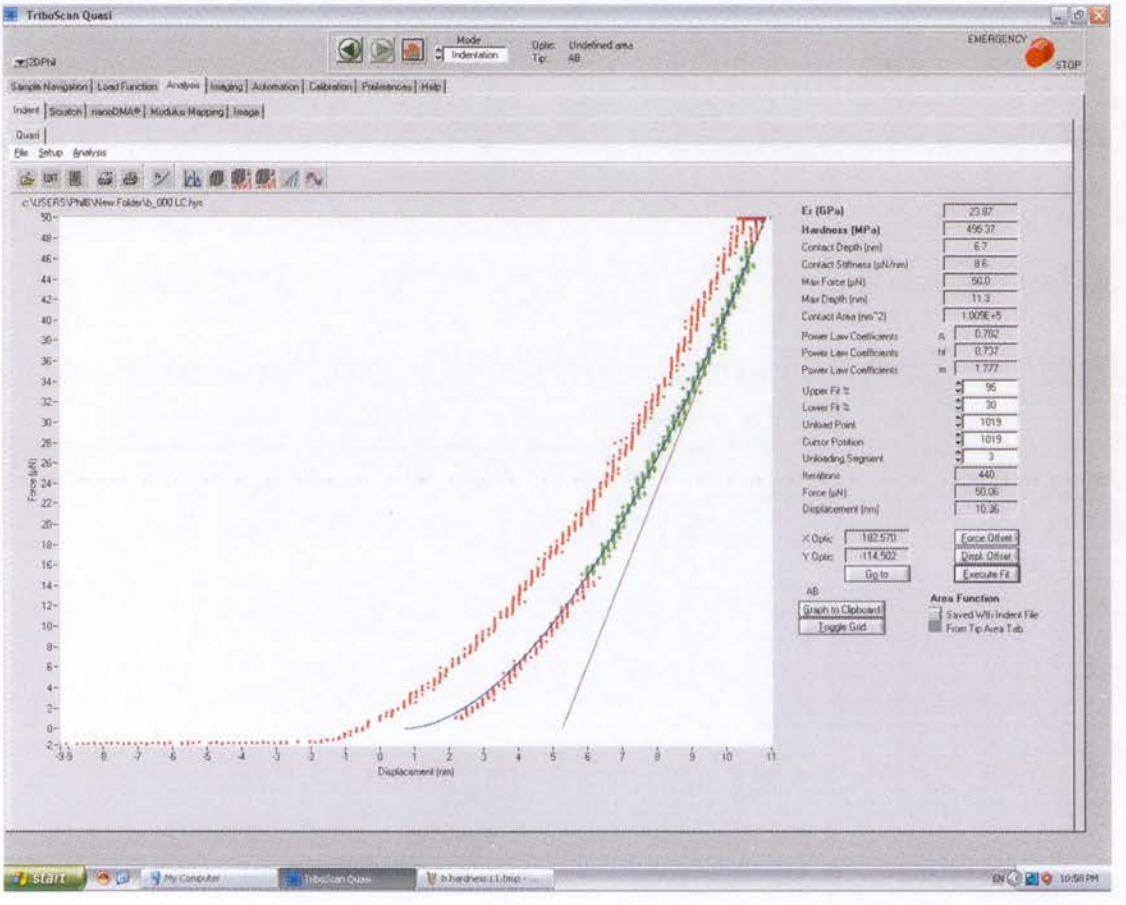


Figure 4.33. Force-displacement curve obtained using the Hysitron TI 900 Triboindenter.

4.5.2.1. Hardness Measurements (Experiment 1)

The indentation results for experiment 1 are shown in Fig. 4.34 and Table 4.9. The mean hardness increased with increasing proportions of silica, for the 45S5, 49S4.9 and 52S4.6 glass samples. However, the mean hardness for the Ba-doped samples decreased with increasing silica component. Increasing of the Zn component from 0.2% to 2% resulted in a doubling of the hardness.

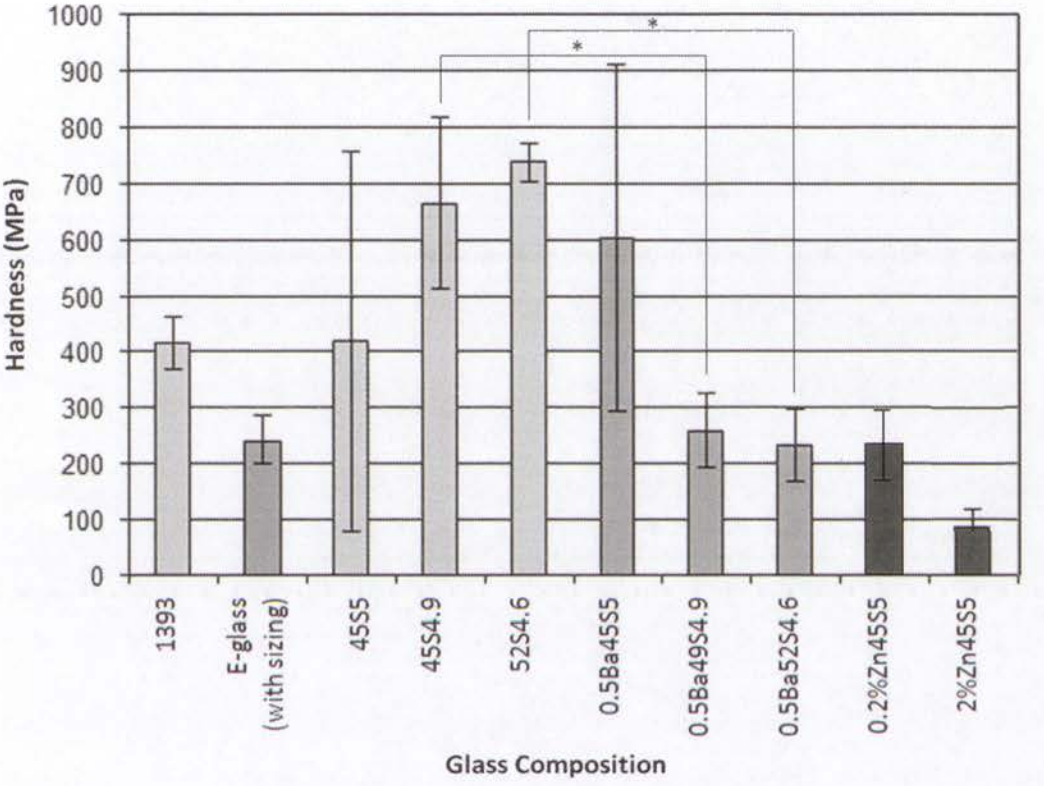


Figure 4.34. Hardness results for experiment 1.

Table 4.9. Nanoindentation results for experiment 1.

No.	Composition	Modulus (GPa)	Hardness (GPa)
Sx3	1393	17.26±1.53	415.87±45.78
Sx4	E-glass (with sizing)	1.96±0.21	240.89±47.45
Ax1	45S5	15.90±11.90	417.97±338.12
Sx1	49S4.9	37.37±21.19	664.54±151.05
Sx2	52S4.6	14.20±0.43	736.69±34.86
Rx1	0.5Ba45S5	-	603±304
Rx2	0.5Ba49S4.9	6.86±1.25	601.45±307.89
Rx3	0.5Ba52S4.6	6.17±5.56	258.63±66.12
Nx1	0.2%Zn45S5	13.25±4.65	232.62±64.97
Nx2	2%Zn45S5	1.24±0.39	87.74±31.04

4.5.2.2. Hardness Measurements (Experiments 2 & 3)

The quantitative results for experiment 2 & 3 are shown in Tables 4.10 & 4.11. The results from experiment 2 indicated a modulus of approximately 31 GPa for 45S5 glass. The vertical-tube furnace synthesised 45S5 displayed a very high contact depth.

Table 4.10. Nanoindentation results for experiment 2.

No.	Composition	Contact Depth (nm)	Modulus (GPa)	Hardness (GPa)
Ax1	45S5	76.82±49.12	30.96±8.26	3.63±2.86
Ax4	45S5	242.59±143.11	1.37±0.53	0.08±0.04
Nx3	5%Zn45S5	29.88±5.26	16.61±3.13	2.23±0.59
Fx1	5%Fe45S5	18.48±3.26	135.80±34.82	6.79±3.79

Table 4.11. Nanoindentation results for experiment 3

No.	Composition	Contact Depth (nm)	Modulus (GPa)	Hardness (GPa)
Ax1	45S5	186.93±74.18	28.74±81.60	2.16±6.43
Ax4	45S5	185.74±88.48	27.26±79.56	2.05±6.27
Nx3	5%Zn45S5	24.67±1.95	15.81±0.99	2.93±0.37
Fx1	5%Fe45S5	-	-	-

The hardness of these samples were measured a second time with an increased number of indentation points (experiment 3). Points were not included if they showed excessive stiffness, as this most likely indicated cracking of the glass sample. Results from experiment 3 showed some differences from experiment 2, most notably more similar contact depths for the conventional furnace melted and vertical tube derived samples (186.93 nm and 185.74 nm respectively). In addition, their moduli and hardness were similar (approx. 28 GPa and 2.10 GPa). The moduli and hardness of the vertical tube derived samples had increased significantly compared to experiment 2. If a further two of the stiffest points on the melt-derived 45S5 sample were regarded as outliers, the modulus and hardness reduced to less than half the original value. This is consistent with the idea that both the melt and tube-derived samples showed a variety of characteristics at different regions.

Nanoindentation techniques were used to determine the hardness and moduli of a range of novel glass compositions. This would help verify the quality of the glass produced.

From experiment 1, the Young's Modulus increased as the proportion of silica increased, although this trend is not obvious due to high standard deviations. Addition of barium and zinc significantly decreased the moduli- to about 1/3 the value of their undoped counterparts. The moduli of the zinc doped glasses were reduced in all three experiments (e.g. 5%Zn45S5: 17 GPa, 24.67 GPa). From experiment 2 (10 μm/s), the iron-doped glass was extremely stiff (130.80±34.82 GPa) with a high hardness (6.8G±3.79 Pa), as expected. A modulus of 30.96±8.26 GPa was measured for the 45S5 glass which had been melted with a molybdenum furnace (indentation speed 10 μN/s) (Table 4.10). This is in accordance with the literature range of 30-35 GPa [412]. The glass melted with the vertical tube furnace was softer, as exhibited by a high contact depth, extremely low modulus (1.37 GPa) and low hardness (0.08 GPa).

Variation between results for the same glass sample can be attributed to: the flatness of the region selected and the presence of cracks on the surface. During the fritting process, the glasses are super chilled in water and stress and microfragments form within the glass. These glasses were not annealed. This process could be included in future, and involves relaxing of internal stresses. The resulting glasses can either be stronger or slightly softer. Another reason for variable results could be due to residual on the glass or the indenter tip. In this case, the hardness might not be accurate even though the modulus could be. This is because the modulus is the elastic response measured during the unloading sequence. This may have been the case for experiment 1 (Table 6.9, Fig. 4.34), which yielded a relatively reasonable Young's Modulus (1-40 GPa) but an excessively high hardness (87-736 GPa). For this reason, these hardnesses were thought not to be representative of the true properties of the glasses.

Future work using nanoindentation could trial methods for determining the bonding strength of cells to scaffolds and glasses.

4.6. BIOACTIVITY AND DISSOLUTION

4.6.1. METHODS

4.6.1.1. SBF Soaking Study

Glasses were soaked in SBF according to the following protocol, in order compare dissolution rates and relative bioactivities of the glasses.

Samples of various bioactive glass compositions (altered levels of Si and Ba: Ax1, Sx1, Sx2, Rx1, Rx2, Rx3), each weighing 0.08525±0.00025g were measured into glass vials. Three replicates per composition were used. The majority of the glass powders had diameters <30μm (mean: 19.04±17.77μm). 1.5mL of simulated body fluid (1.5SBF) at 37°C was added to each glass vial to a depth of approx. 5mm. The composition of SBF has been previously described by Rhee & Tanaka [526]. The vials were placed in a water bath so they were immersed in 10-15mm of water, in a large plastic insulated tub. An immersion heater (Korjo water boiler) controlled by a thermocouple attached to a temperature controller (CAL990) were immersed in the water bath and set to 37°C. The vials were kept at a temperature between 36-39°C as there was some fluctuation in the actual water temperature. At each timepoint, one sample of each composition of the bioactive glass was removed from the water bath. The SBF was decanted and the vials were then placed in a convection oven and heated at 110-120°C for 2 hours [583]. The samples were rinsed with deionised water and the water was decanted. This was repeated at least ten times to dissolve and remove residual salts from the SBF. The samples were dried in a laboratory oven (HACH Gravity Oven, 115 volt) at 120°C for 16 to 24 hours. The samples were reweighed using a high-precision microbalance accurate to ±0.01 mg (Sartorius BP 210 D). Steps 4 to 6 were repeated for timepoints at 1, 3 and 7 days.

4.6.1.2. Examination of Pre-Soaked Glasses using SEM/EDS

The appearance and composition of the glass surfaces were analysed using SEM/EDS prior to the soaking experiment (day 0) and after 1 and 7 days soaking. The methods for these were described previously in section 4.4.1. The formation of calcium phosphate precipitates would indicate high levels of bioactivity on the surfaces.

4.6.2.1. Dissolution Rates of Bioactive Glasses

The dissolution curves of the SBF-soaked glass samples are shown in Fig. 4.35. Most of the samples exhibited a massive weight loss between days 0-1, a smaller weight loss between days 3-7 and a small weight gain from days 1-3.

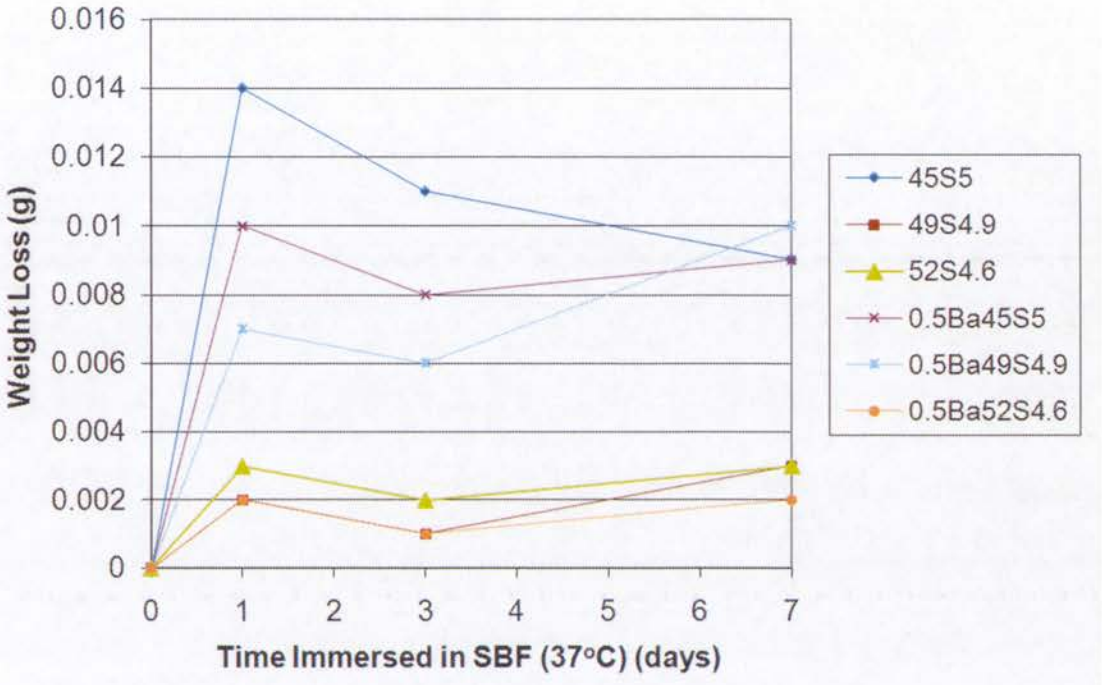


Figure 4.35. Dissolution curve of glasses after immersion in SBF.

4.6.2.2. Bioactivity of Glasses

4.6.2.2.1. Effect of SBF Soaking on Silica-Altered Glass

Figure 4.36 shows the surface of the 45S5 glass using SEM. Prior to soaking, there were small, angular particles on the surface, which were likely to be glass fragments or contaminants. After 1 day soaking in SBF, these particles seemed to disappear. The formation of patches on the surface at day 1, which became more widespread by day 7 were also evident. These patches seemed to form a thick layer on the glass surface and take on a more discrete appearance, appearing as spherical shaped deposits (Fig. 4.36a). These could suggest the formation of a Ca-P layer which gradually crystallised to form more discrete HCA particles.

Figure 4.36e & Table 4.12 depict the spectral composition of the glasses, as measured using EDS. The level of silica decreased over 7 days of soaking, from 54 to 42mol%. Correspondingly, the proportion of calcium increased from 25 to 53%. The Ca:Si ratio also consistently increased, from 0.47 to 1.26. The phosphate levels remained steady or decreased.

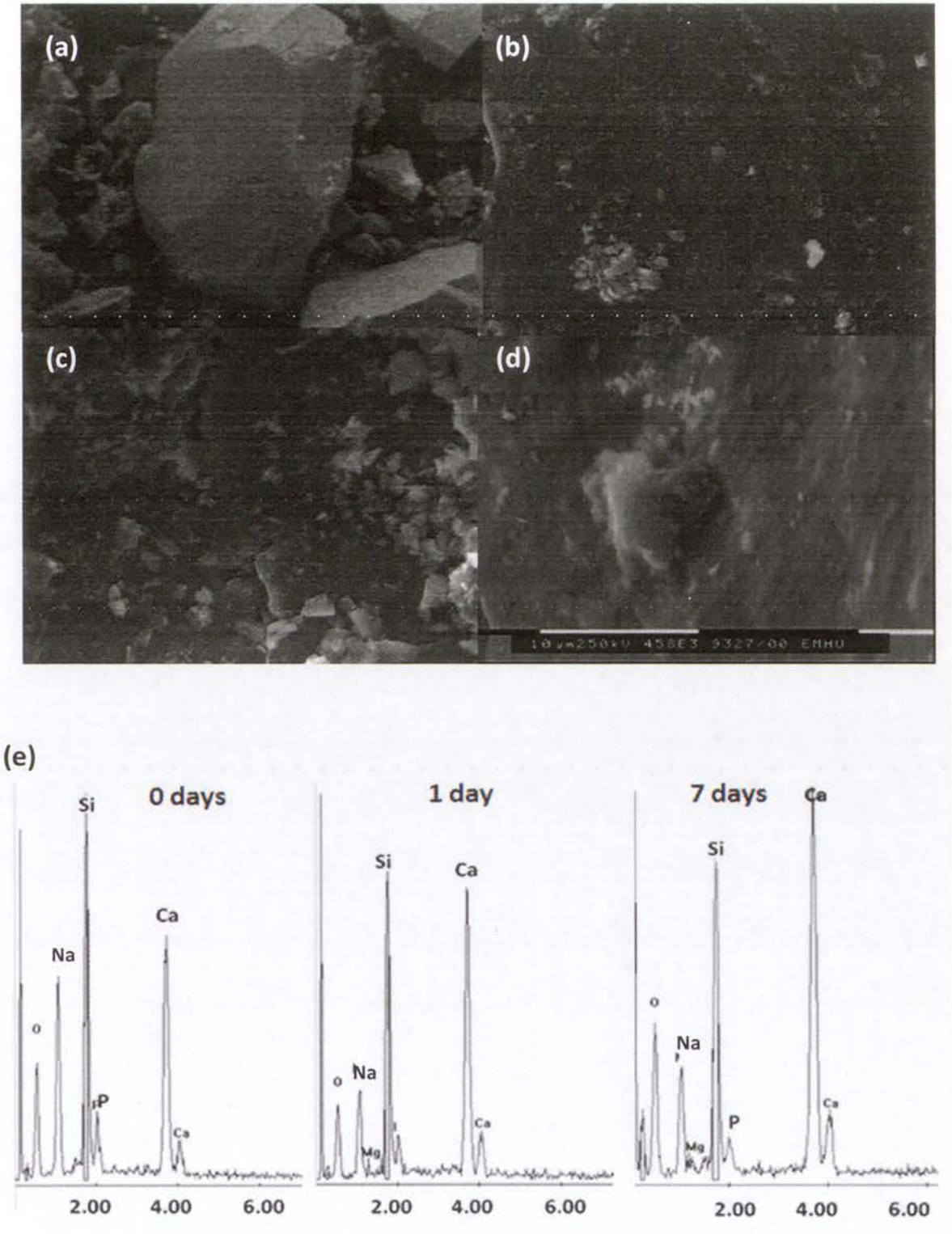


Figure 4.36. SEM micrographs of the surface of a 45S5 particle (a) prior to immersion, and (b) 1 day (c,d) 7 days after immersion in in SBF at 37°C. (e) The corresponding EDAX spectrums.

Table 4.12. EDAX of the 45S5 glass after soaking in SBF at 37°C.

	Time of SBF soaking		
Oxide	0 day (%mol)	1 day (%mol)	7 days (%mol)
SiO_2	48	40	42
CaO	34	37	53
Na_20	28	12	14
P_2O_5	8	7.4	7
Ca:Si RATIO	0.71	0.93	1.26
Ca:P RATIO	4.25	6.2	4

The 49S4.9 sample (results not shown) appeared very stable and unreactive. Silica and phosphate levels remained constant over the soaking period. Calcium increased after 1 day but then remained constant.

The 52S4.6 bioactive glass clearly demonstrated an abundance of Ca-P precipitates or HCA crystals by day 7 (Fig. 4.37a). These precipitates were formed in tight clusters and were a few microns in diameter (Fig. 4.37b). The EDS results (Fig. 4.37c, Table 4.13) demonstrated a reduction of sodium and silica over time, and a significant increase in the calcium and phosphate levels by day 7. This is strong evidence that the clustered precipitates were Ca-P precipitates.

4.6.2.2.2. Effect of SBF Soaking on Barium-Doped Glass

The SEM and EDAX results for 0.5Ba45S5 glass are shown in Fig. 4.38 and Table 4.14. Visible in Fig. 4.38a, small, angular particles observed on the surface of the 0.5Ba45S5.9 glass also seemed to disappear after SBF soaking. By 7 days, rounded particles similar in appearance to hydroxyapatite crystals were observed (Fig. 4.38b-d). These spherical features were generally less than 2μm. EDS analysis showed similar trends to the 45S5 sample. Initially there was a massive drop in Si, although levels recovered by day 7. Calcium levels also dropped at day 1 but were still elevated in comparison to the unsoaked sample. As with the 45S5 samples, the phosphate levels were relatively unaffected for the duration of the experiment. The 0.5Ba49S4.9 glass (data not shown) showed a lower bioactivity, with calcium levels remaining unchanged between days 0 and 1, and increasing by day 7. The formation of spindle-like features was observed on the day 7 sample.

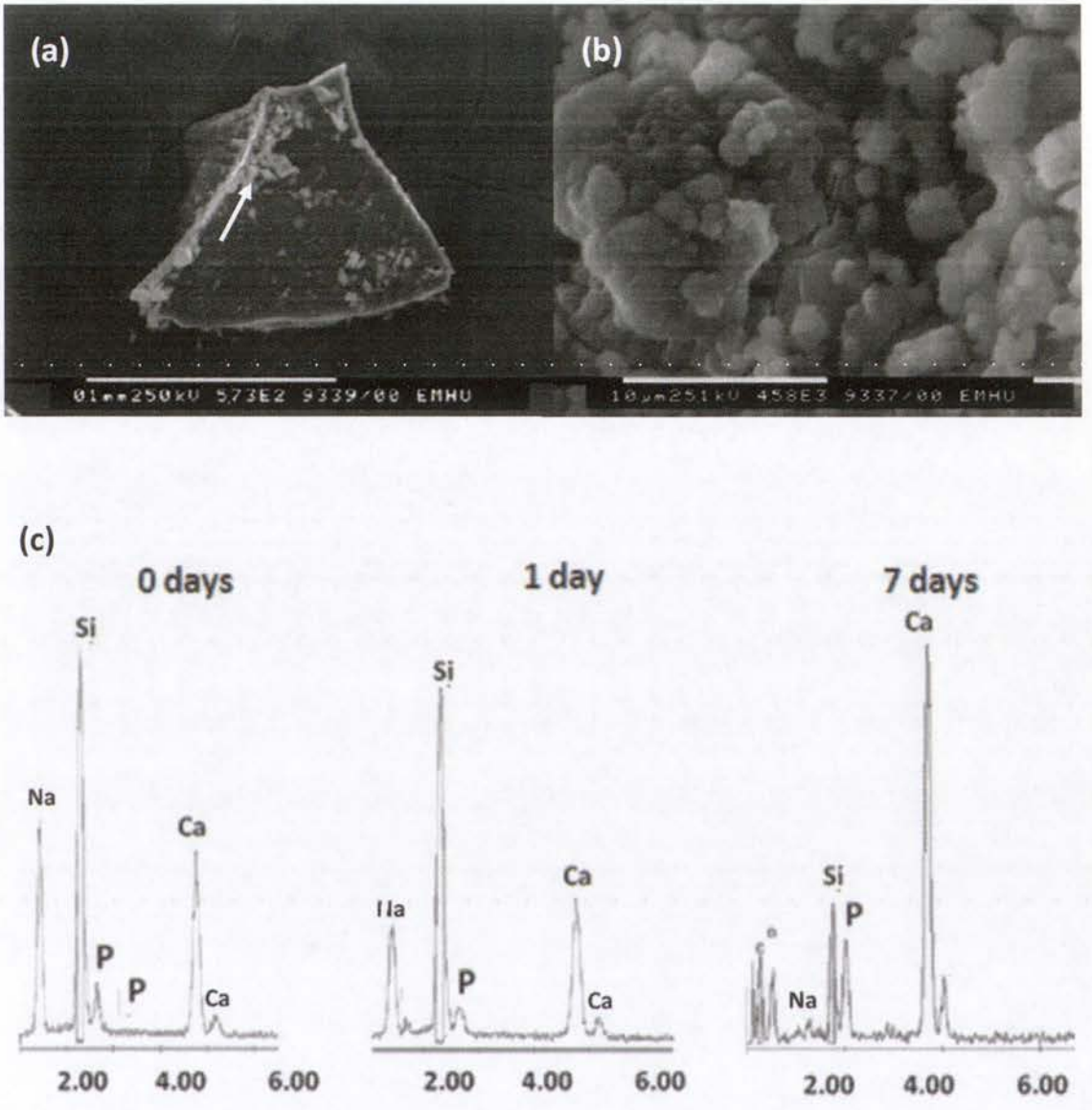


Figure 4.37. (a,b) Spherical precipitates on 52S4.6 glass (Sx2) after 7 days SBF soaking, Arrow: rounded precipitates. (c) Corresponding EDAX spectrums.

Table 4.13. EDAX of 52S4.6 glass (Sx2) after SBF soaking.

	Time of SBF soaking		
Oxide	0 day (%mol)	1 day (%mol)	7 days (%mol)
SiO_2	52	48	19
CaO	27	21	55
Na_20	28	16	8
P_2O_5	8	4	17
Ca:Si RATIO	0.52	0.44	2.89
Ca:P RATIO	3.38	5.25	3.24

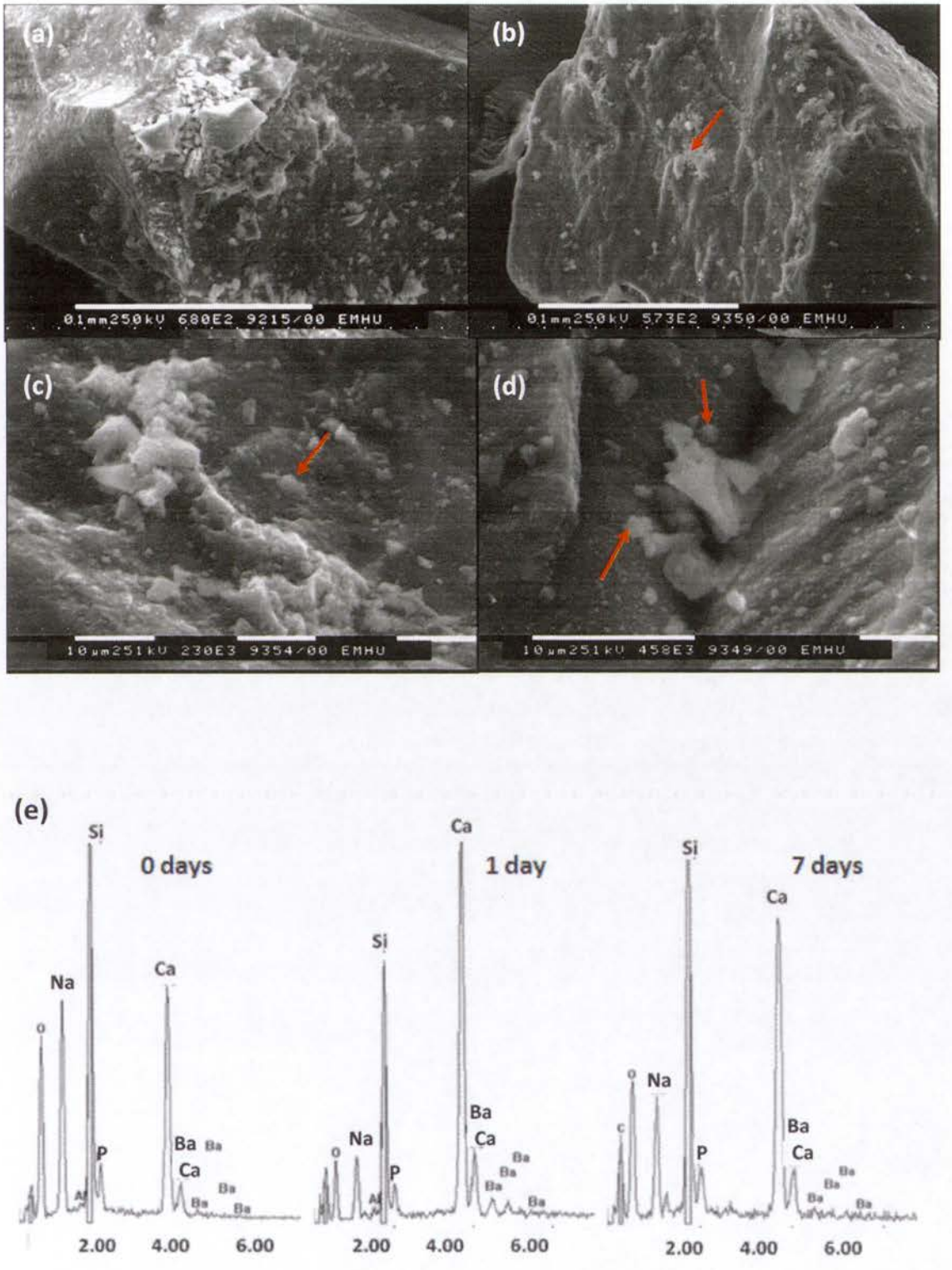


Figure 4.38. 0.5mol%Ba4SS5 (a) prior to immersion and after (b-d) 7 days immersion in SBF at 37°, (e) EDAX analyses of the 0.5Ba45S5 glass sample after soaking in SBF. Arrows: precipitate formation.

Table 4.14. EDS of 0.5Ba45S4.9 glass (Rx2) after SBF soaking.

	Time of SBF soaking		
Oxide	0 day (%mol)	1 day (%mol)	7 days (%mol)
SiO_2	57	35	53
CaO	32	55	44
Na_20	30	9	15
P_2O_5	8	5	9
Ca:Si RATIO	0.56	1.57	0.83
Ca:P RATIO	4	11	4.89

Figure 4.39 shows the surface of the 0.2%Zn45S5 glass prior to soaking and after 1 and 7 days soaking. Prior to soaking, the glasses showed a smooth surface with some non-crystalline glass residuals or contaminants. After 1 day of soaking, a small amount of hydroxyapatite crystals start to appear on the surface of the glass (Fig 4.39b,c). They are easily identified as clusters of crystalline structures. After 7 days of soaking, large areas of the surface were covered by hydroxyapatite crystals. The crystal size appeared to be increasing with soaking time.

4.6.2.2.2. Effect of SBF Soaking on Zinc-Doped Glass

2% zinc containing bioactive glass demonstrated similar results to the 0.2% zinc composition. After one day of soaking there was small amounts of precipitate formation-slightly less crystal structures than the 45S5. After seven days of soaking, the amount of crystals formed increased dramatically compared to after one day of soaking. The HA crystals were observed to be larger than that of the 45S5 sample after seven days of soaking.

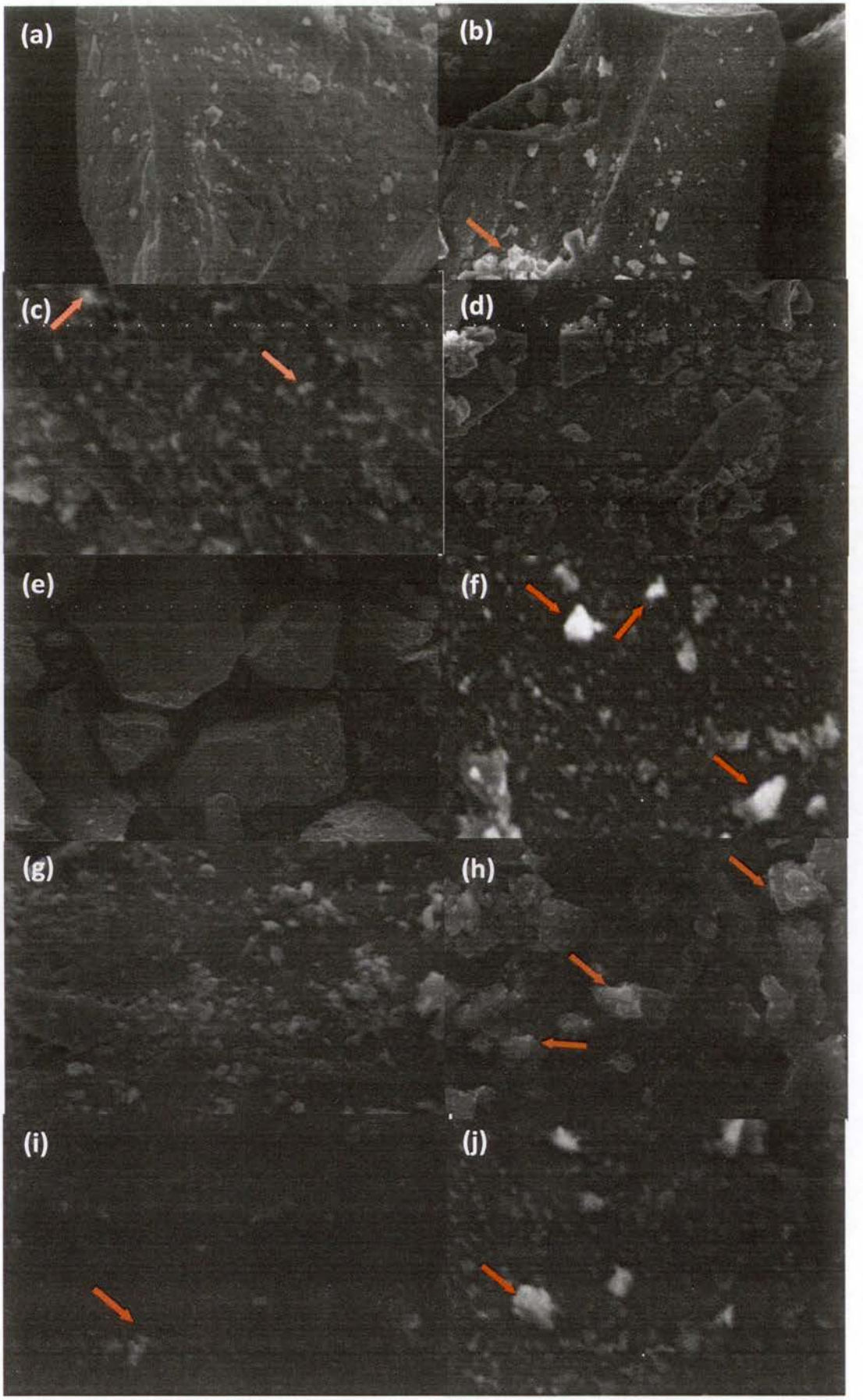


Figure 4.39. 0.2%Zn45S5 glass after (a) 0 days (b, c) 1 day (d) 7 days.). 2%Zn45S5 glass after (a) 0 days (b) 1 day (c,d) 7 days soaking in SBF at 37°C. 5%Zn45S5 after (e) 1 day (f) 7 days sbf soaking. Arrows: Spherical precipitates.

The relative bioactivity of biomaterials is an important indicator of its biological activity and could affect an implant's long term acceptance and bonding strength. SBF soaking is a standard test thought to give some indication of relative *in vivo* bioactivity [526]. In this section, glasses varying in Si, Ba or Zn levels were soaked in SBF for a period of 7 days. Upon contact with body fluids, bioactive glasses experience protein adsorption, calcium phosphate precipitation and the formation of a thick silica gel layer which facilitates bonding to soft and hard tissues [3, 8, 52, 140]. Soaking in SBF does not contain the proteins present in body fluid, however it does represent some of the ion exchange activity occurring with Calcium, Silica etc. The effects of the substitution of CaO with certain levels of zinc or barium on the physical properties of melt-derived bioactive glass are not well documented and were therefore of interest in this study.

4.6.3.1. Effect of Silica Proportion on Glass Bioactivity

Comparison of the weight loss during soaking time showed a high weight loss for the 45S5 (Fig. 4.35). This corresponded to the formation of widespread spheroidal shaped deposits on the glass (Fig 4.36). This is consistent with the low level of silica for this glass, which gives it reduced stability and therefore higher bioactivity. The rounded calcium phosphate precipitates were assumed to be hydroxyapatite; however this was difficult to confirm with the EDS results. An increase of 30% of the calcium and phosphorous on the surface of the glass was observed from day 0 to 7. A Ca:P ratio of 1.67 would confirm the presence of HA, however the ratios measured were 4.25-13.25 (Table 4.12). This is due to the EDS readings being measured over the entire region of an SEM image. Future studies should examine the composition at a single point. The 49S4.9 glass was unreactive- reflected in both the dissolution curve and EDS results. This anomalous result is likely attributable to the production of a flawed and possibly overcrystalline 49S4.9 glass sample. Clusters of precipitates were highly visible on the 52S4.6 glass at day 7 and likely to be hydroxyapatite. This was supported by a doubling of the level of calcium and phosphorous from days 0 to 7 (Fig. 4.37, Table 4.13). This increase in calcium levels and decrease in silica and sodium levels are what would be expected for bioactive surfaces- with the rapid release and dissolution of soluble ion species and the development of a calcium rich film. These results demonstrate the high level of bioactivity for the 45S5 and 52S4.6 glasses which were synthesised.

4.6.3.2. Effect of Zinc Doping on Glass Bioactivity

The barium-doped samples showed a slower increase in calcium levels, corresponding to reduced weight loss (Fig. 4.35, Table 4.13, 4.14) compared to the undoped samples. Small spherical precipitates were visible on the 0.5 mol%Ba45S5 samples after 7 days and calcium levels increased for days 1 and 7. The 0.5 mol%Ba49S4.9 sample exhibited spindle-shaped precipitates, suggesting immature Ca-P precipitates which could later develop into spherical shapes [791]. The levels of phosphorous on these glasses were relatively constant and reflected the composition of the entire glass surface, rather than the calcium phosphate precipitates only. Small amounts of barium were detected as was expected due to the inclusion of only 0.5 mol% was included in the glass. Addition of Ba did show a decreased bioactivity when compared to their silica-based counterparts. This phenomenon has previously been reported in the literature [795]. Future studies could increase the level of barium to determine how pronounced the retardation effects are.

4.6.3.3. Effect of Zinc Doping on Glass Bioactivity

Of particular interest to a wound healing application is the effect of zinc on the bioactivity. Zinc is an essential element in the human body and plays a vital role during wound healing [337, 664, 668]. The presence of zinc did seem to slow the dissolution of the glasses, at least in the short term. The 0.2% and 2% Zn samples viewed after 1 day of soaking showed slightly less crystal formation than the 45S5 sample at the same time (Fig. 4.39). However, by 7 days, the Zn samples showed at least as much crystal formation as the 45S5 samples. The 2% Zn sample displayed a larger surface area which was covered by hydroxyapatite nuclei. There were significantly fewer precipitates on the surface of the 5% Zn containing bioactive glass after both 1 and 7 days of soaking. The retardation effect of Zn containing glass was noted in a study by Rui and coworkers [169]. They soaked sol-gel derived 58S and 4% Zn containing bioactive glass in SBF for a period of 5 days. XRD analysis revealed the presence of HA on the Zn glass after 5 days, but not at 3 days. The 58S glass, in contrast, showed evidence of crystalline HA formation after 3 days. One explanation for this effect may be that during SBF soaking, there is a migration of Zn from the inside to the surface of the bulk glass. Now usually when a zinc free bioactive glass is soaked in SBF, the Ca^{2+} ion is migrated to the surface to combine with $PO4^{3-}$ ion from the solution to form a Ca-P rich layer, which is later crystallised into hydroxyapatite crystals. In case of zinc containing bioactive glass, both Ca^{2+} ion and the Zn^{2+} ion migrate to the surface. However, because of the low solubility product constant of $Zn_3(PO_4)_2$, a zinc rich layer is formed. The incorporation of Zn^{2+} with PO_4^{3-} therefore causes a decrease of HA nucleation. In addition, the inclusion of ZnO into the glass also retards the release of Ca^{2+} ions in the early stages of SBF soaking, because of the lower CaO content, when compared to 45S5 Bioglass®.

Although the addition of Zn retarded the nucleation of HA at the early timepoint, it did not affect the growth of HA after prolonged soaking. This could be explained by the fact that the zinc on the surface of the glass becomes covered by a hydroxyapatite layer. This makes it more difficult for the zinc inside the glass samples to diffuse from the network to the solution, than compared to Ca^{2+} because of the higher bond energy [169] of Zn-O (180 kJ/mol) as compared to that of Ca-O (110 kJ/mol). This means that influence of Zn^{2+} ions on the growth of the HA is reduced and HA can grow steadily with soaking time. For the 5% Zn sample, the retardation effect is prolonged as the zinc rich layer takes longer to be covered by the HA layer. These results show that both Zn and Ba-rich glasses may be useful for controlling the biodegradability of bioactive glasses to some extent, without losing their bioactivity.

4.7. MEASUREMENT OF GLASS RADIOPACITY

4.7.1. METHODS

4.7.1.1. Preparation of Ba-Glass/Silicone Samples

Cylindrical samples of 5% of 45S5, 49S4.9, 0.5Ba45S5, 0.5Ba49S4.9 and 0.5Ba52S4.6 bioactive glass and 10 wt% of 52S4.6 bioactive glass embedded in silicone matrices (Fig. 4.40) were prepared using the following procedure. 100 mg of bioactive glass powder was weighed into a plastic vial using a microbalance (Sartoris BP 210D). 2 mL (2 g) of uncured silicone was dispensed into the plastic vial using a silicone mixer gun. 1 mL was dispensed for the sample containing 10% bioactive glass. The bioactive glass and silicone were well mixed together using an aluminium stirrer to evenly distribute the bioactive glass within the silicone matrix. The plastic vial was centrifuged at 100rpm for 1min to force the silicone-glass mixture to the bottom of the vial. The plastic vial was removed from the centrifuge and maintained upright, allowing the silicone-glass mixture to cure to form a silicone-glass composite. Controls for this experiment were undoped silicone, and 5wt% barium sulphate doped silicone.



Figure 4.40. Silicone/bioactive glass samples.

4.7.1.2. Measurement of Radiopacity via Fluoroscopy

Fluoroscopy was performed on the samples using an OEC Series 7600 Fluoroscopic C-arm set to 48kV. The fluoroscopy images were relayed to the fluoroscope monitors and the monitor displays were photographed. The pixel intensity was measured from the .tif images using Phoretix 1D Advanced (v3.01) (Fig 4.41). This was done via selecting the number/width of 'lanes', defining the baseline reading and measuring the pixel intensity.

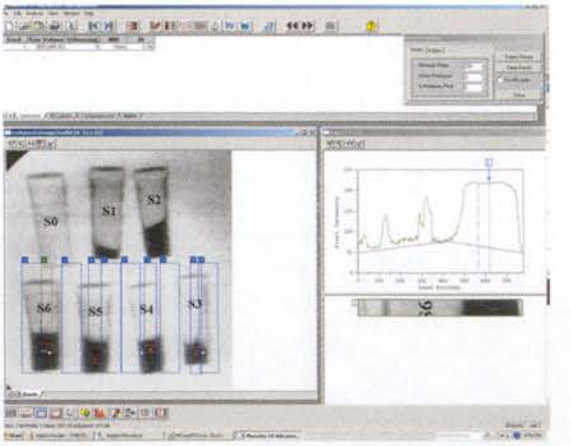


Figure 4.41. Calculation of pixel intensity using Phoretix 1D.

4.7.2. RESULTS

4.7.2.1. Radiopacity of Ba-doped Glasses

Figure 4.42 demonstrates the pixel intensity measurements of the composite glass/silicone samples, taken using the fluoroscope. The bioactive glass-doped samples were all more radiopaque than the undoped silicone control. However, this was not significant for 45S5, 49S4.9 or 52S4.6. A significant increase was shown between the standard glasses and their Ba doped counterparts. Up to a 25% increase was observed. As anticipated, the positive control 5wt% Barium sulphate sample showed the highest radiopacity- an increase of 30% compared to the undoped silicone.

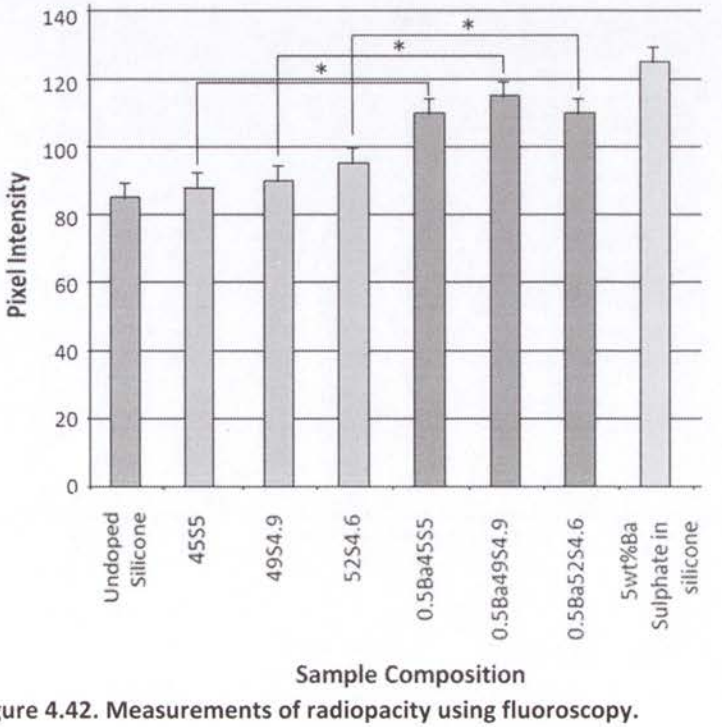


Figure 4.42. Measurements of radiopacity using fluoroscopy.

The ability to impart radiopacity to bioactive glass could be useful for determining whether an implant has been delivered in the correct location, to track implant migration or to determine the degree of degradation. Barium sulphate has previously been successful for increasing the radiopacity of bone cements [790]. The development of bioresorbable, radiopaque materials which could be used in soft tissue regions could have many clinical applications such as osteochondral tissue, skin and intervertebral disks.

In the current study, barium sulphate was successfully used as an opacifier in the creation of radio-opaque bioactive glass. When suspended in silicone, fluoroscopic measurements indicated a significant increase in radiopacity for 45S5, 49S4.9 and 52S4.6 glasses when doped with 0.5 mol% barium sulphate (Fig. 4.42). However, visual observations did not detect a noticeable change in opacity. Barium sulphate was added to bioactive glass at a concentration of 10% by Madanat and coworkers [795]. In the current study, only 0.5% was included. A higher proportion of barium could enable detection of a more significant change and this should be investigated in future studies.

Since the addition of barium sulphate seems to reduce bioactivity [795] (ref section 4.6), this would need to be considered in any medical applications where the use of barium-doped glass is being considered.

4.8. METHODS FOR MOUNTING GLASS POWDERS ONTO SCAFFOLD DISKS

In this section, cylindrical scaffold compacts were made and powdered biomaterials were mounted. Methods were sought which could enable a researcher to test small quantities of biomaterials using the scaffold. Disks synthesised via protocol B were utilised to investigate the biocompatibility of bulk metallic glasses and bioactive glasses. Bulk Metallic Glasses, introduced in section 4.1.3, were mounted on PCL scaffold disks, in preparation for biological testing in section 5.5.

4.8.1. METHODS

4.8.1.1. Method A. Synthesis of Glass-Coated Compact Scaffold Disks via Direct Heating

Fig. 4.43. shows a schematic of this protocol.

8. Bulk metallic glasses (ref 5.5.1.1. for details) were crushed into powder using a granite mortar and pestle and their particle size distribution was characterised (ref section 5.5. 2.1). The glass powders were placed into a well of a 96-well plate.
9. PCL variotis™ scaffolds (10.5x16.5x17.8mm) were cut into 1/2 using sharp scissors to form scaffolds (10.5x16.5x8.9mm). The scaffold was rolled between two fingers to form a cylinder. The scaffold was pushed into the end of a syringe (with the nozzle removed).
10. The scaffold was heated with a heat gun using the following settings: heat setting=1, power=1, <65°C for 15-20sec. Although the temperature at the tip of the heat gun was close to 65°C, the actual temperature experienced by the scaffold was 55-58°C.
11. The syringe was pressed onto a Teflon surface, compressing the scaffold (2kg force).
12. The scaffold was heated again to 65°C using a heat gun and pressed onto glass powder, in a 96-well tissue culture plate (2kg force). The scaffold was heated for a third time to 65°C and removed from the syringe.

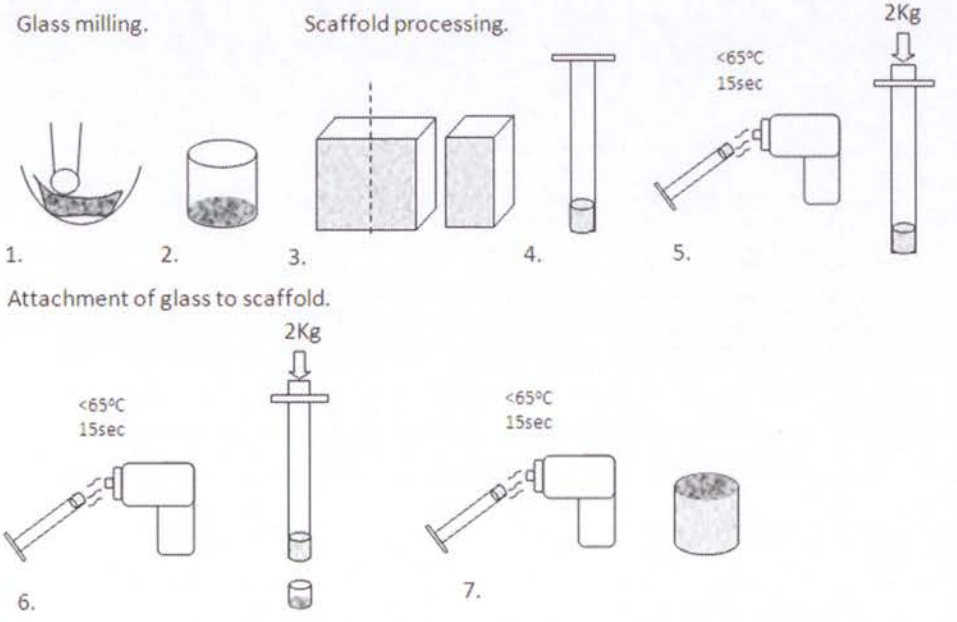


Figure 4.43. Synthesis of cylindrical shaped, glass coated scaffolds for cell culture wells (method A).

4.8.1.2. Method B. Synthesis of Glass-Coated Scaffold Disks via Warm Water

Figure 4.44. shows a schematic of this protocol.

1. Bioabsorbable glasses were crushed into powder using a granite mortar and pestle.
2. Glass powders were placed into wells of a 96-well plate.
3. A transfer pipette was modified by melting the tip using a heat gun (110°C).
4. The warmed pipette was pressed into a 96-well plate in order to flatten the end.
5. PCL variotis™ scaffolds were cut in ½ using sharp scissors (10.5x16.5x8.9 mm).
6. Scaffolds were placed into wells, on top of glass powder. Hot water (55°C) was poured into the gaps between the wells in the tissue culture plate.
7. The scaffold was compressed using a flattened transfer pipette.
8. The compressed scaffold was removed from the well using a syringe needle.
9. The scaffold was inverted and steps 6 and 7 were repeated.

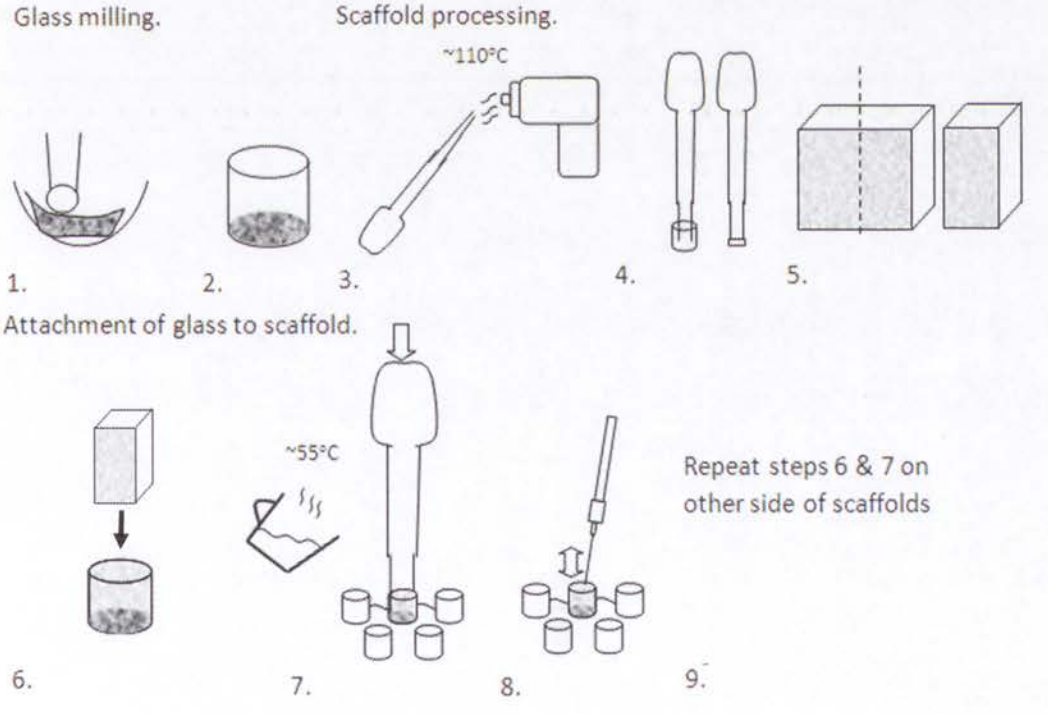


Figure 4.44. Synthesis of cylindrical shaped, glass coated scaffolds for cell culture wells (method B).

4.8.1.3. Method C. Synthesis of Glass-Coated Bulk PCL Disks

Figs 4.45. depicts this protocol in schematic form

1. A custom-made mold was made from a 3 mm-thick metal plate. Cylindrical holes (d=5 mm) were drilled into the metal to create molds.
2. 2-3 PCL beads were placed into each mold, on a Teflon-coated steel plate. The PCL was melted using a heat gun (>65°C). Alternatively, the PCL beads were melted on a teflon surface using a heat gun (>65°C), and then fit to the molds.
3. Powdered bioactive glass was spread onto a Teflon surface.
4. The warm PCL cylinders, still in the mold, were pressed down onto the glass powder.
5. PCL cylinders were allowed to cool and then removed from the mold using a metal tool.

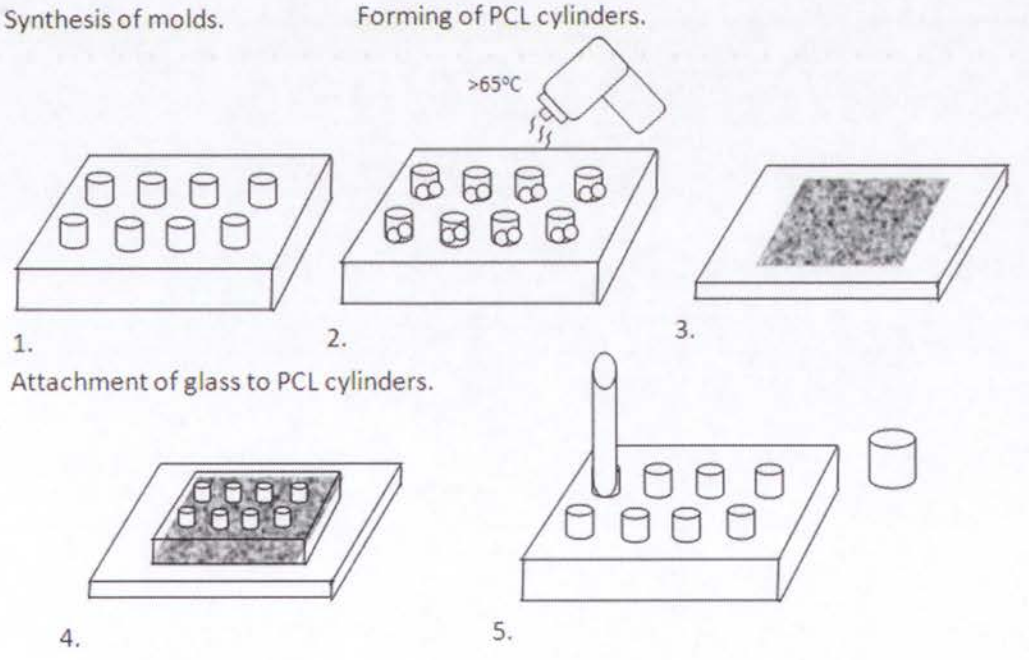


Figure 4.45. Synthesis of glass coated PCL cylinders for cell culture (Method C).

Figure 4.46 shows photographs of the three aforementioned protocols.

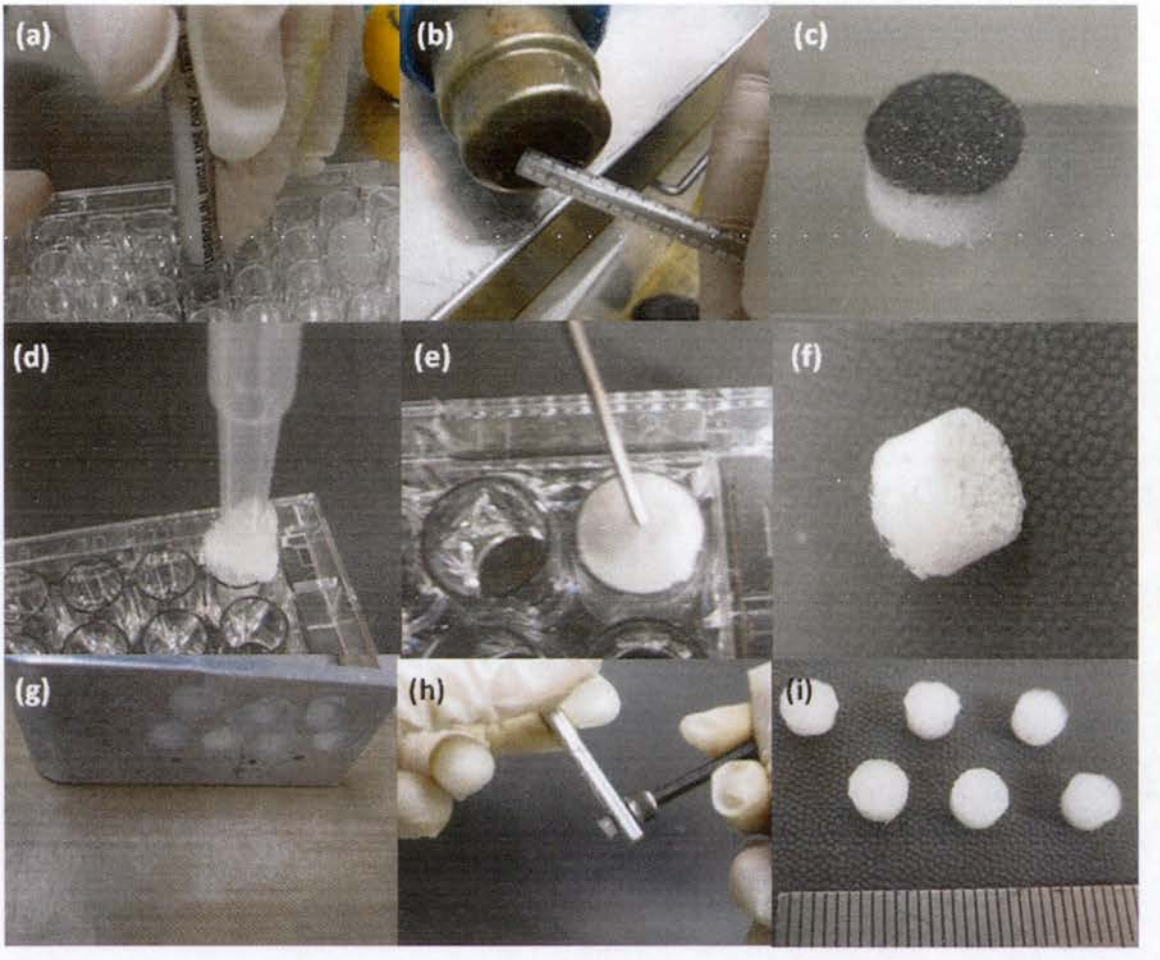


Figure 4.46. Fabrication of cylindrical shaped scaffolds using (a-c) method A, (d-f) method B and (g-i) dense PCL cylinders using method C. These images demonstrate coating with (c) Magnesium-rich BMG and (f, i) 45S5 bioactive glass.

4.8.2. RESULTS

The consistency of the specimens synthesised using method B was compared. The mounted glass occupied an area of 8.22±1.95 mm^2. This is equivalent to a variation of 23.77%. The weights for all the PCL disks and mounted glass powders are listed in Table 4.15. Each scaffold held an average of 0.001g of glass. The variation between weights for the PCL disks and glass-mounted PCL disks were 12.08 and 11.79% respectively. The variation for the mounted glass weights was 43.14%. Fig. 4.47 contains a histogram of the weights when broken down according to each glass composition. This data is also included in Table 4.16.

Table 4.15. Comparison of the weight of PCL disks mounted with glass powders (average of all samples).

	Weight (g)	% variation
PCL stubs	0.03114±0.00376	12.08
Glass/PCL	0.03200±0.00375	11.79
Glass	0.00111±0.00049	43.14

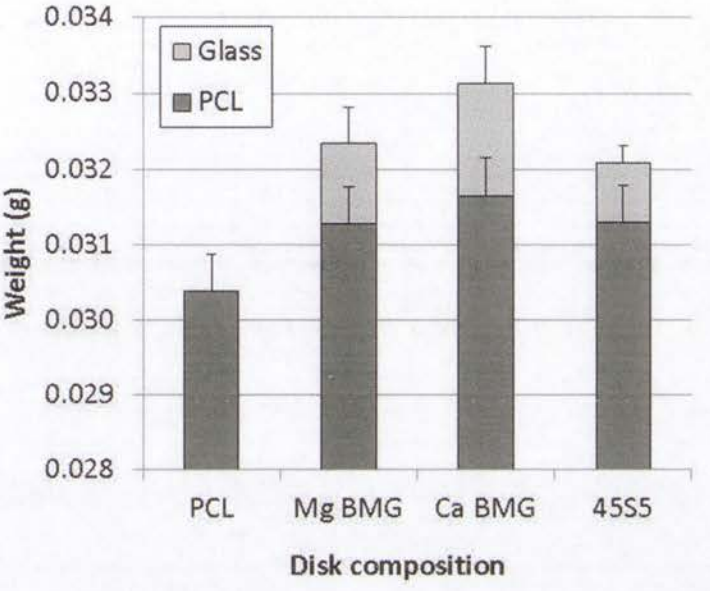


Figure 4.47. Histogram of weights for the PCL disks and mounted glasses (average for each glass composition).

Table 4.15. Weights for the PCL disks and mounted glasses (average for each glass composition).

	PCL	Mg/PCL	Ca/PCL	45S5/PCL
PCL disk	0.0304±0.004	0.0331±0.0046	0.0317±0.0031	0.0042±0.0313
Glass/PCL disk	-	0.0325±0.0032	0.0331±0.004	0.0321±0.0041
Glass	-	0.0011±0.0004	0.0015±0.0005	0.0008±0.0002

4.8.3. DISCUSSION

Three novel methods were developed for the synthesis of compact variotis™ scaffold disks and bulk PCL disks. The disks showed a variation of ~12% for the neat PCL disks and glass-mounted disks (Table 4.14). An average of 0.0011g glass could be mounted on each scaffold, with a variation of 43.14%. These methods also provide simple techniques for the mounting of small amounts of biomaterial, in preparation for biological testing. Often bulk bioabsorbable biomaterials are either expensive or overly reactive when tested in bulk form. This can lead to cell death and display a different response than would be observed in the body. Testing of a

small amount of material has the ability to overcome these difficulties, whilst still providing useful biological data. Realistically, many bioabsorbables, including bioactive glass, metallic glasses and metals, are more likely to find clinical applications as coatings and fillers (powders/fibers) than in bulk form. Delivery of glass powders directly into culture wells can be time consuming and inaccurate. In addition, glass can accidently be removed from the well during media changes. This novel method ensures a constant cross-sectional area of glass of 8.22±1.95 mm^2. Control of the cross-sectional area is important for cell tests. Researchers could mount a biomaterial of their choice on the scaffold disks, before adjoining the disk to the well using a warm water bath.

4.9. HONEY-COATED VARIOTIS™ SCAFFOLDS

4.9.1. METHODS

Honey was incorporated into the PCL scaffold using two alternate approaches.



Figure 4.48. Manuka Honey UMF25+.

4.9.1.1. Scaffold Honey Infusion Method

1. Manuka Active UMF25+ honey (Manuka Health, New Zealand) (Fig 4.48) was warmed to 40°C for 3 minutes to reduce viscosity.
2. The scaffold was submerged within a 4mm layer of honey.
3. The scaffold was subject to 3 cycles of compression to 10% of original scaffold height
4. The scaffold was left on stainless steel gauze to allow excess honey to drip off for 3 minutes.
5. The honey filled scaffold was cooled to ambient temperature (20 °C).
6. The scaffold was photographed and inspected with optical microscopy to verify filling with honey.

4.9.1.2. Honey Infiltrated Scaffold Method (to remove excess honey and restore interconnected porosity)

1. The infusion method was undertaken.
2. The scaffold was sandwiched in a lintless cloth.
3. The scaffold was subject to 3 cycles of compression to 10% of original scaffold height.
4. The scaffolds were removed from the lintless cloth sandwich.

5. Steps 2-4 were repeated.
6. The scaffold was photographed and inspected with optical microscopy to verify interconnected pores.

4.9.2. RESULTS

The scaffold appeared to be fully wetted with Manuka honey using both methods (Fig 4.49). All vacancies were substituted with the honey and there weren't any visible air bubbles present in the infused scaffold. The infiltrated scaffold was lined with honey and displayed good interconnected porosity.

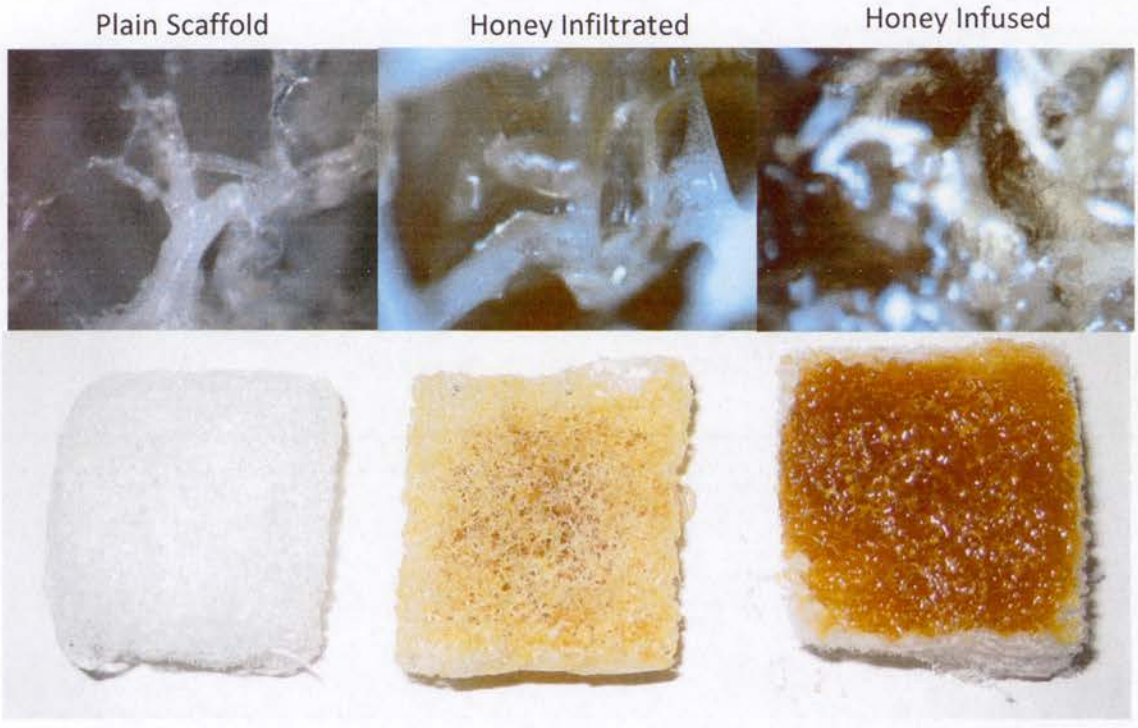


Figure. 4.49. The variotis™ scaffold with infiltrated and infused Manuka honey. Microscopy images are 200x magnification.

4.9.3. DISCUSSION

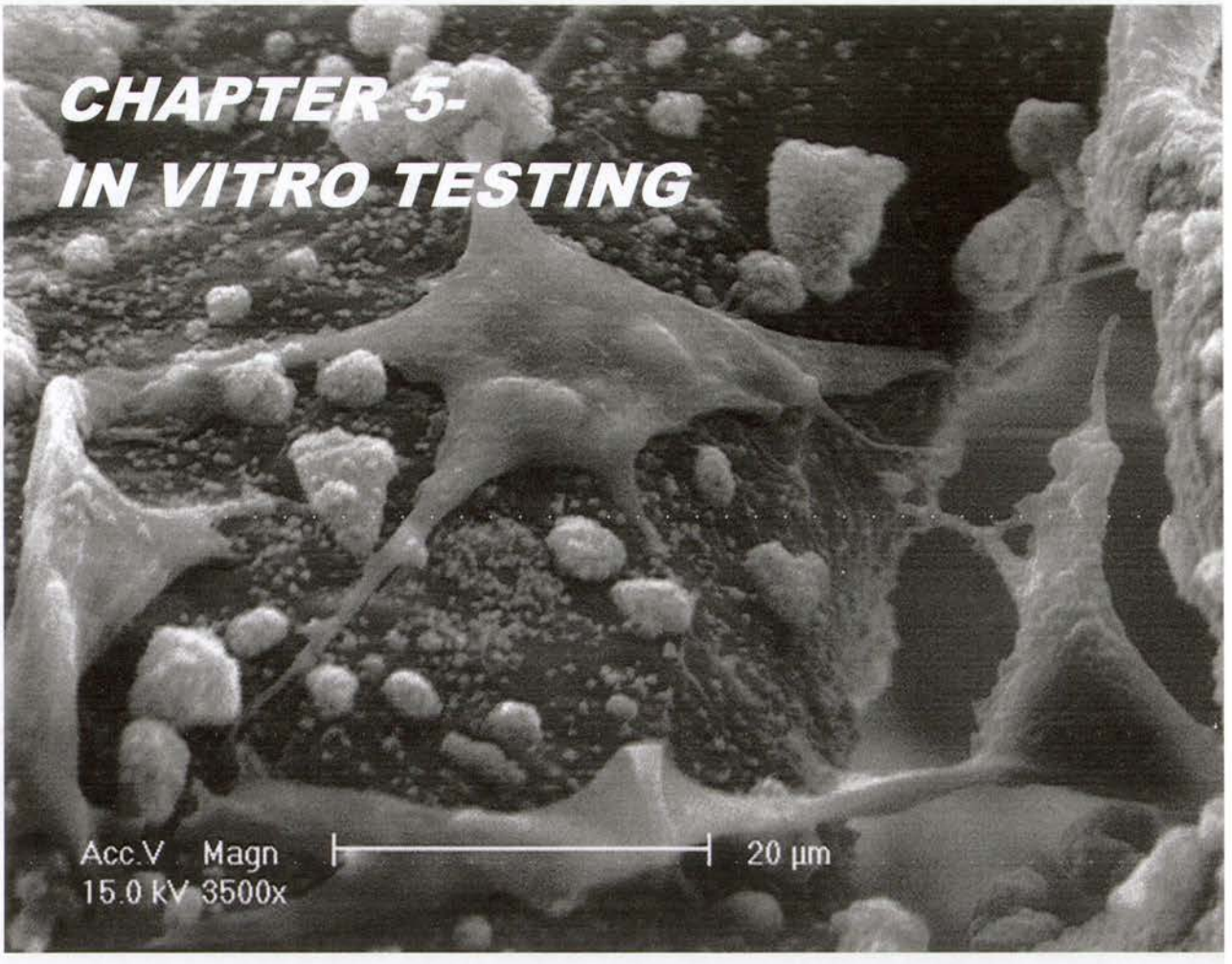
This study shows the capability of the variotis™ scaffold to support a gel phase. As a proof of concept, honey was used due to evidence suggesting its efficacy for aiding healing in chronic wounds. The infused scaffold could be suitable for in vivo use as a wound dressing or localised infection control device for treatment of antibiotic-resistant bacteria. For *in vitro* studies, the honey infiltrated scaffold could be more suitable.

There is good evidence that bioburden in honey can be addressed with gamma irradiation [739] without affecting the antibacterial activity. A study by Postmes and coworkers has demonstrated glucose oxidase, which produces hydrogen peroxide, is not easily damaged by irradiation. A sterility assurance limit of 10^6 can be attained after 25 kGy gamma [739].

Dressings for clinical use could be therefore formed by the following steps (1) Honey infusion in a clean room (2) Packaging in air tight poly(ethylene terephthalate) (PET) (3) Terminal sterilization with 25 kGy gamma irradiation.

4.10. CONCLUSION

- A range of Si-based bioactive glasses were formulated and synthesised, including established Si-doped glasses and novel Zn, Ba and Iron-doped compositions.
- The compositions of a selection of these glasses were verified as the expected formulations. Alumina contamination due to the alumina crucible or ball mill was identified in numerous samples.
- Nanoindentation hardness measurements showed a wide variation according to the positioning of the indenter tip. Iron-doped glass had a high hardness and Zn-doped specimens had a low hardness. The modulus of the 45S5 glass was similar to literature (31 GPa). Glass synthesised using a vertical tube furnace had a lower hardness than glass melted in the molybdenum or induction oven.
- Bioactivity studies demonstrated the ability of all glasses to form increasing calcium phosphate precipitation on their surface. The introduction of zinc led to a slower rate of hydroxyapatite formation in the short term (1 day) but did not affect medium term apatite formation (7 days). The rate of precipitate formation decreased as the amount of ZnO was increased in the glass. An attenuation of the dissolution rate was noted for Ba-doped samples compared to silica-based glasses. These results indicate both barium and zinc could potentially be used to control the degradation rate of bioactive glasses.
- The radiopacity of Ba-doped glasses seemed to increase with the proportion of Ba included.
- Novel methods were developed for mounting glasses onto variotis™ disks which would enable biocompatibility testing of a small quantity of material.
- Honey infused and infiltrated variotis™ scaffolds were successfully synthesised, which could have potential for wound dressings or addressing infection in other tissues.



5.0. CHAPTER OVERVIEW

In vitro biological verification data for composite variotis™ scaffolds and bioactive glasses were obtained in this chapter. Initial biocompatible and long-term viable cell attachment and proliferation were analysed. Long-term *in vitro* culture of mouse fibroblasts (3T3-L1) was performed on PCL and 45S5 or 13-93-coated PCL scaffolds, for 4 weeks. Using SEM, cell growth was evident on the scaffolds at all time-points. Cell proliferation peaked at 3 weeks before decreasing at 4 weeks. Examination of levels of MMP-2 and MMP-9 showed the inflammatory response of the scaffolds was less than the control well. Test models for cell culture and characterisation on variotis™ scaffold was developed. Fluorescence measurement was examined as a potential method for cell population quantitation. Fibroblasts were also cultured on various bioactive glass compositions (altered silica, zinc, barium). Cell attachment to and spreading on the glass slurries was evident using fluorescence microscopy with staining for viable cells using. Calcein. MMP-2 and MMP-9 levels were determined. Fibroblasts were cultured on Ca and Mg-rich monolithic and powdered bulk metallic glasses (BMGs) fused to variotis™ disks. MMP-2 and MMP-9 levels were measured after 3 days. In bulk form, the Ca-rich glass showed high reactivity which inhibited cell growth. When mounted on variotis™ disks this response was attenuated and good cell growth was achieved on both the BMGs as well as 45S5 glass mounted on the variotis™.

5.1. INTRODUCTION

The term "*in vitro*" literally means "in glass", and refers to laboratory culture assays performed on substrates such as petri dishes and culture plates. *In vitro* testing can be used to assess cells and tissues seeded on new implantable materials for:

- cell attachment. proliferation, differentiation;
- biocompatibility or inflammatory response (acute response, giant cells, capsule etc);
- elution of degradation by-products and bioactive/therapeutic agents;
- material stability in the presence of near-physiologic fluid (moisture, salts, lipids, sugars etc); and
- indirect verification of sterility and cleanliness.

In vitro tests also provide insight into whether a device needs further development prior to in vivo testing and ultimately clinical trial validation. In vivo testing is most commonly performed in rodent models prior to clinical trials. Effective *in vitro* testing enables verification of aspects relating to safety and efficacy of a medical device. Well designed in vitro studies can also provide a more ethical development route by reducing the number of animal studies. Mechanisms of cell-material interaction can be readily studied due to meticulous control of variables. The low cost and minimal lead-time of *in vitro* experiments also enables statistically significant numbers of experiments to be rapidly undertaken. *In vitro* testing is therefore useful to help optimise composition, form or delivery kinetics of a device, tissue engineering scaffold or therapeutic components.

5.1.1. DEVICE BIOCOMPATIBILITY AND EFFICACY

Demonstration of the safety and efficacy of a biomaterial is required according to ISO13485 medical device quality standards before the material could be placed in routine clinical use. In a specific sense, this means the cytotoxicity, mutagenicity and gene toxicity of a new material must be demonstrated to be within acceptable levels, so that the risk of an adverse response by the patient is minimised. Both PCL and bioactive glass have an extensive history of biocompatibility, having been used clinically in medical devices for over 20 years.

As detailed in ISO13485, the manufacturing process can adversely impact device safety and efficacy independent of materials biocompatibility. *In vitro* testing can provide an indirect assessment of manufacturing process by detecting cytotoxic levels of contaminants and bioburden introduced during fabrication and storage. Although the biocompatibility of PCL and bioactive glass have been demonstrated in a wide range of *in vitro* and in vivo studies, this is

the first published account of testing soft tissue cells on PCL/bioactive glass composite scaffolds manufactured using the novel batch coagulation and powder-coat methods described in chapter 3.

Previous *in vitro* studies have primarily focused on demonstration of the ability of PCL and bioactive glass to sustain attachment, proliferation and promote the osteogenic phenotype of osteoblasts [117, 147-149, 150, 203, 204, 208, 214-216-220]. Other work using PCL formed using different manufacturing routes has focused on the response of soft tissue cells including fibroblasts, tumor cells and endothelial cells [85, 86, 143, 149, 153, 154, 202, 204-206, 209, 210, 212, 213, 217, 222, 223]. These previous studies have been included earlier in Table 1.3. From the work of others it is known that the speed and quality of tissue attachment and cell proliferation will differ according to the form of the composite; including the macro-, micro- and nano-scale properties. Previous experiments have been performed using PCL in the form of electrospun fibres [150, 222], and bioactive glass in either powdered [86, 201, 202, 204] or sintered fibrous scaffold [198, 200] forms. Occasionally, composite foams have been studied which have incorporated bioactive glass, or other silica-based components, into either PCL [148, 149, 218, 219] or other matrices [153, 154, 209- 212].

Due to the unique structure of the variotis™ scaffold, it was important to study its ability to support attachment and proliferation of cells. In addition, it was of interest to study the scaffold's effect on soft tissue remodelling and inflammatory markers, as very little work has been done in this area. For this reason, in the current study matrix metalloproteinase expression was also investigated.

5.1.2. TECHNIQUES FOR *IN VITRO* CULTURE IN SCAFFOLDS

Often the analysis of cell-biomaterial interactions is limited due to the properties of the biomaterial and the nature of the scaffold form. Thus, an important design criterion for our scaffold was to ensure that a range of standard culture techniques would be possible. It was anticipated that a synthetic scaffold would show increased *in vitro* and in vivo technique capacity compared to a naturally derived scaffold.

5.1.2.1. Cell Seeding

Cells can be seeded on scaffolds in a variety of ways. Standard static seeding involves depositing the cells in a solution of culture media, using a pipette. The cells can be then left to attach for a few hours before additional media is added to the well. Cells can then migrate throughout the scaffold, depending upon its characteristics. Alternately, a uniform cell distribution within the well could lead to well-distributed cell attachment, depending on the scaffold form. Alternate seeding techniques include perfusion seeding [222] and oscillation culture [745] which could be necessary when cell migration is difficult and there is a high risk of cell accumulation.

5.1.2.2. Cell Culture

Cells can be cultured using a variety of static or dynamic methods, which can dramatically affect cell morphology, phenotype and ECM composition/structure. Examples of culture techniques include:

- standard static culture [149];
- stirring culture [108];
- rotating or oscillating culture [745, 746]; and
- mechanically actuated- pulsile, stretched, compressed [22, 402, 440].

5.1.2.3. Characterisation Techniques

A range of standard techniques used to characterize the behaviour of cell cultures on scaffolds are described in Table 5.1. Commonly, analysis is limited to relatively simple techniques such as metabolic assays and cell visualisation using SEM or epifluorescent microscopy. Live and dead cells can be detected via staining techniques and visualised using a fluorescent microscope or counted using flow cytometry [204]. Rarely do researchers investigate the capacity for the scaffold to support cell migration throughout the scaffold. Quite often, cell accumulation occurs on one edge of the scaffold, and this is not reflected in data from metabolic assays or overall cell counts.

Table 5.1. Techniques for characterizing cell attachment and spreading in porous polymer scaffolds.

	Technique	Common Challenges	Ref
Cell proliferation	Metabolism e.g. MTS, DNA assay, glucose consumption	Cannot determine cell position within scaffold. Some scaffolds demonstrate poor handling properties and cannot be transferred into clean culture plates.	125, 132, 223, 751
	Cytotoxicity (manual cell count; flow cytometry; fluorescence)	Can be difficult to remove cells from scaffold; destructive.	234, 746
	Total Protein or RNA content	Scaffold components can interfere with measurements.	747, 748
Cell attachment, spreading and morphology in 3D space	Epifluorescent microscopy	Low depth of field.	221, 222, 746
	SEM	Limited 3D view.	221, 222, 746
	Phase contrast microscopy	Low depth of field.	748
	Confocal Microscopy	Limited imaging thickness.	219
	Histology/ Immunohistochemistry	Scaffold can be difficult to slice or dissolve in solvents.	14, 59, 84, 85, 202, 234, 262, 830
	MicroCT	Lack of contrast between cells/scaffold. Cells can die/detach due to dehydration.	446, 365
Gene expression- Cell phenotype, inflammation	RT-PCR	Difficulty removing cells from some scaffolds.	244, 746
	Protein activity e.g. Gelatin Zymography, ELISA, Western Blot	Naturally-derived scaffolds can contain unknown protein types or concentrations. Some materials demonstrate protein adsorption or release.	495, 496, 749, 750
	Immunohistochemistry	Scaffold can be difficult to section or dissolve in solvents. Cell quantitation can be difficult using automatic methods due to visual interference with scaffold.	202, 234

5.1.2.4. Non-Destructive Cell Characterisation Techniques

Development of non-destructive techniques to effectively investigate cell behaviour in thick, 3D tissue scaffolds is still an area of great need. Such techniques would enable tracking of cell migration and measurement of biomarkers within a particular sample, over time.

Several techniques potentially enable the position of cells within a scaffold to be ascertained. These include scanning electron microscopy, confocal microscopy, microCT and standard microscopy techniques. SEM is commonly used for investigation of cells on biomaterials, however, cell counting is difficult with these images. In addition, SEM does not fully enable 3D cell spreading to be investigated, as only a cross-sectional surface could be viewed at a time. Although confocal microscopy could be used to visualize cells in 3D space, its depth of field is

limited to about 100 μM. MicroCT has the capacity to view cells in 0.5 cm thick scaffolds. However, techniques are currently only optimised for mineralised tissue. Using optical or fluorescence microscopy, intact scaffolds or histological sections can potentially be visualised, depending on the scaffold characteristics. Other specialised microscopy techniques include time-lapse photography or video microscopy.

The conditioned media, in which cells were cultured, can be analysed to give information about the biomaterial degradation or cell behaviour. Measurements could be taken of protein activity, pH, dissolved ions/corrosion products or glucose consumption [234, 677, 751, 752]. Such methods are particularly useful if the scaffold is expensive, difficult to produce or if the culture period is long-term and labour intensive.

Over the next 10 years, useful novel, nondestructive techniques are likely to be further developed, and applied to scaffold systems.

5.1.3. CHALLENGES POSED BY SCAFFOLD SYSTEMS

Characteristics of scaffold systems will make them more or less suited to these various analysis and culture techniques. These characteristics include the physical, chemical and biological properties of the biomaterial. A range of commercially available scaffold systems were included earlier in Table 1.6. Although tissue engineering systems consisting of gel beads, bulk gels or fibrous membranes could provide beneficial micromechanical and biological cues to the cells, such constructs are usually difficult to handle. This can lead to a loss of integrity upon transfer out of the cell well. Such systems are therefore limited to well-based techniques including MTS or cell counts. Ideally, a scaffold system would have sufficient mechanical integrity to be cut, manipulated and transferred between culture plates and eppendorf tubes. In addition, Cell removal can be difficult from many scaffolds (e.g. elastin, collagen, hydrogels). This can make obtaining cell counts or RNA analysis inaccurate or impossible. Some scaffolds are also difficult to embed, slice or stain for histology or TEM, and could experience problems such as compression, dehydration, autofluorescence or dissolution in solvents. Many naturally-derived ECM scaffolds consist of unknown concentrations or types of proteins (e.g. Matrigel) or encourage protein adsorption, so accurate profiling of protein activity or RNA expression is not possible. Gel networks are frequently too dense to allow a high level of cell migration, penetration and proliferation throughout the construct [746], so culture is limited to thin (<3 mm) systems.

A wide range of scaffolds are unsuitable for long-term cultures (3+ weeks). Scaffolds such as collagen can experience premature contraction and degradation due to the cell cultures. Gels are metastable materials which experience varying water content over time, and the influence

of salts and ions. Few scaffolds could be used for long-term mechanically stimulated culture, due to a poor capacity to strain before tearing, and the inability to return to their original length after straining.

The above difficulties are sometimes more pronounced when it comes to analysis of the in vivo explants. It is these limitations which can make it difficult to transfer pre-seeded scaffolds to an in vivo situation, or compare results between *in vitro* and in vivo models. In addition to these difficulties, the rapidly evolving degradation byproducts of scaffolds (e.g. PGA) can raise the local pH, leading to an early decrease in cell viability [234].

5.1.4. PREVIOUS *IN VITRO* STUDIES ON PCL/BG COMPOSITES

5.1.4.1. Studies with Hard Tissue Cells

PCL/Bioactive glass composites have demonstrated increased bone cell proliferation and a corresponding stimulation of bone formation [147-150, 753-755]. For example, Lee and coworkers [147] synthesised thin membranes (~260μm) from nanofibrous bioactive glass embedded into PCL, and investigated their potential as a guided bone regeneration membrane. Murine derived osteoblastic cells (MC3T3-E1) grew actively over the membrane with the cell viability and osteoblastic activity (as assessed by MTS assay and expression of alkaline phosphatase) significantly improved with those on the pure PCL membrane. The results for this study are included in Fig. 5.1. In another study, Jo and coworkers [150] detected higher cell proliferation and osteoblastic activity on PCL/Bioactive glass (powder or nanofibre) composite electrospun meshes, as compared to pure PCL. This corresponded with an increase in bone formation, particularly for the nanofibrous composite. A similar finding was reported in a study by Yun and coworkers [148]. Bioglass®/PCL composites demonstrated higher levels of osteoblast proliferation than PCL scaffolds, and this finding was even more pronounced when mesoporous Bioglass® was used [148]. The biocompatibility of PCL/Bioactive glass scaffolds (synthesised using salt leaching) was demonstrated by Cannillo and coworkers [219]. Lu and coworkers [221] cocultured endothelial hybridoma and osteoblast cells on rapid prototyped PCL scaffolds which were created using a sucrose porogen. They demonstrated cell spreading and multiple layers of cells over 6 days of culture, using epifluorescence and scanning electron microscopy.

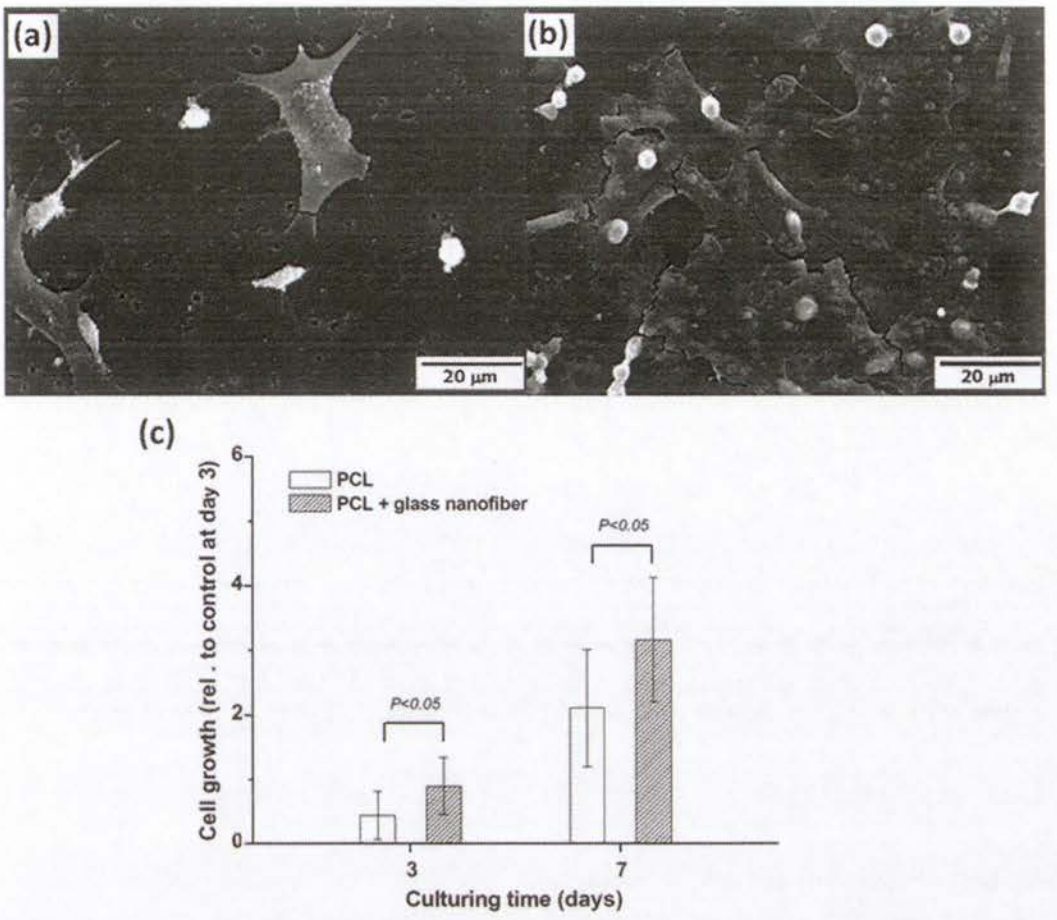


Figure 5.1. Osteoblastic cell proliferation after 4 days on (a) PCL, (b) Nanofibrous bioactive glass/PCL composite (c) Comparison of cell growth, as measured by MTS assay [147]

5.1.4.2.Studies with Soft Tissue Cells

To the author's knowledge, there are no *in vitro* studies reported in the literature concerning PCL/BG composites for soft tissue. Whitehead and coworkers demonstrated PCL/mesoporous silicon scaffolds (prepared using salt leaching or freeze drying) were non-toxic for kidney fibroblasts and bone-derived mesenchymal cells [149].

Previous studies have investigated PCL alone for soft tissue cells such as endothelial cells, dermal fibroblasts and smooth muscle cells [206, 221, 222, 234]. For example, Sung and coworkers [234] synthesised thin porous PCL scaffolds (cut to 10μm thickness) using salt leaching, and demonstrated increased *in vitro* cell viability compared to PLGA scaffolds, when seeded with smooth muscle cells. Lowery [222] seeded dermal fibroblasts onto thin electrospun PCL mats using perfusion seeding. SEM and epifluorescent imaging (DAPI and Calcein) were used to demonstrate cell proliferation over a period of 21 days. The cells were observed to bridge the pore voids and deposit ECM. Good attachment of human foreskin fibroblasts was observed on PCL microporous matrices (pore size: 10-20μm) over 2 weeks of culture by Yeh and coworkers [206]. Higher cell proliferation was noted on high molecular weight PCL (CAPA 6500 and 6800) (as used for the current study) than for the low molecular

weight PCL (CAPA 6400), which is more waxy [206]. Chen [223] used MTT assay to demonstrate good proliferation of fibroblasts on PCL and PCL/silk composite scaffolds over a period of 7 days, with confluence being reached at 7 days. The PCL scaffold showed a higher level of cell attachment in the first 24 hrs than the composite scaffolds.

5.1.5. PREVIOUS *IN VITRO* STUDIES ON BIOACTIVE GLASSES

Few studies have investigated the in vitro response of soft tissue cells to bioactive glass [86, 202]. *In vitro* studies have been performed on bioactive glass in powdered [86, 201-204], fibrous [205] or sintered fibre form [198, 200]. Cells studied have included osteoblasts [200, 203-205], fibroblasts, [86, 202, 204, 205], adipose stem cells [198] and nucleus fibrosis cells [202]. Cell densities on biomaterials which include bioactive fillers have generally been observed to increase over time [108, 209, 211, 212]. For example, Takahashi [108] incorporated various levels of β-TCP into gelatin sponges and cultured MSCs on the sponges for 6 days (shown in Fig. 5.2). Generally, cell proliferation increased with the proportion of β-TCP (5.2d). This effect was more pronounced when a stirred culture method was used (Fig. 5.2e). One of the reasons for the increased proliferation on the TCP/Gelatin scaffolds was thought to be an increased stiffness, which ensured the scaffolds held their volume and allowed for a higher level of cell proliferation within the scaffolds. The extent of scaffold deformation was measured in this study and a relationship was demonstrated between these aspects.

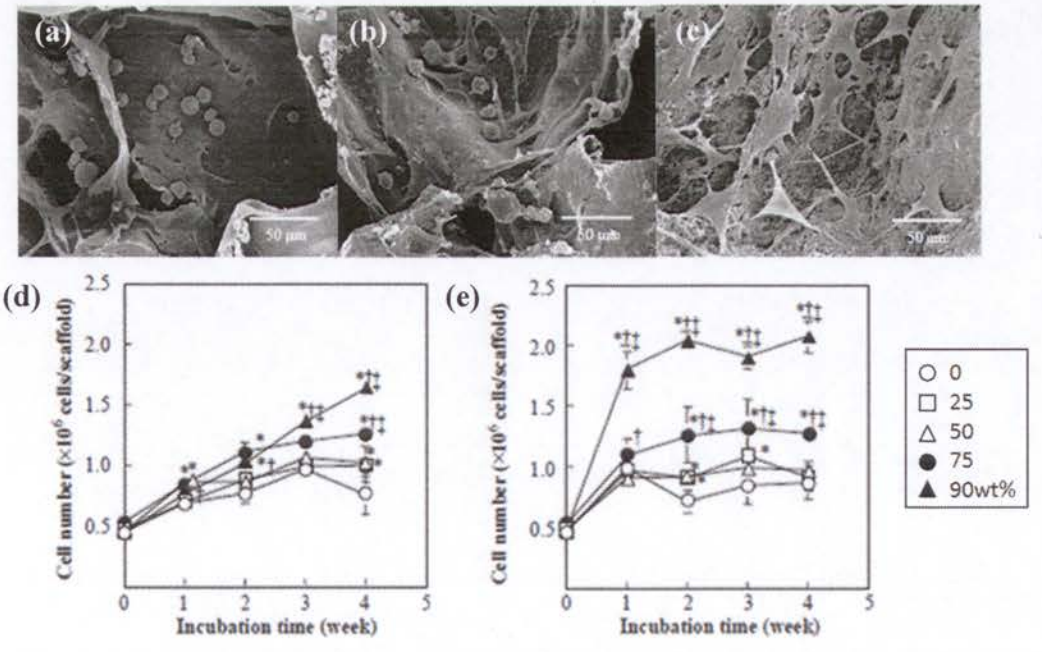


Figure 5.2. Scanning Electron Micrographs of MSCs proliferating on gelatin sponges incorporated with (a) 0, (b) 25%, (c) 75% TCP. Time course of MSC proliferation of gelatin sponges incorporating various levels of TCP by the (d) static or (e) stirring culture method. The TCP particles used in this study had an average diameter of 2.9μm [108].

However, the beneficial effect of bioactive fillers on cell proliferation does not always correspond with an increase in glass concentration. Verrier and coworkers [212] detected an increase in human lung carcinoma cell proliferation, when cultured on PDLLA/5 wt% Bioglass®, as compared to PDLLA (shown in Fig. 5.3). However, proliferation of cells on PDLLA/40 wt% Bioglass®, was lower than both these materials. This effect was dependent on the cell type; little difference was detected between the material compositions for a human osteosarcoma cell line. Verrier's demonstrated that using 3D cell culture, it is possible to observe an increase in cell number for at least 4 weeks. In contrast, when the cells were cultured on tissue culture plastic, the cell numbers decreased from weeks 2 to 4. This is due to layering of cells which occurs due to limited surface area, which leads to cell detachment and death. In another study, Day and coworkers [86] found low concentrations of 45S5 bioactive glass (0.01-0.2% wt/vol) showed a stimulatory effect on fibroblasts for 24 hrs *in vitro*, which corresponded with high levels of secretion of the angiogenic factor VEGF. However, cell proliferation was reduced at higher concentrations and longer periods of incubation (48 and 72 hrs). A key aspect of this study which could have hindered cell proliferation are the rapid accumulation of ionic byproducts which would have been released from the dissolution of the bioactive glass particles, which had a small particle size of <5 μM.

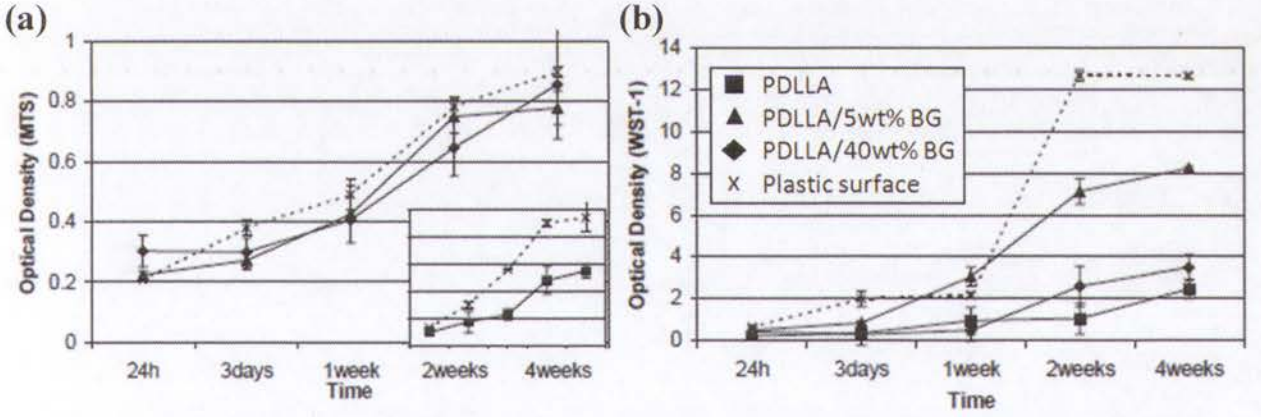


Figure 5.3. Cell proliferation assays on PDLLA scaffolds (a) Human osteosarcoma cell line (MG63) or (b) Human lung carcinoma cells (A549) cultured on PDLLA foams containing 0, 5 or 40 wt% of 45S5 Bioglass® and compared with a plastic control surface [212].

The inclusion of bioactive glass within a composite provides a higher surface area and more attachment sites for cells. This results in cells which exhibit multiple protrusions as they stretch the glass particles. As shown in Fig. 5.4, Tsigkou and coworkers [208] observed protrusions from osteoblasts which attached to bioactive glass particles embedded in PDLLA films (Fig. 5.4).

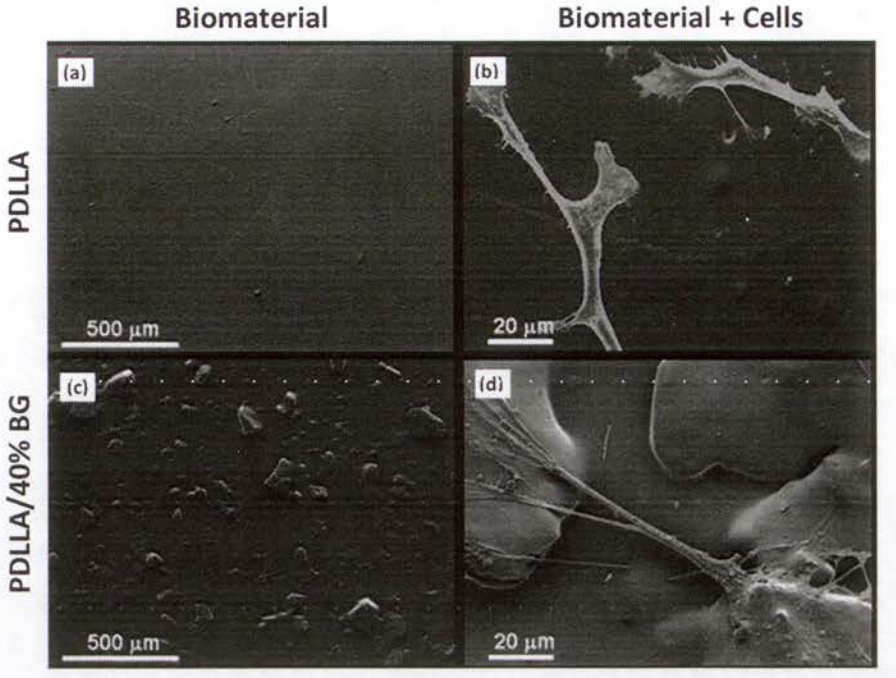


Figure 5.4. Scanning Electron Microscopy images of (a, c) Substrate surfaces (b, d) Osteoblasts on the surface after 7 days of culture. (a, b) PDLLA films (c, d) PDLLA/40% BG [208]

This cell attachment could contribute to the ability of some cell types (e.g. cartilage and nucleus pulposis) to retain their phenotype on bioactive glass composites. Gan [202] suggested that the proliferation of nucleus pulposis cells could be an anchorage dependent event, where the cells utilize the CaP rich layer to facilitate adhesion and proliferation. Cell accumulation leads to a high level of surface contact and pressure which aids in phenotype retention. Shown in Fig. 5.5, Gan and coworkers cultured rabbit-derived nucleus pulposis disks on powdered 45S5 bioactive glass and found rapid attachment and colonisation within 12 hours. By 21 days, confluency was achieved. DNA measurements showed a progressive increase in cell number with time. Levels of collagen I, II, proteoglycan and aggrecan were maintained, consistent with phenotype retention [202, 154]. 5.1.4. Detection of Wound Modelling Biomarkers

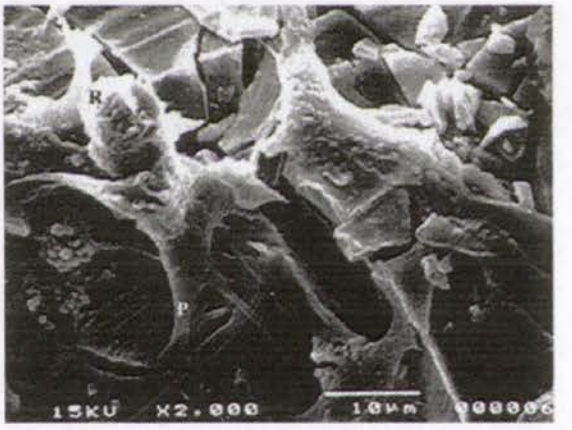


Figure 5.5. Nucleus pulposis cells on 45S5 bioactive glass. Some cells exhibited a rounded shape (R) and others had cytoplasmic processes (P) [202].

In the current *in vitro* studies, matrix degrading enzymes termed matrix metalloproteinases (MMPs) have been used to monitor matrix remodelling. The MMPs are a family of zinc-dependent proteolytic enzymes which are responsible for the extracellular degradation of connective tissue. They are involved in tissue modelling during tumor progression, cell migration, angiogenesis and wound healing [756]. Matrix metalloproteinases are present in both the active and inactive (i.e. zymogen or proMMP) forms in body fluids such as wound fluids, blood and urine [757]. MMPs require divalent ions such as Ca^{2+} or Zn^{2+} in the catalytic domain to display enzymatic activity [758].

In terms of wound healing, the balance between growth factor activation and degradation has to be carefully controlled to ensure correct progression towards healing. MMPs are produced by both inflammatory cells (e.g. neutrophils and macrophages) and wound cells (e.g. epithelial cells, fibroblasts and vascular endothelial cells). Although they play an important role in healthy skin, certain MMPs are present in high levels in chronic wound exudate, including MMP-1, -2, -3, -8 and -9. This leads to the degradation of key elements in the wound healing process [499].

MMPs are also involved in other biological processes important to wound healing. These include growth factor activation and immune system regulation [771]. Some MMPs, such as MMP-2, demonstrate a positive effect during the later stages of healing and repair [761]. MMP-2 (gelatinase-A, 72-kDa) has a vital role in ECM turnover and has been shown to have a role in collagen lattice reorganisation *in vitro* [760, 487]. A study by Jung-Yu and coworkers found the presence of MMP-2 aided functional recovery after spinal cord injury by regulating the formation of a glial scar whilst sparing axonal plasticity [761]. The MMPs are thought to play an important role in the processes of endothelial cell migration and matrix remodelling during angiogenesis [762]. Haas and coworkers [763] demonstrated, using gelatin zymography, that levels of MMP-2 mRNA and protein increased when endothelial cells were cultured in 3-D as compared to 2-D monolayer cultures (51% and 3.5%, respectively). MMP-9 (gelatinase-B, 92-kDa) has shown to have the ability to degrade collagen types I, II, III, IV and V into small peptides [764]. MMP-9 (gelatinase-B) is primarily produced by inflammatory cells, neutrophils, macrophages and keratinocytes [496].

Several techniques have been investigated to address the imbalance of MMP activity in chronic wounds [497, 496, 497, 499, 750, 765]. These include coupling protease inhibitors (e.g. bisphosphonates) to cotton wound dressings [497, 765] and binding of MMPs to particular biomaterials (e.g. polyacrylate superabsorber particles) which bind to Ca^{2+} and Zn^{2+} divalent

ions. Among the synthetic inhibitors of MMPs, are bisphosphonates (e.g. clodronate, alendronate) [767]. Bisphosphonates have been shown to inhibit MMP-1, -2, -3, -8, -9, -12, -13 and 20 at both therapeutically obtainable and noncytotoxic concentrations [765]. Incorporation of alendronate into a poly(2-hydroxy methacrylate) (PHEMA) hydrogel for treatment of chronic wounds has been investigated by Rayment and coworkers [499]. Collagen-based dressings have been shown to reduce protease levels in wound fluid [496, 497]. Delivery of MMP-2 to chronic wounds from PCL matrices was an approach recently developed by Smith et al [750]. This could be an avenue for therapeutic treatment of chronic wounds which could be explored in the future.

MMPs are adsorbed onto various biomaterials to differing degrees [757]. Reno and coworkers used western blot and substrate zymography to observe the adsorption of MMP-2 and MMP-9 onto the surface of polymers, especially the hydrophilic ones (PMMA and PHEMA) and PLA, in both the active and inactive forms. Evidence was obtained that it could be possible to use a gelatinase inhibitor to reduce the inflammation associated with some biomaterials. Reno demonstrated that, using a gelatinase inhibitor, the adhesion of neutrophils to PMMA was reduced by more than 50%.

Biomaterials will stimulate MMPs to varying extents. Hydroxyapatite has been shown to induce an increase in MMP-9 expression, along with other pro-inflammatory mediators such as IL-1α and chemotactic factors such as IL-8, macrophage inflammatory protein -α and -β [768]. Bosetti [637] demonstrated that oxidation of UHMWPE using radiation resulted in a decrease in the release and activity of MMP-2 after 4 and 8 days osteoblast culture compared to cells grown on non-oxidised UHMWPE disks. MMP-9 release was not significantly influenced. Upregulation of MMP-2 (also MMP-4, and the MMP inhibitors; TIMP-1, TIMP-2) was detected following culture of the ionic products of 45S5 Bioglass® dissolution with osteoblasts, in a study by Xynos and coworkers [752]. Increased levels of MMP-9 are often associated with increased inflammatory cell invasion and more pronounced angiogenic response within scaffolds [770].

In the current study, MMP-2 and MMP-9 levels were measured in the media (supernatant) in which cells were cultured on the variotis™ scaffold or bioactive biomaterials which were synthesised in previous chapters. Zymography was also performed in chapter 6 on wound fluid taken from the in vivo study.

5.2. *IN VITRO* TESTING OF FIBROBLASTS ON COMPOSITE SCAFFOLDS

5.2.1. METHODS

5.2.1.1. Specimen Preparation and Cell Seeding

Polycaprolactone scaffolds (10.5 x 16.5 x 17.8 mm) were rapidly synthesised using the novel coagulating batch process developed by the authors (ref 3.2.2.1B). Some composite scaffolds were synthesised by coating with either 1393 bioactive glass fibres (~10 wt%) or 45S5 bioactive glass powder (~10 wt%) (ref 3.2.2.3.A and 3.2.2.3C). The 45S5 glass was synthesised by a melt-derived technique, as previously described in chapter 4 (batch Ax2). Rectangular prism scaffolds with final dimensions 10.5 x 8.25 x 8.9 mm were prepared by cutting the scaffolds into quarters using a sharp, sterile blade. Scaffolds were attached to the base of 24-well culture plates using warm water. Scaffolds were sterilised in a UV laminar flow cabinet (30 mins), rinsed with sterile PBS and then washed with 70% ethanol (20 mins). Samples were soaked in sterile medium (11 mM RPMI, 10% FCS) overnight to remove residual ethanol.

Fig. 5.6. shows a schematic representation of the cell seeding procedure. Mouse 3T3L1 fibroblasts (P24) were cultured to confluence in 150 cm^2 flasks at 37°C and 5% CO_2. Culture was undertaken in complete media consisting of 11 mM RPMI (Sigma), 10% Fetal Calf Serum (HyClone). All cells were cultured in the presence of antibiotics, e.g. 1% Penicillin/streptomycin (Sigma). Cells were removed from flasks using trypsin (0.2 mL/mL). Cells were spun at 1200 rpm to form a cell pellet and were resuspended in complete media. Prior to placing cells on the scaffold 500 mL complete media was placed into each well. 500µL of the cell solution (10 x 10^3 cells) was placed onto each scaffold, resulting in a final cell density of 6666 cells/mL. Control wells consisted of cells or media alone. Cells were cultured in an incubator at 37°C and 5% CO_2 for the duration of the experiment, with media replacement at least every 48 hours. The media was replaced with 11 mM serum-free RPMI 24 hrs before each timepoint. Scaffolds were removed with a scalpel for further analysis.

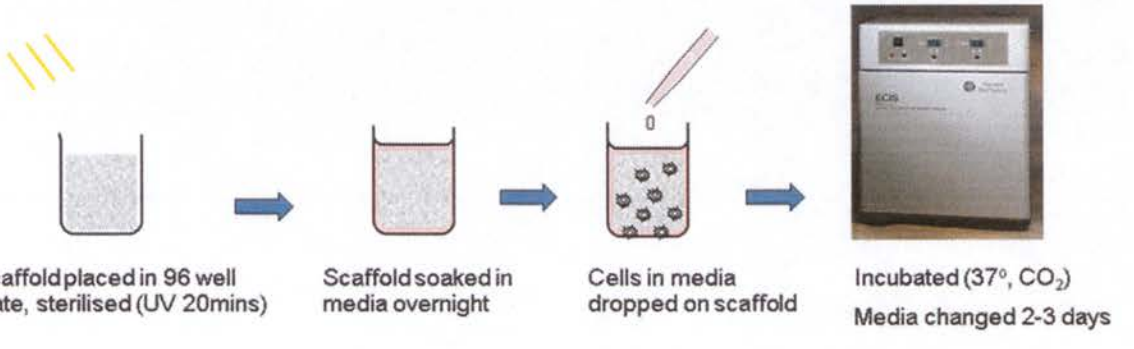


Figure 5.6. The protocol for fibroblast seeding on variotis™ scaffolds.

5.2.1.2. Optical and Fluorescent Microscopy Examination

3D scaffolds were stored at -80°C after 48 hours of culture, then embedded in Optimum Cutting Temperature Compound (OCT- Tissue-Tek, ProScitech, QLD, Australia). OCT embedded sections were cryosectioned at -15°C. Sections (7μm) were mounted onto gelatinised slides (Superfrost Plus) and air dried. Other 3D scaffolds were stained with the nuclear marker DAPI (0.2% (v/v) in PBS. Cell attachment after 2 weeks of culture was examined using a using a Leitz DMRXE optical microscope and Leica DFC420 digital camera system. Additional scaffolds were stained after 2 weeks culture using a cytoplasmic marker. Viable cells were marked using 500 μL Calcein AM (1:100 in RPMI) for the last 20mins of the incubation period. After removal, scaffolds were rinsed with PBS. Scaffolds were also stained using the nuclear marker DAPI (0.2% (v/v) in PBS. DAPI stained nuclei were visualised as blue (350 nm) and cytoplasmic stains were visualised as green (520 nm) using a fluorescent microscope (Olympus AX70, Olympus, Tokyo, Japan) equipped with an Olympus DP60 camera.

5.2.1.3. Scanning Electron Microscopy (SEM) Examination

The scaffolds were prepared for SEM by removal from culture after 2, 3 and 4 days. Fixation was performed as previously described in section 2.4.1.4. Cross-sectioned specimens were mounted on aluminium stubs and sputter coated with 10 nm gold and 10 nm platinum. SEM Imaging was performed on a Philips XL30.

5.2.1.4. Measurement of Cellular Metalloproteinase Activity

Gelatin zymography was used to measure MMP activity after 4, 7 and 14 days of culture. For these studies supernatant (10 μL) was loaded onto a 8% SDS-PAGE gel containing 10% MDPF labeled gelatin (0.75 mm thick). The samples were separated by electrophoresis at a constant voltage (130 V) for approximately 1.5 hr at room temperature, and activities determined as described in detail previously [776]. The results are expressed as the average of 2 wells from 2 gels for each timepoint. Results were corrected for initial wound fluid volume and protein concentration and are expressed as X μg/mgP.

5.2.1.5.Examination of Cells on Scaffold using MicroCT

Phosphomolybdic acid was explored as a potential contrast agent for visualising the cells within the scaffold. It was chosen due to proven ability to enhance the density of molluscan soft tissue in a previous study [410]. Fibroblasts cultured on chamber slides for 24 hrs were treated with 0.25, 1.25 and 2.5% phosphomolybdic acid (Sigma-Aldrich) in media. Cells were examined using light microscopy to assess the depth of staining. A concentration of 1.25% was

chosen to stain 4-week cultured scaffolds. Scaffolds were visualised using a desktop MicroCT (Skyscan 1072, The Netherlands) as detailed in section 3.2.2.7.

5.2.2. RESULTS

5.2.2.1. Examination of Cell Attachment and Morphology on 3D Scaffolds

Optical and fluorescent microscopy of the 3D scaffolds demonstrated cell adhesion to the scaffold (Fig. 5.7). Webs of cells were observed stretching between glass fibres. Cell nuclei were identified using the fluorescent stain DAPI. Agglomerates of cells were visible on the glass and the scaffold struts. However, difficulty focusing on the 3D scaffold matrix meant it was difficult to ascertain a qualitative indication of cell density using this method. Scattering of light caused by the 3D nature of the scaffold made clear detection of the Calcein stain especially difficult (results not shown).

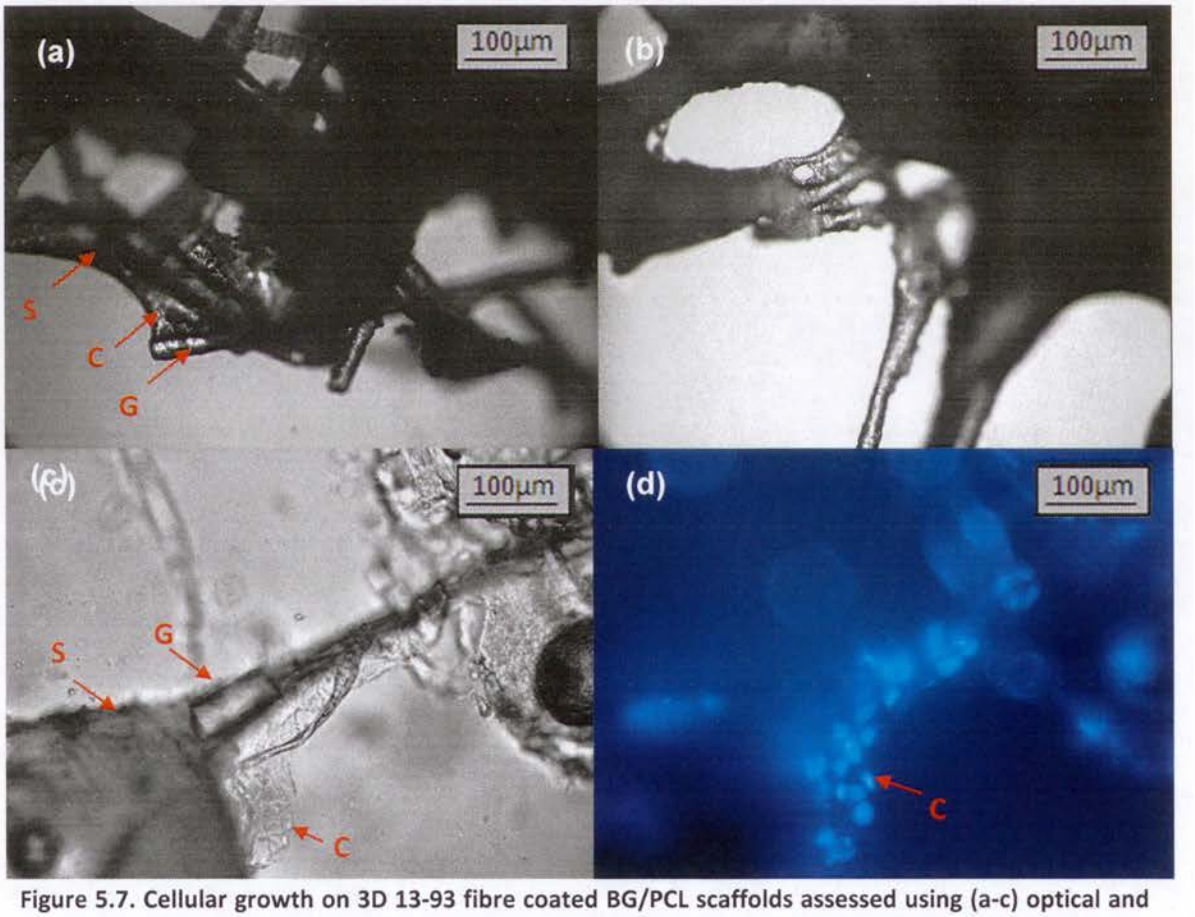


Figure 5.7. Cellular growth on 3D 13-93 fibre coated BG/PCL scaffolds assessed using (a-c) optical and (d) fluorescent microscopy (DAPI). Images (c) and (d) show the same region. S: scaffold, G: glass, C: cells

Cell proliferation was also examined on scaffold fragments which had broken off the scaffold during the culture period (Fig. 5.8). Large numbers of live cells were observed on all scaffold types using DAPI and Calcein. Cell spreading was evident on both the PCL and glass particles.

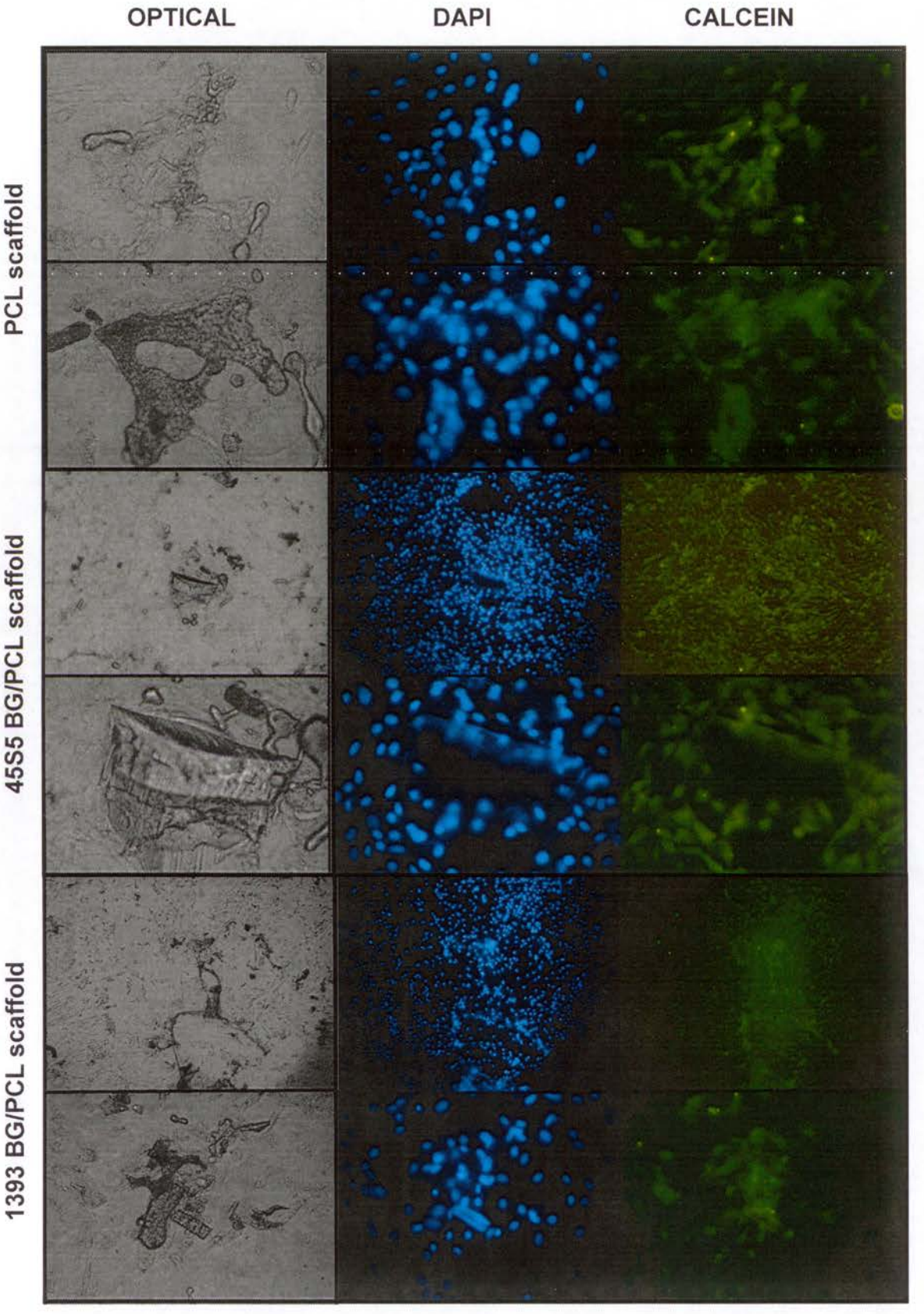


Figure 5.8. Fibroblast proliferation on scaffold fragments using DAPI and Calcein fluorescent staining.

The PCL scaffolds were successfully mounted in OCT, cryosectioned and mounted on slides. Cells were visualised attached to the scaffold, using DAPI (Fig. 5.9). Due to the scaffold's highly porous nature, the sectioned scaffolds did not always adhere to the slide intact. Overlapping of scaffold segments occurred in some cases. The composite scaffolds were more difficult to section than the PCL scaffolds (not shown). This was due to the bioactive glass splitting the sections. Blunting of the blade also occurred prematurely.

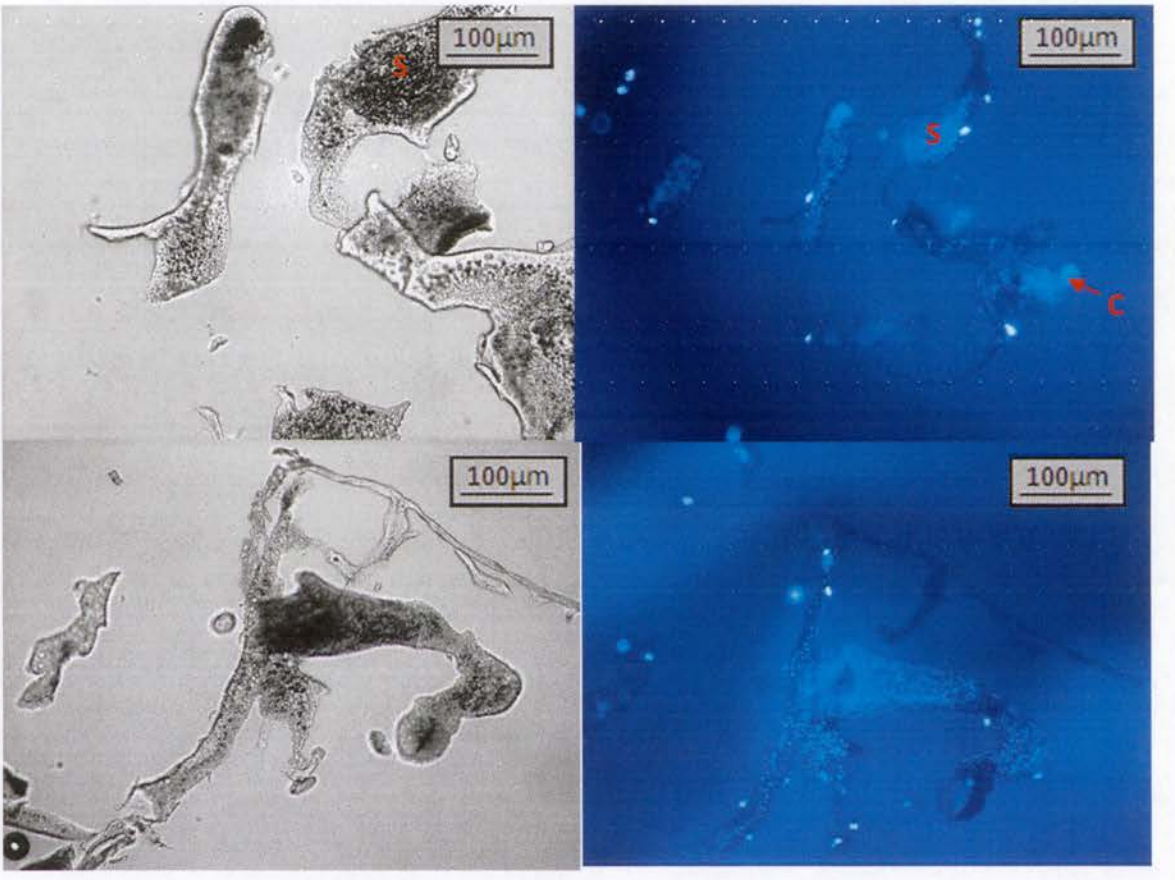


Figure 5.9. Histological sections of DAPI-stained fibroblasts cultured on PCL variotis™ scaffolds for 48 hrs. C: cell, S: scaffold.

Cells were observed on all scaffolds after 14, 21 and 28 days of culture, using SEM (Fig. 5.10). This gave a qualitative indication of the relative number of cells in each scaffold.

The PCL scaffold showed low levels of cells for all timepoints. The 45S5 BG/PCL scaffold demonstrated a moderate-high level of cells at 14 days. This increased to confluent layers on many of the struts by 3 weeks, but had reduced to a moderate level by 28 days. The 1393 BG/PCL scaffold also supported a moderate-high level of cells by 14-21 days, but this dropped to a moderate level by 28 days. These results indicate that between 21 and 28 days, the cells could be detaching from the scaffolds. This is a common phenomenon on tissue culture plastic, usually occurring after about 1 week. Therefore using the variotis™ scaffold, 3D cell culture could be sustained for at least 3x longer than 2D tissue culture plastic, before detachment occurs. An alternate explanation for this finding could be that not enough nutrients were being supplied to the scaffold to support further cell growth. If this were the case, this could be improved via using a smaller scaffold for the culture or replacing the media more often.

Although the cell coverage for the PCL scaffold was generally more sparse than the glass-coated scaffolds (Fig. 5.11), some regions in the PCL scaffold were more dense in cells, particularly near the base of the scaffold (Fig. 5.12a,b). Cells were observed stretching into the microporous surface of the PCL scaffold (Fig. 5.12c). Cell debris was present near the base of the PCL scaffold, however these regions still supported live cells (Fig. 5.13).

The 45S5-coated scaffolds exhibited excellent cell proliferation in many regions throughout the scaffold, particularly at 3 weeks (Fig. 5.14-5.18). Cells appeared to take a flattened, elongated morphology, and were larger than those on the PCL scaffold. Many of the cells exhibited a flattened, star-like shape. Cell filopodia observed stretching in multiple directions, attaching to the textured scaffold surface. Cells were observed to stretch large distances across the pores. For example, Fig. 5.18 depicts a cell stretching 200μM. The inset shows the cell attachment to the calcium phosphate precipitates.

Rounded, cauliflower-shaped precipitates (1μm diameter) were observed covering the glass powders, and also lining the scaffold surface. These features were evident after 14, 21 and 21 days of culture on the 45S5 and 1393 coated samples. The microporous scaffold surface was not as evident on the glass-coated scaffolds as it was for the PCL. However, upon examination of strut cross-sections, it was obvious that there was still a network of microporous channels within the struts (Fig. 5.17).

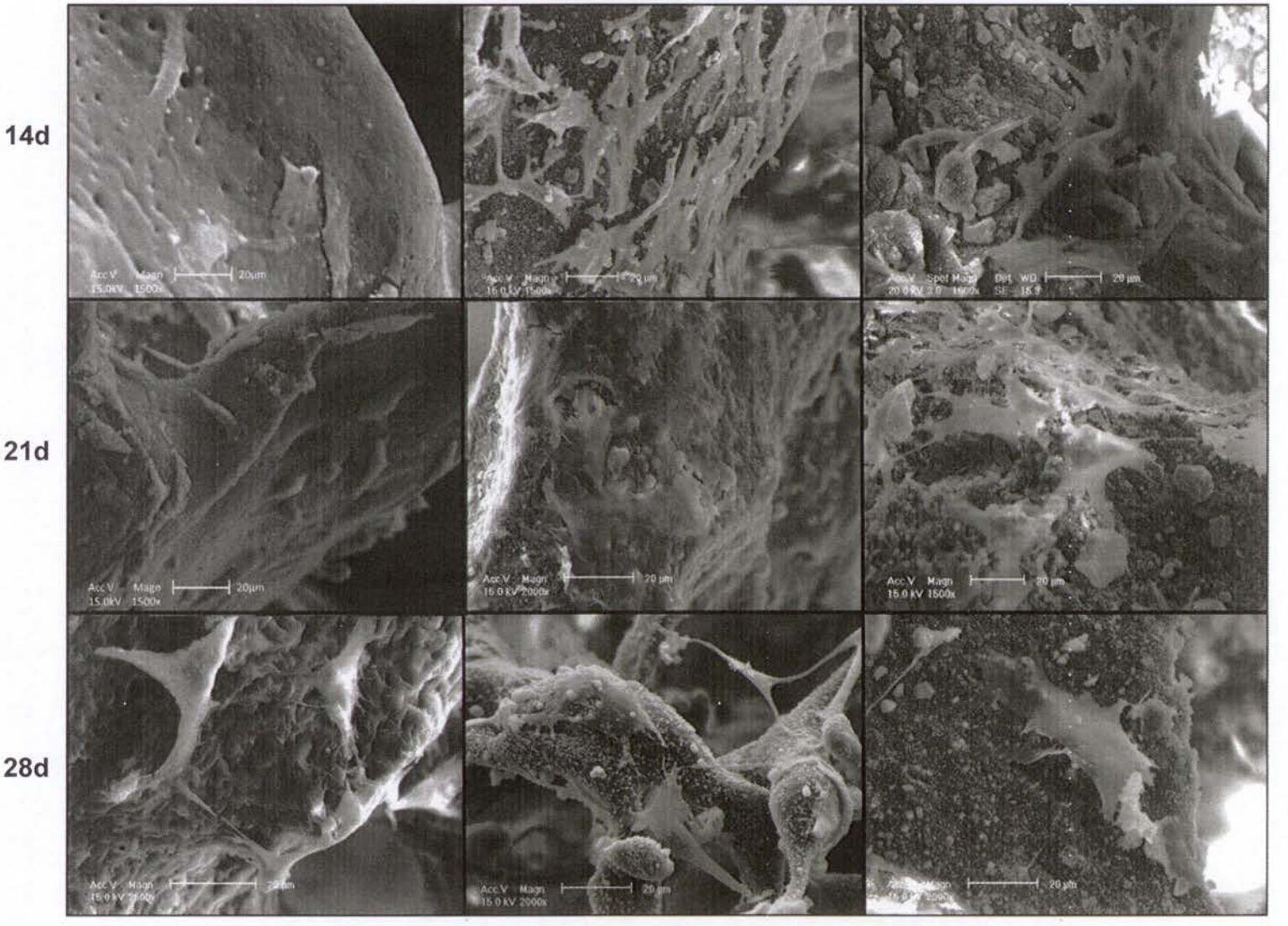


Figure 5.10. Scanning Electron Microscopy images of mouse fibroblasts on variotis™ scaffolds after culture for 14, 21 and 28 days.

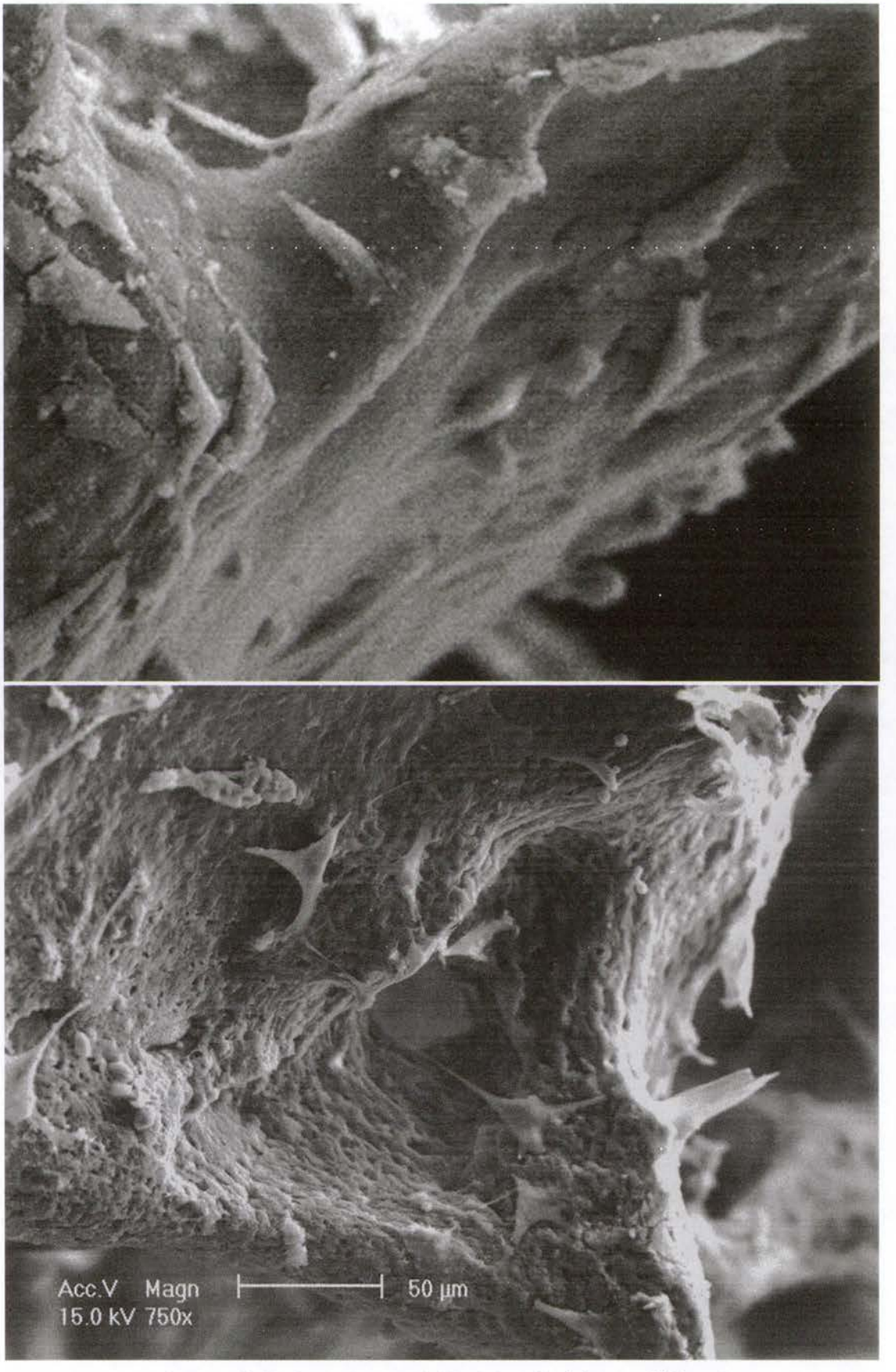


Figure 5.11. SEMs of PCL scaffold after culture with fibroblasts for (a) 21 and (b) 28 days.

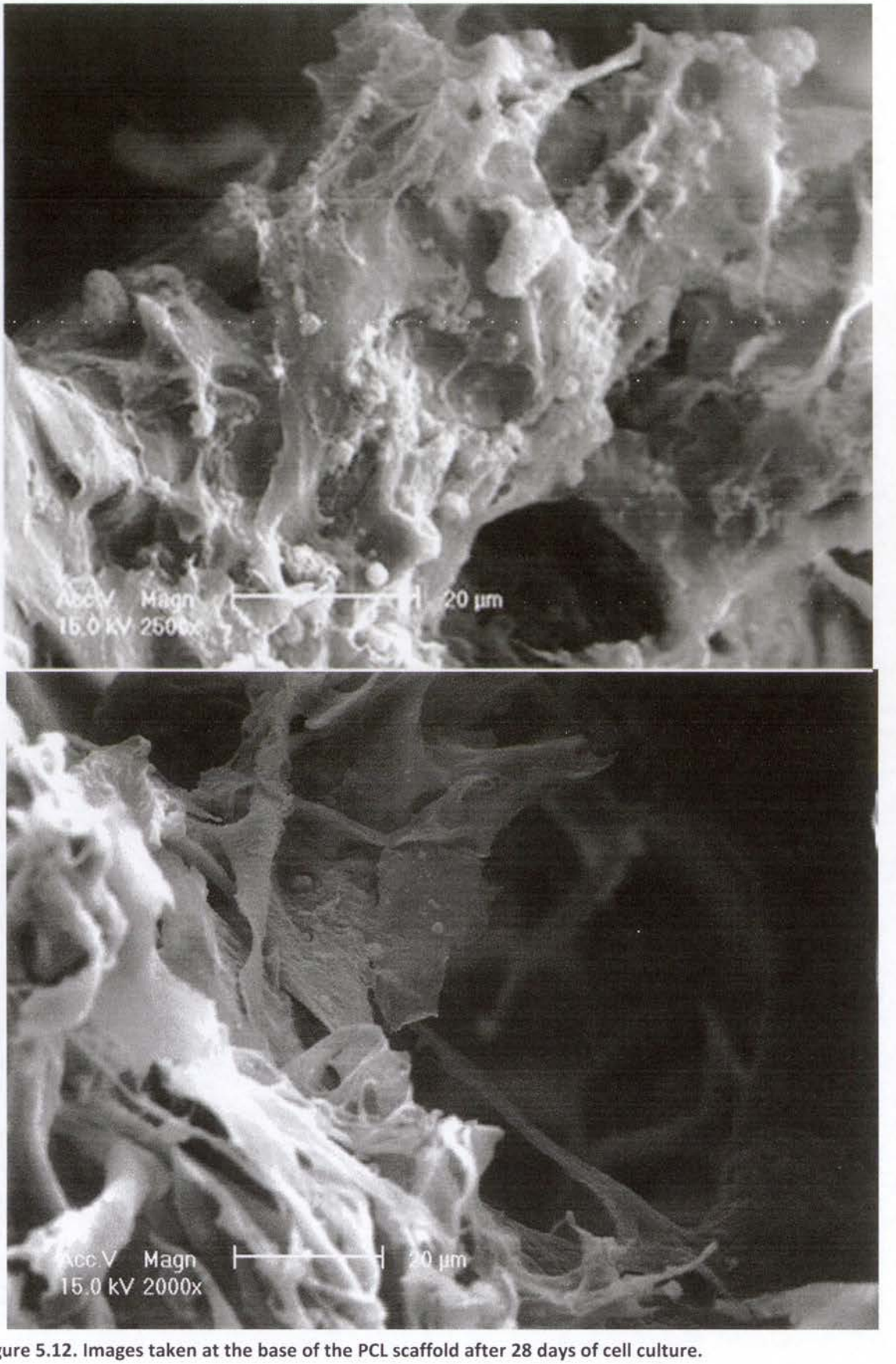


Figure 5.12. Images taken at the base of the PCL scaffold after 28 days of cell culture.

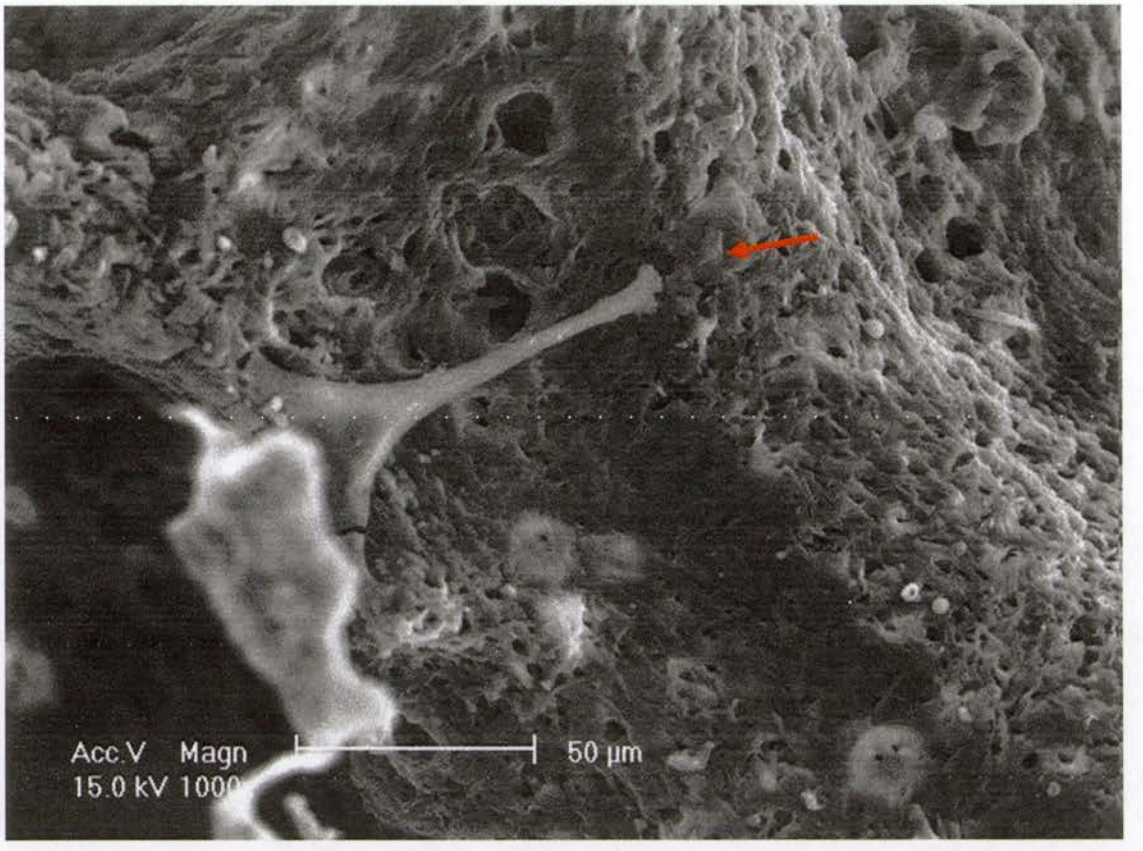


Figure 5.13. SEMs of PCL scaffold after culture with fibroblasts for 28 days. Arrow: cell reaching into a micropore.

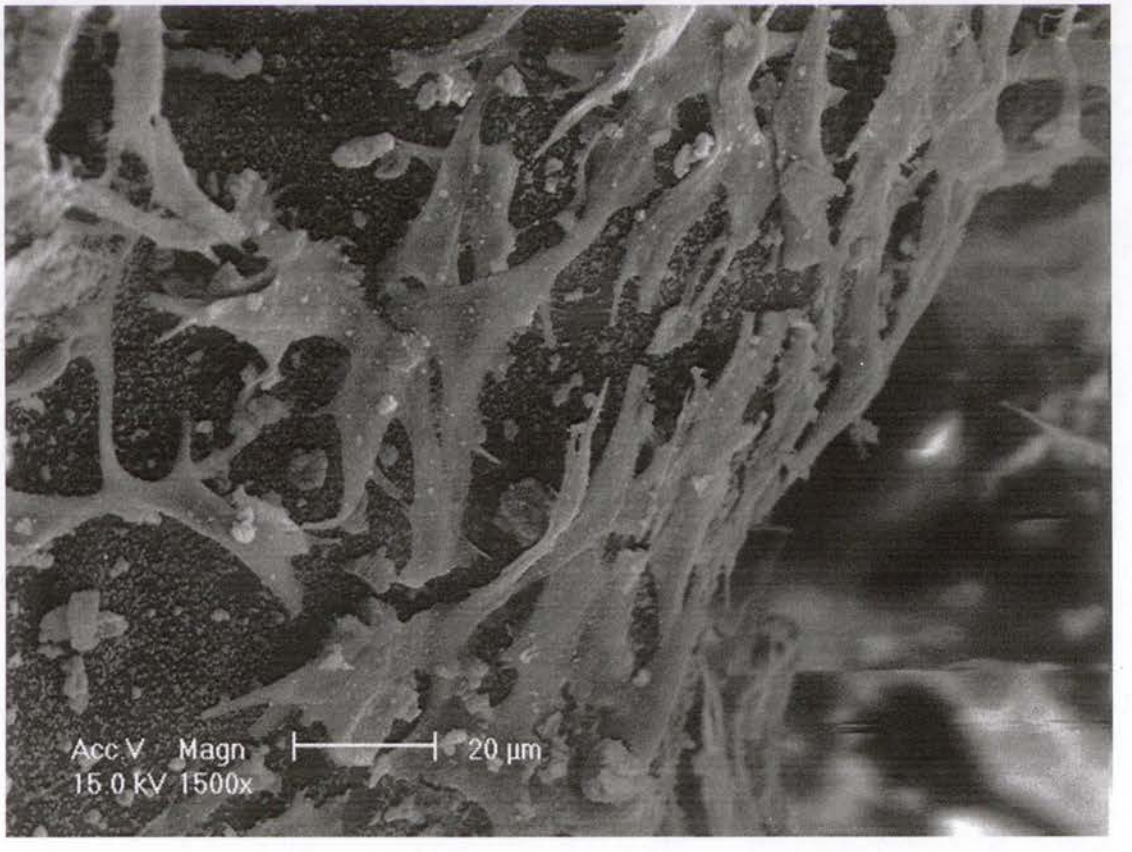


Figure 5.14. SEMs showing spreading of fibroblasts over the 45S5/PCL scaffolds after 14 days.



Figure 5.15. SEMs showing spreading of fibroblasts over the 45S5/PCL scaffolds after 21 days.

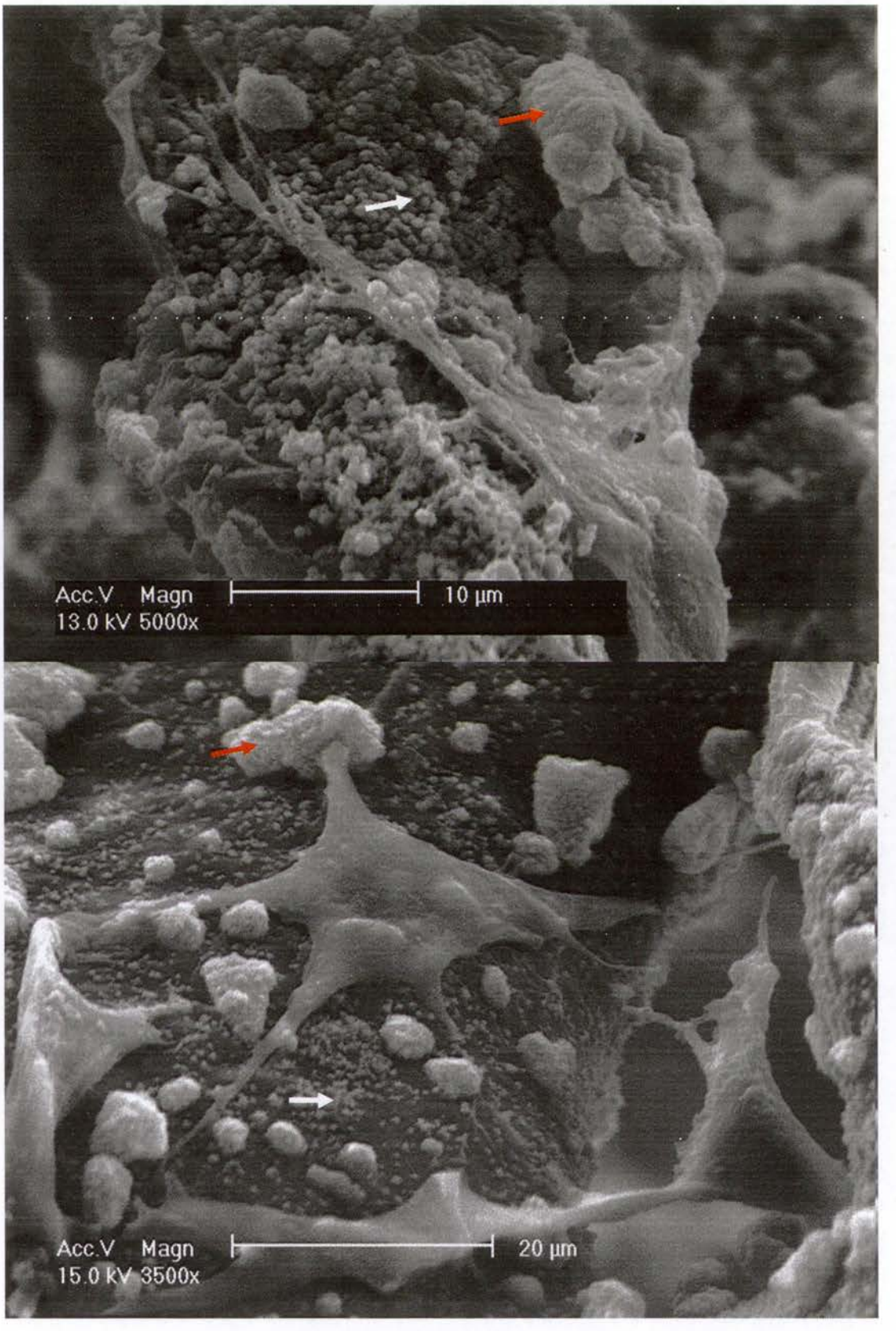


Figure 5.16. Rounded precipitates were observed on the surface of the 45S5 glass and the polymer after *in vitro* culture for 28 days (red and white arrows, respectively).

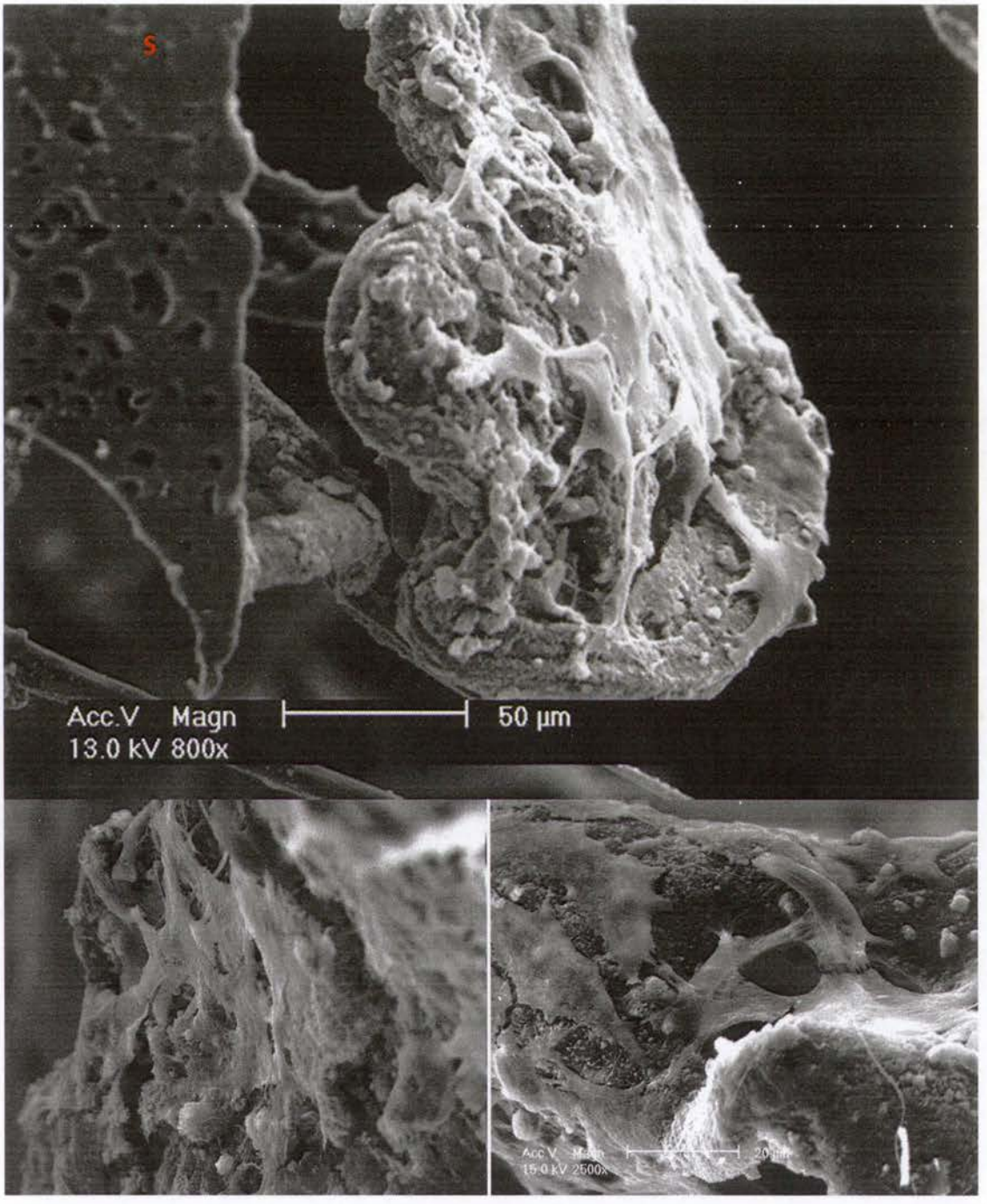


Figure 5.17. Star-like morphology of cells on 45S5 BG/PCL scaffolds. S: Scaffold cross-section, showing microporosity.

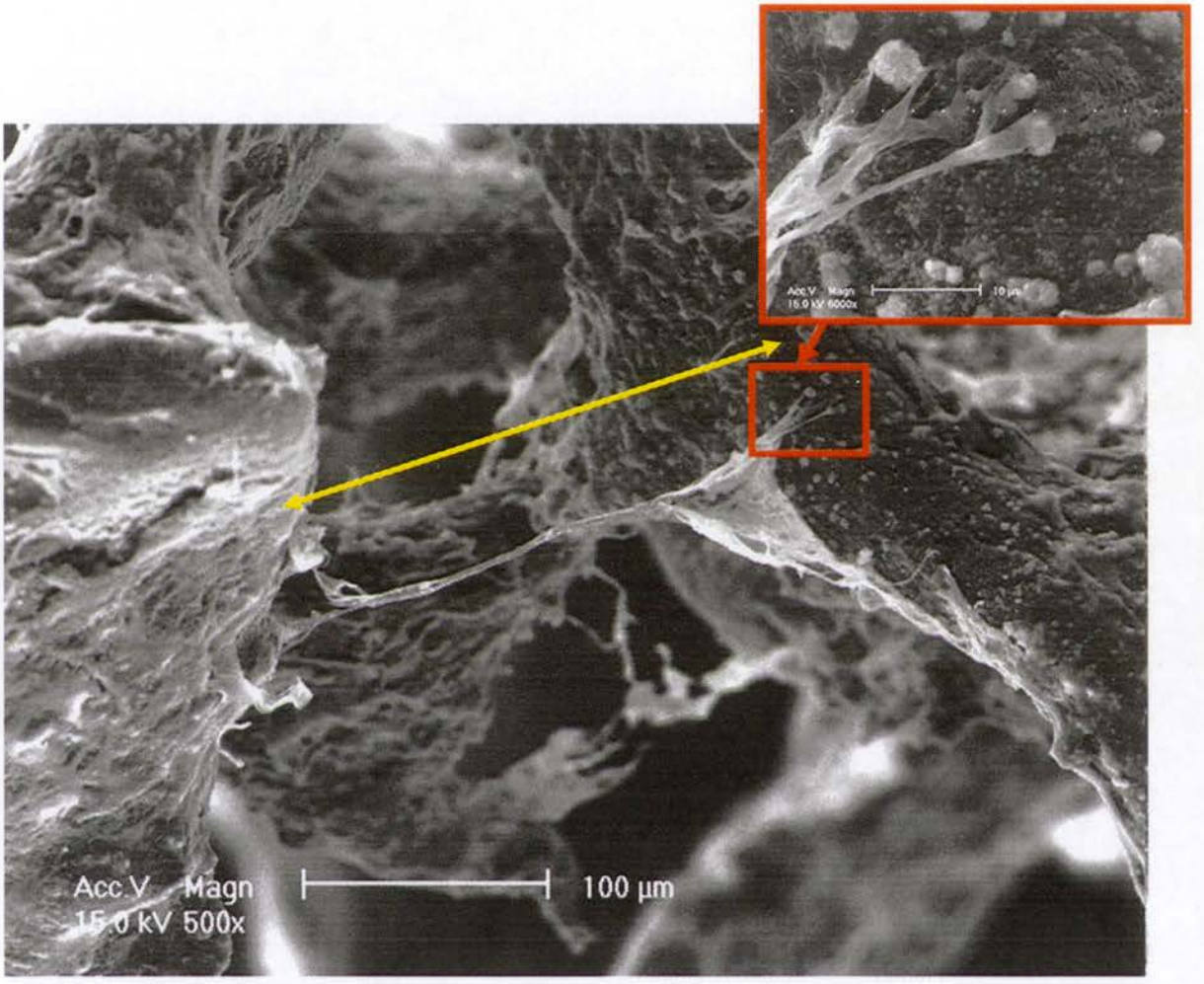


Figure 5.18. A dehydrated cell observed stretching to a length of 200µm (45S5/PCL scaffold, 28days). Inset: cell philopodia attachment to glass particles.

The cells on the 1393 glass coated scaffold also exhibited a stretched morphology, with extended protrusions attaching to the scaffold (Fig. 5.19-5.22). The highest levels of cell spreading were observed in the regions which were covered with the rounded precipitates (Fig. 5.19a). Other regions showed virtually no cell activity (Fig. 5.20b).

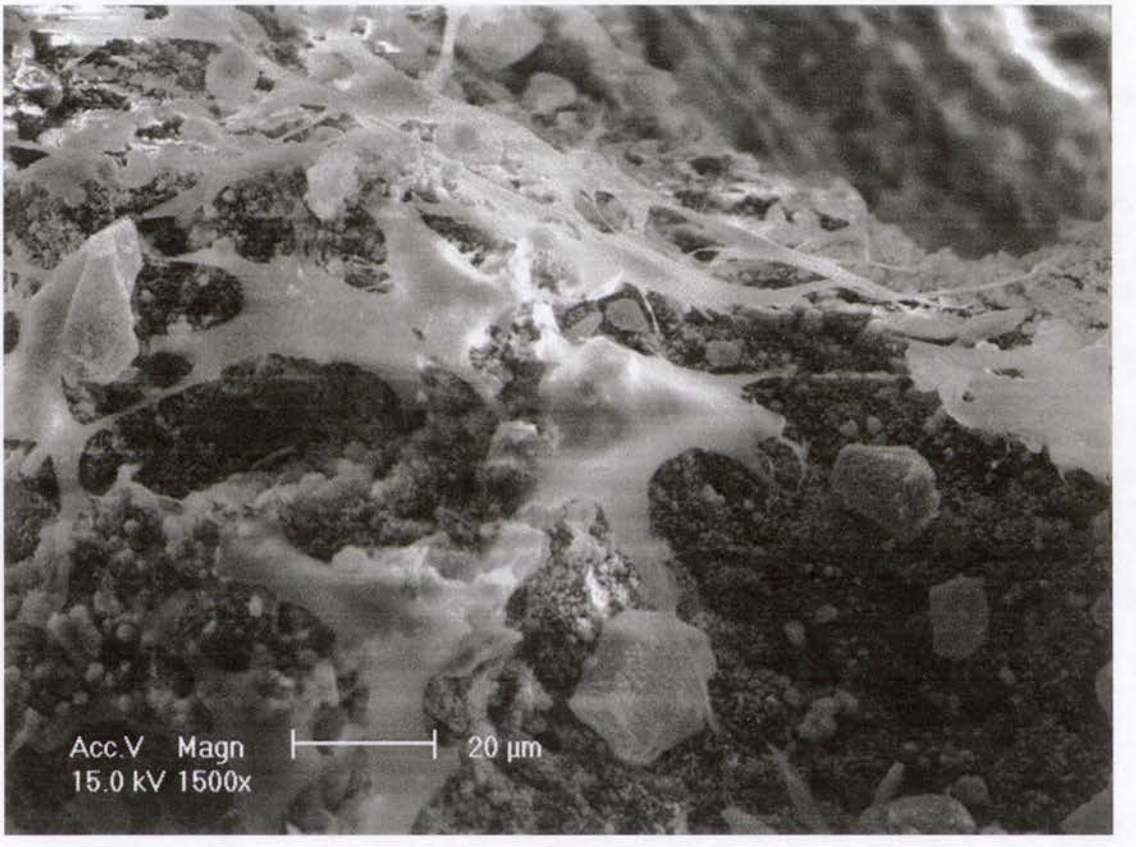


Figure 5.19. SEM of fibroblast proliferation on the 1393/PCL scaffold (21 days).

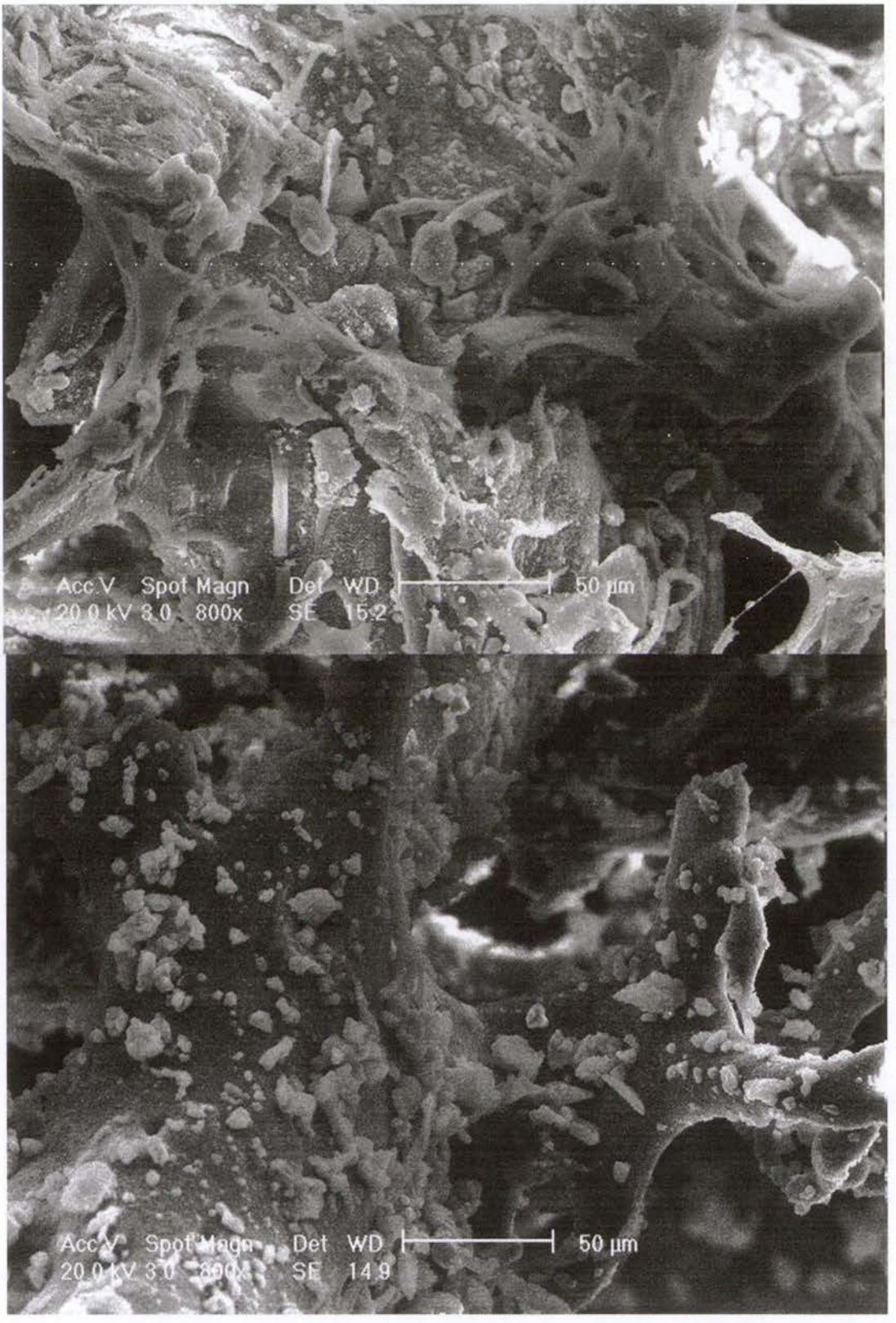


Figure 5.20. Regions of (a) high and (b) low cell density on the 1393 Bioactive Glass coated PCL scaffold (21 days).

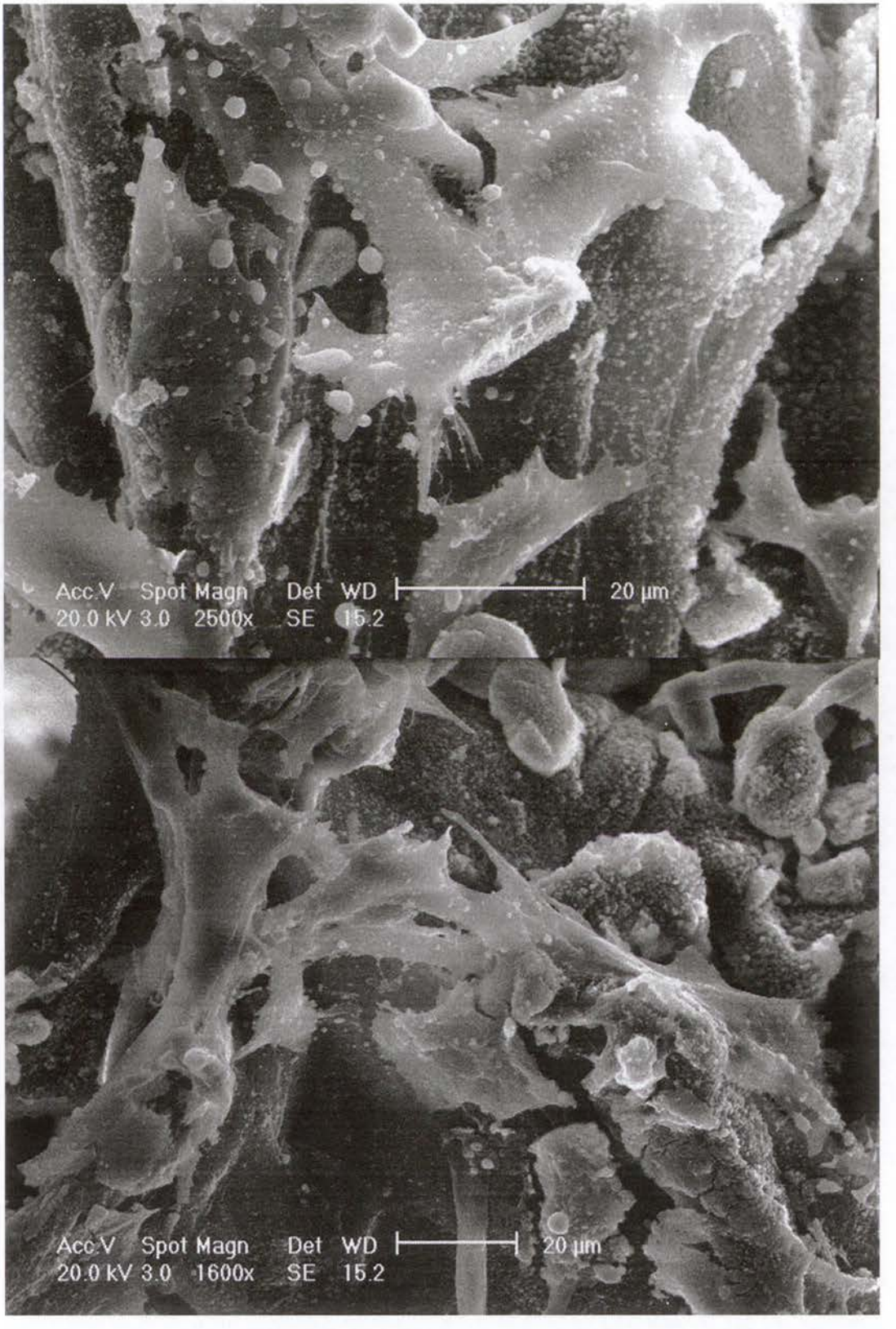


Figure 5.21. Highly magnified scanning electron micrographs of cells on 1393 BG/PCL scaffold (21 days).

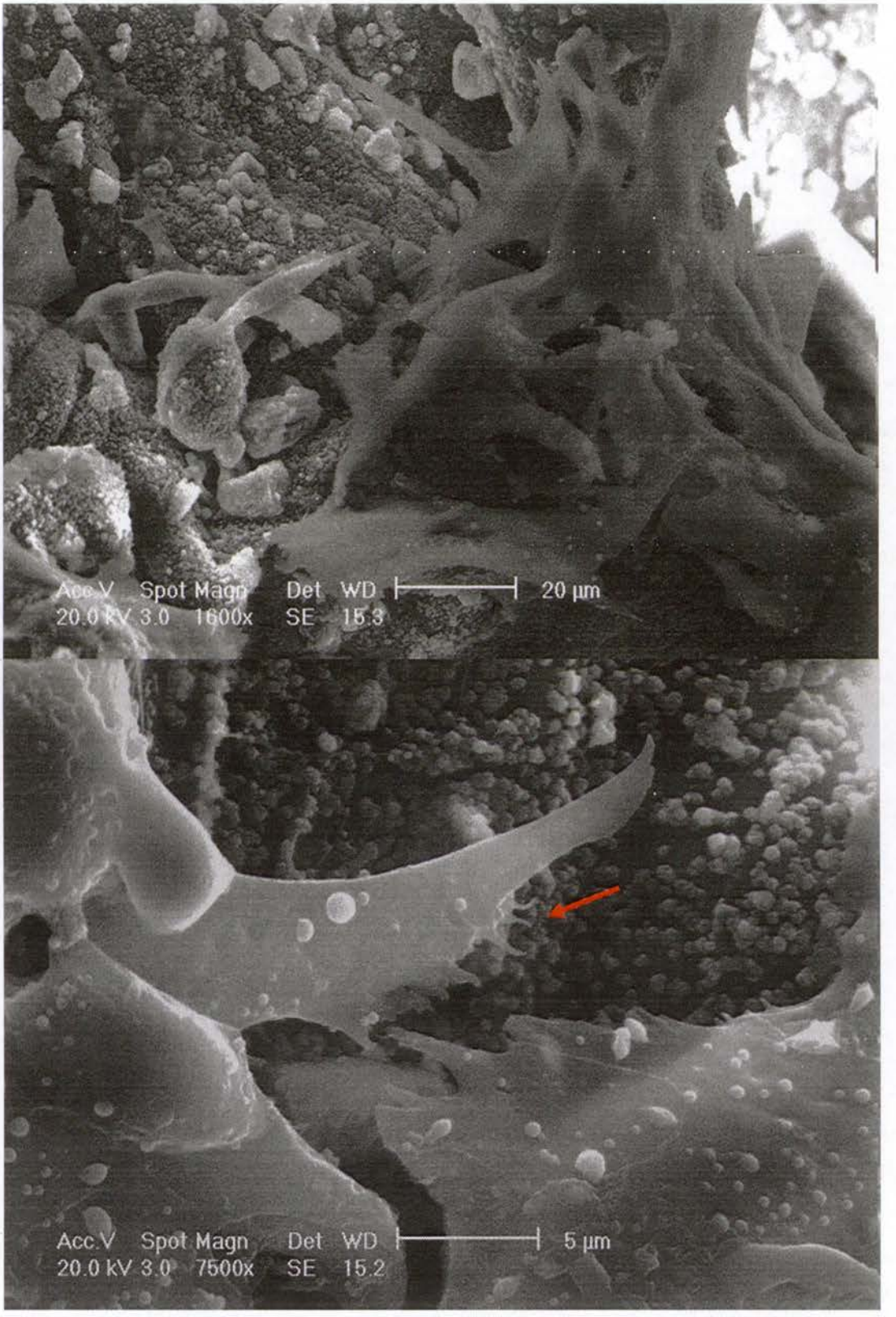


Figure 5.22. Highly magnified scanning electron micrographs of cells on 1393 BG/PCL scaffold (21 days). Arrow: cell protrusions attaching to scaffold.

5.2.2.2. Examination of the Effect of the Scaffolds on In Vitro Inflammatory Response

Gelatinase activity was measured after day 4, 7 and 14 of cell culture on the various scaffolds (Fig. 5.23). No active MMP bands were observed. Latent MMP-2, which is associated with cell growth, reached a maximum in the cell only control at day 7. The decrease evident at day 14 indicates detachment of the cells from the cell culture plate, due to cell layering. A similar trend was seen with the PCL scaffold. The composite scaffolds did not show this trend, and continued to increase in cell proliferation to day 14. All scaffolds showed low levels of inflammation, as suggested by MMP-9 measurements. The presence of the glass in the composite scaffolds did not increase levels of proMMP-9.

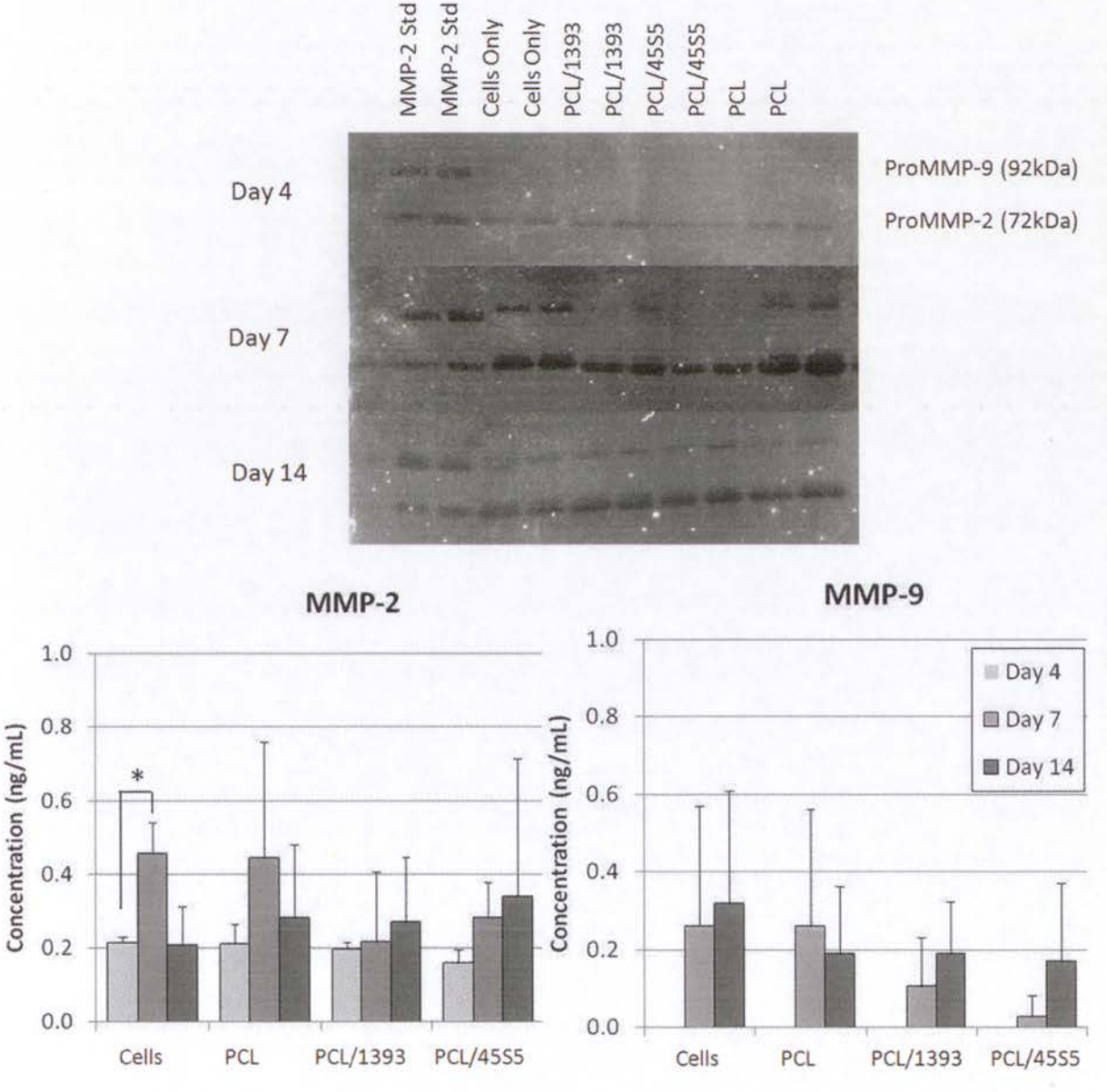


Figure 5.23. Gelatinase activity of mouse fibroblasts on composite variotis™ scaffolds, after 4, 7 and 14 days of culture.

5.2.2.3. Examination of Cells in Scaffold using MicroCT

Staining of cells in 2D culture with phosphomolybdic acid was accomplished for a range of concentrations (0.25, 1.25, 2.5%). A concentration of 1.25% gave similar levels of contrast to 2.25% and is shown in Fig 5.24a. MicroCT models were constructed of 1.25% phosphomolybdic acid-stained cells on the scaffold (Fig . 5.24b). However, neither the scaffold nor the cells were visible due to the presence of media. This fluid filled the pores and obscured the model. Thus it is unclear whether this staining method has the ability to provide sufficient density contrast between the cells and scaffold.

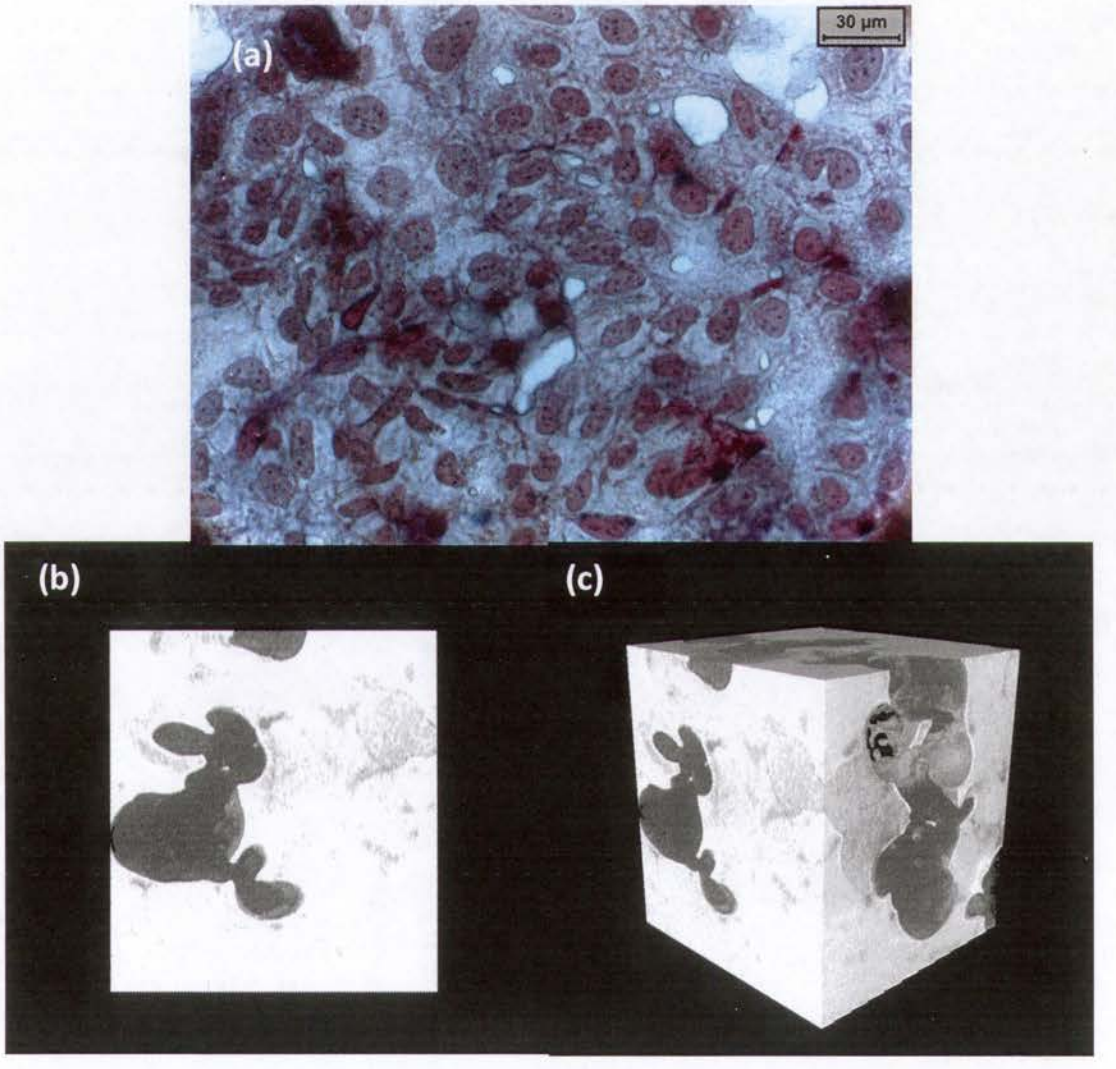


Figure 5.24. (a) Fibroblasts stained with 1.25%phosphomolybdic acid, (b, c) MicroCT of media-filled scaffold with stained cells.

5.2.3.1. *In vitro* Cell Culture on variotis™ Scaffolds

The aims of this study were to verify the *in vitro* biocompatibility of the variotis™ scaffold, and also ascertain whether the addition of 1393 or 45S5 bioactive glass coating to the scaffold changed cell morphology, proliferation or induced inflammation. This was also necessary to confirm if the manufacturing process produces scaffolds suitable as a host for biological components. Unclean production processes or sources of bioburden would result in high rates of cell death or infection compared to controls. This in vitro study also provides some preliminary results of the composition design for in vitro and in vivo use. Evidence also of the scaffold to support cell culture verifies design capabilities. Ideally, autologous or allogenic cells would be seeded on a subdermal graft prior to implantation, in order to build ECM and provide factors to the tissue.

5.2.3.2. Visualisation of Cells on Scaffolds

All scaffolds supported viable mouse fibroblasts for up to 28 days. In long-term studies, while initially seeded on top of the scaffold, cells were observed throughout the scaffolds. Observations of the cells via histology, optical (phase contrast) microscopy and SEM were taken. The scaffolds were able to be sectioned using cryosectioning techniques, however, sections sometimes displayed some distortion. Cells were visible on the scaffold using optical phase contrast and fluorescence microscopy using DAPI staining. Future experiments could utilise DAPI staining to count cells during long-term culture. Staining could also be performed on collagen deposited by the fibroblasts. Distortion of sections would be less likely to occur when cells are confluent throughout the scaffolds. Attempts were made to visualise cells using MicroCT when cells were doped with phosphomolybdic acid [410]. However, the scaffold and cells were not sufficiently contrasted due to the presence of media within the scaffold. This protocol therefore requires further optimization. In addition to further study using phosphomolybdic acid, alternate approaches could include fixation and dehydration of the cells on the scaffold prior to scanning as well as other doping techniques such as gold and silver [446] (ref 2.1.6.2).

5.2.3.3. Cell Morphology via SEM

Using SEM, the cells appeared to take a healthy, flattened morphology on the scaffold surfaces. The cells exhibited both 2D and 3D spreading behaviour (Fig. 5.10-5.18, 5.16); attaching to glass particles and precipitates on the PCL. Although cell numbers were not counted in this study, qualitatively there appeared to be more cell attachment and

proliferation on the 1393 or 45S5 bioactive glass-coated scaffolds, when compared to the neat PCL foams. Cell numbers peaked at 21 days, but decreased by 28 days. This is acknowledged to be the limiting timespan in literature. This could be due to cell layering or a lack of nutrition. Further 3D stretching across scaffold pores could be more evident if larger numbers of cells were seeded and cultured to confluence. Scaffolds with smaller customised pore sizes can also be formed to suit specific cell types or groups. This experiment highlighted the importance of regular media changes for cell-filled scaffolds. In the current experiment, media was changed every 24-48hrs, and required more regularly as the experiment progressed. Visualisation of cells on scaffolds using SEM has previously been undertaken by many researchers [221, 108].

5.2.3.4. Precipitate Formation on Scaffolds

Rounded precipitates were obvious on the surfaces of the glass-coated scaffolds. These were likely to be calcium phosphates; possibly hydroxyapatite [209]. Increase in hydrophilicity and surface area of the PCL, and subsequent increase protein and lipid deposition is expected [661], with a corresponding increase in bioactivity [631]. For these reasons, cell proliferation was at a maximum in regions high in these precipitates. In SEM images (Fig 5.16, 5.19, 5.20), larger glass particles were still visible after 21 days of culture. This indicates that these particles took longer to react and form precipitate on the surrounding PCL surfaces.

5.2.3.5. Scaffold Micropores

Textured PCL surface with interconnected micropores were observed throughout the scaffold struts. These were formed due to solvent exchange occurring subsequent to the polymer solution ingress into the sucrose templates (ref 3.2.4). This was obvious in the PCL scaffolds, but less so for the glass-coated scaffolds. Surface micropores may have progressively sintered closed during bonding of the glass to the thermoplastic PCL. The micropores provided additional attachment points for cell protrusions, and a higher surface area for precipitate formation. The level of surface texture is much higher than compared with several previous studies [147].

5.2.3.6. Comparison with Literature

To the author's knowledge this is the first study to investigate the proliferation of soft tissue cells on PCL/BG scaffolds. Some previous studies have examined osteoblast culture on other composite polymer/BG meshes or foams [148, 150, 219]. These constructs were much thinner than the variotis™ scaffolds (<20%). Numerous studies have also demonstrated increased cell proliferation in the presence of specific bioactive glass compositions or tri-calcium phosphate compared to pure polymers [108, 116, 147-150, 154, 208, 209, 212, 753-755]. Specifically,

Helen and coworkers [154] demonstrated increased proliferation (3x) of human annulus fibrosis cells over 4 weeks, on PDLLA scaffolds coated with 5 or 30% BG, as compared to the neat PDLLA scaffolds. This is one of the few long-term studies reported in the literature. Tsigkou and coworkers [208] demonstrated increased elongation and protrusions from human osteoblasts on composite films consisting of PDLLA embedded with 40 wt%45S5 (particle size: >90um), as compared to PDLLA/5 wt%45S5 or neat PDLLA, when cultured for 1 week. Cell spreading in the current study was more pronounced, due to the glass being coated on the outside of the polymer, rather than embedded in the matrix. In addition, the size of the glass particles in the current study were smaller with a surface area. These factors led to a faster dissolution rate and subsequent higher levels of CaP formation in the current study. Another study, by Haimi and coworkers [198] demonstrated the opposite effect. Addition of or 45S5 bioactive glass (75-106μm) or tri-calcium phosphate (75-106μm) to PLA scaffolds showed no effect on the morphology of adipose stem cells after 2 weeks of *in vitro* culture. This could be due to slow dissolution of the glass, as it was embedded within the matrix. The cells were observed to be stretching and forming projections on the porous surface of the scaffolds and forming bridges between the granules on the composite scaffolds. However, cell infiltration was limited into the pores and glass accumulation on the scaffold surface. This could be related in part to the small pore size (<100μm) and limited interconnectivity, resulting from the TIPs fabrication process. A dense superficial surface layer is formed when the frozen solvent sublimates from the top surface. For these reasons, glass and cell distribution was not even throughout the scaffold. A high density of cells was observed on the outer surface of the scaffold. This demonstrates the limitations of scaffolds with a pore size equivalent to a single cell diameter.

5.2.3.7. Investigation of MMP Levels

Measurement of MMP levels using gelatinase zymography (Fig 5.23) showed increasing levels of latent MMP-2 (cell growth) in all groups until day 7. After this point, the cell only and PCL scaffold wells showed depressed levels. This is likely indicative of detachment due to confluent cell layering. In contrast, the composite scaffolds did not show this trend. Increasing yet insignificant levels of MMP-2 were observed. Levels of MMP-9 were lower for the cells cultured on the scaffolds, than compared to tissue culture plastic, when measured up to day 14. Protein absorption onto the scaffold remains a possibility, as previously observed on biomaterials [757] (ref 5.1.4). Previous studies have demonstrated that the ionic products of 45S5 glass increase MMP-2 [752] and that hydroxyapatite increases MMP-9 and other inflammatory markers [768]. This can in turn increase the angiogenic response within scaffolds. Future studies with various bioactive glass compositions, scaffold porosities and cell

densities could determine whether bioactive glasses significantly change MMP levels and whether this will provide benefits to a wound healing environment.

5.3. INVESTIGATION OF CELL NUMBER MEASUREMENT TECHNIQUES

5.3.1. METHODS

5.3.1.1. MTS Assay

Thick section PCL scaffolds (dimensions: 5.25x5.25x10mm) were placed into IWAKI 96-well culture plates. 3T3L1 mouse fibroblasts were seeded at concentrations of $5x10^3$, $1x10^3$ and $2x10^3$ (3 replicates) and allowed to attach for 4 hours at 37°C and 5% CO_2. MTS solution was made up using Promega Cell Titer 96® Aqueous One Solution Reagent (16.5%, 1:5 in complete culture media). Media was removed from culture plates. 200µL of MTS solution was added to each well. Control wells were blank wells (no cells) and cells only (no scaffold). The plate was incubated at 37°C for a further 1-2 hours to allow cells to convert the reagent into a coloured product. Scaffolds were moved to empty wells. Optical density was read at 490nm using a LabSYS Multiskan 96 well plate reader. Prior to reading, the plate was subjected to a one minute program consisting of repeated cycles of 15secs agitation and 5sec lag periods. Readings were taken for (a) the cells (b) cells remaining after scaffolds were moved and (c) scaffolds with attached cells. The optical density of the blank wells was subtracted from the readings of the control and test wells. This was to account for background absorbance which could be affected by conditions such as media/serum, pH, light exposure or the presence of other chemicals.

5.3.1.2. Fluorescence Measurement

This section of work outlines the method for direct quantification of the number of cells contained within the scaffold. For this measurement a fluorescent dye was used to label the cells and the number of cells were counted relative to fluorescence intensity.

Effect of solution type- PBS/Ethanol/DAPI on fluorescence

3T3L1 mouse fibroblasts were plated into IWAKI 96-well plates at a concentration of 1000 cells per well (7 replicates) and allowed to attach for 4 hours at 37°C and 5% CO_2. 200 µL 70% ethanol was placed into wells and fluorescence measured at 355-460 nm using a Fluoroscan OMEGA. This value was 'termed EtOH'. Ethanol was removed and wells were rinsed using PBS. 200 µL PBS was placed into wells and fluorescence measured 'termed PBS'. DAPI was placed into wells and replaced with 200 µL PBS. Fluorescence was measured and termed 'DAPI (in PBS)'. The fractional difference between the Ethanol and PBS was measured using the formula:

$$\frac{Fluorescence_{EtOH} - Fluorescence_{PBS}}{Fluorescence_{PBS}}$$

Fluorescence of 5000 cells on scaffolds

PCL and 45S5 BG-coated PCL Scaffolds were placed into IWAKI 96-well plates and sterilised for 20mins in the UV laminar flow cabinet (3 replicates per condition). 3T3L1 mouse fibroblasts were plated onto half the scaffolds at a concentration of 5000 cells per well. The scaffolds were incubated for 4 hours to allow cell attachment, at 37°C with 5% CO_2. Media was removed and rinsed with PBS. 70% ethanol was applied for fixation of cells. DAPI was applied to the wells. DAPI was replaced with 200 µL PBS and the fluorescence was measured at 355-460 nm using a Fluoroscan OMEGA.

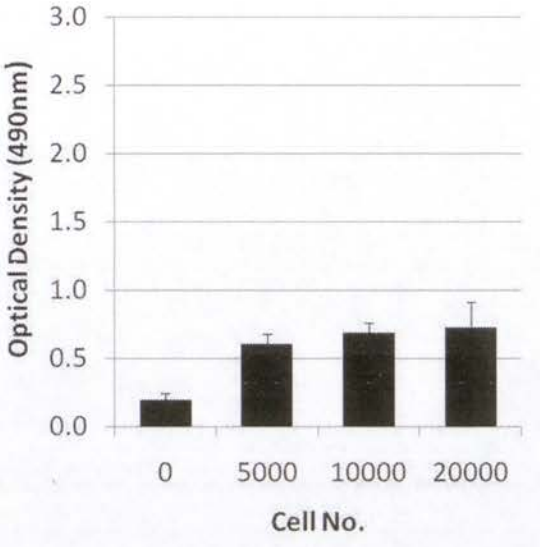
Effect of various cell densities/presence of scaffold on fluorescence

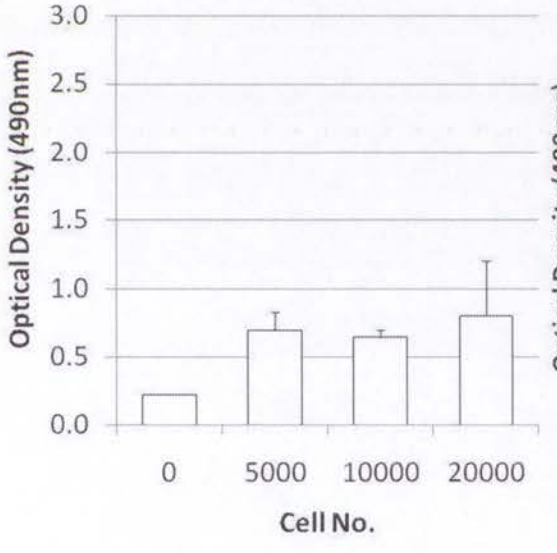
3T3L1 mouse fibroblasts were seeded in an IWAKI 24-well plate, at cell numbers of 1000, 5000, 25000 and 125000 (3 replicates per condition). Cells were also seeded on PCL and 45S5 BG powder coated PCL scaffolds which had been sterilised for 20mins in the laminar flow cabinet. Cells were allowed to attach for 4 hrs at 37°C with 5% CO_2. Samples were air dried then rinsed with PBS x2. DAPI (0.2% (v/v) in PBS was applied and removed. Samples were rinsed with PBS, then filled with PBS. The fluorescence of the DAPI was measured at 355-460 nm using a Fluoroscan OMEGA.

5.3.2. RESULTS

5.3.2.1. MTS assay

Figure 5.25 shows the results of the MTS assay. For the cell only wells, the optical density increased for increasing cell numbers (Fig. 5.25a). The readings for the cells remaining after the scaffolds were moved are recorded in Fig. 5.25b. These readings were only 10-15% lower than the cell controls, indicating that this was the proportion of cell attachment which occurred. No difference in optical density was detected for the scaffolds with attached cells as compared to the scaffold alone (Fig. 5.25c).





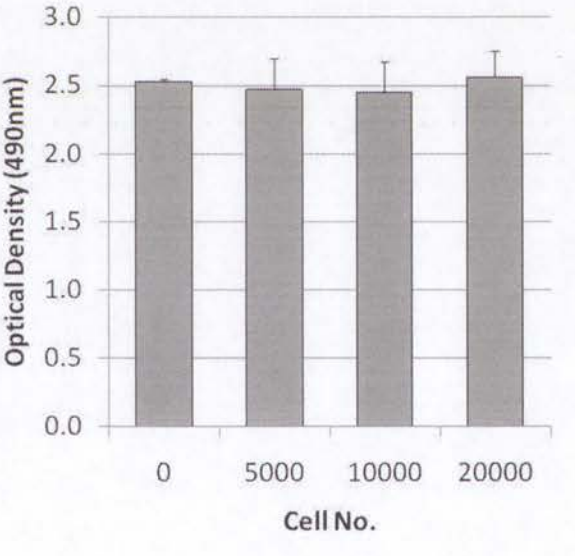
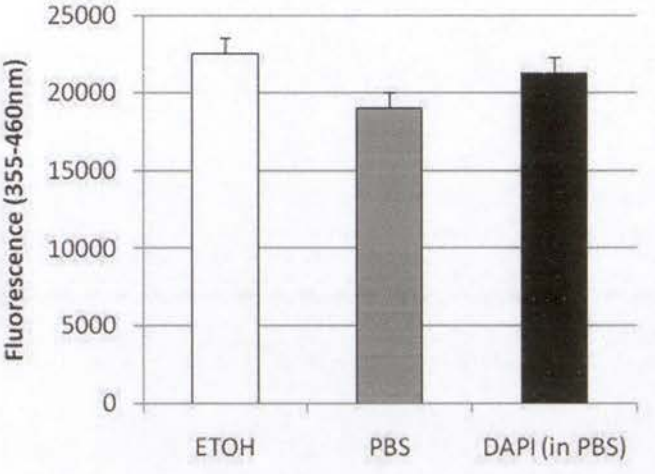


Figure 5.25. MTS readings for (a) Cells only (b) Cells remaining after scaffolds were moved (c) Scaffolds and attached cells.

5.3.2.2. Fluorescence Readings

As shown in Fig. 5.26, fluorescence measurements taken through ethanol led to an apparent increase in fluorescence relative to PBS (3,500 increase, fractional difference: 0.187+-0.10). This suggests ethanol autofluoresced. It is important that ethanol is thoroughly replaced with PBS prior to obtaining fluorescence readings.



Treatment	Fluorescence
ETOH	22538.86±1495.05
PBS	19069.57±1609.76
DAPI (in PBS)	21289.14±1922.99
Fractional Difference	0.187±0.10

Figure 5.26. Comparison of fluorescence measured for 1000 cells in ethanol, PBS and stained with DAPI.

A reduction of 50,000 in fluorescent readings were observed for BG/PCL scaffold compared to the PCL scaffold (Fig. 5.27) when no cells or low cell numbers (n=5000) were used. The scaffolds with 5000 cells showed little difference in fluorescence measurements compared to the acellular scaffolds, indicating that higher cell densities should be used.

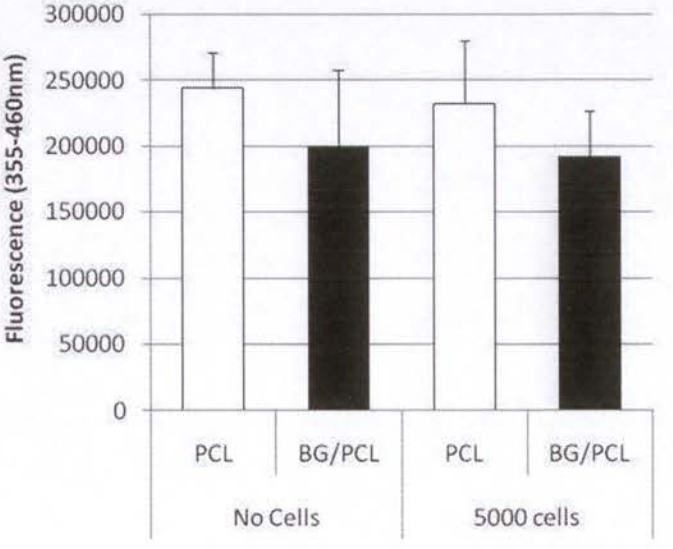


Figure 5.27. Fluorescence for acellular and 5000 cell seeded PCL and BG/PCL scaffolds (in PBS).

Higher cell densities demonstrated a similar drop in fluorescence for the BG/PCL sample (Fig. 5.28). A drop in fluorescence of at least 25,000 was obtained when readings were taken for PCL scaffolds seeded with 125,000 cells, as compared with 125,000 cells (no scaffold).

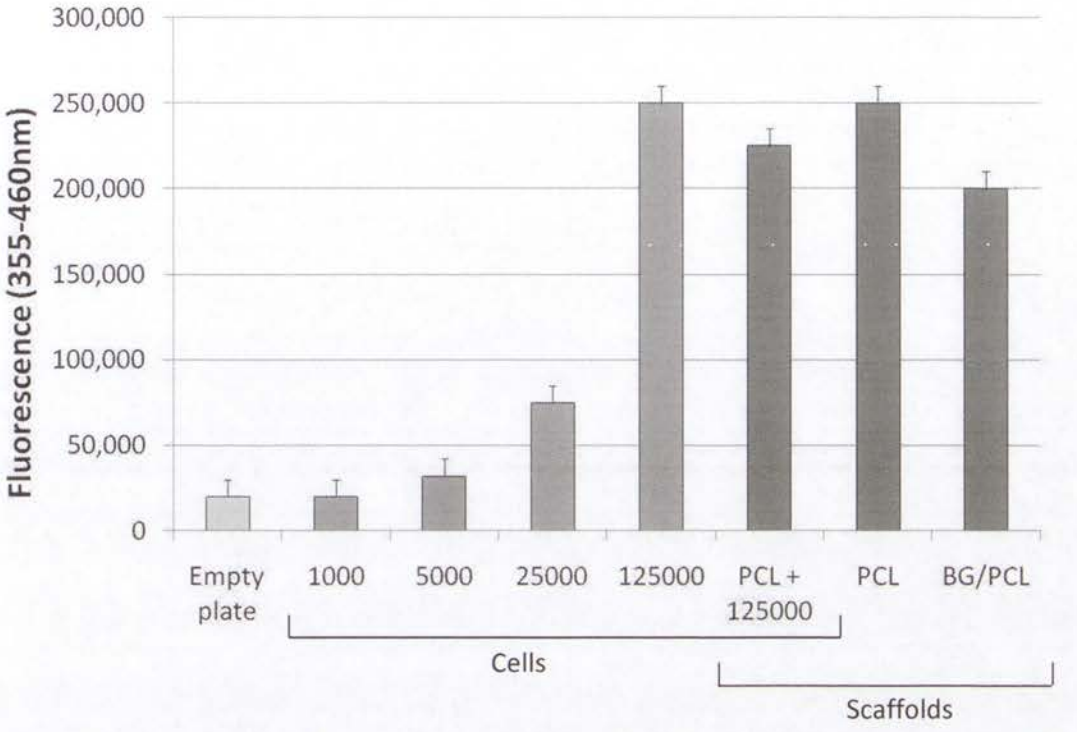


Figure 5.28. Measurement of fluorescence after DAPI staining for a range of cell densities (in PBS).

The results for all 3 experiments are summarised in Table 5.2.

Table 5.2. Summary of approximate fluorescence values for all experiments.

Condition	~Fluorescence (355-460nm)
Empty plate	20,000
PCL scaffold- DAPI (in PBS)	250,000
PCL/BG scaffold- DAPI (in PBS)	200,000
PCL scaffold- in ethanol	32,000
PCL/BG scaffold- in ethanol	33,000
Ethanol- 1000 cells	22,500
PBS- 1000 cells	19,000
DAPI (in PBS)- 1000 cells	21,300
DAPI (in PBS)- 0 cells	15,000
PCL scaffold, DAPI (in PBS)- 0 cells	200,000
Cells only (DAPI)- in PBS- 1000 cells	20,000
Cells only (DAPI)- in PBS- 5000 cells	32,000
Cells only (DAPI)- in PBS- 25000 cells	75,000
Cells only (DAPI)- in PBS- 125000 cells	250,000(+)
PCL scaffold + cells (DAPI)- in PBS- 125000 cells	225,000
PCL/BG scaffold + cells (DAPI)- in PBS- 125000 cells	250,000(+)

5.3.3. DISCUSSION

Quantitative techniques were investigated to determine cell numbers on the scaffolds. When measured using MTS, cell proliferation (cell number: 0-20,000) on tissue culture plastic increased. However, this change was not evident when cells were cultured on the scaffolds, due to excessively high readings. High fluorescence levels were noted for cells which had not attached to the scaffolds, and had instead proliferated on the base of the well. Future studies will need to investigate methods to retain cells within the scaffolds (e.g. pore size, thin membrane on base of scaffold). This fluorescence method could be a useful method for ascertaining approximately how many cells attach.

Likewise, when the fluorescence values of DAPI or calcein-stained cells were determined, the cells which were on the scaffolds could not be detected. The scaffolds, particularly when containing bioactive glass, could be scattering the light, as it is white and reflective. This could be the main reason for the findings of both techniques. Additionally, fluorescence readings reached the limit of the scanner in some instances. These readings normally reflect the cell populations within one plane of the scaffold. A large proportion of cells would have been obstructed due to the 3D opaque nature of the scaffold. From these precursory experiments, several recommendations can be made for developing future fluorescence measurement methods.

All measurements should be undertaken in PBS, so as not to detect autofluorescence from ethanol. High cell numbers over long time periods should be utilised. The media should be diluted prior to scanning to ensure the reading is within the limit of the scanner. To quantify 3D cell proliferation scanning of scaffolds could be summated for all surfaces of the scaffolds, by rotating the scaffold along all planes prior to additional scans. Excess fluorescence was also detected due to cell layering on the base of the culture plate, so for this reason scaffolds should always be moved to clean plates. There is a remaining question of how much the scaffold interferes with the fluorescence measurements. In future, a control could be run consisting of cells cultured on tissue culture plastic, with an acellular scaffold on top to determine obscurance effects.

A more useful technique for determining cell numbers within the scaffold would be either histological sectioning and counting using DAPI, or removing the cells by trypsinisation, followed by counting (either manually or through flow cytometry).

5.4. *IN VITRO* TESTING OF FIBROBLASTS ON BIOACTIVE GLASSES

5.4.1. METHODS

5.4.1.1. Specimen Preparation and Cell Seeding

Silica-based bioactive glass was synthesised using the melt process as described in section 4.2. A range of established and novel compositions were tested, including: 45S5, 49S4.9, 52S4.9, 0.5Ba45S5, 0.5%Ba45S5, 2%Zn45S5, 5%Zn45S5. Glass powders synthesised using a mortar and pestle (ref 4.2.5) (particle size: <100 μm, 80% of glass powders were <30 μm in length). The glass was sterilised under UV in a laminar flow cabinet for 20 mins. The glass powders were suspended in RPMI, and aliquoted into 96-well cell culture plates. Some samples were suspended in NaCMC

Cells were cultured to confluence and removed from flasks using trypsin. Cultures were performed in complete media consisting of 11mM RPMI, 10% Fetal Calf Serum and 1% Penicillin/streptomycin. Cells were diluted to a density of 5 x 10^4 cells/mL in complete media. 200 mL of cell solution was placed into each well, yielding a cell number of 10x10^3 cells per well. Specimens were placed in incubator at 37°C with 5% CO_2 and media was replaced every 24 hrs. At timepoints of 4, 8 and 11 days, media was replaced with serum free media for 24 hrs then stored at -20°C for subsequent measurement of metalloproteinase activity and total protein content (2 wells were combined and divided between 2 eppendorfs).

5.4.1.2. Fluorescent Microscopy Examination

Cells were treated with 100 μL Calcein AM (1:100 in RPMI) for the last 20 mins of incubation. Calcein is taken up into the cytoplasm of viable cells. At the 48 hr timepoint, the calcein was removed and samples rinsed with PBS. Scaffolds were also stained using the nuclear marker DAPI (0.2% (v/v) in PBS. DAPI was rinsed and replaced with 100 μL PBS. DAPI stained nuclei were visualised as blue (350 nm) and cytoplasmic stains were visualised as green (520 nm) using a fluorescent microscope (Olympus AX70, Olympus, Tokyo, Japan) equipped with an Olympus DP60 camera. Using a hybrid filter approach (between phase contrast optical and 520 nm), both the glasses and calcein stain were visible.

5.4.1.3. Measurement of Cell Spreading

Two non-destructive methods were trialed for quantitation of the extent of cell spreading on the glasses; fluorescence quantitation and area of cell occupation quantitation. Fluorescence was measured using a Fluoroscan Omega in attempt to quantify cell number (DAPI: 355-460 nm, Calcein: 485-520 nm). The area of the fluorescent images which was covered by cells was quantified using AxioVision Release 4.4.0.0. (Carl Zeiss Vision). The area occupied by the

calcein-stained cells was reported as a percentage of the entire image. Results were calculated from images which had been captured at 10x magnification and are reported as mean ± stdev from 3 images.

5.4.1.4. Measurement of Cellular Metalloproteinase Activity

Gelatin Zymography was used to measure wound fluid proteolytic activity after 4, 7 and 14 days of culture. For these studies supernatant (10 µL) was loaded onto a 8% SDS-PAGE gel containing 10% MDPF labeled gelatin (0.75 mm thick). The samples were separated by electrophoresis at a constant voltage (130 V) for approximately 1.5 hr at room temperature, and activities determined as described in detail previously [776]. The results are expressed as the average of 3 wells from 2 gels for each timepoint. Results were corrected for initial wound fluid volume and protein concentration and are expressed as Xg/mgP.

5.4.1.5. Protein Measurement

Total protein concentration was determined from the supernatant using a Biorad protein detection system (BioRad DC, Sigma, Australia). A standard curve was constructed from Bovine Serum Albumin (BSA) of known concentration. The protein concentration of the supernatant samples was then estimated to give an indication of cell number/activity.

5.4.2. RESULTS

5.4.2.1. Cell Attachment, Morphology and Spreading on Bioactive Glass Powders

Using fluorescent imaging, a high level of viable cells was observed on all the glasses. No autofluorescence was observed. The fibroblasts preferentially attached and spread along the glass particles as compared to the tissue culture plastic (Fig. 5.2-5.33). In some cases, the cells appeared as large, pale cells, due to flattening behaviour on the top or side surfaces of the glass. Cells were also noted to stretch between glass particles (Fig. 5.3), and were observed tracking along the glass. These features were consistent across all the glass compositions. The cell morphology appeared to be more influenced by surface topography and particle size than the compositions of these glasses at the timepoints examined. Cells were observed to accumulate in regions where there was a concentration of small particles. Cell-cell joins were also widely observed.

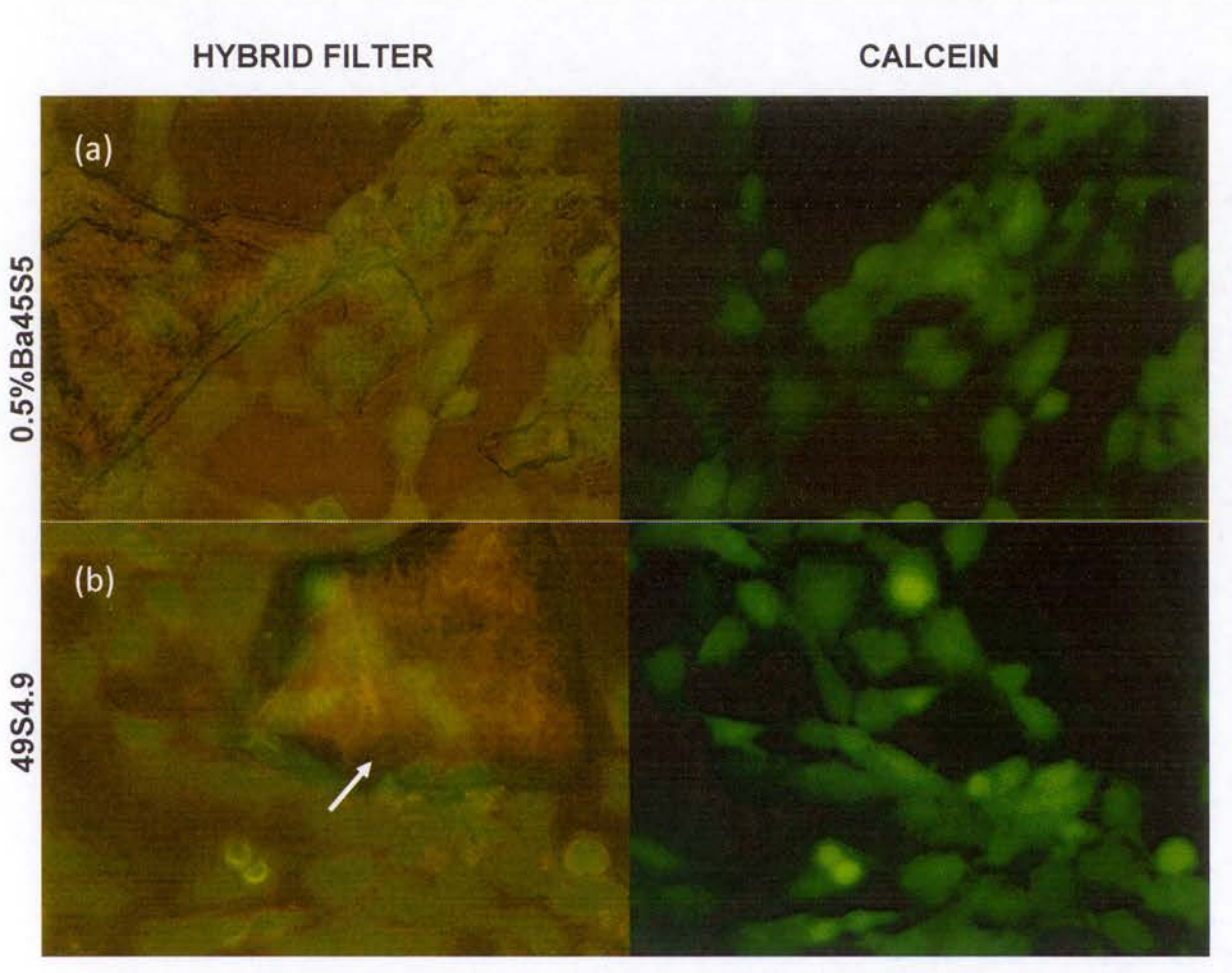


Figure 5.29. Morphology of fibroblasts cultured on bioactive glasses for 24 hrs for (a) 0.5%Ba45S5 and (b) 49S4.9 Bioactive Glass (Calcein, 40x). Arrows: cells tracking along glass edges or ridges.

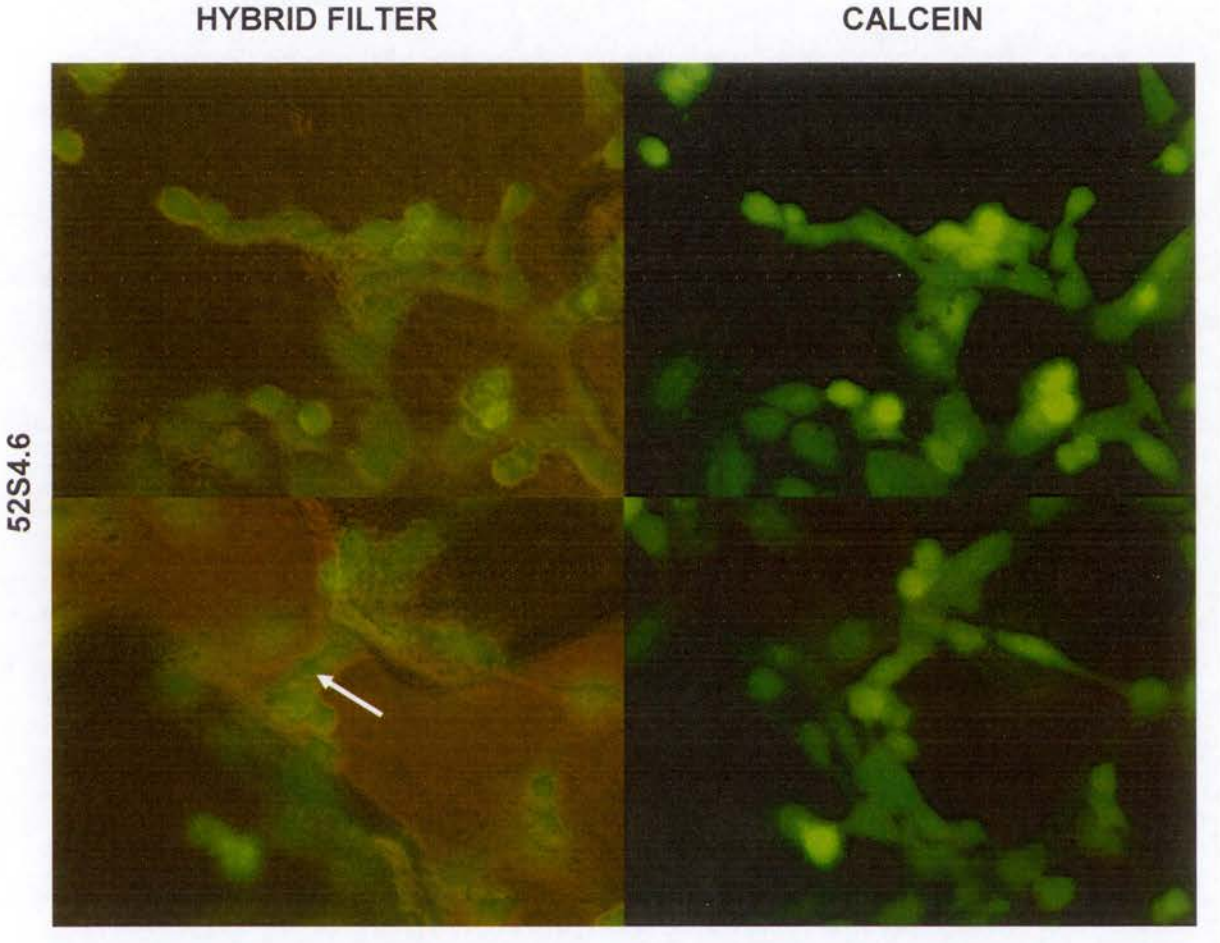


Figure 5.30. Morphology of fibroblasts cultured on 52S4.6 bioactive glasses for 24 hrs (Calcein, 40x). Arrow: Cells bridging between glass granules.

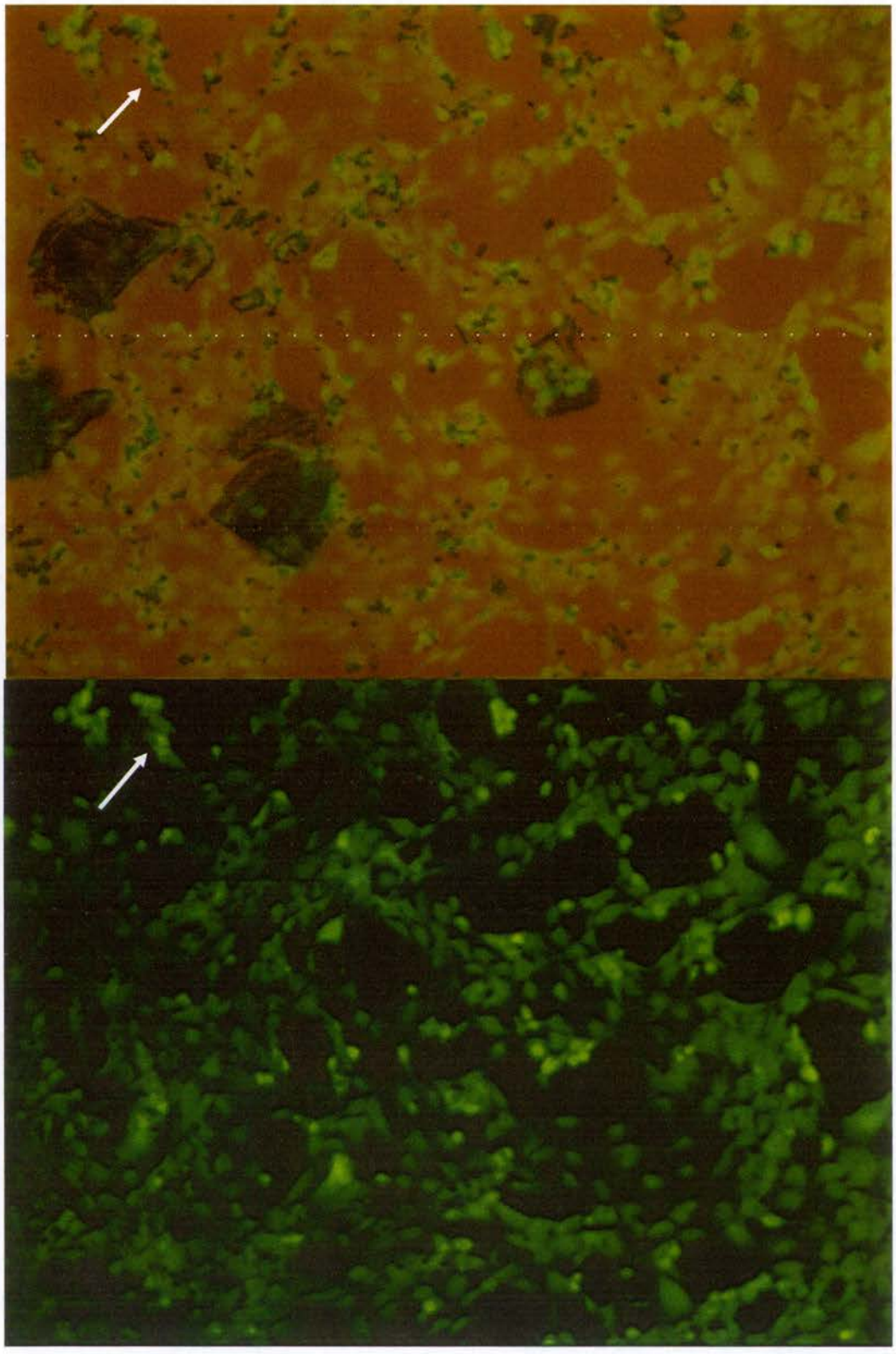


Figure 5.31. Morphology of fibroblasts cultured on 49S4.9 bioactive glasses for 24 hrs (Calcein). Arrows: Cell accumulation in regions with collections of small glass particles

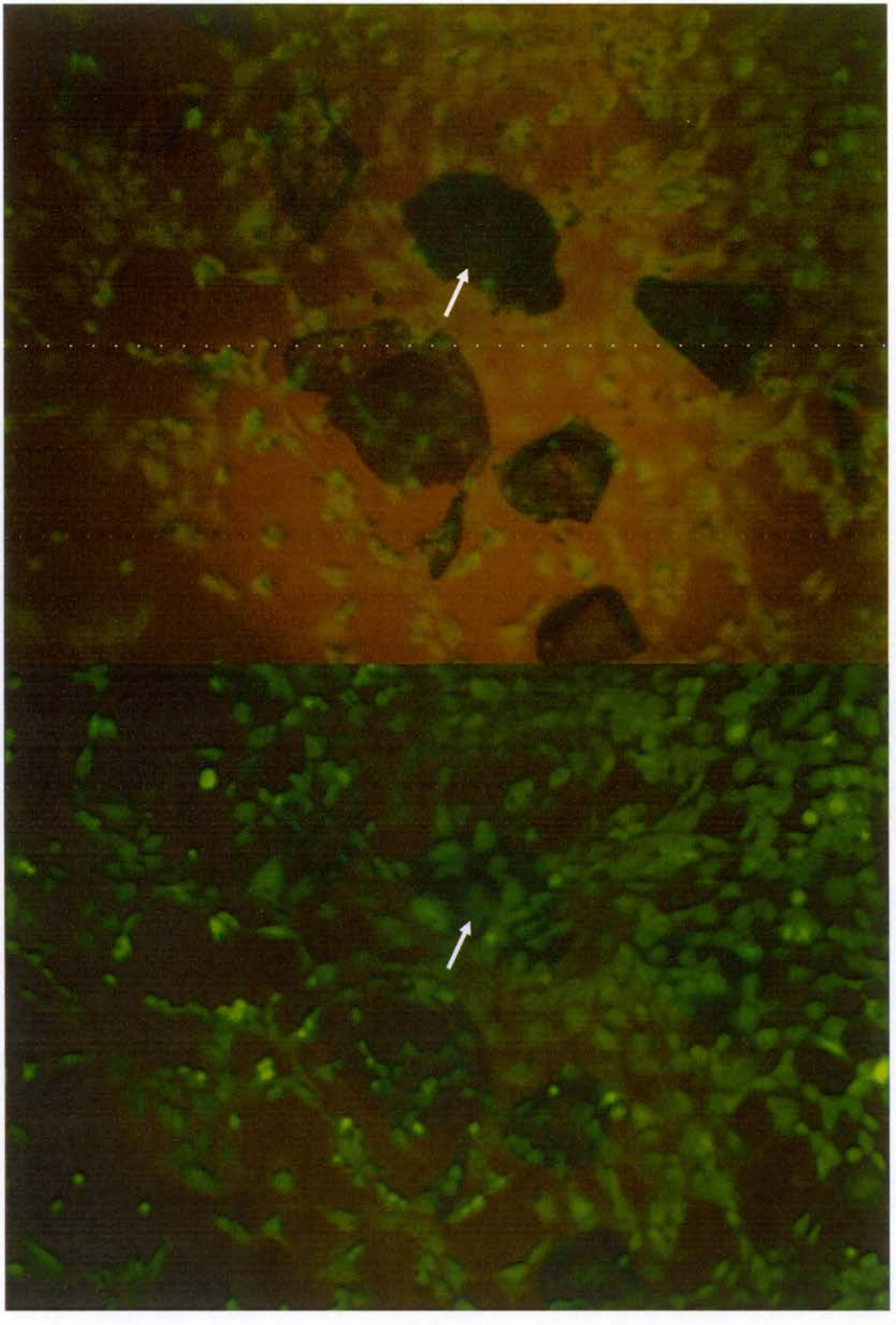


Figure 5.32. Morphology of fibroblasts cultured on 0.5%Ba45S5 bioactive glasses for 24 hrs (Calcein). Arrows: Cells showing flat spreading on glass granules.

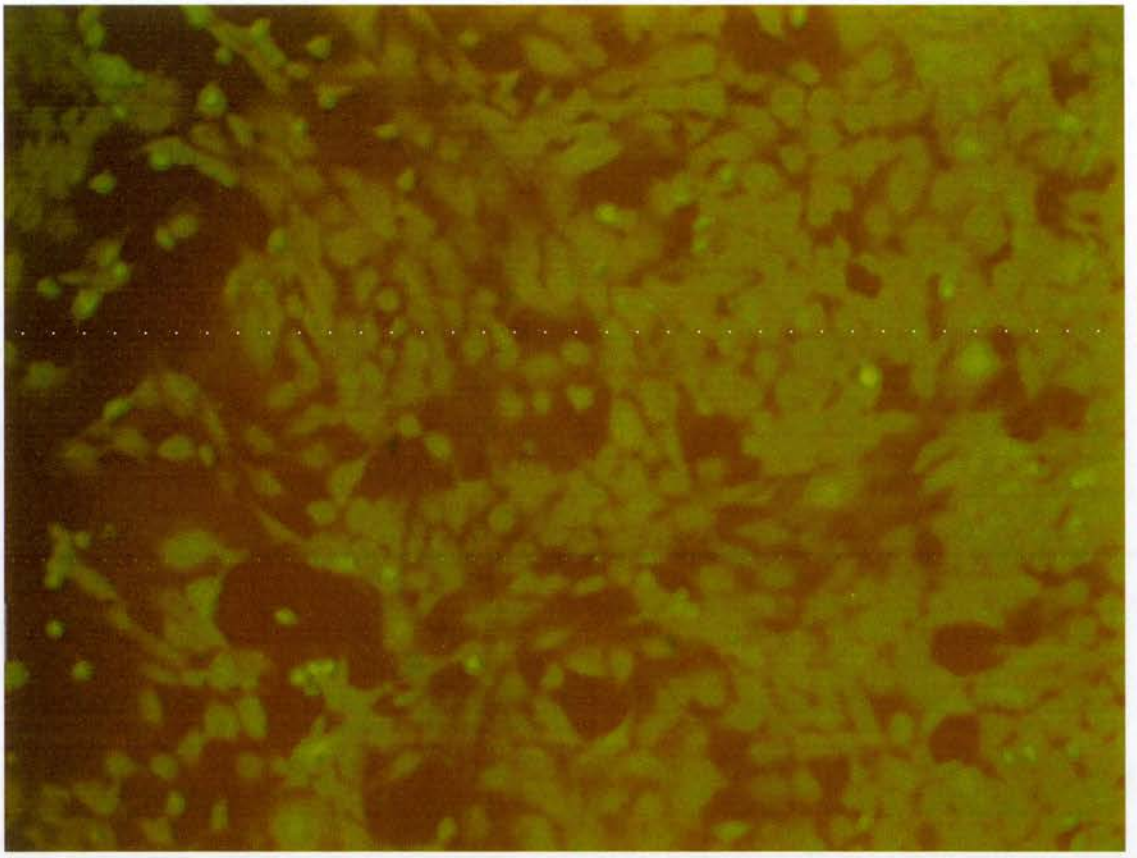


Figure 5.33. Morphology of fibroblasts cultured on tissue culture plastic for 24 hrs (Calcein).

Using fluorescence quantitation for the DAPI staining, there was no significant difference for any of the glass compositions, compared to the cell control well (Fig 5.34). The fluorescence did appear to decrease as the proportion of silica increased (45S5, 49S4.9, 52S4.9) (Fig. 5.34a). This corresponds to a decrease in stability and could indicate a loss of cell viability for the wells containing higher levels of ionic products. The 0.5%Ba45S5 bioactive glass displayed the highest fluorescence (620±115), although 0.5Ba49S4.9 had low levels of fluorescence (250±260). The zinc-doped specimens appeared to decrease in fluorescence as the proportion of zinc was increased (Fig 5.34a).

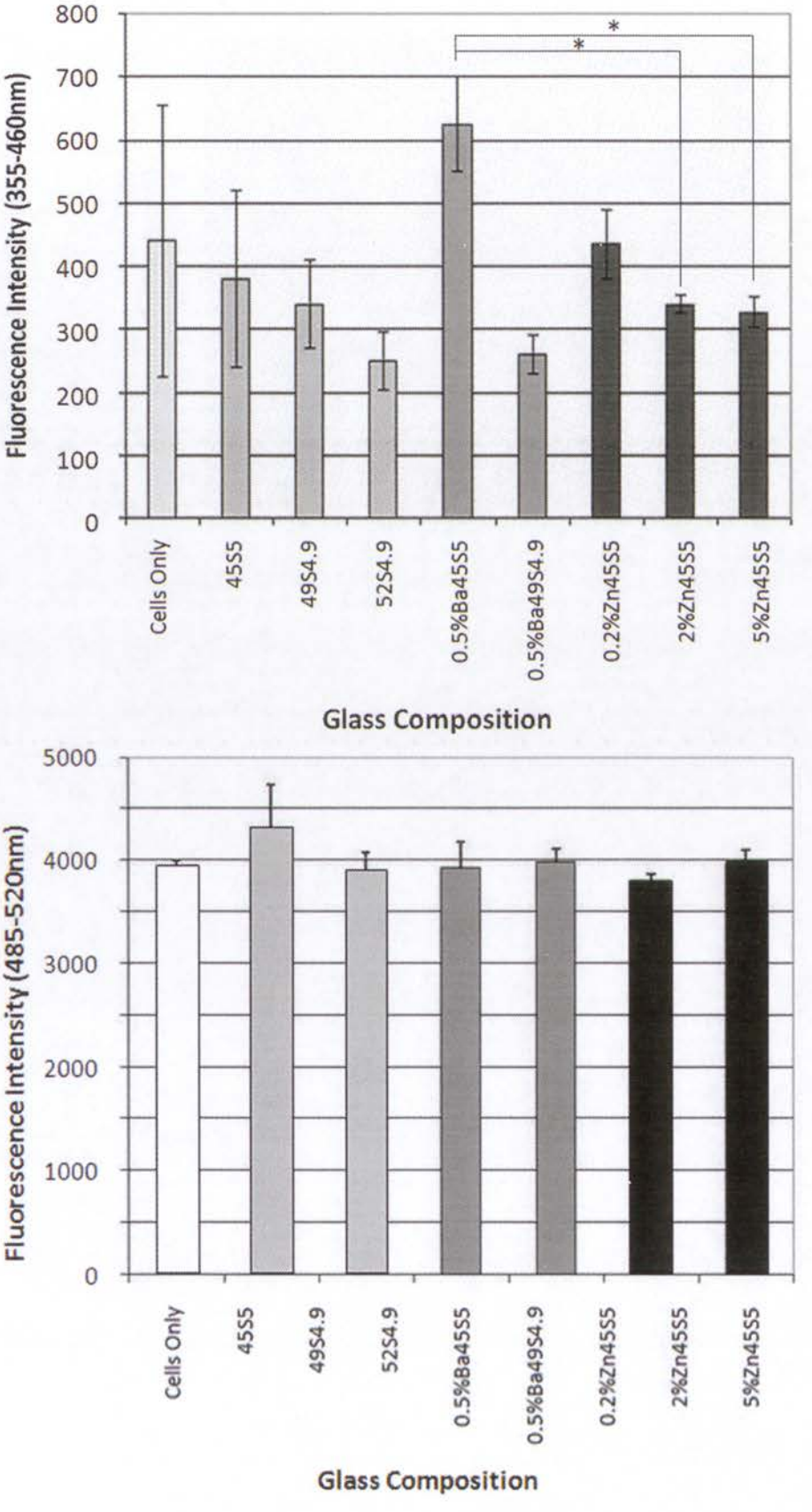


Figure 5.34. Cell fluorescence after 48 hr culture on bioactive glass powders (a) DAPI, (b) Calcein.

Digital selections of the regions occupied by the cells or glass particles are shown in Fig. 5.35. Quantification of the area quantification of the area covered by the calcein-stained cells is shown in Fig. 5.36. All glass compositions showed equally high levels of fluorescence when measured using this method. A slight decrease was seen for 0.5Ba52S4.6. There was a range of values for the area occupied by glass in each culture well, from 1.32-36.43% (13.62±12.68%: 98% variation).This is equivalent to a cross-sectional area ranging from 0.42-11.54 mm^2.

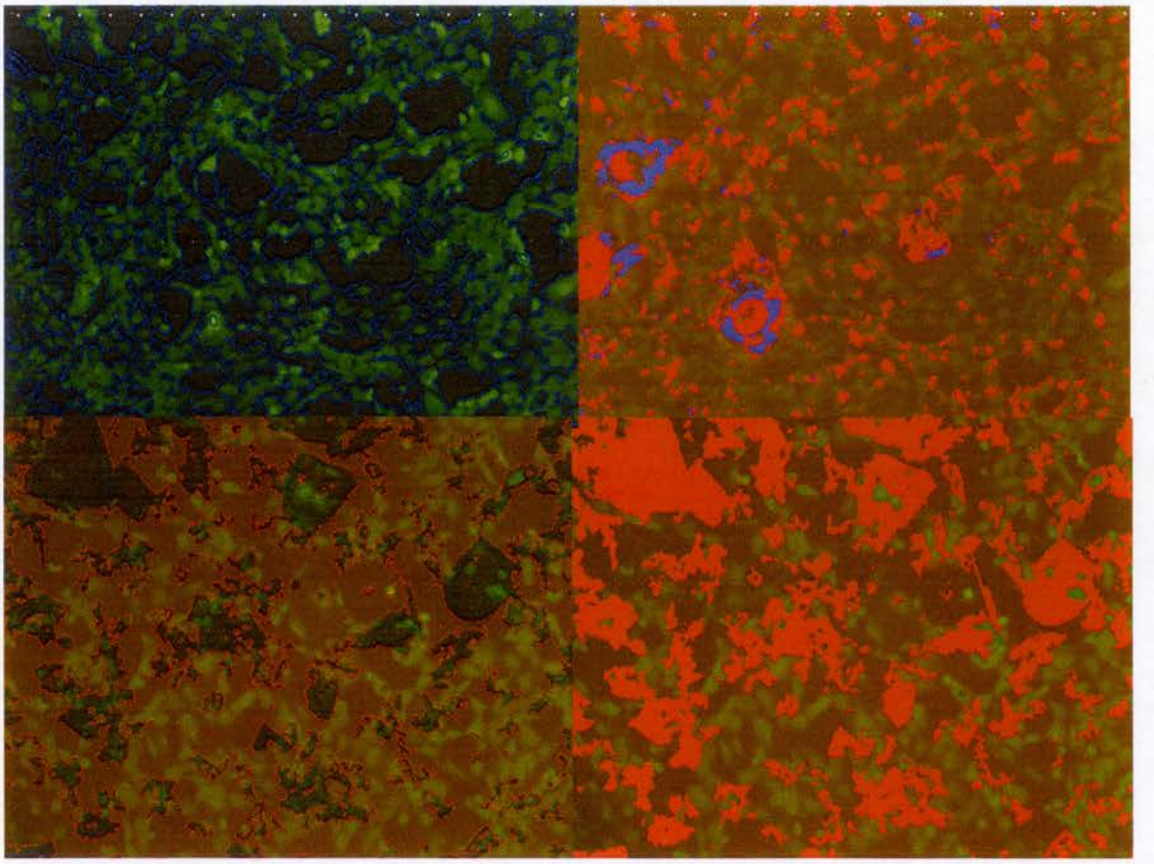


Figure 5.35. (a) Original image (b) Selection of the cell area (c) Selection of the outer perimeter of glass particles (d) Selection of the area occupied by glass. (red: digital selections, green: calcein staining)

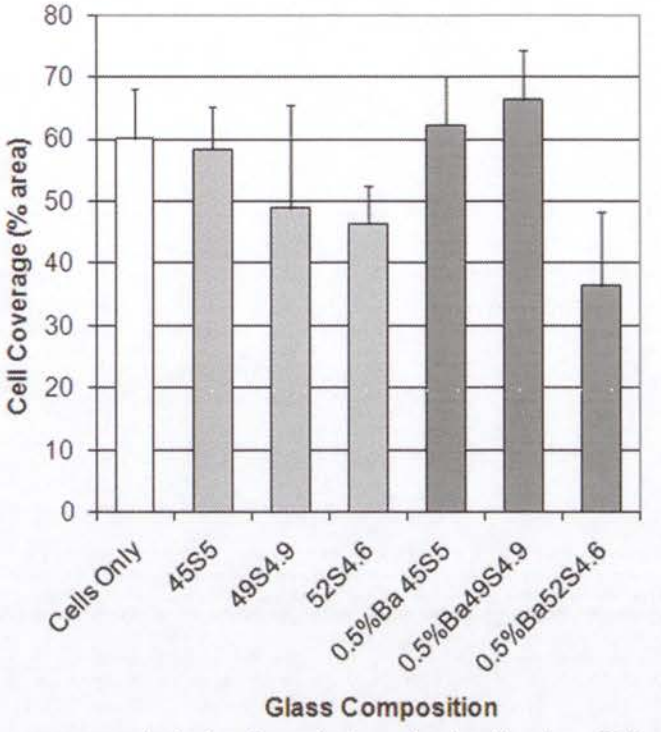


Figure 5.36. Digital cell coverage calculation for calcein-stained cells after 48 hrs culture on glass powders.

5.4.2.2. Measurement of Protein Concentration

A standard curve was constructed from bovine albumin serial dilutions (Fig. 5.34, blue). The absorbance readings for the bioactive glass supernatant samples were also determined. The day 4 samples are included in Fig. 5.37 in red.

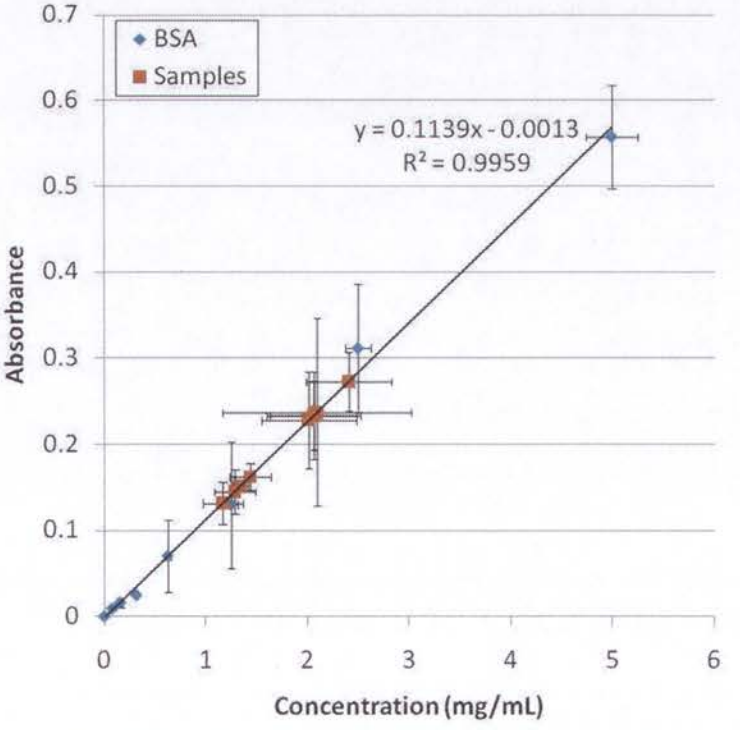


Figure 5.37. Standard curve for protein measurement showing the BSA control and the samples (day 4, fibroblast proliferation on bioactive glass)

The protein concentrations measured for the day 4, 8 and 11 samples are shown in Fig. 5.38. Overall, the concentrations were similar to the cell control wells. In some samples, including the cell control well, there was a slight decrease in protein over time. This could indicate a decrease in cell proliferation as the cell wells were already confluent.

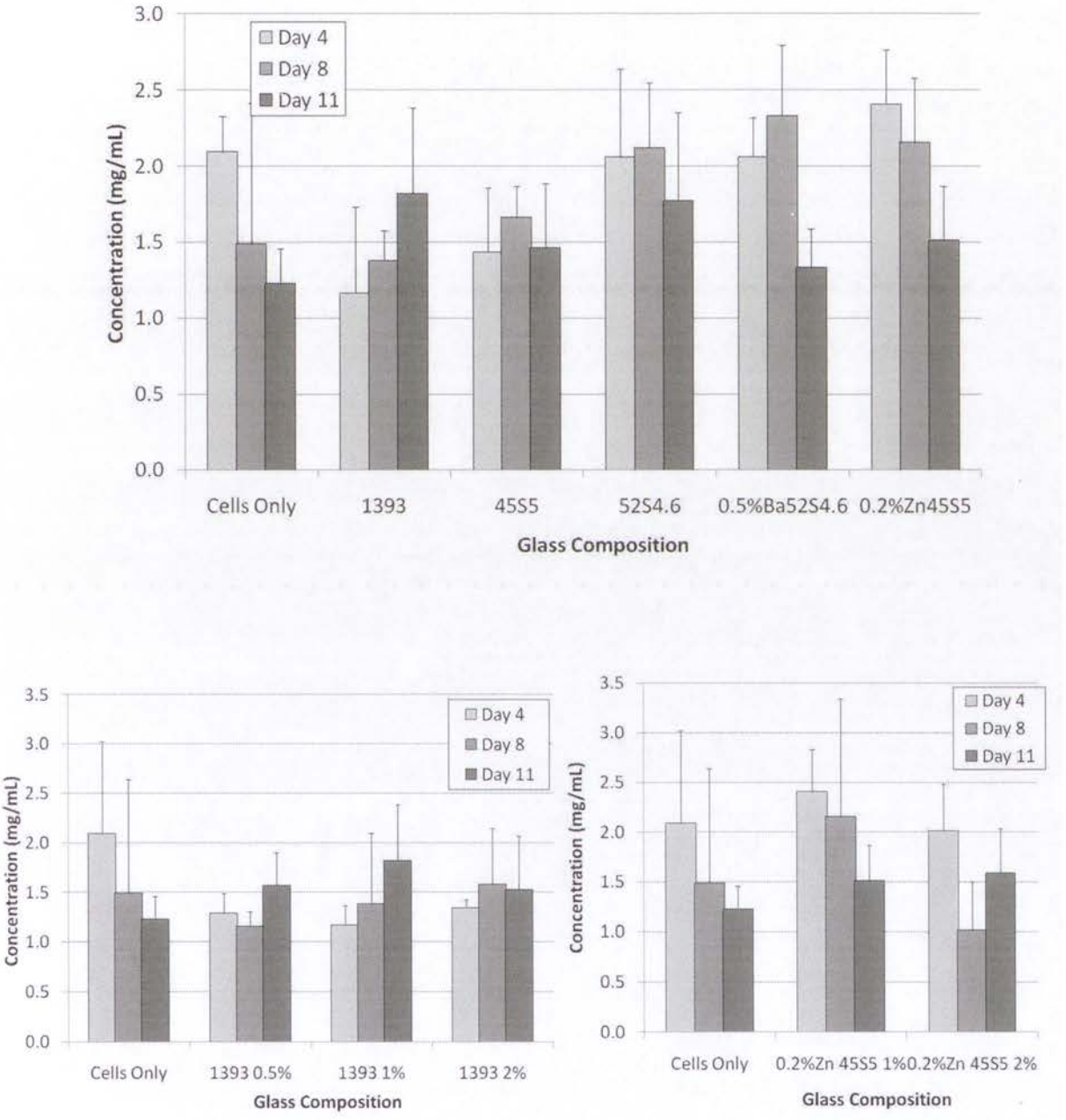


Figure 5.38. Protein measurement from supernatant taken from fibroblasts grown on glass after 4, 8 and 11 days. (a) All glass concentrations were 1% (b) Glass concentrations are included after the composition.

5.4.2.3. Examination of the Effect of the Glasses on MMPs

Gelatinase zymography (Fig. 5.39) results indicated an increase in latent MMP-2 and MMP-9 over time for all glass compositions. Active MMP-2 bands were observed for some of the glasses at day 11.

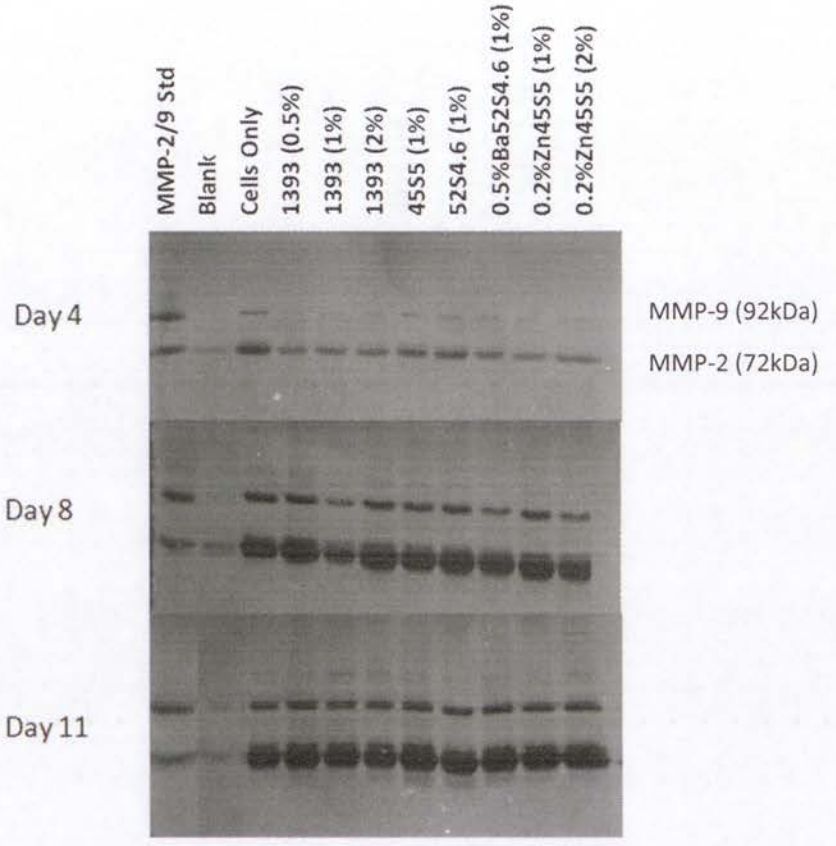


Figure 5.39. Gelatin zymography gels for fibroblast cultures on various bioactive glass compositions.

Results for the MMP-2 and MMP-9 band quantification are shown graphically in Fig. 5.40 and Fig 41. Most of the samples showed an increase in both MMP-2 and MMP-9 levels over time. Day 11 values were about double those of the day 4 values. By day 11 (and sometimes day 8), the MMP-2 expression had increased more than the cell control wells. Day 11 results showed slightly higher levels of MMP-9 compared to the cell control well for most of the samples. The barium, zinc (1 and 2 wt%) and 45S5 samples showed particularly high levels of MMP-2 and MMP-9, with the day 11 values being 50% higher than the cell control. On the other hand, the 1393 samples were similar to the cell controls at day 11 at concentrations of 0.4, 1 and 2 wt% glass in the cell well.

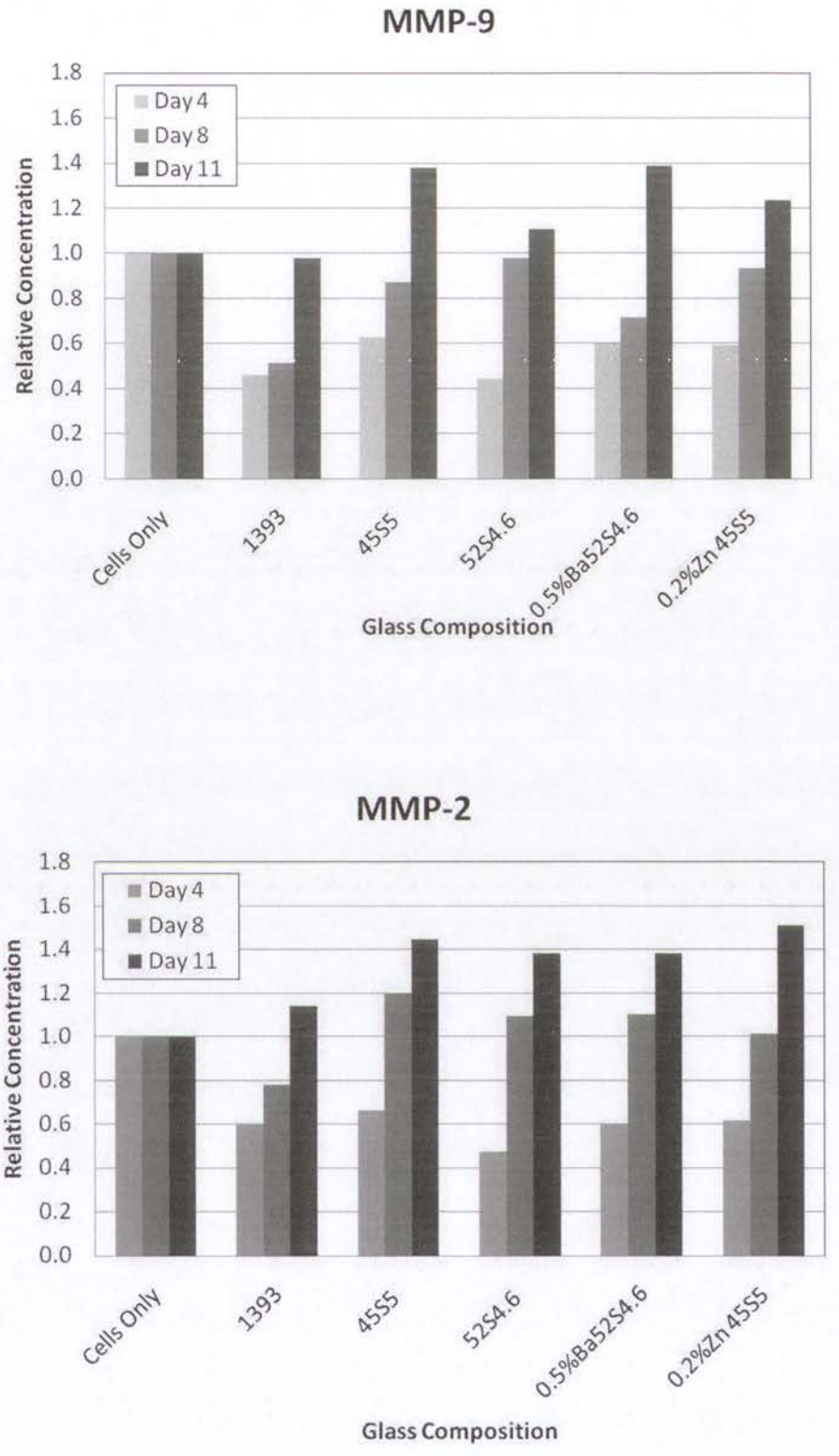


Figure 5.40. proMMP-9 and proMMP-2 expression for fibroblasts cultured on glasses (1% concentration in wells) for 4, 8 and 11 days.

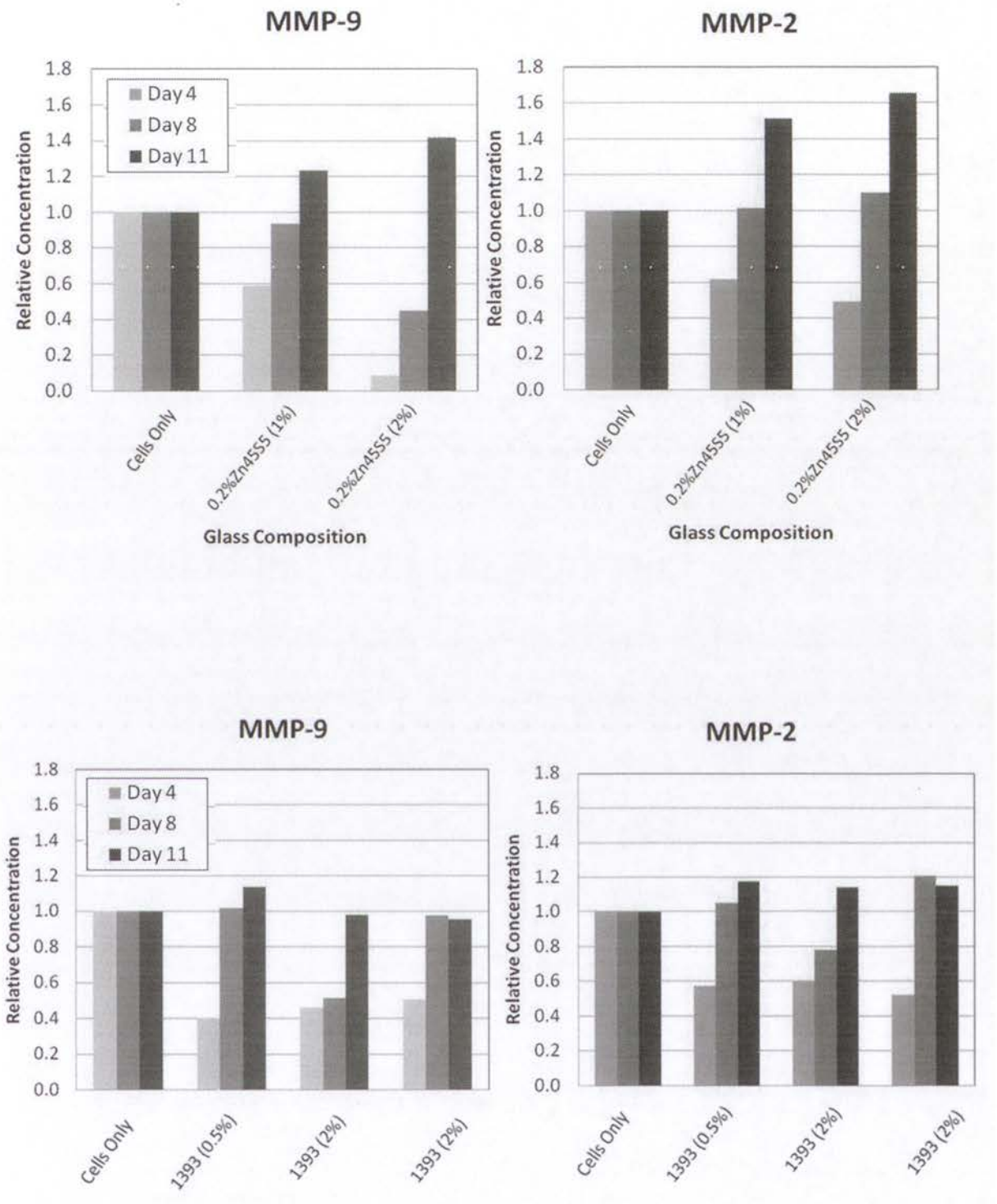


Figure 5.41. proMMP-9 and proMMP-2 expression for fibroblasts cultured on glasses (1% concentration in wells) for 4, 8 and 11 days.

The aims of this study were to provide preliminary evidence of the biocompatibility of synthesised bioactive glasses, develop test models for glasses and investigate the morphology of fibroblasts on glasses with various compositions (altered silica, barium, zinc). The majority of previous studies have focused on the behaviour of osteoblasts in contact with bioactive glasses. This is despite evidence that bioactive glasses can also form strong bones to soft tissues [53]. Few studies have been performed using soft tissue cells [86, 202, 204]. To the author's knowledge, this was also the first study to investigate MMP response to these glasses.

5.4.3.1. Cell Spreading and Morphology on Glass Powders

The viability and morphology of fibroblasts were investigated on the glasses using calcein staining and fluorescent microscopy (Fig. 5.29-5.33). The cells exhibited a high degree of attachment, spreading and viability on all samples up to at least 11 days of culture. No differences in morphology were noted between the glass compositions. Cells often displayed flattened morphologies and others showed 2D stretching behaviour with many cytoplasmic processes (Fig. 5.32). They preferentially attached to glass particles than tissue culture plastic (coated polystyrene) (Fig. 5.31) and agglomerated in regions of high glass density (Fig. 5.31).

5.4.3.2. Methods for Quantitating Cell Number

Test models were investigated in order to non-destructively quantitate the cell number, including measurement of fluorescence and quantitation of cell area. Fluorescence measurements of 0.5%Ba45S5 showed a significantly higher cell density for dapi-stained cells compared to the other glass compositions (Fig. 5.34a). However, this trend was not observed with calcein staining, which showed no change across the glasses (Fig 5.34b). Calculation of cell area occupied by calcein-stained cells using digital methods showed different trends for the level of cell density for some compositions (particularly 0.5%Ba49S4.9), compared to the fluorescence quantitation technique (Fig. 5.36). Calculation of the area occupied by glass particles showed a wide variation across culture wells (1.32-36.43%). This is likely to indicate there was a difference in the weight of glass powders actually delivered into each well. The amount of glass in the wells could have also decreased due to accidental removal when media changes were undertaken. This can be partially controlled by tipping the culture plate before the media is removed, and removing media manually rather than using a suction device. The method used in the current study for glass delivery into the wells was similar to that used in previous studies [86]. No data has been reported in these previous studies which validate the amount of glass which was actually coated on the base of the culture wells. Novel alternate techniques for glass delivery were therefore sought. These included (1) cutting the tops off

200 µL pipette tips to reduce glass agglomeration within the tip, (2) individually weighing the amount of dry glass delivered to each well, followed by UV sterilization of the culture plate (2) suspension of the glass in NaCMC and (4) mounting of glass powder on variotis™ discs (ref. section 4.8, 5.5).

Measurement of protein concentration showed similar levels of protein across all samples (Fig. 5.38). This technique is thought to be an effective, non-destructive technique which can easily be undertaken using the supernatant. A decrease in cell proliferation between day 8 and 11 were detected for some samples, likely to be indicating cell detachment due to confluence and layering. This problem could be reduced if the glasses are mounted on the scaffolds and culture undertaken in 3D.

5.4.3.3.MMP Levels

Measurement of MMP-2 and MMP-9 activity was successfully undertaken for a range of the glasses from days 4-11 of culture (Fig. 5.39-5.41). Both MMP-2 and MMP-9 increased over time for all samples and did not show a decrease at day 11, which was observed using total protein measurement. Low levels of MMP-9, which were detected for the 0.2%Zn45S5 (2%) glass, could be due to the increased stability of the glass which occurs with zinc doping. Some active MMP-2 bands were detected at day 11, particularly for 45S5 and 52S4.6. At day 11, the glasses all showed higher levels of MMP-9 and MMP-2 than the cell control well. The maximum MMP-9 level recorded was only 1.4, relative to the cell control well. This is still a low level of MMP-9, indicative of low inflammatory markers. Higher levels of MMP-9 which were noted for 45S5 as compared to 13-93 are attributed to the lower stability of 45S5, due to its lower silica level and lack of potassium. This is consistent with MMP-9 stimulation by hydroxyapatite [768] which, within certain levels, can be beneficial for stimulation of angiogenesis and wound healing [770].

5.4.3.4. Comparison with Previous Studies

Previous studies have investigated cell behaviour on bioactive glass powders or fibres [86, 200-205]. The current findings show increased cell proliferation on surfaces incorporating bioactive glass, as commonly observed on glass/polymer surfaces (incorporating 5 wt% or less bioactive glass) [147, 202, 209, 211, 212]. This result can largely be attributed to the increased surface area and attachment sites for cells. It could also be due to dissolution products released by the cells and formation of hydroxyapatite on their surface. Hydroxyapatite formation has been demonstrated as early as 3 days during SBF soaking studies of 45S5 glass/PDLLA foams, for a glass particle size <5 µm. Future studies could use SEM/EDAX to investigate the correlation between hydroxyapatite formation and in vitro cell proliferation on the current glass

compositions. This would more easily be done for PCL disk-mounted glass powders, than loose powders. The findings of the current study are different to those found by Day and coworkers [86]. This group found that fibroblast proliferation was stimulated for low concentrations of 45S5 glass (0.01-0.1% wt/vol over 24 hrs), over longer periods and higher concentrations (0.2-10% wt/vol) growth was inhibited and cells became vacuoled. No signs of cytoplasmic vacuole formation were noticed in the current study. Cell growth did not appear to be inhibited by the glass (concentrations 0.5-2 wt%) in the current study, although the 24-72 hr timepoints were not investigated. The differences in these results can be accounted for by the reduced particle size used by Day (<5um). It is likely the cells had vacuoles due to earlier degradation of the glass, leading to the release of silica. Previous studies have found high silica glasses (60%) result in high silica levels inside the vacuoles of osteoblasts- 75% higher than other regions of the cell [792]. Another study has demonstrated the release of silica into the media over a period of 7 days (due to 1% mesoporous 85%silica bioactive glass) has a stimulatory effect on osteoblast proliferation and does not have any negative effects on parameters such as cell cycle, viability or oxidation [204]. The rapid initial release of calcium could have an inhibitory effect on cells for high-silica glasses [204]. A study by Foppiano [793] has demonstrated increased osteoblast proliferation on bioactive glass disks (50, 55% silica), compared to both titanium alloy (Ti6Al4V) and tissue culture polystyrene.

As in the current study, elongated cell morphologies with multiple protrusions were noted in a study by Tsigkou [208], for osteoblasts attaching to glass particles embedded in PDLLA. Gan and coworkers observed flattened cells, displaying long cytoplasmic processes, when nucleus pulposus cells were grown on 45S5 porous disks [202]. These features were also noted in the current study. They were particularly obvious on larger granules; consistent with the larger particle size used in Gan's study (40-71 μm). DNA measurements for Gan's study increased over a 6-day period. This is in contrast to Day's study as the more slowly dissolving large particles, which would not change the pH in the cell well significantly. The high viability and absence of cell damage shown in the current study demonstrate the good biocompatibility of a range of novel melt-derived bioactive glasses. Future studies will examine the antibacterial effects of these novel glass compositions.

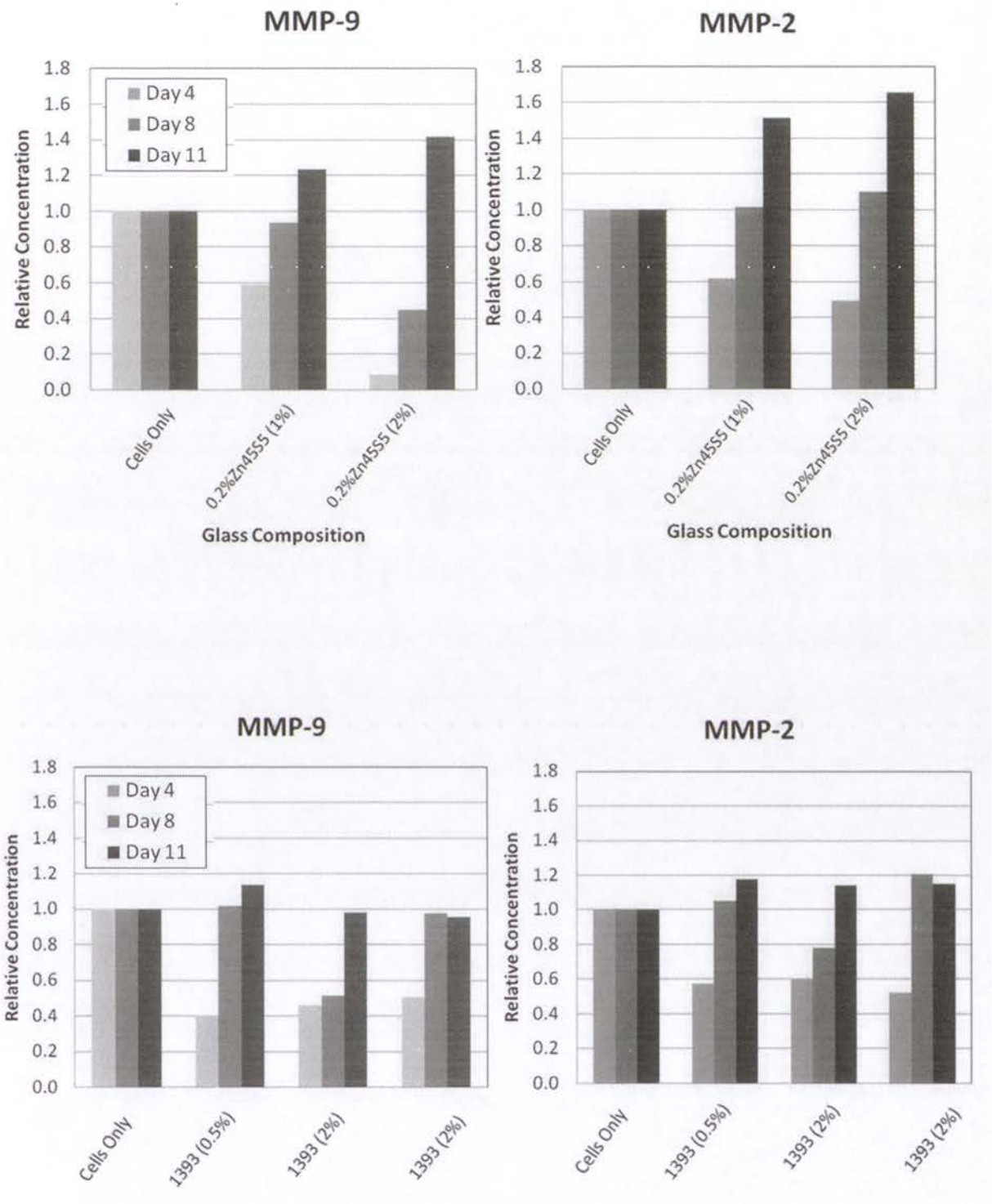


Figure 5.41. proMMP-9 and proMMP-2 expression for fibroblasts cultured on glasses (1% concentration in wells) for 4, 8 and 11 days.

The aims of this study were to provide preliminary evidence of the biocompatibility of synthesised bioactive glasses, develop test models for glasses and investigate the morphology of fibroblasts on glasses with various compositions (altered silica, barium, zinc). The majority of previous studies have focused on the behaviour of osteoblasts in contact with bioactive glasses. This is despite evidence that bioactive glasses can also form strong bones to soft tissues [53]. Few studies have been performed using soft tissue cells [86, 202, 204]. To the author's knowledge, this was also the first study to investigate MMP response to these glasses.

5.4.3.1. Cell Spreading and Morphology on Glass Powders

The viability and morphology of fibroblasts were investigated on the glasses using calcein staining and fluorescent microscopy (Fig. 5.29-5.33). The cells exhibited a high degree of attachment, spreading and viability on all samples up to at least 11 days of culture. No differences in morphology were noted between the glass compositions. Cells often displayed flattened morphologies and others showed 2D stretching behaviour with many cytoplasmic processes (Fig. 5.32). They preferentially attached to glass particles than tissue culture plastic (coated polystyrene) (Fig. 5.31) and agglomerated in regions of high glass density (Fig. 5.31).

5.4.3.2. Methods for Quantitating Cell Number

Test models were investigated in order to non-destructively quantitate the cell number, including measurement of fluorescence and quantitation of cell area. Fluorescence measurements of 0.5%Ba45S5 showed a significantly higher cell density for dapi-stained cells compared to the other glass compositions (Fig. 5.34a). However, this trend was not observed with calcein staining, which showed no change across the glasses (Fig 5.34b). Calculation of cell area occupied by calcein-stained cells using digital methods showed different trends for the level of cell density for some compositions (particularly 0.5%Ba49S4.9), compared to the fluorescence quantitation technique (Fig. 5.36). Calculation of the area occupied by glass particles showed a wide variation across culture wells (1.32-36.43%). This is likely to indicate there was a difference in the weight of glass powders actually delivered into each well. The amount of glass in the wells could have also decreased due to accidental removal when media changes were undertaken. This can be partially controlled by tipping the culture plate before the media is removed, and removing media manually rather than using a suction device. The method used in the current study for glass delivery into the wells was similar to that used in previous studies [86]. No data has been reported in these previous studies which validate the amount of glass which was actually coated on the base of the culture wells. Novel alternate techniques for glass delivery were therefore sought. These included (1) cutting the tops off

200 µL pipette tips to reduce glass agglomeration within the tip, (2) individually weighing the amount of dry glass delivered to each well, followed by UV sterilization of the culture plate (2) suspension of the glass in NaCMC and (4) mounting of glass powder on variotis™ discs (ref. section 4.8, 5.5).

Measurement of protein concentration showed similar levels of protein across all samples (Fig. 5.38). This technique is thought to be an effective, non-destructive technique which can easily be undertaken using the supernatant. A decrease in cell proliferation between day 8 and 11 were detected for some samples, likely to be indicating cell detachment due to confluence and layering. This problem could be reduced if the glasses are mounted on the scaffolds and culture undertaken in 3D.

5.4.3.3.MMP Levels

Measurement of MMP-2 and MMP-9 activity was successfully undertaken for a range of the glasses from days 4-11 of culture (Fig. 5.39-5.41). Both MMP-2 and MMP-9 increased over time for all samples and did not show a decrease at day 11, which was observed using total protein measurement. Low levels of MMP-9, which were detected for the 0.2%Zn45S5 (2%) glass, could be due to the increased stability of the glass which occurs with zinc doping. Some active MMP-2 bands were detected at day 11, particularly for 45S5 and 52S4.6. At day 11, the glasses all showed higher levels of MMP-9 and MMP-2 than the cell control well. The maximum MMP-9 level recorded was only 1.4, relative to the cell control well. This is still a low level of MMP-9, indicative of low inflammatory markers. Higher levels of MMP-9 which were noted for 45S5 as compared to 13-93 are attributed to the lower stability of 45S5, due to its lower silica level and lack of potassium. This is consistent with MMP-9 stimulation by hydroxyapatite [768] which, within certain levels, can be beneficial for stimulation of angiogenesis and wound healing [770].

5.4.3.4. Comparison with Previous Studies

Previous studies have investigated cell behaviour on bioactive glass powders or fibres [86, 200-205]. The current findings show increased cell proliferation on surfaces incorporating bioactive glass, as commonly observed on glass/polymer surfaces (incorporating 5 wt% or less bioactive glass) [147, 202, 209, 211, 212]. This result can largely be attributed to the increased surface area and attachment sites for cells. It could also be due to dissolution products released by the cells and formation of hydroxyapatite on their surface. Hydroxyapatite formation has been demonstrated as early as 3 days during SBF soaking studies of 45S5 glass/PDLLA foams, for a glass particle size <5 µm. Future studies could use SEM/EDAX to investigate the correlation between hydroxyapatite formation and in vitro cell proliferation on the current glass

compositions. This would more easily be done for PCL disk-mounted glass powders, than loose powders. The findings of the current study are different to those found by Day and coworkers [86]. This group found that fibroblast proliferation was stimulated for low concentrations of 45S5 glass (0.01-0.1% wt/vol over 24 hrs), over longer periods and higher concentrations (0.2-10% wt/vol) growth was inhibited and cells became vacuoled. No signs of cytoplasmic vacuole formation were noticed in the current study. Cell growth did not appear to be inhibited by the glass (concentrations 0.5-2 wt%) in the current study, although the 24-72 hr timepoints were not investigated. The differences in these results can be accounted for by the reduced particle size used by Day (<5um). It is likely the cells had vacuoles due to earlier degradation of the glass, leading to the release of silica. Previous studies have found high silica glasses (60%) result in high silica levels inside the vacuoles of osteoblasts- 75% higher than other regions of the cell [792]. Another study has demonstrated the release of silica into the media over a period of 7 days (due to 1% mesoporous 85%silica bioactive glass) has a stimulatory effect on osteoblast proliferation and does not have any negative effects on parameters such as cell cycle, viability or oxidation [204]. The rapid initial release of calcium could have an inhibitory effect on cells for high-silica glasses [204]. A study by Foppiano [793] has demonstrated increased osteoblast proliferation on bioactive glass disks (50, 55% silica), compared to both titanium alloy (Ti6Al4V) and tissue culture polystyrene.

As in the current study, elongated cell morphologies with multiple protrusions were noted in a study by Tsigkou [208], for osteoblasts attaching to glass particles embedded in PDLLA. Gan and coworkers observed flattened cells, displaying long cytoplasmic processes, when nucleus pulposus cells were grown on 45S5 porous disks [202]. These features were also noted in the current study. They were particularly obvious on larger granules; consistent with the larger particle size used in Gan's study (40-71 μm). DNA measurements for Gan's study increased over a 6-day period. This is in contrast to Day's study as the more slowly dissolving large particles, which would not change the pH in the cell well significantly. The high viability and absence of cell damage shown in the current study demonstrate the good biocompatibility of a range of novel melt-derived bioactive glasses. Future studies will examine the antibacterial effects of these novel glass compositions.

5.5. *IN VITRO* BIOCOMPATIBILITY TESTING OF MG-BASED AND CA-BASED BULK METALLIC GLASSES

5.5.1. METHODS

5.5.1.1. Specimen Preparation and Cell Seeding

Figure 5.42 shows the specimen preparation for this experiment. Bulk metallic glasses (BMGs) (ref section 4.1.3) were kindly provided by Michael Ferry (Materials Science and Engineering, UNSW, Australia). BMGs were chosen for this study due to their potential for coating the variotis™ scaffold in a clinical situation. BMGs could show antibacterial actions, and deliver beneficial nutrients to tissue such as calcium, magnesium and zinc. Calcium and Magnesium rich BMGs (termed 'Ca BMG' and 'Mg BMG') were formed [674]. Magnesium ('Mg') and stainless steel (S. steel) controls were used. In addition, silica-based 45S5 bioactive glass ('45S5') was synthesised by the author via a melt-derived process, according to the procedures in section 4.2 (Batch Ax2). Bulk, cylindrical specimens were prepared with the following sample dimensions: Ca BMG:h-=1.88±0.12, d=4.95±0.18, Mg BMG:h=1.77±0.19, d=4.83±0.15, Mg: h=2.29±0.50, d=5.3±0.00, S. steel: h=3.19±0.46, d=3.82±0.21 mm.

In addition, some glass (Ca BMG, Mg BMG, 45S5) was crushed to powders using a mortar and pestle. Particle size histograms were developed using the protocol described in 4.3.1. The particle size was expressed as mean ± standard deviation and range. The glass powders were mounted on PCL scaffold disks, in order to minimize the amount of material tested in a single cell well. PCL scaffold disks (d=3.2±0.4, h=4.57±0.07 mm) were formed from PCL variotis™ scaffolds. The various metal, BMG and bioactive glass powders described above were mounted onto the PCL stubs using the technique described in section 4.8.1. These specimens were termed 'PCL/Ca BMG', 'PCL/Mg' and 'PCL/45S5'.



Figure 5.42. (a) BMG powder, (b) BMG mounted on PCL variotis disk, (c,d) Ultrasound treatment of the disks.

Prior to cell culture, the BMG and metal specimens were removed from the silicone oil in which they had been stored to prevent corrosion. The samples were subjected to ultrasound in acetone to remove residual oil. Specimens were weighed and dimensions measured. Samples placed in 24-well polystyrene tissue culture plates and immersed in 70% ethanol for 20 mins.

Samples were rinsed with sterile culture medium (11 mM RPMI), which was then removed. Specimens were sterilised using a UV laminar flow cabinet for 30mins. The samples were immersed in sterile medium (11 mM RPMI) for 3 days, at 37°C.

All culture was performed using a culture medium as previously described. 500 µL complete media was placed into each well with the disks. Confluent 3T3L1 mouse fibroblast cells (P19) were trypsinised from 25 cm^2 flasks, pelleted and counted. 500 µL of a 40,000 cells/mL solution was placed in each well, resulting in a final cell density of 20,000 cells/well/mL. Controls were cells only or media only. Plates were then placed in an incubator at 37°C and 5% CO_2. Photos and observations of the wells were taken every 24 hrs. Media was changed every 24 hrs. After 3 days of culture, medium was replaced with serum-free media. After 4 days of culture, supernatant was stored at -20°C for protein quantification and zymography.

5.5.1.2. Examination of Disks using Light Microscopy

The top surface of the dry bulk BMG, magnesium and stainless steel samples were imaged using a Wild Heerbrugg Intralux 5000 stereoscopic microscope and Leica DFC420 digital camera system.

5.5.1.3. Measurement of Weight Loss

4-5 specimens of each type were transferred to clean culture plates. Specimens were rinsed with PBS and dried using 70% ethanol and blotting with Kimwipes. Samples were air dried for 4 days then weighed, so the weight loss over the culture period could be determined.

5.5.1.4. Scanning Electron Microscopy and Energy Dispersive X-Ray Spectroscopy

Specimens were air-dried and mounted on aluminium stubs and sputter coated with 10 nm gold. SEM Imaging was performed on a Philips XL30. Cells on the disks were not visible as biological fixation was not performed. Deposits formed on the Ca-based glasses were identified using Energy Dispersive X-Ray Spectroscopy (EDAX). This was achieved using an integrated EDS detector (EDAX) while the specimens were placed in a Phillips XL30 Scanning Electron Microscope.

5.5.1.5. Total Protein Quantification

Total media protein concentration was determined using a Biorad protein detection system (BioRad DC, Sigma, Australia). A standard curve was constructed from Bovine Serum Albumin (BSA) of known concentration. The protein concentration of the supernatant samples was then estimated to give an indication of cell number/activity. The protein levels were normalised to the cell control well.

5.5.1.6. Measurement of Cellular Metalloproteinase Activity

Gelatin Zymography was used to measure proteolytic activity after 4 days of culture. For these studies wound fluids (1 µl) were loaded onto a 8% SDS-PAGE gel containing 10% MDPF labeled gelatin (0.75 mm thick). The samples were separated by electrophoresis at a constant voltage (130 V) for approximately 1.5 hr at room temperature, and activities determined as described in detail previously [776]. The results are expressed as the average of 2 wells from 2 gels for each timepoint. Results were corrected for initial fluid volume and protein concentration and are expressed as Xg/mgP.

5.5.1.7. Fluorescent Microscopy

Viable cells were marked at day 4 using 500µL Calcein AM (1:100 in RPMI) for the last 20 mins of the incubation period. The calcein was removed and disks were rinsed with PBS. Scaffolds were also stained using the nuclear marker DAPI (0.2% (v/v) in PBS. DAPI was removed and replaced with 100 µL PBS. DAPI stained nuclei were visualised as blue (350 nm) and cytoplasmic stains were visualised as green (520 nm) using a fluorescent microscope (Olympus AX70, Olympus, Tokyo, Japan) equipped with an Olympus DP60 camera.

5.5.2.1. Particle Size Distribution

Histograms for the BMG powder lengths are shown in Fig. 5.43. For the Ca BMG, the mean particle length was 21.42±16 μm, with a range of 4.48-91.83 μm. 60.28% of the glass had a particle size less than 20 μm, and 87.66% of the glass was <40 μm. For the Mg BMG, the mean particle length was 23.63±28.07 μm, with a range of 4.48-146.7.68.95% of the particles were <20 μm in length and 81% of the glass was <40 μm.

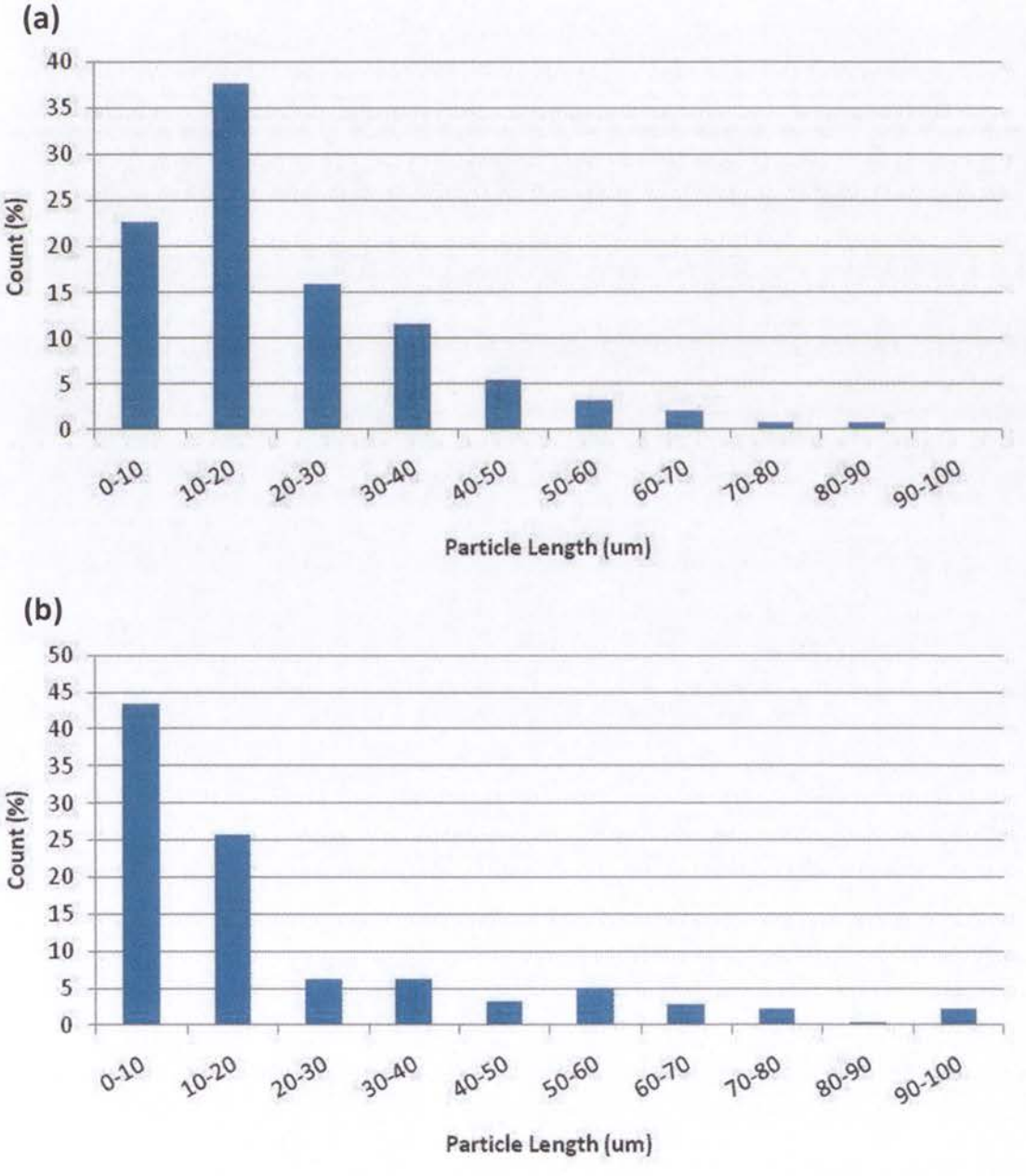


Figure 5.43. Particle distribution histograms for (a) Ca BMG and (b) Mg BMG.

5.5.2.2. Chemical and Physical Changes in the Materials

Fig. 5.44 shows the appearance of the bulk samples after 1 day of soaking. Particulate degradation products were released from the bulk Mg-based BMG throughout the entire experiment, from the first day of soaking. The release of degradation products did reduce after the first few days of soaking in media. The pink media in the wells containing the bulk Ca-based BMG and bulk magnesium disks had turned fairly transparent. Bubbles were evident on the surface of the bulk stainless steel samples, but the colour of this media remained unchanged. The specimens mounted on the PCL scaffolds did not show such obvious changes.

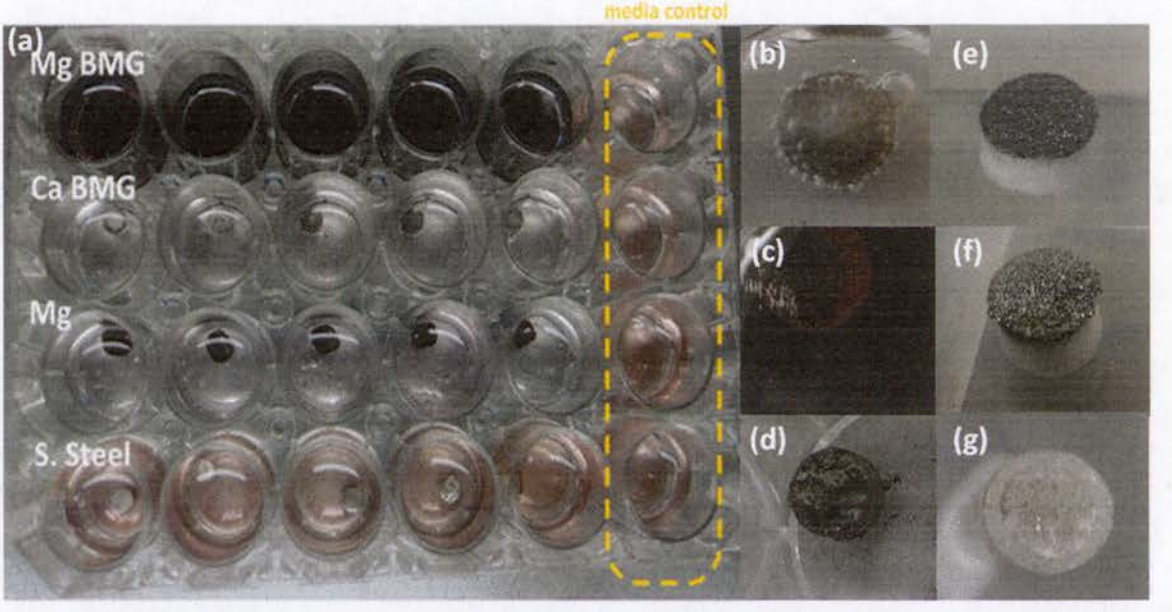


Figure 5.44. (a) The appearance of the bulk samples after 1 day of soaking in media (b) Bubbles on the Ca BMG disk (c) Degradation products from the Mg-based BMG (d) Ca BMG (e) PCL/Mg BMG (f) PCL/Ca BMG (g) PCL/45S5 disk.

Fig. 5.45 shows the surface of the bulk glasses, as viewed using light microscopy at the end of the culture period. Whilst there were no changes observed on the stainless steel or magnesium samples, deposits of metallic salts were evident on the surfaces of the Mg-based and Ca-based BMGs (Fig. 5.44c-f).

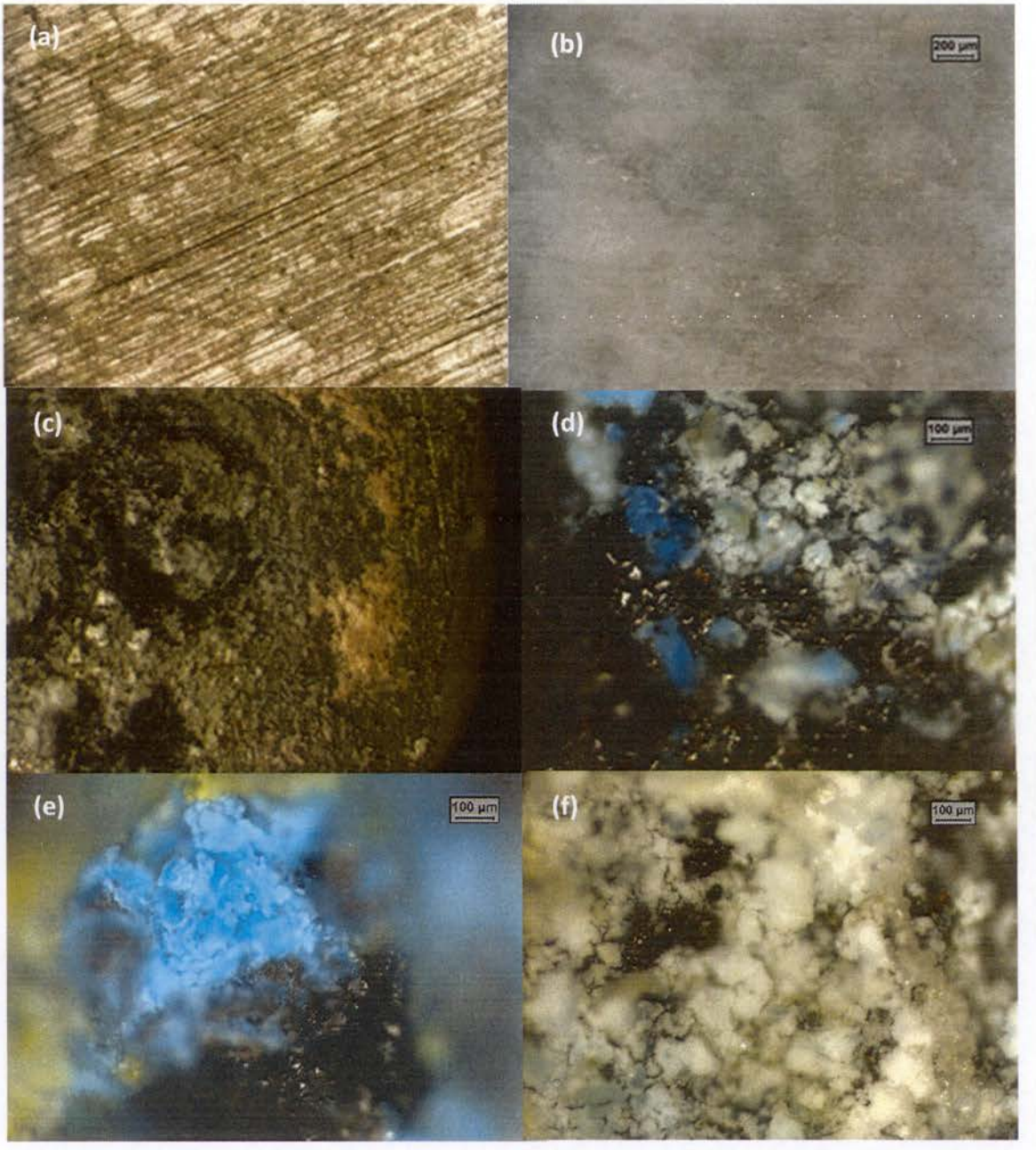
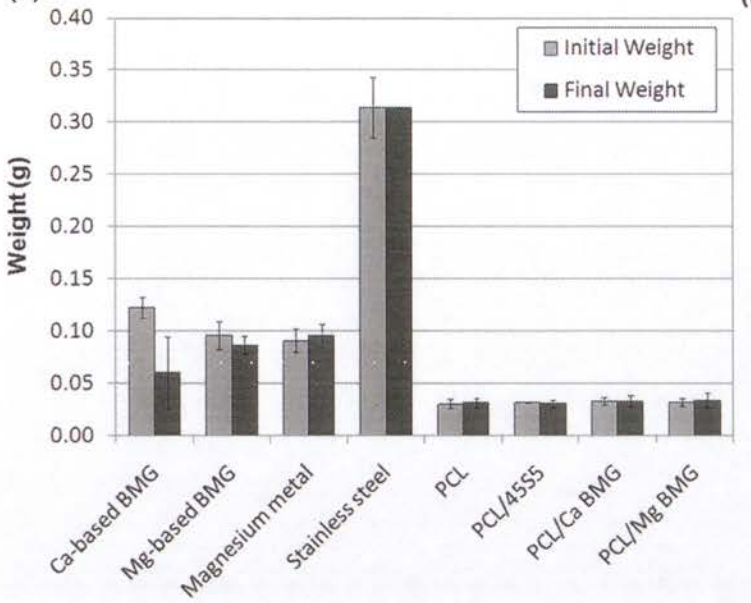


Figure 5.45. Light microscopy of the surface of the bulk disks after the culture period (a) S. Steel, (b) Mg, (c) Mg BMG, (d-f) Ca BMG.

Weight loss measurements for the disks are shown in Figure 5.46. The calcium-rich bulk BMG experienced the highest weight loss (~50%). The Mg rich BMG also demonstrated weight loss (~8.5%). These findings reflect their relative reactivity on the redox scale. Magnesium indicated a weight increase (6%), due to the formation of a magnesium oxide layer, which stabilizes the metal. Little weight change was observed for the stainless steel or the PCL scaffold based specimens.

(a)



(b)

	Average ± stdev
Ca BMG	-49.551 ± 29.352
Mg BMG	-8.575 ± 7.665
Magnesium metal	6.104 ± 7.677
Stainless steel	0.081 ± 0.092

Figure 5.46. Weight loss for the BMG, metallic and bioactive glass disks and scaffold samples.

5.5.2.3. Cellular Activity

Protein levels were measured in the supernatant to give an indication of cellular activity on and around the disks (Fig. 5.47). Protein measurements actually indicate the amount of biological proteins present in the well, whether due to cells, bacteria or the media itself. The calcium-based bulk BMG showed protein levels much lower than the media alone (0.2 vs 2.0 mg/mL), which could be due to the precipitation of proteins from the media in a high pH environment. It could also signify a lack of viable cells and cell proliferation. The protein concentration for the variotis™-mounted Ca BMG (2.2 mg/mL) was higher than the other variotis™-mounted samples. All samples showed a good protein concentration which was similar to the cell control well (1.7-2.2 mg/mL), which could indicate cell growth in these wells.

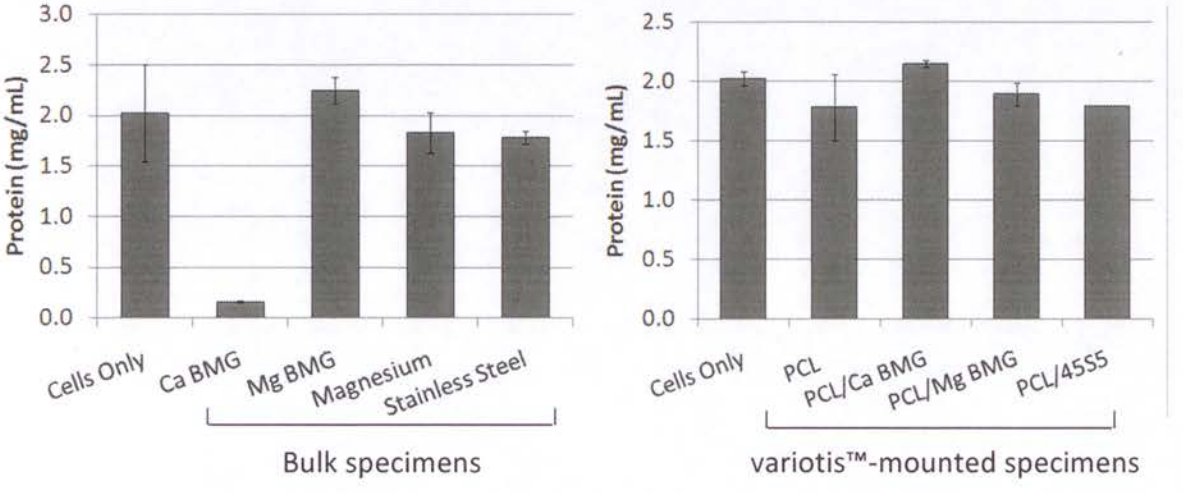


Figure 5.47. Measurement of protein levels in the supernatant.

The metalloproteinase activity was measured to give an indication of cell growth (MMP-2) and inflammation (MMP-9) (Fig. 5.48, 5.49). No active gelatinase bands were observed, which indicated lack of expression. Low levels of proMMP-2 were measured for the 3T3L1 Mouse Fibroblast cell line which was cultured on the bulk Ca-based and Mg-based BMGs. Levels of proMMP-2 were statistically higher for the same BMGs embedded in the PCL variotis™ scaffold, with an increase of 30% and 300+% for the Ca-based and Mg-based BMGs respectively. High levels of MMP-2 were noted for the cell only and stainless steel controls, as well as most of the PCL disk samples.

High levels of proMMP-9 were detected for surgical stainless steel disks, however proMMP-9 was lower than the cell control for Ca-based and Mg-based BMGs, as well as for the Magnesium metal. Most of the PCL-based samples had similar MMP-9 levels to the cell control. The low level of proMMP-9 measured for PCL/Ca BMG corresponded with low levels of proMMP-2, due to low levels of cell growth.

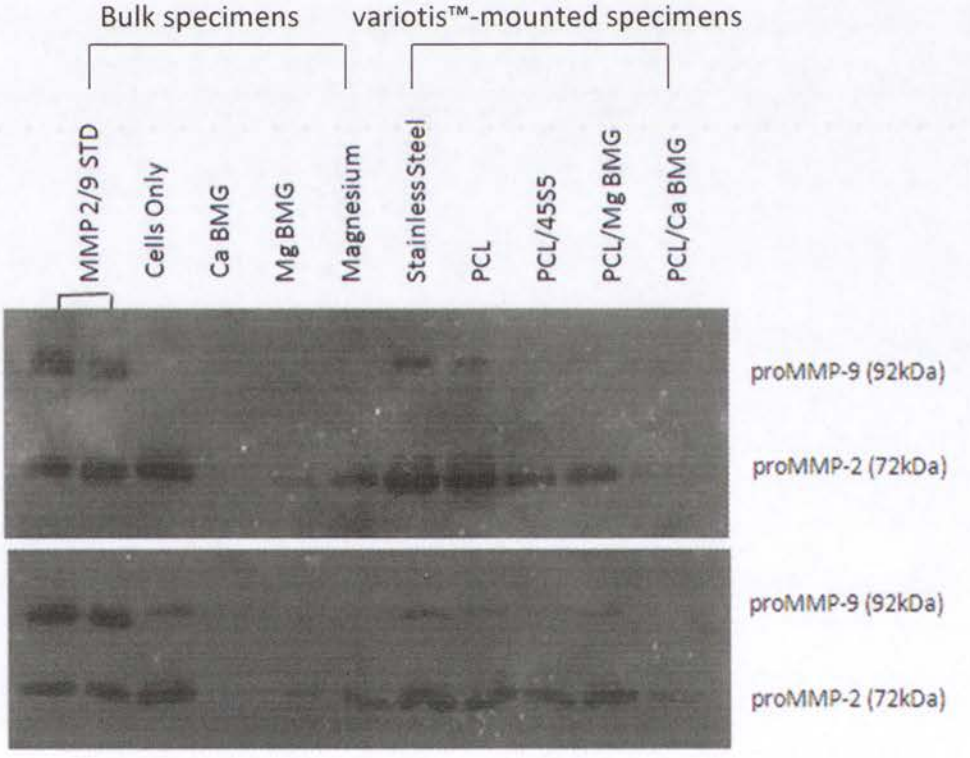


Figure 5.48. Gelatin zymography gel for matrix metalloproteinase expression.

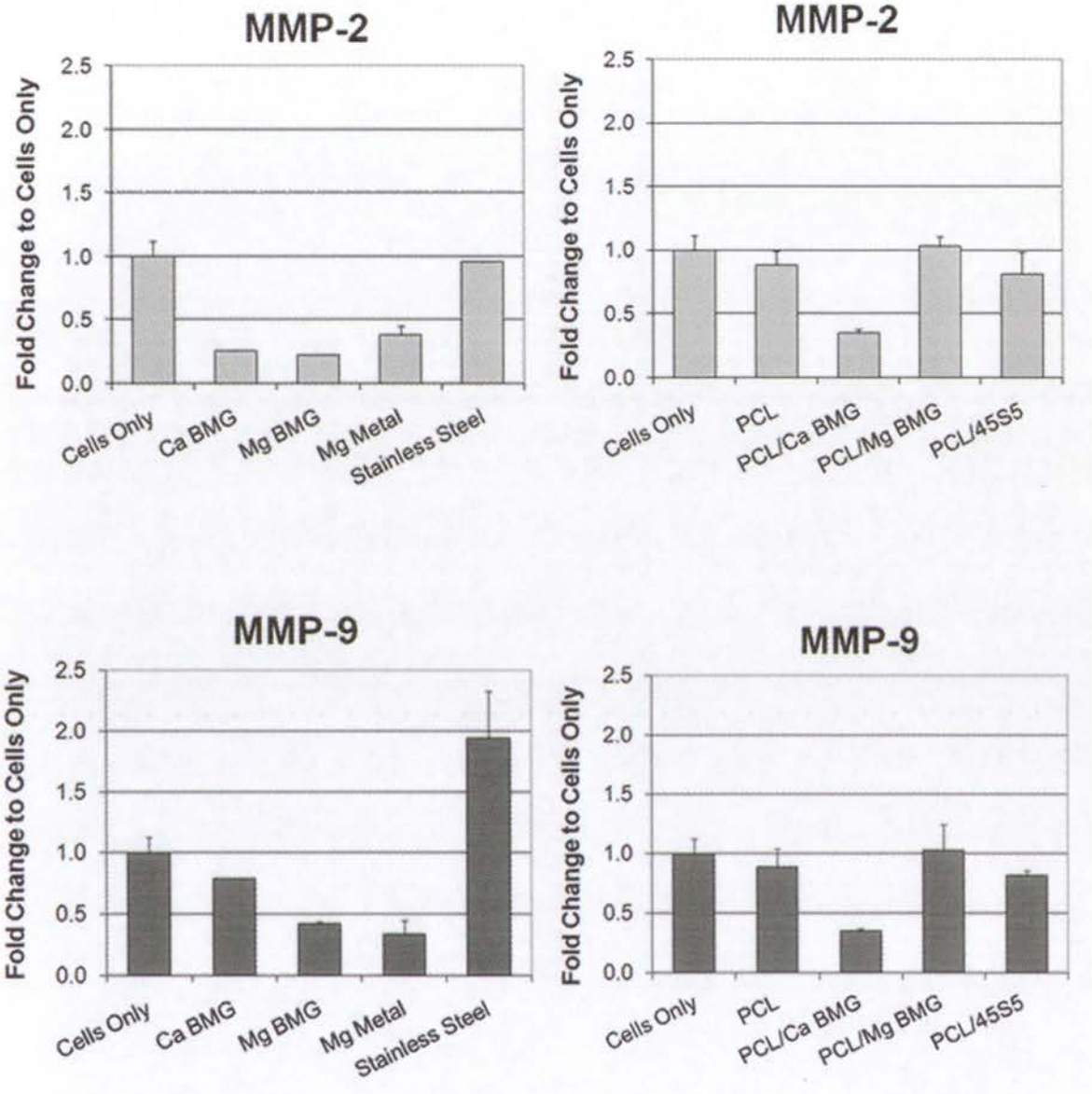


Figure 5.49. Matrix metalloproteinase expression for proMMP-2 and proMMP-9 of fibroblasts cultured on bulk BMGs and variotis™ scaffold-mounted powders.

Shown in Fig. 5.50, fluorescent microscopy demonstrated excellent levels of viable cells in the wells containing the Cells Only, Stainless Steel, PCL, PCL/45S5, PCL/Mg/BMG and PCL/Ca BMG. Cells were also observed attaching to and spreading on BMG powders.

In contrast, cells were not observed in the bulk Mg BMG cell well. Autofluorescing material was evident within this well, likely to be from cellular debris.

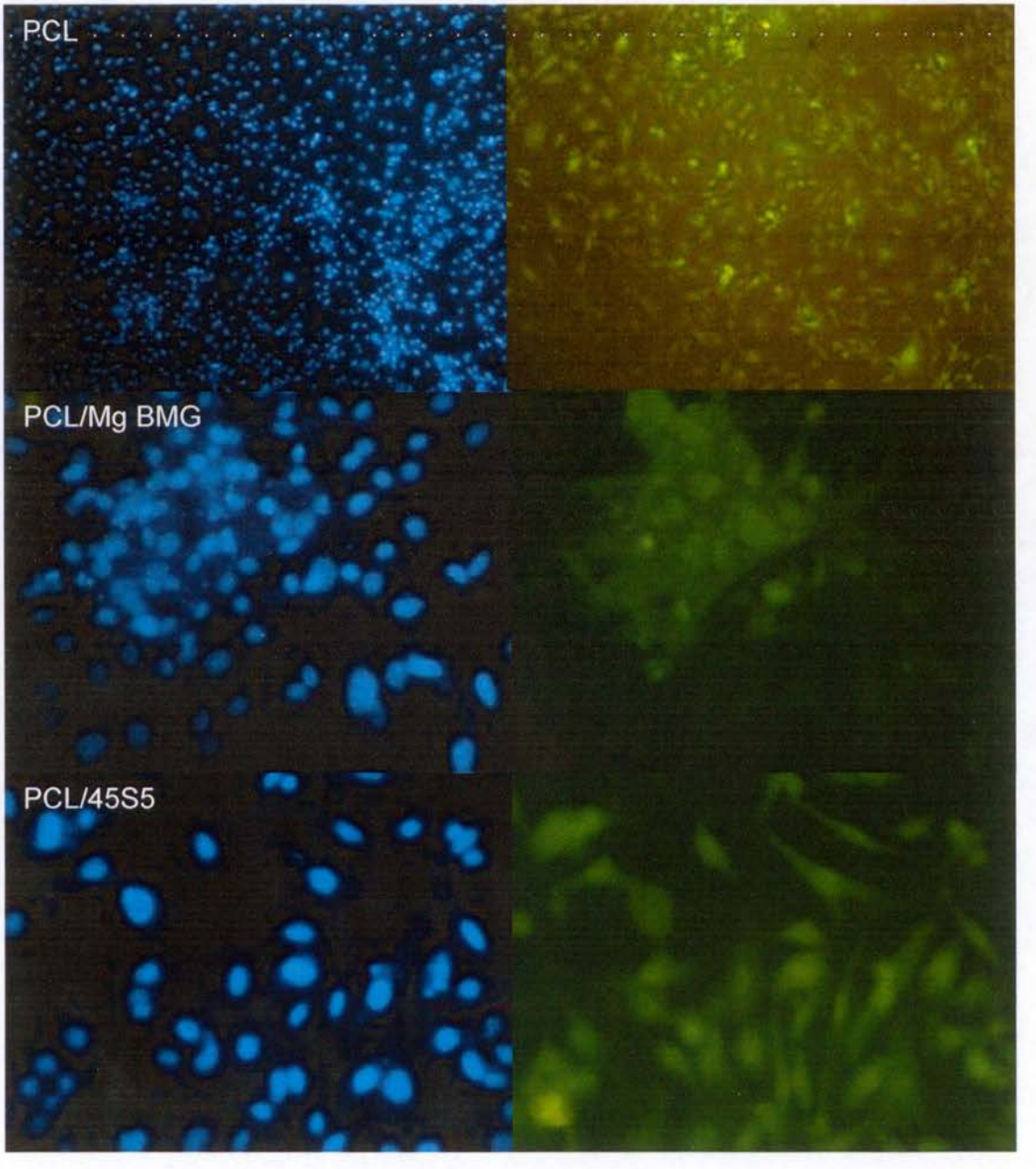


Figure 5.50. Representative images showing viable cells in the wells containing the PCL Variotis ™ disks. The three sets of images indicate plain PCL, PCL/Mg BMG and PCL/45S5. (DAPI, calcein).

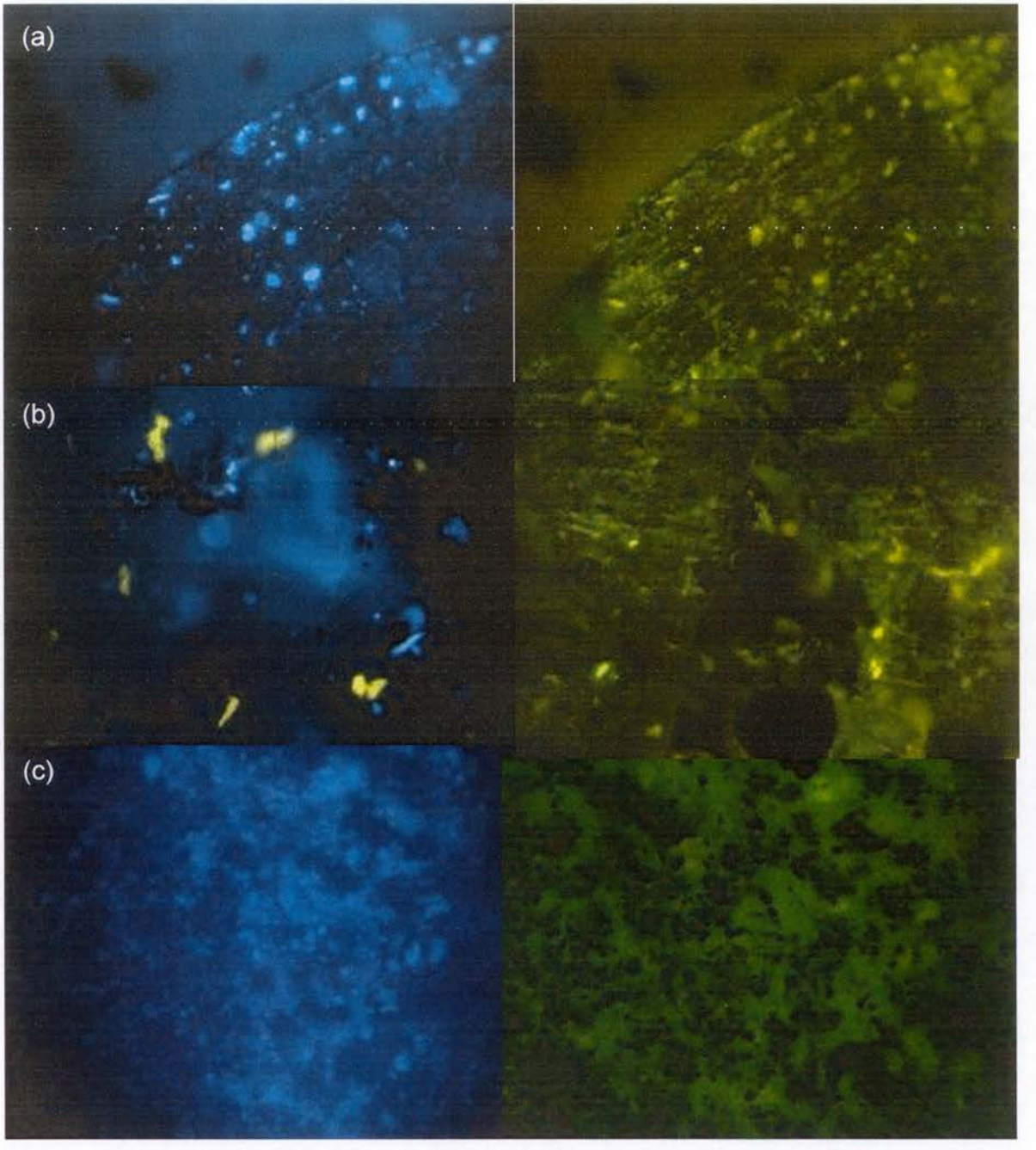


Figure 5.51. (a) Cells on the edge of the Ca-BMG (b,c) Autoflouorescing cell material and BMG fragments from the Mg-based BMG well. (left) DAPI (right) Calcein.

Table 5.3. contains a comparison of the data from this experiment, including the weight loss (% original weight), protein concentration and proMMP-9 and proMMP-2 levels.

Table 5.3. Relative weight loss, protein, MMP-9 and MMP-2 levels for the samples. Legend: 1=low levels, 5=high levels.

Sample	Weight Loss	Protein	MMP-9	MMP-2	Observations from Fluorescent Microscope
Cells Only	N/A	5	1	5	High levels of viable cells
Ca BMG	5	1	2	1	No viable cells, high inflammation
Mg BMG	3	5	1	1	Low level of viable cells, high levels of cell debris
Magnesium Metal	1	4	2	2	Slight precipitation, some viable cells
Stainless Steel	2	4	5	4	High levels of viable cells
PCL	2	5	2	4	High levels of viable cells
PCL/45S5	2	4	2	3	Moderate level of viable cells
PCL/Mg BMG	2	4	2	3	Moderate level of viable cells
PCL/Ca BMG	2	5	3	5	High level of viable cells, equal to stainless steel

5.5.3. DISCUSSION

The goals of this study were twofold: demonstrate the capacity of a novel technique for mounting biomaterial powders on scaffold disks, and to demonstrate the biocompatibility of biodegradable biometallic glasses which could be used as thin coatings on the variotis™ scaffold (ref section 4.1.3). Analysis of MMP expression of cells on BMGs was performed for the first time in the literature.

5.5.3.1. Findings of this BMG study

This study showed low or zero levels of viable cells after 4 days on Ca-rich or Mg-rich bulk BMG disks (which had been pre-soaked in media for 3 days). This is due to the extremely high reactivity of these materials. This was reflected in weight loss measurements after a total of 7 days in media (50 and 8.5% respectively). The evolution of hydrogen from the Ca BMG was observed, as has been previously reported [Mani 2007]. Pure magnesium metal disks also showed low levels of viable cells. Magnesium disks exhibited the formation of a magnesium oxide layer, corresponding with a weight increase of 6%. Stainless steel disks displayed a high level of cells and almost zero change in specimen weight. In contrast, when mounted on PCL variotis™ scaffold disks, the Ca-rich and Mg-rich BMGs showed high levels of cell growth, which

were similar to PCL or tissue culture polystyrene substrates. This was demonstrated by measurement of total protein content in the supernatant.

5.5.3.2. MMP Levels

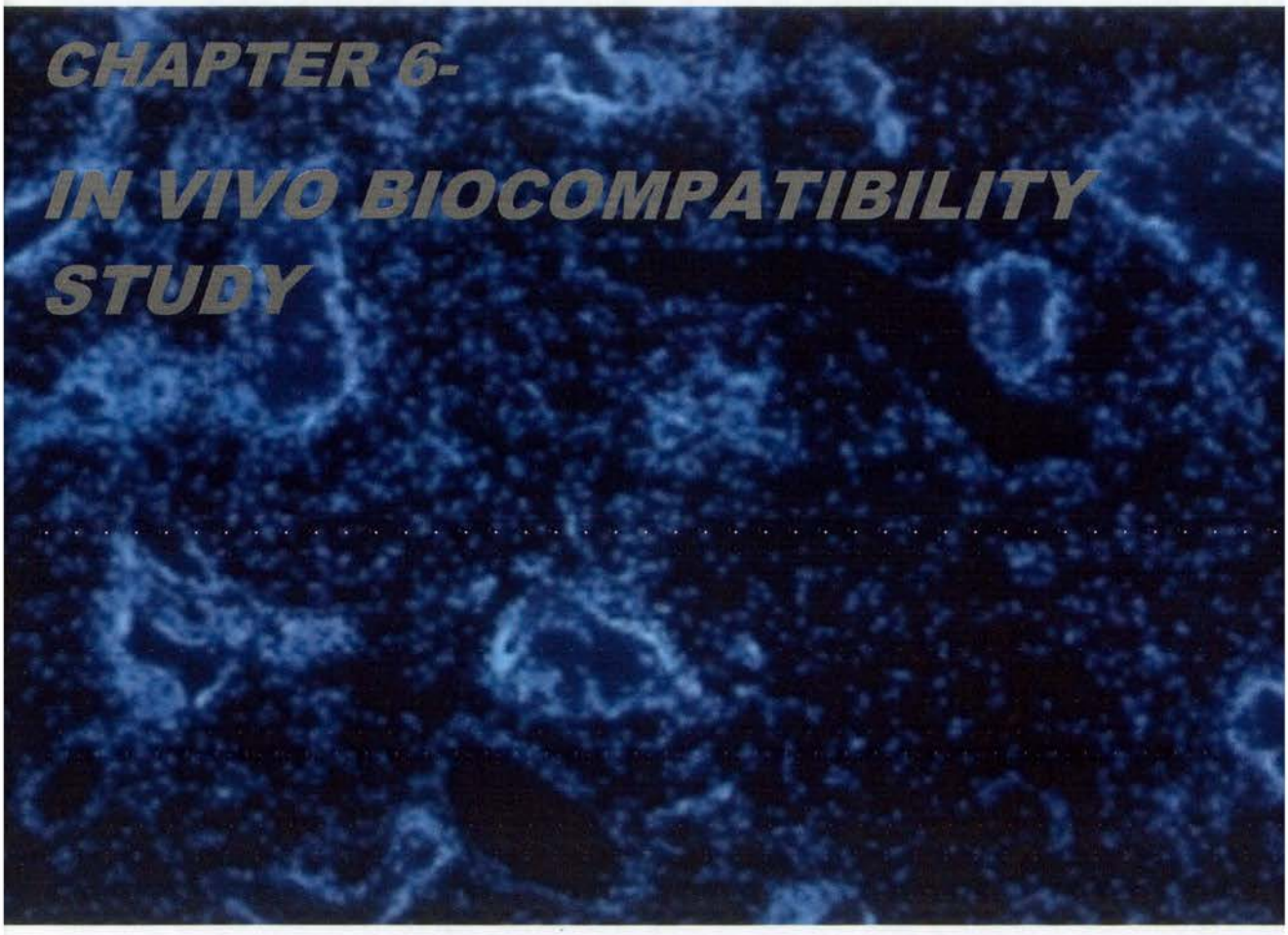
When MMP protein levels were measured using gelatinase zymography, there were no active bands observed. proMMP-2 levels were low for Ca-rich and Mg-rich bulk BMGs. proMMP-2 levels were increased when the BMGs were mounted on the scaffold disks, particularly for the Mg-rich BMG which showed an increase of 300%- to the same level as the cell only well. 45S5 glass mounted on the scaffold also showed high proMMP-2 levels. MMP-9 levels generally corresponded to levels of proMMP-2. Exceptions to this were bulk Ca-rich BMG disk and stainless steel which both showed high proMMP-9 levels. All the PCL-mounted specimens showed levels of proMMP-9 which were less than the cell control.

5.5.3.3. Comparison with previous studies

Previous studies have demonstrated the good biocompatibility and osteoconductive properties of BMGs [671, 672, 675, 682]. Their unique properties have led to worldwide interest as implant coatings or stent materials. The current study was the first cell study performed on BMGs which were synthesised by Michael Ferry's group at UNSW [674]. Recent studies have demonstrated the potential of BMGs for soft tissue applications [677]. A study by Gu [677] also showed higher cell viabilities for Mg-Zn-Ca glass supernatants than pure magnesium, in studies using murine fibroblasts and human osteosarcoma cell lines. Corrosion products of $Mg(OH)_2$ were identified- as would be the case in the current study. Obviously, these BMGs require optimisation of the level of Ca, Mg and Zn to reduce hydrogen evolution. For example, levels of >28% zinc has displayed no hydrogen evolution in vivo [671].

5.6. CONCLUSION

- Scaffolds with and without bioactive glasses (10% 45S5, 20% 13-93) were found to support fibroblast cell attachment, differentiation and proliferation. Higher cell proliferation and cytoplasmic processes stretching in 3D were evident on the glass coated scaffolds.
- PCL and Bioglass® composite scaffolds did not contribute to inflammatory response (MMP-9), but did stimulate positive modelling response (MMP-2) not dissimilar to that necessary for wound healing
- A range of novel methods were investigated to non-destructively obtain semi-quantitative indications of cell growth on thick scaffolds.
- Scaffolds were found to be relatively biostable throughout *in vitro* testing
- The manufacturing process of the glass and scaffolds was indirectly verified to be free of cytotoxic levels of contaminants and bioburden.
- Novel methods to use scaffolds to be a vehicle for miniscule yet controlled amounts of bioactive materials for cell tests were developed.
- Novel metallic glass coatings were found to be biocompatible using the scaffold mounting approach.



CHAPTER 6-

IN VIVO BIOCOMPATIBILITY STUDY

6.0. CHAPTER OVERVIEW

In this chapter, *in vivo* validation work for variotis™ scaffolds is reported. Subcutaneous implantation of PCL and Bioglass®-PCL composite scaffolds in 56 healthy rats was undertaken. Scaffolds were excised from days 2-42. Cellular infiltrate, collagen accumulation and vessel formation were examined through SEM, histology and immunohistochemistry. Observations on gross changes in scaffold volume or integrity were recorded. White cell counts were determined for circulating blood and wound fluids. Widespread fibrin coagulation was evident by day 2, and vascularised granulation tissue had formed within the scaffolds by day 7. Within 14 days, scaffolds were infiltrated through to the centre with neotissue which was rich in crystalline collagen and new vasculature networks. A slight increase in the rate of tissue infiltration and maturation was achieved for the Bioglass®-PCL scaffold. This study demonstrates that rapid neotissue formation and vasculature can develop within soft yet mechanically supportive scaffolds without the need for therapeutic growth factors. The mechanical stabilisation of the vascularised de novo tissues indicate potential for utilizing a similar type of scaffold in a novel burns graft to prevent debilitating wound contraction from occurring.

6.1. INTRODUCTION

6.1.1. ANIMAL MODELS

Animal models are often used to demonstrate the soft tissue biocompatibility of materials [7, 10, 14, 18, 58, 59, 61, 62, 68, 73, 84-87, 773]. Models include insertion of an implant into a subcutaneous pocket [10, 772], cutaneous wound closure [256, 544], abdominal wall [68] or muscle implantation [73]. Although the biocompatibility of PCL and Bioactive glass are well established, the form of the material should always be tested for a particular application.

6.1.2. TISSUE INGROWTH AND VASCULARISATION OF SCAFFOLDS

The restoration of fully functional tissue is an extremely important goal of tissue engineering. Functional tissue is less likely to become a loci for infection [61, 773]. This was a major impetus for a study by Misaki and coworkers [61], who were investigating the potential for polylactic acid/polycaprolactone copolymer biodegradable matrices to induce tissue filling in the dead space which remains after pneumonectomy in the thoracic cavity.

Animal studies rarely demonstrate adequate, functional tissue restoration. The majority of studies involve incomplete or immature tissue formation within porous scaffolds [14, 61, 84, 86, 87]. Reasonable tissue ingrowth is generally achieved using thin scaffolds [59, 62], over a long period of time (generally >6 weeks) [168]. Good tissue ingrowth has been achieved by 6 weeks in porous polyethylene ocular implants, although these are permanent implants [771].

The vascular network which forms within scaffold pore vacancies is usually absent or insufficient to sustain long term tissue health [14, 84, 87]. In addition, vascularisation reported in the literature often lies within the fibrous capsule surrounding the scaffold, rather than within the pores [85]. This is an important distinction- almost any biomaterial will illicit an increase in capillary density surrounding it, as the result of an inflammatory response. However, there are few reports of vessel formation within scaffolds. Vessel ingrowth to the scaffold is important to aid restoration of healthy tissue.

Reasons for incomplete tissue infiltration and vascular development include inadequate porosity/pore diameter/pore throat dimensions, aggravated inflammatory response due to acidic byproducts [14], fibrous capsule formation [61, 62], poor interconnectivity [85] and inefficient, tortuous pathways from the outer edge to the centre of the scaffold.

Examples of porous scaffolds which have achieved varying levels of tissue and vessel ingrowth are described in Table 6.1 and will now be reviewed in detail. Scaffolds will be examined according to their structure and fabrication process as introduced in section 3.1.6. This includes woven meshes, sintered scaffolds, rapid prototyped scaffolds, and freeze drying/porogen techniques. Hydrogels are also examined due to their popularity for skin engineering. The *in vivo* effect of the addition of bioactive glass to scaffolds will then be reviewed.

6.1.3.1. Hydrogels

6.1.3.1.1. Elastin (Kurane 2007)

Kurane and coworkers [627] subcutaneously implanted porcine artery-derived elastin tubes, into rats, for harvest after 7 or 28 days (shown in Fig. 6.1). Some scaffolds were loaded with FGF via agarose gel. After 28 days, the scaffolds with the growth factors achieved tissue infiltration to a depth of 107 μm. This is quite a poor result as it only reflects only 45% of the depth of the thin scaffolds. The scaffolds which did not contain growth factor achieved an even lower level of tissue infiltration (42 μm). Macrophages were present within the scaffold at 7 days but this had reduced by 28 days. These findings indicate that the permanent elastin scaffold was not being remodeled by macrophages, and the limited interconnectivity did not favor cell infiltration. Mature collagen bundle formation would be difficult within this scaffold, and a wound treated with this material could lack strength.

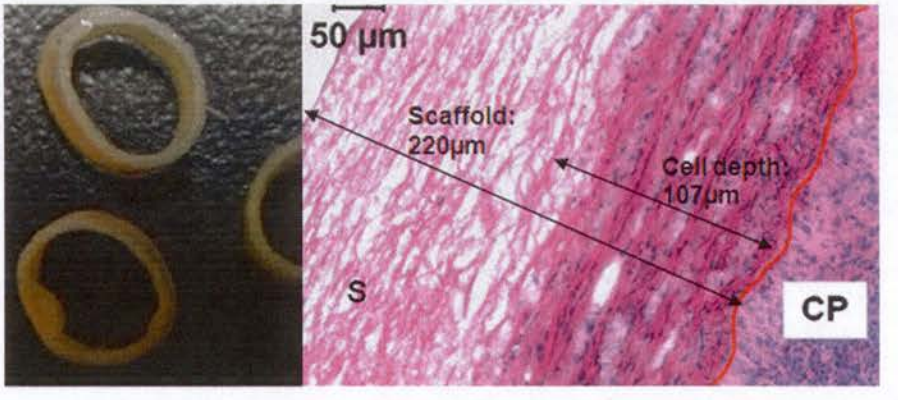


Figure 6.1. Elastin tubes before and after subcutaneous implantation for 28 days (H&E staining). S: scaffold, CP: capsule. The red line indicates the boundary between the scaffold and capsule [627].

Table 6.1. Degree of in vivo tissue filling and vascularisation within polymer scaffolds.

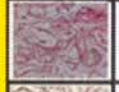
	Image	Author	Material (Synthesis Process)	Thickness	Pore Size	Tissue in Scaffold	Vascularisation in Scaffold	Comments	Ref
Hydrogel		Kurane 2007	Elastin	220um	<50um b/w fibres	50% infiltration by 28 days with bFGF delivery	No		627
		De Jong 2007	Dextran (methacrylate)	1mm	Nonporous	No	No	Fibrous capsule. Minimal cells within gel. Skin ulcer formation and wound healing impairment due to inflammation.	628
		Kimura 2010	Collagen	3mm	<100um between fibers	Adipose by 4 weeks	Capillaries		16
		Rhodes 2007	Hyaluronan (SL scaffolds)	5mm	400um	Fibrous tissue (12wks)	Low levels		57
		Rhodes 2007	Hyaluronan (viscous gel)	-	Nonporous	Mature adipogenesis (12wks)	High levels		57
Woven mesh		Day 2004	PGA/BG	1cm	~10um b/w fibres	Infiltration by 14 days, however little collagen as low porosity, due to thick fibers	Vessels with lumens by 2 wks	Acidic byproducts from PGA	86
		Nienhuiis 2004	GORE PGA/TMC	-	-	Unclear. Most collagen deposition between 3-6 months (38-91% increase), as material absorbed.	Yes	Clinical product	68
Sintered		Park 2005	Medpor PE	-	>100um	Substantial ingrowth by 4 wks and almost complete by 6 wks.	Yes	Clinical product	7, 168
Rapid Prototyped		Low 2009, Schantz, 2003, 2007	Osteoplug PCL	14mm	400-600um	Some bone ingrowth by 4 mths, unclear whether complete ingrowth was achieved	Yes	Clinical product	58, 18, 71
		Lam 2009	Osteopore PCL, PCL/TCP	2.5mm	<700x500um	PCL- 3mths-adipose, 6mths fibroblasts PCL/TCP- 3,6mths- fibroblasts	Yes,	Stress shields soft tissue- lack of collagen deposition	83
		Woodfield 2004	PEGT/PBT	4mm	185x600um	Tissue ingrowth complete by 3 wks (rich in cartilage ECM)	N/A	Precultured with bovine chondrocytes	59

Table 6.1. cont...

	Image	Author	Material (Synthesis Process)	Thickness	Pore Size	Tissue in Scaffold	Vascularisation in Scaffold	Comments	Ref
Porous Foams		Day 2005	PDLA (NaCL porogens, compression)	3mm	<100um	Tissue ingrowth incomplete by end of study (<20% infiltration by 6 wks)	No	Poor interconnectivity	85
		Day 2005	PDLA (TIPS)	3mm	3mm, <200um	Tissue ingrowth incomplete by end of study (50% infiltration by 6 wks).	No	Tissue infiltration greater along one axis	85
		Cao 2006	PLGA (TIPS)	6mm	-	Some ingrowth by 2 wks. Some tissue death at 8 wks. Tissue survival in 300-400um pores.	Yes in larger pores- much less than surrounding tissue	Polycarbonate chamber & AV loop. Aggravated foreign body response.	14
		Cao 2006	PLGA (SC/NaCL PL)	6mm	<300um	Some ingrowth by 2 wks. Some tissue death at 8 wks. Tissue survival in 300-400um pores.	Yes- in wider pores by 2 wks	Polycarbonate chamber & AV loop. Aggravated foreign body response.	14
		Yamamoto 2000	PVA (starch PL)	2mm	250, 350 or 700um	Incomplete by end of study (At 6 wks, <80% infiltration for pore sizes 250, 350, 700um)	Yes; for pore size 350um only.		84
		Lee 2003	PGCL (NaCL PL)	2.5mm	200-300um	Good tissue by 3 wks	Not reported	Highly elastic scaffold	60
		Hofer 2003	PLGA (NaCL PL)	7mm	7mm, 95um	Incomplete by end of study (8 wks)	Vessels with lumens by 2 wks	Polycarbonate growth chamber & AV loop	87
		Misaki 2007	PLAC (TIPS/NaCL porogens)	8mm	200-400um	Complete by 2 months	Not reported	Fibrous collagen layer surrounding scaffold at 1 month.	61
		Bezuidenhout 2008	PU (TIPS/gelatin porogens)	2mm	147um	Compete by 4 wks	By 4 wks	Fibrous capsule. Vascularisation invreased by heparin.	62

6.1.3.1.2. Dextran (methacrylate) (De Jong 2007)

De Jong and coworkers [628] examined the tissue responses of hydroxyethyl-methacrylated dextran (dex-HEMA) hydrogels which had been subcutaneously implanted in mice or rats. Implants were examined after 2, 6 and 13 weeks. Shown in Fig. 6.2, after 2 weeks, the implants from the rats demonstrated a slight fibrous capsule with minimal levels of cell infiltrate-including macrophages and fibroblasts. Fragments of the hydrogel were taken up by macrophages (giant cells) as the hydrogel degraded. The implants in the mice showed a moderate-strong capsule formation after 2 weeks. Draining lymph node activation was observed at 2 weeks, as a reflection of the marked inflammation surrounding the implant, however this had subsided by weeks 6 and 13. As these implants were bulk gels, cellular ingrowth occurred as the implant degraded. However, ½ the implants in this study formed skin ulcers due to the excessive levels of inflammation and capsule formation. In addition, in a relatively large number of the implants, the healing of the surgical wound was not complete by 2 weeks. This study indicates that even though a material exhibits minimal levels of inflammation *in vitro*, it could cause unacceptable responses *in vivo*. These implants, due to their lack of porosity, contained a high level of foreign material, which exacerbated the *in vivo* inflammatory reaction.

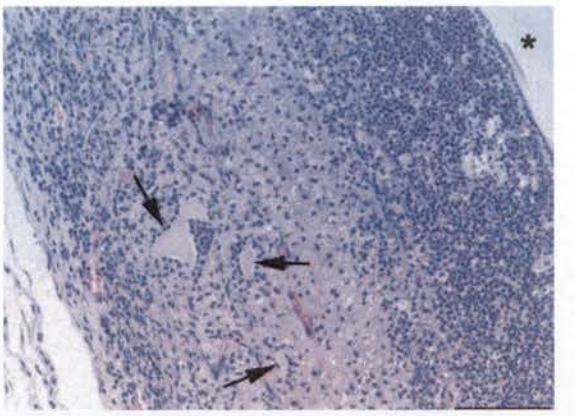


Figure 6.2. Two weeks after implantation in mice a marked inflammatory response was evoked. The implant (*) was surrounded by Polymorphonuclear Neutrophils and macrophages, which were also degrading the implant (arrows) [628].

Collagen (Kimura 2010)

Kimura and coworkers [16] observed adipose tissue regeneration within porous collagen sponges. The sponges had degradation times which varied from 1-4 weeks. The sponges were made from bovine collagen, preseeded with human preadipocytes and implanted subcutaneously in mice. The highest level of adipose tissue regeneration and capillary formation was observed in the scaffold which degraded in 2 weeks (Fig. 6.3a). Less tissue regeneration was observed in the fast-degrading scaffolds (<2 weeks). The 4 week sample contained eosin-stained ribbon-like matrices at the implantation site.

This study highlights problems which can occur with rapidly degrading scaffolds. Such scaffolds often provide a lack of support for the developing tissue. In addition, these collagen scaffolds are likely to have small pore sizes and poor long-range interconnectivity. Therefore, to allow tissue ingrowth into the scaffold, it is important that the material degradation occurs at a

similar rate to tissue ingrowth and vascularisation. For a highly porous, interconnected scaffold, like variotis, this degradation property is not so important.

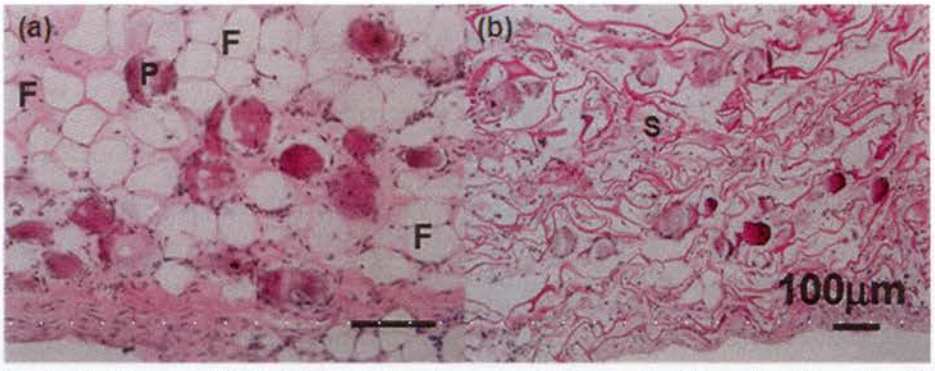


Figure 6.3. Histological images (H&E staining) of collagen scaffolds excised 4 weeks after subcutaneous implantation. (a) Collagen scaffold which degraded in 2 weeks, (b) Collagen which degraded in 4+ weeks. F: mature adipose, P: preadipocyces, S: scaffold [16].

6.1.3.1.4. Hyaluronan (Rhodes 2007)

Rhodes and coworkers [57] compared the *in vivo* response of modified hyaluronan porous scaffolds (400 μm, salt leaching) and viscous gels. The hyaluronan was implanted subcutaneously into rats for periods of up to 26 and 12 weeks respectively. The results are shown in Fig. 6.4. below. While the gels resulted in significant angiogenesis and the formation of mature adipocytes within the implant by 12 weeks, the scaffolds demonstrated fibrous tissue ingrowth and much lower levels of adipogenesis. It is likely that the viscous gels were actually in a form which enabled quicker degradation and therefore a more pronounced, early inflammatory response. This would lead to increased vascularisation and potential for adipogenesis. The authors suggest that previous work has also demonstrated the potential for macrophages to transdifferentiate into adipocytes [785].

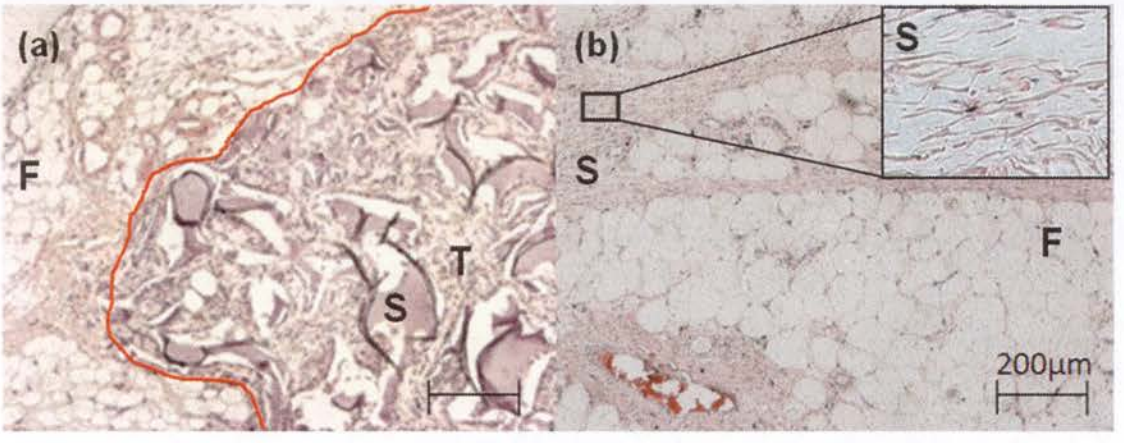


Figure 6.4. (a) Acellular porous hyaluronan-based scaffold and (b) Acellular, hyaluronan-based viscous gel scaffold, after 12 weeks subcutaneous implantation in rats. S: scaffold, F: mature adipose, T: tissue (collagen, fibroblasts etc) [57].

6.1.3.2. Woven Meshes

6.1.3.2.1. PGA/BG Mesh (Day 2004)

Day and coworkers [86] used a subcutaneous implant model in rats to investigate the *in vivo* response of PGA and PGA/BG knitted meshes. Although the 1 cm thick meshes were fully cellularised after 14 days, limited collagen was able to form due to the small, unidirectional spaces between fibers (Fig. 6.5). Blood vessels were present inside the scaffold from day 14, and at day 42 some were quite sizable as the scaffold degraded.

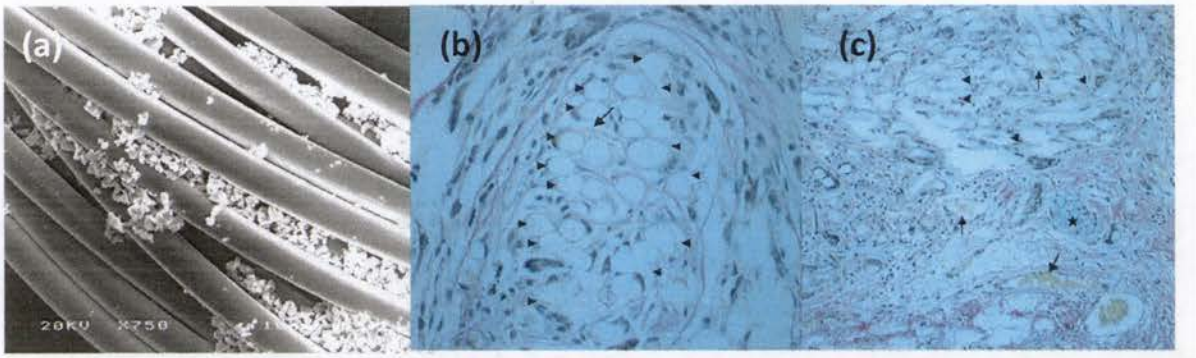


Figure 6.5. (a) SEM of PGA/45S5 Bioglass® composite mesh. Subcutaneously implanted meshes with surrounding tissue at (b) 14 days and (c) 42 days (H&E and van Gieson staining, arrows show blood vessels, arrow heads show woven mesh fibers and * indicates Bioglass®) [86].

6.1.3.2.2. PGA-TMC Hernia Mesh- BIO-A® Hernia Plug, GORE (Nienhuijs 2004)

Nienhuijs and coworkers [68] designed a copolymer Polyglycolic acid/ trimethylene carbonate (67% PGA-33% TMC) biodegradable hernia mesh plug. It is now commercially available as the GORE® BIO-A® Hernia Plug, and indicated for the reinforcement of soft tissue in the groin, abdominal and umbilical regions. The plug has the structure of a flat disk crowned with 12 hollow, flexible tubes, made from woven polymer fabric. These plugs have been shown to beneficially reduce unwanted adhesion to abdominal structures, migration and nerve entrapment, compared to the current polypropylene plugs.

When implanted into the inguinal floor during clinical trials, the plugs were observed to experience mass loss from 40-5% during 3-6 months. During this period, a loss of crystallinity of the PGA-TMC was observed using polarised light microscopy. New collagen grew in the spaces remaining from the absorbed PGA-TMC, with the level of collagen increasing from 38-91% from the 3-6 month timepoints. In the space around the bioabsorbable plug the presence of macrophages, foreign body giant cells, fibroblasts and some blood vessels were observed. In contrast, the traditional permanent polypropylene plug demonstrated a higher level of lymphocytes, indicating an ongoing inflammatory reaction which increases pain for patients. No blood vessels were observed surrounding the polypropylene plug. [68].

The GORE bioabsorbable plug has been adapted for gastrointestinal closure (Fig. 6.5.), since no biosynthetic materials are currently on the market for this purpose. Gastrointestinal closure requires a prosthetic to form an effective seal, allow tissue ingrowth and tolerate the local environment. Such bioabsorbable plugs can be implanted using minimally invasive techniques. The PGA-TMC plug was tested in a gastrointestinal model in canines. At 8 weeks, the maximum level of collagen ingrowth was detected. At 12 weeks, as the matrix was dissolving, the collagen was less prominent but more organised [775].

Several other bioabsorbable meshes have been proposed as soft tissue repair systems. A Finnish group led by Tormala described a woven polyglocolic acid (PGA)/P(D,L)LA mesh which is combined with two other polymer layers, in order to prevent attachment to the abdominal wall [69]. Dexon (PGA) and Vicryl (polyglactin 910) meshes [777] have also been investigated for breast surgery. They have been shown to create fluid-filled cysts lined with granulated scar, which fill the undesirable dead space. The meshes fully degrade within 30 days, and the cysts slowly reduce in size. However, calcification has been noted in some breast reconstructive surgery using meshes of polyglactin/polyester [778]. Calcification is a common problem in many implants, which can be minimised with proper tissue integration.

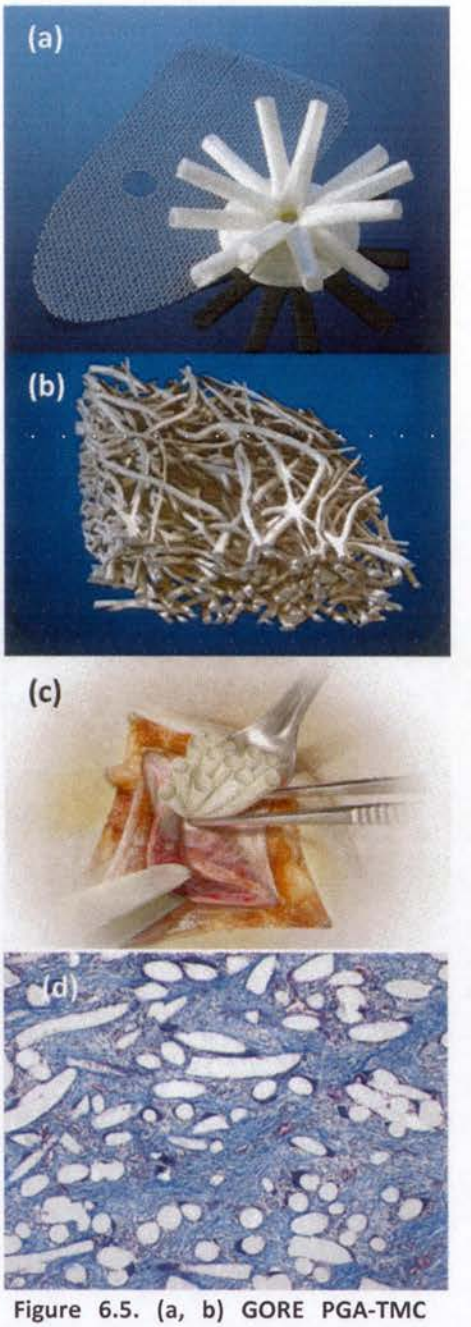


Figure 6.5. (a, b) GORE PGA-TMC Hernia plug (c) Insertion of the plug into a gastrointestinal wound (d) Collagen ingrowth around the plug remnants at 8 weeks (10x, trichrome stain) during a gastrointestinal perforation study [775, 776].

6.1.3.2.3. Polydioxanone (PDS) Hernia Mesh (Entenmann 1999)

Entenmann and coworkers [73] designed a novel, ellipsoid-shaped knitted PDS mesh for treatment of abdominal wall defects. The implants were positioned in the abdominal wall of rats with explantation occurring after 21, 42 and 180 days. By 21 days, infiltration of tissue components from the adjacent abdominal wall was evident. 42 days post implantation the implant showed a progressive ingrowth of connective tissue including fibroblasts, the formation of collagenous networks and blood vessels. At the ventral portion of the implant,

the collagen fascicles were more homogenously arranged. This suggests that the ventral region is preferentially exposed to tension forces, which are known to stimulate the proliferation of fibroblasts and to induce a functionally effective arrangement of the collageneous network [779]. In contrast to the ventral portion of the implant, the dorsal region showed a more irregular arrangement of collagen fascicles and a relatively thin neo-fascia. The presence of adipocytes, most likely due to the differentiation of connective into fat tissue, further supports the assumption that the dorsal portion of the implant has been insufficiently exposed to tension forces 130 days post implantation the meshes began to bulge out of the ventral abdominal wall. The authors concluded that in the future a material with longer absorption time would be necessary to allow a sufficient consolidation of the ingrowing connective tissue to resist the tensile forces present in the abdominal muscle.

6.1.3.3. Sintered Scaffolds

6.1.3.3.1. Polyurethane Orbital Implants- Medpor, Porex (Park 2005)

Sintered polyurethane porous scaffolds are available commercially for craniofacial reconstruction and augmentation, particularly in the orbital cavity (eye socket) [7, 169, 771] (Fig. 6.6). In a rabbit study, 14mm Medpor implants were placed into the right orbit. By 4 weeks, substantial fibrovascular ingrowth was noted into the polyethylene implants (Fig. 6.6c). The fibrovascular growth had increased by 6 weeks to 80-100% of the implant volume. Vascularisation was observed throughout the scaffold. This is a high level of tissue ingrowth and vascularisation, and was achieved despite the scaffold's low porosity (50%), omnidirectional pores, limited pore size (>100 μm) and thick struts (200 μm+). However, this is a permanent implant and so comparisons are difficult to make with bioabsorbable implants. Had it been made of certain bioabsorbable materials, excessive inflammation could have occurred due to high volumes of material which needs to degrade. In addition, this implant is extremely rigid, due to its choice of material and low porosity. This is an advantageous property for enabling carving and molding of custom implant shapes for bone interfaces. However, this implant is unsuitable for most soft tissue applications.



Figure 6.6. (a,b) Polyethylene Medpor implants for craniofacial reconstruction (c) Fibrovascular ingrowth into the scaffold after 4 weeks orbital implantation (white=scaffold) [7]

6.1.3.4. Rapid Prototyped Scaffolds

6.1.3.4.1. PCL Bone Burr plug- Osteoplug, Osteopore (Low 2009)

Osteoplug (*Osteopore* International Pty Ltd., Singapore), is an FDA approved, bioresorbable PCL implant. It is designed to cover burr hole skull defects, which commonly occur during neurosurgery [58, 71, 251]. Human studies have shown good osseointegration into the surrounding calvarial bone at 1 year and excellent cosmetic results. No infection or adverse systemic reactions have been noted. This scaffold has a high level of repetition and interconnectivity, due to synthesis via rapid prototyping. It is 60-70% porous, with a pore size of 400-600 μm and strut diameter of 300 μm. The scaffold is designed to be placed snugly within the scull, with a snap-fit, without the need for plates and screws. Fibrin glue is used to seal the defect. After 3 months, osseointegration was not visible using CT, but was observed at 4 months. Multifocal mineralisation was noted in one patient, after 1 year. Most patients did not undergo a CT at 1 year and so it is unclear how the implant was responding in all patients. The stiffness of the implant after 3 months was 60% that of healthy bone [18]. These PCL implants have advantages over polyethylene, hydroxyapatite and titanium, generally used for burr plugs/mini plates, such as biodegradability. Neovascularisation was observed in implants placed in animal models, whether they were unseeded or seeded with osteoblasts or mesenchymal stem cells [18]. A later study by the same group using PCL implants demonstrated native cell migration and angiogenesis, however this was not achieved without the presence of the cytokines (VEGF, SDF-1) [780]. This study provided a novel technique of providing cell guidance via directed cytokine delivery which can enable polarised tissue formation.

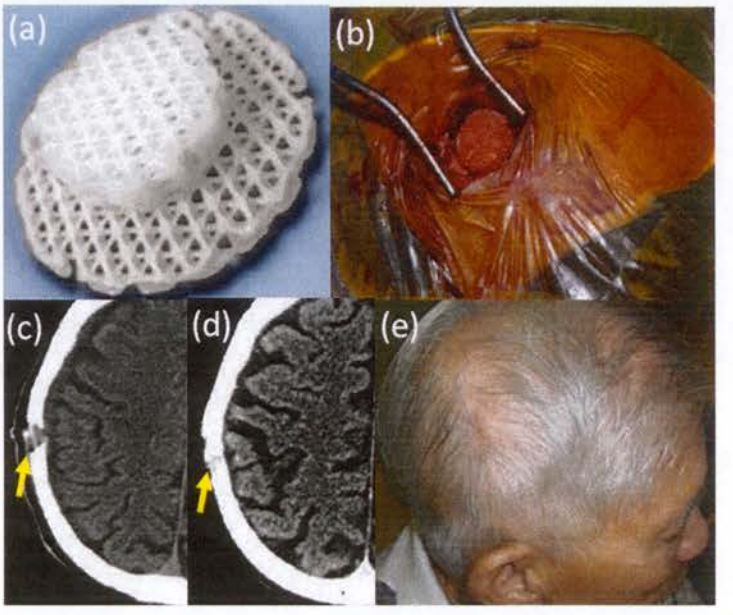


Figure 6.7. (a) Osteoplug implant, designed for a 14mm burr hole, (b) Implantation into the burr hole. Axial CT image of a burr hole in the skull, taken at (c) 1 month post operation and (d) 1 year post operation. (e) A good cosmetic result [18].

6.1.3.4.2. PCL Bone Scaffold (Lam 2009)

Lam, Hutchmacher and coworkers [83] synthesized PCL scaffolds from fused deposition modeling, and demonstrated the scaffolds showed little degradation after 6 months *in vitro* (Fig. 6.8a,b). When implanted into rabbit calvarial defects, many pores and some scaffold struts had been replaced by bone after 2 months. Subcutaneous rabbit studies achieved adipose within the scaffold after 3 months, but by 6 months this had been replaced by fibroblasts (Fig 6.8d,e). When tricalcium phosphate (TCP) was incorporated into the PCL scaffold, high levels of fibroblasts were present after both 3 and 6 months (Fig. 6.8f,g). Some vascularisation was observed at all of these timepoints. No generalised inflammatory activities were detected for the PCL scaffolds. The crystallinity of this PCL scaffold increased by 3% over the 6 month *in vitro* degradation study, corresponding to a rise of 150% in scaffold stiffness (2.5 MPa to 3.6 MPa).

This scaffold was extremely stable due to structure of the PCL scaffold, which had thick, nonporous struts (250 μm diameter). Fibroblast migration within this scaffold could have been facilitated by the high porosity, large pore size and good level of interconnectivity. However, a lack of collagen deposition could indicate stress shielding of the tissue. This scaffold is extremely stiff (modulus=2.5 MPa) and this limits the force transferred to the developing tissue.

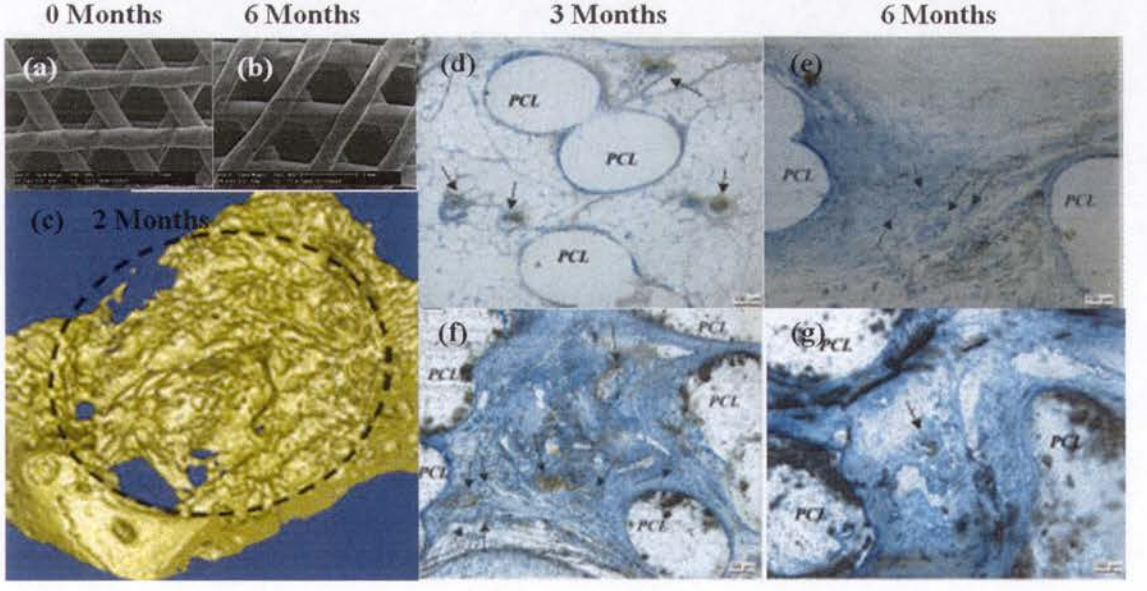


Figure 6.8. Fused deposition modeling PCL scaffold at (a) 0 months (b) and after 6 months *in vitro* degradation. (c) MicroCT of bone growth after 2 years of the scaffold in a rabbit calvarial defect model. Soft tissue growth in the PCL scaffold at (d) 3 months and (e) 6 months. Soft tissue ingrowth into a PCL/TCP scaffold at (f) 3 months and (g) 6 months (Giemsa stain, scale bar 400 μm). The arrows indicate blood vessels, black dots are TCP particles, erythrocytes are grey/yellow, collagen is pink, mast cells are purple, leukocytes are red/orange and most cells are pale blue [83].

6.1.3.4.3. Poly(butylene terphthalate) (PEGT/PBT) Osteochondral Scaffold (Woodfield 2004)

Woodfield and coworkers produced a poly(butylene terphthalate) (PEGT/PBT) scaffold with a 100% interconnecting pore network using FDM [59]. These scaffolds had a porosity of 70%, and average interconnecting pores of 185μm in one direction and ~600μm in the others. The scaffolds were dynamically cultured with bovine chondrocytes in spinner flasks, for 7 days, prior to subcutaneous implantation in mice. After 21 days, the mice were sacrificed and the tissue was examined using SEM and histology (Fig. 6.9). Cells were observed throughout the scaffold, although there was a thick fibrous capsule around the scaffold. *In vitro* culture of this scaffold had resulted in a thin capsule of fibroblast-like cells. This was previously observed by other studies involving dynamic culture of cartilaginous constructs *in vitro* [781, 782]. After *in vitro* dynamic culture, ECM cartilage products were produced (GAG and Col II), which the chondrocytes were suspended in.

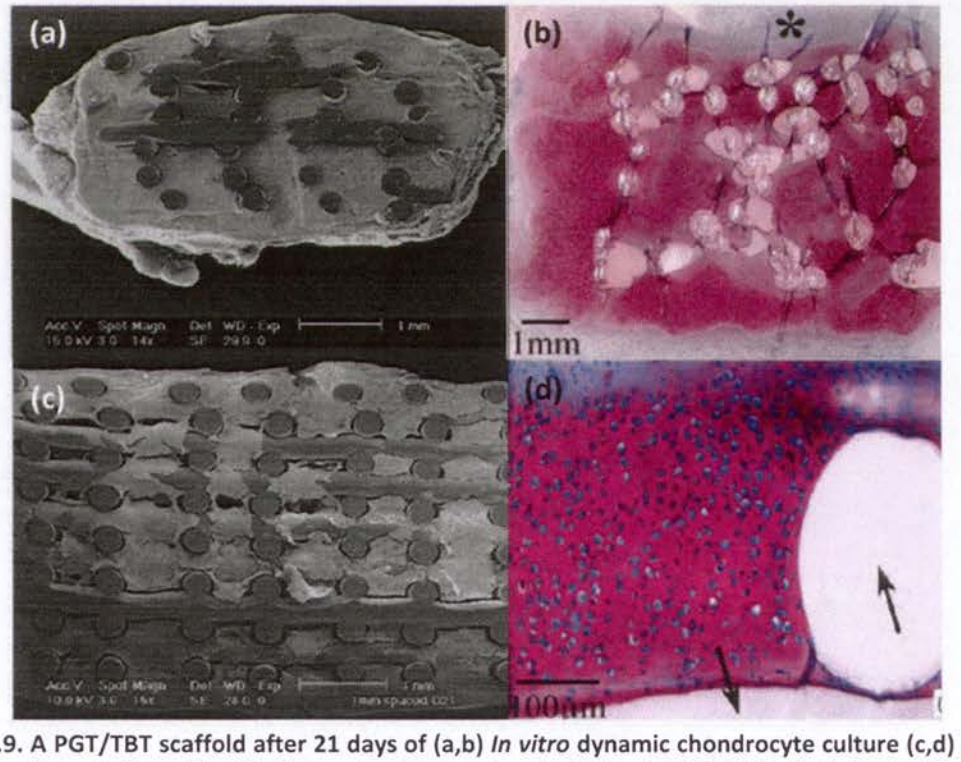


Figure 6.9. A PGT/TBT scaffold after 21 days of (a,b) *In vitro* dynamic chondrocyte culture (c,d) *In vitro* dynamic culture followed by 21 days subcutaneous implantation (a,c) SEM (b,d) Stained with H&E. * denotes a thick fibrous capsule and arrows refer to the lacunae (spaces) left from polymer struts [59].

6.1.3.5. Freeze Drying/Porogen Techniques

6.1.3.5.1. PLGA Scaffolds (Day 2005)

PLGA scaffolds investigated by Day and co-workers [85], were synthesised using 2 methods: (1) Compression Molding with porogens (2) Freeze Drying (also known as Thermally Induced Phase Separation- TIPS) (Fig. 6.10a,b). When subcutaneously implanted into mice, both scaffolds failed to be completely infiltrated by fibrovascular tissue by 6 weeks (Fig. 6.10c,d). The compression foams, whose pores were cuboidal and walls thicker, exhibited less tissue infiltration. The freeze dried foams exhibited greater tissue infiltration, however, this was dependent on the pore orientation of the foam (Fig. 6.10e,f). The authors found the layer of granulation tissue surrounding the scaffolds to be thicker when a 0.1% BG coating was used. This suggests a stimulatory effect of bioactive glass on blood vessel inducing factors, or could be due to the earlier dissolution of PLGA. An increase in this granulation tissue layer was also observed with the freeze drying method. The thickness of the granulation tissue layer decreased between weeks 4 and 6 for many of the scaffolds tested in this study.

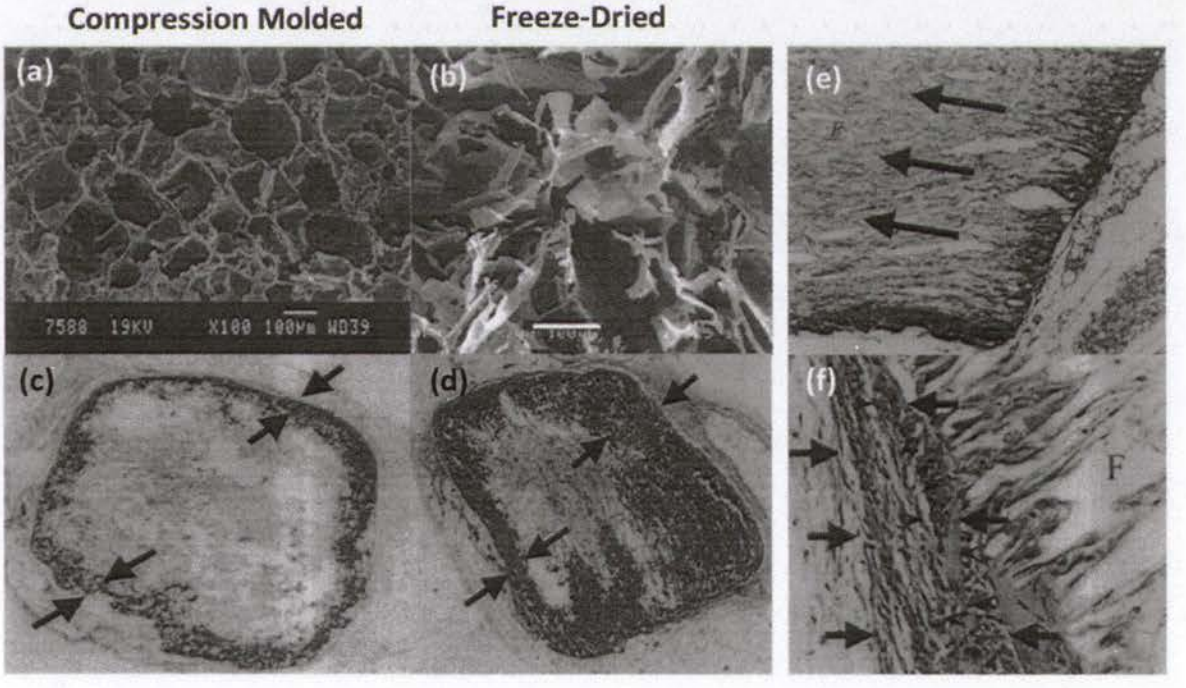


Figure 6.10. SEMs of (a,c) Compression Molded and (b,d) Freeze Dried PLGA scaffolds. (a,b) Prior to implantation and (c,d) Incomplete tissue filling by 6 weeks. (e) Tissue infiltration was greater along the direction of the pores of the freeze dried foam. (f) The arrows indicate the granulation tissue layer surrounding the foam (F), in which blood vessels were counted [85].

6.1.3.5.2. PLGA Scaffolds (Cao 2006)

Justin Cooper-White's group at the University of Melbourne synthesised PLGA scaffolds using TIPs or solvent casting and NaCl porogen leaching [14, 87]. The scaffolds were implanted subcutaneously in rats within a polycarbonate chamber with a microsurgically created arterio-venal vascular loop (AV), to improve perfusion (Fig. 6.11a,b). By 2 weeks, some tissue ingrowth was observed into the scaffolds, in the region adjacent to the AV loop. Most scaffold pores displayed no tissue ingrowth, being either empty or filled with a loose fibrin network (Fig. 6.11c). Multinucleated giant cells were observed aligning themselves around individual surfaces of PLGA. Some blood vessels were observed within the widest pores. Tissue within the scaffold pores was considerably less vascular than the surrounding tissue.

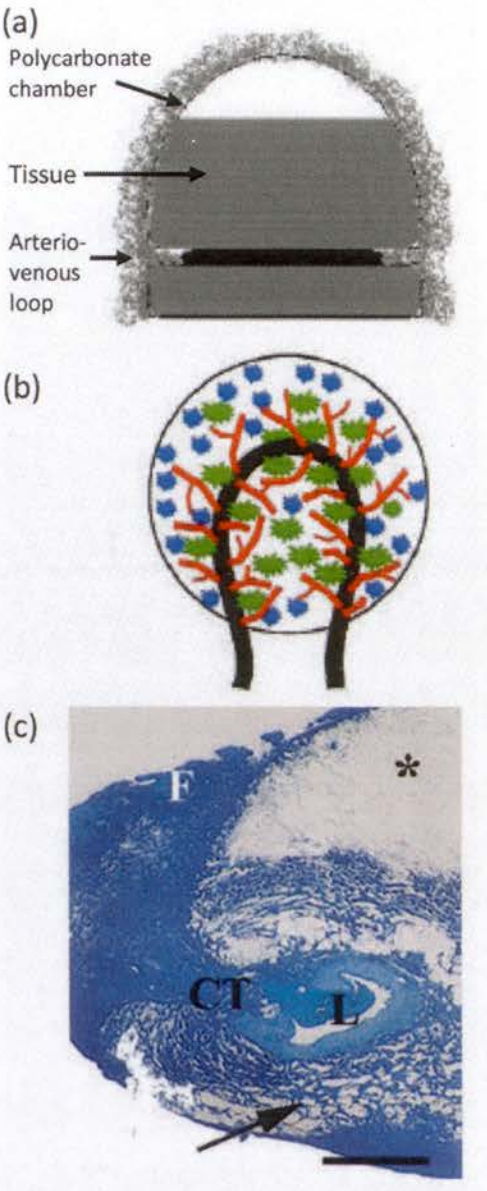


Figure 6.11. (a) Scaffold-filled polycarbonate chamber, indicating tissue level at 8 weeks- longitudinal view, (b) AV loop- horizontal view (c) PLGA scaffold after 2 weeks, demonstrating tissue growth into some pores. (*) an unfilled pore. CT: Connective tissue, F: Fibrin clot on scaffold edge, L: AV vessel loop. Scale: 100 μm [14].

However, complete tissue filling was not achieved even to the study end at 8 weeks. At this timepoint, substantial tissue death was observed. Tissue survival was predominantly in the larger pores (300-400 μm). Tissue survival was probably hindered by the limited pore size (particularly on the surface of the TIPS scaffold, where pores were 10 μm), interconnectivity and degradation products. Superior tissue ingrowth was noted for the porogen leached scaffold.

A blood clot was not able to form within this scaffold during the early periods after implantation. The lack of vascularisation was thought to lead to a build-up of acidic degradation products, resulting in tissue death due to the drop in pH. An aggravated foreign body response was observed due to the PLGA's degradation products. At 6 weeks, macrophage influx was observed within the scaffold- thought to be related to either scaffold breakdown or as a consequence of tissue death.

6.1.3.5.3. PVA Scaffold (Yamamoto 2000)

Yamamoto and coworkers [84] examined tissue and capillary growth into 2mm PVA scaffolds at 1, 3 and 6 weeks after subcutaneous implantation into mice. Fig. 6.12 shows the scaffold appearance after 3 weeks. The scaffolds had been formed using a starch porogen technique, which formed 1mm scaffolds which were then layered. Tissue infiltration was achieved throughout this study but was still incomplete at 6 weeks (Fig. 6.12). A variety of pore sizes were tested, including 30, 60, 110, 250, 350 and 700 μm. Vascularisation was detected for pore diameters of 350 μm, to a depth of <400-600 μm from the outer edge of the scaffold (arrows in Fig 6.12). No vascularisation was observed for pore sizes <250 μm. The depth of vascularisation was increased via delivery of bFGF, to 800-1000 μm.



Figure 6.12. PVA sponges (pore size 250 μm) incorporating bFGF 3 weeks after subcutaneous implantation. Arrows indicate capillaries [84].

PGCL Scaffold (Lee 2003)

Lee and coworkers [262] seeded PGCL scaffolds with smooth muscle cells before implantation subcutaneously in mice. These scaffolds are only 2.5mm thick- a limited by the porogen leaching process. However they are highly elastic (>250% strain before failure) and well interconnected scaffolds (porosity 90%, pore size 200-300 μm). They showed a good biological response, with good tissue formation within the scaffold at 3 weeks (the only timepoint for the study) (Fig. 6.13). The authors did not report whether complete scaffold filling was achieved, nor did they comment on vascularisation which did not appear to have formed. The variotis™ scaffold shows a similar degree of elasticity to this scaffold, a key feature for determining the *in vivo* tissue response.

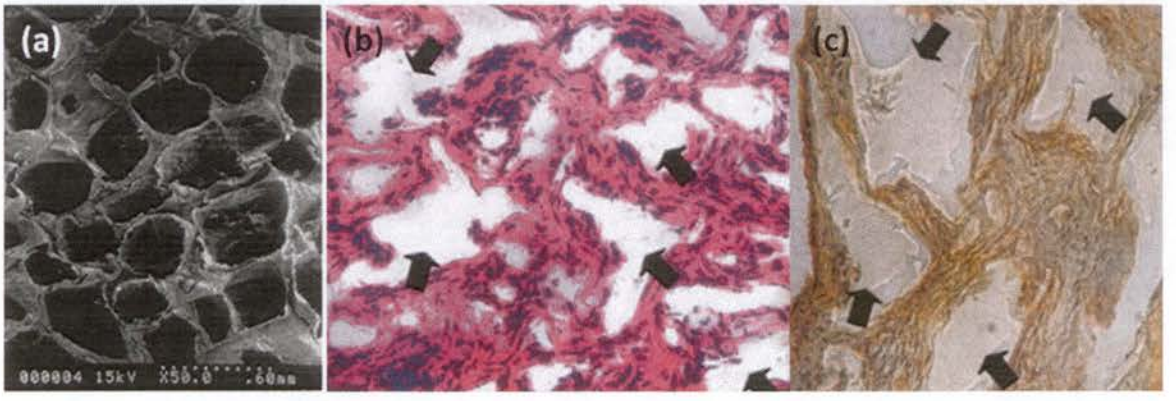


Figure 6.13. (a) SEM of PGCL scaffold morphology, (b) H&E staining (c) α-smooth muscle actin staining after 3 weeks implantation [262].

6.1.3.5.4. Polylactide-Caprolactone (PLAC) Thoracic Scaffold (Misaki 2007)

Misaki and coworkers [61] investigated the ability of a PLAC scaffold for fibrous soft tissue incorporation in the intraplueral space of rabbits (Fig. 6.14). The impetus for this study was to reduce the incidence of infection in this dead space remaining after pneumonectomy (lung resection). This study highlights the effectiveness of a scaffold-based approach to tissue-filling of defects, when compared to growth factor or scaffold-free approaches. The scaffolds had been synthesised using NaCl porogen leaching followed by the TIPs process, and had a honeycomb appearance with 200-400 μm pores. Fibroblasts and collagen fibrils were observed within some of the pores after 1 month of implantation. Macrophages and inflammatory cells were also present surrounding the scaffold. After 2 and 3 months, collagen deposition was present within all the pore spaces. By this stage the scaffold structure was collapsing due to degradation. Vascularisation was not reported in this study so was likely to have been absent or limited. The scaffolds were surrounded by fibrous collagen layers and the scaffolds did not integrate fully with the surrounding adipose tissue. Similar results to these were found for PLAC scaffolds supplemented with bFGF. Tissue was not observed for the control group (no scaffold), or a group treated with bFGF-embedded gelatin microspheres (no scaffold). Some of the design features of this scaffold which could have promoted new tissue include the relatively large pore size and the lack of an aggravated inflammatory response, due to a moderately slowly degrading polymer blend. Fibrous layers around the scaffold may have formed due to implant movement in the thoracic cavity, and poor integration due to limited pore interconnectivity.

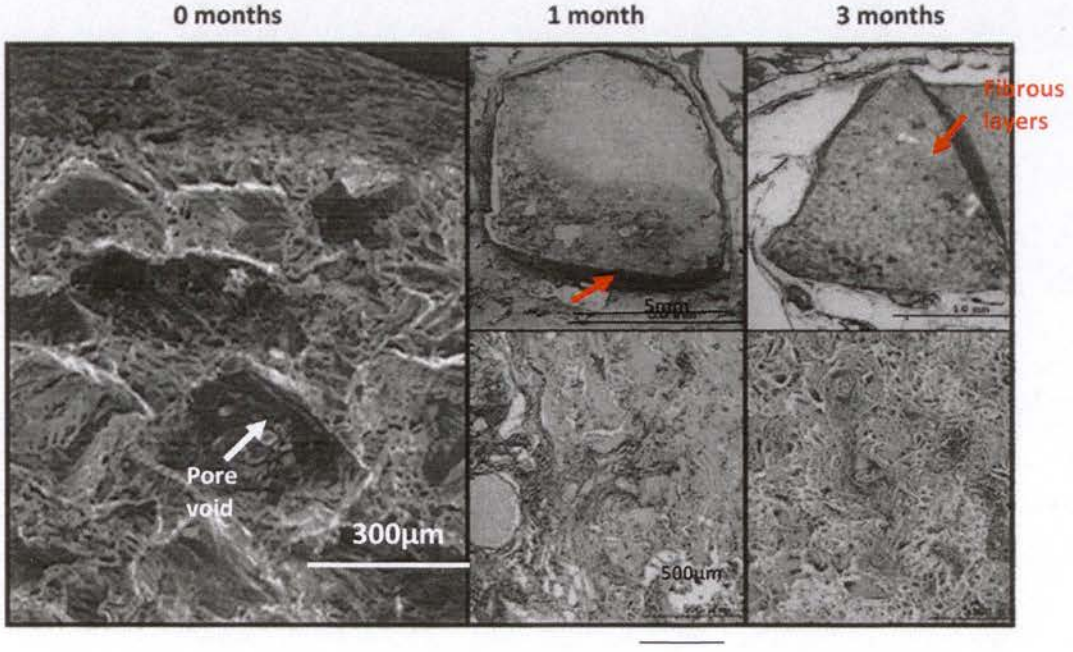


Figure 6.14. PLAC scaffold, and scaffold after 1 and 3 months of implantation. Red arrows: fibrous layers surrounding the scaffold [61].

6.1.3.5.5. Polyurethane (PU) Scaffold (Bezuidenhout 2008)

Bezuidenhout and coworkers [62] synthesised permanent PU scaffolds using phase inversion and porogen extraction (gelatin spheres). Subcutaneous implantation into rats demonstrated tissue ingrowth and vascularisation by 4 weeks, which was the earliest timepoint for the study. The effect of surface heparanisation was determined, with an increase in vessel number but not vessel diameter being detected. The size of the blood vessels were probably limited by the pore size (<147 μm) and pore interconnects (67 μm). In this study, blood vessels were identified by staining using CD31 endothelial marker and the alpha smooth muscle. Inflammatory cells were identified by ED-1 positive macrophages and giant body cells and an adverse inflammatory response was not observed. A fibrous capsule was noted, probably due to the high stiffness of this implant. The successful tissue growth in this study is largely due to the high porosity and interconnected pores which encouraged early fluid flow and connection of the tissue and vessels with the surrounding tissue/vessel attachment.

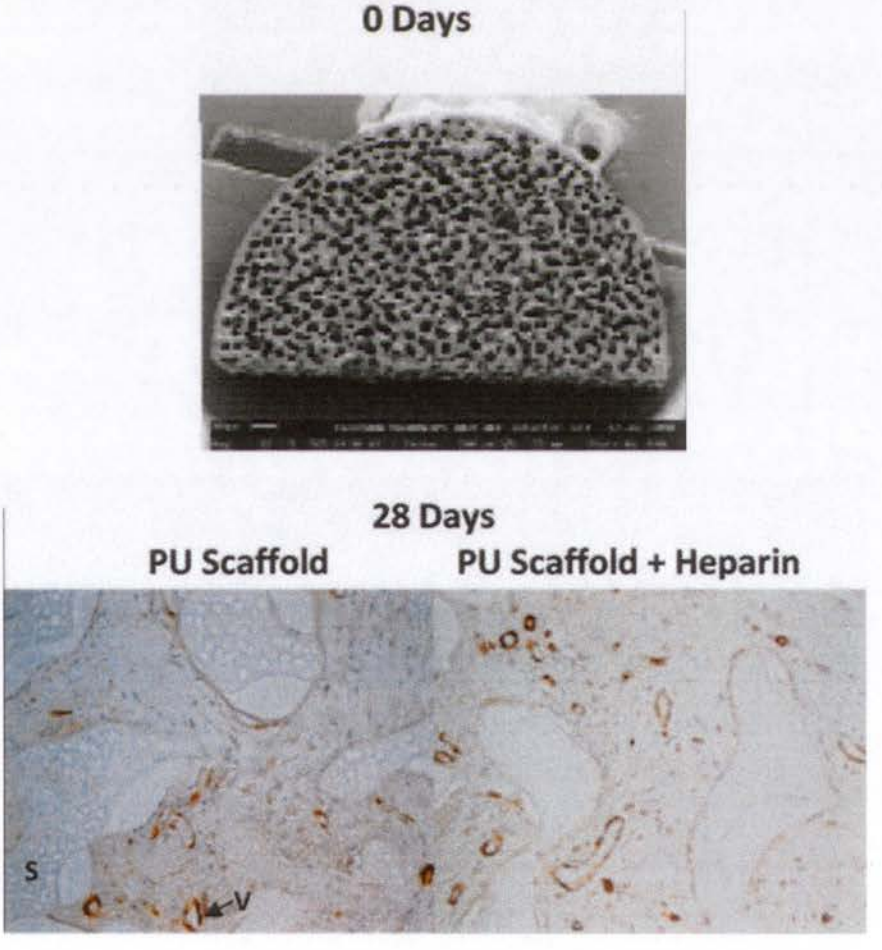


Figure 6.15. Polyurethane scaffold before implantation and after 28 days subctuaneously. V: Histological staining shows α-smooth muscle surrounding the vessels. S: Cross-sections of scaffold struts displaying microporosity [62].

In this chapter, variotis™-containing bioactive glass scaffolds were tested *in vivo* to determine whether there was a change in the amount or speed of tissue ingrowth or vascularisation inside the scaffold, compared to the neat variotis™ foams.

6.1.4.1. In vivo Effect of Bioactive Glass on Tissue Ingrowth and Vascularisation

Few studies have examined the effect of bioactive glass on soft tissue ingrowth into scaffolds. Animal models examining the effect of bioactive glass have included subcutaneous rat studies [53, 85, 86, 226, 783] and bone grafts [229], and are listed Table 6.2. Coating implants with BG clearly improves tissue attachment [53] and can increase the rate of bone and soft tissue integration, although this effect could be temporary. The more reactive 58S and 77S glasses promoted osteoconduction while resorbing at a faster rate than 45S5 Bioactive glass. However, after 12 weeks, bone growth was similar for all glasses, whether porous or nonporous. Increased tissue infiltration and surrounding bloods vessels were noticed in 45S5 filled PLGA foams [85]. Increased vascularisation was also observed within 45S5 coated PGA meshes [86].

Therefore, in the current study, it was of interest to investigate whether the addition of bioactive glass to the variotis™ scaffold would show an increase in the rate and quality of tissue infiltration or blood vessels inside the scaffolds. Future work could investigate whether the newly formed tissue imparted an increased strength to tissue wounds, via the addition of bioactive glass.

Table 6.2. *In vivo* studies investigating the effect of bioactive glass.

Animal Model	Tissue/Vascularisation	Ref
Rat- subcutis	Soft tissue bonding to BG-coated tube. No tissue attachment for uncoated tube, but a fibrous capsule formed (50μM). Increased blood vessels surrounding BG-coated tube.	53
Rat- subcutis (1, 2, 4, 6 wks)	Significantly increased granulation tissue for BG (6wks). Increased blood vessels surrounding BG scaffold (4 and 6 wks).	85
Rabbit-bone (4,8,12 wks)	58S and 77S showed increased bone at 4 and 6 weeks. Equivalent bone growth at 12 weeks for all glasses.	226
Rat- subcutis (1,2,4,6 wks)	Rapid integration of microspheres with host tissue, including vascularisation of voids within the microporous spheres.	783
Rat- subcutis (2,4,6 wks)	Both meshes infiltrated with collagen/fibroblasts. Increased vascularisation at 2 and 4 wks for the BG scaffold (not significant). Spaces existed between the tissue and agglomerates of BG.	86

6.1.4.2. *Effect of Bioactive Glass on In vivo Inflammation*

Studies of monocytes and macrophages on 45S5 bioactive glass have demonstrated ingestion by macrophages, corresponding with increased TNF-α (Fig. 6.16) [784]. Bioactive glasses appear to activate an autocrine-like process in which the response evoked by the material (for example monocyte and macrophage activation with cytokine production) enhances subsequent interactions with cells in contact with the material [784]. Bioactive glass has been shown to not modify *in vitro* T-cell (lymphocyte) response, and this underlies it's biocompatibility [204]. Previous studies have noted the presence of multinucleated giant cells surrounding bioactive glasses to precede their degradation. Asikanen [785] observed these giant cells at 12 weeks (Fig. 6.16d), however by 24 weeks the bioactive glass particles could no longer be detected. Eosinophilic granulocytes were also noted in this study, possibly indicating an allergic response. This is largely thought to be due to the inclusion of chitosan, a reaction which has been previously noted [785].

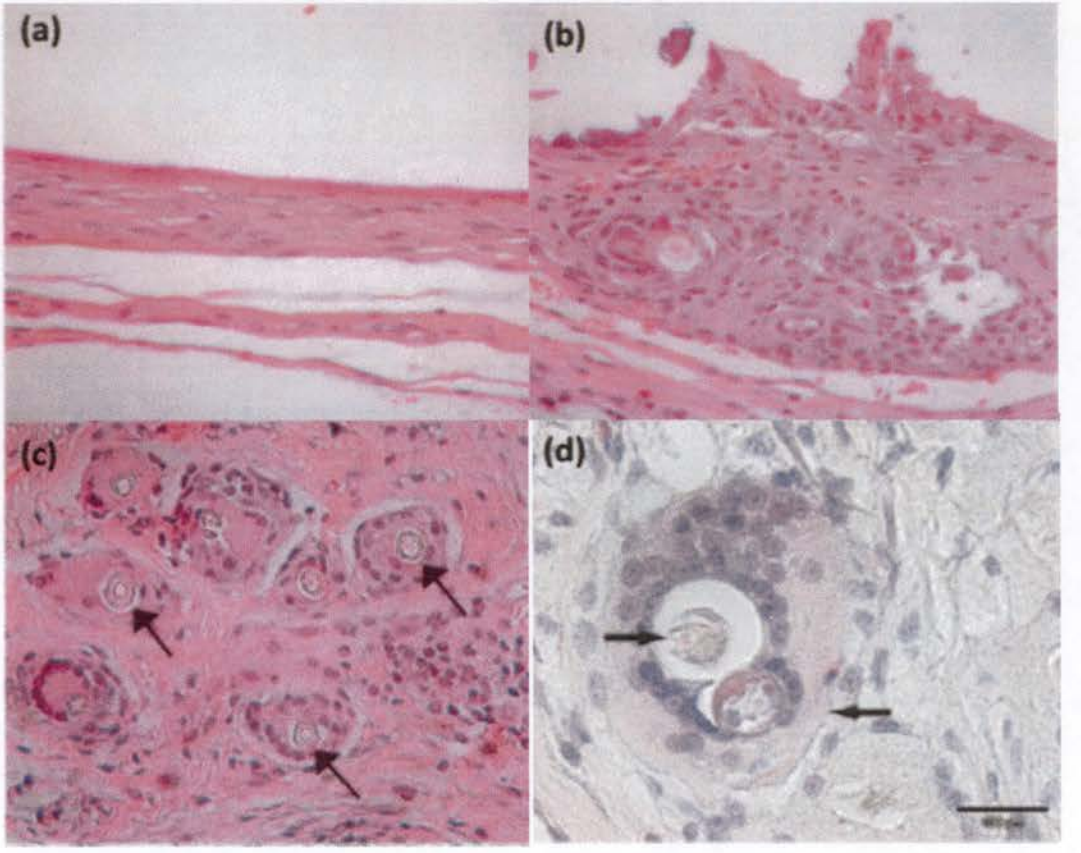


Figure 6.16. *In vivo* response to (a) Silicone implant (b) Bioactive glass-coated silicone implant. Note the increased presence of inflammatory cells associated with the bioactive glass. (c, d) Arrows: Multinucleated giant cells surrounding bioactive glass particles (100x mag) [53, 785].

6.1.5. BLOOD VESSEL COUNTS

Counts of blood vessels inside scaffolds have been done by some previous studies. Day and coworkers [86] counted vessels in sections stained with H&E and van Gieson stain, as identified by erythrocytes within the blood vessel lumen (average of 6 fields). More blood vessels were counted in PGA/45S5 Bioglass® composite meshes than PGA control meshes. These results are shown in Fig. 6.17.

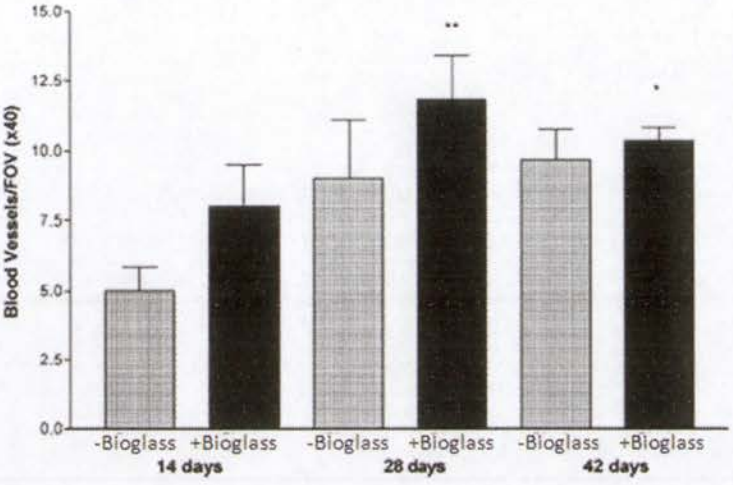


Figure 6.17. The number of blood vessels counted at 40x magnification within a PGA/45S5 mesh [86].

Vessels are usually, however, counted surrounding the scaffolds due to low levels of tissue infiltration into the scaffolds. For example, in another study Day [85] showed an increase in vessel density around 0.1% BG coated PLGA scaffolds (compression molded), when compared to uncoated scaffolds, 4 and 6 weeks after subcutaneous implantation. In addition, Ross and coworkers [53] demonstrated the presence of more blood vessels in the surrounding region (mean: 33 vessels) of Bioglass®-coated silicone tubes compared with uncoated implants (mean: 20 vessels). These results are graphed in Fig. 6.18.

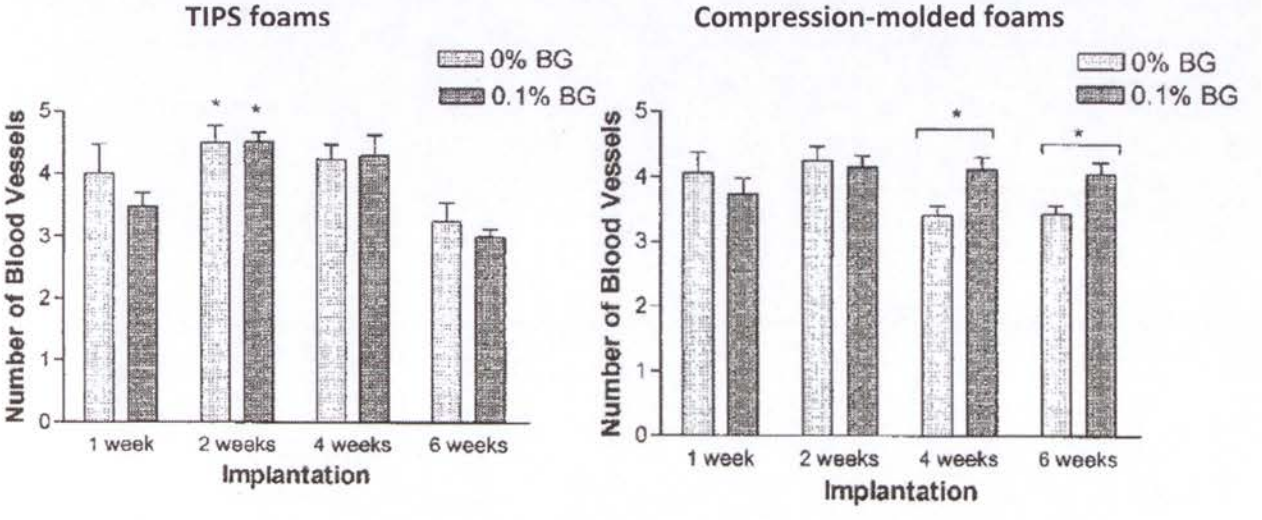
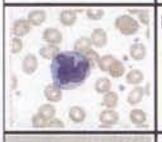
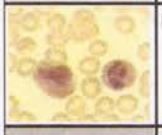


Figure 6.18. Vessel counts surrounding PLGA scaffolds, with or without bioactive glass coating [85].

6.1.6. INFLAMMATORY CELL ANALYSIS

Inflammatory cell infiltration is a normal response to biomaterials. Commonly used biomaterial show the presence of multinucleated giant cells and small numbers of macrophages and lymphocytes. For example, silicon shows this reaction due to the leaching of silica [53]. Inflammatory cells which were identified are listed in Table 6.3.

Table 6.3. Descriptions of inflammatory cells.

Appearance	Cell	Appearance	Role
	Monocyte	Largest cell. Nuclei can appear jelly-bean shaped or multi-lobed	Can evolve into macrophages
	Macrophage	Large, 'fried egg' appearance, contain vacuoles	Phagocytose foreign material including bacteria & biomaterial. Can form multi-nucleated giant cells.
	Eosinophil	Small, bright pink	Associated with allergic reactions and some infections
	Neutrophil	Multiple, 'tear drop' shaped nuclei, H&E: neutral pink	Phagocytose bacteria &release antimicrobial agents. Account for 70% of WBC. Lifespan only 12hrs.
	Basophil	H&E: dark blue	Phagocytose bacteria & other foreign bodies
	Lymphocyte	Single nucleus	Associated with viral and bacterial infections

Note: PMNs include basophils, eosinophils and neutrophils.
Neutrophils are also known as: Neutrophil granulocytes, Polymorphonuclear Neutrophils (PMN)

The purpose of this present study was to assess the biocompatibility of PCL and PCL/bioactive glass composite scaffolds with highly interconnective porosity, and secondly, to characterise the extent and rate of tissue ingrowth and vessel development into the scaffold core. It was of interest whether an improved biological response was stimulated by the presence of bioactive glass, as has been suggested in other studies.

6.2. METHODS

6.2.1. SYNTHESIS OF BIOACTIVE GLASS POWDERS AND SCAFFOLDS

Bioactive glass was chosen for incorporation into the scaffold in order to increase bioactivity, wettability, degradation rate and potentially upregulate biological factors beneficial to wound healing. The composition chosen was 45S5 (Bioglass®), as this is the most commonly used Bioactive Glass, known for its high bioactivity. Bioglass® with a final composition of 45 w/v% SiO_2, 25.5% Na_2O, 24.4% CaO, 6% P_2O_5, was synthesised using a melt-derived technique, as previously described (ref section 4.2). Powders were formed using a mortar and pestle and particle size was characterised using a computerised image analysis system (Leica QWin Plus v3.5, Leica Microsystems Imaging Solutions Ltd., Cambridge, UK).

10mm-thick PCL variotis™ scaffolds were rapidly synthesised using a novel coagulating batch process developed by the author (ref section 3.2). Some scaffolds were synthesised by coating with the 45S5 bioactive glass powder, (~10 wt% of the total weight of the scaffolds) and were termed the composite Bioglass® scaffold ('BG') (ref section 3.2.2.3.3). Results were compared with those synthesised in the absence of the bioactive glass (termed 'PCL'). Scaffolds were sterilised using 25 kGy gamma radiation (Steritech Pty Ltd, Wetherill Park, NSW, Australia).

6.2.2. ANIMAL STUDY

Male Sprague Dawley rats (n=56) were used for these studies. Scaffolds (n=4) control PCL or bioactive glass/PCL composite scaffolds were inserted subcutaneously into the flanks of each rat. Animals were terminated at days 2, 4, 7, 14, 21, 28 and 42 post-implantation. These time periods were chosen to investigate the tissue infiltration during the inflammatory phase (approx 2-7 days), proliferative phase (approx 7-21 days) and remodeling phase (approx 21-42 days).

The rats were anaethesised using 5 mg/kg Ketamine and 0.3 mg/kg Xylazine (Bayer Health Care). A region approx 10 x 10 cm on the dorsum of each animal was shaved and the skin was disinfected with betadine (10% povidone-iodine in water). Two incisions were created on each side of the animal (2 cm long) and a subcutaneous pocket was formed at each site by blunt dissection. A sterile scaffold (dimensions: 5.25 x 5.25 x 10 mm) was placed in each pocket and the incision sites were sutured. Animals were treated at the time of wounding with subcutaneous Temgesic (0.03 mg/kg) and Carprofen (0.9 mg/kg) to minimise pain and inflammation and Ampicillin (50 mg/kg) to reduce chance of infection. At termination, animals were anaesthetised with ketamine and xylazine and blood was obtained by cardiac puncture. Ethics approval for this study was obtained from the Sydney South Western Area Health

Service (Protocol no. 2007-024). At each time point animals were anaethetised as above and whole blood was obtained for measurement of circulating inflammatory cell number by FACs. Scaffolds were excised and treated as follows i) snap frozen in Optimum Cutting Temperature Compound (OCT) (Tissue-Tek, ProScitech, QLD, Australia) and stored at -80^{0}C for immunohistochemical analysis, ii) frozen in liquid nitrogen for SEM imaging and RNA extraction (later expt) or iii) placed on ice for wound fluid extraction for counting inflammatory cells and measurement of matrix metalloproteinase activities. Optical photos were taken of the excised scaffolds at each time-point and the outer dimensions of the scaffolds were measured and compared.

6.2.2.1. Examination of Tissue Ingrowth into the Scaffold

Snap frozen OCT embedded sections were cryosectioned at -15°C. Sections (10 μm) were mounted onto gelatinised slides (Superfrost Plus) and air dried.

6.2.2.2. Histological Examination

For histological examination of cellular infiltrate, and collagen content, sections were fixed in in 70% ethanol for 5 mins and stained using haemotoxylin and eosion (H&E). For identification of collagen sections were stained with PicoSirius Red (PSR) both according to standard protocols. Slides were mounted with DPX mounting medium (BDH Laboratory Supplies, Poole, UK) and viewed by light microscopy using Olympus AX70 (Olympus, Tokyo, Japan). Collagen content was quantified after scanning using the Dako Automated Cellular Imaging System (ACIS) as follows: 6 regions of approx 220000 pixels^2 were selected per slide, and collagen quantified using the ACIS. All measurements were performed on two sections per scaffold, for 2 scaffolds (different animals). The amount of collagen was expressed as a % of the total region area.

6.2.2.3. Immunohistochemical Examination

Sections of scaffolds were also obtained for identification and localisation of collagen IV and macrophages using rabbit anti rat collagen IV (1:400, Invitrogen) and anti-rat CD68 antibody (1:200, Invitrogen) respectively. For these studies sections were fixed for 10 mins in 4% Paraformaldehyde prior to treatment with 0.3% hydrogen peroxide (in H_2O, Merck, Kilsyth, Victoria) for 20 mins. Slides were rinsed with TBST and tissue was blocked with 10% Normal Goat Serum for 30 mins to ensure specific binding. Immunostaining was carried out for 1hr at room temperature and for collagen IV visualised with biotinylated goat anti-rabbit secondary antibody (1:400) for 20 mins. This was followed by 30 min incubation with avidin-biotin-peroxidase detection system (Vectastain ABC kit, Vector Laboratories Inc., USA), using

diaminobenzidine (DAB) as a chromogen. The sections were counterstained with haemotoxylin, and mounted as before.

Vessels were studied by immunofluorescence and staining with CD31. For these studies OCT embedded sections were fixed in paraformaldehyde and then incubated with the primary antibody CD31 (1:100, mouse-anti-rat) and the secondary antibody FITC (fluorescein isothiocyanate, 1:500, Alexafluor 488, chicken-anti-mouse, Invitrogen) for 45 mins. Nuclei were stained with 0.2% DAPI and slides were mounted with antifade (Prolong Gold; Invitrogen) in 50%glycine/50%PBS.

Images were captured on a fluorescent microscope (Olympus AX70, Olympus, Tokyo, Japan.) equipped with an Olympus DP60 camera. The numbers of blood vessels and arterioles were determined as follows: Blood vessels were defined as CD31 positive structures with a visible lumen. Arterioles were defined as CD31 positive or collagen IV positive structures with no visible lumen. Vessel numbers were counted in 4 regions of 1.5 cm x 1.5 cm, from a single slide and are reported as the mean±SD of these 4 regions.

The sizes of the mesopores were measured using collagen 4 immunostained sections. An image analysis program, Irfanview 4.25, was used to determine the range of particle sizes over 4 fields of view at 60x magnification.

6.2.2.4. Scanning Electron Microscopic (SEM) Examination

The scaffolds were prepared for SEM by freezing in liquid nitrogen immediately upon excision from the animal. Primary fixation was achieved by immersion in 2% gluteraldehyde (in 0.1 M Na-cacodylate buffer) overnight at 4°C and post-fixation with 1% osmium in 0.1 M Na-cacodylate buffer. Samples were dehydrated in ethanol solutions at 70%, 80%, 90% and 3x 100% for 10 min each, before being immersed for 3 min in 100% hexamethyldilazane (HMDS) for dehydration. Cross-sectioned specimens were mounted on aluminium stubs and sputter coated with 10 nm platinum. SEM Imaging was performed on a Philips XL30.

6.2.2.5. Stereoscopic Microscopy Examination

Cross-sectioned scaffolds which had been fixed for SEM imaging were also viewed using a stereoscopic optical microscope.

6.2.3. EXAMINATION OF THE EFFECT OF THE SCAFFOLD ON INFLAMMATORY RESPONSE

6.2.3.1. Measurement of Circulating Inflammatory Cell Number

Blood obtained at termination by cardiac puncture was used for counting of whole blood white cell number by flow cytometry according to standard protocols. Counts included: whole blood count, neutrophil, leukocyte and monocyte counts.

6.2.3.2. Measurement of Cell Types in Scaffolds

Two of each type of scaffold at days 2, and 14 were used for collection of wound fluid. Fluid was removed from the scaffold by squeezing onto a petri dish. Fluids were then collected using a pipette and the fluid volume was measured. Fluids were aliquoted and either stored at -80^{0}C for later analysis or diluted 1:20 and the cells collected for analysis of cell type. For analysis of cell type, fluid were cytospun onto slides and the cells stained using May-Grunwald-Geimsa, and myeloperoxidase stains, using established techniques (ref Table 6.3). Positive and negative neutrophils, macrophages and eosinophils were counted in 5 regions at 40x magnification.

6.2.3.3. Measurement of Wound Fluid Matrix Metalloproteinase Activity

Gelatin Zymography was used to measure wound fluid proteolytic activity. For these studies wound fluids (1 µL) were loaded onto a 8% SDS-PAGE gel containing 10% MDPF labeled gelatin (0.75 mm-thick). The samples were separated by electrophoresis at a constant voltage (130 V) for approximately 1.5 hr at room temperature, and activities determined as described in detail previously [773]. Results were corrected for initial wound fluid volume and protein concentration and are expressed as Xg/mgP.

6.2.3.4. Statistical Analysis

All data were expressed as mean ±standard deviation (SD) and were analysed using the NCSS package and one-way ANOVA with post hoc comparisons with Bonferroni test. P-values of <0.05 were considered statistically significant.

6.3. RESULTS

6.3.1. EXAMINATION OF TISSUE INGROWTH INTO THE EXCISED SCAFFOLDS

The subcutaneously implanted scaffolds (Fig. 6.20) were well tolerated and the wounds healed well in all animals. No wound or implant infections were detected. All animals continued to gain weight throughout the experiment. Scaffolds were quickly incorporated into the connective tissue layer between the skin and the muscle (i.e. dermis) (Fig. 6.20a).

Shown in Fig. 6.20b, The volume of the scaffolds doubled during the first 7 days and provided early support to the developing tissue. This increase in volume could be due to the filling of the scaffold with the blood clot, and was possible because of the good extensibility of the scaffold. From day 7-42, the scaffold slowly returned to its original volume. This is likely to be due to both tissue contraction and material degradation. The BG scaffolds had a larger volume than the PCL scaffolds at day 14 and 28.

Tissue and capillaries were visible on the outside of the scaffolds which were excised from day 4 to 42 (Fig. 6.20c). Granulation tissue was visible within the scaffolds by 7 days, as shown using H&E staining in Fig. 6.20d. Both scaffolds were completely filled with granulation tissue by 14 days. Fig. 6.20e shows a photograph of the cross-section of a BG scaffold after 28 days, demonstrating an excellent level of tissue filling.

The granulation tissue front developed quicker in the Bioglass® scaffold which was examined. In Fig. 6.20d, it progressed 2-3x further than the PCL scaffold in some regions. As the experiment continued, the tissue in both scaffolds continued to mature. The pink haemotoxylin stain darkened in both scaffolds approaching day 42. The stain was darker in the BG scaffold at all timepoints. Fig. 6.21 depicts the tissue entering edge of the scaffold (Fig. 6.21a) and the centre of the scaffold (Fig. 6.21b), stained with H&E. The tissue within the scaffold was also successfully viewed using stereoscopic microscopy (Fig 6.22, 6.23). In these images, the tissue was visible as brown and scaffold was white.

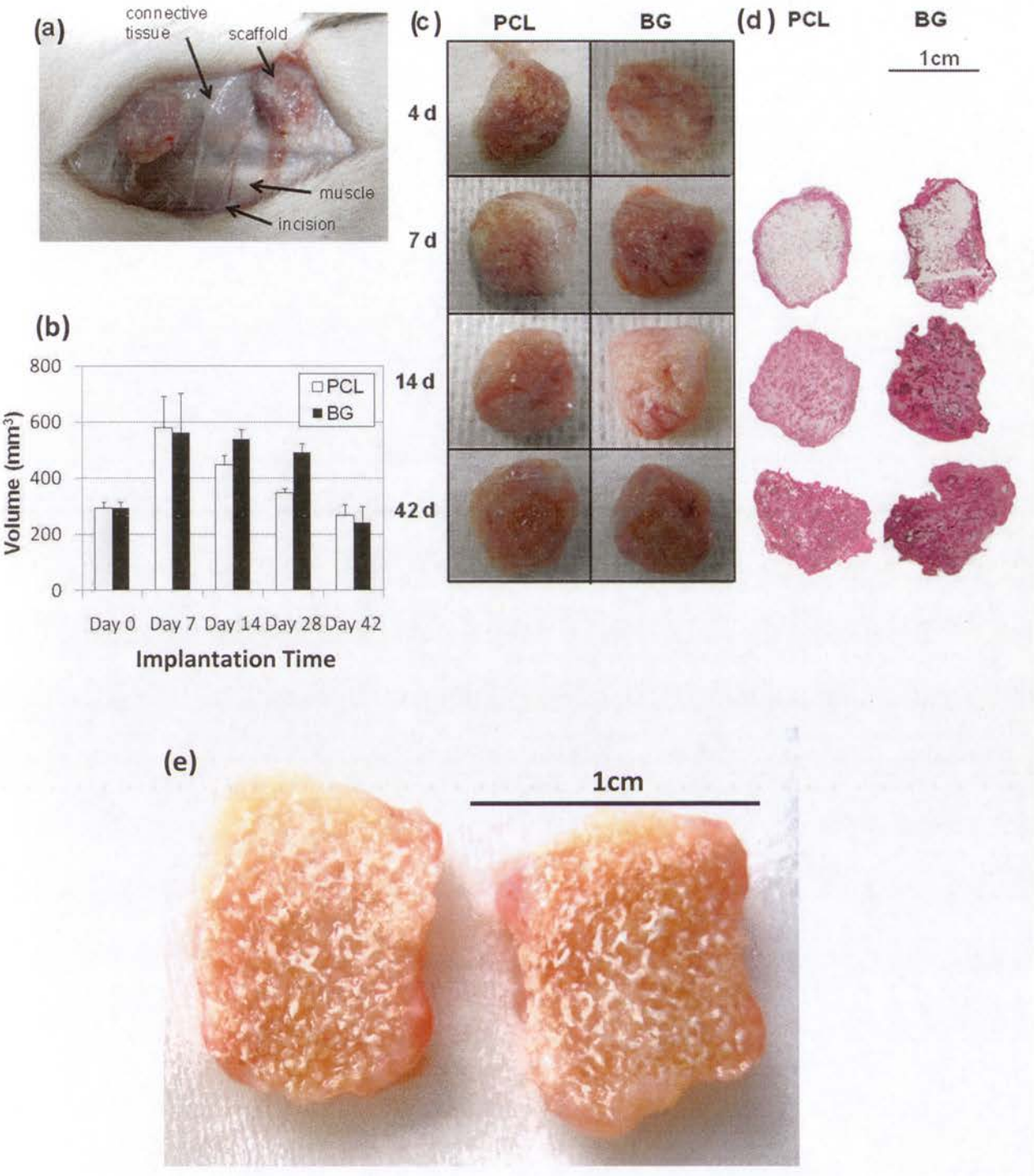


Figure 6.19. (a) A subcutaneous pocket in rat skin showing the implantation site of the scaffolds (Day 4, BG), (b) Measurements of the volume of the excised scaffolds, (c) Photographs of the excised scaffolds (d) H&E stained cryosections from the centre of the scaffolds (PCL day 14), (e) Cross-section of the Bioglass® composite scaffold at day 28.

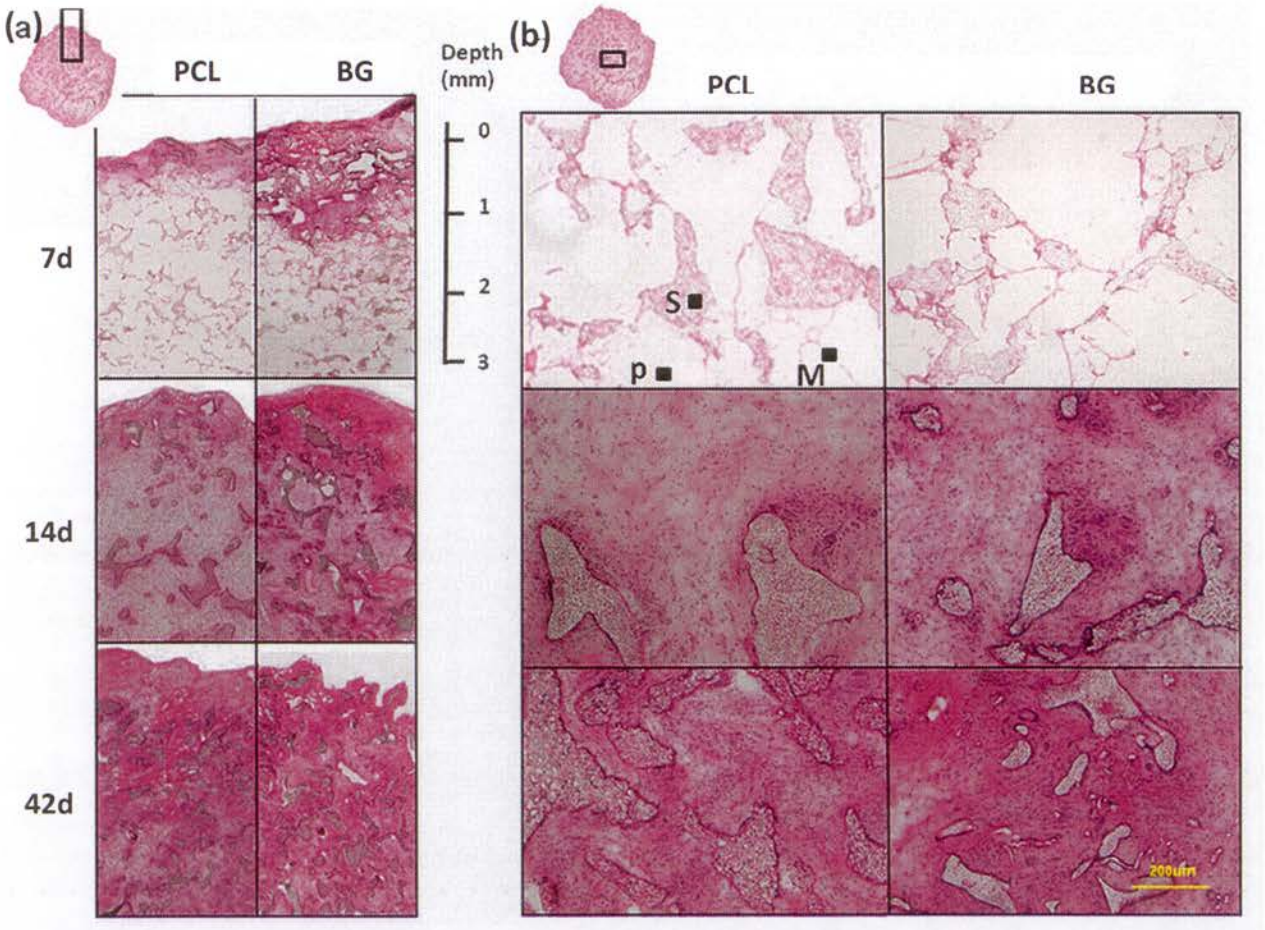


Figure 6.21. H&E- stained sections showing tissue ingrowth into the scaffolds (a) edge profiles and (b) scaffold centres.

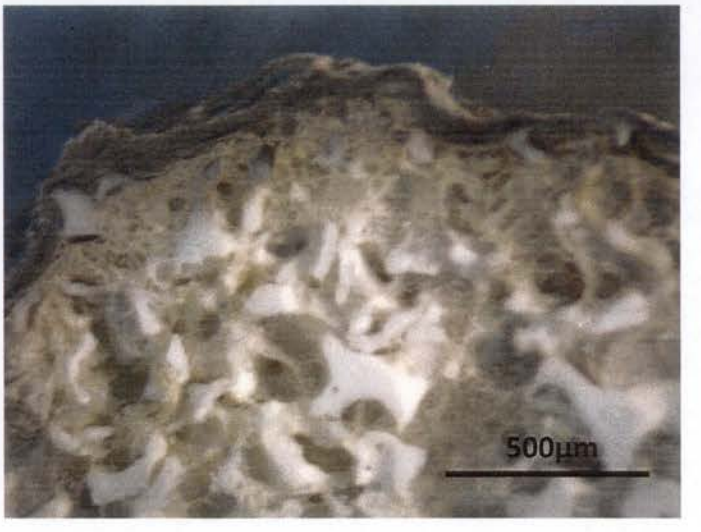


Figure 6.22. PCL scaffold after 14 days tissue infiltration, taken using stereoscopic microscopy after preparation for SEM.

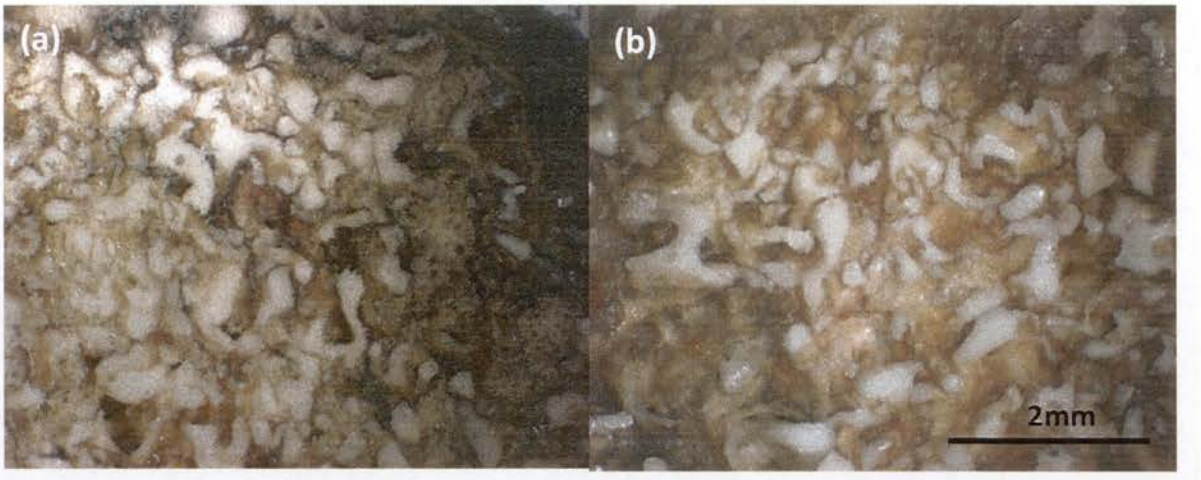


Figure 6.23. (a) PCL and (b) BG scaffold, after 21 days tissue infiltration, taken using stereoscopic microscopy after preparation for SEM.

Scanning electron microscopy was a useful tool for visualizing the stages of tissue ingrowth into the scaffold. These scaffolds could easily be prepared for SEM, due to their mechanical integrity, inherent thickness and ease of cutting. Using SEM, it was possible to see tissue and blood vessels filling up the scaffold pores at day 42 (Fig. 6.23). Figure 6.25 shows a timecourse of the tissue filling the scaffolds, taken using SEM. The corresponding phases of wound healing are indicated next to these images.

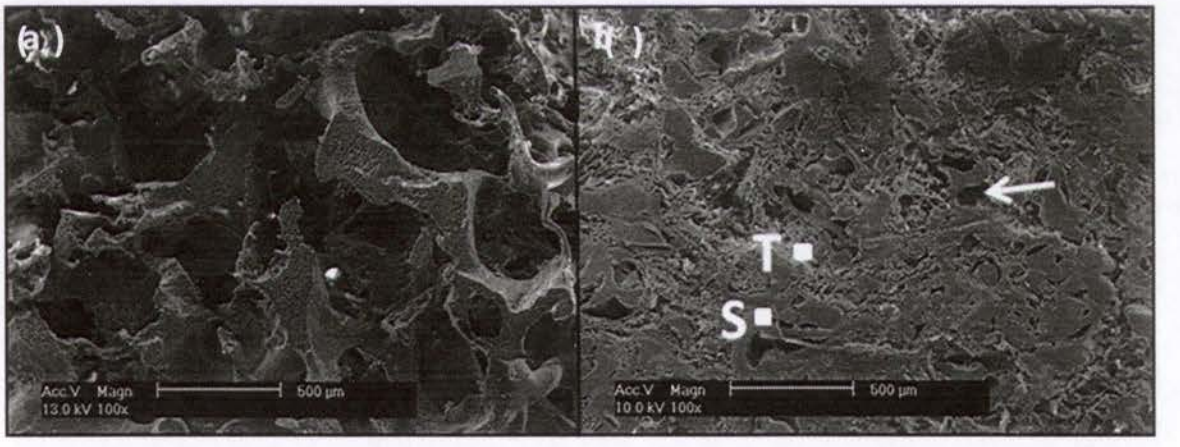


Figure 6.24. Scanning Electron Micrographs of central cross-sections of the a) the PCL scaffold before implantation and (b) the tissue-infiltrated scaffold after 42 days *in vivo*. S: scaffold, T: tissue and arrow: blood vessel. (Scale: 500 µm)

By day 2, a blood clot had formed. This consisted of a provisional fibrin matrix and blood and inflammatory cells such as platelets, leukocytes and neutrophils. By 28 days, the ECM had formed a loose woven structure within scaffold. Although the PCL scaffold showed similar tissue formation at days 2 and 7, by 28 and 42 days thick collagen bundle arrangements were visible. These results suggest a difference in morphology of the tissue between the PCL and Bioglass® scaffolds, however this trend is difficult to confirm as only one scaffold was imaged

using SEM. Figures 6.26 and 6.27 show the clot which was visible at day 2. The fibrin and blood cells bridged the large pores with a web-like provisional matrix. This matrix consisted of fibers which were ~1 μm in diameter. The blood clot also lined the struts of the scaffolds.

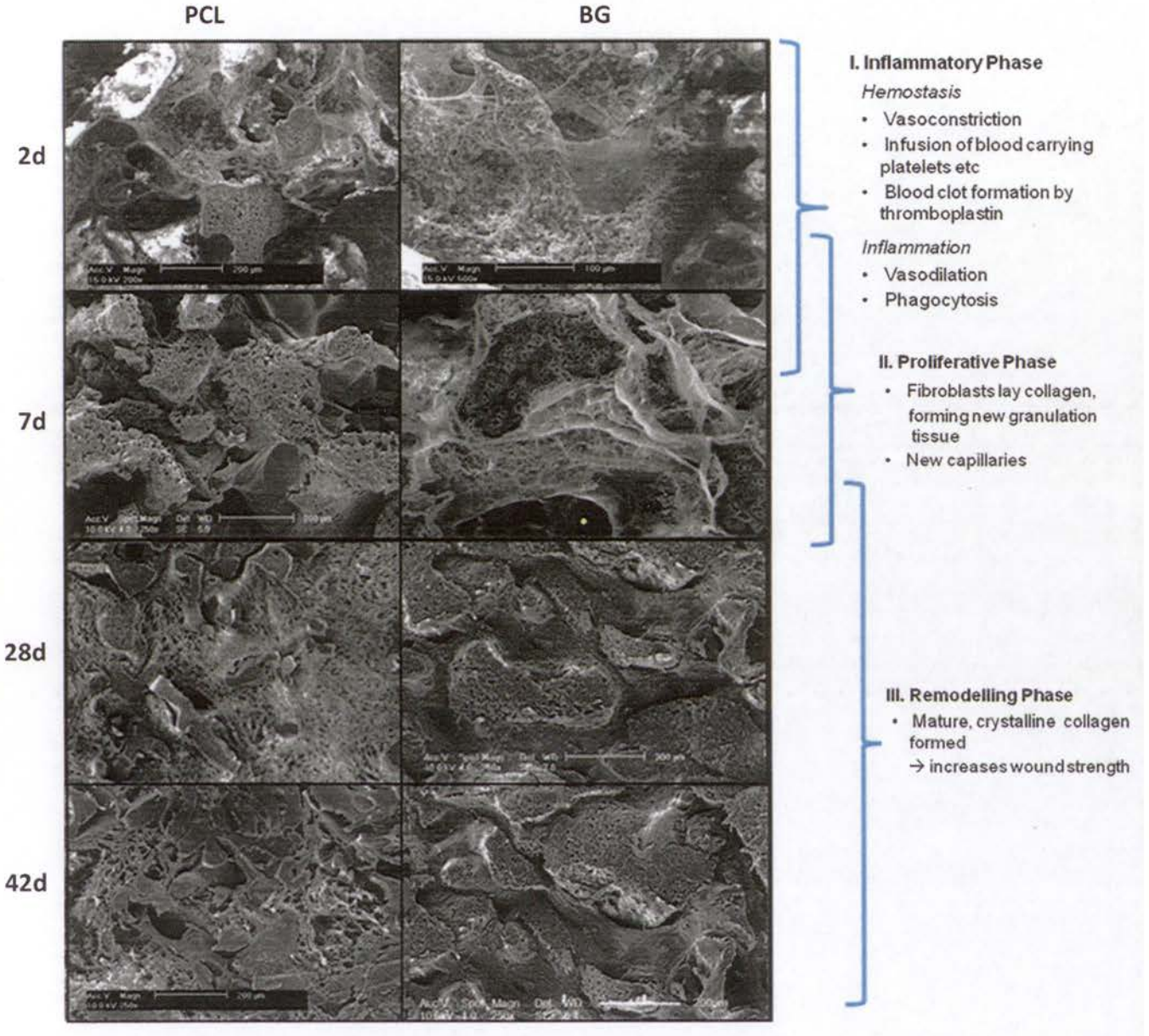


Figure 6.25. Scanning Electron Micrographs of central cross-sections of the scaffolds showing the phases of wound healing 2, 7, 28 and 42 days. b) (top) Blood and inflammatory cells visible on the surface of the scaffold (Scale: 10 μm) (middle) A thromboplastin clot lining the surface of the scaffold struts (Scale: 100 μm) (bottom) The Bioglass® scaffold at 42 days, showing the presence of collagen bundles (Scale: 200 μm).

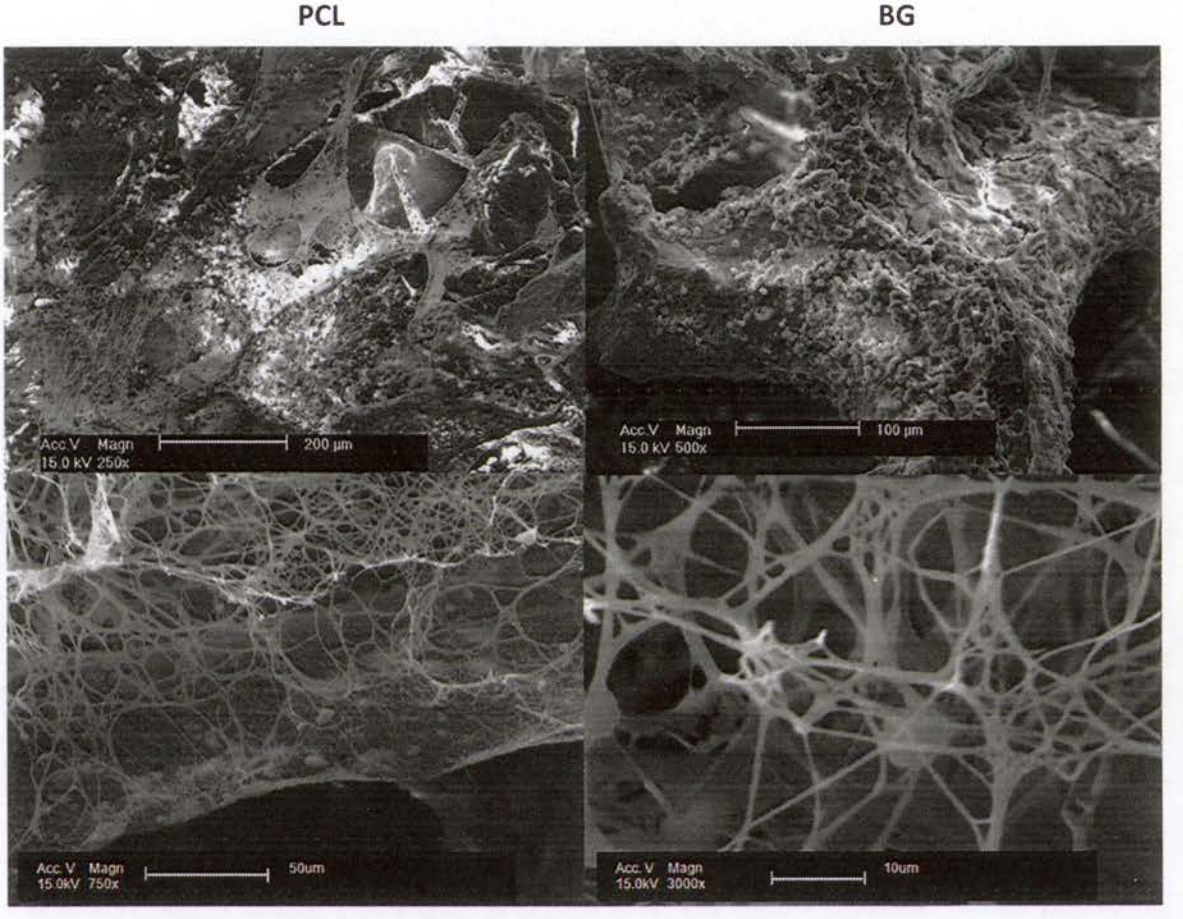


Figure 6.26. Fibrin provisional matrix between the pores (2 days, PCL scaffold).

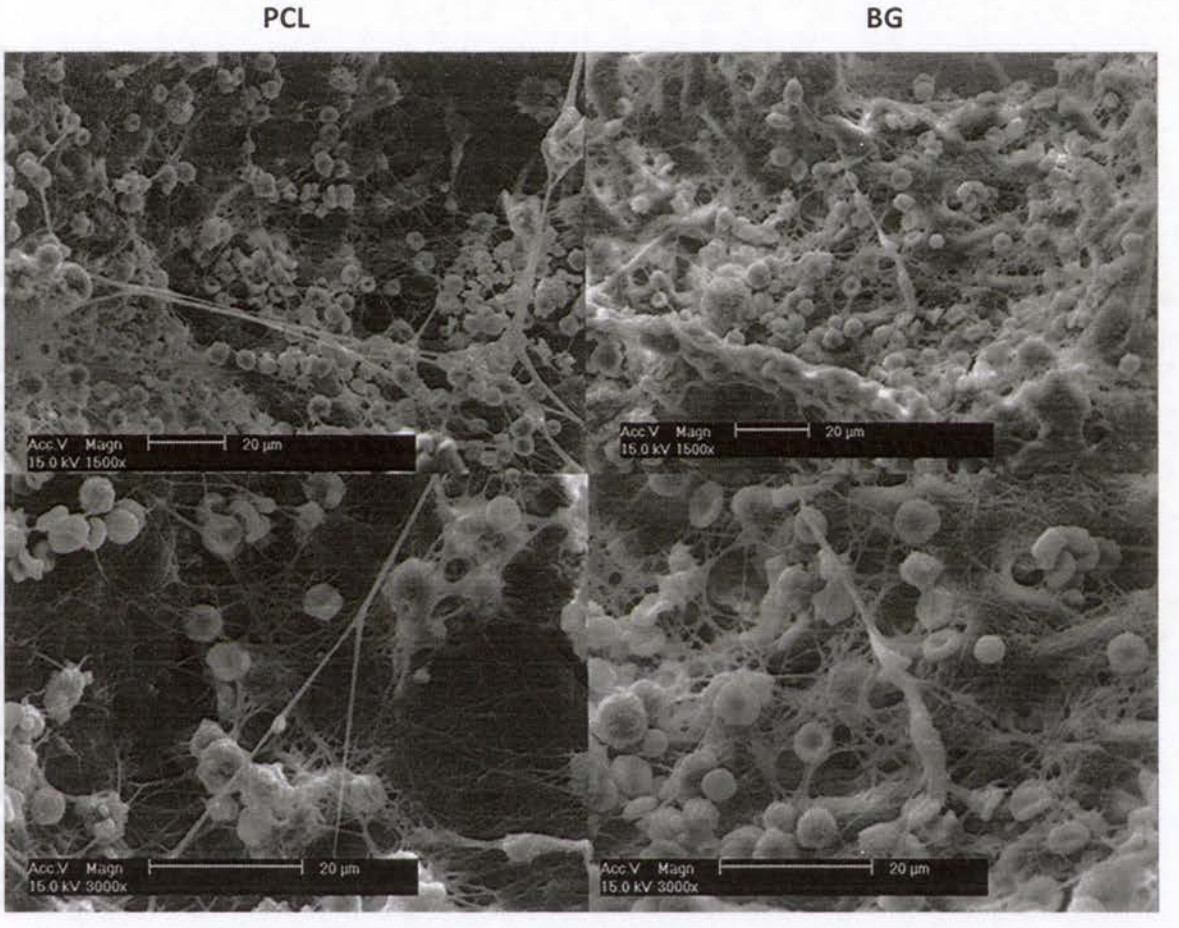


Figure 6.27. High magnification images of the blood clot within the scaffold (2 days, PCL scaffold).

The amount and quality of the collagen inside the scaffold was investigated. This was to confirm the increase in maturity over time and to determine whether there was a difference between the two scaffolds. Total collagen within the scaffold, visualised using PSR, is depicted in Fig. 6.28 and 6.29. Fig. 6.28 shows complete filling of both scaffolds with collagen by day 14. Complete collagen filling was also observed in day 7 sections which were sliced ~200μM in from the edge. Increasingly dense collagen was observed in the day 42 sections, particularly in the BG scaffold.

Fig. 6.29 shows the quantification of collagen as a % of the area of the scaffold section. This showed an increase in collagen content over time for both scaffolds. The intensity of the collagen staining also increased over time for both scaffolds. A slight increase in collagen intensity was evident for the BG scaffold at days 14 and 42.

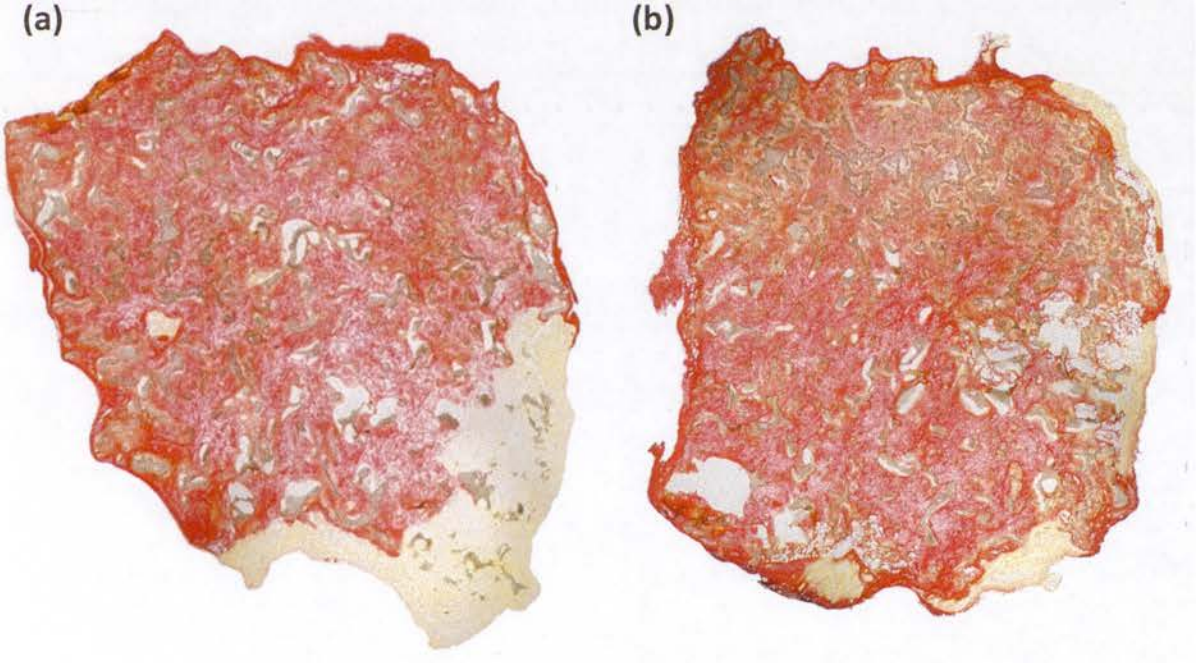


Figure 6.28. PSR -stained section taken from scaffold centres, at day 14 (left) PCL and (right) BG.

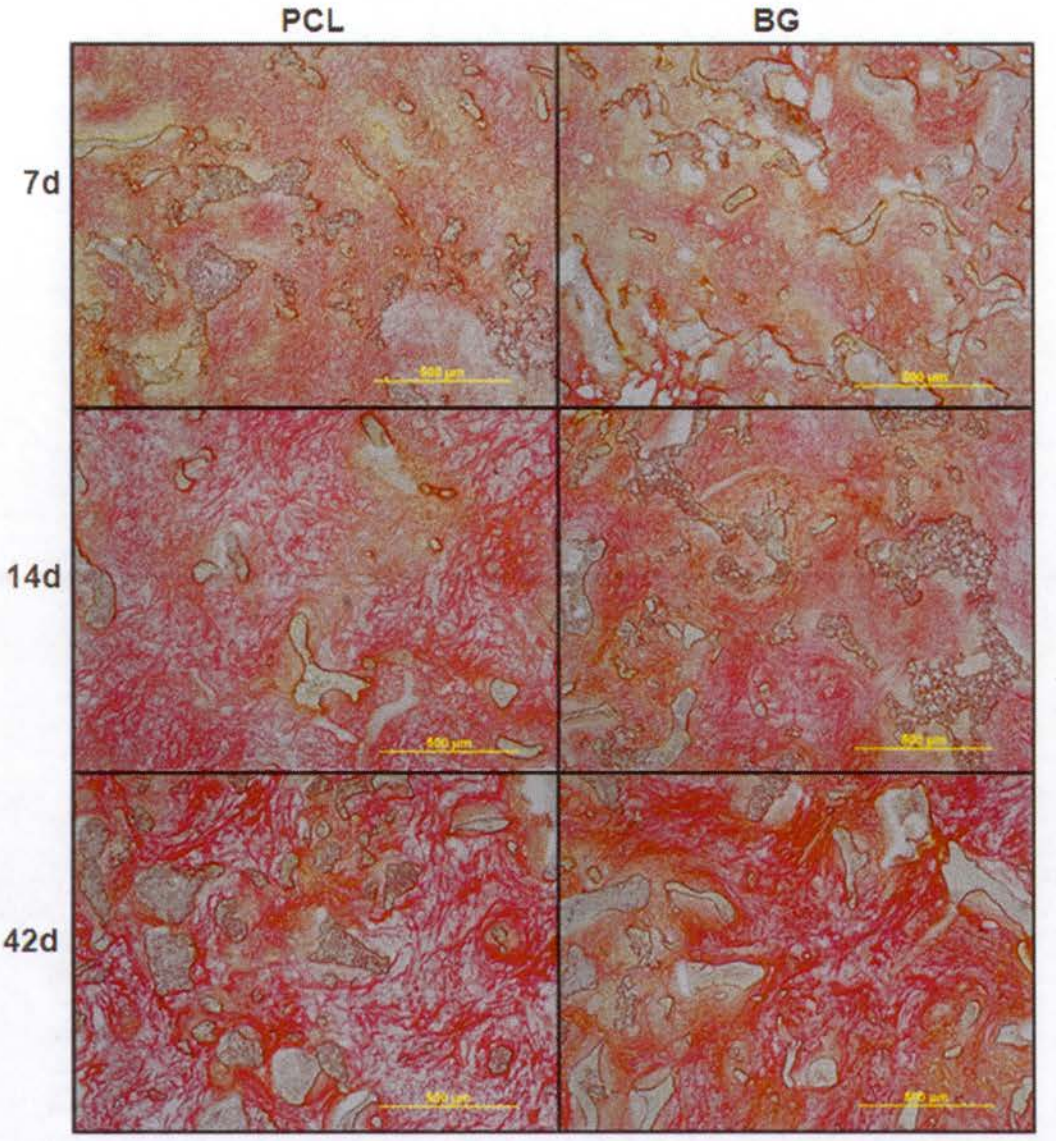


Figure 6.29. Top row: PSR- stained sections taken from 200μM into the scaffold at day 7. Centre row: Sections from the centre of the scaffolds at day 14. Bottom row: Sections from the centre of the scaffolds at day 42 (scale bar: 500 μm).

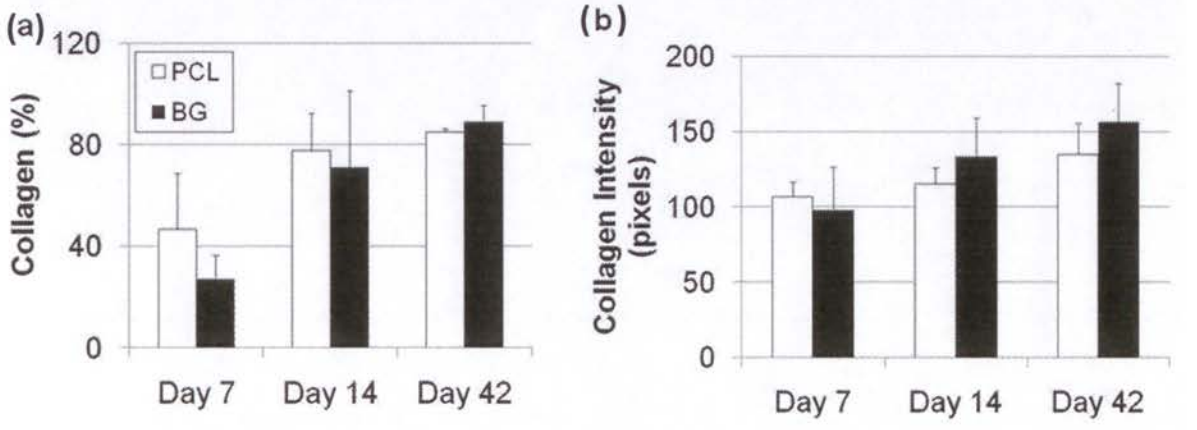


Figure 6.30. Quantification of collagen from PSR sections showing (a) % Collagen (b) Collagen intensity, which are both increasing over time and similar across the two scaffolds.

The collagen in the scaffolds was birefringent when examined under polarizing light microscopy. This was indicative of the oriented molecular structure of collagen (Figs 6.31, 6.32). In many regions, the collagen in the Bioglass® scaffold appeared more dense and crystalline than in the PCL scaffolds. The amount of polarised collagen increased from day 14 to day 42. The collagen appeared to be aligned in 2, perpendicular, directions, most likely corresponding to lines of force [Timmenga 1991].

Interestingly, the regions with the largest empty pores showed the highest level of mature collagen deposition. This is particularly evident in Fig. 6.32f, where the contrast between 2 regions is seen. Towards the upper right corner of the image is a region consisting of large pores with ample room for collagen deposition. In contrast, in the lower left portion of the image, the scaffold has experienced more pronounced degradation, resulting in small polymer fragments which have reduced the pore size. This suggests that there are advantages to delaying degradation of the scaffold, such as the ability to make space for a good level of collagen deposition and remodeling.

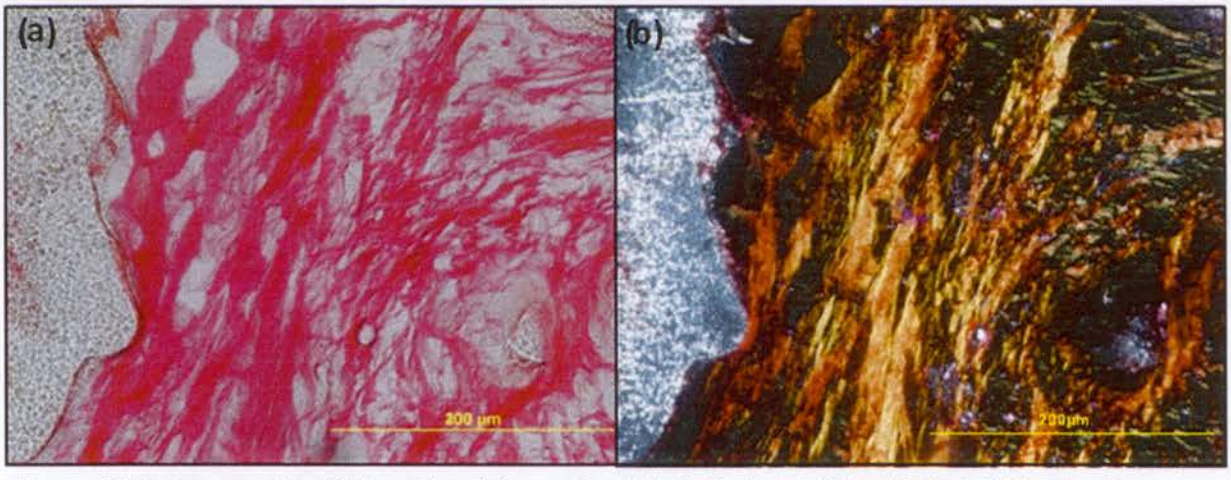


Figure 6.31. Images of a PSR section taken using (a) Optical and (b) polarised light, showing molecularly aligned collagen bundles in yellow (Scale bar: 200 µm).

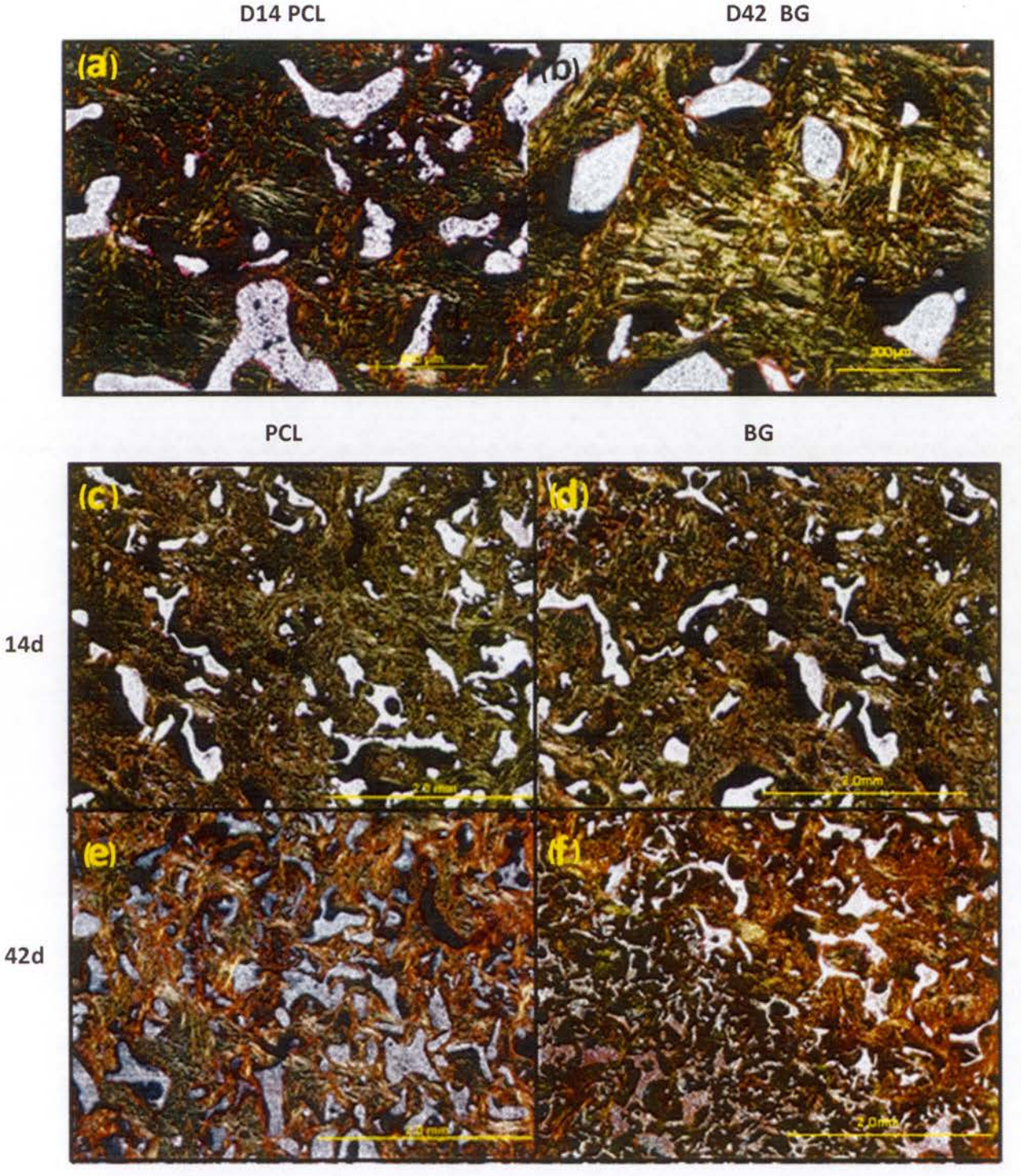


Figure 6.32. PSR stained sections imaged using polarised light, showing mature collagen bundles in the centre of the scaffolds, (a) Day 14, PCL (b) Day 42, BG (Scale bars: 500 µm), (c-f) Day 14 and 42 images show increasing collagen maturity over time. At day 42, the Bioglass® shows less mature collagen formation in regions where the scaffold is partially degraded (Scale bar: 2 mm)

The scaffolds were shown to be high in collagen 1 (Fig. 6.33). The scaffolds also facilitated the migration of cells and deposition of collagen within the mesopores inside the scaffold struts (Fig. 6.34). Cells (probably including fibroblasts and macrophages) and collagen (including collagen 4) were observed within the mesopores. Collagen was also observed to line the surface of the scaffold struts and mesopores. These features were visible throughout both scaffolds from day 14-42. The size of the mesopores increased from 2-40 μm (mean: 10.61±7.3 μm) prior to implantation to 12.5-75 μm (mean: 25.88±11.77 μm) by day 21.

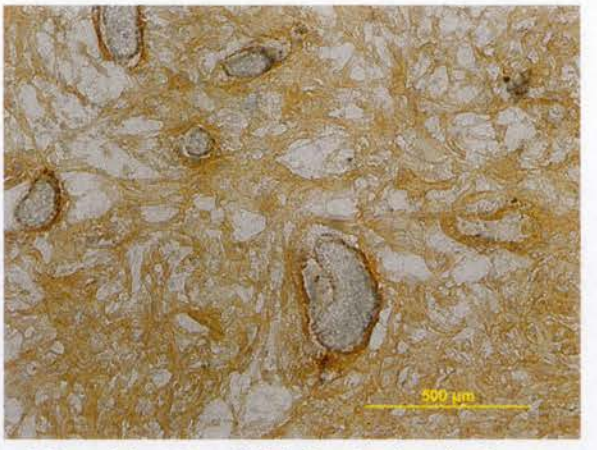


Figure 6.33. Collagen 1 staining of the BG scaffold after 21 days *in vivo*.

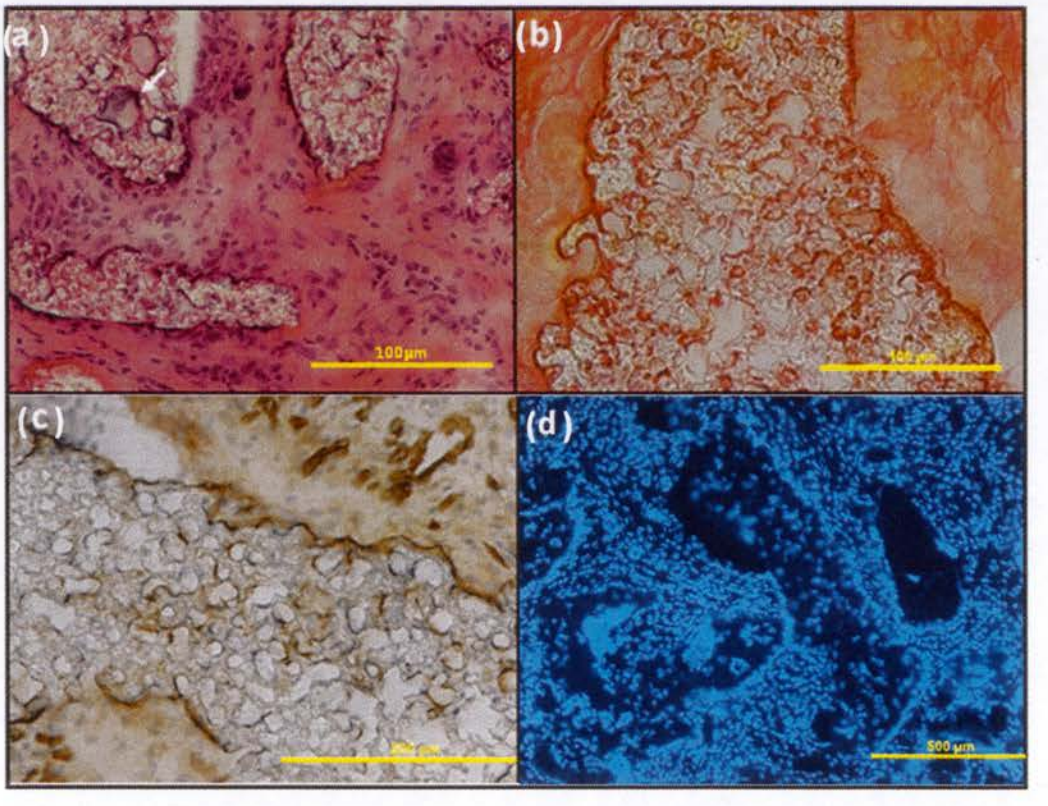


Figure 6.34. Micropores within the struts after 42 days subcutaneous implantation show the presence of collagen and cells. (a) H&E (b) PSR (c) Collagen 4/Eosin (Scale: 100 μm). Nuclei (blue) indicate cells within the pores in a & c, which are likely to include fibroblasts and macrophages. (d) DAPI (Scale:500 μm).

In some of the scaffolds, agglomerates of ellipsoid-shaped voids were visible, shown in Fig. 6.35 and Fig. 3.36. These features were 30-50μM in diameter and their outline stained positive for collagen IV. They were observed within 3 different BG scaffolds excised on day 14. In addition, these voids were observed on the outer edges of some scaffolds. It was hypothesised that this could be adipose tissue. Using SEM, the cell membranes of adipocytes take on a honeycomb structure. These adipocytes are empty as the lipid deposits of the cells (their major component) has been removed.

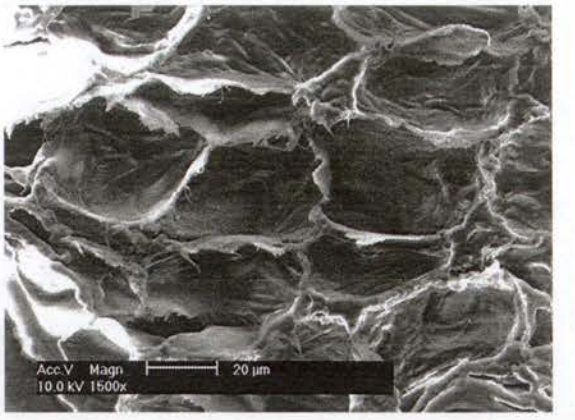


Figure 6.35. Possible adipose tissue within a Bioglass® composite scaffolds excised at day 14.

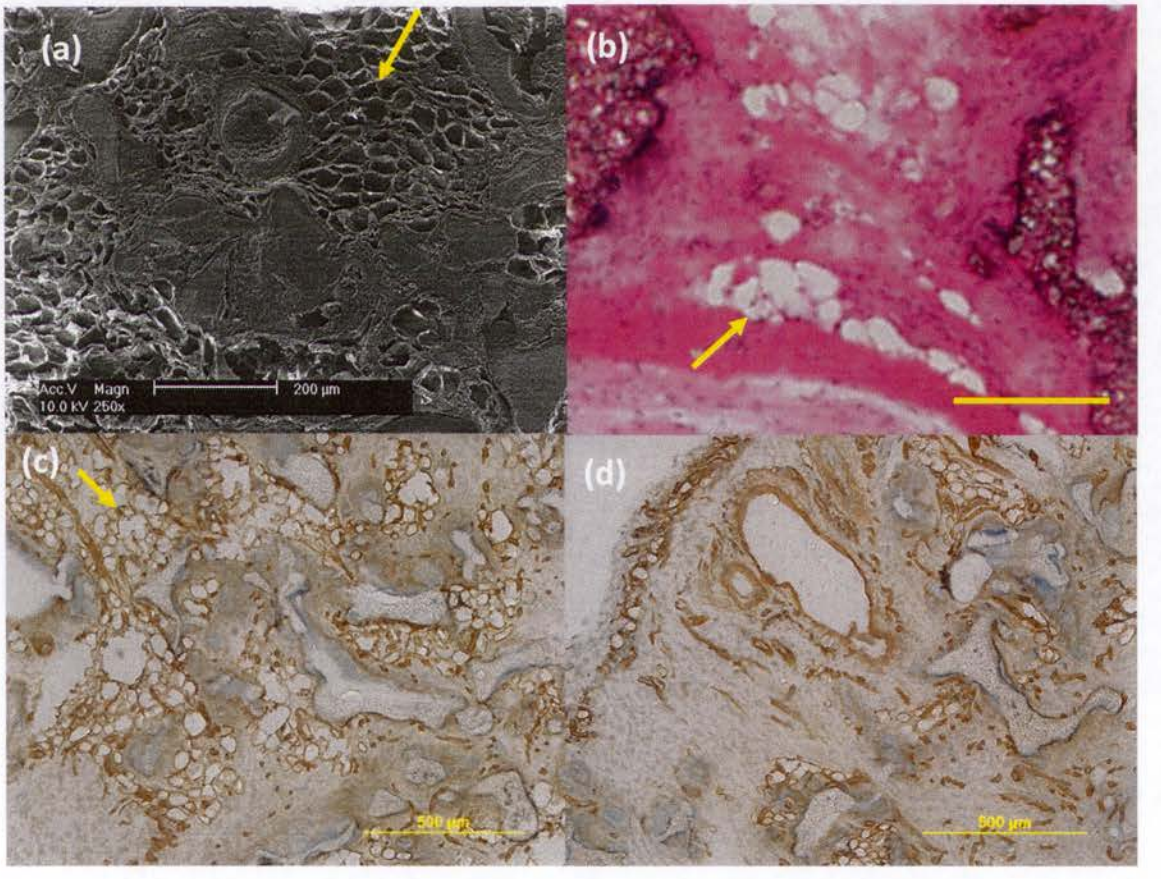


Figure 6.36. Possible adipose tissue was observed in BG scaffolds excised at day 14. (a) SEM (b) H&E (c, d) Collagen IV.

6.3.2. BLOOD VESSEL INGRESS INTO THE SCAFFOLDS

Blood vessels were present throughout all regions wherever granulation tissue had formed (Fig 6.37-6.39). Vessels were visualised at day 7, at a depth of 500μM into the BG scaffold. These vessels are pictured in Fig. 6.36 by CD31 endothelial cell staining (green) and dapi nuclear staining (blue). Shown in Fig. 6.38, the presence of vessels throughout both the scaffolds from day 14-42 was confirmed. Blood vessels inside the scaffolds were observed to have a lumen of >400μM in cross-sectional diameter.

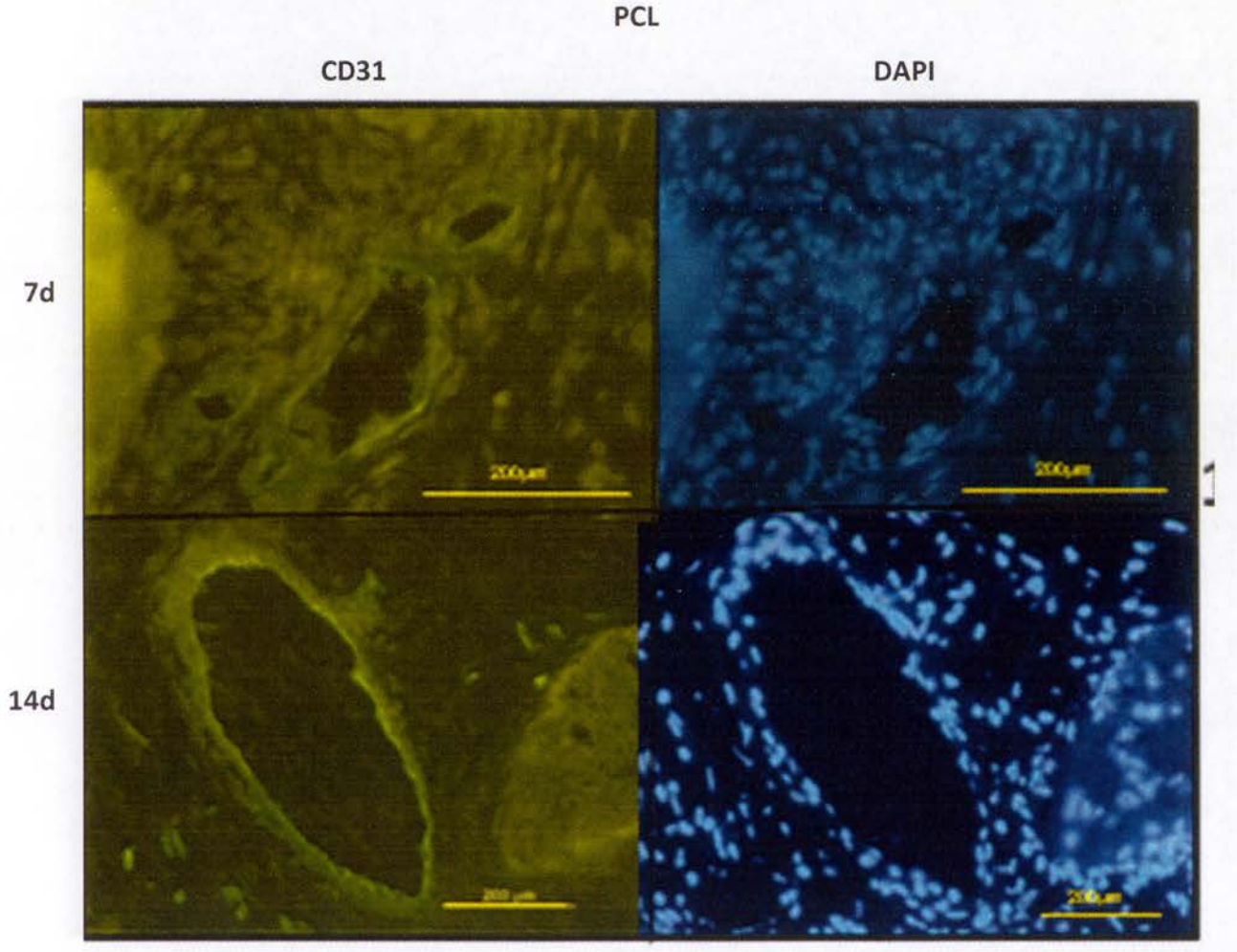


Figure 6.37. (top) Blood vessels 500 μm into the BG scaffold at 7 days, (bottom) Blood vessel in the centre of the PCL scaffold at day 14 (CD31 immunofluorescence- green, DAPI-blue, scale bars: 200 μm).

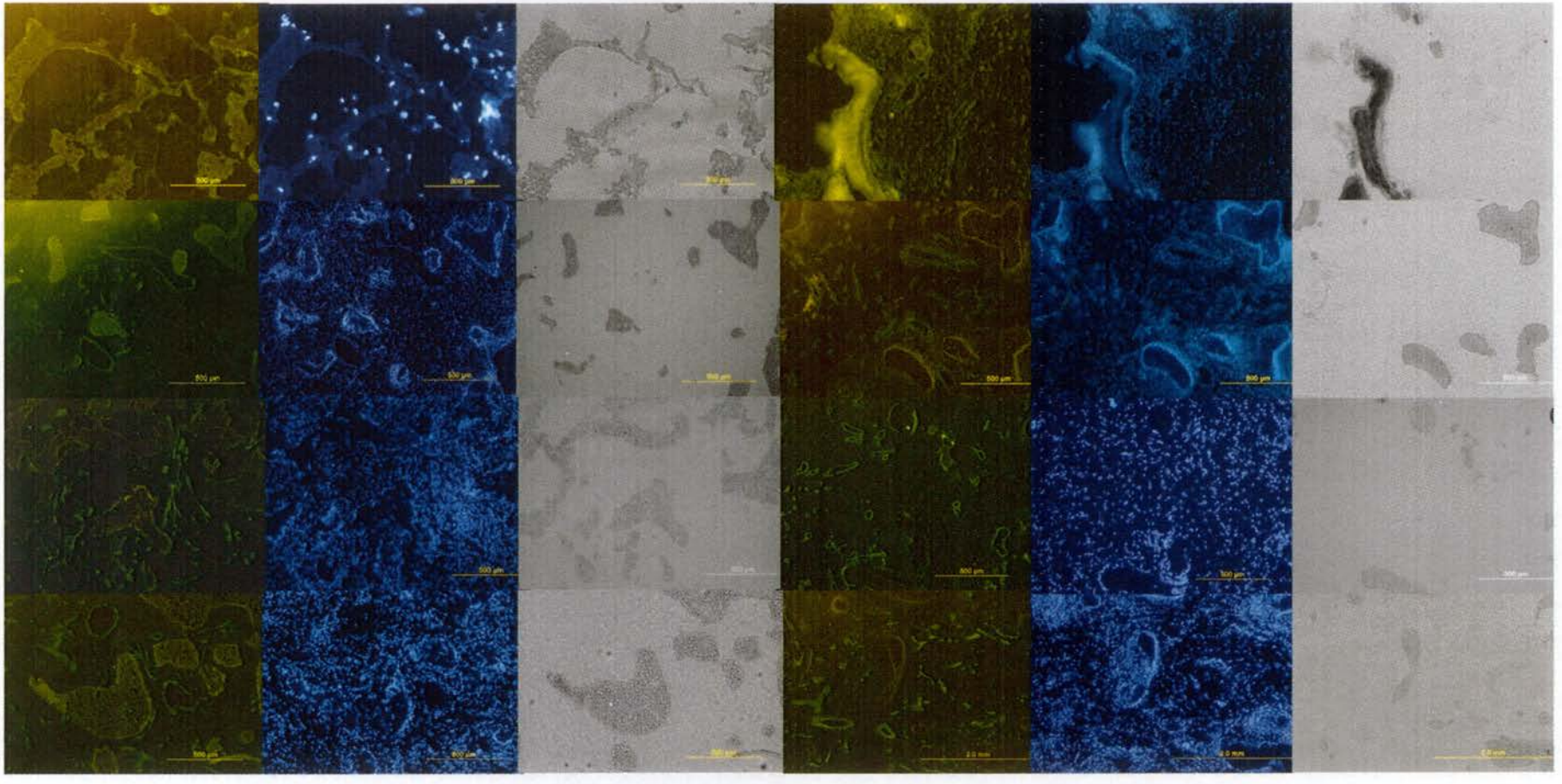


Figure 6.38. Blood vessels in the centre of the scaffolds using CD31 & DAPI fluorescent stains. For the BG scaffold, the day 7 images are taken close to the edge, in order to capture the fibrovascular ingress. (scale:500 µm)

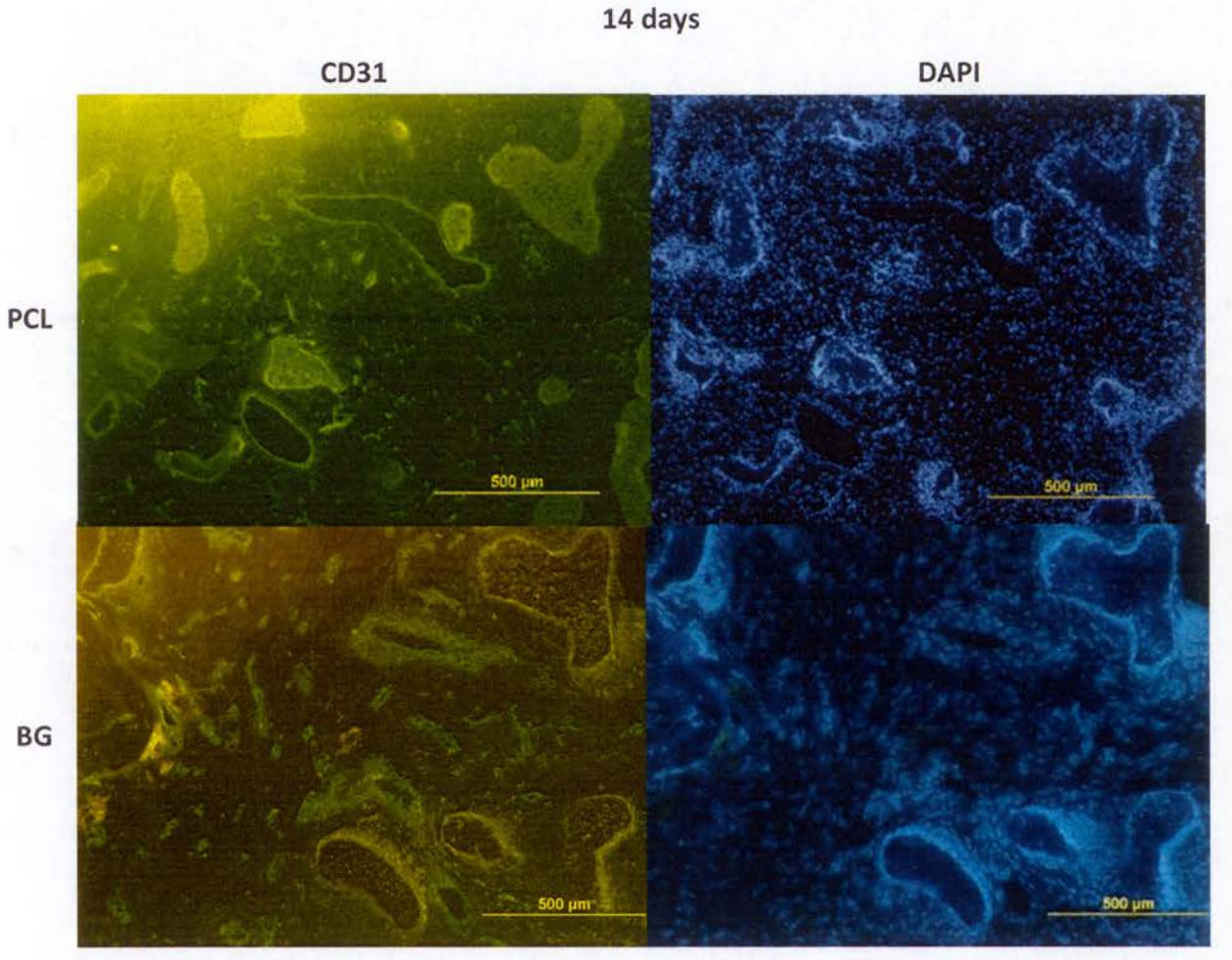


Figure 6.39. Blood vessels after 14 days in the centre of PCL and BG scaffolds (CD31, DAPI)

Vessels were also visualised using collagen 4 immunostaining, shown in Fig. 6.40. Large numbers of vessels with open lumens were observed.

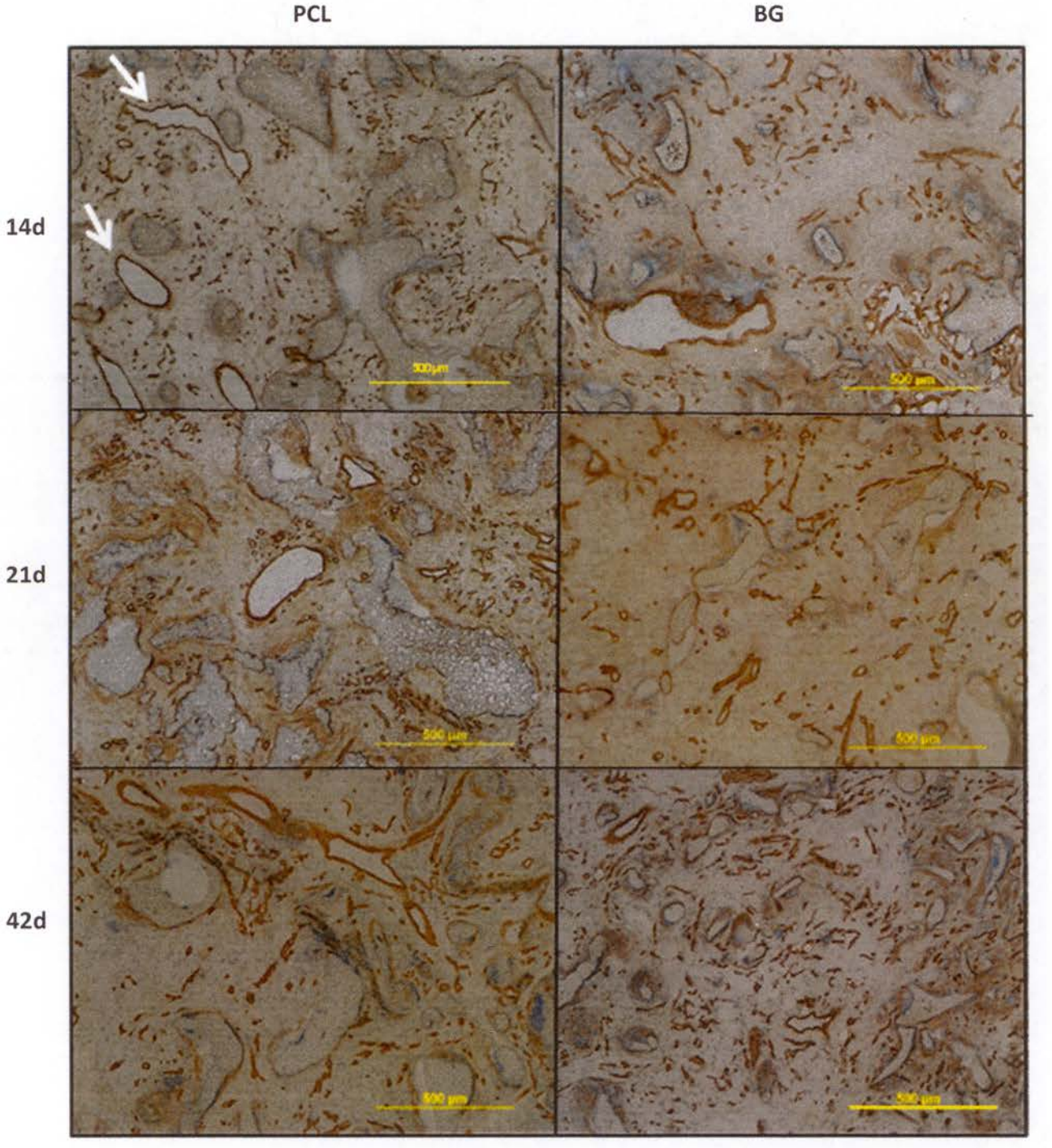


Figure 6.40. Blood vessels in the centre of the scaffolds (Collagen 4 immunohistochemistry, dark brown) (Scale: 500 μm)

Figure 6.41 shows vessel counts which were obtained from collagen 4 stained sections. Vessel numbers increased to day 21 followed by a subsidence at day 42. This corresponded with an inverse trend for arterioles. This trend is likely to indicate a resolution of the proliferation phases of wound healing. Higher number of vessels and arterioles were detected for the BG scaffolds. These differences were particularly pronounced for day 14 and day 42, respectively. This is likely to correspond with the earlier granulation tissue ingrowth and to indicate an earlier resolution of the proliferation phase for the BG scaffold.

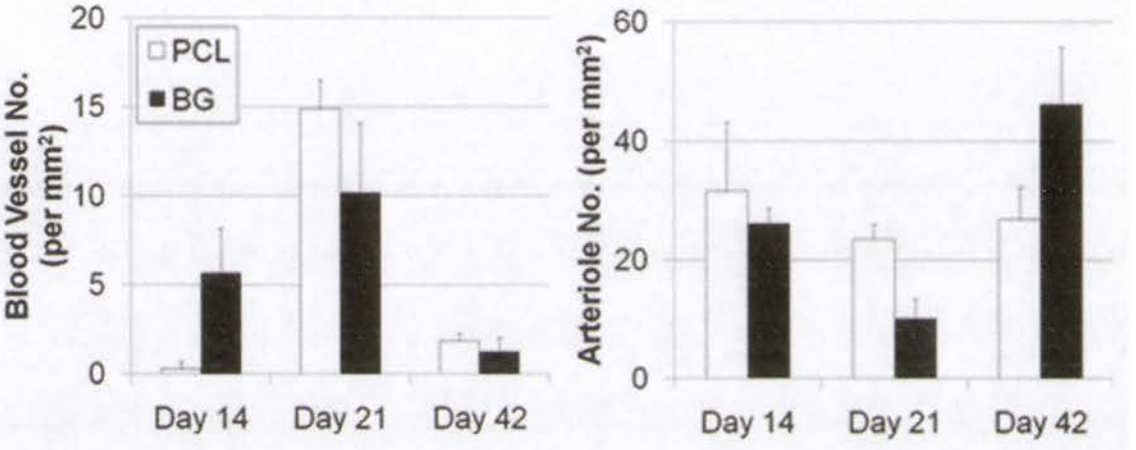


Figure 6.41. Blood vessel counts inside the scaffolds.

The tissue surrounding the scaffolds was highly vascularised and appeared to form a stable adherent bond with the scaffold (Fig. 6.42). Large vessels (>600 μm) were identified along the edge of the scaffolds (Fig. 6.43a,c). A 1 mm vessel was identified which had penetrated a degrading BG scaffold, at day 42 (Fig. 6.43d, inset). In this image, the deformation of this entire scaffold was further evidence of degradation occurring. In some of the SEM images, features were identified which could be endothelial cells, however this was not confirmed (Fig 6.43e,f).

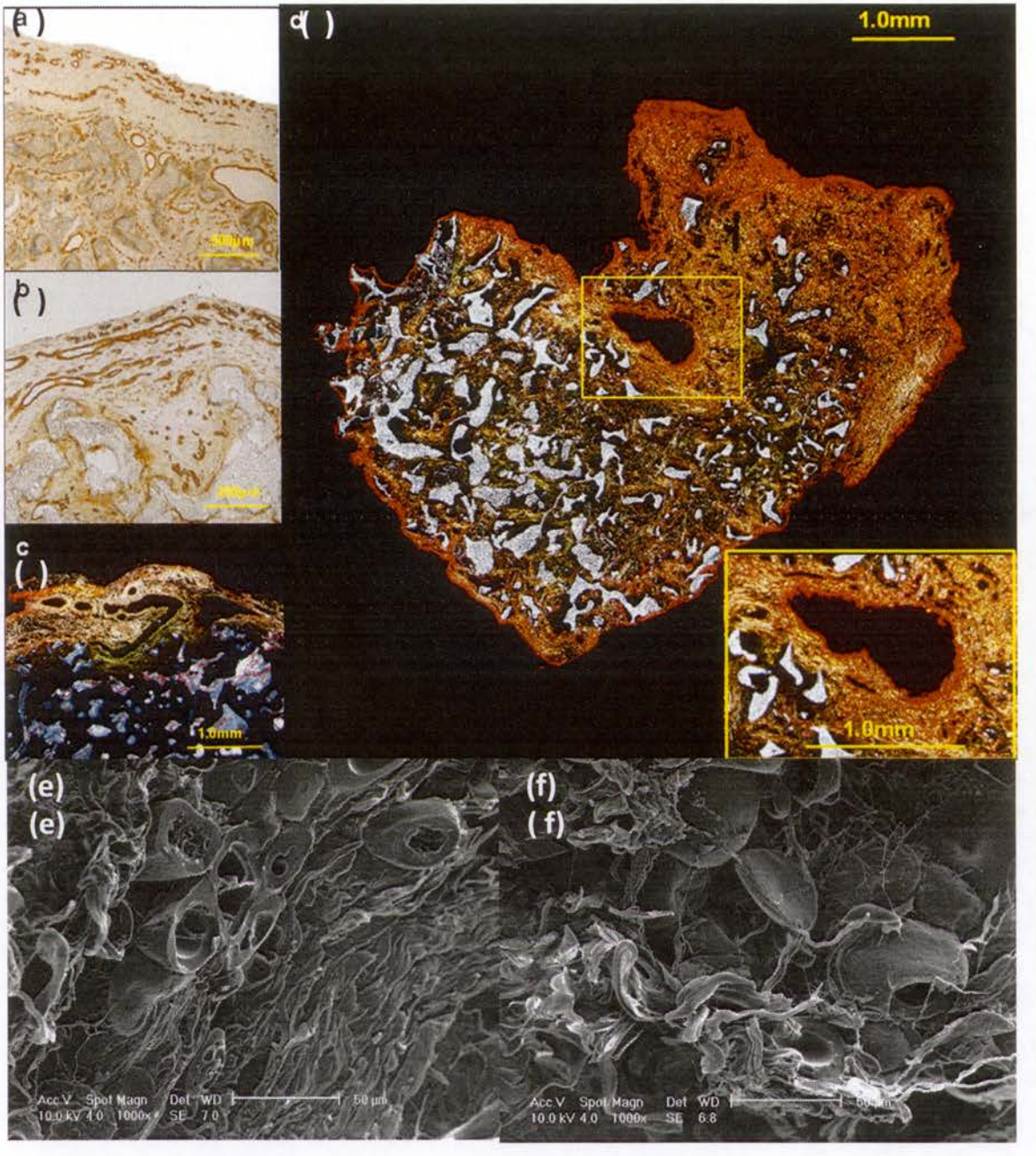


Figure 6.42. The tissue surrounding the scaffolds was highly vascularised. (a) Large vessel lining the scaffold (day 21, PCL, collagen 4 immunostaining scale bar 500 µm) (b) Vascularisation surrounding the scaffold (day 42, BG, collagen 4 immunostaining, scale bar 200 µm) (c) cross-section of a vessel on the outer edge of the scaffold (day 7, PCL, PSR, polarised filter, scale bar 1 mm), (d & inset) 1 mm+ vessel inside the degrading scaffold (D42, BG, PSR, polarised filter, scale bars 1 mm). (e,f) SEMs of tissue surrounding a PCL scaffold which was excised after 14 days *in vivo*. The round cells in these images could be endothelial cells. (scale bar: 10 µm)

6.3.3. EXAMINATION OF THE EFFECT OF THE SCAFFOLD ON INFLAMMATORY RESPONSE

Shown in Fig. 6.43, macrophage immunostaining using CD68 showed an aggregation of macrophages on the edge of the scaffold struts. This was more pronounced for the BG scaffolds. At day 42, it was evident that the BG scaffold has broken into smaller pieces than the PCL scaffold. Macrophages were particularly prominent surrounding the small pieces of biomaterial (arrow).

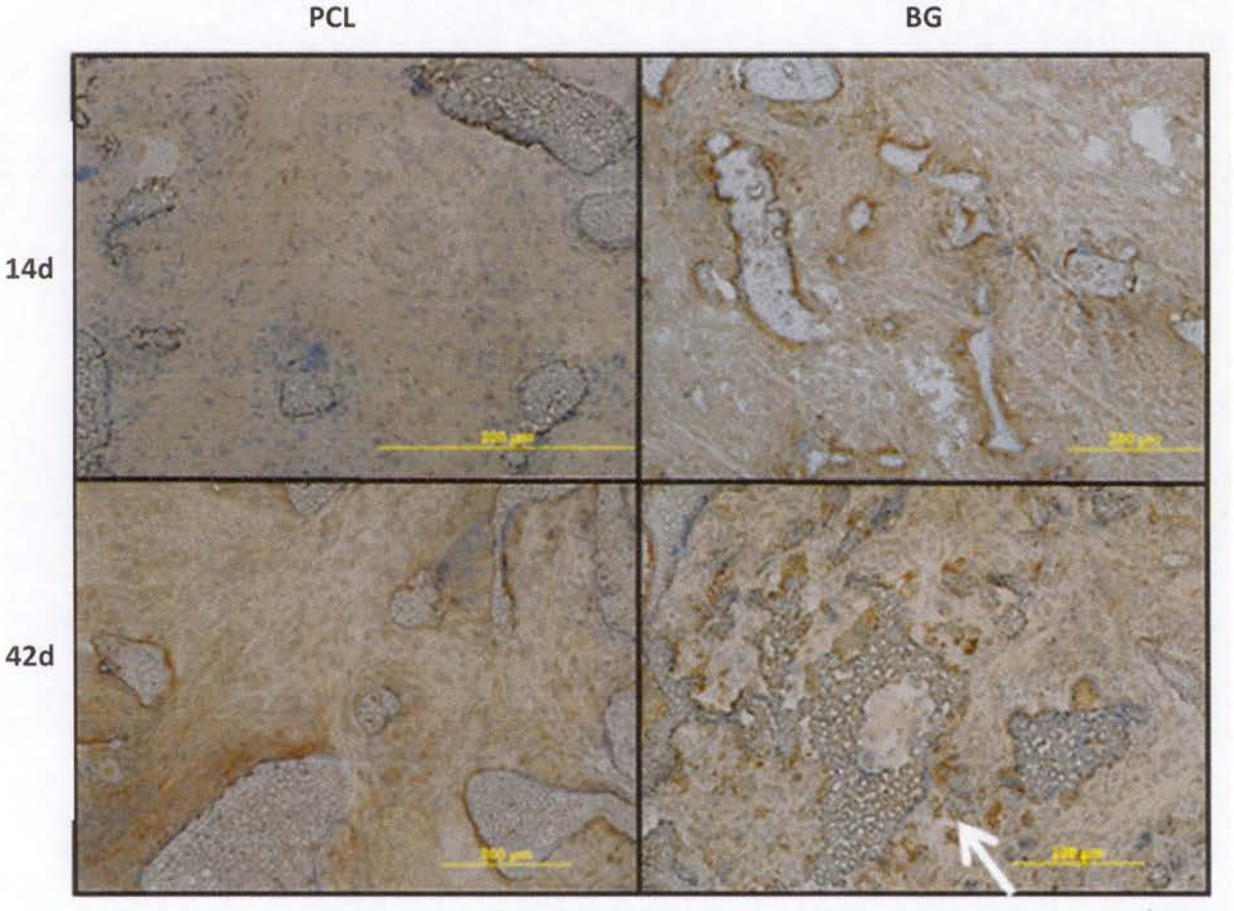


Figure 6.43. Scaffold sections stained for macrophages, which particularly accumulate near the scaffold (CD68 immunostaining, dark brown, Scale bar: 200um, arrow indicates macrophages near disintegrating scaffold)

The circulating white blood cell counts showed similar levels of inflammatory cells over time (Fig. 6.44). This indicated there was no major adverse systemic reaction occurring due to infection in the animals. For both scaffold types, white blood cells tended upwards at day 7 and day 42. When white cell subsets were examined it appeared that this increase could be caused by an increase in monocytes and lymphocytes which followed the same trends. The level of neutrophils stayed constant over time. In addition the level of circulating eosinophils was very low, indicating minimal allergic response.

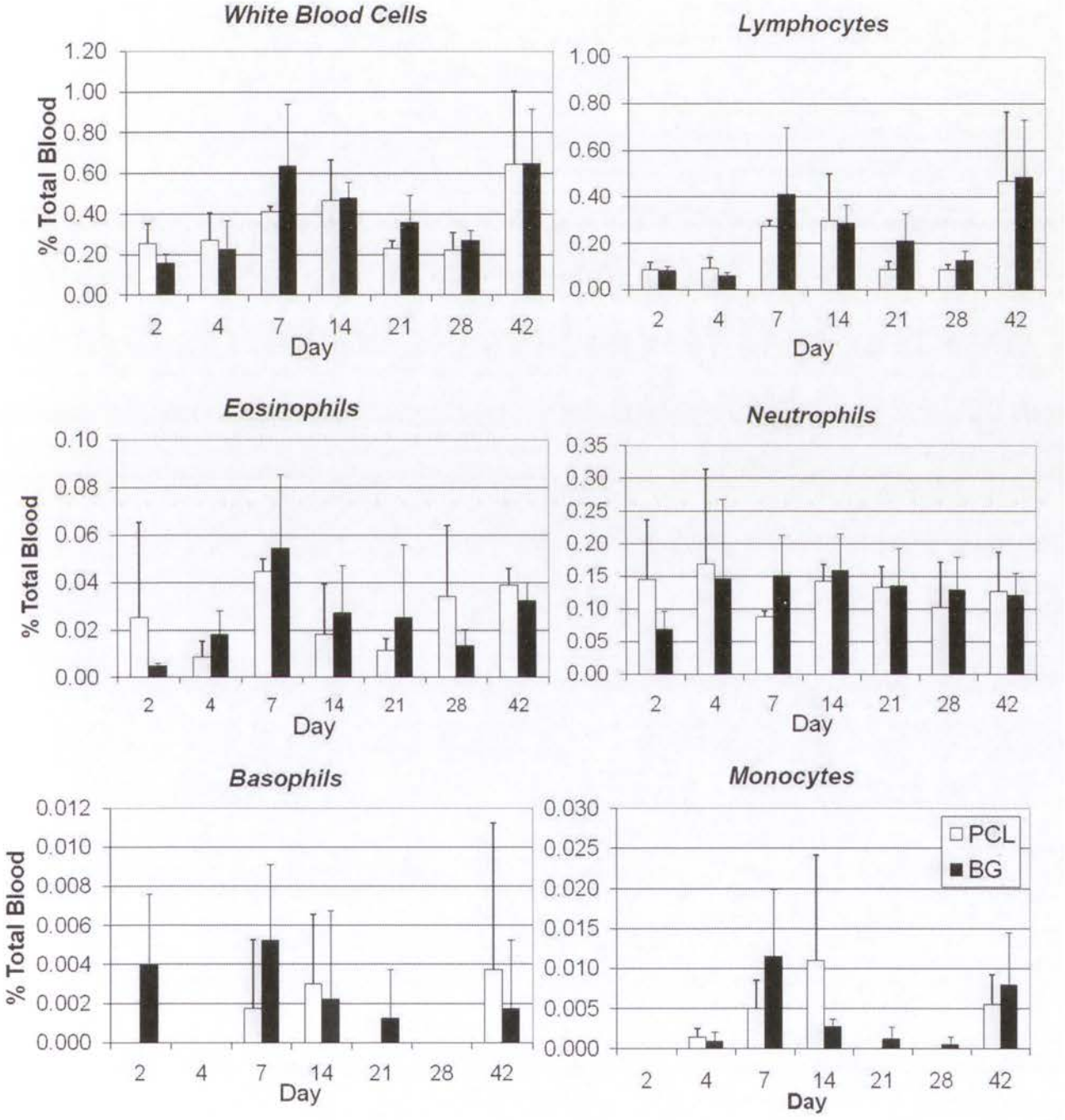


Figure 6.44. Circulating blood counts for various cell types.

Fluid was successfully extracted from the excised scaffolds and decreased with time (Fig. 6.45). There was a tendency towards increased fluids in the BG scaffold at later timepoints.

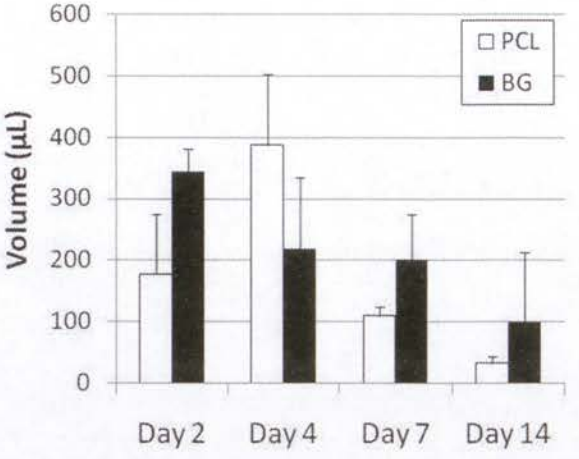


Figure 6.45. Volume of wound fluid collected from scaffolds.

Fluid cell counts are illustrated in Fig. 6.46. Neutrophils were all MPO negative, and showed a fall in numbers from day 2 to day 14. The number of eosinophils decreased with time in both scaffolds. In contrast macrophage numbers varied between the scaffolds at each timepoint. At day 2 macrophage numbers were lower in BG compared to PCL scaffold. The opposite was true at day 14.

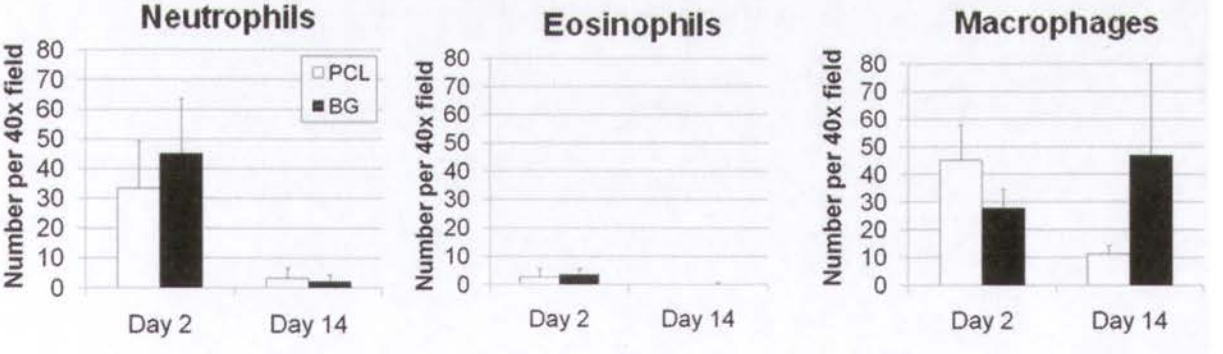


Figure 6.46. (a) Counts of neutrophils, eosinophils and macrophages from the wound fluid (MPO negative).

Gelatinase zymography (Fig. 6.47) revealed bands of enzymatic activity in fluids corresponding to latent MMP-2 (72kDa), MMP-9 (92kDa) and their active forms at 62kDa and 82kDa respectively. There was a significant decrease of proMMP-2 from day 2 to 7, with no difference between the scaffolds. Over this period there was an increase in the active form of MMP-2, a result consistent with the remodeling and laying down of the new collagen seen with earlier results. Levels of active MMP-2 expressed in the PCL matrix was significantly higher than the BG matrix at days 4 and 7. There was no change in MMP-9, either for the pro or active forms,

over time or between the scaffolds. These results indicate a good host response to the scaffolds.

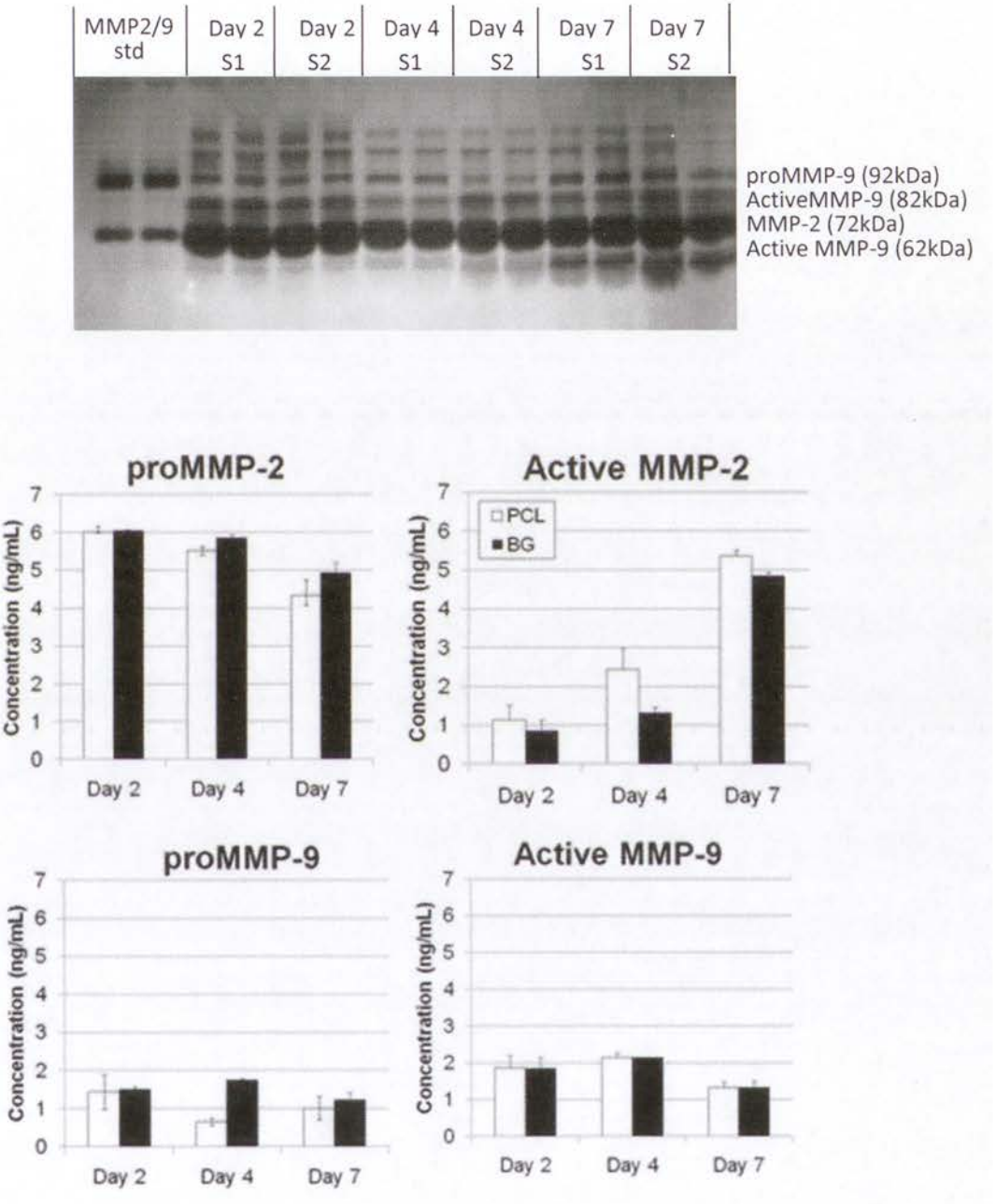


Figure 6.47 (a) Gelatin zymography results obtained from the wound fluid showing the concentration of MMP-2, MMP-9 (and their active forms), indicating increasing growth and decreasing inflammation over the first 7 days

6.4. DISCUSSION

This preliminary study assesses the biocompatibility of the variotis™ scaffold and tests the hypothesis that 45S5 Bioglass® infused scaffolds are safe and efficacious for use in soft tissue engineering. To the author's knowledge, this is the first study to investigate *in vivo* cellularisation and de novo tissue formation in 45S5 Bioglass®/PCL composite foams. A total of 124 scaffolds were implanted subcutaneously into 56 rats. Complete tissue filling and vascularisation was achieved inside scaffolds within 2 weeks. All scaffolds were well-tolerated and wounds healed well with no signs of infection. This is reliable evidence for the cleanliness of the synthesis process and validity of the gamma sterilisation process. The scaffolds needed to be cut out of the tissue, indicating good integration with the surrounding tissue, with no isolating, fibrous encapsulation. This is a promising result which demonstrates the potential for variotis™ to serve as a soft tissue scaffold. This study suggests that variotis™ could have the ability to make space for developing tissue whilst transferring physiologic levels of load to developing tissue.

6.4.1. Rapid and Complete Fibrovascular Tissue Ingrowth Inside Scaffold

A fibrin clot network was observed to have filled the scaffold 2 days after implantation (Figs. 6.20d, 6.26, 6.27). This network is associated with distribution of inflammatory and blood cells throughout the scaffolds. This presumably serves as a provisional matrix on which fibrovascular tissue develops [457]. Tissue infiltration was observed progressing into the scaffold after 1 week (Fig 6.20d, 6.25). Within 2 weeks, complete filling of the variotis™ scaffold with fibrovascular tissue was evident. This is an excellent result demonstrating tissue formation which more rapidly than the majority of other tissue scaffolds reported in literature. In addition, tissue filling was achieved in 10 mm-thick scaffolds, which have the ability to be formed into even thicker constructs. A major reason for this is the high permeability of the scaffold to inflowing blood carrying progenitor cells and necessary factors.

The process of tissue ingrowth was successfully observed using a range of techniques, including histology and SEM. The granulation tissue-filled scaffolds were readily sectioned for histology, and did not experience fragmentation as the tissue acted as a reinforcing phase. The volume of the scaffolds increased over the first 7 days (2x original volume) (Fig 6.20b), indicating its shape and compliant nature accommodated for the infiltrating blood clot and fluids. From days 7-42, the scaffold returned to its original volume as the tissue matured and contracted the material. The new tissue was high in collagen content, particularly collagen 1 (Fig. 6.28, 6.29, 6.30). Under polarised light, mature aligned collagen bundles were observed throughout the scaffolds. The Bioglass® composite scaffold some increase in the rate of tissue

ingrowth than the PCL scaffold (6.21a). This is consistent with previous findings [85]. Under SEM, more mature collagen bundles were observed in the Bioglass® scaffold compared to the control PCL scaffold, which displayed a less dense and more disordered tissue structure.

The ability of the variotis™ scaffold to facilitate rapid de novo tissue can be attributed in part to its large pore size, high level of porosity, interconnectivity and permeability. The biocompatibility and biostability of the scaffold may play an important role in ensuring degradation byproducts do not hinder or interfere with tissue formation.

6.4.2. Vessel Formation Inside Scaffolds

Healthy degrees of vascularization were seen within both scaffold groups. Vessels were evident by 1 week, 500um in from the edge of a Bioglass® composite scaffold (Fig 6.37). By 2 weeks, good vessel ingress was observed throughout all scaffolds using CD31 and collagen 4 staining (Fig. 6.38-40). These vessels had lumens and thick vessel walls. Counts of blood vessels peaked at 21 days and had decreased by 42 days. This was consistent with the resolution of the proliferative phase of wound healing in which vascularisation to a wound decreases as the tissue remodels. Vessel counts within the Bioglass® composite scaffold peaked and resolved earlier than the PCL scaffolds; consistent with the earlier tissue front. A vessel was observed within the Bioglass® composite scaffolds with a diameter greater than 1mm (Fig. 6.42d). To the author's knowledge, this is the first time that vessels this large have been observed inside synthetic soft tissue scaffolds within 6 weeks.

The tissue around the scaffold was highly vascularised (Fig 6.42) and did not form an isolating fibrous/fluid-filled capsule, as has been previously reported for many scaffolds [61, 62, 628]. Examples of scaffolds which have formed these capsules include bulk dextran hydrogel [628], PLAC foam [61] and polyurethane porous scaffolds [62]. The formation of a stable interface of a scaffold with the tissue is a critical factor in reducing the chance of fibrous encapsulation [632]. The stiffness of an implant can focus stress at the interface, leading to poor integration and overall function of the implant, prolonged healing times and associated pain and morbidity. In the current study, capsule formation is likely to have been minimised by reduction of stress shielding, due to the interweaving nature of the scaffold with the tissue (via macro/meso pores and textured strut surfaces) and the anisotropic mechanical compliance of the foam as a whole. Porous or textured materials have been shown to produce a less densely packed, random capsule structure that is more vascularised [29, 786].

6.4.3. Inflammatory Response and Scaffold Bioresorption

Circulating blood counts (Fig 6.46) showed little change in the numbers of inflammatory cells over time. Peaks in whole blood counts were noted for both scaffolds at days 7 and 42. The level of neutrophils stayed constant over time. The volume of fluid extracted from the scaffold reduced over time (Fig. 6.45). Wound fluid cell counts showed neutrophils were MPO negative and reduced over time. The numbers of macrophages were higher in the PCL scaffold after 14 days, compared to the PCL (Fig. 6.46). These are good indications that a normal wound healing process was progressing. Gelatin zymography results (Fig. 6.47) indicated no change in MMP-9 over time. Levels of proMMP-2 decreased from days 4 to 7, corresponding to an increase in the active form.

Immunostaining revealed macrophage aggregation near the scaffold struts, particularly for the Bioglass® composite scaffold, consistent with the wound fluid cell counts (Fig. 6.43). This may have contributed to the increased fragmentation which was observed for the Bioglass® scaffold at day 42. Scaffold change is likely to have occurred through both hydrolysis and biodegradation, through the action of the macrophages [83, 246]. The mode of degradation of PCL, particularly in the presence of Bioglass should be the subject of future studies.

The low inflammatory levels during this study can be partly attributed to the bio-stability of the scaffold. The current scaffolds are anticipated to completely bioresorb in 8-12 months, although in bulk form PCL takes 2+ years to degrade. Bioresorption will occur at an increased rate to the bulk material due to the high surface area created by the multi-leveled pores, surface texture, and the addition of Bioglass® (which creates an alkaline environment) [188]. PCL eventually degrades into a sole metabolite, hexanoic (caproic) acid, and essential fatty acid found in fats and oils and causes a negligible change in local pH over time [247]. This is in contrast with rapidly degrading materials such as PGA and PLA which liberate byproducts (glycolide, lactic acid) which rapidly accumulate and can adversely alter the pH. This can interfere with modeling and remodeling of wound tissues [14, 27, 28, 234, 235]. The good level of vascularisation achieved in the current study is also likely to aid in the removal of toxins and degradation products from the site. Vascularisation is often limited by an intense inflammatory response [14]. In addition, the volume of material implanted in the variotis™ scaffold is minimised due to its high porosity. This is likely to reduce the foreign body response to the implant. This is in contrast to other scaffold designs such as rapid prototyped structures. In a previous study, bioactive glass-derived hydroxyapatite coated cellulose sponges evoked a massive inflammatory reaction 1-3 days post subcutaneous implantation in rats [230]. These sponges particularly attracted macrophages and fibroblasts, and favoured angiogenesis. However, from 1 month to 1 year after implantation these sponges showed no change from

the cellulose controls. Tissue formation was histologically normal and the major ECM molecules were synthesised in a normal ratio. A similar phenomenon may be evident in the current study.

6.4.4. Possible Adipose Tissue within Scaffold

In some of the scaffolds, tissue was observed which is could be vacant adipocytes which are lacking lipid droplets (Fig. 6.35-6.36). These structures were visible in at least two of the bioactive glass scaffolds excised at day 14, but were not observed in any other scaffolds. Further staining is required to confirm whether this is in fact adipose tissue.

Two vital factors in adipose tissue formation which have been overcome in this study are volume retention and adequate angiogenesis [13]. For adipose tissue to form, the scaffold must provide sufficient mechanical stability to withstand *in vivo* compressive forces [787]. Adipose tissue formation is rarely reported in synthetic scaffolds. This is likely to be largely due to the lack of scaffold vascularity, and space making ability of many bioabsorbable materials and constructs. Examples of reported adipose tissue within avascular, synthetic polymer scaffolds, include rigid, rapid prototyped PCL meshes [83] and soft, polyethylene glycol diacrylate (PEGDA) matrices [13]. Stosich and coworkers demonstrated adipose tissue formation inside PEGDA matrices, after 4 weeks [13]. This scaffold maintained its shape and dimensions for at least 12 weeks, and this is likely to be an important factor for its success. Some researchers have commented that although porous scaffolds can provide a suitable environment for cell penetration and vascularisation and cell penetration, the conversion of preadipocytes into mature adipocytes does not always occur [13]. This is attributed to a lack of contact inhibition which is required for differentiation to occur [13]. Contact inhibition is less likely to occur in the variotis™ scaffold due to the presence of the supportive ECM network throughout the PCL matrix.

6.4.5. Comparison with Literature- Tissue Infiltration and Vascularisation

This study demonstrated 100% new tissue formation throughout the variotis™ scaffold. This tissue has formed more rapidly and is of a superior quality to most previous work. As shown in Table 6.1, most scaffolds reported in the literature are unable to achieve complete tissue filling after 6+ weeks [84, 85]. For example, a PDLA scaffold tested by Day and coworkers demonstrated <50% subcutaneous tissue infiltration by the end of the study (6 weeks) [85]. This could be due to the small pore size (<200 μm), oriented pore structure and limited interconnectivity resulting from the TIPs synthesis process (ref 3.1.6). Similarly, PDLA scaffolds (formed using NaCl porogens and compression molding) by the same group achieved <20% tissue. Both these scaffolds exhibit poor pore interconnectivity that is associated with

incomplete tissue infiltration. These *in vitro* studies provide insight into how scaffold fabrication routes can directly impact scaffold dorm and subsequently its suitability for infiltration by various tissues. The novel synthesis method has addressed the limitations associated with other popular methods. The rate and proportion of tissue filling achieved in this study validates the form and fabrication routes. Even scaffolds consisting of a naturally derived, biomimetic molecular architecture exhibit poor tissue infiltration. This is apparent in a study by Kurane and coworkers in which 220 μm –thick fibrous, elastin matrices only achieved 50% tissue, even with bFGF delivery [627]. This result can be attributed to the low porosity and minimal free space between the fibers (<50 μm) and poor long-range interconnectivity.

Fig. 6.48 contains a comparison of the thickness of acellular, polymer scaffolds which have previously achieved complete soft tissue filling (ref Table 6.1 and section 6.1.3). The thickest scaffold reported is an 8 mm-thick PLAC (TIPS/PL) scaffold by Misaki and coworkers [61]. It is likely this scaffold only facilitated fibroblast migration and collagen deposition and not widespread vascularization. Fibrous layers were visible on the outer surface, isolating the scaffold from the surrounding adipose tissue and vascular networks. Comparison cannot be readily be made due to the differing site of implantation (thoracic cavity). A lack of pore interconnectivity could be partly responsible for the low levels of tissue integration. The other scaffolds in this figure showed suboptimal fibrovascular growth. A lack of collagen deposition was observed, even though the 2.5 mm-thick PCL (RP) scaffold tested by Lam [83] showed good interconnectivity and porosity and facilitated adipose tissue (3 months) and fibroblast migration (6 months). This was likely to have been partly due to the rigid nature of this scaffold, which stress shields the tissue. A 2 mm-thick PU (TIPS/PL) scaffold synthesized by Bezuidenhout did achieve a good level of vessel formation and could have facilitated collagen deposition, although this was not discussed by the authors. Fibrous encapsulation was, however, present during this subcutaneous study. A hyaluronan (SL) scaffold studied by Rhodes [57] did fill with fibrous tissue by 12 weeks, however, only low levels of vascularization were reported. In addition to the constructs included in this graph, a PGA/TMC mesh plug, studied by Nienhuiis, has demonstrated good levels of vascularisation and collagen ingrowth [68].

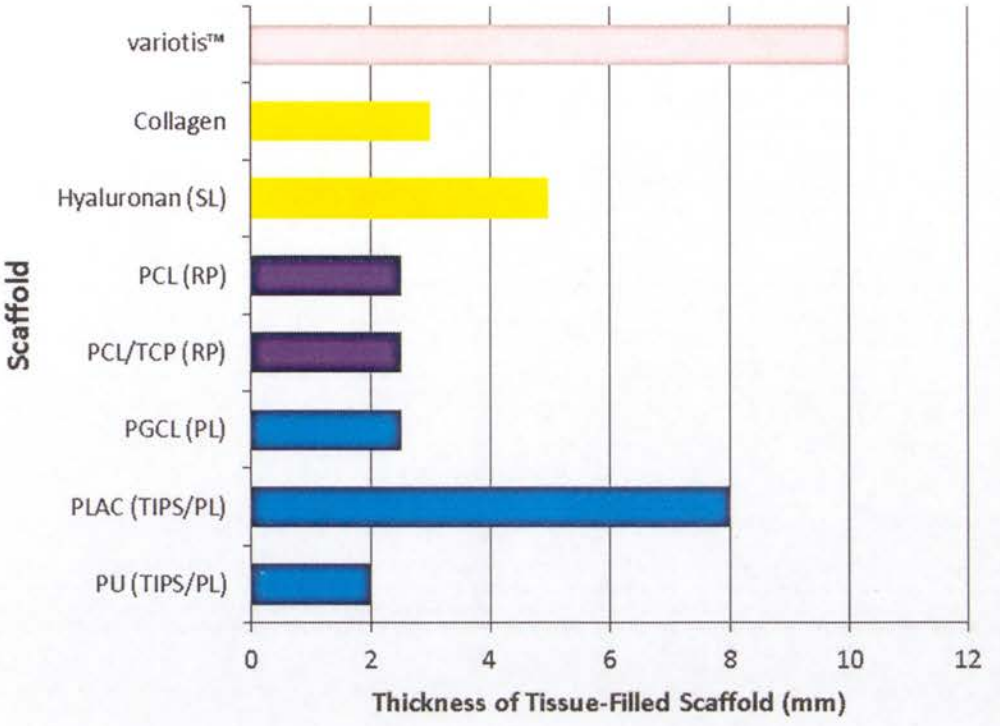


Figure 6.48. Comparison of cellular polymer scaffold thickness with complete tissue infiltration (references included in Table 6.1).

The majority of previous studies have reported vessels within scaffolds which are much smaller than detected in the current study. Often they are <80 μm in diameter [365] or limited to small capillaries. Studies which have reported the presence of vessels with lumens occur in scaffolds with large pore sizes (>300 μm) and good mass transfer [16, 63, 84, 86]. These are both key benefits provided by the variotis™ scaffold. Previous studies have shown a clear correlation between an increase in vessel diameter with increasing pore dimensions [84]. The importance of the pore size was demonstrated by Yamamoto and coworkers who detected vessels in PVA scaffolds with an average pore diameter of 350 μm pores but not 250 μm [84]. A number of previous studies have been unable to accomplish substantial vascularisation within scaffolds without the use of angiogenic growth factors, including bFGF, platelet-derived growth factor, and VEGF [363-365). Risk of cancer developing exists with their usage [299]. They are also costly. Scaffold designs that can facilitate vascularisation without dependence on these factors are pertinent. Pre-seeding of scaffolds with cells has also been reported as potential stimulus for vascularisation [60, 788]. To the author's knowledge, the current study has shown superior, rapid angiogenesis within a porous, synthetic scaffold, than previously reported, without the need for growth factors or pre-seeding with cells.

This *in vivo* study provides preliminary evidence that validates the scaffold design suitability for wound healing subcutaneous soft tissue. Variotis™ composition, structure, mechanical characteristics and sterilisation approach are validated. Studies to determine whether the

scaffold increases wound strength in healthy and diabetic animals are recommended. The ability of keratinocytes to proliferate on the scaffold would also be important to study *in vitro* and *in vivo*.

6.5. CONCLUSION

- A subcutaneous small animal study demonstrated fibrovascular tissue infiltration into 10 mm-thick PCL and Bioglass®-PCL composite scaffolds after 7 days of implantation. By 14 days, both scaffolds were completely filled with highly vascular and mature tissue.
- Tissue inside the scaffolds contained a high proportion of crystalline collagen 1 and mature collagen bundles, suggesting the elastic scaffold could have facilitated force transfer to assist tissue modeling.
- High levels of vascularisation were observed within the scaffold pores. Vessels with lumens increased in number from day 7-21 and decreased by day 42. Vessels measuring up to 1 mm were detected within the scaffold after 42 days, as the scaffold had partially degraded.
- Cells and collagen deposition were observed within the microporous scaffold struts from days 14-42.
- The Bioglass®-PCL scaffold showed a slightly earlier progression of fibrovascular tissue and the presence of higher levels of macrophages.
- Tissue surrounding the scaffold was highly vascular and did not form an isolating capsule.
- Low inflammatory levels were observed for the circulating blood counts and fluids. Neutrophil levels were low.
- This study provides evidence that supports the biocompatibility and validates the variotis™ scaffold design. The scaffold could have potential for further development into a subcutaneous skin graft for chronic wounds.

CHAPTER 7- CONCLUSION

- Two novel soft tissue scaffolds were developed and characterised.
- A biphasic osteochondral bed construct, consisting of a porous calcium silicate or sphene matrix, with a gel phase to support cartilage, supported chondrocyte culture to a period of 4 weeks.
- The calcium silicate had a low compression strength (262kPa) but this was increased to 1048kPa with PDLLA coating.
- Therapeutic testing showed zoledronic acid reduced breakdown of cartilage ECM, while S100A9 increased the degradation.
- A bioactive, high interconnective porosity composite Bioglass®-PCL scaffold (variotis™) was developed with high extensibility and a low modulus which avoids causing trauma to the skin.
- Variotis™ was readily manufactured in large, consistent batches and could be post-formed to vary the shape, porosity and mechanical properties.
- The porosity of the variotis™ scaffolds can be readily modified without losing void interconnectivity.
- Variotis scaffolds could readily be formed with functionally graded porosity and modulus.
- A minimally invasive method was developed for repair of a cartilage surface via a functionally graded variotis™ mounted on an osteochondral pin.
- Bioactive glasses with a range of novel compositions (Ba, Zn, Fe-doped) were synthesised. Both Zn-and Ba-doped glasses showed redduced bioactivity compared to 45S5 Bioglass. Iron increased the modulus.
- In vitro tests showed cells attaching throughout the entire scaffold.
- In vivo tests demonstrated the good biocompatibility of the variotis™ scaffold. Highly vascularized tissue infiltration was evident progressing into the scaffold by day 7.
- Synthesised bioactive glass was shown to be bioactive and biocompatible (ch 6).
- Two patents were lodged from the intellectual property developed in this thesis. This has led to the commercialization of the scaffolds and Bioglass.
- A novel method for the cell testing of biomaterials was developed.

REFERENCES



1 Guan J, Stankus JJ, Wagner WR. Preparation and characterization of highly porous, biodegradable polyurethane scaffolds for soft tissue applications. Biomaterials 26:3961-3971:2005

2 Jones AC, Arns CH, Hutmacher DW, Milthorpe BK, Sheppard AP Knackstedt MA. The correlation of pore morphology, interconnectivity and physical properties of 3D ceramic scaffolds with bone ingrowth. Biomaterials 30(7): 1440-1451:2009

3 Hench LL, Polak JM. Third-generation biomedical materials. Science 295:1014–1017:2002

4 Jones JR, Hench LL. Regeneration of trabecular bone using porous ceramics. Current Opinion in Solid State and Materials Science 7:301-307:2003

5 Jones JR, Lee PD, Hench LL. Hierachical porous materials for tissue engineering. Phil Trans R Soc A 364:263-281:2006

6 Guan J, Stankus JJ, Wagner WR. Soft Tissue Scaffolds. Wiley Encyclopedia of Biomedical Engineering. Wiley-Interscience, US, 2006

7 Park WC, Han SK, Kim NJ, Chung TY, Khwarg SI. Effect of basic fibroblast growth factor on fibrovascular ingrowth into porous polyethylene anophthalmic socket implants. Korean J Opthalmol 19(1-8):2005

8 Hench LL, Bioceramics: From Concept to Clinic. J Am Ceram Soc 74(7):1487-1510:1991

9 Mikirova NA, Casciari JJ, Riordan NH. Ascorbate inhibition of angiogenesis in aortic rings ex vivo and subcutaneous Matrigel plugs in vivo. Journal of Angiogenesis Research 2:2:2010

10 Wang HL, Greenwell H, Fiorellini J, Giannobile W, Offenbacher S, Salkin L. J Periodontol 76:1601:2005

11 Park WC, Han SK, Kim NJ, Chung TY, Khwarg SI. Effect of basic fibroblast growth factor on fibrovascular ingrowth into porous polyethylene anophthalmic socket implants. Korean J Opthalmol 19(1-8):2005

12 Hemmerich, KJ. Polymer Materials Selection for Radiation-Sterilized Products. Medical Device & Diagnostic Industry Magazine. 78-89:2000

13 Stosich MS, Moioli EK, Wu JK, Lee CH, Rohde C et al. Bioengineering strategies to generate vascularized soft tissue grafts with sustained shape. Methods 47:116-121:2009

14 Cao Y, Mitchell G, Messina A, Price L, Thompson E, Penington A et al. The influence of architecture on degradation and tissue ingrowth into three-dimensional poly(lactic-co-glycolic acid) scaffolds in vitro and in vivo. Biomaterials 27:2854–2864:2006

15 Wang DA, Varghese S, Sharma B, Strehin I, Fermanian S, Gorham J et al. Multifunctional chondroitin sulphate for cartilage-tissue biomaterial integration Nature Materials 6:385-392-2007.

16 Kimura y, Inamoto T, Tabata Y. Adipose Tissue Formation in Collagen Scaffolds with Different Biodegradabilities, Journal of Biomaterials Science 21:463-476:2010

18 Schantz JT, Teoh SH, Lim TC, Endres M, Lam CX, Hutmacher DW. Repair of Calvarial Defects with Customised Tissue-Engineered Bone Grafts II. Evaluation of Cellular Efficiency and Efficacy in Vivo. Tissue Engineering 9:S127-139:2003

19 Lanza RP, Langer RS, Vacanti J. Principles of tissue engineering. Academic Press. San Diego, CA. 2000

20 Fundamentals of Tissue Engineering and Regenerative Medicine. Eds. Meyer U, Handschiel, Meyer T, Wiesmann HP. p 468, Springer Berlin Heidelberg, 2009

21 Chen S, Jones JA, Xu Y, Low HY, Anderson JM. Characterization of topographical effects on macrophage behavior in a foreign body response model. Biomaterials 31:3479-3491:2010

22 Freed L, Guilak F, Guo XE, Gray ML, Tranquillo R, Holmes JW et al. Advanced tools for tissue engineering: scaffolds, bioreactors and signalling. Tissue Engineering 12(12):3285-3305:2006

23 Clark RA, Ghosh K, Tonnesen MG. Tissue Engineering for Cutaneous Wounds. Journal of Investigative Dermatology 127:1018-1029:2007

24 Ueda H, Tabata Y. Polyhydroxyalkanonate derivatives in current clinical applications and trials. Advanced Drug Delivery Reviews 55:501-518:2003

25 Thadani V, Penar PL, Partington J, Kalb R, Janssen R, Schonberger LB et al. Creutzfeldt-Jakob disease in a patient with a cadaveric dural graft, J Neurosurg 69(5):766-769:1988

26 Dolores W, Christian R, Harald N, Hildegunde P, Georg W. Cellular and molecular composition of fibrous capsules formed around silicone breast implants with special focus on local immune reactions. Journal of Autoimmunity 23:81-91:2004

27 Bostman O, Pihlajamaki H. Late Foreign-Body Reaction to an Intraosseous Bioabsorbable Polylactic Acid Screw. A Case Report. J Bone Joint Surg Am 80:1791-1794:1990

28 Bergsma EJ, Rozema FR, Bos RR, de Bruijn WC. Foreign body reactions to resorbable poly(L-lactide) bone plates and screws used for the fixation of unstable zygomatic fracture. J Oral Maxillofac Sug 51:666-70:1993

29 Ward WK, Slobodzian EP, Tiekotter KL, Wood MD. The effect of microgeometry, implant thickness and polyurethane chemistry on the foreign body response to subcutaneous implants Biomaterials 23:4185-4192:2002

30 Jones JR, Gentleman E, Polak J. Bioactive Glass Scaffolds for Bone Regeneration. Elements 3:393-399

31 Ksander GA, Vistnes LM. Collagen and Glycosaminoglycans in Capsules around Silicone Implants. Journal of Surgical Research 31:433-439:1981

32 Ratner BD, Bryant SJ. Biomaterias. Where we have been and where we are going. Ann Rev Biomed Eng 6:41-75:2004

33 Jones KS. Effects of biomaterial-induced inflammation on fibrosis and rejection. Seminars in Immunology 20:130–136:2008

34 Cohen K, Diegelmann R, Linbladt WJ, eds. Biochemical and Clinical Aspects of Wound Healing. WB Saunders, Philadelphia 562-580:1999

35 Maloney WJ, Smith RL. Periprosthetic osteolysis in total hip arthroplasty: the role of particulate debris. J Bone Joint Surg 77A:1448–1461:1995

36 Nascimento C, Issa JP, Oliveira RR, Iyomasa MM, Siessere S, Regalo SC. Biomaterials Applied to the Bone Healing Process. Int J Morphol 25(4):839-846:2007

37 Rubin JP, Yaremchuk MJ. Complications and toxicities of implantable biomaterials used in facial reconstructive and aesthetic surgery: a comprehensive review of the literature. Plast Reconstr Surg 100(5):1336-53:1997

38 Jacobson JA. Hip replacement: multimedia. http://emedicine.medscape.com/article/398669-media. 2009. Accessed 25/3/2011

39 Bronzino JD. The Biomedical Engineering Handbook. CRC Press. USA. 2000

41 Campbell R, Agrawal C. Bioabsorbable Intermedullary Implant System and Methods of Use. US Patent 5836040. Nov 1998

42 Anderson JM. Tissue Engineering and Artificial Organs. In: Bronzino JD, ed. The Biomedical Engineering Handbook. Third ed CRC Press. Boca Raton. 36–35:2006

43 Elst M et al. Tissue Reaction on PLLA versus Stainless Steel Interlocking Nails for Fracture Fixation: an Animal Study. Biomaterials 16:103-106:1995

44 Wise D, ed. Biomaterials and Bioengineering Handbook. Marcel Dekker Inc. USA, 2000

45 Kunz E et al. Resorbable Osteosynthesis Rods. An Experimental Study of the Biomechanics and Degradation of Various Rods of Polyglycolide and Poly(-L-lactide). Unfallchirurgie 21:1-7:1995

46 Spoerke ED, Murray NG, Li H, Brinson LC, Dunard DC, Stupp SI. A bioactive titanium foam scaffold for bone repair. Acta Biomaterialia 523-533:2005

47 Soballe K, Hansen ES, Rasmussen HB, Jorgensen PH, and Bunger C. Tissue ingrowth into titanium and hydroxyapatite-coated implants during stable and unstable mechanical conditions. Ortho Res 10:285-299:1992

48 Burr DB, Mori S, Boyd RD, Sun TC, Blaha, JD, Lane L & Parr J. Histomorphometric assessment of the mechanisms for rapid ingrowth of bone to HA/ TCP coated implants. J Biomed Mater Res, 27(5):645-53:1993

49 Dumronglert E. A follow-up study of chronic wound healing dressing with pure natural honey. J Nat Res Counc Thail 15(2):39-66; 1983

50 Geesink RG. Osteoconductive Coatings for Total Joint Arthroplasty. Clin Orthop Relat Res 395:53:2002

51 Tsui YC, Doyle C and Clyne TW. Plasma sprayed hydroxyapatite coatings on titanium substrates. Part 1: Mechanical properties and residual stress level. Biomaterials 19:2015:1998

52 Suchanek W and Yoshimura M. Processing and properties of hydroxyapatite-based biomaterials for use as hard tissue replacement implants. J Mater Res 13(1):94:1998

53 Ross EA, Batich CD, Clapp WL, Sallustio JE, Lee NC. Tissue adhesion to bioactive glass-coated silicone tubing in a rat model of peritoneal dialysis catheters and catheter tunnels. Kidney International 63:702-708:2003

54 Taksali S, Gauer JN, Vaccaro AR, Material considerations for intervertebral disc replacement implants, The Spine J. 6:S231-S238:2004

55 Bobyn JD, Poggie RA, Kygier JJ, Lewallen DG, Hanssen AD, Lewis RJ, et al. Clinical validation of a structural porous tantalum biomaterial for adult reconstruction, J Bone Joint Surg. 86:123-129:2004

56 Akin FA, Zreiqat H, Jordan S, Wijesundara, MB and Hanley L. Preparation andanalysis of macroporous TiO_2 films on Ti surfaces for bone-tissue implants. J Biomed Mater Res 57(4):588-96:2001

57 Rhodes NP. Inflammatory signals in the development of tissue-engineered soft tissue. Biomaterials 28:5131-5136:2007

58 Low SW, Ng YJ, Yeo TT, Chou N. Use of Osteoplug polycaprolactone implants as novel burr-hole covers. Singapore Med J 50:777:2009

59 Woodfield TB, Malda J, de Wijn J, Péters F, Riesle J, van Blitterswijk CA. Design of porous scaffolds for cartilage tissue engineering using a three-dimensional fiber-deposition technique. Biomaterials 25:4149–4161:2004

60 Lee CR, Grodzinsky AJ, Hsu H-P, Spector M. Effects of a cultured autologous chondrocyte-seeded type II collagen scaffold on the healing of a chondral defect in a canine model. J Orthop Res 21:272–81:2003

61 Misaki N. Intra-thoracic fibrous tissue induction by polylactic acid and epsilon-caprolactone copolymer cubes, with or without slow release of basic fibroblast growth factor. Eur J Cardiothorac Surg 32:761-765:2007

62 Bezuidenhout D, Davies N, Black M, Schmidt C, Oosthuysen A, Zilla P. Covalent Surface Heparinization Potentiates Porous Polyurethane Scaffold Vascularization. Journal of Biomaterials Applications. 00:1-18:2008

63 van den Dokler J, Farber E, Spauwen PH & Jansen JA. Bone tissue reconstruction using titanium fiber mesh combined with rat bone marrow stromal cells. Biomaterials 24(10):1745-50:2003

65 Vats A, Tolley NS, Polak JM, Gough JE. Review. Scaffolds and biomaterials for tissue engineering: a review of clinical applications. Clin Otolaryngol 28:165-172:2003

66 Moreno-Sanz C, Picazo-Yeste JS, Manzanera-Diaz M, Herrero-Bogajo ML, Cortina-Oliva J, Tadeo-Ruiz G. Prevention of trocar site hernias: Description of the safe port plug technique and preliminary results. Surgical Innovation 15:100:2008

67 Abed A, Deval B, Assoul N, Bataille I, Portes P, Louedec L et al. Tissue Engineering Part A 14(4):519-527:2008

68 Nienhuijs S, Kortmann B, Boerma M, Strobbe L, Rosman C. Preferred mesh-based inguinal hernia repair in a teaching setting. Arch Surg 139:1097-1100:2004

69 Tormala P, Paasimaa S, Antikainen T. Hernia Mesh, US Patent 6,319,264 B1, Nov 20 2001

70 Hutmacher DW. Scaffolds in tissue engineering bone and cartilage. Biomaterials 21(24):2529-2543:2000

71 Schantz JT, Lim TC, Ning C, Teoh SH, Tan KC, Wang SC, Hutmacher DW. Cranioplasty after trephination using a novel biodegradable burr hole cover: technical case report. Neurosurgery 58(1 Suppl):ONS-E176:2006

73 Entenmann A, Wedel T, Kolbert G, Kiihnel W and Bruch H-P. Scanning electron microscopy study including maceration techniques of an absorbable alloplastic implant designed for the reconstruction of ventral abdominal wall defects. Ann Anat 181:237-245:1999

74 Ng TH, Chan KH, Leung SY, Mann KS. An Unusual Complication of Silastic Dural Substitute: Case Report. Neurosurgery 27:491:1990

75 Cohen AR, Aleksic S, Ransohoff J. Inflammatory reaction to synthetic dural substitute. Case report. Journal of Neurosurgery 70(4):633-635:1989

76 Ongkiko CM, Keller JT, Mayfield FH, et al. An unusual complication of Dura Film as a dural substitute. Report of two cases. J Neurosurg 60:1076–1079:1984

77 Chan C, Thompson, Robinson P, Wilson J, Hench L. Evaluation of Bioglass/dextran composite as a bone graft substitute. Int J Oral Maxillofac Surg 31:73-77:2002

78 Enderle J, Blanchard S, Bronzino J. Introduction to Biomedical Engineering, 2nd ed. Academic Press, California, 2005

79 Falanga V, Margolis D, Alvarez O, Auletta M, Maggiacomo F, Altman M, Jensen J, Sabolinski M, Hardin-Young J. Rapid healing of venous ulcers and lack of clinical rejection with an allogeneic cultured human skin equivalent. Human Skin Equivalent Investigators Group. Arch Dermatol, 134(3): 293-300, 1998.

80 Jones DS, Djokic J, McCoy CP, Gorman SP. Poly(epsilon-caprolactone) and poly(epsilon-caprolactone)- polyvinylpyrolidone-iodine blends as ureteral biomaterials: characterization of mechanical and surface, properties, degradation and resistance to encrustation in vitro. Biomaterials 2002:23:4449-58:2002

81 Rigberg D, Tulloch A, Chun Y, Mohanchandra KP, Carman G, Lawrence. Thin-film nitinol (NiTi): A feasibility study for a novel aortic stent graft material. J Vasc Surg 50:375-80:2009

82 Lewandrowski KU, Wise DL, Trantolo DJ., White AA. Advances in spinal fusion: molecular science, biomechanics and clinical management. New York. 2005.

83 Lam CX, Hutmacher DW, Schantz JT, Woodruff MA, Teoh SH. Evaluation of polycaprolactone scaffold degradation for 6 months in vitro and in vivo. J Biomed Mater Res 90A: 906–919:2009

84 Yamamoto M, Tabata Y, Kawasaki H, Ikada Y. Promotion of fibrovascular tissue ingrowth into porous sponges by basic fibroblast growth factor, Journal of Materials Science: Materials in Medicine 11:213-218:2000

85 Day RM, Maquet V, Boccaccini AR, Jérôme R, Forbes A. In vitro and in vivo analysis of macroporous biodegradable poly(D,L-lactide-co-glycolide) scaffolds containing bioactive glass. J Biomed Mater Res A 75: 778-87:2005

86 Day RM, Boccaccini AR, Shurev S, Roether JA Forbes A, Hench LL, et al. Assessment of polyglycolic acid mesh and bioactive glass for soft-tissue engineering scaffolds. Biomaterials 25:5857–5866:2004

87 Hofer SO, Knight KM, Cooper-White JJ, O'Connor AJ, Perera JM, Stevens GW, et al. Increasing the volume of vascularized tissue formation in engineering constructs—an experimental study in rats. Plast Reconstr Surg 111:1186–92:2003

88 Hollister S, Scaffold engineering: a bridge to where? Biofabrication 1(1):2009

89 Velema J, Kaplan, Biopolymer-Based Biomaterials as Scaffolds for Tissue Engineering. Adv Biochem Engin/Biotechnol 102: 187–238:2006

90 Scotti C, Wirz D, Wolf F, Schaefer DJ, Bürgin V, Daniels AU et al. Engineering human cell-based, functionally integrated osteochondral grafts by biological bonding of engineered cartilage tissues to bony scaffolds. Biomaterials 31:2252-2259:2010

92 Hung CT, Lima EG, Mauck RL, Taki E, LeRoux MA, Lu HH, et al. Anatomically shaped osteochondral constructs for articular cartilage repair. Journal of Biomechanics 36(12):1853–1864:2003

94 Drury JL, Mooney DJ. Hydrogels for tissue engineering: scaffold design variables and applications. Biomaterials 24:4337–51:2003

94 Mithieux, S, Tu, Y, Korkmaz, E, Braet, F, Weiss, A. In situ polymerization of tropoelastin in the absence of chemical cross-linking.Biomaterials. 30:431-5: 2009

95 Hoffman AS. Hydrogels for biomedical applications. Ann NY Acad Sci 944:62–73:2001

96 Hoffman AS. Hydrogels for biomedical applications Advanced Drug Delivery Reviews 45:3-12:2002

99 Miller BE, et al. Factors affecting growth and drug sensitivity of mouse mammary tumor lines in collagen gel cultures. Cancer Res. 45:4200–4205:1985

100 Ho ST, Hutchmacher DW. A comparison of micro CT with other techniques used in the characterization of scaffolds. Biomaterials 27:1362-1376:2006

101 Maurer PK, McDonald JV. Vicryl (polyglactin 910) mesh as a dural substitute. Journal of neurosurgery. 1985; 63(3):448-52.

102 von Wild KR. Examination of the safety and efficacy of an absorbable dura mater substitute (Dura Patch®) in normal applications in neurosurgery. Surgical Neurology 52(4):418-425:1999

103 Vincenzini P, Giardino R, Development of bioabsorbable dura mater, Adv Sci Tech. 49:165-167:2006

104 Navarro M, Michiardi A, Castano O Planell JA. Biomaterials in orthopaedics 5(27):1137-1158:2008

105 Vogel M, Voigt C, Gross UM, Muller-Mai CM. *In vivo* comparison of bioactive glass particles in rabbits, Biomaterials. 22(4):357-362:2001

106 Socola G, Macoveib AM, Miroiua F, Stefana N, Dutaa L, Dorciomana G, et al. Hydroxyapatite thin films synthesized by pulsed laser deposition and magnetron sputtering on PMMA substrates for medical applications, Materials Science and Engineering: B. 169(1-3):159-168:2009

107 Bhattari N, Gunn J, Zhang M, Chitosan-based hydrogels for controlled, localized drug delivery. Adv Drug Del Reviews. 62(1):83-99:2010

108 Takahashi Y, Yamamoto M, Tabata Y. Osteogenic differentiation of mesenchymal stem cells in biodegradable sponges composed of gelatin and beta-tricalcium phosphate. Biomaterials 26(17):3587–3596:2005

109 Blouin S, Moreau MF, Weiss P, Daculsi G, Basle MF, Chappard, D, Evaluation of an injectable bone substitute (TCP/hydroxyapatite/hydroxy-propyl-methyl-cellulose) in severely osteopenic and aged rats, Journal of Biomedical Materials Research Part A. 78A(3):570-580:2006

110 Teoh EY, Chong MS, Zhang Z, Lu J, Moochhala S, Ho B, Teoh SH, Polycaprolactone-based fused deposition modeled mesh for delivery of antibacterial agents to infected wounds, Biomaterials. 31(1):279-287:2011

111 Monvisade P, Siriphannon P, Jermsingnern R, Rattanabodee S, Preparation of hydroxyapatite/poly(methyl methacrylate) and calcium silicate/poly(methyl methacrylate) interpenetrating hybrid composites, J Mater Sci: Mater Med. 18:1955-1959:2007

112 De Aza PN, Luklinska ZB, Martinez A, Anseau MR, Guitian F, De Aza S. Morphological and structural study of pseudowollastonite implants in bone. J Microsc 197:60–67:2000

113 Banchet V, Michel J, Jallot E, Wortham L, Bouthors S, Laurent-Maquin D, Blossier G. Interfacial reactions of glasses for biomedical application by scanning transmission electron microscopy and microanalysis. Acta Biomaterialia 2(3): 349-359:2006

114 Li H, Chang J. Fabrication and characterization of bioactive wollastonite/PHBV composite scaffolds. Biomaterials 25(24):5473–80:2004b

115 Wu C, Ramaswamy Y, Boughton P, Zreiqat H. Improvement of mechanical and biological properties of porous $CaSiO_3$ scaffolds by poly(D,L-lactic acid) modification. Acta Biomater 4(2):343–53:2008a

116 Wu C, Ramaswamy Y, Zhu Y, Zheng R, Appleyard R, Howard A, et al. The effect of mesoporous bioactive glass on the physiochemical, biological and drug-release properties of poly(DL-lactide-co-glycolide) films. Biomaterials 30:2199-2208:2009

117 Wu C, Ramaswamy Y, Zreiqat H. Porous diopside ($CaMgSi_2O_6$) scaffold: A promising bioactive material for bone tissue engineering. Acta Biomaterialia 6:2237-2245:2010

118 Wu C, Zhang Y, Zhu Y, Friis T, Xiao Y. Structure-property relationships of silk-modified mesoporous bioglass® scaffolds. Biomaterials 31(13): 3429-3438:2010

119 Wu CT & Zreiqat H. Conference Proceedings: Society For Biomaterials, April 18 - 21, Chicago, 2007, Tissue Engineering and Developmental Biology, April 12-17, Salt Lake City 2007

120 Nonami T, Tsutsumi S. Study of diopside ceramics for biomaterials. J Mater Sci Mater Med 10:475-479:1999

121 Cheng W, Li H, Chang J. Fabrication and characterization of β-dicalcium silicate/poly(d,l-lactic acid) composite scaffolds. Materials Letters 59(17):2214–2218:2005

122 Zehnder M, Söderling E, Salonen J, Waltimo T. Preliminary evaluation of bioactive glass S53P4 as an endodontic medication in vitro. J Endod 30: 220-224:2004

123 Tai BG, Bian Z, Jiang H, Greenspan DC, Zhong J, Clark AE, et al. Anti-ginivitis effect of a dentifrice containing bioactive glass (NovaMin) particulate. J Clin Peridontol 33:86-91:2006

124 Aho AJ, Tirri T, Kukkonen J, Strandberg N, Rich J, Seppälä J, et al. Injectable bioactive glass/biodegradable polymer composite for bone and cartilage reconstruction: concept and experimental outcome with thermoplastic composites of poly(epsilon-caprolactone-co-D,L-lactide) and bioactive glass S53P4. J Mater Sci Mater Med 15:1165-1173:2004

125 Bhattarai S, Bhattarai N, Yi HK, Hwang PH, Cha D, Kim HY. Novel biodegradable electrospun membrane: scaffold for tissue engineering. Biomaterials 25:2595-2602:2004

126 Food and Drug Administration, USA (Online). K061554, approval to Market Mepilex Ag in USA. 510(k) Summary 2009 (accessed Oct 4 2010) Available from: http://www.accessdata.fda.gov/cdrh_docs/pdf9/K091013.pdf

127 Fathi MH, Doostmohammadi A. Bioactive glass nanopowder and bioglass® coating for biocompatibility improvement of metallic implant. Journal of Materials Processing Technology 209:1385-1391:2009

128 Dumbleton J, Manley MT. Hydroxyapatite-Coated Prostheses in Total Hip and Knee Arthroplasty. J Bone Joint Surg Am 86:2526:2004

129 Y Kotani, K Abumi, Y Shikinami, M Takahata, K Kadoya, T Kadosawa, A Minami, K Kaneda. Two-year observation of artificial intervertebral disk replacement: results after supplemental ultra-high strength bioresorbable spinal stabilization. J Neurosurg (Spine 4) 100:337-342:2004

130 Shikinami Y, Kawarada H. Potential application of a triaxial three-dimensional fabric (3-DF) as an implant. Biomaterials 19(7-9):617-635:1998

131 Kotani Y, Abumi K, Shikinami Y, Takada T, Kadoya K, Shimamoto N. Artificial Intervertebral Disc Replacement Using Bioactive Three-Dimensional Fabric: Design, Development, and Preliminary Animal Study. Spine 27(9):929-935:2002

132 Chen W, Liu Y, Courtney HS, Bettenga M, Agrawal CM, Bumgardner JD, et al. In vitro anti-bacterial and biological properties of magnetron co-sputtered silver-containing hydroxyapatite coating. Biomaterials 27:5512–5517:2006

133 Li H, Chang J. pH-compensation effect of bioactive inorganic fillers on the degradation of PLGA. Composites Science and Technology 65:2226-2232:2005

134 Tomsia AP, Launey ME, Lee JS, Mankani MH, Wegst UGK, Saiz E, Nanotechnology Approaches to Improve Dental Implants, Int J Oral Max Impl. 26:25-44:2011

135 Aho AJ, Hautamaki M, Mattila R, Alander P, Stranberg N, Rekola J, et al. Surface porous fibre-reinforced composite bulk bone substitute. Cell & Tissue Banking 5(4): 213-221:2004

136 Oonishi H, Hench LL, Wilson J, Sugihara F, Tsuji E, Matsuura M, et al. Quantitative comparison of bone growth behavior in granules of Bioglass®, A-W glass-ceramic, and hydroxyapatite. J Biomed Mater Res 51:37-46:2000

137 Lopez-Esteban S, Fuijino ES, Oku T, Suganuma K, Tomsia AP, Bioactive glass coatings for orthopedic metallic implants, J Eur Cer Soc 23(15):2921-2930:2003

138 Jones JR, Ehrenfried LM, Hench LL. Optimising bioactive glass scaffolds for bone tissue engineering Biomaterials 27:964–973:2006

139 Allan I, Newman H, Wilson M. Antibacterial activity of particulate Bioglass® against supra- and subgingival bacteria, Biomaterials 22: 1683-1687:2001

140 Gillette RL, Swaim SF, Sartin EA, Bradley DM, Coolman SL. Effects of a bioactive glass on healing of closed skin wounds in dogs, AJVR 62:1149:2001

141 Fencher J. Bioactive glasses as a potential new class of anti-oxidative ingrediants for personal care products. SOFW-Journal. 131(4):1-5:2005

142 Keshaw H, Forbes A, Day RM. Release of angiogenic growth factors from cells encapsulated in alginate beads with bioactive glass, Biomaterials, 2005;26:4171-9:2005

143 Leu A, Leach JK. Proangiogenic potential of a collagen/bioactive glass substrate. Pharmaceutical Research 25(5):1222-1229:2008

144 Gorustovich AA, Roether JA, Boccaccini AR. Effect of Bioactive Glasses on Angiogenesis: A Review of In Vitro and In Vivo Evidences, Tissue Engineering: Part B 00:1-9:2009

145 Aina V, Malavasi G, Pla AF Munaron L, Morterra C. Zinc-containing bioactive glasses: Surface reactivity and behaviour towards endothelial cells. Acta Biomaterialia 5:1211–1222:2009

146 Nandi SK. In vitro and in vivo release of cefuroxime axetil from bioactive glass as an implantable delivery system in experimental osteomyelitis Ceramics International 35:3207-3216:2009

147 Lee HH, Yu HS, Jang JH, Kim HW. Bioactivity improvement of poly(e-caprolactone) membrane with the addition of nanofibrous bioactive glass. Acta Biomaterialia 4:622-629:2008

148 Yun HS, Kim SE, Hyun YT, Heo SJ, Shin JW. Three-Dimensional Mesoporous-Giant porous Inorganic/Organic Composite Scaffolds for Tissue Engineering Chemistry of Materials 19(26):6363-6366:2007

149 Whitehead MA, Fan D, Mukherjee P, Akkaraju GR, Canham LT, Coffer JL. High-Porosity Poly(ε-Caprolactone)/Mesoporous Silicon Scaffolds: Calcium Phosphate Deposition and Biological Response to Bone Precursor Cell. Tissue Engineering Part A. 14(1):195-206:2008

150 Jo JH, Lee EJ, Shin DS, Kim HE, Kim HW, Koh YH, Jang JH. In vitro/in vivo biocompatibility and mechanical properties of bioactive glass nanofiber and poly(ε-caprolactone) composite materials. Journal of Biomedical Materials Research Part B: Applied Biomaterials 91B(1) 213-220:2009

151 Moosvi SR, Day RM. Bioactive glass modulation of intestinal epithelial cell restitution. Acta Biomaterilia 5:76-83:2009

152 Leach JK, Kaigler D, Wang Z, Krebsbach PH, Mooney DJ et al. Coating of VEGF-releasing scaffolds with bioactive glass for angiogenesis and bone regeneration. Biomaterials 27:3249-55:2006

153 Boccaccini AR, Stamboulis AG, Rashid A and Roether JA. Composite surgical sutures with bioactive glass coating. J Biomed Mater Res B Appl Biomater 67(1):618-626:2003

154 Helen W, Gough JE. Cell viability, proliferation and extracellular matrix production of human annulus fibrosus cells cultured within PDLLA/Bioglass composite foam scaffolds in vitro. Acta Biomaterialia 4:230–243:2008

155 Allan I, Newman H, Wilson M. Particulate Bioglass reduces the viability of bacterial biofilms formed on its surface in an in vitro model. Clin Oral Impl Res 13:53–58:2002

156 Yli-Urpo H, Närhi T, Söderling E. Antimicrobial effects of glass ionomer cements containing bioactive glass (S53P4) on oral micro-organisms in vitro' Acta Odontologica Scandinavica 61:4:241-246:2003

157 Bellantone M, Williams HD, Hench LL. Broad-Spectrum Bactericidal Activity of Ag_2O-Doped Bioactive Glass, Antimicrobial agents and chemotherapy 1940–1945:2002

158 Mortazavi V, Nahrkhalaji MM, Fathi,MH, Mousavi SB, Esfahani BN. Antibacterial effects of sol-gel-derived bioactive glass nanoparticle on aerobic bacteria. J Biomed Mater Res 94A:160–168:2010

159 Hu S, Chang J, Liu M, Ning C. Study on antibacterial effect of 45S5 Bioglass®. Journal of Materials Science: Materials in Medicine 20:281-286:2009

160 Niiranen H, Paatola T, Bioabsorbable polymer plates coated with bioactive glass spheres, J Mater Sci: Mater Med. 10:707-710:1999

161 Wang M, Developing bioactive composite materials for tissue replacement. Biomaterials. 24:2133-2151:2003

162 Martina M, Hutmacher DW. Biodegradable polymers applied in tissue engineering research: a review. Polymer International 56(2):145-157:2007

163 Ramakrishna S, Mayer J, Wintermantel E, Leong KW. Biomedical applications of polymer-composite materials: a review. Composites Science and Technilogy 61(9):1189-1224:2001

164 Corden TJ, Jones IA, Rudd CD, Christian P, Downes S, McDougall KE. Physical and biocompatibility properties of poly-e-caprolactone produced using in situ polymerisation: a novel manufacturing technique for long-fibre composite materials, Biomaterials 21:713-724:2000

165 Hutmacher DW. Loessner D, Rizzi S, Kaplan DL, Mooney DJ, Clements JA. Can tissue engineering concepts advance tumor biology research? Trends in Biotechnology 28(3):125-133:2010

166 Hexsel D, Hexsel C, Iyengar V. Liquid Injectable Silicone: History, Mechanism of Action, Indications, Technique, and Complications. Seminars in Cutaneous Medicine and Surgery. 22(2):I07-I 14:2003

167 Ananthakrishnan N, Rao RS, Shivam S. Bacterial adherence to cotton and silk sutures. Natl Med J India 5(5):217-8:1992

168 Porex Website http://www.porexsurgical.com/english/surgical/skull.asp Accessed 1/9/10

169 Du RL, Chang J, Ni SY, Zhai WY, Wang JY. J Biomater Appl 20(4):341-360:2006

170 Moyer KE, Saggers GC, Allison GM, Mackay DR, Ehrlich HP. Effects of interleukin-8 on granulation tissue maturation. Journal of Cellular Physiology 193(2):173-179:2002

171 Kyriakides TR, Bornstein P. Matricellular proteins as modulators of wound healing and the foreign body response. Thromb Haemost 90(6):986–992:2003

172 Nam SY, Nho YC, Hong SH. Evaluations of Poly(vinyl alcohol)/Alginate Hydrogels Cross-linked by γ -ray Irradiation Technique. Macromol Res. 12(2):219–224:2004

173 Sanger C, Soto A, Mussa F, Sanzo M, Sardo L, Donati PA, et al. Maximizing results in craniofacial surgery with bioresorbable fixation devices. J Craniofac Surg 18:926-930:2007

174 Hench LL, Jones JR, Spulveda P. Ch 1, Bioactive Materials for Tissue Engineering Scaffolds-Future Strategies for Tissue and Organ Replacement Ed. Polak JM, Hench LL, Kemp P. Imperial College Press. London, 2002

175 Woodruff MA, Hutmacher DW. The return of a forgotten polymer- Polycaprolactone in the 21st century. Progress in Polymer Science 35(10):1217-1256:2010

176 Bezwada RS, Jamiolkowski DD, Lee IY, Agarwal V, Persivale J, Trenka-Benthin S, et al. Monocryl suture, a new ultra-pliable absorbable monofilament suture, Biomaterials 16:1141-1148:1995

177 Onal L, Cozien-Cazuc S, Jones IA, Rudd CD. Water absorption properties of phosphate glass fiber-reinforced poly-epsilon-caprolactone composites for craniofacial bonme repair. J Appl Polym Sci 107:3750-5:2008

178 Alani A, Knowles JC, Chrzanowski W, Ng YL, Gulabivala K. Ion release characteristics, precipiatate formation and sealing ability of a phosphate glass-polycaprolactone-based composite for use as a root canal obturation material. Dent Mater 25:400-10:2009

179 Sun H, Mei L, Song C, Cui X, Wang, P. The in vivo degradation, absorption and excretion of PCL-based implant. Biomaterials 27:1735-40:2006

180 Shin'oka T, Imai Y, Ikada Y. Transplantation of a tissue-engineered pulmonary artery. New Engl J Med 344:352:2001

181 Vitale-Brovarone C, Verné E, Robiglio L, Martinasso G, Canuto RA and Muzio G. Biocompatible glass-ceramic materials for bone substitution. Journal of Materials Science-Materials in Medicine 19(1):471-478:2008

182 Chouzouri G and Xanthos M. In vitro bioactivity and degradation of polycaprolactone composites containing silicate fillers. Acta Biomaterialia 3(5):745-756:2007

183 Fu K, Griebenow K, Hsieh L, Klibanov AM, Langer R. FTIR characterization of the secondary structure of proteins encapsulated within PLGA microspheres. J Control.Rel 58: 357-366:1999

184 Boccaccini AR, Chen Q, Lefebvre L, Gremillard L, Chevalier J. Sintering, crystallisation and biodegradation behaviour of Bioglass-derived glass-ceramics. Faraday Discussions 136: 27-44 & 107-123:2007

185 Brovarone CV, Appendino P. Macroporous bioactive glass-ceramic scaffolds for tissue engineering. J Mater Sci: Mater Med 17:1069-1078:2006

186 Rainer A, Giannitelli SM, Abbruzzese F, Traversa E, Licoccia S, Trombetta M. Fabrication of bioactive glass–ceramic foams mimicking human bone portions for regenerative medicine. Acta Biomaterialia 4(2):362-369:2008

187 Boccaccini AR, Maquet V. Bioresorbable and bioactive polymer/Bioglass® composites with tailored pore structure for tissue engineering applications, Composites Science and Technology 63:2417–2429:2003

188 Bil M, Ryszkowska J, Roether JA, Bretcanu O, Boccaccini AR. Bioactivity of polyurethane-based scaffolds coated with Bioglass®. Biomed Mater 2: 93-101:2007

189 Roether JA, Boccaccini AR, Hench LL, Maquet V, Gautier S, Jérôme R. Development and in vitro characterisation of novel bioresorbable and bioactive composite materials based on polylactide foams and Bioglass for tissue engineering applications. Biomaterials 23(18):3871-3878:2002

190 Maquet V, Boccaccini AR, Pravata L, Notingher I, Jerome R. Preparation, characterization, and in vitro degradation of bioresorbable and bioactive composites based on Bioglass®-filled polylactide foams. Journal of Biomedical Materials Research Part A. 66A(2):2003

191 Niemela T, Niiranen H, Kellomaki M, Tormala P. Self-reinforced composites of bioabsorbable polymer and bioactive glass with different bioactive glass contents. Part I: Initial mechanical properties and bioactivity. Acta Biomaterialia 1(2):235-242:2005

192 Couto DS, Hong Z, Mano JF. Development of bioactive and biodegradable chitosan-based injectable systems containing bioactive glass nanoparticles. Acta Biomaterialia 5(1):115-23:2009

193 Rich J, Jaakkola T, Tirri T, Narhi T, Yli-Urpo A, Seppala J. In vitro evaluation of poly(ϵ-caprolactone-co-dl lactide)/bioactive glass composites, Biomaterials 23:2143-2150:2002

194 Li Z, Gu X, Lou S, Zheng Y. The development of binary Mg–Ca alloys for use as biodegradable materials within bone. Biomaterials 29:1329-1344:2008

195 Jaakkola T, Rich J, Tirri T, Narhi T, Jokinen M, Seppala J et al. In vitro Ca-P precipitation on biodegradable thermoplastic composite of poly(e-caprolactone-co-dl-lactide) and bioactive glass (S53P4). Biomaterials 25:575-581

196 Maquet V, Boccaccini AR, Pravata L, Notingher I, Jerome R. Porous poly(a-hydroxyacid)/Bioglass® composite scaffolds for bone tissue engineering. I. Preparation and in vitro characterisation. Biomaterials 25(18):4185–94:2004

197 Zhang K, Ma Y, Francis LF. Porous polymer/bioactive glass composites for soft-to-hard tissue interfaces. J Biomed Mater Res 61:551-563:2002

198 Haimi S, Suuriniemi N, Haaparanta AM, Ellä V, Lindroos B, Huhtala H, et al. Growth and osteogenic differentiation of adipose stem cells on PLA/bioactive glass and PLA/beta-TCP scaffolds. Tissue Eng Part A 15(7):1473-1480:2009

199 Brown RF, Rahaman MN, Dwilewicz AB, Huang W, Day DE, Li Y, Bal BS. Effect of borate glass composition on its conversion to hydroxyapatite and on the proliferation of MC3T3-E1 cells. J Biomed Mater Res 88A:392–400:2009

200 Brown RF, Day DE, Day TE, Jung S, Rahaman MN, Fu Q. Growth and differentiation of osteoblastic cells on 13–93 bioactive glass fibers and scaffolds. Acta Biomaterialia 4:387-396:2008

201 Levy S, Dalen MV, Agonafer S, Soboyerjo WO. Cell/surface interactions and adhesion on bioactive glass 45S5 J Materi Sci: Mater Med 18:89-102:2007

202 Gan JC, Ducheyne P, Vresilovic E, Shapiro IM. Bioactive glass serves as a substrate for maintenance of phenotype of nucleus pulposus cells of the intervertebral disc. J Biomed Mater Res 51(4):596-604:2000

203 Gao T, Aro HT, Ylänen H, Vuorio E. Silica-based bioactive glasses modulate expression of bone morphogenetic protein-2 mRNA in Saos-2 osteoblasts in vitro. Biomaterials 22(12):1475-1483:2001

204 Alcaide M, Portoles P, Lopez-Noriega A, Arocs D, Vallet-Regi M, Portoles MT. Interaction of an ordered mesoporous bioactive glass with osteoblasts, fibroblasts and lymphocytes, demonstrating its biocompatibility as a potential bone graft material. Acta Biomater 6(3):892-899:2010

205 Bitar M, Salih V, Knowles JC, Lewis MP. Iron-phosphate glass fiber scaffolds for the hard-soft interface regeneration: the effect of fiber diameter and flow culture condition on cell survival and differentiation. J Biomed Mater Res A 87(4):1017-26:2008

206 Yeh CC, Li YT, Chiang PH, Huang CH, Wang, Chang HI. Characterizing microporous PCL matrices for application of tissue engineering, J Med Bio Eng. 29(2):92-97:2009

207 Vance RJ, Miller DC, Thapa A, Haberstroh KM, Webster TJ. Decreased fibroblast cell density on chemically degraded poly-lacticco- glycolic acid,polyure thane,and polycaprolactone. Biomaterials 25:2095-2013:2004

208 Tsigkou O, Hench LL, Boccaccini AR, Polak JM, and Stevens MM. Enhanced differentiation and mineralization of human fetal osteoblasts on PDLLA containing Bioglass® composite films in the absence of osteogenic supplements. J Biomed Mater Res A 80(4):837–851:2007

209 Blaker JJ, Gough JE, Maquet V, Notingher I, Boccaccini AR. In vitro evaluation of novel bioactive composites based on Bioglass®- filled polylactide foams for bone tissue engineering scaffolds. J Biomed Mater Res 67A(4):1401–11:2003

210 Helen W, Merry CL, Blaker JJ, Gough JE. Three-dimensional culture of annulus fibrosus cells within PDLLA/Bioglass® composite foam scaffolds: assessment of cell attachment, proliferation and extracellular matrix production. Biomaterials 28(11):2010-2020:2007

211 Gough JE, Arumugam M, Blaker J, Boccaccini AR. Bioglass® coated poly(DL-lactide) foams for tissue engineering scaffolds. Mat.-wiss. u. Werkstofftech 34:654–661:2003

212 Verrier S, Blaker JJ, Maquet V, Hench LL, Boccaccini AR. PDLLA/Bioglass® composites for soft-tissue and hard-tissue engineering: an in vitro cell biology assessment. Biomaterials 25(15):3013-3021:2004

213 Keshaw H, Georgiou G, Blaker JJ, Forbes A, Knowles JC, Day RM. Microporous Spheres for Tissue Regeneration Applications. Tissue Engineering: Part A 15:1451:2009

214 Yao J, Radin S, Leboy PS, Ducheyne P. The effect of bioactive glass content on synthesis and bioactivity of composite poly (lactic-co-glycolic acid)/bioactive glass substrate for tissue engineering. Biomaterials 26:1935–1943:2005

215 Lu HH, El-Amin SF, Scott KD, Laurencin CT. Three-dimensional, bioactive, biodegradable, polymer–bioactive glass composite scaffolds with improved mechanical properties support collagen synthesis and mineralization of human osteoblast-like cells in vitro. J Biomed Mater Res 64A:465-474:2003

216 Kim TG, Chung HJ, Park TG. Macroporous and nanofibrous hyaluronic acid/collagen hybrid scaffold fabricated by concurrent electrospinning and deposition/leaching of salt particles. Acta Biomaterialia 4:1611-1619:2008

217 Mo X, Weber HJ, Ramakrishna S. PCL-PGLA composite tubular scaffold preparation and biocompatibility investigation. Int J Artif Organs 29(8):790-9:-2006

218 Yun HS, Kim SE, Kyun Park E. Bioactive glass-poly(ε-caprolactone) composite scaffolds with 3 dimensionally hierarchical pore networks. Materials Science & Engineering C 30:191-205:2011

219 Cannillo V, Chiellini F, Fabbri P, Sola A. Production of Bioglass® 45S5 – Polycaprolactone composite scaffolds via salt-leaching. Composite Structures 92:1823-1832:2010

220 Wei J, Wu X, Liu C, Jia J, Heo S, Kim S et al. Fabrication of Bioactive Scaffold of Poly(e-Caprolactone) and Nanofiber Wollastonite Composite J Am Ceram Soc 92(5):1017-1023:2009

221 Lu L, Zhang Q, Wootton D, Lelkes PI, Zhou J. A novel sucrose porogen-based solid freeform fabrication system for bone scaffolds manufacturing. Rapid Prototyping Journal 16(5):365-376:2010

222 Lowery JL, Datta N, Rutledge GC. Effect of fiber diameter, pore size and seeding method on growth of human dermal fibroblasts in electrospun poly(3-caprolactone) fibrous mats. Biomaterials 31:491-504:2010

223 Chen G, Zhou P, Mei N, Chen X, Shao Z. Silk fibroin modified porous poly(ε-caprolactone) scaffold for human fibroblast culture in vitro. Journal of Materials Science: Materials in Medicine 15:671-677:2004

224 Bretcanu O, Chatzistavrou X, Paraskevopoulos K, Conradt R, Thompson I, Boccaccini AR. Sintering and crystallisation of 45S5 Bioglass® powder, Journal of the European Ceramic Society 29:3299-3306:2009a

225 Bretcanu O. Electrospun nanofibrous biodegradable polyester coatings on Bioglass®-based glass-ceramics for tissue engineering. Materials Chemistry and Physics 118:420-426:2009b

226 Miao X, Tan DM, Li J, Xiao Y, Crawford RW. Mechanical and biological properties of hydroxyapatite/tricalcium phosphate scaffolds coated with poly(lactic-co-glycolic acid). Acta Biomaterialia 4:638-645:2008

227 Wheeler DL, Eschbach EJ, Hoellrich RG, Montfort MJ, Chamberland DL. Assessment of Resorbable Bioactive Material for Grafting of Critical-size Cancellous Defects. Journal of Orthopaedic Research. 18:140-148:2000

228 Pohunkova H, Adam M, Reactivity and the fate of some composite bioimplants based on collagen in connective tissue. Biomaterials 18:67-71:1995

229 Ekholm E, Tommila M, Forsback AP, Martson M, Holmbom J, Aaritalo V. Hydroxyapatite coating of cellulose sponge does not improve its osteogenic potency in rat bone. Acta Biomaterialia 1:535-544:2005

230 Tommila M, Jokinen J, Wilson T, Forsback AP, Saukko P, Penttinen R, et al. Bioactive glass-derived hydroxyapatite-coating promotes granulation tissue growth in subcutaneous cellulose implants in rats. Acta Biomaterialia 4:354-361:2008

231 Shin'oka T, Matsumura G, Hibino N, Naito Y, Watanabe M, Konuma T, et al. Midterm clinical results of tissue-engineered vascular autografts seeded with autologous bone marrow cells, J Thorac Cardiovasc Surgery 129:1330–1338:2005

232 Acharya NK, Kumar RJ, Varma JK, Menon VK. Hydroxyapatite-Bioactive Glass Ceramic Composite as Stand-alone Graft Substitute for Posterolateral Fusion of Lumbar Spine: A Prospective, Matched, and Controlled Study. Journal of Spinal Disorders & Techniques. 21(2):106-111:2008

234 Sung HJ, Meredith C, Johnson C, Galis ZS. The effect of scaffold degradation rate on three-dimensional cell growth and angiogenesis Biomaterials 25:5735–5742:2004

235 Ceonzo K, Gaynor A, Shaffer L, Kojima K, Vacanti CA, Stahl GL. Polyglycolic acid-induced inflammatrion: role of hydrolyxis and resulting complement activation. Tissue Eng, 12(2):301-308:2006

236 Bergsma JE, de Bruijn WC, Rozema FR, Bos RRM, Boering G. Late degradation tissue response to poly(-lactide) bone plates and screws. Biomaterials. 16:25-31:1995

237 Cordewener FW, Dijkgraaf LC, Ong JL, Agrawal CM, Zardeneta G, Milam SB, Schmitz JP. Particulate retrieval of hydrolytically degraded poly(lactide-co-glycolide) polymers. Journal of Biomedical Materials Research 50(1):59-66:2000

238 Poandl T, Trenka-Benthin S, Azri-Meehan S, Contiliano J, Li Y, Yuan J, et al. A new faster-absorbing biocomposite material: Long-Term In-Vitro tissue reaction and absorption. Spring Arthroscopy Association of North America (AANA) Meeting May 2005, Vancouver

239 Bostman O, Pihlajamaki H. Clinical biocompatibility of biodegradable orthopaedic implants for internal fixation: a review. Biomaterials 21:2615–2621:2000

240 Bostman O, Pihlamajaki. Adverse Tissue Reactions to Bioabsorbable Fixation Devices, Clinical Orthopaedics and Related Research 371:216-227:2000

241 Moore JW, Brekke JH. Foreign body giant cell reaction related to placement of tetracycline-treated polylactic acid: report of 18 cases. J Oral Maxillofac Surg 48:808–812:1990

242 Miller RA, Brady JM, Cutright DE. Degradation rates of oral resorbable implants (polylactates and polyglycolates): rate modification with changes in PLA/PGA copolymer ratios. J Biomed Mater Res 11:711–719:1977

243 Lee KH, Won CY, Chu CC, Gitsov I. Hydrolysis of absorbable polymeric biomaterials by superoxide. J Polym Chem 37:3558-3587:1999

244 Li X, Chang J. Preparation and characterization of bioactivecollagen/wollastonite composite scaffolds. J Mater Sci Mater Med 2005;16(4):361–5:2005

245 Yang X, Yang F, Walboomers XF, Bian Z, Fan M, Jansen JA. The performance of dental pulp stem cells on nanofibrous PCL/gelatin/nHA scaffolds. J Biomed Mater Res 93A:247-257:2010

246 Woodward SC, Brewer PS, Moatamed F, Schindler A, Pitt CG. The intracellular degradation of poly (epsilon-caprolactone). J Biomed Mater Res 19:437-444:1985

247 Traul KA, Driedger A, Ingle DL, Nakhasi D. Review of the Toxicologic Properties of Medium-chain Triglycerides. Food and Chemical Toxicology 38:79-98:2000

248 Dhall GI, Krishna U, Sivaraman R. Phase II- Clinical trial with biodegradable subdermal contraceptive implant Capronor® 44(4):1991

249 Sun H, Qu Z, Guo Y, Zhang G, Yang B. In vitro and in vivo effects of rat kidney vascular endothelial cells on osteogenesis of rat bone marrow mesenchymal stem cells growing on polylactide-glycolic acid (PLGA) scaffolds. Biomed Eng Online 6:1:2007

250 Ma G, Song C, Sun H, Yang J, Leng X.Abiodegradable levonorgestrel releasing implant made of PCL/F68 compound as tested in rats and dogs. Contraception 74:141–7:2006

251 Osteopore. www.osteopore.com.sg Accessed 16/1/2011

252 Braun Website. www.bbraun.com Accessed 30/2/2011

253 Roby MS, Bennett SL, Liu CK. Absorbable block copolymers and surgical articles fabricated therefrom. US Pat. 5 (403) (1995) 347:1995

254 Suru International Pvt Ltd. www.suru.com Accessed 29/2/2011

255 Ratner BD, Hoffman AS, Schoen FJ, Lemons JE. Biomaterials science an introduction to materials in medicine. Elsevier Academic Press, 2004

256 Merrell JG, McLaughlin SW, Tie L, Laurencin CT, Chen AF, Nair LS. Curcumin-loaded Poly(ϵ-Caprolactone) Nanofibres: Diabetic Wound Dressing with Anti-oxidant and Anti-Inflammatory Properties. Clin Exp Pharm Physiol 36:1149:2009

257 Venugopal JR, Zhang Y, Ramakreishna S. In vitro culture of human dermal fibroblasts on electrospun polycaprolactone collagen nanofibrous membrane. Artif Organs 30:440:2006

258 Medlicott NJ, Jones DS,Tucker IG, Holborow D. Preliminary release studies of chlorhexidine (base and diacetate) from poly(epsilon-caprolactone) films prepared by solvent evaporation. Int J Pharm 84:85-9:1992

260 Barralet JE, Wallace LL, Strain AJ. Tissue engineering of human biliary epithelial cells on polyglycolic acid/polycaprolactone scaffolds maintains long-term phenotypic stability, Tissue Engineering 9:1037–1045:2003

261 Barnes CP, Sell SA, Boland ED, Simpson DG, Bowlin GL. Nanofiber technology: Designing the next generation of tissue engineering scaffolds, Advanced Drug Delivery Reviews 59:1413-1433:2007

262 Lee S-H, Kim B-S, Kim S-H, et al. Elastic biodegradable poly(glycolide-co-caprolactone) scaffold for tissue engineering. J Biomed Mater Res 66A:29:2003

263 Almarza AJ, Athanasiou KA. Design characteristics for the tissue engineering of cartilaginous tissues. Ann Biomed Eng 32(1):2-17:2004

264 Currey J, Unsworth A, Hall DA, Properties of bone, cartilage and synovial fluid. In: Dowson D, Wright V, ed. An introduction to the biomechanics of joints and joint replacement. Bury St. Edmunds: Mechanical Engineering Publications 285:1981

265 Paulsen DF. Histology & Cell Biology: Examination and Board Review, 4th ed., Lange/McGraw-Hill, New York 376:2000

266 Klein TJ, Chaudhry M, Bae WC, Sa RL. Depth dependent biomechanical and biochemical properties of fetal, newborn, and tissue engineered articular cartilage. Journal of Biomechanics 40:182–190:2007

267 Mankin HJ. The response of articular cartilage to mechanical injury. J Bone Joint Surg 64:460:1982

268 Radhakrishnan P, Lewis NT, Mao JJ. Zone-specific micromechanical properties of the extracellular matrices of growth plate cartilage. Annals of Biomedical Engineering. 32(2):284-291:2004

269 Langrana NA, Parsons JR, Lee CK, Vuono-Hawkins M, Yang SW, Alexander H., Materials and design concepts for an intervertebral disc spacer. I. fiber-reinforced composite design, J Appl Biomater. 1994 Summer;5(2):125-32.

270 Buckwalter JA, Brown TD. Joint injury, repair and remodeling: roles in post-traumatic osteoarthritis. Clin Ortop Relat Res 423:7-16:2004

271 MendMeShop. What causes osteoarthrisis in the knee? http://www.mendmeshop.com/knee/knee_osteoarthritis_causes.php. Accessed 12/2/2011

272 Roach HI, Aigner T, Soder S, Haag J, Welkerling H, Pathobiology of osteoarthritis: pathomechanisms and potential therapeutic targets, Current drug targets. 8(2):271-282:2007

273 Young AA, Smith MM, Smith SM, Cake MA, Ghosh P, Read RA, et al, Regional assessment of articular cartilage gene expression and small proteoglycan metabolism in an animal model of osteoarthritis, Arth Res Therapy. 7(4):R851-R862:2005

274 Ghosh P. The pathobiology of osteoarthritis and the rationale for the use of pentosan polysulfate for its treatment. Sem Arthritis Rheum 28:211–67:1999

275 Arthritis Foundation. www.arthritis.org. Accessed 13/09/10

276 Aigner T, Haag J, Martin J, Buckwalter. Osteoarthritis: aging of matrix and cells--going for a remedy. Curr Drug Targets 8:2:325-31:2007

277 Morrison G. Advances in the Skin Trade. Mechanical Engineering. CIME. Feb 1999

278 Currie LJ, Sharpe JR, Martin R. The use of fibrin glue in skin grafts and tissue-engineered skin replacements: a review. Plast Reconstr Surg 108:1713–26:2001

278 ShandsHealth. Melanoma and other skin cancers. 2009. http://www.shands.org/health/In-depth%20Reports/10/000032.htm. Accessed 12/2/2011

279 Demling R, DeSanti L & Orgill D. Moist Healing and Wound Care including Burns. http://www.burnsurgery.org/Betaweb/Modules/moisthealing/images/mid_dermal_burn_web.jpg. 2000. Accessed 8/10/06

280 Anderson GG and O'Toole GA. Innate and Inuced Resistance Mechanisms of Bacterial Biofilms. Current Topics in Microbiology and Immunology. 322:85-105:2008

281 Rhoads DD, Wolcott RD, Percival SL. Biofilms in wounds: management strategies. J Wound Care 17:502–8:2008

283 Blakytny R and Jude E. The molecular biology of chronic wounds and delayed healing in diabetes. Diabet Med 23:594:2006

284 Frykberg RG, Zgonis T, Armstrong DG, Driver VR, Giurini JM, Kravitz SR, et al. Diabetic foot disorders. A clinical practice guideline (2006 revision), J Foot Angle Surg. 39(5S):S1-66:2006

285 Brown University Division of Biology and Medicine. Skin Grafts & Transplants. biomed.brown.edu. Accessed 15/2/2011

286 Barrett D, Muhammed N. Design & Applications of Biodegradable Polyester Tissue Scaffolds Based on Endogenous Monomers Found in Human Metabolism. Molecules 14:4022-4050:2009

287 Eshel H, Lanir Y. Effects of Strain Level and Proteoglycan Depletion on Preconditioning and Viscoelastic Responses of Rat Dorsal Skin. Annals of Biomedical Engineering 29(2):164-172:2009

288 Iatridis JC, Wu J, Yandow JA, Langevin H. Subcutaneous tissue mechanical behavior is linear and viscoelastic under uniaxial tension. Connective Tissue Research 44:208-217:2003

289 Shepherd DE, Seedhom BB. The 'instantaneous' compressive modulus of human articular cartilage in joints of the lower limb. Rheumatology 38:124–132:1999

291 Parsons JR. Cartilage. In: Black J and Hastings G e+A781ds. Handbook of Biomaterials Properties. New York: Chapman & Hall 40–46:1998

292 Woo SY, Levine RE. Ligament, tendon and fascia. In: Black J and Hastings G eds. Handbook of Biomaterials Properties. New York: Chapman & Hall 59–65:1998

293 Yang S, Leong KF, Zhaohui D, Chua CK. The Design of Scaffolds for Use in Tissue Engineering. Part I. Traditional Factors. Tissue Engineering. 7(6):679-689:2001

294 Chung S, Hazen A, Levine JP, Baux G, Olivier WA, Yee HT, et al. Vascularized Acellular Dermal Matrix Island Flaps for the Repair of Abdominal Muscle Defects. Plastic & Reconstructive Surgery. 111(1):225-232:2003

296 Metcalfe AD, Ferguson MW. Bioengineering skin using mechanisms of regeneration and repair. Biomaterials. 28(34):5100-5113:2007

297 Cao Y, Vacanti JP, Paige KT, Upton J, Vacanti CA. Transplantation of chondrocytes utilizing a polymer-cell construct to produce tissue-engineered cartilage in the shape of a human ear. Plast Reconstr Surg 100: 297:1997

298 Huang YC, Kaigler D, Ricfe KG, Krebsbach PH, Mooney DJ. Combined angiogenic and osteogenic factor delivery enhances bone marrow stromal cell-driven bone regeneration. J Bone Miner Res 20:848:2005

299 Bremnes RM, Camps C, Sirera R. Angiogenesis in non-small cell lung cancer: The prognostic impact of neoangiogenesis and the cytokines VEGF and bFGF in tumors and blood. Lung Cancer 51:143—58:2006

300 Olsen D, Jiang J, Chang R, Duffy R, Sakaguchi M, Leigh S, et al. Expression and characterization of a low molecular weight recombinant human gelatin: development of a substitute for animal-derived gelatin with superior features. Protein Expression and Purification 40:346-357:2005

301 Birchall IE, Lee VW, Ketharanathan V. Retention of endothelium on ovine collagen biomatrix vascular conduits under physiological shear stress, Biomaterials 22(23):3139-3144:2001

302 White JF, Werkmeister JA, Edwards GA, Ramshaw JA. Structural analysis of a collagen--polyester composite vascular prosthesis. Clin Mater 14(4):271-276:1993

303 Apel PJ, Garrett JP, Sierpinski P, Ma J, Atala A, Smith TL, et al. Peripheral Nerve Regeneration Using a Keratin-Based Scaffold: Long-Term Functional and Histological Outcomes in a Mouse Model, 33(9):1541-1547:2008

304 Ravin AG, Olbrich KC, Levin LS, Usala A-L and Klitzman B. Long- and short-term effects of biological hydrogels on capsule microvascular density around implants in rats. J Biomed Mater Res. 58(3): 313-8, 2001

305 "Hamada K, et al. Spatial distribution of mineralized bone matrix produced by marrow mesenchymal stem cells in self-assembling peptide hydrogel scaffold.

J Biomed Mater Res A. 2008 Jan;84(1):128-36"

306 Martin I, et al. J Orthopaedic Res 16:181, 1998

307 Gough JE, Notingher I, Hench LL. Osteoblast attachment and mineralized nodule formation on rough and smooth 45S5 bioactive glass monoliths. J Biomed Mater Res 68A(4):640–50:2004

308 Baume A, Coleman N, Boughton P. Methods for Achieving Soft Tissue Scaffold Sterility. J Biomimetics, Biomaterials & Tissue Engineering 2009

309 Freed LE, Vunjak-Novakovic G, Biron RJ, Eagles DB, Lesnoy DC, Barlow SK, et al. Biodegradable polymer scaffolds for tissue engineering. Biotechnology (NY) 12(7):689–93:1994

310 Suzuki S, Matsuda K, Maruguchi T, Nishimura Y, Ikada Y. Further applications of "bilayer artificial skin. Br J Plast Surg 48(4):222-9:1995

311 Chernyshov A, Allard S. Biocompatible porous Ti-Ni Material. European Patent EP1663330

312 Pal K, Bag S, Pal S. Development of porous ultra high molecular weight polyethylene scaffolds for the fabrication of orbital implant. J Porous Materials 15(1):53-59:2008

313 Woodfield TB, van Blitterswijk CA, de Wijn J, Sims TJ, Hollander AP, Riesle J. Polymer scaffolds fabricated with pore size gradients as a model for studying the zonal organization within tissue engineered cartilage constructs. Tissue Engineering 11:1297–1311:2005

313 Kotani Y, Abumi K, Shikinami Y, Takahata M, Kadoya K, et al. Two-year observation of artificial intervertebral disc replacement: results after supplemental ultra-high strength bioresorbable spinal stabilization, J Neurosurg, Spine 4:100:337-342:2004

314 Hollister SJ, Lin CY, Saito E, Lin CY, Schek RD, Taboas JM, et al. Engineering Craniofacial Scaffolds. Orthodontics and Craniofacial Research 8:162-173:2005

315 Hutmacher D, Sittinger M, Risbud M. Scaffold-based tissue engineering: rationale for computer-aided design and solid free-form fabrication systems, TRENDS in Biotechnology, 22(7), 354-362, 2004

316 Adhikari R. Biodegradable injectable polyurethanes: Synthesis and evaluation for orthopaedic applications, Biomaterials 29:3762–3770:2008

317 Yamada KM, Cukierman E. Modeling tissue morphogenesis and cancer in 3D. Cell. 4;130(4):601-10:2007

318 Williamson MR, Woollard KJ, Griffiths HR, Coombes AGA. Gravity spun polycaprolactone fibres for applications in vascular tissue engineering. Proliferation and function of human vascular endothelial cells. Tissue Engineering. 12, 45-51 (2006)

319 Roosa SM, Kemppainen JM, Moffitt EN, Krebsbach PH, Hollister SJ. The pore size of polycaprolactone scaffolds has limited influence onbone regeneration in an in vivo model. J Biomed Mat Res Part A. 91(1): 359-68:2010

320 Taboas CK, Huang GT, Tuan RS in: Translational Approaches in Tissue Engineering and Regenerative Medicine. Mao JJ, Vunjak-Novakovic G, Mikos AG, Atala A, Artech House, Eds. p. 83. Boston, 2008

321 Hulbert SF, Young FA, Mathews RS, Klawitter JJ, Talbert CD, Stelling FH. Potential of ceramic materials as permanently implantable skeletal prostheses. J Biomed Mater Res 4:433:1970

322 Otsuki B, Takemoto M, Fukibayashi S, Neo M, Kokubo T, Nakamura T. Pore throat size and connectivity determine bone and tissue ingrowth into porous implants: Three-dimensional micro-CT based structural analyses of porous bioactive titanium implants. Biomaterials 27:5892-5900:2006

323 Moore MJ, Jabbari E, Ritman EL, Lu L, Currier BL, Windebank AJ, et al. Quantitative analysis of interconnectivity of porous biodegradable scaffolds with micro-computed tomography. J Biomed Mater Res 71A:258-267:2004

324 Brauker JH, Carr-Brendel VE, Martinson LA, Crudele J, Johnston WD, and Johnson RC. Neovascularization of synthetic membranes directed by membrane microarchitecture, Journal of Biomedical Materials Research 29:1517-1524:1995

325 Slaaf D, Tangelder GJ, Reneman R. The physics of heart and circulation. In: Physics of the Microcirculation. Institute of Physics. Bristol 383-416:1993

326 Vogt S, Larcher B, Beer B, Wilke I, Schnabelrauch M. Fabrication of highly porous scaffold materials based on functionalized oligolactides and preliminary results on their use in bone tissue engineering, Cells & Materials. 4:30-38:2002

327 Gao TJ, Crapo PM, Wang Y. Macroporous Elastomeric Scaffolds with Extensive Micropores for Soft Tissue Engineering. Tissue Eng 8:429:2002

328 Yunos DM, Bretcanu O, Boccaccini AR. Polymer-bioceramic composites for tissue engineering scaffolds J Mater Sci. 43:4433–4442:2008

329 Coombes AG, Heckman JD. Gel casting of resorbable polymers. 2. In vitro degradation of bone graft substitutes. Biomaterials 13(5):297:1992

330 Miao X, Sun D. Graded/Gradient Porous Biomaterials, Materials. 3:26-47:2010

331 Li S, De Wijn JR, Li J, Layrolle P, De Groot K. Macroporous biphasic calcium phosphate scaffold with high permeability/porosity ratio. Tissue Engineering 9(3):535-48:2003

332 Hui PW, Leung PC, and Sher A. Fluid conductance of cancellous bone graft as a predictor for graft-host interface healing. J Biomech 29:123:1996

333 Schmitt EA, Flanagan DR, Linhardt RJ. Importance of distinct water environments in the hydrolysis of poly(dl-lactide-coglycolide) Macromolecules 27:743-748:1994

334 Li SM, Garreau H, Vert M. Structure property relationships in the case of the degradation of massive aliphatic poly- (alpha-hydroxy acids) in aqueous-media.1. Poly(dl-lactic acid). J Mater Sci Mater Med 1:123-130:1990

335 Li SM, Garreau H, Vert M. Structure-property relationships in the case of the degradation of massive poly(alpha-hydroxy acids) in aqueous-media. 3. Influence of the morphology of poly(llactic acid). J Mater Sci Mater Med 1:198-206:1990

336 Godstein J. The use of bioresorbable material in craniofacial surgery. Clin Plast Surg 28:653-659:2001

337 Holbrook MC. The resistance of polyglycolic acid sutures to attach by infected human urine. Br J Urol 54:313:1982

338 Tomihata K, Suzuki M, Ikada Y. The ph dependence of monofilament sutures on hydrolytic degradation. Appl. Biomater. 58:511:2001

339 Luong-Van E, Grøndahl L, Song SJ, Nurcombe V, Cool S. The in vivo assessment of a novel scaffold containing heparin sulfate for tissue engineering with human mesenchymal stem cells. J Mol Hist 38:459–46:2007

340 Stamm C, Westphal B, Kleine HD, Petzsch M, Kittner C, Kllinge H, et al. Autologous bone-marrow stem-cell transplantation for myocardial regeneration. Lancet 361:45–6:2003

341 Breinan HA, Minas T, Hsu HP, Nehrer S, Sledge CB, Spector M. Effect of cultured autologous chondrocytes on repair of chondral defects in a canine model. J Bone Joint Surg 79–A:1439–51:1997

342 Soto-Gutierrez A, Yagi H, Uygun BE, Navarro-Alvarez N, Yang YG, Yarmush ML. Cell delivery: from cell transplantation to organ engineering. Cell Transplant. 19(6):655-665:2010

343 Kasten P, Vogel J, Luginbuhl R, Niemeyer P, Tonak M, Lorenz H, et al. Ectopic bone formation associated with mesenchymal stem cells in a resorbable calcium deficient hydroxyapatite carrier. Biomaterials 26:5879-5889:2005

344 Shea LD, Smiley E, Bonadio J, Mooney DJ. DNA delivery from polymer matrices for tissue engineering. Nature Biotech 17:551-4:1999

345 Mikos AG, Herring W, Ochareon P, Elisseeff J, Lu HH, Kandel R, et al. Engineering Complex Tissues. Tissue Eng 12:3307:2006

346 Maquet V and Jerome R. Design of macroporous biodegradable polymer scaffolds for cell transplantation. Mater Sci Forum 250:15:1997

347 Mundargi RC, Srirangarajan S, Agnihotri SA, Patil SA, Ravindra S. Development and evaluation of novel biodegradable microspheres based on poly(d,l-lactide-co-glycolide) and poly(epsilon-caprolactone) for controlled delivery of doxycycline in the treatment of human periodontal pocket: in vitro and in vivo studies. J Control Release 119:59-68:2007

348 Holland TA, Bodde EW, Cuijpers VM, Baggett LS, Tabata Y, Mikos AG, et al. Degradable hydrogel scaffolds for in vivo delivery of single and dual growth factors in cartilage repair. Osteoarthritis Cartilage 15:187:2007

349 Cevher E, Orhan Z, Mulazimoglu L, Sensoy D, Alper M, Yildiz A, Ozsoy Y. Characterization of biodegradable chitosan microspheres containing vancomycin and treatment of experimental osteomyelitis caused by methicillin-resistant Staphylococcus aureus with prepared microspheres. Int J Pharm 317:127–35:2006

350 Woo BG, Fink BF, Page R, Schrier JA, Jo YW, Jiang G, et al. Enhancement of bone growth by sustained delivery of recombinant human bone morphogenetic protein-2 in a polymeric matrix. Pharm Res 18:1747:2001

351 Ikenaga M, Ohura K, Nakamura T, Kotoura Y, Yamamuro T, Oka M, et al. In: Bioceramics (W. Bonfield, GW Hastings, and KE Tanner, Eds.), Butterworth-Heinemen, London 4:255-262:1991

352 Bodde EW, Boerman OC, Russel FG, Mikos AG, Spauwen PH, Jansen JA. The kinetic and biological activity of different loaded rhBMP-2 calcium phosphate cement implants in rats. J Biomed Mater Res. 87:780:2008

353 Paul W, Sharma CP. Ceramic drug delivery: a perspective. J Biomater Appl 17:253–64:2003

354 Kawanabe K, Okada Y, Matsusue Y, Iida H, Nakamura T. Treatment of osteomyelitis with antibiotic-soaked porous glass ceramic. J Bone Joint Surg 80:527-30:1998

355 Mortera R, Onida B, Fiorilli S, Cauda V, Vitale Brovarone C, Baino F, et al. Synthesis and characterization of MCM-41 spheres inside bioactive glass–ceramic scaffold. Chem Eng J 137:54-61:2007

356 Rai B, Teoh SH, Hutmacher D, Tong C, Ho KH. Novel PCL-based honeycomb scaffolds as drug delivery systems for rhBMP-2. Biomaterials. 26(17):3739-3748:2005

357 Noble ML. Drug Delivery Systems. University of Washington Engineered Biomaterials. http://www.uweb.engr.washington.edu/research/tutorials/drugdelivery.htm. 2004. Accessed 12/2/2011

358 Zhang X, Jia W, Gu Y, Xiao W, Liu X, Wang D, et al. Teicoplanin-loaded borate bioactive glass implants for treating chronic bone infection in a rabbit tibia osteomyelitis model. Biomaterials 31(22):5865-5874:2010

359 Zhang Y & Zhang M. Calcium phosphate/chitosan composite scaffolds for controlled in vitro antibiotic drug release. J Biomed Mater Res 62:378-386:2002

360 Chang HI, Perrie Y, Coombes AG. Delivery of the antibiotic gentamicin sulphate from precipitation cast matrices of polycaprolactone. J Control Release 110(2):414-21:2006

361 Fujita M. Vascularisation in vivo caused by the controlled release of fibroblast growth factor-2 from an injectable chitosan/non-anticoagulant heparin hydrogel. Biomaterials 25:699:2004

362 Ruhe PQ, Boerman OC, Russel FG, Spauwen PH, Mikos AG, Jansen JA. Controlled release of rhBMP-2 loaded poly(dl-lactic-co-glycolic acid)/calcium phosphate cement composites in vivo. J Controlled Release 106:162:2005

363 Wang JW, Aspenberg P. Basic fibroblast growth factor promotes bone ingrowth in porous hydroxyapatite. Clin Orthop Rel Res 333:252:1996

364 Ahrendt G, Chickering DE, Ranieri. Angiogenic growth factors: A review for tissue engineering, Tissue Eng 4:117:1998

365 Schmidt C, Bezuidenhout D, Beck M, Van der Merwe E, Zilla P, Davies. Rapid three-dimensional quantification of VEGF-induced scaffold neovascularisation by microcomputed tomography. Biomaterials 30:5959–5968:2009

366 Nillesen ST, Geutjes PJ, Wismans R, Schalkwijk J, Daamen WF, et al. Increased angiogenesis and blood vessel maturation in acellular collagen–heparin scaffolds containing both FGF2 and VEGF. Biomaterials 28:1123–1131:2007

367 Novak MT, Bryers JD & Reichert WM. Biomimetic strategies based on viruses and bacteria for the development of immune evasive biomaterials. Biomaterials 30:1989–2005:2009

368 Duarte AR, Mano JF & Reis RL. Dexamethasone- loaded scaffolds prepared by supercritical-assisted phase inversion. Acta Biomater. 5:2054–2062:2009

369 Cigna E, Tarallo M, Bistoni G, Anniboletti T, Trignano E, Tortorelli G, et al. Evaluation of Polyurethane Dressing with Ibuprofen in the Managementof Split-thickness Skin Graft Donor Sites, In Vivo. 23(6):983-986:2009

370 Mourino V, Boccaccini AR. Bone tissue engineering therapeutics: controlled drug delivery in three-dimensional scaffolds. J R Soc Interface 7(43):209-27:2010

371 Nieto A, Balas F, Colilla M, Manzanto M, Vallet-Regi M. Functionalization degree of SBA-15 as key factor to modulate sodium alendronate dosage. Microporous Mesoporous Mater. 116:4–13:2008

372 Fauchex C, Verron E, Soueidan A, Josse S, Arshad MD, Janvier P, et al. Controlled release of bisphosphonate from a calcium phosphate biomaterial inhibits osteoclastic resorption in vitro. J Biomed Mater Res Part A 86:46–56:2009

373 Santin M, Huang SJ, Iannace S, Ambrosio L, Nicolais L, Peluso G. Synthesis and characterization of a new interpenetrated poly(hydroxyethyl methacrylate)–gelatin composite polymer. Biomaterials 17:1459–67:1996

374 Sheng J, Nguyen PT, Marquis RE. Multi-target antibacterial actions of zinc against oral anaerobes, Arch Oral Biol. 50(8):747-57:2005

375 Petrini P, Arciola CR, Pezzali I, Bozzini S, Mondanaro L, Tanzi MC, et al. Antibacterial activity of zinc modified titanium oxide surface. Int J Artif Organs 29:434–42:2006

376 Cho YH, Lee SJ, Lee JY, Kim SW, Lee CB, Lee WY, et al. Antibacterial effect of intraprostatic zinc injection in a rat model of chronic bacterial prostatitis. Int J Antimicrob Agents 19:576–82:2002

377 Gray D & Cooper P. Nutrition and wound healing: What is the link? Journal of Wound Care 10(3):86-89:2001

378 Baena MI, Marquez MC, Matres V, Botella J, Ventosa A. Bactericidal activity of copper and niobium-alloyed austenitic stainless steel. Curr Microbiol 53:491–5:2006

379

380 Levy A.S, Lohnes J, Sculley S, LeCroy M and Garrett W. Chondral delamination of the knee in soccer players. Am. J. Sports Med. 24:634:1996

381 Smith and Nephew. Bioabsorbable Product Details http://www.endo.smith-nephew.com/us/ Accessed 6/5/2005

382 Hunziker EB. Articular cartilage repair: Basic science and clinical progress. A review of the current status and prospects. Osteoarthritis Cartilage 10:432–463:2002

383 Schmalzried TP, Callaghan JJ. Current Concepts Review - Wear in Total Hip & Knee Replacements, J Bone Joint Surg. 81:115-136:1999

384 Treatment of Articular Cartilage Defects: Surgical Procedure. 2000 http:/B1032/www.medscape.com/viewarticle/408519_5. Accessed 5/10/2010

385 Cao T, Ho KH, Teoh SH. Scaffold design and in vitro study of osteochondral coculture in a three-dimensional porous polycaprolactone scaffold fabricated by fused deposition modeling. Tissue Eng 9 (Suppl. 1):S103–12:2003

386 Goldberg VM, and Caplan AI. Biologic restoration of articular surfaces. In: Zuckerman, J.D., and Rosemont, J.D., eds. Instructional Course Lectures. Rosemont, IL: American Academy of Orthopaedic Surgeons 623–627:1999

387 Spalazzi JP, Vyner MC, Jacobs MT, Rich CV, Luh HH. Mechano0active scaffold induces tendon remodeling and expression of fibrocartilage markers, Clin Orth Rel Res. 466(8):1938-1948:2008

388 Martin I. Osteochondral tissue engineering. Journal of Biomechanics 40(4):750-765:2007

389 Wise DL. Encyclopedic handbook of biomaterials and bioengineering. Marcel Dekker B4812(2):1995

390 Mimura T, Imai S, Kubo M, Isoya E, Ando K, Okumura N, et al. A novel exogenous concentration-gradient collagen scaffold augments full-thickness articular cartilage repair,Osteoarthritis and Cartilage. 16:1083-1091:2008

391 Buckley CT, Thorpe SD, Kelly DJ. Engineering of large cartilaginous tissues through the use of microchanneled hydrogels and rotational culture, Tissue Engineering: Part A. 15(11):3213-3220:2009

392 Xu Y, Balooch G, Chiou M, Bekerman E, Ritchie RO, Longaker MT. Analysis of the material properties of early chondrogenic differentiated adipose-derived stromal cells (ASC) using an in vitro three-dimensional micromass culture system, Biochem. Biophys. Res. Com. 359:311-316:2007

393 Williams CG, Kim TK, Taboas A, Malik A, Manson P, Elisseeff J. In vitrochondrogenesis of bone marrow-derived mesenchymal stem cells in a photopolymerizing hydrogel, Tissue Engineering. 9(4):679-688:2003

394 Moutos FT, Freed LE & Guilak. A biomimetic three-dimensional woven composite scaffold for functional tissue engineering of cartilage Nature Materials 6(2):162-167:2007

395 Yaylaoglu MB, Yildiz C, Korkusuz F, Hasirci V. A novel osteochondral implant. Biomaterials 20:1513-1520:1999

396 Wise JK, Yarin AL, Megaridis CM, Cho M. Chondrogenic differentiation of human mesenchymal stem cells on oriented nanofibrous scaffolds: engineering the superficial zone of articular cartilage, Tissue Engineering. 15(4):913-921:2009

397 Li WJ, Tuli R, Okafor C, Derfoul A, Danielson KG, Hall DJ, Tuan RS. A three-dimensional nanofibrous scaffold for cartilage tissue engineering using human mesenchymal stem cells, Biomaterials. 26:599-609:2005

398 He L, Bin L, Xipeng G, Xie G, Liao S, Quan D, et al. Microstructure and properties of nano-fibrous pcl-b-plla scaffolds for cartilage tissue engineering, Euro. Cells & Materials. 18:63-74:2010

399 Schaefer D, Martin I, Shastri P, Padera RF, Langer R, Freed LE, Vunjak-Novakovic G. In vitro generation of osteochondral composites. Biomaterials 21:2599:2000

400 Eriksen C, Kaylon DM, Wang H. Biomaterials 29:4065–4073:2008

401 Sherwood JK, Riley SL, Palazzolo R, Brown SC, Monkhouse DC, Coates M, et al. A three-dimensional osteochondral composite scaffold for articular cartilage repair. Biomaterials 23(24):4739–51:2002

402 Chang CH, Lin FH, Lin CC, Chou CH, Liu HC. Cartilage tissue engineering on the surface of a novel gelatin-calcium-phosphate biphasic scaffold in a double-chamber bioreactor. J Biomed Mater Res 71B:313:2004

403 Hsu SH, Chang SH, Yen HJ, Whu SW, Tsai CL, Chen DC. Evaluation of biodegradable polyesters modified by type II collagen and Arg-Gly-Asp as tissue engineering scaffolding materials for cartilage regeneration, Artif Organs. 30(1):42-55:2006

405 Isogai N, Sinichi A, Higashi T, Ikada Y, Morita S, Hillyer J, et al. Tissue Engineering of an Auricular Cartilage Model Utilizing Cultured Chondrocyte Poly(L-lactide-e-caprolactone Scaffolds, Tissue Engineering,10(5-6):673-687:2004

406 Lee NK, Oh HJ, Hong CM, Suh H, Hong SH. Comparison of the Synthetic Biodegradable Polymers, Polylactide (PLA), and Polylactic-glycolic acid (PLGA) as Scaffolds for Artificial Cartilage, Biotechnology and Bioprocess Engineering. 14: 180-186:2009

407 Kreklau B, Sittinger M, Mensing MB, Voigt C, Berger G, Burmester GR, et al. Tissue engineering of biphasic joint cartilage transplants. Biomaterials 20:1743–1749:1999

408 Fecek C, Yao D, Kacorri A, Vasquez A, Iqbal S, Sheikh H, et al. Chondogenic derivatives of embryonic stem cell seeded into 3D polycaprolactone scaffolds generated cartilage tissue in vivo, Tissue Engineering: Part A. 14(8):1403-1413:2008

409 Niederauer GG, Slivka MA, Leatherbury NC, Korvick DL, Harroff HH, et al. Evaluation of multiphase implants for repair of focal osteochondral defects in goats. Biomaterials 21(24):2561–2574:2000

410 Golding RE, Jones AS. Micro-CT as a novel technique for 3D reconstruction of molluscan anatomy. Molluscan Research 27(3):123-128:2007

411 Chen QZ, Thompson ID, Boccaccini AR. 45S5 Bioglass-derived glass–ceramic scaffolds for bone tissue engineering. Biomaterials 27(11):2414–25:2006

413 Miao X, Tan LP, Tan LS, Huang X. Porous calcium phosphate ceramics modified with PLGA-bioactive glass, Mater Sci Eng C. 27(2):274-279:2007

414 Kim HW, Knowles JC, Kim HE. Hydroxyapatite porous scaffold engineered with biological polymer hybrid coating for antibiotic vancomycin release. J Mater Sci Mater Med 16(3):189–95:2005

415 Ramaswamy Y, Wu C, Van Hummel A, Combes V, Grau G, Zreiqat H. The Responses of Osteoblasts, Osteoclasts & Endothelial Cells to Zirconium Modified Calcium-Silicate Based Ceramic, Biomaterials. 29:4392-402, (2008).

416 Wu CT, Ramaswamy Y, Chang J, Woods J, Chen YQ, Zreiqat H. The Effect of Zn Contents on Phase Composition, Chemical Stability and Cellular Bioactivity in Zn-Ca-Si System Ceramics. J Biomed Mater Res Part A, 87B: 346-353, 2008

417 Ramaswamy Y, Wu C, Zreiqat H. Orthopedic coating materials: considerations and applications. Orthopaedic Expert Reviews in Medical Devices, Review. 6(4):423-30 (2009)

418 Jakob M, Démarteau O, Schäfer D, Hintermann B, Dick W, Heberer M, et al. Specific growth factors during the expansion and redifferentiation of adult human articular chondrocytes enhance chondrogenesis and cartilaginous tissue formation in vitro. J Cell Biochem 81:368:2001

419 Baksh D, Yao R, Tuan RS. Comparison of proliferative and multilineage differentiation potential of human mesenchymal stem cells derived from umbilical cord and bone marrow, Stem Cells 25:1384-1392:2007

420 Coleman RM, Case ND, Gulberg RE. Hydrogel effects on bone marrow stromal cell response to chondrogenic growth factors. Biomaterials 28:2077-2086:2007

421 Schagemann JC, Mrosek EH, Landers R, Kurz H, Erggelet C. Morphology and function of ovine articular cartilage chondrocytes in 3D hydrogel culture. Cells Tissues Organs 182:89-97:2006

422 Liu H, Lee YW and Dean MF. Re-expression of differentiated proteoglycan phenotype by dedifferentiated human chondrocytes during culture in alginate beads. Biochim Biophys Acta 1425:505:1998.

423 Kolambkar YM. Chondrogenic differentiation of amniotic fluid-derived stem cells. J of Mol Hist 38(5):405-413:2007 2007

424 Hauselmann HJ, Fernandes RJ, Mok SS. Phenotypic stability of bovine articular chondrocytes after long-term culture in alginate beads. J Cell Sci 107(93):751–757:17–27:1994

425 Guaccio A, Borselli C, Oliviero O, Netti PA. Oxygen consumption of chondrocytes in agarose and collagen gels: a comparative analysis, Biomaterials. 29:1484-1493:2008

426 Tabata Y, Ikada Y. Protein release from gelatin matrices. Adv Drug Deliv Rev 31:287-301:1998

427 Robinson MJ, Tessier P, Poulsom R, Hogg N. The S100 family heterodimer MRP-8/14, bindswith high affinity to heparin and heparan sulfate glycosaminoglycans on endothelial cells, J Biol. Chem. 277:3658-3665:2002

428 Ornitz DM. FGFs, heparan sulfate and FGFRs: complex interactions essential for development. Bioessays 22:108-12:2000

429 Kumarasuriyar A, Jackson RA, Grondahl L, Trau M, Nurcombe V, and Cool SM. Poly(beta hydroxybutyrate-co-beta-hydroxyvalerate) supports in vitro osteogenesis. Tissue Eng 11:1281-95:2005

430 Burrage PS, Mix KS, Brinkerhoff CE. Matrix Metalloproteinases: Role in Arthritis, Front Biosci. 11:529-543, 2006

431 Zometa® Website. www.zometa.com. Accessed 10/10/2011

432 Novartis Oncology Website. novartisolcology.com. Accessed 1/3/2011

433 Ural AU and Avcu F. Therapeutic role of bisphosphonate and radiation combination in the management of myeloma bone disease. Breast Cancer Research 8(R52):2006

434 Senaratne SG, Pirianov G, Mansi JL, Arnett TR, Colston KW. Bisphosphonates induce apoptosis in human breast cancer cell lines, Br J Cancer, 82(8):1459-1468:2000

435 Fromique O, Lagneaux L, Body JJ. Bisphosphonates induce breast cancer cell death in vitro, J Bone Miner Res. 15(11):2111-21:2000

436 Zreiqat H, Binder W, Little CB, Geoczy CL and Youssef P. Poster: Zoledronic acid modulates the expression of S100A8 in adjuvant arthritis. 2006

437 Foell D. Wittkowski H. Roth J. Mechanisms of disease: a 'DAMP' view of inflammatory arthritis. [Review] Nature Clinical Practice Rheumatology 3(7):382-90:2007

438 Liao H, Wu J, Kuhn E, Chin W, Chang B, Jones MD, et al. Use of mass spectrometry to identify protein biomarkers of disease severity in the synovial fluid and serum of patients with rheumatoid arthritis. [Journal Article] Arthritis & Rheumatism 50(12):3792-803:2004

439 Henke MO, Renner A, Rubin BK, Gyves JI, Lorenz E, Koo JS. Up-regulation of S100A8 and S100A9 protein in bronchial epithelial cells by lipopolysaccharide. [Journal Article. Research Support, Non-U.S. Gov't] Experimental Lung Research. 32(8):331-47, 2006

440 Hsu SH, Kuo CC, Yen HJ, Whu SW, Tsai CL. The effect of two different bioreactors on the neocartilage formation in type II collagen modified polyester scaffolds seeded with chondrocytes, Artif Organs: 29(6):467-74:2005

441 Zreiqat H, Howlett CR, Gronthos S, Hume D, Geczy CL. S100A8/S100A9 and their association with cartilage and bone. J Mol Histol. 38, 381-391, 2007

442 Cancedda R, Cedola A, Giuliani A, Komlev V, Lagomarsino S, et al. Bulk and interface investigations of scaffolds and tissue-engineered bones by X-ray microtomography and X-ray microdiffraction. Biomaterials 28:2505-2524:2007

443 Matthieu LM, Mueller TL, Bourban PE, Pioletti DP, Muller R, Manson JA. Architecture and properties of anisotropic polymer composite scaffolds for bone tissue engineering. Biomaterials 27:905-916:2006

444 Mather ML, Morgan SP, White LJ, Tai H, Kockenberger W, et al. Image-based characterization of foamed polymeric tissue scaffold, Biomed Mater 3;2008

445 Lin AS, Barrows TH, Cartmell SH, Guldberg GE. Microarchitectural and mechanical characterization of oriented porous polymer scaffolds. Biomaterials 24:481-489:2003

446 Zehbe R, Goebbels J, Ibold Y, Gross U, Schubert H. Three-dimensional visualization of in vitro cultivated chondrocytes inside porous gelatine scaffolds: A tomographic approach. Acta Biomaterialia 6(6):2097-2107:2010

447 Gössl M, Bentley MD, Lerman LO. Review- 3D Micro CT Imaging of Renal Micro-Structural Changes, Nephron Clinical Practice 103(2):c66-70:2006

448 Bentley M D, Ortiz M C, Ritman E L, and Romero J C. The use of micro computed tomography to study microvasculature in small rodents. Am. J. Physiol. Regul. Integr. Comp. Physiol. 282: R1267–R1270:2002

449 Alberich-Bayarr A, Moratal D, Ivirico JL, Hernandez JC, Valles-Lluch A, Marti-Bonmati L, et al. Microcomputed tomography and microfinite element modeling for evaluating polymer scaffolds architecture and their mechanical properties. Journal of Biomedical Materials Research Part B: Applied Biomaterials 91B(1):2009

450 Melchels F, Rijckaert B, Grijpma D and Feijen J. Micro-CT analysis of tissue engineering scaffold architectures. In: BMTI/iBME Symposium : Highlights in BioMedical Technology, Enschede, Netherlands 2008

451 Stanton H, Rogerson FM, East CJ, Golub SB, Lawlor KE, Meeker CT, et al. ADAMTS-5 is the major aggrecanase in mouse cartilage in vivo and in vitro. Nature 434:648-652:2005

452 Braun B, Zimmerman MB, Dretchmer N, Spargo RM and Gracey M. Risk factors for diabetes and cardiovascular disease in young Australian Aborigines. Diabetes Care 19:472-479:1996

453 Yang J, Goto M, Ise H, Cho CS, Akaike T. Glycosylated alginate as a scaffold for hepatocytes entrapment. Biomaterials 23:471-9:2002

454 Masuda T, Takahashi I,Anada T, Arai F, Fukuda T, Takano-Yamamoto T, et al. Development of a cell culture system loading cyclic mechanical strain to chondrogenic cells, J Biotech. 133:231-238:2008

455 Lee JH, Kisiday J, Grodzinsky AJ. Tissue-engineered versus native cartilage: linkage between cellular mechano-transduction and biomechanical properties. Novartis Found Symp 249:52-64:2003

456 Figure 3.2 wound healing

457 Clark RA, Lanigan JM, DellaPelle P, Manseau E, Dvorak HF, Colvin RB. Fibronectin and fibrin provide a provisional matrix for epidermal cell migration during wound reepithelialization. J Invest Dermatol 79(5):264-69:1982.

458 Grinnell F. Fibroblasts, myofibroblasts, and wound contraction. J Cell Biol 124:401-404:1994

459 Tonnesen MG, Feng X, Clark RA. Angiogenesis in wound healing. J Investig Dermatol Symp Proc 5(1): 40-06:2000

460 Clark RA. Wound repair. Curr Opin Cell Biol 1(5):1000-08:1989

461 Winter GD. Formation of the scab and the rate of epithelization of superficial wounds in the skin of the young domestic pig. Nature 193:293-94:1962

462 Clark RA, Nielsen LD, Welch MP, McPherson JM. Collagen matrices attenuate the collagen-synthetic response of cultured fibroblasts to TGF-beta. J Cell Sci 108(3):1251:1995

463 Levenson SM, Geever EF, Crowley LV, Oates JF, Berard CW, Rosen H. The healing of rat skin wounds. Ann Surg 161:293-308:1965

464 Lobman R, Schultz G, Lehnert H. Proteases and the diabetic foot syndrome: mechanisms and therapeutic implications. Diabetes Care 28:461–471:2005

465 Harrison CA, Gossiel F, Layton CM, Bullock AJ, Johnson T, Blumsohn A, et al. Use of an in vitro model of tissue-engineered skin to investigate the mechanism of skin graft contraction. Tissue Eng 12(11):3119–33:2006

466 Chen C, Schultz GS, Bloch M, Edwards PD, Tebes S, Mast BA. Molecular and mechanistic validation of delayed healing rat wounds as a model for human chronic wounds. Wound Repair and Regeneration 7(6):486-494:1999

467 Stadelmann WK, Digenis AG, Tobin GR. Physiology and healing dynamics of chronic cutaneous wounds. The American Journal of Surgery 126(Suppl 2A):26S-38S:1998

468 Multimedia Healthcare. http://www.mmhc.com/2010/11/28/signs-of-infection-in-chronic-wounds-6/ Accessed 2/2/2009

469 Alavi SM, Khosravi AD, Sarami A, Dashtebozorg A, Montazeri EA. Pakistan Journal of Medical Sciences Quarterly. 23(5):2007

470 Lennox J. Chapter 2- Biofilm Formation and Growth. The biofilms hypertextbook-Intermediate Level 2008. http://biofilmbook.hypertextbookshop.com/public_version Accessed 1/12/10

471 Hollis G. Dechra Vetinary Products. Types of wound. http://dechra-eu.com/Therapy-Areas/Woundcare/Types-of-wound.aspx. Accessed 13/1/2010

472 Williams D, Enoch S, Miller D, Harris K, Price P, Harding KG. Effect of sharp debridement using curette on recalcitrant nonhealing venous ulcers: a concurrently controlled, prospective cohort study. Wound Repair Regen 13(2):131-7:2005

473 Mekkes JR, Le Poole IC, Das PK, Bos JD, Westerhof W. Efficient debridement of necrotic wounds using proteolytic enzymes derived from Antarctic krill: a double-blind, placebo-controlled study in a standardized animal wound model. Wound Repair Regen 6(1):50-57:1998

474 Bucalo B, Eaglstein W, Falanga V. Inhibition of cell proliferation by chronic wound fluid. Wound Repair Regen 1:181-186:1993

475 Rogers AA, Burnett S, Moore JC, Shakespeare PG, Chen WYJ. Involvement of proteolytic enzymes, plasminogen activators, and matrix metalloproteinases levels in the pathology of pressure ulcers. Wound Repair Regen. 3:273-283:1995

476 Falanga V, Williams R. Wound Bed Preparation and the Role of Enzymes: Overview of Wound Bed Preparation Wounds. 14(2):2002. Health Management Publications, Inc. http://www.medscape.com/viewarticle/430899_2. Accessed 13/1/2010

477 Wound Care Information Network. Types of Wound Debridement. http://www.medicaledu.com/debridhp.htm. Accessed 16/1/2011

478 Morykwas MJ, Simpson J, Punger K, Argenta A, Kremers L, Argenta J. Vacuum-assisted closure: State of basic research and physiologic foundation. Plastic and reconstructive surger 1117:121S-126:2006

479 Horch RE, Kopp J, Bach AD, Kneser U. Pre-treatment of pressure ulcers using subatmospheric pressure dressings enhances plastic surgical coverage. 8th EPUAP Open Meeting. http://www.epuap.org/aberdeen/page4.htm. Accessed 26/1/2011

480 US Food and Drugs Administration. Preliminary Public Health Notification: Serious Complications Associated with Negative Pressure Wound Therapy Systems 13/11/09 http://www.fda.gov/MedicalDevices/Safety/AlertsandNotices/PublicHealthNotifications/ucm190658.htm Accessed 9/12/10

481 Petrulyte S. Advanced textile materials and biopolymers in wound management. Dan Med Bull:55:72-77:2008

482 Parish, LC, Dryjski M, Cadden S. Prospective clinical study of a new adhesive gelling foam dressing in pressure ulcers. Int Wound J. 2008;5:60-67 7. Robinson BJ. The use of a hydrofiber dressing in wound management. J Wound Care 2000;9:32-34.

483 Brown CD and Zittelli JA. Choice of wound dressings and ointments. Otolaryngol Clin N Amer 28(5):1081-91:1995

484 Margolis DJ, Kantor J, Berlin JA. Healing of diabetic neuropathic foot ulcers receiving standard treatment. A meta-analysis. Diabetes Care 22(5):692-5:1999

485 Steffansen B, Herping SP. Novel wound models for characterizing ibuprofen release from foam dressings. International Journal of Pharmaceutics 364:150-155:2008

487 Parks WC. Matrix metalloproteinases in repair. Wound repair and regeneration 7(6):423-432:1999

488 Li X & Hou Y. The treatment of osteomyelitis with gentamicin-reconstituted bone xenograft-composite. J Bone Joint Surg Br 1063-1068:2001

489 Cabanas MV, Pena J, Roman J, Vallet-Regi M. Tailoring vanomycin release from x-TCP/agarose scaffolds Eur J Pharm Sci 37:249-256:2009

490 Jia WT, Zhang X, Luo SH, Liu X, Huang WH, Rahaman MN, et al. Novel borate glass/chitosan composite as a delivery vehicle for teicoplanin in the treatment of chronic osteomyelitis. Acta Biomater 6(3):812-819:2010

491 Kim TG, Lee DS, Park TG. Controlled protein release from electrospun biodegradable fiber mesh composed of poly(e-caprolactone) and poly(ethylene oxide), Pharm Nanotech. 338(1-2):276-283,2007

492 Forner-Cordero I, Navarro-Monsoliu R, Muñoz-Langa J, Alcober-Fuster P, Rel-Monzó P. Use of nanocrystalline silver dressing on lymphatic ulcers in patients with chronic lymphoedema. Journal of Wound Care 16:235-8:2007

493 Silver S, Phung le T, Silver G. Silver as biocides in burn and wound dressings and bacterial resistance to silver compounds. J Ind Microbiol Biotechnol 33:627–34:2006

494 Poon VK, Burd A. In vitro cytotoxicity of silver: implication for clinical wound care. Burns 30:140-7:2004

495 Cullen B, Smith R, McCulloch E, Silock D, Morrison L. Mechanism of action of POMOGRAN, a protease modulating matrix, for the treatment of diabetic foot ulcers. Wound repair and regneration 10(1):16-25:2002a

496 Cullen B, Watt PW, Lundqvist C, Silcock D, Schmidt RJ, Bogan D, et al. The role of oxidised regenerated cellulose/collagen in chronic wound repair and its potential mechanism of action. The International Journal of Biochemistry & Cell Biology December 34(12):1544-1556:2002b

497 Edwards JV, Yager DR, Cohen IK, Diegelmann RF, Montane S, Bertoniere N, et al. Modified cotton gauze dressings that selectively absorb neutrophil elastase activity in solution. Wound Repair Regen 9:50–8:2001

498 Vachon DJ, Yager DR. Novel sulfonated hydrogel composite with the ability to inhibit proteases and bacterial growth. J Biomed Mater Res A 76:35-43:2006

499 Rayment EA, Shooter GK, George GA, Upton Z. Elevated matrix-metalloproteinase activity in chronic wound fluid. In: 16th European Tissue Repair Society Annual Meeting, Pisa, Italy 2006

500 Fimiani M, Pianigiani E, Simplicio FC, SbanoP, Cuccia A, Pompella G. Other uses of homologous skin grafts and skin bank bioproducts. Clinics in Dermatology 23:396-402:2005

501 Hierner R, Degreef H, Vranckx JJ, Garmyn M, Massage P, van Brussel M. Skin grafting and wound healing- the "dermato-plastic team approach". Clinics in Dermatology 23:343-352:2005

502 Steed DL, Goslen JB, Holloway GA, Malone JM, Bunt TJ and Webster MW. Randomized prospective double-blind trial in healing chronic diabetic foot ulcers. CT-102 activated platelet supernatant, topical versus placebo. Diabetes Care 15(11):1598-604:1992

503 Bernhardt A, Lode A, Boxberger S, Pome W, Gelinsky M. Mineralised collagen – an artificial, extracellular bone matrix – improves osteogenic differentiation of bone marrow stromal cells. J Mater Sci Mater. Med 19:269:2008

504 Yannas IV, Burke JF, Orgill DP, Skrabut EM. Wound tissue can utilize a polymeric template to synthesize a functional extension of skin. Science. 215:174-176:1982

505 Landsman A. Management of Complex Wounds, The North American Journal of Medicine and Science 3(1):14-16:2010

505 Hodde J. Naturally occurring scaffolds for soft tissue repair and regeneration, Tissue Engineering 8(2):295-308:2002

506 Auger FA, Rouabhia M, Goulet F, Berthod F, Moulin V, Germain L. Tissue-engineered human skin substitutes developed from collagen populated hydrated gels: clinical and fundamental applications. Med Biol Eng Comput. 36:801-812:1998

507 Langer A, Rogowski. Systematic review of economic evaluations of human cell-derived wound care products for the treatment of venous leg and diabetic foot ulcer, BMC Health Ser Res 9:115:2009

508 Warren SM, Fong K, Nacamuli R, Song H, Fang T, Longaker. Biomaterials for Skin and Bone Replacement and Repair in Plastic Surgery, Operative Techniques in Plastic and Reconstructive Surgery 9:1:10-15:2003

510 Sabolinski ML, Alvarez O, Mulder G, Parenteau NL. Cultured skin as a 'smart material' for healing wounds: experience in venous ulcers. Biomaterials 17(3):311-320:1996

511 Gentzkow GD, Iwasaki SD, Hershon KS, Mengel M, Prendergast JJ, Ricotta JJ, et al. Use of dermagraft, a cultured human dermis, to treat diabetic foot ulcers. Diabetes Care 4:350–354:1996

511 Gentzkow GD, Iwasaki SD, Hershon KS, Mengel M, Prendergast JJ, Ricotta JJ. Use of Dermagraft, a cultured human dermis, to treat diabetic foot ulcers. Diabetes Care. 1996;19(4):350-354.

512 Kim PJ, Dybowski KS, Steinberg JS. A closer look at bioengineered alternative tissues 19(7):38-55:2006 http://www.podiatrytoday.com/article/5820?page=1

513 Eldor R, Raz I, A Yehuda, Boulton A. New and experimental approaches to treatment of diabetic foot ulcers: a comprehensive review of emerging treatment strategies, Diabetes Medicine. 24:1161-1173:2004

514 Cooper ML, Hansbrough JF, Spielvogel RL, Cohen R, Bartel RL, Naughton G. In vivo optimization of a living dermal substitute employing cultured human fibroblasts on a biodegradable polyglycolic acid or polyglactin mesh, Biomaterials. 12:243-248:1991

515 Elsenbud D, Huang NF, Luke S, Silberklang M. Skin Substitutes and Wound Healing: Current Status and Challenges Wounds 16(1):2004

516 The Whitaker Foundation 2000

517 Waugh HV and Sherratt JA. Modeling the effects of treating diabetic wounds with engineered skin substitutes.Wound Repair Regen 15(4):556-65:2007

519 Kassel KS. Dermagraft helps heal diabetic foot ulcers. 2004 www.mbmc.org/healthgate Accessed 20/1/2011

520 Hu S, Kirsner RS, Falanga V, Phillips T and Eaglstein WH. Evaluation of Apligraf persistence and basement membrane restoration in donor site wounds: a pilot study. Wound Repair Regen 14(4):427-33:2006

521 Philips TJ, Manzoor J, Rojas A, Isaac C, Carson P, Sabolinski M, et al. The longevity of a bilayered skin substitute after appliation to venous ulcers, Arch Dermatol. 138(8):1079-1061:2002

522 Organogenesis. The science behind Apligraf®. http://www.apligraf.com/patient/what_is_apligraf/how_works/the_science_behind_apligraf.html. Accessed 14/01/2010

523 Silverstein G. Dermal regeneration template in the surgical management of diabetic foot ulcers: a series of five cases. J Foot Ankle Surg 45(1):28-33:2006

524 Voigt DW, Paul CN, Edwards P, Metz P. Economic study of collagen-glycosaminoglycan biodegradable matrix for chronic wounds. Wounds 18(1):1-7:2006

525 Lattari V, Jones LM, Varcelotti JR, Latenser BA, Sherman HF, Barrette RR. The use of a permanent dermal allograft in full-thickness burns of the hand and foot: a report of three cases. Journal of Burn Care and Rehabilitation 18(2):147-155:1997

526 Rhee SH and Tanaka J. Effect of citric acid on the nucleation of hydroxyapatite in a simulated body fluid. Biomaterials 20(22):2155-2160:1999

528 Deodato B, Arsic N, Zentilin L, Galeano M, Santoro D, Torre V, Altavilla D, et al. Recombinant AAV vector encoding human VEGD165 enhances wound healing. Gene Ther 9:12:777-85:2002

529 Steed DL. Clinical evaluation of recombinant human platelet-derived growth factor for the treatment of lower extremity ulcers. Plast Reconstr Surg 117:143S:2006

530 Liechty KW, Nesbit M, Herlyn M, Radu A, Adzick NS, Crombleholme TM. Adenoviral-mediated overexpression of platelet-derived growth factor-B corrects ischemic impaired wound healing. J Invest Dermatol 113:3:375-83:1999

532 EMEA Scientific Discussion for the approval of Regranex 2004 http://www.emea.europa.eu/docs/en_GB/document_library/EPAR_-_Scientific_Discussion/human/000212/WC500050140.pdf Accessed 20/1/2011

533 Aggarwal S and Pittenger MF. Human mesenchymal stem cells modulate allogenic immune cell responses. Blood 105:1815:2005

534 Quesenberry PJ, Colvin GA, Lambert JF, Frimberger AE, Dooner MS, Mcauliffe CI, et al. The new stem cell biology. Trans Am Clin Climatol Assoc 113: 182-207:2002

535 Badiavas EV, Abedi M, Butmarc J, Falanga V, Quesenberry P. Participation of bone marrow derived cells in cutaneous wound healing. Journal of Cellular Physiology. 196(2):2003

536 Yoshikawa T, Mitsuno H, and Nonaka I. Wound therapy by mesenchymal cell transplantation. Plast Reconstr Surg 121: 860:2008

537 ImmuneRegen Biosciences. Stem Cells. http://www.immuneregen.com/stem-cells.php. Accessed 15/1/2011

538 Rezwan K, Chen QZ, Blaker JJ, Boccaccini AR. Biodegradable and bioactive porous polymer/inorganic composite scaffolds for bone tissue engineering, Biomaterials:3413-3431:2006

539 Hutmacher DW. Scaffold design and fabrication technologies for engineering tissues-state of the art and future perspectives. J Biomat Sci. 12:107-124:2001

540 Hou Q, Grijpma DW, Feijen J. Porous polymeric structures for tissue engineering prepared by a coagulation, compression moulding and salt leaching technique, Biomaterials 24:1937-1947:2003

541 Robertson DB, Daniel DM and Biden E. Soft tissue fixation to bone. Am J Sports Med 14:398:1986

542 Spalazzi JP, Doty SB, Moffat KL, Levine WN and Lu HH. Development of controlled matrix heterogeneity on a triphasic scaffold for orthopedic interface tissue engineering. Tissue Eng 12:3497:2006

543 Barnes PC, Sell SA, Boland ED, Simpson DG, Bowlin GL. Nanofiber technology: designing the next generation of tissue engineering scaffolds, Advanced Drug Delivery Reviews. 59:1413-1433:2007

544 Powell HM, Supp DM, Boyce ST. Influence of electrospun collagen on wound contraction of engineered skin substitutes. Biomaterials 29:834-843:2008

545 Nam YS, Yoon JJ and Park TG. A novel fabrication method of macroporous biodegradable polymer scaffolds using gas foaming salt as a porogen additive. J Biomed Mater Res Appl Biomater 53:1:2000

546 Perera DS, Mukherjee SK, Moricca CJ, Fabrication of porous iron using sucrose, J Mat Sci Lett. 16:1437-1440:1997

547 Olah L, Filipczak K, Jaegermann Z, Czigany T, Borbas L, Sosnowski S, et al. Synthesis, structural and mechanical properties of porous polymeric scaffolds for bone tissue regeneration based on neat poly(e-caprolactone) and its composites with calcium carbonate, Polymers for Adv Tech. 17:11-12:2006

548 Gao J, Crapo P, Wang Y. Macroporous Elastomeric Scaffolds with Extensive Micropores for Soft Tissue Engineering, Tissue Engineering 12(4):917-925:2006

549 Reignier K, Huneault MA. Preparation of interconnected poly(e-caprolactone) porous scaffolds by a combination of polymer and salt particulate leaching, Polymer. 47:4703-4717:2006

550 Mano JF, Hungerford G, Ribelles JL. Bioactive (poly(L-lactic acid)- chitosan hybrid scaffolds. Materials Science and Engineering C 28:1356-1365:2008

551 Li J, Rickett TA, Shi R. Biomimetic Nerve Scaffolds with Aligned Intraluminal Microchannels: A "Sweet" Approach to Tissue Engineering Langmuir 25:1813-1817:2009

552 Silver IA, Deas J, Erecinska M. Interactions of bioactive glasses with osteoblasts in vitro: effects of 45S5 Bioglass®, and 58S and 77S bioactive glasses on metabolism, intercellular ion concentrations and cell viability. Biomaterials 22(2):175–85:2001

552 Khasim HR, Henning S, Michler GH, Brand J. Development of nanocomposite scaffolds for bone tissue engineering, Macromol Symp. 294(1):144-152:2010

553 Di Nunzio S & Verne E. Process for the production of silver-containing prosthetic devices. Italian Patent no. PCT/EP2005/056391

554 Thomson RC, Yaszemski MJ. Powers JM & Mikos AG. Hydroxyapatite fiber reinforced poly(a-hydroxylester) foams for bone regeneration. Biomaterials 18:1935–1943:1998

555 Meratoja W, Helminen AO, Korventausta JJ, Haapa-aho V, Seppala JV, Narhi TO. Crosslinked poly(epsilon-caprolactone/D,L-lactide)/bioactive glass composite scaffolds for bone tissue engineering, J Biomed Mater Res A. 77(2):261-268:2006

556 Nazarov R, Jin HJ, Kaplan D. Porous 3-D Scaffolds from Regenerated Silk Fibroin. Biomacromolecules. 5:718-726:2004

557 Oates M, Chen R, Duncan M, Hunt JA. The angiogenic potential of three-dimensional open porous synthetic matrix material, Biomaterials. 28:3679-3686:2007

558 Mikos AG, Sarakinos G, Leite SM, Vacanti JP, Langer R. Laminated Three-Dimensional Biodegradable Foams for Use in Tissue Engineering. Biomaterials 14:323:1993

559 Timmenga EJ, Andreassen TT, Houthoff HJ, and Klopper PJ. The effect of mechanical stress on healing skin wounds: An experimental study in rabbits using tissue expansion. Br J Plast Surg. 44:514–519, 1991

560 Stamboulis A, Hench LL and Boccaccini AR. Mechanical properties of biodegradable polymer sutures coated with bioactive glass, J Mater Sci Mater Med 13(9):843-848:2002

561 Bretcanu O, Verné E, Borello L and Boccaccini AR. Bioactivity of degradable polymer sutures coated with bioactive glass. J Mater Sci Mater Med. 15(8):893-899:2004

562 Chen QZ, Blaker JJ, Boccaccini. Bioactive and mechanically strong bioglass-poly(D,L-lactic acid) composite coatings on surgical sutures, J Biomed Mater Res B Appl Biomater. 76(2):352-363:2006

563 Niemala T, Niiranen H, Kellomaki M, Tormala P. Self-reinforced composites of bioabsorbable polymer and bioactive glass with different bioactive glass contents. Part I: initial mechanical properties and bioactivity. Acta Biomaterialia. 1(2):235-242:2004

564 tussa- cannot find on comp. pg 33 ch 4 BG powders dry pressed onto polymer composite

565 Blaker JJ, Nazhat SN, Boccaccini AR. Development and characterisation of silver-doped bioactive glass-coated sutures for tissue engineering and wound healing applications. Biomaterials 25(7-8):1319-1329:2004

566 Blaker JJ, Boccaccini AR, Nazhat SN. Thermal Characterizations of silver-containing bioactive glass-coated Sutures. Journal of Biomaterials Applications 20:1: 81-98:2005

567 Shin KH, Sung JH, Koh YH, Lee JH, Choi WY, Kim HE. Direct coating of bioactive sol–gel derived silica on poly(ε-caprolactone) nanofibrous scaffold using co-electrospinning. Materials Letters 64:1539-1542:2010

568 Misra SK, Mohn D, Brunner TJ, Stark WJ, Philip S, Roy I, et al. Comparison of nanoscale and microscale bioactive glass on the properties of P(3HB)/Bioglass composites. Biomaterials 29(12):1750-1761:2008

569 Leong KF, Chua CK, Sudarmadji N, Yeong WY. Engineering functionally graded tissue engineering scaffolds- Review. J Mech Behav Biomed Mat 1:140-152:2008

570 Hench L, Jones JR. Biomaterials, artificial organs and tissue engineering. Cambridge: Woodhead Publishing Ltd 2005

571 Prendergast PJ. In: Cowin, S.C. (Ed.), Bone Mechanics Handbook. CRC Press LLC, Boca Raton, 351–3529:2001

572 Kreke MR, Huckle WR, Goldstein AS. Fluid flow stimulates expression of osteopontin and bone sialoprotein by bone marrow stromal cells in a temporally dependent manner. Bone 36:1047–1055:2005

573 Wang X, Wenk E, Zhang X, Meinel L, Vunjak-Novakovic G, Kaplan DL. Growth factor gradients via microsphere delivery in biopolymer scaffolds for osteochondral tissue engineering. J Controlled Release 134(2):81-90:2009

574 Oh SH, Park IK, Kim JM, Lee JH. In vitro and in vivo characteristics of PCL scaffolds with pore size gradient fabricated by a centrifugation method. Biomaterials 28(9):1664-71:2007

575 Buhler M, Bourban P-E, Manson J-A. Cellular thermoplastic composites with microstructural gradients of fibres and porosity. Composites Science and Technology 68:820–828:2008

576 Liu C, Han Z, Czernuszka JT. Gradient collagen/nanohydroxyapatite composite scaffold: Development and characterization, Acta Biomaterialia 5(2):661-669:2008

577 Shen M, Bever MB, Gradients in polymeric materials, J Mat Sci 741-746:1972

578 Zha G, Liao W, Wang Y, Wu G. Morphological observation on repairing articular cartilage defects with collagen complex gradient TCP [Chinese] Chung Kuo Hsiu Fu Chung Chien Wai Ko Tsa Chih 22(8):989-92:2008

579 Bignon A, Chouteau J, Chevalier J, Fantozzi G, Carret JP, Chavassieux P, et al. Effect of micro and macroporosity of bone substitutes on their mechanical properties and cellular response. Journal of Materials Science Materials in Medicine 14:1089–1097:2003

580 Seavey R. Sterilisation of surgical implants: Did you know..... Managing Infection Control Nov 2006

581 Schultz, Janet. Monitoring and Load Release for Implants Sterilized by Steam Within Healthcare Facilities. Managing Infection Control. Jan 2004

582 Nakagawa Y, Murai T, Hasegawa C, Hirata M, Tsuchiya T, Yagami T, et al. Endotoxin contamination in wound dressings made of natural biomaterials. J Biomed Mater Res 66B:347–55:2003

583 Hench LL. Bioactive Ceramics, in Bioceramics: Material characteristics versus in vivo behavior. Vol. 523. Ducheyene P and Lemons J, Eds. Annals of New York Academy of Sciences. New York. 1988

584 Niiranen H, Pyhalto T, Rokkanen P, Kellomaki M, Tormala P. In vitro and in vivo behavior of self-reinforced bioabsorbable polymer and self-reinforced bioabsorbable polymer/bioactive glass composites. J Biomed Mater Res A 69A:699–708:2004

585 Cottam E, Hukins DW, Lee K, Hewitt C, Jenkins MJ. Effect of sterilisation by gamma irradiation on the ability of polycaprolactone (PCL) to act as a scaffold material. Medical Engineering & Physics 31(2):221-226:2009

586 Oláh L, Filipczak K, Czvikovsky T, Czigány T, Borbás L. Changes of porous poly([epsilon]-caprolactone) bone grafts resulted from e-beam sterilization process. Radiation Physics and Chemistry 76(8-9):1430-1434:2007

586 Olah L, Filipezak K, Czvikovsky T, Czigany T, Borbas L. Changes of porous (poly(e-caprolactone) bone grafts resulted from e-beam sterilization process. Radiation Physics and Chemistry 76:1430-1434:2007

587 Fischbach C, Tessmar J, Lucke A, Schnell E, Schmeer G, Blunk T, et al. Does UV irradiation affect polymer properties relevant to tissue engineering? Surface Science 491(3):333-345:2001

588 Plikk P, Odelius K, Hakkarainen M, Albertsson AC. Finalizing the properties of porous scaffolds of aliphatic polyesters through radiation sterilization. Biomaterials 27:5335-5347:2006"

589 Croonenborghs B, Smith MA and Strain P. X-ray versus gamma irradiation effects on polymers. Radiation Physics and Chemistry 76(11-12):1676-1678:2007

590 Dinarello CA. Thermoregulation and the pathogenesis of fever. Infectious Disease Clinics of North America 10:433-499:1996

591 Denyer SP, Hodges NA, Gorman SP eds. Hugo and Russell's Pharmaceutical Microbiology 7th Edition Wiley-Blackwell Publishing 2004

592 Gao B, Tsan MF. Endotoxin contamination in recombinant Human Heat Shock Protein 70 (Hsp70) preparation is responsible for the induction of TNFa release by murine macrophages. J Biol Chem 278:174–9:2003

593 Gorbet MB, Sefton MV. Endotoxin: The uninvited guest. Biomaterials 26:6811-6817:2005

594 Suri RM, Austyn JM. Bacterial lipopolysaccharide contamination of commercial collagen preparations may mediate dendritic cell maturation in culture. J Immunol Methods 214:149–63:1998

595 Ragab AA, Van de Motter R, Lavish SA, Goldberg VM, Ninomiya JT, Carlin CR, et al. Measurement and removal of adherent endotoxin from Titanium particles and implant surfaces. J Orthop Res 17:803–9:1999

596 Greenfield EM, Bi Y, Ragab AA, Golberg VM, Nalepka JL, Seabold JM. Does endotoxin contribute to aseptic loosening of orthopedic implants? Journal of Biomedical Materials Research Part B: Applied Biomaterials 72B(1):179-185:2005

597 Iverson SL, Barnard JW, Mehta KK. Electron-beam processing for sterilization. Radiation Physics & Chemistry. 42(4-6):601-604:1993

598 Yixiang D, Yong T, Liao S, Chan CK, Ramakrishna S. Degradation of electrospun nanofiber scaffold by short wave length ultraviolet radiation treatment and its potential applications in tissue engineering. Tissue Eng Part A 14(8):1321-9:2008

599 Silva MM, Cyster LA, Barry JJ, Yang XB, Oreffo RO, Grant DM, et al. The effect of anisotropic architecture on cell and tissue infiltration into tissue engineering scaffolds. Biomaterials 27(35):5909-5917:2006

600 Hedberg EL, Shih CK, Lemoine JJ, Timmer MD, Liebschner MA, Hansen JA, et al. In vivo degradation of porous poly(propylene fumarate)/poly(DL-lactic-co-glycolic acid) composite scaffolds. Biomaterials 26(22):4616-4623:2005

601 Steritech www.steritech.com.au. Accessed 12/10/10

602 Zhang YZ, Bjursten LM, Freij-Larsson C, Kober M, Wesslén B. Tissue response to commercial silicone and polyurethane elastomers after different sterilization procedures. Biomaterials 17(23):2265-2272:1996

603 Odelius K, Plikk P, and A-C Albertsson. The influence of composition of porous copolyester scaffolds on reactions induced by irradiation sterilization. Biomaterials 29(2):129-140:2008

604 O'Neill P, Birkinshaw C, Leahy JJ, Barkli R. The role of long lived free radicals in the ageing of irradiated ultra high molecular weight polyethylene. Polymer Degradation and Stability 63:31-39:1999

605 Jahan MS, King MC, Haggard WO, Sevo KL, Parr JE. A study of long-lived free radicals in gamma-irradiated medical grade polyethylene. Radiation Physics and Chemistry 62:141–144:2001

606 Ries MD, Weaver K, Rose RM, Gunther J, Sauer W, Beals N. Clin Orthop Relat Res. 333:87-95:1996

607 Park K, Mishra S, Lewis G, Losby J, Fan Z, Park J. Quasi-static and dynamic nanoindentation studies on highly crosslinked ultra-high molecular-weight polyethylene Biomat 25:2427-2436:2004

608 Gorna K, Gogolewski S. The effect of gamma radiation on molecular stability and mechanical properties of biodegradable polyurethanes for medical applications, Polymer Degradation and Stability 79:465-474:2003

609 Zdaniewski WA, Easler TE, Bradt RC. Gamma Radiation Effects on the Strength of a Borosilicate Glass. J Am Cer Soc 66(5):1983

610 Sakuri Y, Nagasawa K, Nishikawa H, Ohki Y. Point defects in high purity silica induced by high-dose gamma irradiation. J Appl Phys 75:1372:1994

611 Bharati S, Soundrapandian C, Basu D, Datta S. Studies on a novel bioactive glass and composite coating with hydroxyapatite on titanium based alloys: Effect of gamma-sterilization on coating. J. Eu Ceram Soc 29:12:2527:2009

612 Boughton PC. Personal Communication. Operations Manager, Biometic Pty Ltd., 9/12/10

613 Gibson LJ, Ashby MF. Cellular solids, structure and properties. Oxford, UK: Pergamon Press 1988

613 mechanical verification figure ch3

614 Annabi N, Mithieux SM, Weiss AS, Dehghani F. Electrospun nanofibrous structure: A novel scaffold for tissue engineering. Biomaterials 31:1655-1665:2010

615 Li WL, Laurencin CT, Caterson EJ, Tuan RS, Ko FK. Electrospun nanofibrous structure: A novel scaffold for tissue engineering. J Biomed Mat Res 60(4):613-621, 2002

616 Xu C, Inai R, Kotaki M, Ramakrishna S. Electrospun Nanofiber Fabrication as Synthetic Extracellular Matrix and Its Potential for Vascular Tissue Engineering. Tissue Engineering 10(7/8):1160:2004

617 Kim SS, Park MS, Jeon O, Choi CY, Kim BS. Poly(lactide-co-glycolide)/hydroxyapatite composite scaffolds for bone tissue engineering. Biomaterials 27:1399-1409:2006

618 Eshraghi S, Das S. Mechanical and microstructural properties of polycaprolactone scaffolds with one-dimensional, two-dimensional, and three-dimensional orthogonally oriented porous architectures produced by selective laser sintering, Acta Biomaterialia 6(7):2467-76:2010

619 Powell HM, Boyce ST. EDC cross-linking improves skin substitute strength and stability. Biomaterials 27:5821-5827:2006

620 Burks CA, Bundy K, Fotuhi P, Alt E. Characterization of 75:25 poly(L-lactide-co-ε-caprolactone) thin films for the endoluminal delivery of adipose-derived stem cells to abdominal aortic aneurysms. Tissue Eng 12:2591–2600:2006

621 Stammen JA, Williams S, Ku DN, Gulber RE. Mechanical properties of a novel PVA hydrogel in shear and unconfined compression. Biomaterials 22:799-806:2001

622 Annabi N, Mithieux SM,Weiss AS, Dehghani F. The fabrication of elastin-based hydrogels using high pressure CO_2. Biomaterials 30:1–7:2009

623 Baker SC, Rohman G, Southgate J, Cameron NR. The relationship between the mechanical properties and cell behavior on PLGA and PCL scaffolds for bladder tissue engineering, Biomaterials 30:1321-1328:2009

624 DuttaRoy T, Wang FW, Stone JJ, Cho EH, Lockett SJ. Mechanisms Of Osteoblast Adhesion On 3D Polymer Scaffolds Made By Rapid Prototyping, Citation: Society For Biomaterials 30th Annual Meeting Transactions, 347:2005

625 Ma PX, Choi JW. Biodegradable Polymer Scaffolds with Well-Defined Interconnected Spherical Pore Network. Tissue Engineering 7(1):23-33:2001

626 Heydarkhan-Hagvall S, Schenke-Layland K, Dhanasopon AP, Rofail F, Smith H, Wu BM, et al, Influence of systematically varied nano-scale topography on cell morphology and adhesion, Cell Commun Adhes. 14:181-194:2007

627 Kurane A, Simionescu DT, Vyavahare NR. In vivo cellular repopulation of tubular elastin scaffolds mediated by basic fibroblast growth factor, Biomaterials. 28:2830-2838:2007

628 De Jong WH, Dormans JA, Steenbergen MJ, Verharen HW, Hennink WE. Tissue response in the rat and the mouse to degradable dextran hydrogels. J Biomed Mater Res 83A:538-545:2007

629 Weir NA, Buchanan FJ, Orr JF, Farrar DF. Influence of processing and sterilisation on properties of poly-ε-caprolactone. Plastics, rubber and composites. 32(6):265-270:2003

630 Hench LL, Andersson O. Bioactive glasses. In: Hench LL, Wilson J, eds. An introduction to bioceramics. Singapore: World Scientific Publishing 1993

631 Hench LL. Bioactive glasses and glass-ceramics: a perspective, in CRC Handbook of Bioactive Ceramics: Volume I: Bioactive Glasses and Glass-Ceramics, Yamamuro T, Hench LL, and Wilson J. Eds. CRC Press, Boca Raton Florida 7-23:1990

632 Hench LL. The story of Bioglass®. J Mater Sci Mater Med. 17: 967-978:2006

633 Amaral M, Costa MA, Lopes MA, Silva RF, Santos JD, Fernandes MH. Wettability and surface charge of Si3N4-bioglass composites in contact with simulated physiological liquids. Biomaterials 23(20):4123-4129:2002

634 Quintero F, Pou J, Comesaña R, Lusquiños F, Riveiro A, Mann AB, et al. Laser Spinning of Bioactive Glass Nanofibers. Advanced Functional Material 19 (19):3084:2009

635 Dept Materials. Imperial College London. Research in Progress 2008-2009 http://workspace.imperial.ac.uk/materials/Public/MaterialsRIP.pdf Accessed 10/12/10

636 Hill M. Unbreakable Glass- Chemists Steal Engineering Tricks from Sponges. Science Daily Sept 2005. http://www.sciencedaily.com/videos/2005/0909-unbreakable_glass.htm

637 Bosetti M, Zanardi L, Hench L, Cannas M. Type I collagen production by osteoblast-like cells cultured in contact with different bioactive glasses. J Biomed Mater Res 64A(1):189–95:2003

638 Vrouwenvelder WC, Groot CG, de Groot K. Behaviour of fetal rat osteoblasts cultured in vitro on bioactive glass and nonreactive glasses. Biomaterials 13(6):382–92:1992

639 Vrouwenvelder WC, Groot CG, de Groot K. Better histology and biochemistry for osteoblasts cultured on titanium doped bioactive glass: Bioglass® 45% compared with iron-, titanium-, fluorine- and boron-containing bioactive glasses. Biomaterials 15(2):1994

640 Vrouwenvelder WCA. Histological and biochemical evaluation of osteoblasts cultured on bioactive glass, hydroxylapatite, titanium alloy, and stainless steel. J Biomed Mater Res 27:465-475:1993

641 Xynos ID, Edgar AJ, Buttery LD, Hench LL, Polak JM. Ionic products of bioactive glass dissolution increase proliferation of human osteoblasts and induce insulin-like growth factor II mRNA expression and protein synthesis. Biomed Biophys Res Commun 276:461–465:2000

642 Asselin A, Hattar S, Oboeuf M, Greenspan D, Beral A, Sautier JM. The modulation of tissue-specific gene expression in rat nasal chondrocyte cultures by bioactive glasses. Biomaterials 25(25): 5621-5630:2004

643 Bunting S, Di Silvo L, Deb S, Hall S. Bioresorbable glass fibers facilitate peripheral nerve regeneration. Journal of Hand Surgery British and European Volume 30B:3:242–247:2005

644 Wilson J and Nolletti D. Bonding of soft tissues to Bioglass®, in CRC Handbook of Bioactive Ceramics: Volume I: Bioactive Glasses and Glass-Ceramics. Yamamuro, T, Hench, LL, and Wilson J, Eds., CRC Press, Boca Raton Florida 283-302:1990

645 Kokubo T. Surface chemistry of bioactive glass-ceramics. J Noncrystal Solids 120:138-51:1995

646 Lobel KD, Hench LL. In vitro adsorption and activity ofenzymes on reaction layers ofbioactive glass substitutes. J Biomed Mater Res 39:576-9:1998

647 TheraGlass. 2010 http://www.theraglass.co.uk. Accessed 14/2/2011

648 Lenihan DV, Carter AJ, Gilchrist T, Healy DM, Miller IA, Myles LM, Glasby MA. Biodegradable Controlled Release Glass in the Repair of Peripheral Nerve Injuries. J Hand Surg 23:588:1998

649 Gao J, Dennis JE, Solchaga LA, Awadallah AS, Goldberg VM, Caplan AI. Tissue engineered fabrication of an osteochondral composite graft using rat bone marrow-derived mesenchymal stem cells. Tissue Eng 7(4):363–71:2001

650 Andrade AL, Valerio P, de Goes AM, Leite MF, Domingues RZ. Influence of recovering collagen with bioactive glass on osteoblast behavior. Journal of Biomedical Materials Research. Part B, Applied Biomaterials 83(2): 481-489:2007

651 Sepulveda P, Jones JR, Hench L. In vitro dissolution of melt-derived 45S5 and sol–gel derived 58S bioactive glasses. J Biomed Mater Res 61(2):301–11:2002

653 Gan JC, Ducheyne P, Vresilovic EJ, Shapiro IM. Intervertebral disc tissue engineering. II. Cultures of nucleus pulposus cells. Clin Orthop Relat Res 411:315–24:2003

654 Jell G, Notingher I, Tsigkou O, Notinger P, Polak JM, Hench LL, et al. Bioactive glass-induced osteoblast differentiation: a noninvasive spectroscopic study. Journal of Biomedical Materials Research. Part A 86(1):31-40:2008

655 Griss P, Greenspan DC, Heimke G, Krempien B, Buchinger R, Hench LL, et al. Evaluation of a bioglass®-coated Al_2O_3 total hip prosthesis in sheep. Journal of Biomedical Materials Research 10(4):511-518:1976

656 Hench LL & Wilson J. An Introduction to Bioceramics. Chapter 1 Bioceramics. J Am Ceram Soc 81:1705–28:1998 http://www.icpress.co.uk/etextbook/p252/p252_chap1.pdf

657 Ylänen HO. Porous bioactive glass matrix in reconstruction of articular osteochondral defects. Ann Chir Gynaecol. 88(3):237-45:1999

658 Munukka E, Leppäranta O, Korkeamäki M, Vaahtio M, Peltola T, Zhang D. Bactericidal effects of bioactive glasses on clinically important aerobic bacteria. Journal of Materials Science-Materials in Medicine 19(1):27-32:2008

659 Waltimo T, Brunner TJ, Vollenweider M, Stark WJ, Zehnder M. Antimicrobial effect of nanometric bioactive glass 45S5. Journal of Dental Research 86(8):754-757:2007

660 Shackelford JF Ed. Bioceramics: Applications of Ceramic and Glass Materials in Medicine Trans Tech Publications, Materials Science Forum. Switzerland 1999

661 Hench LL and Paschall HA. Histo-chemcial responses at a biomaterials interface. J Biomed Mater Res. Symp 2:345:1974

662 Igarashi A, Yamaguchi M. Stimulatory effect of zinc acexamate administration on fracture healing of the femoral diaphyseal tissues in rates. General Pharmacology. 32: P463 – 469:1999

663 McIlwaine C. Importance of holistic nutritional assessment in wound healing. Journal of Wound Care 12(8):285-288:2003

664 Brandao-Neto J, Stefan V, Mendonca B.B, Bloise W and Castro AV. The essential role of zinc in growth. Nutritional research. 15(3):335-358:1995

665 Osak M. Nutrition and wound healing. Plastic Surgical Nursing 3:29-36:1993

666 Bretcanu O, Spriano S, Verne E, Coisson M, Tiberto P, Allia P. The influence of crystallised Fe_3O_4 on the magnetic properties of coprecipitation-derived ferrimagnetic glass-ceramics. Acta Biomater 1(4):421-9:2005

667 Wahlqvist M. Ed. Food & nutrition in Australia (3rd ed.) Melbourne: Thomas Nelson Australia 1998

668 Meyer NA, Muller MJ, Herndon DN. Nutrient support of the healing wound. New-Horiz. 2(2):202-214:1994

669 Cannillo V, Sola A. Potassium-based composition for a bioactive glass, Ceramics Int. 35(8):3389-3393:2009

670 Lusvardi G, Malavasi G, Menabue L, Aina V, Morterra C. Fluoride-containing bioactive glasses: surface reactivity in simulated body fluids solutions, Acta Biomaterialia. 5:3548-3562:2009

671 Zberg B, Arata ER, Uggowitzer PJ, Löffler JF. Tensile properties of glassy MgZnCa wires and reliability analysis using Weibull statistics, Acta Materialia 57:3223-3231:2009

672 Zberg B, Loffler JF. MgZnCa glasses without clinically observable hydrogen evolution for biodegradable implants. Nature Materials 8:887-891:2009b

673 Hänzia AC, Schinhammer M, Loffler JF, Uggowitzer PJ. On the in vitro and in vivo degradation performance and biological response of new biodegradable Mg-Y-Zn alloys. Acta Biomaterialia 6(5):1824-2833:2010

674 Laws KJ, Gun B, Ferry M. Large-scale production of Ca65Mg15Zn20 bulk metallic glass samples by low-pressure die-casting. Materials Science and Engineering:A 475(1-2):348-354:2008

675 Staiger MP, Pietak AM, Huadmai J, Dias G. Magnesium and its alloys as orthopedic biomaterials: A review. Biomaterials 27:1728-1734:2006

676 Witte F, Voigt C, Cohen S, Kainer KU, Willumeit R, Feyerabend F. Degradable biomaterials based on magnesium corrosion. Current Opinion in Solid State and Materials Science 12(5-6):63-72:2008

677 Gu X, Zhong S, Xi T, Wang J, Wang W. Corrosion of, and cellular responses to Mg-Zn-Ca bulk metallic glasses. Biomaterials 31(6):1093-1103:2010

678 Heublein B, Rohde R, Kaese V, Niemeyer M, Hartung W, Haverich A. Biocorrosion of magnesium alloys: a new principle in cardiovascular implant technology? Heart 89:651-656:2003

679 Chikushi S. Metallic Glass opens a new field in materials science- Development of new light-weight, high-strength materials. Japan Nanonet Bulletin 2004. http://www.nanonet.go.jp/english/mailmag/2004/014a.html

680 Alexander S. Amorphous solids: their structure, lattice dynamics and elasticity. Physics Reports 296:65-236:1998

681 Scoperta. Amorphous Alloys, http://scopertainc.com/amorphous_alloys.html, Updated 2009, Accessed 28/12/10

682 Witte F. The history of biodegradable magnesium implants: A review. The THERMEC'2009 Biodegradable Metals. Acta Biomaterialia 6:5:1680-1692:2010

683 Mani G, Feldman MD, Patel D, Agrawal CM. Coronary stents: A materials perspective. Biomaterials 28:1689-1710:2007

684 Inoue A, Masumoto T. Mg-based amorphous alloys. Materials Science and Engineering A 173:1-8:1993

685 Inoue A. Stabilization of Metallic Supercooled Liquid and Bulk Amorphous Alloys. Acta Materialia 48:279-306:2000

686 Johnson WL. Bulk glass-forming metallic alloys: science and technology. Materials Research Society 24:42-56:1999

687 Molan PC. Re-introducing honey In the management of wounds and ulcers: theory and practice. Ostomy/Wound Manage 48:11:28-40:2002

688 Herszage L, et al. Tratamieno de las heridas supuradas con azucar granulado commercial. Biol Trab Soc Argent 31:315-330:1980

689 Molan PC. A brief review of the use of honey as a clinical dressing. Primary Intention (The Australian Journal of Wound Management) 6:(4):148-158:1998

690 The People's Pharmacy. Sugar Speeds Wound Healing. 2007 http://www.peoplespharmacy.com/2007/09/17/sugar-speeds-wo/ Accessed 14/2/2011

691 Universal Healing solutions. WoundCare Healing Powder 4oz http://www.tradekey.com/product_listall/uid/3898947/Universal-Healing-Solutions.htm Accessed 2/1/2011

692 Douglas J, Johnson J, Forrey C, LaVan D, Curtis J, M Cicerone. Protein Preservation, Materials Science and Engineering Laboratory. National Institute of Science and Technology 2009 http://www.nist.gov/mml/polymers/upload/854_03_04a.pdf

693 Middleton JC, and Tipton A.J. Synthetic biodegradable polymers as medical devices. Med. Plastics Biomater. Mag. 3:30:1998

694 Marraccini PA. Healing powder and method of use thereof, US Patent 2008/0107734

695 Ambrose U, Middleton K, Seal D. In vitro studies of water activity and bacterial growth inhibition of sucrose-polyethylene glycol 400-hydrogen peroxide and xylose-polyethylene glycol 400-hydrogen peroxide pastes used to treat infected wounds. Antimicrob Agents Chemother 35:1799-803:1991

696 Gordon H, Middleton K, Seal D, Sullens K. Sugar and wound healing Lancet. 2:663-664:1985

697 Ambrose U. An investigation into the mode of action of Northwick Park Hospital sugar pastes. Hatfield Polytechnic B Sc Applied Biology Thesis 1986

698 Hersel U, Dahmen C, Kessler H. RGD modified polymers: biomaterials for stimulated cell adhesion and beyond. Biomaterials 24 4385–4415:2003

699 Chung JW, Yang J, Akaike T, Cho KY, Nah JW, Kim SI, et al. Preparation of alginate/galactosylated chitosan scaffold for hepatocyte attachment Biomaterials 23:2827-2834:2002

700 Park TG. Perfusion culture of hepatocytes within galactose-derivatized biodegradable poly(lactide-co-glycolide) scaffolds prepared by gas foaming of effervescent salts. J Biomed Mater Res 59:127–135:2002

701 Gianetti S, Lauretti L, Fernandez E, Salvinelli F, Tamburrini G, Pallini R. Acrylic hydrogel implants after spinal cord lesion in the adult rat. Neurol Res 23:405-409:2001

702 Ransome HM. The Sacred Bee in Ancient Times and Folklore. George Allen and Unwin London. 1937

703 Molan PC. The Antibacterial Activity of Honey. 1. The Nature of the Antibacterial Activity. Bee World73, 5-28:1992a

704 Molan PC. The Antibacterial Activity of Honey. 2. Variation in the Potency of the Antibacterial Activity. Bee World 73, 59-76:1992b

705 Molan PC. The antibacterial activity of honey. 1.The nature of the antibacterial activity. Bee World 73(1):5-2:1992

706 Aristotle (350 BC). Translated by Thompson DÕA W. Historia Animalium in: The Works of Aristotle. Smith JA, Ross WD, eds. Oxford University Press Oxford Volume IV 1910

707 Blomfield R. Honey for Decubitus Ulcers. J Am Med Assoc 224:905:1973

708 Molan PC. Honey as a topical antibacterial agent for treatment of infected wounds, World Wide Wounds, 2001 http://www.worldwidewounds.com/2001/november/Molan/honey-as-topical-agent.html#ref20

709 Molan PC. The role of honey in the management of wounds. J Wound Care 8(8):415–8:1999

710 Molan PC. Clinical usage of honey as a wound dressing: an update, J Wound Care. 13(9):353-356:2004

711 Armon P J. The Use of Honey in the Treatment of Infected Wounds. Trop Doct 10:91:1980

712 Bose B. Honey or sugar in treatment of infected wounds? Lancet 1 (8278):963:1982

713 McInerney R J. Honey - a Remedy Rediscovered. J Royal Soc Med 83:127:1990

714 Lusby PE, Coombes AB, Wilkinson JM. Honey: A potent agent for wound healing? Journal of Wound, Ostomy & Continence Nursing. 29(6):295-300:2002

715 Conklin AR. UW Study Tests Topical Honey as a Treatment for Diabetic Ulcers. University of Wisconsin-Madison, University Communications, 5/2/07 http://www.news.wisc.edu/releases/13738

716 Efem SEE. Clinical observations on the wound healing properties of honey. Br J Surg 75:679-681:1988

717 Beattie T, Mayze J. Anti-microbial properties of Australian honeys. 2000 http://www.dpi.qld.gov.au/cft/cft_honey.html

718 Farouk A, Hassan T, Kashif H, Khalid SA, Mutawali I, Wadi M. Studies on Sudanese Bee Honey: Laboratory and Clinical Evaluation. Int J Crude Drug Res 26:161-168:1988

719 Cho CY & Lo JS. Dressing the part. Dermatol Chin 16(1):25-47:1998

720 Oryan A, Zaker SR. Effects of Topical Application of Honey on Cutaneous Wound Healing in Rabbits. J Vet Med A 45:181-188:1998

721 Condon RE. Curious interaction of bugs and bees. Surgery 113(2):234-5:1993

722 Somerfield SD. Honey and healing. J R Soc Med 84(3): 179:1991

723 Chirife J, Herszage L, Joseph A, Kohn ES. In vitro study of bacterial growth inhibition in concentrated sugar solutions: microbiological basis for the use of sugar in treating infected wounds. Antimicrob Agents Chemother 23(5):766-73:1983

724 Cooper RA, Molan PC, Harding KG. Antibacterial activity of honey against strains of Staphylococcus aureus from infected wounds. J R Soc Med 92(6):283-5:1999

725 White JW, Subers MH, Schepartz AI. The identification of inhibine, the antibacterial factor in honey, as hydrogen peroxide and its origin in a honey glucose-oxidase system. Biochim Biophys Acta 73:57-7:1963

726 Cavanagh D, Beazley J, Ostapowicz F. Radical Operation for Carcinoma of the Vulva. A New Approach to Wound Healing. J Obstet Gynaecol Br Cmwlth 77:1037-1:1970

727 Postmes TJ, Bosch MM, Dutrieux R, van Baare J, Hoekstra MJ. Speeding up the healing of burns with honey. An experimental study with histological assessment of wound biopsies. In: Mizrahi A, Lensky Y, eds. Bee Products: Properties, Applications and Apitherapy. New York: Plenum Press 27-37:1997

728 Hyslop PA, Hinshaw DB, Scraufstatter IU, Cochrane CG, Kunz S, Vosbeck K. Hydrogen peroxide as a potent bacteriostatic antibiotic: implications for host defense. Free Radic Biol Med 19(1):31-7:1995

729 Allen KL, Molan PC, Reid GM. A survey of the antibacterial activity of some New Zealand honeys. J Pharm Pharmacol 43(12):817-22:1991

730 Majtan J. Methylglyoxal – a Potential Risk Factor of Manuka Honey in Healing of Diabetic Ulcers, ecam 2010 http://ecam.oxfordjournals.org/cgi/reprint/neq013v2

731 Tonks A, Cooper RA, Price AJ, Molan PC, Jones KP. Stimulation of tnf-alpha release in monocytes by honey. Cytokine 14(4):240-2:2001

732 Beretta G, Orioli M, Facino RM. Antioxidant and radical scavenging activity of honey in endothelial cell cultures (EA.hy926), Planta Med. 73(11):1182-1189:2007

733 Molan PC. The evidence supporting the use of honey as a wound dressing, The Int J Low Ext Wounds. 5(1):40-54:2006

734 Burlando F. Sull'azione terapeutica del miele nelle ustioni. Minerva Dermatol 113:699-706:1978

735 Gethin G & Cowman S. Manuka honey vs. hydrogel – a prospective, open label, multicentre, randomised controlled trial to compare desloughing efficacy and healing outcomes in venous ulcers. Journal of Clinical Nursing. 18:466-474:2008

736 Al-Waili NS, Saloom KY. Effects of topical honey on post-operative wound infections due to gram positive and gram negative bacteria following caesarean sections and hysterectomies. Eur J Med Res 4(3):126-30:1999

737 Subrahmanyam M. Topical application of honey in treatment of burns. Br J Surg 78(4): 497-8:1991

738 Subrahmanyam M. A prospective randomised clinical and histological study of superficial burn wound healing with honey and silver sulfadiazine. Burns 24(2):157-61:1998

739

740 Fernandes Júnior A, Leomil L, Fernandes AAH, Sforcin JM. The antibacterial activity of propolis produced by Apis mellifera L. and Brazilian stingless bees. J Venom Anim Toxins 7:173–82:2001

741 Fernandes Júnior A, Balestrin EC, Cunha ML. Anti- Staphylococcus aureus activity of bee propolis extracts prepared with different ethanol concentrations. Rev Ciênc Farm 24:147–52:2003

742 Lofty M. Combined use of honey, bee propolis and myrrh in healing a deep, infected wound in a patient with diabetes mellitus. British Journal of Biomedical Science 63(4):2006

743 Stepanovic S, Antic N, Dakic I, Svabic-Vlahovic M. In vitro antimicrobial activity of propolis and synergism between propolis and antimicrobial drugs. Microbiol Res 158:353–7:2003

744 McLennan S, Jia J, Milne S, Lo L, Bonner J, Yue D, Twigg S. Propolis. The anti-inflammatory agent Propolis improves wound healing in a rodent model of experimental diabetes. Wound Rep Regen 16:706-713:2008

745 Grad S, Gogolewski S, Alini M, Wimmer MA. Effects of simple and complex motion Patterns on gene expression of chondrocytes seeded in 3D scaffolds. Tissue Engineering 12(11):2006

746 Brown RQ, Mount A, Karen K, Burg L. Evaluation of polymer scaffolds to be used in a composite injectable system for intervertebral disc tissue engineering, J BiomedMat Res Part A .74(1):32-39:2005

747 Jeong SI, Kwon JH, Lim JI, Cho SW, Jung Y, Sung WJ, et al. Mechano-active tissue engineering of vascular smooth muscle using pulsatile perfusion bioreactors and elastic PLCL scaffolds, Biomaterials. 26:1405-1411:2005

748 Rai B, Teoh SH, Hutmacher DW, Cao T, Ho KH. Novel pcl-based honeycomb scaffolds as drug delivery, Biomaterials. 26:3739-3748:2005

749 Haas T, Davis SJ, Madri JA. Three dimensional type I collagen lattices induce coordinate expression of matrix metalloproteinases MT1-MMP and MMP-2 in microvascular endothelial cells, J Biol Chem. 273(6):3604-3610:1998

750 Smith ME. Dissertation: Biologically functional scaffolds for tissue engineering and drug delivery, produced through electrostatic processing. Dept. Chem Eng, Case Western Reserve University 2010

751 Takagi M, Fukui Y, Wakitani S, Yoshida T. Effect of poly dl-lactic-co-glycolic acid meshon a three-dimensional culture of chondrocytes. J Bioscience & Bioengineering. 98(6):477-481:2004

752 Xynos DI, Edgar AJ, Buttery DK, Hench LL, Polak JM, Gene-expression profiling of human osteoblasts following treatment with the ionic products of Bioglass 45S5 dissolution, J Biomed Mat Res: Part A. 55(2):151-157:2001

753 Lovelace TB et al. Clinical evaluation of bioactive glass in the treatment of periodontal osseous defects in humans. J Periodontol 69:1027–35:1998

754 Moimas L, Biasotto M, Di Lenarda R, Schmid C. In situ tissue engineering, effect of a porous bioactive glass scaffold on bone healing: in vivo rabbit study. In 10th ceramics, cells and tissues—materials for tissue engineering, chemistry and microstructure: the role for ceramics. Faenza, Italy: Consiglio Nazionale Delle Ricerche; 2006.

755 Valimaki VV, Yrjans JJ, Vuorio EI, Aro HT. Molecular biological evaluation of bioactive glass microspheres and adjunct bone morphogenetic protein 2 gene transfer in the enhancement of new bone formation. Tissue Eng 11:387–94:2005

756 Powell WC, Matrisian LM. Complex roles of matrix metalloproteinases in tumor progression. Attempts to understand metastasis formation. In Gunthert U, Schlag M, Birchmeier W (eds) Metastasis Related Molecules. Heidelberg: Springer-Verlag, Heidelberg, pp1-21:1996

757 Reno F, Traina V, Cannas M, Mechanical stretching modulates growth direction and MMP-9 release in human keratinocyte monolayer, Cell Adhesion & Migration. 3(3):239-242:2009

758 Gill SE, Parks WC. Metalloproteinases and their inhibitors: regulators of wound healing. Int J Biochem Cell Biol 2007

759 Weckroth M, Vaheri A, Lauharanta J, Sorsa T, Konttinen YT. Matrix metalloproteinases, gelatinase and collagenase in chronic leg ulcers. J Invest Dermatol 106:1119-1124:1996

760 Cook HP. Defective extracellular matrix reorganization by chronic wound fibroblastsis associated with alterations in TIMP-1, TIMP-2 and MMP-2 activity. Journal of Investigative Dermatology 115(2):225-233:2000

762 Cornelius LA, Nehring LC, Roby JD, Parks WC, Welgus HG. Human dermal microvascular endothelial cells produce matrix metalloproteinases in response to angiogenic factors and migration. J Invest Dermatol 105:170–176:1995

762 Hsu JY, McKeon R, Goussev S, Werb Z, Lee JU, Trivedi A et al. Matrix Metalloproteinase-2 facilitates wound healing events that promote functional recovery after spinal cord injury. The Journal of Neuroscience. 26(39):9841-9850:2006

763 Skyscan 1172 instruction manual 2005 http://www.itg.uiuc.edu/help/microct/1172_Manual.pdf Accessed 18/1/2011

764 Okada Y, Gonoji Y, Naka K, Tomita K, Nakanishi I, Iwata K et al. Matrix metalloproteinase-9 (92-kDa gelatinase type-IV collagenase) from Ht-1080 human fibrosarcoma cells-purification and activation of the precursor and enzymatic properties. Journal of Biologicel Chemistry 267(30):21712-21719:1992

765 Heikkilä P, Teronen O, Moilanen M, Konttinen Y, Hanemaaijer R, Laitinen M et al. Bisphosphonates inhibit stromelysin-1 (MMP-3), matrix metalloelastase (MMP-12), collagenase-3 (MMP-13) and enamelysin (MMP-20), but not urokinase-type plasminogen activator, and diminish invasion and migration of human malignant and endothelial cell lines. Anti-Cancer Drugs 13:245-254:2002

766 Rayment EA, Dargaville TR, Shooter GK, George GA, Upton Z, Attenuation of protease activity in chronic wound fluid with bisphosphonate-functionalised hydrogels, Biomaterials. 29:1785-1795:2008

767 Valleala H, Hanemaaijer R, Mandelin J, Salminen A, Teronen O, Mönkkönen J et al. Regulation of MMP-9 (gelatinase B) in activated human monocyte/macrophages by two different types of bisphosphonates. Life Sciences 73(19):2413-2420:2003

768 Velard F, Laurent-Maquin D, Guillaume C, Bouthors S, Jallot E, Nedelec J-M. Polymorphonuclear neutrophil response to hydroxyapatite particles, implication in acute inflammatory reaction. Acta Biomaterialia 5:1708-1715:2009

769 Bosetti M, Reno F, Bracco P, Costa L, Cannas M, Ultra-high molecular weight polyethylene oxidation reduces metalloproteinase 2 secretion in human osteoblast-like cells in vitr:A mechanism of modulation of extracellular matrix, J Biomed Mat Res: Part A. 64A(4):698-705:2003

770 Hak-Joon, S. Matrix Metalloproteinase 9 (MMP-9) and Biodegradable Polymers in the Engineering of a Vascular Construct, DIssertation- Georgia Institute of Technology, http://hdl.handle.net/1853/5106

771 Gearing A, Thorpe SJ, Miller K, Mangan M, Varley PG, Dudgeon T et al. Selective cleavage of human IgG by the matrix metalloproteinases, matrilysin and stromelysin. Immunology Letters 81:41-48:2002

771 Porex. Options: Medpor Biomaterial and Surgical Implants 2004 http://www.porexsurgical.com/english/surgical/smedpor.asp Accessed 2/12/2010

772 Huang MH, Yang MC, Evaluation of glucan/poly(vinyl alcohol) blend wound dressing using rat model, Int J Pharmaceutics 346:(38-46):2008

773 Min D, Lyons JG, Jia J, Lo L, McLennan SV. 2-Methoxy-2,4-diphenyl-3(2H)-furanone-labeled gelatin zymography and reverse zymography: A rapid real-time method for quantification of matrix metalloproteinases-2 and -9 and tissue inhibitors of metalloproteinases. Electrophoresis 27:357–364:2006

774 Vargis EV, Mesones RV, Bretcanu O, Lopez JM, Boccaccini AR, Gorustovich A. Biocompatibility and bone mineralization potential of 45S5 bioglass-derived glass-ceramic scaffolds in chick embryos, Acta Biomaterialia. 5(1):374-380:2009

775 Cios TJ, Reavis KM, Renton DR, Hazey JW, Mikami DJ, Narula VK et al. Gastrotomy closure using bioabsorbable plugs in a canine model. Surg Endosoc 22:961-966:2008

776 GORE, GORE® BIO-A® Hernia Plug Video http://www.goremedical.com Accessed 20/01/2011

777 Kwag JH. Imaging Findings of Implanted Absorbable Mesh in Patients with Breast Partial Resection. Yonsei Medical Journal 49(1):2008

778 Goes JC, Landecker A, Lyra EC, Henriquez LJ, Goes RS, Godoy PM. The application of mesh support in periareolar breast surgery: clinical and mammographic evaluation. Aesthetic Plast Surg 28:268-74:2004

779 Michna H. Funktionelle, experimentelle und klinische Anatomie kollagenfaserigen Bindegewebes. Med Habil University, Liibeck 1988

780 Schantz JT, Chim H, Whiteman M, Cell guidance in tissue engineering: SDF-1 mediates site-directed homing of mesenchymal stem cells within three-dimensional polycaprolactone scaffolds, Tissue Engineering. 13(1):2615-2624:2007

781 Martin I, Obradovic B, Treppo S, Grodzinsky AJ, Langer R, Freed LE, Vunjak-Novakovic G. Modulation of the mechanical properties of tissue engineered cartilage. Biorheology 37(1–2):141–7:2000

782 Vunjak-Novakovic G, Martin I, Obradovic B, Treppo S, Grodzinsky AJ, Langer R, Freed LE. Bioreactor cultivation conditions modulate the composition and mechanical properties of tissue-engineered cartilage. J Orthop Res 17(1):130–8:1999

783 Kenshaw H, Georgiou G, Blaker JJ, Forbes A, Knowles JC, Day RM, Assessment of polymer/bioactive glass-composite microporous spheres for tissue regeneration applications. Tissue Engineering Part A. 15(7):1451-1461:2009

784 Bosetti M, Hench L, Cannas M. Interaction of bioactive glasses with peritoneal macrophages and monocytes in vitro. Journal of Biomedical Materials Research 60(1): 79-85:2002

785 Saillan-Barreau C, Cousin B, Andre M, Villena P, Casteilla L, Penicaud L. Human adipose cells as candidates in defense and tissue remodeling phenomena. Biochem Biophys Res Commun 39:502-5:2003

786 Sharkawy AA, Klitzman B, Truskey GA, Reichert WM. Engineering the tissue which encapsulates subcutaneous implants. III. Effective tissue response times. J Biomed Mater Res 40:598-605:1998

787 Hemmrich K, Heimburg D, Rendchen R, Bartolo CD, Milella E, Pallua N, Implantation of preadipocyte-loaded hyaluronic acid-based scaffolds into nude mice to evaluate potential for soft tissue engineering, Biomaterials. 26:7025-7037:2005

788 Von Heimburg D, Zachariah S, Heschel I, Kühling H, Schoof H, Hafemann B et al. Human preadipocytes seeded on freeze-dried collagen scaffolds investigated in vitro and in vivo. Biomaterials 22:429-438:2001

789 Tran RT, Thevenot P, Zhang Y, Gyawali D, Tang L, Yang J. Scaffold sheet design strategy for soft tissue engineering. Materials 3:1375-1389:2010

790 Lewis G, van Hooy-Corstjens CS, Bhattaram A, Koole LH. Influence of the radiopacifier in an acrylic bone cement on its mechanical, thermal, and physical properties: barium sulfate-containing cement versus iodine-containing cement. J Biomed Mater Res B Appl Biomater 73:77–87:2005

791 Rawlings RD. Composition dependence of the bioactivity of glasses. Jounal of Materials Science Letters 11(20): 1340-1343:1992

792 Valerio P, Pereira MM, Goes AM, Leite MF. The effect of ionic products from bioactive glass dissolution on osteoblast proliferation and collagen production. Biomaterials 25(15):2941–8:2004

793 Foppiano S, Marshall SJ, Marshall GW, Saiz E, Tomsia AP. The influence of novel bioactive glasses on in vitro osteoblast behavior. J Biomed Mater Res A 71:242–249:2004

794 Wilson J, Pigott G, Schoen FJ and Hench LL. Toxicology and biocompatibility of Bioglass®. J Biomed Mater Res 15:805-811:1981

795 Madanat R, Moritz N, Vedel E, Svedstrom E, Aro HT. Radio-opaque bioactive glass markers for radiostereometric analysis. Acta Biomaterialia 5:3497-3505:2009

APPENDIX

A.1. CELL COUNTING

MATERIALS

- Trypsin
- DMEM/FCS

METHOD

1. Cells were trypsinised from approx. 70% confluent flasks using 1:4mL trypsin diluted in PBS. 5mL of this solution was used for 75cm^2 flasks.
2. Flasks were returned to the incubator for 10mins to allow the cells to detach.
3. The trypsin/cell solution was carefully pipette up & down using a 1mL sterile pipette.
4. This cell solution was placed into a 50mL centrifuge tube.
5. An equal volume of media (or PBS) was immediately added to neutrilised the reaction.
6. The tube was centrifuged for 5mins at 1000-1200rpm.
7. The trypsin solution was removed to waste, carefully leaving the cell pellet on the base of the tube.
8. A small amount of media was added to the cell pellet (1-2mL).
9. The cells were counted using the following procedure:
10. A few drops of cell solution were placed in an eppendorf.
11. The haemocytometer was cleaned by rinsing in warm water then 70% ethanol. The haemocytometer was gently wiped (not pressed) using a kimwipe.
12. Trypan blue (Invitrogen) was diluted 1:4 in PBS (e.g. 10µL trypan, 40µL PBS). The cell solution was diluted 1:2 in the diluted trypan blue (e.g. 50µL cell solution).
13. 10µL of this solution was placed into either side of the haemocytometer.
14. The haemocytometer was viewed using a microscope, and the live cells were counted in each of 5 squares. The average of these counts was calculated.
15. The original concentration of cells in the centrifuge tube was calculated by multiplying by the dilution factors.
16. The cell suspension volume for the required cell density was calculated, and media added to this level.
17. Cells were gently constantly resuspended using a transfer pipette, whilst being measured into the wells at the required volumes using a 200µL or 1mL pipette.

A.2. BIOLOGICAL FIXATION FOR SEM

MATERIALS

This procedure was completed in the fume cabinet.

The following buffers were prepared:

0.2M Na-cacodylate (i.e. phosphate buffer):

28mL stock sol'n A ($NaHPO_4$-0.2M sodium dihydrogen orthophosphate) (I2.83g/100mLs)

72mL stock sol'n B (Na_2HPO_4- 0.2M sodium hydrogen orthophosphate) (3.12g/100mLs)

0.1M Na-cacodylate:

50mL 0.2M phosphate buffer + 50mL distilled water

These buffers were stored in the fridge for future use.

2% gluteraldehyde

2% gluteraldehyde was made from 25% gluteraldehyde (Sigma Aldrich) and 0.2M phosphate buffer. (for example, for 8 samples, 8mL 2% gluteraldehyde was req=ured so 7.5mL 0.2M phosphate buffer + 700µL 25% gluteraldehyde was utilized)

Gluteraldehyde was frozen in 1mL aliquots for future use and repeated freeze/thaw cycles were avoided. Care was taken to avoid breathing fumes.

METHOD

1. Media was removed from the cell wells.
2. 2% gluteraldehyde was added for:
    i. 1hr at 37°C (for *in vitro* cells on scaffolds) OR
    ii. overnight at 4°C (for in vivo tissue specimens, 7x7x7mm)
3. Samples were rinsed 2x using 0.1M Phosphate Buffer for 15mins. Tissue specimens required a third rinse.
4. (Samples could be stored for 1-2 weeks in PB if kept in the fridge (0-4°C) (1-2weeks), or even more ideally, following the osmium fixation step).
5. Secondary fixation was completed, particularly for specimens with a high lipid content. 1% Osmium Tetroxyde (OsO4) was added to the specimens by firstly adding 500µL 0.2M Phosphate Buffer to the well, then adding 500µL 2% osmium tetroxide. Special care was taken when using osmium tetroxide as it is a carcinogen. Blue, chemical barrier gloves were used.
6. Osmium was discarded into an osmium waste bottle after 1hr.
7. Osmium was rinsed off using 2x 0.1M PB (discarded into osmium waste bottle). For tissue specimens, each wash was soak for 15mins..

8. Specimens were dehydrated using graded ethanol solutions of 70%, 80%, 90%, 95% and 3x 100%, 10mins each. Care was taken not to let the tissue dry out during the transfer of reagents.
9. (Tissue could then be stored in 100% ethanol in refrigerator if necessary)
10. Specimens were immersed in 100% hexamethyldisilazane (HMDS) for 3mins.
11. Specimens were transferred to a dessicator for at least 25mins (preferably 1+ days).
12. Samples were mounted on alumina stubs and sputter-coated with gold/platinum, before examination using an SEM.

Alternately, it was possible to fix specimens using paraformaldehyde as an alternative to gluteraldehyde, and to FITC, DAPI, imaging using fluorescent microscope, followed by graded ethanol dehydrations as described. This method was not followed in the current study, although recommended by coworkers for future work.

A.3. SUBCULTURE OF OVINE CHONDROCYTES

MATERIALS

- PBS
- T/E (i.e. 0.2% (w/v) trypsin/0.1% (w/v) EDTA)
- DMEM/FCS (+ 2mM Glutamine, 200g/mL gentamicin)

METHOD

1. Media from 70% confluent flasks was removed to waste.
2. Remaining media was removed by rinsing with 1-2mL PBS. This step was repeated.
3. Cells were detached by addition of 1-2mL T/E to the flask. The flask was placed in the incubator at 37°C for 3-5mins.
4. The trypsin was neutralized by addition of 1-2mL of media. The cell suspension was transferred to a 15mL centrifuge tube.
5. Media was added to the tube to a total volume of 10mL.
6. The tube was centrifuged at 20°C, at 2000rpm for 5mins.
7. The trypsin solution was removed to waste.
8. The cells were counted, diluted and plated into tissue culture plates.

A.4. RECOVERY OF CRYOPRESERVED CELLS

MATERIALS

Notes: Media should be used within a week if FCS had been added. Glutamine was added due to possible decay from the media. It was not necessary if the media was fresh.

MATERIALS

- DMEM/F12/10%FCS
- Glutamine
- Gentamicin
- Tissue Culture Flask

METHOD

1. Cryotubes containing cells were thawed in 37°C water.
2. Complete media was prepared, and cells were added, in centrifuge tube.
3. The tubes were centrifuged at 20°C at 12,000rpm for 10mins.
4. The supernatant was removed to waste and the cell pellet was resuspended in 10mL complete media.
5. The tubes were centrifuged at 20 °C at 12,000rpm for 10mins.
6. The supernatant was removed to waste and the cell pellet was resuspended in 15mL complete media.
7. The cell mixture was transferred to a flask for incubation at 37°C. Media in the flask was added to 15mL for a 75mm^2 flask.
8. The cells were checked daily and media was changed every 2 days. Confluent cells (approx. 4 days) were subcultured for the experiment or split 1:3-1:5 into new flasks.

A.5. TOTAL RNA EXTRACTION FROM CELL CULTURE

MATERIALS

Total RNA was isolated using the RNeasy Mini Kit (Qiagen)

Procedure was performed in fume hood.

- Qiagen RNeasy kit (Valencia, CA, USA) (including buffers RW1, RPE, spin columns (1 per sample) & collection tubes (2 per sample)).
- DNase (10µL per sample) (optional)
- DNase buffer

- 2mL eppendorfs
- Frozen pelleted cells or fresh cultured cells
- 18-21 gauge needle (0.9mm)
- RNase free syringe

METHOD

Cell Lysis

1. Cells were lysed by addition of 350µL lysis buffer (RLT) followed by pipetting up and down using a 1mL pipette.
2. Cell solution was passed 5-10 times through an 18-21 gauge needle attached to an RNase free syringe.
3. The homogenate was centrifuged at 3000rpm for 5mins and supernatant was transferred to a clean tube.
4. Equal volumes of 70% ethanol to cell to each aqueous phase. *check this step is correct*
5. The lids were sealed and tubes were gently mixed 10x by inversion. Tubes could sit at room temperature at this stage for up to 30mins.

Loading of Spin Columns

The spin columns were not placed in a rack or the centrifuge without their collection tube underneath them, due to the high risk of contamination.

11. 600µL of the aqueous/EtOH phase from previous step was loaded onto a spin column. This was performed in a rack, not the centrifuge. If the volume was in excess of 600uL, the tip was kept in the tube for later loading of the rest of the sample.
12. The spin columns with collection tubes were transferred to the centrifuge and spun at 12,000 rpm for 20secs.
13. The collection tube was emptied into a waste container and put back under spin column.
14. The remainder (if any) of the aqueous/EtOH phase was loaded onto the appropriate column.
15. The tubes were spun at 12,000 rpm for 20secs.
16. The collection tubes were emptied into a waste container and returned under the spin column.

Washing of the Spin Columns

17. 350µL of RW1 was loaded into each of the spin columns, and let sit for 5mins.

18. The tubs were spun at 12,000rpm for 15secs.
19. The collection tubes were emptied and discarded.
20. New collection tubes were placed under the spin columns.

DNase Digestion (optional)

21. DNase was retrieved from the freezer and a master mix was made consisting of 10µL DNase and 70µL DNase buffer per sample. (e.g. for 18 samples, 20µL DNase was added to 1400µL buffer).
22. Using a master mix, 80µL of DNase/buffer mix was added to each spin column using a fresh tip per sample.
23. Samples were spun at 12,000 rpm for 15 seconds to saturate the columns with DNase.
24. The DNase/buffer mix from the collection tube was reapplied onto the spin column using a fresh tip per sample. Care was taken to ensure the DNase was place directly onto the membrane of the column.
25. Tubes were incubated at 37°C for 1 hr, using either an incubator or heating block.
26. Tubes were spun at 12,000rpm for 15secs.
27. Another 350µL of RW1 was loaded to each of the spin columns.
28. Tubes were spun at 12,000rpm for 15secs.
29. Collection tube were emptied into waste container and returned under the spin columns.
30. 500µL of RPE buffer was loaded onto each of the spin columns.
31. Tubes were spun at 12,000 rpm for 15 secs.
32. Collection tubes were emptied into waste containers and returned under spin column.
33. Another 500µL of RPE buffer was loaded onto each of the spin columns.
34. Tubes were spun at 12,000 rpm for an additional 2 minutes to evaporate the EtOH and to dry the column.
35. The collection tubes were emptied and discarded.
36. Spin columns were transferred to pre-labelled 1.5mL tubes.

Elution of RNA from Columns

37. Depending on expected yield, 30-100µL (for example 32uL- 1µL for sybergreen, 1µL for no RT, 30 for RT) of RNase-free H2O was loaded onto each column. A new tip was used per sample to avoid cross contamination (especially of the water).
38. The collection tubes were emptied and discarded.
39. Care was taken to ensure the H_2O was placed directly onto membrane of column.
40. Tubes were incubated at room temperature for 10-15mins.

41. Ice was collected during this time if required.
42. Tubes were spun at 12,000 rpm for 1min.
43. The spin column was discarded.
44. Tubes containing RNA were stored on ice if continuing process, or tubes were frozen at -80°C if not continuing.
45. A Nanodrop ND-1000 Spectrophotometer was used to measure the concentration and quality of the RNA. A 2µL aliquot was used for this measurement.

A.6. REVERSE TRANSCRIPTION OF RNA TO CDNA

MATERIALS

Note: All samples must be reverse transcribed at the same time. For real time PCR, extra samples were reverse transcribed (use some in which there was excess RNA to use to make standards). If only 1µg was needed, for real time PCR, the RT could be done in the thermal cycler in 0.2mL PCR tubes.

Materials

- Omniscript kit (including 10x RT buffer, RT dNTPs, RT enzyme)
- Random hexamers (primers)- aliquoted at -20°C
- RNase guard (optional- prevents RNA degradation at higher temperatures- diluted to 10U/µL using 1x RT buffer and stored at -20°C)

METHOD

1. The block incubator was preheated at 37°C.
2. 1 set of 1.5 or 2.5mL tubes were labeled to match RNA tubes.
3. The total volume was required to be 10µL RT mix plus RNA and water up to 30µL
4. From sybr green calculations, amount to be RT'd is determined (can be up to 1ug and must be the same for all samples). Using same tip for all samples, place calculated amount of H2O in tubes. Using new tip for each sample, add calculated amount of RNA.
5. Mastermix was made as follows.

   For 50 reactions:
   100µL 10x RT buffer (kit)
   100µL RT NTP (kit) (i.e. DNTP)
   100µL random hexamers (i.e. Oligo primers)
   50µL RNase guard
   50µL RT enzyme (kit)
6. The rest of the mastermix was stored at -20°C if not used.
7. 10µL of RT master mix was placed on the side of each tube (new tip for each sample).

8. Samples were spun down quickly in the centrifuge.
9. Samples were incubated for 1 hour at 37°C. 20mins into this, the heating block (or water bath) was preheat to 93°C.
10. Samples were incubated for 5mins in a 93°C water bath or hot block. Samples were cooled quickly on ice for 5mins.
11. The appropriate amount of H_2O was added to the samples, so that each sample has 500µL H_2O per µg of original RNA (is now cDNA) for SQ; or 150µL H_2O per µg of original RNA for Real time.
12. RT samples (cDNA) were stored at 4°C while in use. For long term storage, they were transferred to -20°C or 80°C.

A.7. RT-PCR

MATERIALS

- Ovine Primers
- Water
- Immomix
- cDNA samples
- Sybrgreen (-80°C freezer, store in aluminium foil so not exposed to light for long periods)
- Pipettors & Art Filter tips

METHOD

1. Materials were gathered and set up near the PCR machine. Sybrgreen was defrosted and spun down. A 1:1000 dilution of 1µL sybrgreen to 1mL water was made. (this could be stored for 1 week) Concentrated sybrgreen was returned to the freezer. Diluted sybrgreen was vortexed and spun.
2. The experiment was designed. Standard curves consisted of 4 different concentrations plus water, plus duplicates (=10 tubes). Only one tube per sample was required (if using biological replicates).
3. Mastermix was combined in an eppendorf using the following proportions (per sample).

1µL sample
1.4µL H2O
5.00µL Immomix
1.00µL Sybrgreen
0.30µL F primer
0.30µL R primer

8.00 TOTAL

4. Extra mastermix was made, enough for 1 sample per every 12 samples. One mastermix was used for every primer.
5. The master mixtures are inverted, tapped several times then vortexed in an eppendorf.
6. PCR tubes were laid out on the rack. 20µL of mastermix was added to each tube. 5µL of standard concentrations or cDNA samples were added.

A.8. OVINE PRIMERS FOR REAL TIME PCR

Molecule	Annealing Temp (°C)	Pos'n	Oligo Bases	Sequence 5' to 3'	Product Size (Base Pairs)	Species Accession #
GAPDH (RT)	58	292F	23	F – CCT GGA GAA ACC TGC CAA GTA TG	139	Ovis aries
		430R	25	R – GGT AGA AGA GTG AGT GTC GCT GTT G		U94889
MMP-1 (RT)	55	124F	24	F – CAT TCT ACT GAC ATT GGG GCT CTG	122	Ovis aries
		245R	22	R – TGA GTG GGA TTT TGG GAA GGT C		AF267156
MMP-2 (RT)	60	84F	23	F – TGC TAC CAC CTC CAA CTA CGA TG	240	Ovis aries
		323R	22	R – GTG CCA GTA TCA ATG TCA GGG G		AF267159
MMP-3 (RT)	58	342F	20	F – TCC CCC AGT TTC CCC TAA TG	124	Bos taurus
		465R	22	R –GAT TTC TCC CCT CAG TGT GCT G		AF135232
MMP-9 (RT)	59	2081F	24	F – AGG TGA ATC AGG TGG ACT ATG TGG	221	Bos taurus
		2301R	23	R – AGA AAG GAA GGT GGG AAG AGA GG		X78324
MMP-9 (RT)	60	354F	24	F – GCA CCA CCA CAA CAT CAC CTA CTG	306	Bos Taurus
		659R	24	R – ATC ACA ACG CCT TTG CCC AGA GAC		X78324
TIMP-1 (RT)	57	362F	22	F - GGT TCA GTG CCT TGA GAG ATG C	265	Ovis aries
		626R	20	R - GGG ATA GAT GAG CAG GGA AAC AC		S67450
TIMP-2 (RT)	57	457F	22	F- ACT CTG GCA ACG ACA TCT ACG G	261	Bos Taurus
		717R	22	R- TCT TCT TCT GGG TGG CAC TCA G		M32303
TIMP-3 (RT)	57	1319F	22	F - CTT CCT TTG CCC TTC TCT ACC C	286	Bos Taurus
		1604R	20	R - TCT GGT CAA CCC AAG CAT CG		NM01045871
Collagen I (a1) (RT)	57	379F	22	F – ATC CCT GGA CAA CCT GGA CTT C	107	Ovis aries
	-55	485R	24	R – TCA TCA TAG CCG TAA GAC AAC TGG		AF129287
Collagen II (RT)	55	646F	20	F – TGA CCT GAC GCC CAT TCA TC	154	Bos taurus
		799R	22	R – TTT CCT GTC TCT GCC TTG ACC C		X02420
Aggrecan (RT)	58	500F	23	F – TCA CCA TCC CCT GCT ACT TCA TC	105	Bos taurus
	-55	604R	20	R – TCT CCT TGG AAA TGC GGC TC		U76615
ADAMTS1 (RT)	55	2242F	22	F – CCA ACT GGA GCC ACA AAC ATT G	126	Bos taurus
		2367R	22	R – GGA CAG AGT GAA GTC GCC ATT C		XM589626
ADAMTS4 (RT)	56	3307F	22	F – GGA AAT CCA GGG TGG TGG TGA T	171	Bos taurus
		3477R	23	R – TCC CTG AAG GCG TAT CCT ACC CT		AF516915
ADAMTS 5 (RT)	55	128F	20	F – GCA TTG ACG CAT CCA AAC CC	97	Bos taurus
		224R	25	R – CGT GGT AGG TCC AGC AAA CAG TTA C		AF192771

A.9. PROTEIN MEASUREMENT

MATERIALS

- Bovine Serum Albumin (BSA)
- ddH_2O

METHOD

1. BSA controls were made by a serial dilution of 10mg/mL BSA in ddH_2O as follows:

		Dilution Factor	ddH_2O	BSA
1	5mg/mL	½	25µL	25µL of 10mg/mL
2	2.5mg/mL	¼	25µL	25µL of protein std #1
3	1.25mg/mL	1/8	25µL	25µL of protein std #2
4	0.625mg/mL	1/16	25µL	25µL of protein std #3
5	0.3125mg/mL	1/32	25µL	25µL of protein std #4
6	0.156mg/mL	1/64	25µL	25µL of protein std #5
7	0.078mg/mL	1/128	25µL	25µL of protein std #6

2. Samples were serially diluted to similar dilution factors by adding 20µL of the sample in 20µL ddH_20.
3. 5µL of d-H_2O (blank), 5µL standard and 5µL sample were placed in the appropriate wells of the microtitre plate.
4. To each well was added: 5µL sample (or BSA), 20µL assay reagent A, 200µL assay reagent B.
5. Plates were shaken for 15mins at room temperature on a platform. Absorbance was measured immediately at 690nm (filter 8) using a Biorad.
6. A standard curve was created from the controls of known concentration. These were used to estimate the concentrations of the samples.
7. Each resuLt was the average of 2 replicate samples measured in the Biorad, taken from 2 replicate tissue culture wells.

A.10. GELATIN ZYMOGRAPHY

METHOD

Chemicals were obtained from Sigma-Aldrich (St. Louis, MO) or BioRad (Hercules, CA)

Gelatin SDS-PAGE making

8% polyacrylamide gels were prepared using the following dilutions:

8% polyacrylamide gel (ml)	5	10	15	40
40% Acrylamide/Bis	1.00	2.00	3.00	8.00
1M Tris pH 8.8	2	4	6	16
10mg/ml MDPF-gelatin	0.5	1	1.5	4
10%APS	0.05	0.1	0.15	0.4
10%SDS	0.05	0.1	0.15	0.4
ddH_2O	1.40	2.80	4.20	11.20
TEMED	5ul	10ul	15ul	40ul

Note: the MDPF gelatin required defrosting for 10-20mins in the heat wells prior to use. TEMED was added immediately prior to gel pouring, as it was responsible for setting the gel.

1. Plates of the minigel apparatus were prepared by rinsing with ethanol and set up using a 7.5mm space plate. Care was taken to align the base of the two plates to prevent leakage. Leakage was checked using water, which was then removed.
2. The gel solution (about 3.5mL/gel) was loaded into the gap between the plates of the minigel apparatus. Space was left for the stacking gel (approx 1cm).
3. H_2O-saturated butanol was loaded to just cover the top of the gel.
4. The gel was left to set at RT for 30-40mins.
5. Meanwhile, the 3% stacking gel was made as follows:

3% stacking gel (ml)	3.75	7.5	10	30
40% Acrylamide/Bis	0.281	0.563	0.75	2.25
1M Tris pH 6.8	0.225	0.45	0.6	1.8
10%APS	0.030	0.06	0.08	0.24
10%SDS	0.0375	0.075	0.1	0.3
ddH_2O	3.17	6.35	8.47	25.41
TEMED	4ul	7.5ul	10ul	30ul

6. After the polyacrylamide gel had set, the butanol was poured off and the top of the gel was rinsed with ddH_2O.
7. The stacking gel was loaded onto the top of the acrylamide gel.
8. The comb (usually 15 wells) was inserted and more stacking gel was added to fill the spaces.
9. The gel was kept at room temperature for 1 hour until set. (Alternately, the gel was kept overnight, covered in foil at this stage).

10. The comb was removed and the gel was rinsed using 1 x Tris-Glycine-SDS buffer.

Sample Preparation

8. Solutions of the sample + 1x Laemmli sample buffer were mixed (e.g. 2µL sample, 18µL Laemmli sample buffer, 4µL loading buffer- used for *in vivo* study)
9. A similar solution of the MMP-2/-9 std was prepared. 2.5x MMP-2/9 std was prepared by diluting 25uL10x MMP2/9 STD, 25µL loading buffer, 75µL PBS (=125uL, enough for 11-12 gels)

Running of Gel

10. Gel tanks were prepared for either 2 or 4 gels.
11. 1 x Tris-Glycine-SDS buffer was added to the gel tank.
12. The gels (still between the 2 plates) were fit into the gel tanks.
13. A small amount of sample buffer was added to the wells (using a long pipette tip) to enable the wells to be visualized.
14. The samples were carefully loaded into the wells in the gels.
15. The gels were run at 135V until the blue dye nearly reached the end of the gel (about 1.5hours).

Development of the Activity

16. The gels were rinsed while shaking for 20-30mins at RT with 50mL of buffer 1, followed by buffer 2 and buffer 3.
17. The gel was incubated at 37°C for several hours or overnight in the No.3 buffer.
18. The gel was photographed under UV illumination on a long wavelength UV light box.

No. 1 buffer	**10 x**	**1 x**	**final con.**
2 M Tris pH 7.5	250ml	25ml	50mM
10%NaN_3	20ml	2ml	0.02%
1 M $ZnCl_2$	10µl	1µl	1µM
100% Triton X-100	250ml	25ml	2.5%
Adjust pH to 7.5			
Add H_2O to	1000ml	1000ml	

No. 2 buffer	**10 x**	**1 x**	**final con.**
2 M Tris pH 7.5	250ml	25ml	50mM
10% NaN_3	20ml	2ml	0.02%
1 M $ZnCl_2$	10ul	1uL	1uM
100% Triton X-100	250ml	25ml	2.5%

1 M $CaCl_2$	100ml	10ml	10mM
Adjust pH to	7.5		
Add H_2O to	1000ml	1000ml	
No. 3 buffer	**10 x**	**1 x**	**final con.**
2 M Tris pH 7.5	250ml	25ml	50mM
10% NaN_3	20ml	2ml	0.02%
1 M $ZnCl_2$	10µL	1µL	1uM
1 M $CaCl_2$	100ml	10ml	10mM
Adjust pH to	7.5		
Add H_2O to	1000ml	1000ml	

Band Quantification

Gelatinase bands were quantified by analyzing *.tif files using the analysis program Phoretix 1d.

1. The background threshold was set.
2. Lanes were defined.
3. Bands of interested were selected.
4. Bands were quantified using the program.
5. The values of the samples were adjusted according to the values found for the MMP2/9 standard well.

A.11. HISTOLOGICAL & IMMUNOHISTOLOGICAL STAINING

Haemotoxylin & Eosin.

1. Slides were fixed in 70% Ethanol for 5mins and taken to water.
2. Slides were immersed in Haemotoxylin for 2mins, rinsed in water.
3. Slides were dipped in acid alcohol 3x, rinsed in water.
4. Slides were blued in Schott's blueing solution for 30secs, rinsed in water.
5. Slides were checked under the microscope to ensure the nuclei have stained blue & the cytoplasm is unstained. If staining was incomplete, steps 2-5 were repeated. Slides were rinsed in water for an additional 30secs.
6. Slides were taken to 70% ethanol for 30secs, then counterstained in eosin for 40secs.
7. Slides were dehydrated quickly using graded ethanol solutions: 95%, 95%, 100%, 100% and cleared with 2 changes of histolene.
8. Slides were mounted with OPX using 22x60mm coverslips.

NB: Bubble formation on the slide was minimized by (1) Immersing the entire slide holder in

the ethanol rinses to prevent water entering the histolene (2) Applying the OPX to the coverslips and allowing the slides to gently pick up the coverslip (3) Utilisation of a tooth pick to press the coverslip after mounting.

Picosirius Red

MATERIALS

Pico-sirius red solution

Sirius Red (F3BACCI.35780)	0.1g
Saturated aqueous picric acid	100mL

0.1% Acidified Distilled Water

Hydrochloric Acid	0.1mL
Distilled Water	100mL

Procedure was performed in fume cabinet.

METHOD

1. Slides were fixed for 5mins in 70% ethanol and rinsed in water.
2. Slides were stained with Picosirius-Red solution for 1hr.
3. Slides were rinsed in acidified water for 2mins.
4. Slides were taken to water and dehydrated via ethanol and histolene, as described in H&E protocol.

NB: water-based mounting medias (such as Aquatex- BDH, England) cannot be used with Picosirius red, as they cause the dye to run.

CD31

MATERIALS

Note: Antibodies were stored in fridge, as they are a protein which can degrade

CD31 (mouse α rat precam-1 monoclonal antibody 1mg/mL stock, Chemicon International MAB1393)

FITC (AlexaFluor 488 chicken α mouse IgG (H+L) 2mg/mL stock, Molecular Probes, A21200)

10x TBST:

60.57g Tris-base & 58.44g NaCl were added to 1L distilled H_2O.

Ph was adjusted to 7.5-7.6 and 5% tween was added.

10% TBST was diluted to 1x TBST by addition of distilled water.

1. The primary antibody, CD31(mouse-anti-rat) was diluted 1:100 in TBST/1%BSA.
2. CD31 was applied to cryosections for 1hr (100µL on each slide).
3. Cryosections were rinsed 3x with TBST (in dipper)
4. The secondary antibody, FITC (chicken-anti-mouse) was diluted to 1:500 in TBST/1%BSA.
5. FITC was applied to cryosections for 45mins.
6. Sections were rinsed 3x in TBST (in dipper)
7. Sections were rinsed with 0.2% DAPI (in PBS)
8. Sections were mounted with antifade (Prolong Gold- Invitrogen P26930, stored at -20°C) in 50% glycine/50% PBS (reagents were at room temperature). Slides were viewed in 1-3 days, when antifade properties were optimal. Slides were stored at room temperature in the dark for 24hrs, then slide corners were sealed with nail polish. Slides were stored at room temperature, 4°C or -20°C.
9. Slides were viewed using fluorescent light, but exposure to light was limited where possible.

Collagen 1, 4 or CD68

Note: this protocol is only relevant for frozen sections

MATERIALS

- TBST (need 700uL-1.5L)
- 4% Paraformaldehyde
- 0.3% Hydrogen Peroxide (Merck, Kilsyth, Victoria) (diluted 1:100 from 30%)
- 10% Normal Goat Serum (NGS)
- Avidin-Biotin Complex (Vectastain ABC kit, Vector Laboratories Inc.)
- Diaminobenzidine (DAB)
- Aquatex (Aqueous Mounting Media- Company: BDH,Poole, England, prod. No. 363123S

The following antibodies were used:

For Collagen 1:

1^0 Antibody- Collagen 1 (1:400, rabbit-anti-rat)

2^0 Antibody: Biotintilated goat-anti-rabbit (IgG) (1:400)

For Collagen 4:

1^0 Antibody- Collagen 4 (1:400, rabbit-anti-rat)

2^0 Antibody: Biotintilated goat-anti-rabbit (IgG) (1:400)

For CD68: (macrophages)

1^0 Antibody- CD68 (1:400, mouse anti-rat McA341)

2^0 Antibody: Biotintilated goat-anti-mouse (IgG) (1:400, BA-9200, Vector Laboratories, Inc, Burlingame, CA)

METHOD

Tissue Fixation

1. Tissue was fixed using 4% paraformaldehyde for 10mins (RT, slide box, lid on- few drops using transfer pipette).

Endogenous Peroxidase Block

2. Slides were rinsed with 1% TBST for a few mins in a coplin jar.
3. The specimen was outlines using a mini pap pen (Zymed Lab Inc.).
4. Specimens were treated with 0.3% hydrogen peroxide for 20mins (coplin jar, lid on) and rinsed with TBST.
5. Excess liquid was tapped off slide onto a tissue, but specimen was not allowed to dry out at any stage.
6. Tissue was blocked with 10% normal goat serum for 30mins (slide box, lid on).
7. Primary antibodies were prepared by dilution in 1% NGS (in TBS).
8. NGS was not rinsed off but was dabbed lightly on tissue.

Primary and Secondary Antibody Incubation

9. Primary antibodies were placed onto slides for 1hr.
10. Secondary antibodies were diluted in 1% NGS (in TBS).
11. Slides were rinsed 3x in TBST, 1-2mins each.
12. Secondary antibodies were placed onto the slides for 20mins.

Amplification and Visualisation

13. Meanwhile, ABC was prepared (1:100) by combining 4µL Avitin, 4µL Biotin, 400µL 1% NGS in eppendorf (RT).
14. Slides were rinsed 3x with TBST and blot on tissue.
15. Slides were treated with 100µL ABC for 30mins, then rinsed with 3x TBST.

16. The following equipment was gathered in the pathology lab: 1mL pipette/tips, eppendorf, slide box, bleach for cleanup, DPX.
17. This step was undertaken in the fume hood, inside a slide box. 1000µL buffer (from DAB kit) was placed in eppendorf and 1 drop DAB was added (approx 20uL).
18. Slides were blotted on tissue and 100µL DAB mixture was placed onto slides for <5mins (1min 20sec is appropriate- individual fibers should still be visible).
19. Slides were placed on metal rack and taken to water.
20. Slides were washed in haemotoxylin 15-20sec then taken to water.
21. Slides were rinsed 1x in acid alcohol.
22. Slides were rinsed in bluing solution (15-20sec) and taken to water.
23. The nuclei were checked to be stained a faint blue colour. (repeat if nec)
24. Slides were mounted using aquatex or dehydrated using ethanol/histolene and mounted with DPX. Slides were dried overnight before viewing on microscope.